THE UNIVERSITY
of EDINBURGH

Neutron Inelastic Scattering Studies of Effective Spin-$\frac{1}{2}$ Magnets

Paul Maximo Sarte, B.Sc. Hons., M.Sc.

Doctor of Philosophy
The University of Edinburgh
January 2019

Lay Summary

Despite the ubiquity of magnetism throughout the history of human civilisation, from its discovery in lodestones during the times of antiquity to its use in almost every technological aspect of our contemporary digital world, a full understanding of magnetism, particularly in the solid state, has remained elusive. The development of new instrumentation and computational techniques, in combination with the continuous discovery of new classes of magnetic materials, has led to not only significant process in our understanding of solid state magnetism, often yielding great technological innovations, but has also inadvertently opened many more questions. One such open question consists of a complete physical description of the cooperative behaviour in the low temperature limit of an interacting macroscopic set of doubly degenerate magnetic spins comprising effective spin-$\frac{1}{2}$ magnets. Driven by their enhanced quantum nature, apparent simplicity and potential role in quantum computing and communication as quantum bits or *qubits*, research of numerous many-body doubly degenerate systems throughout all of physics including effective spin-$\frac{1}{2}$ magnets has experienced a type of renaissance. These effective spin-$\frac{1}{2}$ magnets have and continue to play a pivotal role in the development of a theoretical framework describing not only how magnetic moments interact with one another in the solid state but collective phenomena throughout all the sciences, often yielding a plethora of exotic and often novel types of magnetism. Within this Thesis, the low energy magnetic properties of four different effective spin-$\frac{1}{2}$ magnets constructed from doubly degenerate magnetic cations are investigated with the experimental technique of neutron inelastic spectroscopy.

Abstract

Owing to a combination of both their intrinsic "simplicity" and enhanced quantum nature, effective spin-$\frac{1}{2}$ systems have been subject of intense research for the past three decades. Fuelled by their role in quantum computing and communication as *qubits*, research of many-body doubly degenerate systems has experienced a type of renaissance with one particular noteworthy family being the effective spin-$\frac{1}{2}$ magnets. From the inception of solid state physics, these magnets have and continue to play a pivotal role in the establishment of a theoretical framework describing not only cooperative magnetism but cooperative phenomena in general and have yielded exotic and often novel magnetism. Within this Thesis, the low energy magnetic properties of systems constructed from effective spin-$\frac{1}{2}$ magnetic cations are investigated with neutron inelastic spectroscopy.

The first portion of the Thesis consists of an investigation on the low energy spin fluctuations of $Pr_2Sn_2O_7$. Consisting of rare earth cations placed onto a geometrically frustrated network of corner sharing tetrahedra, these pyrochlores have yielded a multitude of exotic magnetic ground states including spin ice. These spin ices have been of particular interest due to the suggestion that their fundamental excitations behave as monopole-like quasiparticles. Although there is mounting experimental evidence supporting the existence of monopoles in the classical spin ice, the exact nature of the interaction between such monopoles remains unsolved. In an attempt to measure such interactions, our attention has shifted to the quantum spin ice candidate $Pr_2Sn_2O_7$ and its increased monopole density. Neutron inelastic spectroscopic measurements revealed the presence of a hierarchy of unequally-spaced magnetic excitations. These excitations are well-described by a simple model of monopole pairs bound by a linear potential with an effective tension of 0.642(8) K $\cdot$ Å^{-1} at 1.65 K.

The second portion of this Thesis consists of an investigation on the low energy spin fluctuations of the classical Mott insulator CoO. Despite its unique

historic role in the development of the theory underlying both magnetism and neutron scattering, a full understanding of CoO magnetism has remained elusive. A combination of quantum entanglement of the spin-orbit manifolds of the $^4T_1$ ground state multiplet due to a large molecular field and a strong magnetorestrictive monoclinic distortion has led to the extraction of magnetic parameters utilising conventional approaches exceptionally difficult. As an alternative to the conventional pseudo-bosonic method, an approach based on chemical dilution was employed. With sufficient amounts of dilution, both the molecular field and monoclinic distortion are removed from consideration, greatly simplifying the low energy magnetism. The chemical dilution approach used to describe the low energy magnetism of CoO is divided into three chapters.

The first chapter consists of an investigation on the zero field structural and dynamic properties of the mixed valence ternary oxide α-CoV_3O_8. The antiferromagnetic mixed valence ternary oxide α-CoV_3O_8 displays disorder on the Co^{2+} site that is inherent to the *Ibam* space group, thus giving rise to an intrinsically disordered magnet without the need for any external influences such as chemical dopants or porous media. The zero field structural and dynamic properties of α-CoV_3O_8 have been investigated using a combination of neutron and x-ray diffraction, DC susceptibility, and neutron spectroscopy. The low temperature magnetic and structural properties are consistent with a random macroscopic distribution of Co^{2+} over the 16*k* metal sites. However, by applying the sum rules of neutron scattering we observe the collective magnetic excitations are parametrised with an ordered Co^{2+} arrangement and critical scattering consistent with a three dimensional Ising universality class. The low energy spectrum is well-described by Co^{2+} cations coupled *via* a three dimensional network composed of competing ferromagnetic and stronger antiferromagnetic superexchange within the *ab* plane and along *c*, respectively. While the extrapolated Weiss temperature is near zero, the 3D dimensionality results in long range antiferromagnetic order at $T_{\rm N} \sim 19$ K. A crystal field analysis finds two bands of excitations separated in energy at $\hbar\omega \sim 5$ meV and 25 meV, consistent with a $j_{\rm eff} = \frac{1}{2}$ ground state with little mixing between spin-orbit split Kramers doublets. A comparison of α-CoV_3O_8 to the random 3D Ising magnets and other compounds where spin-orbit coupling is present indicates that the presence of an orbital degree of freedom, in combination with strong crystal field effects and well-separated $j_{\rm eff}$ manifolds may play a key role in making the dynamics largely insensitive to disorder.

Consisting of a random distribution of Co^{2+} and V^{4+} on the 16*k* site, α-

CoV_3O_8 may be regarded as being magnetically diluted by 50%. With such dilution, it is located in the $\lambda \gg J$ regime where entanglement is negligible. With the absence of a strong molecular field, the study on α-CoV_3O_8 introduces analysis techniques for addressing Co^{2+} magnetism that will prove important in the two final chapters addressing CoO.

The second chapter consists of an investigation on the magnetic interactions of orbitally degenerate Co^{2+} placed on a non-magnetic host MgO rocksalt lattice where no long range spin or orbital order exists. The paramagnetic nature of the substituted monoxide $Co_{0.03}Mg_{0.97}O$ places the system deep within the $\lambda \gg J$ regime, allowing for the disentanglement of spin-orbit and spin-exchange interactions. By considering the prevalent excitations from Co^{2+} spin pairs, seven exchange constants J out to the fourth coordination shell are extracted. An antiferromagnetic next nearest neighbour 180° exchange interaction is dominant, however dual ferromagnetic and antiferromagnetic interactions are observed for pairings with other pathways. These interactions can be understood in terms of a combination of t_{2g} orbital degeneracy and the Goodenough-Kanamori rules.

The final chapter consists of a reinvestigation of the low energy spin fluctuations of pure CoO. Employing the exchange constants previously extracted from $Co_{0.03}Mg_{0.97}O$, a random phase-type approximation (RPA) in the method of Green's functions was utilised to model $S(\mathbf{Q}, E)$. By approximating CoO as consisting of two [111] cubic magnetic sublattices with all possible orbital orderings present in a molecular field H_{MF}, the multi-level spin wave model successfully accounts for the temporally sharp spin-orbit transitions consistent with orbital ordering observed at $(\mathbf{Q}, E)$ located near the magnetic zone center. However, the model fails to account for higher energy transfers, where well-defined spin waves are replaced by energy and momentum broadened excitations, characterised by steeply dispersive columns of scattering. The concurrent failure of the model and breakdown of spin-orbit excitations observed at higher energy transfers are discussed in terms of coupling to a higher energy process, possibly corresponding to either itinerant or higher energy crystal field excitations.

Declaration of Originality & Co-Authorship

All projects discussed in this Thesis are the result of collaborative efforts.

(i) In Chapter 2, low temperature magnetic diffuse scattering measurements on polycrystalline $Pr_2Sn_2O_7$ were performed by H.D. Zhou.

(ii) In Chapter 3, both x-ray and neutron diffraction were performed by C. Stock, A.M. Arévalo-López and S.C. Capelli on a single crystal of α-CoV_3O_8 grown by C. Stock. Nuclear-magnetic structure determination from x-ray and neutron single crystal diffraction was performed by A.M. Arévalo-López.

(iii) In Chapter 4, the original inelastic neutron scattering measurements were performed by C. Stock and R.A Cowley on polycrystalline samples of CoO, MgO and $Co_{0.03}Mg_{0.97}O$ synthesised by D. Prabhakaran and C. Stock. Energy-dispersive x-ray spectroscopic measurements were performed by E.E. Rodriguez on polycrystalline $Co_{0.03}Mg_{0.97}O$.

(iv) In Chapter 5, the original inelastic neutron scattering measurements were performed by C. Stock, R.A. Cowley and R.A. Ewings on a single crystal of CoO synthesised by D. Prabhakaran.

I declare that this Thesis was composed by myself under the supervision of Professor J.P. Attfield FRS, that the work contained herein is my own except where explicitly stated otherwise, and that this work has not been submitted for any other degree or professional qualification except as specified. All of the research herein has already been published or submitted for publication as detailed in the Publications section.

(*Paul M. Sarte, January 2019*)

Publications

All of the work contained in this Thesis has been published or submitted for publication at the time of submission of this Thesis.

(i) Chapter 2 is published in the *Journal of Physics: Condensed Matter* as P.M. Sarte, A.A. Aczel, G. Ehlers, C. Stock, B.D. Gaulin, C. Mauws, M.B. Stone, S. Calder, S.E. Nagler. J.W. Hollett, H.D. Zhou, J.S. Gardner, J.P. Attfield and C.R. Wiebe, *J. Phys.: Condens. Matter* **29**, 45LT01 (2017) [1].

(ii) Chapter 3 has been published in *Physical Review B* as P.M. Sarte, A.M. Arévalo-López, M. Songvilay, D. Le, T. Guidi, V. Garcìa-Sakai, S. Mukhopadhyay, S.C. Capelli, W.D. Ratcliff, K.H. Hong, G.M. McNally, E. Pachoud, J.P. Attfield and C. Stock, *Phys Rev. B* **98** 224410 (2018) [2].

(iii) Chapter 4 is published in *Physical Review B* as P.M. Sarte, R.A. Cowley, E.E. Rodriguez, E. Pachoud, D. Le, V. Garcìa-Sakai, J.W. Taylor, C.D. Frost, D. Prabhakaran, C. MacEwen, A. Kitada, A.J. Browne, M. Songvilay, Z. Yamani, W.J.L. Buyers, J.P. Attfield and C. Stock, *Phys. Rev. B* **98**, 024415 (2018) [3].

(iv) Chapter 5 has been submitted to *Physical Review Journals* as P.M. Sarte, R.A. Cowley, K.H. Hong, M. Songvilay, R.A. Ewings, A.J. Browne, D. Prabhakaran, Z. Yamani, W.J.L. Buyers, J.P. Attfield and C. Stock.

All published manuscripts have been included in the Reprint of Publications section.

Acknowledgements

First and foremost I would like to convey my sincere gratitude to my amazing team of supervisors. To my primary supervisor Professor Paul Attfield FRS, your deep chemical intuition and seemingly endless source of analogies and literature references have been so instrumental to the success of so many of my projects. Your unwaivering patience and confidence in my abilities has truly been a wonderful experience these past three years and for all your support, I cannot thank you enough. To my second unofficial supervisor, Dr. Chris Stock, your seemingly endless knowledge of everything inelastic is truly inspiring. Words cannot express how grateful I am for all your time, patience and dedication to the Co^{2+} projects. I truly believe we would have made Roger proud! Finally, to my far distant unofficial supervisor Professor Chris Wiebe, I would like to convey my deepest sense of gratitude for all your have done for me. Your support, be it financial, scientific or moral, has proven invaluable throughout these past eight years. Your dedication to scientific research, teaching and ultimately your students has been and will continue to be a personal source of inspiration.

In addition to my university-based supervisors, I would like to convey my gratitude to the instrument scientists at central facilities that have provided me with such invaluable assistance with data collection and their subsequent analysis, making so many of the successes in this Thesis possible. I would like to thank Drs. Adam Aczel, Manh Duc Le, Yixi Su, Matt Stone, Daniel Pajerowski, Andrew Wildes, Lucile Mangin-Thro, Stuart Calder, Georg Ehlers, Gabriele Sala, Vicky Garcìa-Sakai, Tatiana Guidi, Sanghamitra Mukhopadhyay and Mike Cox. I would like to specifically acknowledge Dr. Jason Gardner, Dr. Josh Hollett and Prof. Stephen Nagler for their assistance with the interpretation of the low energy excitations at the heart of Chapter 2. I would also like to specifically acknowledge Dr. Angel Arévalo-López for his assistance with the refinements that form the first portion of Chapter 3. Finally, I would also like to acknowledge my examiners Profs. Euan Brechin and Jon Goff for taking so much of their time and effort in the assessment of this Thesis. A combination of their meticulous analysis and fruitful discussions of the present work has led to not only the removal of inevitable typos, but ultimately has allowed me to produce a much stronger Thesis.

This Thesis is a culmination of more than 12 amazing years of post-secondary education, made possible with the support of many excellent teachers. It is my privilege to acknowledge these great educators: Drs. Pettitt, Frey, Danchura, Bieringer, J. Martin, M. Martin, Vincent, Ata, Goltz, Linek, Stokke, Mitchler

and Mrs. Decelles and Labun. These wonderful teachers have not only influenced me in my own journey but still continue to this day to inspire future generations in their pursuit of higher education.

As is unavoidably cliché, the names of the people that have helped me throughout these past three years in Edinburgh and afar would fill an entire thesis in itself. To the Attfield group past and present: Alex, Jacky, Ed, Graham, Giuditta, Kunlang, Hannah, Padraig, Patricia, Angel, Elena, Paula, James and Elise, I would like to convey my many thanks for your assistance, friendship and support during these past years. To Alex, I would like to thank you for your unrelenting support during the tough times and great experiences we shared during the good. To Jacky, my flatmate and dear friend, I cannot thank you enough for all you have done for me. From the pursuit of common hobbies to some R&R to crystallography, you were always available to provide a helping hand when needed. To Ed, Graham and Giuditta, all of you were there for me during both my deepest struggles and greatest successes. You were all willing to say what I needed to hear in order to accomplish what I thought was once impossible. For your kind and sometimes harsh words, I cannot thank you enough.

I would also like to convey my sincere thanks to the members of the Stock group past and present: Jana, Manila, Harry, Adam, Ryan, Irene, Nathan and Katherine, for welcoming me with open arms. In particular, I would like to thank Jana, you have been my confidante and great friend these past few years. For all the laughs, smiles and giggles, I convey my many thanks.

On a more personal note, I would to acknowledge the many individuals that have enriched my life outside of the laboratory, thus making me a better scientist within. First and foremost, I must thank Stuart. Your unwavering support for me during my most trying times is greatly appreciated. To Alex, Ross and Craig, the lads of HBS, your welcoming attitude and warm smiles are always a great inspiration, especially at 6.00 in the morning. To Ryan, Sally and Raymond, thank you for the constant and uplifting support, especially during my first few months here in Edinburgh. To Katie, Adam and Mike, your constant support and gentle 'pushes' during the finishing stretch of the writing process is greatly appreciated. To the present and past members of the Gaussian Eliminators: Andy, Robbie, Stefan, Sophie and Abilash, thank you for the wonderful times during both the wins and the losses on and off the court. To my friends back home and around the world: Laura, Sam A., Lenny, Lynn, Mara, Jens, Baucis, Hayleigh, Eszter, Gyuri, Mike G., Yue, Joe, David, Aleks, Sam P., Janet, Eric, Kelsey, Cole, Harlyn, Kanisha, Brenden, Arzoo, Joey, Meaghan, Alexis, Nicole, Shelagh, Trevor, Megan, Mimi and Cameron. Despite being located all across the world, your constant words of support are a constant and much appreciated source of encouragement. Finally, I would like to thank my mom Annabelle back home in Winnipeg. None of this would have been possible without your constant warm and very vocal support from six timezones away.

Last but not least, to my dearest Ellie, these final few words are for you.

Je t'aime.

This Thesis is dedicated to the memory of Professor Roger A. Cowley FRS (1939-2015), to whom we all owe a debt of gratitude for his unrelenting pursuit of a much deeper understanding of the fundamental processes underlying our universe.

Table of Contents

List of Figures

List of Tables

Chapter 1

Introduction

1.1 Introductory Remarks

1.1.1 Preamble

Metal oxides occupy a vast and unique realm in materials science [4]. Possessing both rich compositional and structural diversity, these oxides exhibit a plethora of optical, electronic and magnetic properties [5]. Although historically hindered by a lack of understanding of the physical principles underlying magnetism, particularly in the solid state, research into the magnetic properties of these oxides has experienced a type of renaissance, revealing exotic and often novel magnetic ground states, many of which are of both theoretical and practical interest [6].

This Thesis investigates the magnetic properties of four magnetic metal oxide insulators. The general approach employed in each investigation stems from the observation that the magnetic properties of these oxides, although seemingly innumerable and extremely diverse, are all fundamentally governed by a combination of the electron configuration and the lattice geometry [7]. Despite such a deceptively simple approach, in many cases it is often challenging to explain such properties from a first principles atomistic point of view [8]. Instead, if the system in question possesses multiple energy scales that differ significantly from one another in magnitude, it is sometimes advantageous to reformulate the approach based on the particular energy scale of interest, thus significantly reducing the Hilbert space H under consideration [9]. One well-known example

for such a reformulation is the derivation of the effective spin-only model from the Hubbard model in the limit of small $\frac{t}{U}$ [10, 11], where t and U are the hopping and Coulomb repulsion constants, respectively.

Another application for such a reformulation approach that is currently of particular interest corresponds to magnetic systems whose free-ion ground state degeneracy has been removed through a combination of the crystalline electric field and spin-orbit coupling [12–15]. A consequence of this particular combination is that the energy scale associated with the spin-spin interactions is much smaller than the energy gap Δ between the ground state and excited manifolds; thus, only the ground state manifold with its much reduced Hilbert space needs to be considered when addressing magnetic properties in the limit of low temperatures. Such is the case for many magnets constructed from $4f^2$ Pr^{3+} and $3d^7$ Co^{2+}, the two magnetic cations that are investigated in this Thesis. For the case of Pr^{3+} in the pyrochlore structure, the highly distorted cubic coordination often results in a non-Kramers doublet with $\Delta \sim 20$ meV, whilst $J \sim 1$ K [16, 17]. For the case of Co^{2+} in octahedral coordination, a weak-intermediate crystalline electric field in combination with spin-orbit coupling often results in a doublet spin-orbit manifold with $\Delta \sim 30$ meV [18]. Constituting the main unifying theme in this Thesis, the physical realisation of ground state doublet manifolds for both Pr^{3+}-based pyrochlores and magnets based on Co^{2+} in octahedral coordination has naturally led to many employing an effective spin $j_{\text{eff}} = \frac{1}{2}$ model to describe the low temperature magnetic properties for these systems [19–22].

Owing to a combination of both their intrinsic "simplicity" and enhanced quantum nature, $j_{\text{eff}} = \frac{1}{2}$ magnets have been subject of intense research for the past three decades [23]. Although once largely, and still significantly driven by the exotic magnetism that results when their enhanced quantum nature is combined with lower dimensionality [24–26], a recent explosion of interest in these low spin magnets has been fuelled by the central role $j_{\text{eff}} = \frac{1}{2}$ magnetic cations play in Kitaev physics [27–29]. Providing the community with exactly solvable models, $j_{\text{eff}} = \frac{1}{2}$-based Kitaev physics not only represents a potential experimental path for the physical realisation of the elusive quantum spin liquid state but also possesses significant promise for widespread applications in both quantum computing and communications [30, 31].

Motivated by the rich physics exhibited by these $j_{\text{eff}} = \frac{1}{2}$ magnets, the low energy magnetic properties of four magnetic metal oxides constructed from two cations, Pr^{3+} and Co^{2+}, that are commonly treated as $j_{\text{eff}} = \frac{1}{2}$, have been

investigated with neutron inelastic spectroscopy. It will be shown that such an approximation must be approached with caution, being valid only under certain circumstances. Such considerations are of particular interest in the case of Co^{2+}, the second cation investigated in this Thesis, due to recent suggestions that magnets constructed from high spin d^7 cations may host Kitaev physics [32, 33]. Potentially possessing a much richer phase diagram than their more traditionally used d^5 counterparts, the delicate and often subtle balance between spin, orbital and electronic degrees of freedom of the Co^{2+} cation investigated in this Thesis may have both significant and interesting theoretical and practical consequences.

1.1.2 Organisation of the Thesis

This Thesis is organised into six chapters. Chapter 1 is an introductory chapter summarising fundamental concepts from solid state magnetism and neutron inelastic scattering, the primary experimental technique employed in this Thesis. Chapters 2-5 detail the experimental results and are organised into two sections, corresponding to systems whose magnetism are based on Pr^{3+} and Co^{2+}, respectively. Chapter 6 provides a concise summary of the conclusions deduced from the experimental results, whilst providing potential avenues for future research. In addition to the six aforementioned chapters, Appendices A-K have been included to provide both supplementary information (*e.g.* tabulated parameters, crystallographic details) and derivations of key mathematical relations (*e.g.* sum rules of neutron scattering, projection theorem) that are employed in the analysis of experimental data.

1.2 Magnetic Oxides

1.2.1 Introduction & Motivation

From the Stone Age to the Age of Silicon, it can be argued that advancements in our understanding of materials have been a major driving force underlying many seismic shifts in human civilisation [34]. With the use of pigments in the earliest illustrations to the use of silicon dioxide in modern electronics, metal oxides, both transition metal and rare earth oxides, exemplify the crucial role materials have played in human history [4]. Possessing a rich collection of optical,

electronic and magnetic properties, many of which are naturally amenable for a seemingly endless variety of applications, metal oxides have and continue to play a central role in everyday life [35].

One particular class of metal oxides whose potential has only really begun to be physically realised is the magnetic metal oxides [5, 6]. Despite their unique properties being known since the rudimentary studies of lodestone by the Ancient Greeks and Chinese almost two millennia ago, scientific interest in these magnetic metal oxides was intermittent and thus their use was rather limited. It was not until 1600 with Gilbert's *De Magnete* [36] that any attempts were made to investigate the physical principles underlying these magnets, despite already being employed as crude compasses for almost 500 years in Europe and for more than a millennium in China. Beginning with Gowin Knight's discovery of a process for strongly magnetising steel, followed by the development of electromagnetic theory by Ørsted, Ampère, Faraday and Maxwell, and the development of quantum theory and relativity in the early twentieth Century by Einstein, Schrödinger, Planck, Bohr, Heisenberg, Dirac and many more, it would take the scientific community another 400 years for the foundations of magnetism to be firmly established [37, 38].

Despite significant advances in the theory of solid state magnetism occurring decades before with the work of Néel, van Vleck, Curie and many others, it was not until the 1950's and 1960's with the systematic investigations of ferrites that large scale scientific interest was directed towards the magnetic metal oxides [6, 39, 40]. Such investigations led to the discovery of the first ferromagnetic oxide family, the mixed-valence manganites and with them, the discovery of colossal magnetoresistance [41, 42]. After consistent research in the 1970's, a new golden age of magnetic oxides research began with the discovery of high temperature superconductivity in the cuprates [43]. This golden age continues to this day, fuelled by both academia and industry, the study of magnetic metal oxides has resulted in their widespread application spanning all aspects of modern life ranging from information technology to transportation to drug and gene delivery [6, 34, 35, 40]. Beyond the aforementioned applications, magnetic metal oxides have served a unique pedagogical role for the scientific community [44]. In addition to serving as the prototypical system for the study of magnetism in the solid state, the large compositional and structural variation spanned by these oxides [4, 5, 40, 45, 46] has meant that magnetic metal oxides have and will continue to serve as tools to develop and test many scientific concepts, ideas and theories that would otherwise be very difficult or impossible to study

experimentally.

In this section, the reader will be introduced to the fundamental principles underlying magnetism in the solid state, many of which were developed and refined by investigations on magnetic metal oxides. Such a discussion begins with a description of magnetism at the level of the single-ion, consisting of the coupling between spin and orbital degrees of freedom of a multi-electron ion in the presence of Coulombic repulsion from a crystalline electric field. In the solid state, these magnetic ions are not isolated from one another and thus may interact. Thus, this discussion will shift to a description of the mechanisms by which these magnetic ions can interact with each other. This section will then conclude with a description of what may result from such collective behaviour, often yielding emergent, novel and exotic properties.

1.2.2 Magnetism in the Solid State

Single-ion Magnetism

As alluded to in the introductory remarks, the origin of magnetism* in magnetic metal oxide insulators stems from the unpaired electrons of the constituent metal cations. Consequently, a full understanding of the magnetism in both solids and in any general magnetic system of interest, must address all factors that affect the electronic structure of the constituent cations. Some of these factors are addressed quite early in one's chemistry education such as the Pauli Exclusion Principle, the *Aufbauprinzip*, and Hund's rules, whilst others such as the concepts of good quantum numbers and a complete set of commuting observables are often introduced much later and limited to highly specialised courses and pupils. It is the goal of this discussion to introduce the reader to *all* such factors. The discussion is based on Abragam & Bleaney [47], Kittel [37], Cohen-Tannoudji [48], Pauling & Wilson [49], Morrison [50], Judd [51], Stevens [52] and references contained therein. Any additional references will be stated explicitly in the text. This subsection will begin with the isolated hydrogen atom. Corresponding to the most basic problem in atomic physics, the hydrogen atom introduces crucial but often subtle factors that have profound effects on an atom's electronic structure. These concepts will then be generalised to multi-

*This is the particular magnetism of interest in this Thesis. Such magnetism is by far not the only magnetism that exists in solids, as there are other types of magnetism such as Langevin diamagnetism from the paired core electrons.

electron atoms in the presence of a crystalline electric field, corresponding to the physical reality in metal oxides. A particular emphasis will be placed on distinguishing the different regimes that are occupied by the two cations of interest, Pr^{3+} and Co^{2+} (*e.g.* '*j*-*j*' coupling and Russell-Saunders (LS) coupling).

Consisting of one electron of mass m_e with electric charge $-e$ revolving around a single proton of mass m_p with charge $+e$, the isolated hydrogen atom is the most basic problem in atomic physics. The eigenvalue problem is summarised by the time-independent Schrödinger equation given by

$$\hat{\mathcal{H}}_{\mathrm{o}}\psi = E\psi, \tag{1.1}$$

when projected onto a position representation yields the partial differential equation (PDE)

$$\left\{-\frac{\hbar^2}{2\mu}\nabla^2 - \frac{Ze^2}{r}\right\}\psi(\mathbf{r}) = E\psi(\mathbf{r}), \tag{1.2}$$

where $\mathbf{r}$ denotes the electron's position vector[†] of magnitude r with respect to the proton, μ is the reduced mass given by $\frac{m_e m_p}{m_e+m_p}$, and Z is the atomic number, equal to one in the current case of hydrogen. The first term of the Hamiltonian $\hat{\mathcal{H}}_{\mathrm{o}}$, given by the $\{\dots\}$ expression in Eq. 1.2, corresponds to the kinetic energy, whilst the second term corresponds to the potential electrostatic energy. The form of the potential in Eq. 1.2 reflects only the electron-nucleus electrostatic interaction. As will be discussed later, other contributions to the electrostatic potential, in particular interactions between the atom's electrons themselves and the interaction of the atom's electrons with the surrounding ligands will be of particular interest and have significant consequences on an atom's electronic structure.

The conventional approach for solving the PDE given by Eq. 1.2 is well-documented and consists of taking advantage of the fact that the equation is separable in radial (r) and angular components (θ,ϕ). The solutions $\psi_{n,l,m}$ are of the form $R_{n,l}(r)Y_{l,m}(\theta,\phi)$ with each eigenstate of $\hat{\mathcal{H}}_{\mathrm{o}}$ being uniquely defined by the quantum numbers n, l, m and is thus conventionally denoted by $|nlm\rangle$

[†]As will be the convention in this Thesis, vector quantities and their magnitudes are denoted by **bold**-faced and *italicised* characters, respectively, whilst operators are denoted by characters with the circumflex accent (hat). The only exception to this convention is the unit vector that is also denoted by the circumflex accent. In the cases that both uses of the circumflex accents are present in an equation, further clarification will be provided in the text.

using Dirac's bra-ket notation. The principal quantum number n defines the eigenvalues of $\hat{\mathcal{H}}_{\mathrm{o}}$ given by $E_n = \frac{-13.6\ \mathrm{eV}}{n^2}$, whilst the azimuthal (orbital angular momentum) quantum number l and the magnetic quantum number m denote the eigenvalues of the $\hat{L}^2$ and $\hat{L}_z$ operators, respectively, where

$$\hat{L}^2|n,l,m\rangle = l(l+1)\hbar^2|n,l,m\rangle, \tag{1.3}$$

and

$$\hat{L}_z|n,l,m\rangle = m\hbar|n,l,m\rangle. \tag{1.4}$$

Before proceeding, a subtle but crucial observation must be addressed. As aforementioned, each eigenstate of $\hat{\mathcal{H}}_{\mathrm{o}}$ in Eq. 1.2 is completely and uniquely defined by a set of three quantum numbers. These quantum numbers are so-called "good quantum numbers" and the set of their corresponding observables[‡] constitute a complete set of commuting observables (CSCO). A CSCO is defined as a set of operators $\hat{A}$, $\hat{B}$, $\hat{C}$, ... that (i) commute in pairs and (ii) whose set of eigenvalues uniquely specifies each eigenstate of the system. In the case of Eq. 1.2, the operators $\hat{\mathcal{H}}_{\mathrm{o}}$, $\hat{L}^2$ and $\hat{L}_z$ constitute a CSCO since all operators pairwise commute, whilst as stated above, the set of their eigenvalues uniquely specifies an eigenstate of $\hat{\mathcal{H}}_{\mathrm{o}}$.

Based on Eq. 1.2, it is tempting to conclude that the operators $\hat{\mathcal{H}}_{\mathrm{o}}$, $\hat{L}^2$ and $\hat{L}_z$ constitute a CSCO for an isolated hydrogen atom. In fact, this is not the case. In 1922, the Stern-Gerlach experiment revealed that the electron possesses another degree of freedom. Although commonly and erroneously likened to a spinning top where the electron is spinning about its axis, this additional degree of freedom termed spin is now known to be a relativistic effect that is predicted by the Dirac equation. With the introduction of spin, it is clear that two additional operators $\hat{S}^2$ and $\hat{S}_z$, with eigenvalues S and m_s, respectively, must be added to the original set of operators $\hat{\mathcal{H}}_{\mathrm{o}}$, $\hat{L}^2$ and $\hat{L}_z$ to form a CSCO, where

$$\hat{S}^2|s,m_s\rangle = s(s+1)\hbar^2|s,m_s\rangle, \tag{1.5}$$

[‡]Recall that a fundamental postulate of quantum mechanics is that for every measurement, there exists an associated operator called an observable. The eigenvalues of the observable correspond to the possible outcomes of the measurement.

and

$$\hat{S}_z|s, m_s\rangle = m_s\hbar|s, m_s\rangle. \tag{1.6}$$

In the case of an electron, its spin s is $\frac{1}{2}$, whilst m_s may assume the values of $\pm\frac{1}{2}$ and thus, the eigenstates of the isolated hydrogen is given by $|n\ l\ m\ m_s\rangle$, where the eigenvalue s is not conventionally included as it is understood to be $\frac{1}{2}$.

Once again, although one may be tempted to conclude that the set of operators $\hat{\mathcal{H}}_{\rm o}$, $\hat{L}^2$, $\hat{L}_z$, $\hat{S}^2$ and $\hat{S}_z$ form a CSCO, this is still not the case for the isolated hydrogen atom. The failure to form a CSCO is based on an additional complication that results from the introduction of electron spin, namely the interaction of the spin and orbital degrees of freedom, termed spin-orbit coupling. Corresponding to a relativistic interaction between a particle's spin with its motion inside a potential, such an interaction can be motivated from purely classical arguments in the case of the hydrogen atom.

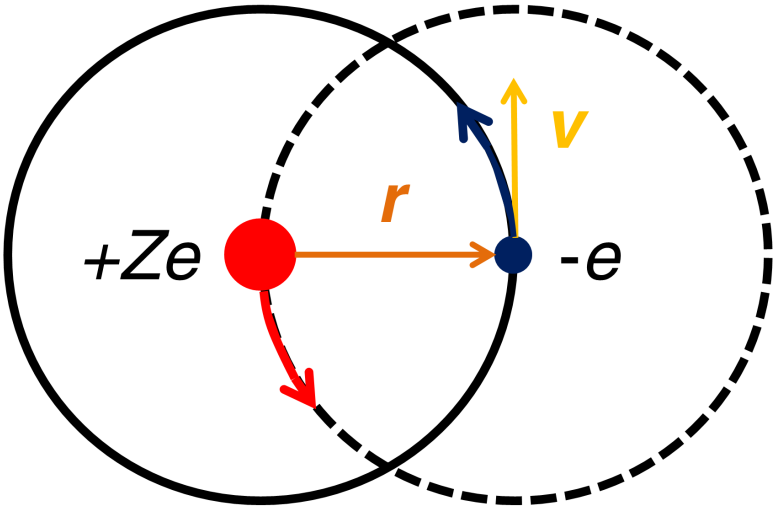

Figure 1.1 Pictorial representation of the Bohr-like orbits of the electron (solid line) of charge $-e$ and nucleus (dashed line) of charge $+Ze$ in the nucleus' and electron's frame of reference, respectively. The vectors **r** and **v** denote the position vector of the electron relative to the proton and the tangential velocity of the electron, respectively.

Although the Bohr model is ultimately incorrect[§], it allows one to "derive" an approximate form of the spin-orbit interaction. As illustrated in Fig. 1.1, the "derivation" begins by considering a frame of reference that is fixed to the electron. In this reference frame, the nucleus of charge Ze now revolves around a stationary electron. The resulting current density $\mathbf{j}$ is equal to $-Ze\mathbf{v}$, where $\mathbf{v}$ is the tangential velocity of the electron in the conventional (*i.e.* nucleus') rest frame. According to classical electromagnetic theory, a current produces a magnetic field $\mathbf{B}$. The value of $\mathbf{B}$ at a particular position $\mathbf{r}$ is given by Ampère's law as

$$\mathbf{B} = \frac{\mu_o}{4\pi}\frac{\mathbf{j}\times\mathbf{r}}{r^3}, \tag{1.7}$$

where μ_o is the permeability of free space and the position vector $\mathbf{r}$ is from the nucleus (*i.e.* the source of current density) to the electron. Since $\mathbf{j} = -Ze\mathbf{v}$, Eq. 1.7 becomes

$$\mathbf{B} = -\frac{Ze\mu_o}{4\pi}\frac{\mathbf{v}\times\mathbf{r}}{r^3}. \tag{1.8}$$

Employing the definition of angular momentum

$$\mathbf{l} = \mathbf{r}\times m\mathbf{v} = -m\mathbf{v}\times\mathbf{r}, \tag{1.9}$$

Eq. 1.8 becomes

$$\mathbf{B} = \frac{Ze\mu_o}{4\pi m_e r^3}\mathbf{l}, \tag{1.10}$$

where the mass has been relabelled explicitly as that of the electron. As a result of its intrinsic angular momentum, *i.e.* spin, the electron possesses a magnetic moment

$$\mu_e = -g_s\frac{\mathbf{s}}{\hbar}\mu_{\mathrm{B}}, \tag{1.11}$$

where $g_s \approx 2$ is the electron g-factor and $\mu_{\mathrm{B}} = \frac{\mathrm{e}\hbar}{2\mathrm{m_e}}$ is the Bohr magneton.

[§]The implication that electrons revolve the nucleus in fixed orbits violates the Heisenberg uncertainty principle.

This magnetic moment interacts with the magnetic field $\mathbf{B}$ (Eq. 1.10) with an associated orientation potential energy given by

$$V = -\mu_e \cdot \mathbf{B}. \tag{1.12}$$

By combining Eqs. 1.10 and 1.11 with the correspondence principle, Eq. 1.12 becomes

$$\hat{V}_{SO} \propto \frac{g_s \mu_{\mathrm{B}} Z e \mu_o}{4\hbar\pi m_e r^3} \hat{\mathbf{S}} \cdot \hat{\mathbf{L}}, \tag{1.13}$$

where the subscript SO denotes spin-orbit and the equality in Eq. 1.12 has been replaced by a proportionality, reflecting the need for a relativistic correction factor of $\frac{1}{2}$, commonly known as the Thomas precession factor or the "Thomas half". Eq. 1.13 is commonly written as $\lambda \hat{\mathbf{L}} \cdot \hat{\mathbf{S}}$, where λ is the spin-orbit coupling constant.

Although deceptively simple, the inclusion of $\hat{\mathbf{L}} \cdot \hat{\mathbf{S}}$ in the potential $\hat{V}_{SO}$ presents a significant problem when attempting to establish a CSCO. The fundamental problem stems from the observation that the inclusion of spin-orbit coupling results in a new Hamiltonian $\hat{\mathcal{H}}$ given by

$$\hat{\mathcal{H}} = \hat{\mathcal{H}}_{\mathrm{o}} + \hat{V}_{SO}, \tag{1.14}$$

that does not commute with $\hat{L}_z$ and $\hat{S}_z$, whilst $\hat{\mathcal{H}}_o$ does not commute with $\hat{\mathcal{H}}$. Thus, the set of operators $\hat{\mathcal{H}}_{\mathrm{o}}$, $\hat{L}^2$, $\hat{L}_z$, $\hat{S}^2$ and $\hat{S}_z$ do not form a CSCO. Such a failure requires certain approximations to be made if a CSCO is to be defined.

One such approximation stems from the observation that the first order energy shift due to the introduction of a perturbation $\hat{V}'$ for a quantum system originally in the unperturbed state $|n^0\rangle$ is given by first order perturbation theory as

$$E_n^1 = \langle n^0 | \hat{V}' | n^0 \rangle. \tag{1.15}$$

In the case of spin-orbit coupling where $\hat{V}' = \hat{V}_{SO}$, Eq. 1.13 implies that

$$E_n^1 \propto Z \left\langle \frac{1}{r^3} \right\rangle. \tag{1.16}$$

Employing the key result[¶]

$$\left\langle \frac{1}{r^k} \right\rangle \propto Z^k, \tag{1.17}$$

suggests that the first order energy shift due to spin-orbit coupling is

$$E_n^1 \propto Z^4, \tag{1.18}$$

in other words, the spin-orbit coupling constant $\lambda \propto Z^4$.

In the case of the hydrogen atom ($Z = 1$), the inclusion of $\hat{V}_{SO}$ results in an energy difference of $\sim 10^{-4}$ eV. Since such an energy difference is significantly smaller than the energy eigenvalues $E_n = \frac{-13.6 \text{ eV}}{n^2}$ of $\hat{\mathcal{H}}_{\text{o}}$, spin-orbit coupling may be treated as a small perturbation and thus the original set of $\hat{\mathcal{H}}_{\text{o}}$, $\hat{L}^2$, $\hat{L}_z$, $\hat{S}^2$ and $\hat{S}_z$ could be considered to form a CSCO with good quantum numbers n (*vis à vis* E_n), l, m, s and m_s. The underlying logic summarised by Eq. 1.18 suggests that such an approximation would be expected to hold in the case of other low Z systems. This particular approximation is commonly referred to as the Russell-Saunders or LS coupling scheme.

Conversely, the same logic summarised by Eq. 1.18 suggests that for large Z systems such an approximation would no longer be valid and thus another must be made in its place. This new approximation is called 'j-j' coupling and as the name suggests, it involves the introduction of the $\hat{J}^2$ and $\hat{J}_z$ operators, such that

$$\hat{J}^2|j, m_j\rangle = j(j+1)\hbar^2|j, m_j\rangle, \tag{1.19}$$

and

$$\hat{J}_z|j, m_j\rangle = m_j\hbar|j, m_j\rangle. \tag{1.20}$$

In the case of large Z systems, such as those contained in the f-block, Eq. 1.18 suggests that the energy scale of spin-orbit coupling will be very large. In the case that $\hat{V}_{SO} \gg \hat{\mathcal{H}}_{\text{o}}$, in particular the electrostatic contribution, then the eigenvalue

[¶]This result can be derived using the Feynman-Hellmann theorem.

problem summarised by Eq. 1.1 may be replaced by

$$\hat{\mathcal{H}}_{SO}|\psi\rangle = E|\psi\rangle, \tag{1.21}$$

where $\hat{\mathcal{H}}_{SO} = \lambda\hat{\mathbf{L}}\cdot\hat{\mathbf{S}}$ and other terms such as the electrostatic contributions in $\hat{\mathcal{H}}_{\mathrm{o}}$ are treated as small perturbations. The eigenvalue problem that is Eq. 1.21 can readily be solved by first noting that the $\hat{\mathbf{J}}$ operator is defined as

$$\hat{\mathbf{J}} = \hat{\mathbf{L}} + \hat{\mathbf{S}}, \tag{1.22}$$

which implies

$$\hat{J}^2 = \hat{L}^2 + \hat{S}^2 + 2\hat{\mathbf{L}}\cdot\hat{\mathbf{S}}. \tag{1.23}$$

or

$$\hat{\mathbf{L}}\cdot\hat{\mathbf{S}} = \frac{1}{2}\left\{\hat{J}^2 - \hat{L}^2 - \hat{S}^2\right\} \tag{1.24}$$

Inserting Eq. 1.24 into Eq. 1.21 and employing definitions 1.19, 1.3 and 1.5, one obtains the following eigenvalues

$$E_{SO} = \frac{\lambda}{2}\left\{j(j+1) - l(l+1) - s(s+1)\right\}, \tag{1.25}$$

where the eigenvalues have been renormalised, *i.e.* the factors of $\hbar$ have been excluded, as will be the convention for the rest of this Thesis. Since the set of operators $\hat{J}^2$, $\hat{L}^2$, $\hat{S}^2$ and $\hat{J}_z$ pairwise commute, completely and uniquely specify the eigenstates of $\hat{\mathcal{H}}_{SO}$, they must form a CSCO with corresponding good quantum numbers j, l, s and m_j, respectively.

Having successfully solved the spin-orbit eigenvalue problem, one of the main potentials in magnetic metal oxides, the crystalline electric field will now be introduced. Commonly denoted as CEF, the crystalline electric field describes the electrostatic interaction between the metal centre's electrons and its surrounding charged ligands. The CEF Hamiltonian for a single electron of charge $-e$ located

at position $\mathbf{r}$ is given by

$$\hat{\mathcal{H}}_{CEF} = -e\hat{V}(\mathbf{r}), \tag{1.26}$$

or in the case of a multi-electron atom,

$$\hat{\mathcal{H}}_{CEF} = -e\sum_i \hat{V}(\mathbf{r}_i), \tag{1.27}$$

where the i^{th} electron has position vector $\mathbf{r}_i$. The potential $\hat{V}(\mathbf{r})$ corresponds to the Coulomb potential at a position $\mathbf{r}$ due to the presence of ligands of charge q_j at position $\mathbf{R}_j$. According to classical electromagnetism, the classical form for such a potential would be given by

$$V(\mathbf{r}) = \sum_j \frac{q_j}{|\mathbf{R}_j - \mathbf{r}|}, \tag{1.28}$$

where $|\ldots|$ denotes the modulus. If one considers a position $\mathbf{r} \ll \mathbf{R}_j \ \forall \ j$, then one can expand the potential in terms of Legendre polynomials such that

$$V(\mathbf{r}) = \sum_j \frac{q_j}{R_j} \sum_{n=0}^{\infty} \left(\frac{r}{R_j}\right)^n P_n(\cos(\theta)), \tag{1.29}$$

where $P_n(\cos(\theta))$ are the Legendre polynomials and the angle θ is defined such that $|\mathbf{r} - \mathbf{R}_j| = r^2 + R_j^2 - 2rR_j\cos(\theta)$. Utilising the simple mathematical relationship between the Legendre polynomials and the tesseral harmonics $Z(\theta, \phi)$ given by

$$P_n(\cos(\theta)) = \frac{4\pi}{2n+1} \sum_\alpha Z_{n\alpha}(\theta, \phi) Z_{n\alpha}(\theta_j, \phi_j), \tag{1.30}$$

then Eq. 1.29 can be rewritten as

$$V(\mathbf{r}) = V(r, \theta, \phi) = \sum_j q_j \sum_{n=0}^{\infty} \frac{r^n}{R_j^{n+1}} \sum_\alpha \left\{ \frac{4\pi}{2n+1} Z_{n\alpha}(\theta, \phi) Z_{n\alpha}(\theta_j, \phi_j) \right\}, \tag{1.31}$$

which is often condensed to

$$V(\mathbf{r}) = V(r, \theta, \phi) = \sum_{n=0}^{\infty} \sum_{\alpha} A_{n\alpha} r^n Z_{n\alpha}(\theta, \phi), \tag{1.32}$$

where

$$A_{n\alpha} = \sum_{j} \frac{4\pi}{2n+1} q_j \frac{Z_{n\alpha}(\theta_j, \phi_j)}{R_j^{n+1}}. \tag{1.33}$$

By rewriting Eq. 1.29 in terms of the tesseral harmonics, the potential can now be written as a function of (x, y, z) explicitly. To explain the importance of such an observation, one must first recall that if the energy scale defined by the CEF Hamiltonian (Eq. 1.26 or 1.27) is much smaller compared to that defined by spin-orbit coupling then $\hat{\mathcal{H}}_{CEF}$ may be considered as a perturbative potential to the eigenstates $|l, s, j, m_j\rangle$ of $\hat{\mathcal{H}}_{SO}$ or simply $|j, m_j\rangle$ for a fixed multiplet with a given l and s. Since the position operator transforms in an identical manner as the angular momentum operator, then one may employ the Wigner-Eckhart theorem[‖] which yields

$$\hat{\mathbf{R}} \propto \hat{\mathbf{J}}. \tag{1.34}$$

By employing both the correspondence principle and the Wigner-Eckhart theorem to Eq. 1.32, the CEF potential and thus the CEF Hamiltonian can be rewritten in terms of the operators $\hat{J}^2$, $\hat{J}_z$ and the corresponding raising and lowering operators defined as

$$\hat{J}_{\pm}|j, m_j\rangle = \sqrt{j(j+1) - m_j(m_j \pm 1)}|j, m_j \pm 1\rangle, \tag{1.35}$$

where the effect of $\hat{J}_{\pm}$ is to raise $(+)$ or lower $(-)$ the value of m_j. Before proceeding, it is worth noting that these raising and lowering operators can be expressed in terms of $\hat{J}_x$ and $\hat{J}_y$ as

$$\hat{J}_{\pm} = \hat{J}_x \pm i\hat{J}_y. \tag{1.36}$$

[‖] In Appendix G, this theorem is discussed in great detail.

Employing definitions 1.19,1.20,1.35 and 1.36, it can be shown that the following commutation relations

$$[\hat{J}_i, \hat{J}_j] = i\epsilon_{ijk}\hat{J}_k \tag{1.37}$$

and

$$[\hat{J}^2, \hat{J}_\xi] = 0, \tag{1.38}$$

for $\xi = x, y, z, \pm$ must hold, where the former is the canonical commutation (quantisation) relation and ϵ_{ijk} is the three dimensional Levi-Civita symbol.

Finally, by rewriting the CEF Hamiltonian in terms of operators whose behaviour on the states $|j, m_j\rangle$ are readily defined by Eqs. 1.19, 1.20, and 1.35, the crystal field eigenvalue problem is greatly simplified.

In the approach employed in this Thesis, conventionally referred to as the Stevens approach, Eq. 1.32 is further condensed into the form

$$\hat{V} = \sum_{l,m} B_l^m \hat{O}_l^m, \tag{1.39}$$

where B_l^m and $\hat{O}_l^m$ are the Stevens coefficients and operators, respectively. The particular Stevens parameters that are present in the sum of Eq. 1.39 are determined by symmetry and have been tabulated by Walter, whilst the expressions of the Stevens operators* in terms of angular momentum operators have been tabulated by Hutchings. The modification of Eq. 1.32 in terms of tesseral harmonics into a sum of Stevens operators given by Eq. 1.39 requires the addition of a proportionality constant α_J and the replacement of r^n with $\langle r^n \rangle$. Although one usually determines the Stevens parameters B_l^m experimentally; in theory the parameters could be calculated using a modified expression of Eq. 1.33 which employs a point-charge model in its current form or could be generalised to charge densities. While the inclusion of a few terms in general is required to achieve numerical convergence, since $B_l^m \propto \frac{1}{R^l}$, one often obtains a reasonable approximation by only considering the Coulomb potential from nearest neighbour ions.

In the analysis so far, it has been assumed that only one particular spin-orbit

*The expressions for the Stevens operators used in this Thesis have been tabulated in Appendix D.

manifold is being considered. Employing spectroscopic nomenclature, such a spin-orbit manifold is conventionally referred to as a multiplet and is represented by a term symbol ${}^{2S+1}L_J$. Although not explicitly stated so far, each of these multiplets under consideration are of fixed j, l and s, whilst their corresponding eigenvalues are given by Eq. 1.25 above. In the systems considered so far, the values of l and s are first determined by a combination of the *Aufbauprinzip*, the Pauli Exclusion Principle and Hund's rules. The first two principles assures that only the valence shell must be considered when assigning a term symbol. In theory, there are numerous, albeit finite ways electrons in the valence shell may be arranged without violating any of the first two principles. Since all measurements performed in this Thesis involve very low incident energies on samples at very low temperatures, only the ground state multiplet is expected to be thermally populated and thus the only multiplet of interest. The procedure for determining the ground state multiplet was well-established in the late 1920's and is now commonly referred to as Hund's rules. This set of three rules incorporate the role of Coulomb repulsion and the Pauli Exclusion Principle and states the following:

1. *Hund's first rule*: For a given electron configuration, the ground state term symbol will be that possessing the largest value for the multiplicity, subject to the Pauli Exclusion Principle. Since the multiplicity is defined by $2S+1$, where S is the total spin quantum number given by $\sum_i s_i$, Hund's first rule can be alternatively stated as the total spin quantum number S must be maximised, again, subject to the Pauli Exclusion Principle.

2. *Hund's second rule*: For a given multiplicity, defined by Hund's first rule, the ground state term symbol will be that possessing the largest value for the total orbital angular momentum number $L = \sum_i l_i$.

3. *Hund's third rule*: For a given term determined by Hund's first and second rules, the ground state term will possess a total angular momentum number J that will be $J = L \mp S$ for a system whose valence shell is less or more than half-filled, respectively.

All of these rules assume that other contributions to the Hamiltonian such as spin-orbit coupling and the crystalline electric field are much weaker than electron-electron Coulombic repulsion. Furthermore, the assignment of the ground state multiplet as simply a direct application of Hund's three rules has an implicit assumption that the $\hat{\mathcal{H}}_{CEF} \ll \hat{\mathcal{H}}_{SO}$, as is the case for the $4f$ metals,

as illustrated in Fig. 1.2(a).

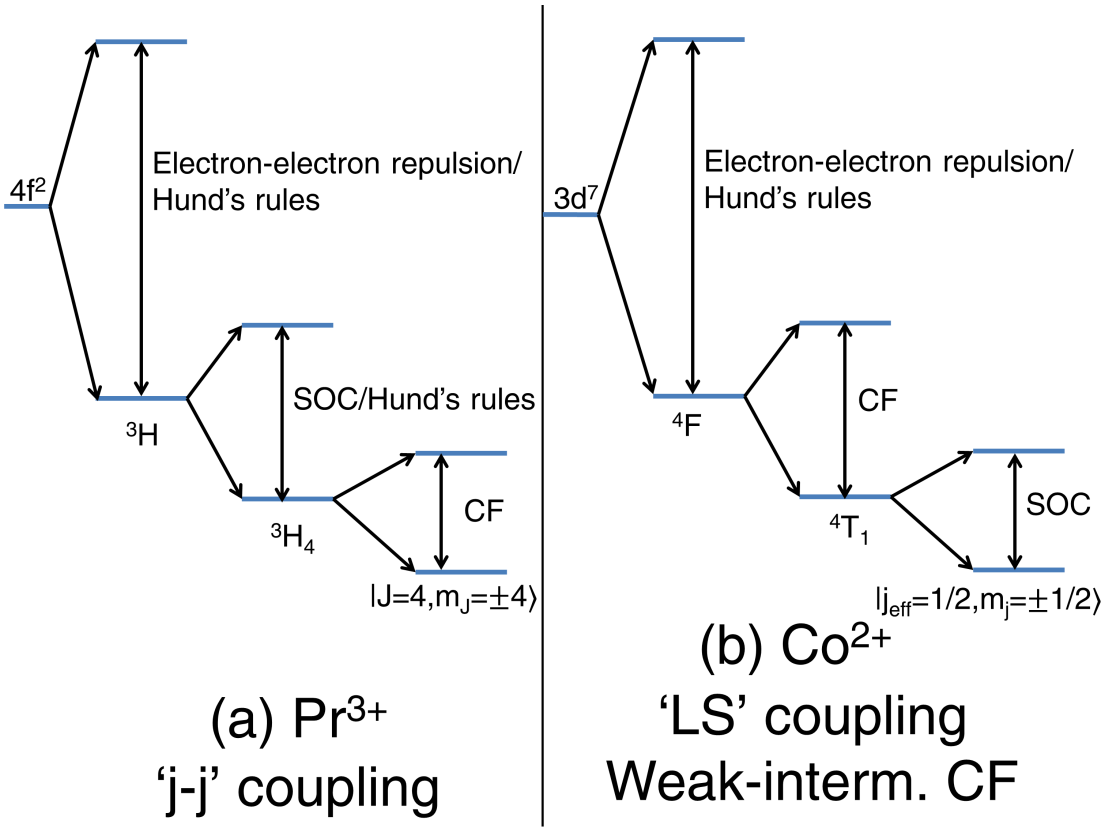

Figure 1.2 Pictorial representation of some select energy scales of interest in the (a) $4f^2$ Pr^{3+} in $Pr_2Sn_2O_7$ and (b) $3d^7$ Co^{2+} in CoO representing 'j-j' coupling and 'weak-intermediate crystal field' schemes, respectively. For simplicity, other splittings due to molecular-induced Zeeman splitting, Jahn-Teller distortions, anisotropy, *etc.* are not included. Energy gaps for both panels (a) and (b) are not to scale.

On the contrary, in the case that $\hat{\mathcal{H}}_{CEF} \gtrapprox \hat{\mathcal{H}}_{SO}$, strong mixing between different terms would be expected, thus the 'j-j' coupling scheme would ultimately not be valid and other approximations must be made. In this particular case, if one assumes that the Coulomb repulsion is still the dominant energy scale, one may apply the so-called 'intermediate crystal field' approximation. Presented in Fig. 1.2(b), such an approximation is particularly valid for the $3d$ metals (*i.e.* lower Z metals) that have crystal field splittings Δ that are not much greater than a few eV (*i.e.* coordinated by weak(er) field ligands). In this approximation, the crystalline electric field contribution $\hat{\mathcal{H}}_{CEF}$ is still considered a perturbation but to the basis states that are defined by Hund's first two rules. These two rules incorporate the effects of Coulomb repulsion and the Pauli

Exclusion Principle, effectively defining an effective[†] unperturbed Hamiltonian $\hat{\mathcal{H}}_o$. An important observation is that in this particular approximation, a good quantum number for $\hat{\mathcal{H}}_o$ is the total orbital angular momentum number L. Thus, the tools employed when addressing the CEF contribution in the 'j-j' coupling scheme (*i.e.* the expansion of $\hat{V}_{CEF}$ in terms of angular momentum operators *via* the Wigner-Eckhart Theorem) is also applicable for this approximation with the main difference being that the manifold of states is defined by L and not J; thus, the Stevens operators $\hat{O}_l^m$ must be defined in terms of $\hat{L}^2, \hat{L}_z, \hat{L}_\pm$ *in lieu* of their total angular momentum counterparts. For systems in this 'intermediate regime' such as many of the $3d$ metals, the presence of such crystalline electric field has a particular substantial influence on their magnetic properties, one such example being the quenching of orbital angular momentum[‡].

Finally, in this approximation the spin-orbit coupling contribution $\hat{\mathcal{H}}_{SO} = \lambda\hat{\mathbf{L}}\cdot\hat{\mathbf{S}}$ is treated as a perturbation to the manifold of states defined by $\hat{\mathcal{H}}_o + \hat{\mathcal{H}}_{CEF}$. Such an approximation is well-represented by the case of the $3d^7$ Co^{2+} in CoO. As will be discussed in further detail in Chapters 3 and 4, Hund's first two rules yield total orbital and spin quantum numbers $L = 3$ and $S = \frac{3}{2}$, respectively, corresponding to a ${}^{2S+1}L$ term symbol of ${}^4F$. In the case of CoO, the Co^{2+} cations are octahedrally coordinated by the relatively weaker field O^{2-} ligand resulting in a $\Delta \sim 900$ meV between the ${}^4T_1$ and ${}^4T_2$ crystal field eigenstates [20]. The triplet orbital degeneracy of the ${}^4T_1$ crystal field ground state is conventionally assigned a fictitious total orbital angular momentum number l=1. In the case of CoO, the spin-orbit coupling constant λ for Co^{2+} is $\alpha\widetilde{\lambda}$ meV, where $\widetilde{\lambda}$ is an effective spin-orbit coupling constant of -16 meV and $\alpha = -\frac{3}{2}$ is a projection factor associated with the projection of $\hat{\mathbf{L}}$ onto $\hat{\mathbf{l}}$ [18]. Consequently, since the energy scale associated with spin-orbit coupling is significantly smaller than the CEF splitting, then the spin-orbital Hamiltonian $\hat{\mathcal{H}}_{SO} = \alpha\widetilde{\lambda}\mathbf{l}\cdot\mathbf{S}$ may be treated

[†]Note the use of the term "effective". The true unperturbed Hamiltonian could be considered the Hamiltonian that defines the atomic orbitals.

[‡]The quenching of angular momentum is discussed in great detail in Abragam & Bleaney [47]. Utilising a simplistic view, orbital angular momentum is present when three conditions are met: (1) there exists degeneracy, (2) the degenerate orbitals can be inter-converted by a simple rotation about a particular axis and (3) the orbitals cannot be empty, half-filled or completely filled. The failure to satisfy any of these conditions will lead to zero orbital angular momentum. Since the crystalline electric field determines the energetic configuration of such orbitals, it is easy to see why it commonly leads to orbital quenching. It is common to present orbital quenching in terms of simple pictorial diagrams but the physical process may be derived rigorously. In the case of the degeneracy requirement, it is known that a non-degenerate system is described by a real wavefunction $|\psi\rangle$, this is conventionally proven by *reductio ad absurdum*. Since $\hat{\mathbf{L}} = -i\hbar(\hat{\mathbf{r}}\times\hat{\nabla})$ is an imaginary operator, then its expectation value given by $\langle\psi|\hat{\mathbf{L}}|\psi\rangle$ must be zero. Such a statement can be quickly derived using integration-by-parts and appropriate boundary conditions employing the fundamental postulates of quantum mechanics.

as a perturbation to the eigenstates defined by $\hat{\mathcal{H}}_o + \hat{\mathcal{H}}_{CEF}$, yielding $j_{\text{eff}} = l + S$ eigenstates with a ground state of $j_{\text{eff}} = \frac{1}{2}$.

In addition to the two approximations presented so far, there exists a third type of approximation called the 'strong crystal field' approximation. In such an approximation, the crystalline electric field $\hat{\mathcal{H}}_{CEF}$ is the dominant energy scale and thus defines an effective[§] unperturbed Hamiltonian $\hat{\mathcal{H}}_o$. The eigenstates for such a Hamiltonian for a cation with a d ($l = 2$) valence shell in octahedral[¶] coordination correspond to the triply degenerate $|t\rangle$ and doubly degenerate $|e\rangle$ states. Both the $|t\rangle$ and $|e\rangle$ states are linear combinations of the d-atomic orbitals given by $|l = 2, m_l\rangle$ in the $|l, m_l\rangle$ basis. The gap between the $|t\rangle$ and $|e\rangle$ states Δ is often denoted as $10Dq$ which is equivalent to $120B_4$, where the Stevens parameter B_4 parametrises the crystal field Hamiltonian for an undistorted octahedron given by

$$\hat{\mathcal{H}}_{CEF} = B_4(\hat{O}_4^0 + 5\hat{O}_4^4) \tag{1.40}$$

in the Stevens formalism defined above. In the 'strong crystal field approximation', $10Dq$ is large compared to the energy scale set by the electron-electron repulsion, thus the ground state is defined by Hund's rules but subject to constraints set by the $|t\rangle$ and $|e\rangle$ eigenstates of $\hat{\mathcal{H}}_{CEF}$. In the case of Co^{2+} in octahedral coordination, using the 'strong crystal field' approximation would imply that the total spin quantum number $S = \frac{1}{2}$ instead of the previously obtained high spin value of $\frac{3}{2}$. The question of what value of $10Dq$ constitutes "large enough" to utilise the 'strong crystal field' approximation is summarised graphically be Sugano-Tanabe diagrams. These diagrams plot the electronic energy levels as a function of $\xi = \frac{10Dq}{B}$, corresponding to the balance between the crystal field ($10Dq$) and Coulomb electron-electron repulsion (B), where small and large ξ correspond to the 'intermediate crystal field' and 'strong crystal field' approximations, respectively. The Sugano-Tanabe diagram for Co^{2+} in octahedral coordination is listed in Abragam & Bleaney [47] and has been measured experimentally by Cowley *et al.* [18]. Although important in understanding the ground state of some $3d$ cations, such an approximation is not relevant to any of the systems discussed in this Thesis. Finally, it is worth noting that although there are many other potential contributions to the

[§]Once again, note the term "effective". The true unperturbed Hamiltonian is the one that defines the atomic orbitals.

[¶]Undistorted.

Hamiltonian that defines single-ion magnetism such as Jahn-Teller distortions, Zeeman splitting and single-ion anisotropy, these contributions are not universal to all systems that are investigated in this Thesis and thus, only when needed will each contribution be introduced in the relevant experimental chapter.

Cooperative Magnetism

Having introduced the multiple energy scales that influence the electronic structure, and ultimately the magnetism at the level of the single-site, the discussion now shifts to the subtle but key observation that these magnetic ions are not isolated and thus *can* interact with one another, resulting in what is known as cooperative magnetism. This discussion is based on Greedan [40], Kittel [37], Ashcroft & Mermin [39], Goodenough [53–55], Kanamori [56], Anderson [57], Heisenberg [58], Dirac [59], Kramers [60], Meislich *et al.* [61], Néel [62] and references contained therein. Any additional references will be explicitly stated in the text. A broad term describing magnetism that is based on correlations between different spins residing on magnetic ions, this phenomenon is the physical mechanism underlying the magnetism of the magnets that are most commonly encountered in everyday life. These correlations can exist for a variety of length scales, ranging from one to a few neighbours, all the way to infinity[‖].

In a sense, the reader has already been introduced to the shortest length scale under consideration, that is the scale of the single-ion. Representing the magnetic analogue of the ideal gaseous state of matter, paramagnetism corresponds to the case when there exists no effective[**] correlation between the spins, even between nearest neighbours. The magnetic moment M for a paramagnetic system consisting of N_{A} non-interacting spins is given by

$$M = N_{\mathrm{A}}\langle\mu\rangle, \tag{1.41}$$

where N_{A} is Avogadro's number and $\langle\mu\rangle$ denotes the average magnetic moment. The value of $\langle\mu\rangle$ can be calculated using statistical mechanics and is given by

$$\langle\mu\rangle = g_{S(J)}SB_{S(J)}(\eta)\mu_B, \tag{1.42}$$

[‖] The term "infinity" essentially denotes the length of the sample probed.

[**] This is simply an approximation. There may be some correlations but may be much weaker than other energy scales under consideration, *e.g.* thermal fluctuations.

where μ_B is the Bohr magneton that was previously introduced, whilst $g_{S(J)}$ denotes the Landé g-factor and S being the spin quantum number. Although the particular expression for $\langle\mu\rangle$ given by Eq. 1.42 is defined in terms of a total angular momentum J, such an equation may be simplified if one assumes that the total spin of the system is described by S. Such an assumption is valid for many of the $3d$ block where crystal field effects often quenches the orbital angular momentum such that $\langle\hat{\mathbf{L}}\rangle = 0$ and thus $\hat{\mathbf{J}} \sim \hat{\mathbf{S}}$, whilst the Landé g-factor given by

$$g_J = g_L \frac{J(J+1) - S(S+1) + L(L+1)}{2J(J+1)} + g_S \frac{J(J+1) + S(S+1) - L(L+1)}{2J(J+1)} \tag{1.43}$$

is reduced to the electron spin g-factor $g_S \sim 2$. The function $B_{S(J)}$ is known as the Brillouin function and is defined as

$$B_{S(J)} = \frac{(S(J) + \frac{1}{2}\cosh(S(J) + \frac{1}{2})\eta - \frac{1}{2}\cosh(\frac{\eta}{2}))}{\sinh(S(J)) + \frac{1}{2}\eta\sinh(\frac{\eta}{2})}, \tag{1.44}$$

where η denotes the ratio between the magnetic and thermal energies given by

$$\eta = \frac{g_{S(J)}\mu_B H_z}{k_B T}, \tag{1.45}$$

where k_B is the Boltzmann constant, T is the absolute temperature and H_z is the relevant component of the applied magnetic field. In the limit of high temperatures or very low fields (*i.e.* $\eta \ll 1$), Eq. 1.44 reduces to

$$B_{S(J)} = \frac{g_{S(J)} H_z \mu_B S(J)(S(J)+1)}{3k_B T}. \tag{1.46}$$

By employing the definition of the magnetic susceptibility as the proportionality constant between the induced magnetisation and the applied magnetic field,

$$\chi = \frac{M}{H_z}, \tag{1.47}$$

and inserting Eq. 1.46 into Eq. 1.42, one obtains

$$\chi = \frac{N_A g_{J(S)}^2 \mu_B^2 S(J)(S(J)+1)}{3k_B T}, \tag{1.48}$$

which is known as the Curie law which is often condensed into

$$\chi = \frac{C}{T}, \tag{1.49}$$

where C is the Curie constant, a value that is a quantitative measure of the spin or total angular momentum. Upon closer inspection of the Curie constant in Eq. 1.48 given by

$$C = \frac{N_A g_{J(S)}^2 \mu_B^2 S(J)(S(J)+1)}{3k_B}, \tag{1.50}$$

it can be shown that its numerator possesses the form that would be assumed by the square of a magnetic moment. By defining an effective paramagnetic moment μ_{eff} given by

$$\mu_{\text{eff}} = g_{J(S)} \sqrt{S(J)(S(J)+1)} \mu_B, \tag{1.51}$$

and noting that

$$\frac{N_A}{3k_B} \sim 8, \tag{1.52}$$

then Eq. 1.50 becomes

$$\mu_{\text{eff}} = \sqrt{8C}. \tag{1.53}$$

Although the form of the Curie law written in Eq. 1.48 describes a hyperbola, it can, and is, conventionally lineralised by taking its inverse such that one obtains

$$\chi^{-1} = \frac{1}{C} T, \tag{1.54}$$

describing a linear dependence on temperature with slope $\frac{1}{C}$.

In contrast to the paramagnetic behaviour described by the Curie law that would be applicable at high temperatures (or low applied magnetic fields), in the limit of $\eta \gg 1$, *i.e.* in the limit of low temperatures or high applied magnetic fields, the Brillouin function approaches a value of 1 and thus Eq. 1.42 reduces to

$$M = N_A g_{J(S)} J(S) \mu_B, \tag{1.55}$$

describing the saturation of the magnetic moment to a value of

$$\mu_{sat} = g_{J(S)} J(S) \mu_B. \tag{1.56}$$

With the discussion of paramagnetism so far, it was assumed that spin-spin correlations were absent. In the case that such correlations are indeed present, a critical temperature T_C should exist where if $T \lessapprox T_C$, a phase transition to a more organised state will occur. Due to the constraints imposed by symmetry, most, but not all, of these magnetic phase transitions are of second order, also referred to as "continuous" transitions, reflecting the continuous nature of the first derivative of the free energy with respect to the state variables at T_C. As with the transition of a gas into a crystalline solid, these magnetic transitions first involve the development of fractal-like clusters from the paramagnetic state as the temperature is lowered into the so-called critical regime. As the temperature is reduced even further, these clusters grow in size until at least one of these clusters becomes "infinite" in size at T_C, forming long range magnetic order (LRO). Since many of these transitions are of second order, anomalies will be present in both the specific heat and magnetic susceptibility, although the so-called latent heat will be absent. As the temperature is lowered below T_C, more and more of these clusters become associated with the "infinite" cluster and the long range ordered magnetic state until the limit of 0 K, where all spins become* correlated by the Third Law of Thermodynamics.

There are three basic types of long range magnetic order: ferromagnetism, antiferromagnetism and ferrimagnetism. Ferromagnetism is the simplest form of long range magnetic order, albeit it is the form that is most rarely found in nature. In the case of long range ferromagnetic order, the critical temperature is called the Curie temperature T_{C}, below which all of the spins are aligned parallel to

*As will be described later in this chapter, this is not always the case for some magnetic systems down to currently experimentally accessible cryogenic temperatures and time scales.

one another. Although there is clearly only one possible spin configuration[†], the spins will tend to align themselves along some preferred direction. In contrast, for the case of long range antiferromagnetic order, the critical temperature is called the Néel temperature T_N, below which the spins are aligned anti-parallel to one another. A common approach in describing long range antiferromagnetic order is to subdivide the magnetic unit cell into magnetic sublattices. The minimum number of sublattices is two, say α and β, with each possessing the same number of spins and with equal total spin magnitudes, *i.e.* $|\mathbf{S}_\alpha| = |\mathbf{S}_\beta|$. Since the spins constituting the α sublattice are aligned antiparallel to those in the β sublattice, the total spin of the system must be zero. For a given magnetic sublattice symmetry, there exists multiple spin arrangements to satisfy the requirement of zero total spin. For example, the simplest case would be that of a primitive magnetic sublattice. As summarised by Fig. 1.3, there exists three possible types of spin configurations that are commonly referred to as: A, C and G-types. In case of the A-type, the magnetic unit cell requires doubling of the nuclear unit cell along **c**, whilst for the C-type, doubling of the nuclear unit cell along both **a** and **b** are required. In the case of G-type, the nuclear unit cell must be doubled in all three crystallographic directions. The third type of long range magnetic order, ferrimagnetism corresponds to a case where there are multiple magnetic sublattices that possess unequal magnetisations. If one defines the sublattice magnetisation $M_\alpha = N_\alpha g_\alpha |\mathbf{S}_\alpha|$ for sublattice α with N_α number of spins with g-factor g_α, then ferrimagnetism could arise if $N_\alpha \neq N_\beta$ or $|\mathbf{S}_\alpha| \neq |\mathbf{S}_\beta|$ in the simplest case of two sublattices with antiparallel coupling, resulting in a net magnetisation of $M = |\mathbf{M}_\alpha - \mathbf{M}_\beta|$. Such type of long range magnetic order can be accomplished in a variety of ways that are dependent on both the crystal and compositional chemistry of the system of interest.

In the discussion of long range magnetic order so far, only collinear states have been considered. There exists also many different types of non-collinear long range magnetic order. These types include the canted antiferromagnet. Canted antiferromagnetism is a consequence of the anisotropic Dzyaloshinskii-Moriya (DM) interaction $\mathbf{D}_{\mathrm{DM}} \cdot \mathbf{S}_\alpha \times \mathbf{S}_\beta$ and thus is most commonly exhibited by low symmetry materials with the lack of an inversion centre. Such order corresponds to the case where the angle between sublattice moments deviates from 180°, usually by no more than 1° or 2°. A consequence of this deviation is that the magnetisation of the sublattices do not completely cancel, resulting in a small net magnetisation, hence why canted antiferromagnetism is sometimes

[†]This is assuming collinear ferromagnetic order.

referred to as weak ferromagnetism. Although equally interesting as numerous and diverse, all long range magnetic order exhibited by the systems investigated in this Thesis are collinear* in nature and thus non-collinear magnetic order shall not be discussed any further.

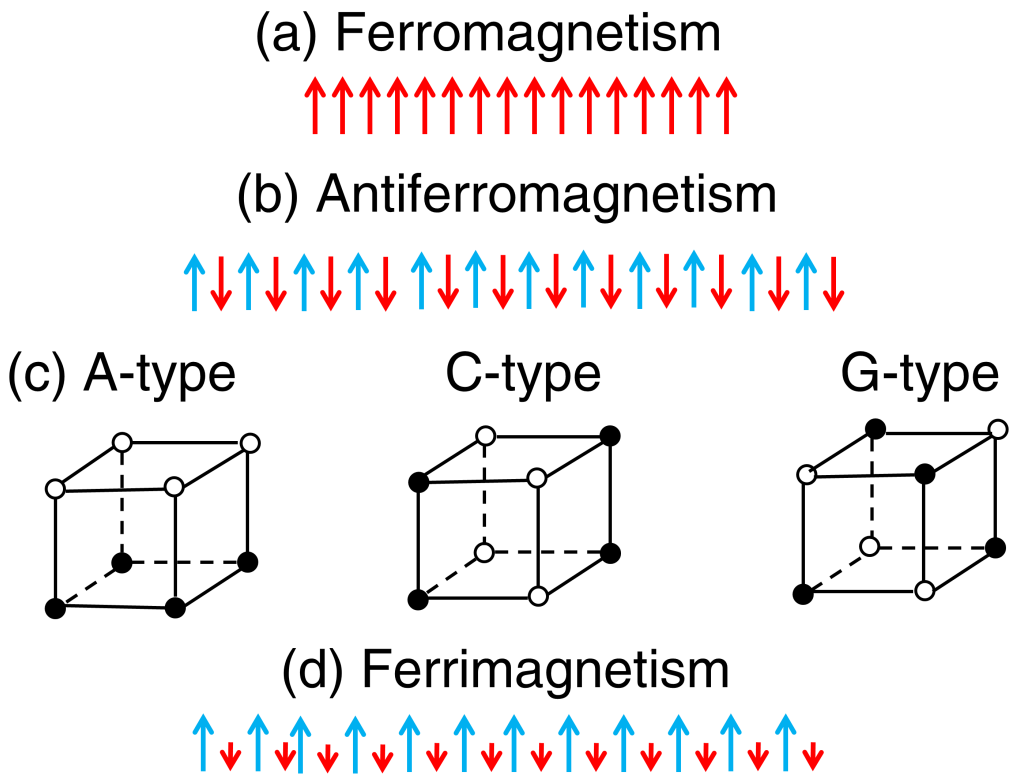

Figure 1.3 Simple collinear (a) ferromagnetic order, (b) antiferromagnetic order, (c) different types of antiferromagnetic order with simple cubic unit cell and (d) ferrimagnetic order. Open and closed circles represent spin up and spin down or *vice versa*, respectively.

Although one would assume that the presence of a large number of magnetic centres combined with strong coupling would be sufficient to guarantee long range magnetic order, in fact this is really generally the case for magnetic systems exhibiting 3D† spatial dimensionality. The term spatial dimensionality d is largely a consequence of crystallography and refers to how the spatial degree to which the spins interact with one another, *i.e.* the relative anisotropy of the exchange

*This is technically still unclear for the case of CoO. The original magnetic structure proposed for CoO is indeed collinear but recent neutron and synchrotron measurements have cast significant doubt on such claim, suggesting some minor spin canting.

†In terms of nomencalture, systems with n-dimensionality are sometimes referred to n-d systems *in lieu* of nD, *e.g.* 1-d systems instead of 1D.

paths. In the case of 3D dimensionality, *i.e.* $d = 3$ the anisotropy is considered small. For the case of $d = 2$, spins are arranged in effective sheets or planes where the exchange interactions within a plane are much stronger than between planes. Such a situation is applicable for magnetic systems that crystallise in the K_2NiF_4 structure, a structure often adopted by many magnetic oxides. The structure consists of layers of corner-sharing NiF_6 octahedra separated by KF layers, resulting in much stronger intra-planar coupling. Finally, in the case of $d = 1$, spins are distributed in a chain-like arrangement with a single dominant intra-planar exchange interaction such as is the case for $CoNb_2O_6$ [63], a low dimensional compound that will play a key role in Chapter 2. In addition to the spatial dimensionality, the spin dimensionality is also a key parameter in determining if a system will assume long range magnetic order. In the case of this Thesis, the spin dimensionality D refers to anisotropy of the Hamiltonian describing spin-spin interactions. The concept of D can be introduced by expanding the Heisenberg-Dirac Hamiltonian

$$\hat{\mathcal{H}} = J \sum_{i,j} \hat{\mathbf{S}}_i \cdot \hat{\mathbf{S}}_i, \tag{1.57}$$

into its components

$$\hat{\mathcal{H}} = \sum_{i,j} \left\{ J_x S_{ix} S_{jx} + J_y S_{iy} S_{jy} + J_z S_{iz} S_{jz} \right\}, \tag{1.58}$$

or more commonly written as

$$\hat{\mathcal{H}} = \sum_{i,j} J_{ij} \left\{ a(S_{iz} S_{jz} + b(S_{ix} S_{jx} + S_{iy} S_{jy})) \right\} \tag{1.59}$$

where i and j are site labels, whilst J_η and $S_{i\eta}$ denote the η component of the exchange constant and the spin operator at site i. Upon closer inspection of Eqs. 1.58 and 1.59, three distinct models may be identified. The Heisenberg model with $D = 3$ refers to when $J_z \sim J_x \sim J_y$, *i.e.* $a = b$. For the case of $D = 2$, when $J_z \ll J_x \sim J_y$, *i.e.* $a \ll b$, is commonly referred to as the XY model, whilst for the case of $D = 1$, when $J_z \gg J_x \sim J_y$, *i.e.* $a \gg b$, corresponds to the so-called Ising model. As will be discussed at the end of this subsection, the dominant physical mechanism underlying cooperative magnetic behaviour

in magnetic insulators is based on the exchange interactions between electronic orbitals. Consequently, much attention has been placed on investigating the Heisenberg-Dirac Hamiltonian and the effects of the dimensionality D and d on these systems' ability to assume long range magnetic order. As is summarised by Tab. 1.1, only certain combinations of D and d allow the Heisenberg-Dirac Hamiltonian to assume long range order, with the only systems possessing spatial dimensionality $d = 3$, with the exception of the $2D$ Ising ($D = 1$) case, and possibly $2D$ XY ($D = 2$). In contrast, 5 (or 4) of the 9 different possible spatial-spin categories assume short range magnetic order whose spin-spin correlations' spatial extent is limited. Such short range magnetic order can persist for a wide temperature range, often over tens of Kelvins and can be viewed as an expansion of the critical regime previously discussed in the context of long range magnetic order which is usually a few degrees at most for 3D systems.

Table 1.1 Ordering of magnetic models as a function of the spatial and spin dimensionality d and D, respectively. LRO denotes the assumption of a long range magnetically ordered state at $T > 0$, whilst SRO denotes a short range magnetically ordered state corresponding to the absence of such long range order.

Model	D	$d = 1$	$d = 2$	$d = 3$
Ising	1	SRO	LRO	LRO
XY	2	SRO	SRO[†]	LRO
Heisenberg	3	SRO	SRO	LRO

The simplicity of the spin-spin interactions described by the Heisenberg-Dirac Hamiltonian and other magnetic Hamiltonians is in stark contrast with those interactions in other standard states of matter such as liquids that are described by much more complicated Hamiltonians. This relative simplicity was a major driving force in the study of magnetic transitions, providing an unparalleled opportunity to study some fundamental properties of critical phenomena. One such property of particular interest is the hypothesis of universality [64]. Commonly viewed as a generalisation of Van der Waals' law of corresponding states, the hypothesis of universality states that for a continuous phase transition, critical exponents can be calculated to describe the transition and these exponents are only dependent on the dimensionality of the system, d and the dimensionality of the order parameter, D, irrelevant of the details of

[†]The 2D XY model is a unique case where the Kousterlitz-Thouless transition is observed.

the microscopic interactions comprising a system of interest, be it quantum or classical. In the case of the magnetic insulators, the former is heavily dependent on the crystal structure, whilst the latter is a measure of the anisotropy of the exchange Hamiltonian. These critical exponents describe the behaviour of the variables of state as one approaches a transition. For the magnetic insulators that are investigated in this Thesis, the critical behaviour of two state variables of particular interest: the magnetisation M and the correlation length ξ are given by

$$M \propto \left(- \left\{ \frac{T - T_C}{T_C} \right\} \right)^{\beta} \tag{1.60}$$

for $T < T_C$ and

$$\xi \propto \left(\frac{T - T_C}{T_C} \right)^{-\nu}, \tag{1.61}$$

for $T > T_C$, respectively, where β and ν are the corresponding critical exponents.

Having described the Heisenberg-Dirac Hamiltonian, this subsection will now conclude with a discussion of exchange interactions. Corresponding to a purely quantum mechanical effect occurring between indistinguishable particles, the need for such an effect can be rationalised by investigating the energy scales involved in a purely classical treatment. In the context of magnetic insulators, such a treatment would address any cooperative magnetism as a consequence of the dipolar interactions between the magnetic centres' electrons' dipolar moments. The interaction energy associated with this magnetic dipole-dipole interaction is given by

$$U_{\text{dipolar}} = \frac{1}{r^3} \left\{ \mathbf{m}_i \cdot \mathbf{m}_j - 3(\mathbf{m}_i \cdot \hat{\mathbf{r}}_{ij})(\mathbf{m}_j \cdot \hat{\mathbf{r}}_{ij}) \right\}, \tag{1.62}$$

where $\hat{\mathbf{r}}_{ij}$ is the unit vector parallel to the displacement vector with magnitude r from the magnetic dipoles $\mathbf{m}_i$ to $\mathbf{m}_j$. By noting that Eq. 1.62 has a maximum when $\mathbf{m}_i \parallel \mathbf{m}_j$, it can be shown that the energy scale defined by the magnetic dipole-dipole interaction is given by

$$U_{\text{dipolar}} \propto \frac{1}{r^3} \left(g\mu_B \right)^2. \tag{1.63}$$

The presence of μ_B^2 in Eq. 1.63 significantly reduces the energy scale set by U_{dipolar}, corresponding to an energy of about 1 K for moments located 2 Å apart. Such low energy scales is in stark contrast to the transition temperatures exhibited by many magnetic insulators, let alone some pure metals such as iron with transition temperatures in the thousands of Kelvin, thus another non-classical physical interaction mechanism was clearly required.

Such a physical mechanism, now known as the exchange interaction, would be discovered in the early 20$^{\text{th}}$ Century with the birth of quantum mechanics. The discovery of the exchange interaction was a consequence of the establishment of a connection between the phenomenon of ferromagnetism and electron bonding by Heisenberg, two areas that physicists once believed were unconnected. Throughout the mid- to late 1800's, it was discovered that certain substances would develop a spontaneous magnetisation if cooled below a critical temperature, even in the absence of an external magnetic field. It was the French physicist Pierre-Ernest Weiss in 1907 that deduced this behaviour was due to the presence of an internal magnetic field $\mathbf{H}_{\text{int}}$, commonly referred to as the molecular or Weiss field. A consequence of the Weiss field is that for a system of atoms in the presence of an external magnetic field, each atom would experience an effective magnetic field given by

$$\mathbf{H}_{\text{eff}} = \mathbf{H} + \mathbf{H}_{\text{int}} = \mathbf{H} + \lambda \mathbf{M}, \tag{1.64}$$

where $\mathbf{M}$ denotes the magnetisation, given by

$$\mathbf{M} = \sum_i \mu_i, \tag{1.65}$$

whilst $\lambda > 0$ is a system-dependent constant. This internal magnetic field plays an ordering effect since a dipole will tend to align itself in the direction of the field and thus giving rise to spontaneous magnetisation. This ordering effect is countered by the randomising effects of thermal energy $k_B T$ that attempts to flip the dipoles away from the ordered ferromagnetic state. Utilising the same logic outlined in the derivation of the Curie law (Eq. 1.49), but now incorporating the Weiss field, one obtains a temperature dependence of the magnetic susceptibility

that is slightly modified from the Curie law given by

$$\chi = \frac{C}{T - \theta_{\mathrm{CW}}}, \tag{1.66}$$

which is called the Curie-Weiss law, where θ_{CW} is called the Curie-Weiss constant (temperature) or simply the Weiss constant (temperature) which is equal to T_{C} for non-frustrated ferromagnets[‡]. Despite the success of the Curie-Weiss law to account for experimental data, the physical origin of the Weiss field remained a mystery for almost two decades.

It was not until the spectroscopic studies of the chemical bond did scientists finally solve the mystery. With the discovery of the electron in 1897, scientists were posed with a dilemma. Since each atom has an outer cloud of electrons, how would these atoms approach one another to form chemical bonds? Epitomised by the studies of Pauli (1926) on helium and Heitler and London (1927) on molecular hydrogen, the exchange interaction was proving to be key in understanding chemical bonding. In the case of the Heitler-London model for molecular hydrogen, there exists an attractive potential between an electron of one atom to the nucleus of the other and *vice versa*, whilst there is electron-electron repulsion between both electrons. In this model, the exchange interaction J appears as the exchange integral term in the list of possible energy eigenvalues. Heisenberg's main contribution to the theory of cooperative magnetism began in 1926 when he began to explore if and how the exchange term — which first came about in the context of chemical bonding — would appear in a system composed of multi-electron atoms. Employing Slater determinants to assure the multi-electron wavefunction would satisfy the Pauli Exclusion Principle, Heisenberg identified that the exchange term did in fact appear. For the next two years, Heisenberg continued to investigate the effects of the exchange interaction, building upon the work of van Vleck and Dirac on the Heitler-London model with the inclusion of spin, culminating in his 1928 paper presenting his theory for ferromagnetism. Using statistical mechanics, Heisenberg was able to confirm that the temperature dependence of the magnetisation of a system of atoms coupled by J would be described by the Curie-Weiss law (Eq. 1.49) if $J < 0$. By reproducing the Curie-Weiss law, Heisenberg proved that J was the underlying physical origin of the Weiss field[§]. The connection between the exchange constants and the Weiss field

[‡]In the discussion, we will focus on ferromagnetism since it wasn't until much later that Louis Néel identified antiferromagnetism.

[§]A rigorous mathematical proof is outlined in Dirac's 1928 paper.

can be established using a mean-field approach. In this particular approach, the magnetic field experienced by an atom at site a i is given by

$$H_i = H + \sum_j \gamma_{ij} M_j, \tag{1.67}$$

where H is the applied magnetic field and the sum is over all surrounding magnetic centres j. The coupling constant γ_{ij} can be shown to be given by

$$\gamma_{ij} = \frac{(2 z_{ij} J_{ij})}{N_A g_{S(J)}^2 \mu_B^2}, \tag{1.68}$$

where z_{ij} is the number of neighbours for a given sublattice. By substituting H_i for H in the definition of the susceptibility (Eq. 1.47), one obtains the expression

$$M_i = \frac{C H_i}{T}. \tag{1.69}$$

By inserting the definition of H_i (Eq. 1.67) into the equation above, it can be shown that

$$\chi = \frac{C}{T - C \sum_j \gamma_{ij}}. \tag{1.70}$$

Comparing the equation above to the Curie-Weiss law (Eq. 1.66), the relationship between the Curie-Weiss temperature and the exchange constants is given by

$$\theta_{\mathrm{CW}} = C \sum_j \gamma_{ij}. \tag{1.71}$$

Inserting the definition of the Curie constant (Eq. 1.50) and γ_{ij} (Eq. 1.68), one obtains

$$\theta_{\mathrm{CW}} = -\frac{2S(J)(S(J)+1)}{3} \sum_j z_{ij} J_{ij}. \tag{1.72}$$

The value of θ_{CW} in this mean field approach is the algebraic sum of all the exchange constants acting on a given atom i and thus is diagnostic of the net

exchange with $\theta < 0$ denoting dominant AFM exchange and $\theta > 0$ denoting dominant ferromagnetic exchange. The negative prefactor has been added to assure the value of θ is consistent with the convention of assigning $J < 0$ for ferromagnetic coupling.

Now known as the Heisenberg model, the spin-spin interactions investigated by Dirac are described by the aforementioned Heisenberg-Dirac Hamiltonian[¶] given by

$$\hat{\mathcal{H}} = \sum_{ij} J_{ij} \hat{\mathbf{S}}_i \cdot \hat{\mathbf{S}}_i, \tag{1.73}$$

where $J < 0$ in the model originally considered by Heisenberg. The consideration of $J < 0$ exclusively presents the reader with an interesting conundrum. It is well-established that the exchange integral for the Heitler-London model incorporating spin is almost always antiferromagnetic, hence why the ground state of molecular hydrogen is the singlet ($S = 0$) spin state. It can be shown that in the case that the overlap integral is zero, ferromagnetic coupling will always be energetically favourable. Such an observation is a key but subtle point. It implies that the Heisenberg model for ferromagnetism is a highly localised model, built upon the already highly localised Heitler-London model, describing interactions between adjacent magnetic centres and thus does not incorporate any covalency effects. Although such a direct exchange mechanism could account for the magnetism of simple ferromagnets, the limitations of Heisenberg's model would become quickly apparent in the late 1940's with the diffraction studies on MnO. In 1949, Shull and Smart using neutron diffraction deduced that the metal monoxide MnO ordered antiferromagnetically, a type of magnetic order proposed by Néel just one year earlier. Not only were the spin-spin interactions antiferromagnetic, all Mn^{2+} magnetic centres were inter-spaced with non-magnetic O^{2-} ligands. Clearly the exchange mechanism underlying antiferromagnetism in MnO was much different to the direct exchange mechanism originally proposed by Heisenberg.

Reflecting the observation that this new exchange mechanism operated over much larger distances compared to its direct counterpart, the mechanism was given the name superexchange and it is this mechanism that is the dominant form of exchange in the magnetic insulators that are investigated in this Thesis.

[¶]It should be noted that it was Dirac, not Heisenberg that first introduced he Hamiltonian in 1928. The key contributions of van Vleck with the inclusion of spin in the Heitler-London model has caused some to call the Heisenberg-Dirac Hamiltonian the Heisenberg-Dirac-van Vleck Hamiltonian instead.

The first investigation on superexchange was performed by Kramers. In 1934, Kramers proposed that spin-dependent perturbations in the wavefunctions of the non-magnetic ligands could be responsible for transmitting the exchange effect over a large distance. In 1950, Anderson proposed a modified Kramers-like approach. This approach is conventionally presented in a collinear arrangement of two Mn^{2+} cations with an intervening O^{2-} ligand. In this particular model, only four electrons must be considered. In the ground state, there are two electrons in the $d\gamma \equiv e_g$ manifold and two electrons in the p_z-orbital. The collinear Mn^{2+}-O^{2-}-Mn^{2+} arrangement results in an overlap of the p_z orbitals of the O^{2-} ligand and the d_{z^2} orbitals on each Mn^{2+}. As a result of the overlap of the atomic wavefunctions, one of the electrons in the p_z orbital can hop into the d_{z^2} orbital of one of the Mn^{2+}, whilst the remaining electron in the p_z orbital enters into a direct exchange with the electron in the d_{z^2} orbital of the other Mn^{2+}. The net result of this particular superexchange mechanism is antiferromagnetic coupling between Mn^{2+} cations. Over the next decade, it was realised that this theory of superexchange appeared as a third order term in perturbation theory. Early terms in this perturbative approach were very large but non-magnetic, whilst the approach was poorly convergent with increasing uncertainties and complexities. In 1959, Anderson proposed a modified theory of the superexchange interaction. In this theory, he considered the role of two molecular orbitals constructed from an admixture of the localised $3d$ metal centres and p orbitals of the intervening negatively charged ligand. The bonding orbital would be mainly occupied by the negative ion, whilst the antibonding orbital would be partially occupied by the $3d$ electrons. This antibonding extends over the negative ion, thus allowing for the possibility of transferring electrons from one $3d$ orbital of one metal centre to another and it is these electrons that result in the presence of magnetism in the system. Anderson pointed out that there are two terms that must be considered. The first is the repulsive Coulomb interaction that prevents such a transition. Commonly denoted as U, this repulsive Coulomb interaction corresponds to the energy increase caused by the placement of a $3d$ electron of one metal centre into an unoccupied site of the neighbouring metal centres. The second term, conventionally denoted by t, corresponds to the transition matrix of the transition of one electron in a metal centre to the neighbour metal centre and may be considered as a kinetic hopping term. In Anderson's modified approach, the first order term in the perturbation theory results in the usual Heisenberg ferromagnetic Hamiltonian, whilst the second-order term gives an

antiferromagnetic exchange

$$4\frac{t^2}{U}\mathbf{S}_1 \cdot \mathbf{S}_2 \equiv 2J_{12}\mathbf{S}_1 \cdot \mathbf{S}_2., \tag{1.74}$$

where $J = 2\frac{t^2}{U}$. It is now well-known that Eq. 1.74 is the Hubbard Hamiltonian in the limit of small $\frac{t}{U}$ [8]. In this particular case, *i.e.* $U \gg t$, the electrons are localised, thus forming an insulator. In contrast, if $U \ll t$, the electrons essentially hop with little hindrance, thus constituting the conduction electrons of a metal. Although it has been deduced that both superexchange and direct exchange share the same general functional form $\hat{H} = 2J_{12}\mathbf{S}_1 \cdot \mathbf{S}_2$, the community up to this point still encountered significant difficulty in evaluating both the magnitude and sign of the exchange constants from first principles.

Throughout the same period of time as Anderson was developing his refined theory of superexchange, Goodenough and Kanamori developed a set of semi-empirical rules for determining the sign and relative strength of the superexchange interactions for a particular set of electronic arrangements on various metal centres placed in given geometric arrangement. Incorporating the effects of orbital symmetry, orbital overlaps and orbital filling, these rules are now known as the Goodenough-Kanamori-Anderson (GKA) rules, or simply the Goodenough-Kanamori rules. For example, these rules predict that two half-filled $3d$ orbitals interacting *via* an overlapping O^{2-} ligand arranged in a collinear manner, *i.e.* the M-O-M angle is 180°, will exhibit strong antiferromagnetic superexchange. In contrast, these rules predict weaker ferromagnetic superexchange for two half-filled $3d$ orbitals interacting *via* an overlapping O^{2-} ligand arranged perpendicularly, *i.e.* the M-O-M angle is 90°.

Despite the perceived underlying complexity of the GKA rules that incorporate multiple aspects of orbital physics, the conclusions of these rules can be obtained pictorially in a relatively straightforward manner. Such a procedure begins by identifying the orbitals of interest and these orbitals depend on both the electron configuration and the bonding geometry. Once the orbitals of interest have been identified, one must determine if the orbitals are orthogonal or not. There are four relevant (dominant) types of relations between the metal centres' orbitals and the p-orbitals of the O^{2-} ligand. These relations are summarised in Tab. 1.2. In the case of orthogonal orbitals, no charge transfer would be possible and direct exchange would be ferromagnetic. Conversely, non-orthogonal orbitals would exhibit charge transfer and direct exchange would be antiferromagnetic. The possibility of charge transfer and type of coupling for each of the four relations

given by Tab. 1.2 are summarised in Tab. 1.3. Examples of the procedure described above are illustrated in Fig. 1.4. Although extremely powerful, the GKA rules are strictly defined in terms of 90° and 180° M-O-M arrangements. In real oxides, the M-O-M angle is rarely exactly 90° or 180°, thus the GKA rules should be treated as a rough guide.

Table 1.2 Relative orbital arrangements for M-O-M 90° and 180° spatial arrangements. $d\epsilon$ denotes the orbitals ($d(xy)$, $d(yz)$ and d_{zx}) belonging to t_{2g} manifold, whilst $d\gamma$ denotes the orbitals ($d_{z^2-r^2}$ and $d_{x^2-y^2}$) belonging to the e_g manifold. Labels σ and π denote p-orbitals that are parallel and perpendicular to the local bonding axis, respectively. Unprimed and primed quantities denote orbitals relative to the first and second metal centres, respectively.

	90°	180°
$d\epsilon \perp p_\sigma$	$p_\sigma(=p'_\pi) \not\perp d\epsilon'$	$p_\sigma(=p'_\sigma) \perp d\epsilon'$
$d\gamma \not\perp p_\sigma$	$p_\sigma(=p'_\pi) \perp d\gamma'$	$p_\sigma(=p'_\sigma) \not\perp d\gamma'$
$d\gamma \perp p_\pi$	$p_\pi(=p'_\sigma) \not\perp d\gamma'$	$p_\pi(=p'_\pi) \perp d\gamma'$
$d\epsilon \not\perp p_\pi$	$p_\pi(=p'_\sigma) \perp d\epsilon'$	$p_\pi(=p'_\pi) \not\perp d\epsilon'$

Table 1.3 Summary of the possibilities of charge transfer at the unprimed site and coupling type for a particular relative orbital arrangement at the unprimed and prime site, respectively. Yes and No denote the possibility and lack thereof for charge transfer, respectively. Labels F and AF denote ferromagnetic and antiferromagnetic coupling, respectively.

Relative Orbital Arrangement	Charge Transfer	Coupling Type
$d\epsilon \perp p_\sigma$	No	F
$d\gamma \not\perp p_\sigma$	Yes	AF
$d\gamma \perp p_\pi$	No	F
$d\epsilon \not\perp p_\pi$	Yes	AF

For the interest of completion, there is a third type of exchange called double exchange that was also discovered in the 1950's by Zener. This particular exchange mechanism assumes that a particular subet of d electrons are highly mobile. These itinerant electrons hop from metal centre to metal centre, resulting in a ferromagnetic coupling of the localised electrons. Such a mechanism is often seen in mixed valence manganate perovskites, where the sole electron in the e_g manifold resulting in ferromagnetic coupling between the localised t_{2g}^3 electrons of both Mn^{3+} and Mn^{4+}.

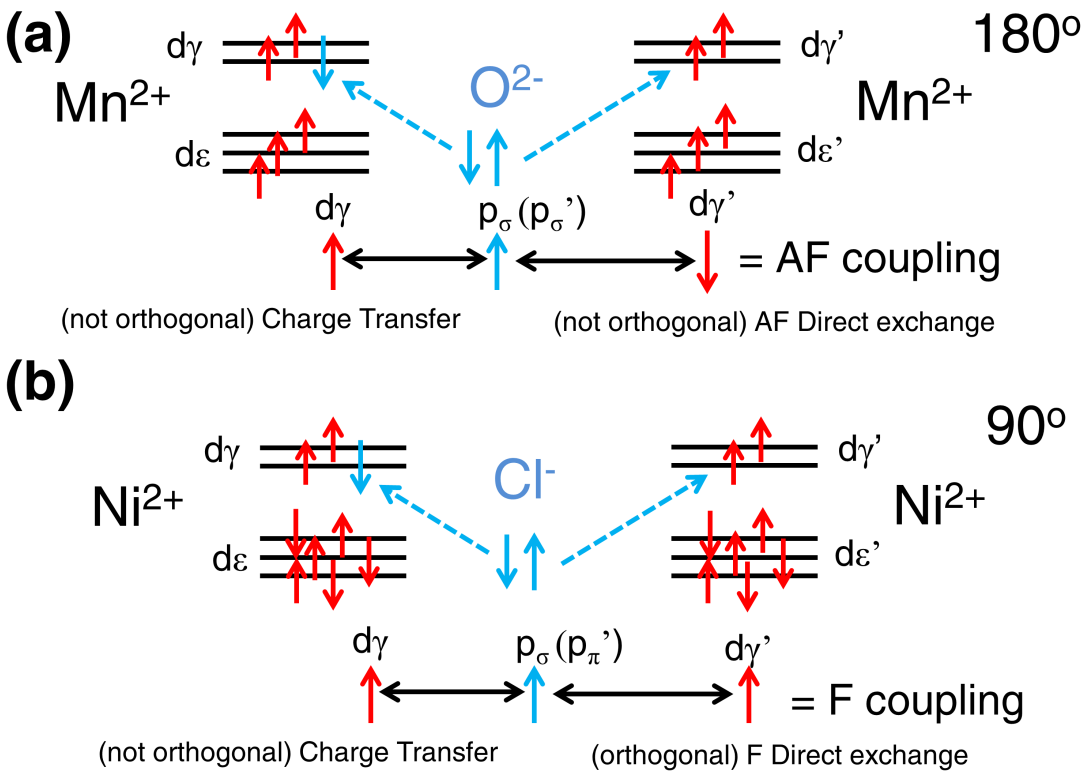

Figure 1.4 Illustration of the determination of the sign of the superexchange coupling in the case of (a) Mn^{2+}-O^{2-}-Mn^{2+} arranged collinearly in MnO and (b) Ni^{2+}-Cl^{-}-Ni^{2+} arranged perpendicularly in $NiCl_2$. In both cases, the ground state electron configuration is determined using Hund's rules. Such a configuration identifies which orbitals are available for charge transfer from the non-magnetic ligands. The requirement of charge transfer determines which p-orbital is employed and based on the M-O-M angle, the relationship between the primed orbitals and thus the type of coupling for the direct exchange can be determined. The overall sign of the superexchange mechanism is determined by comparing the spins from the left to the right.

1.2.3 Crystal Structures

Having provided a general overview of the general physical principles underlying magnetism for the single-ion, and the possible mechanisms by which these magnetic single-ions may interact with one another, the discussion now shifts to how these single-ions and their non-magnetic counterparts are spatially arranged, by providing an introduction to the three crystal structures that are investigated in this Thesis.

As previously alluded to by the introduction of the Goodenough-Kanamori-Anderson rules [53, 54, 56, 57], the three dimensional arrangement of both

magnetic and non-magnetic ions, be it periodic or non-periodic, has a profound effect on a compound's magnetic and non-magnetic properties. Having served as the main motivation for the study of a myriad of phenomena, spanning all fields of the natural sciences, ranging from evolutionary biology to information technology and beyond, the importance of the structure's influence on a compound's physical properties cannot be overstated [46, 65–67]. Even by limiting the discussion to solid state magnetism, the importance of structure is ubiquitous, with significant influences in low dimensional magnets, high temperature superconductors, multiferroics and even frustrated magnets [45, 68, 69]. In addition to its unique historic role, investigations exploring the complex structure-property relationship continue to serve as motivation for the search of exotic and novel phenomena, as evidenced by the rapid development and application of high pressure synthesis and characterisation instrumentation [70, 71] yielding a wealth of exotic behaviours such as magnetic collapse [72]. Most recently, there has been a significant surge of interest in the influence of structure, stemming from the advent of Kitaev physics [27–29]. The continuous search for systems possessing the key ingredients of Kitaev physics (*e.g.* frustration, anisotropic exchange interactions) driven by both significant theoretical and practical interests ensures that the complex, and often subtle structure-property relationship will remain at the forefront of contemporary science for years to come.

$\mathbf{Pr_2Sn_2O_7}$

The rare-earth magnetic oxide $Pr_2Sn_2O_7$ that is the subject of investigation in Chapter 2, crystallises in the pyrochlore structure. This discussion is based on Gardner *et al.* [45], Wiebe & Hallas [71], Ramirez *et al.* [73], Subramanian *et al.* [74] and references contained therein. Any additional references will be stated explicitly in the text. Named after the naturally abundant solid solution $(Na,Ca)_2Nb_2O_6(OH,F)$, the atoms constituting the cubic pyrochlore structure ($Fd\bar{3}m$, S.G. 227/230, Z=8) occupy four unique special Wyckoff positions. For magnetic pyrochlore oxides with the chemical formula $A_2^{3+}B_2^{4+}O_7$, such as $Pr_2Sn_2O_7$, either the trivalent A or tetravalent B or both are magnetic. The A^{3+} and B^{4+} cations occupy the 16d and 16c positions with cubic and octahedral coordination by O^{2-}, respectively. The atomic arrangement is completely specified with the only variable positional parameter being the coordinate x along the a crystallographic axis for the O^{2-} occupying the 48f position. The value of x determines the specific shape of the coordination polyhedra for both the 16d

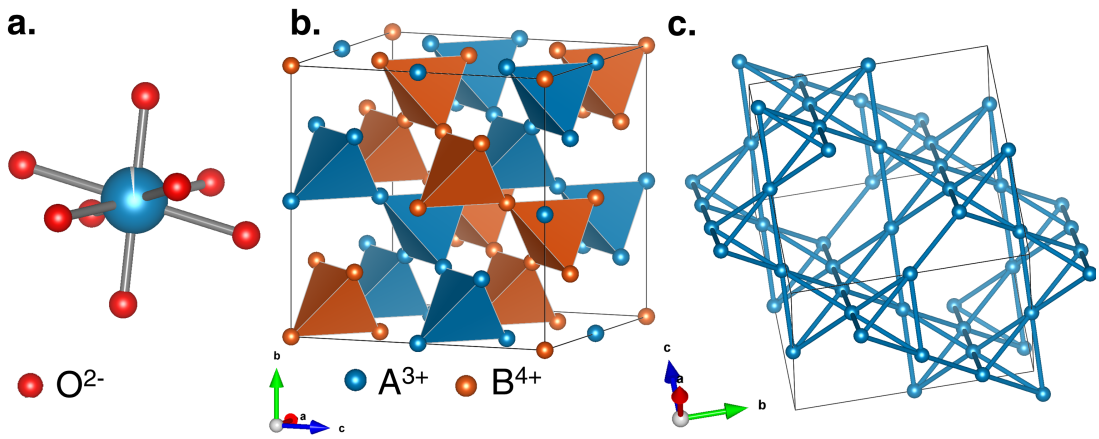

Figure 1.5 Summary of the main structural elements of the pyrochlore ($Fd\bar{3}m$, SG: 227/230) unit cell. (a) Coordination geometry about the A^{3+} site composed of short O′-A-O′ bonds oriented orthogonal to a puckered hexagonal ring of oxygen atoms. (b) Isometric view of the pyrochlore unit cell consisting of two interpenetrating A^{3+} (blue) and B^{4+} (red/orange) sublattices (A=*f*-block and B=*d*- or *p*-block metals in this Thesis), each corresponding to a network of corner-sharing tetrahedra. (c) A^{3+} sublattice displaying alternating Kagomé and triangular planar layers along [111]. The structural motifs summarised in panels (b) and (c) emphasise that the pyrochlore structure is highly susceptible to geometric frustration. Their propensity for geometric frustration, combined with their variability of host cations, has given the pyrochlores a key role in the search for novel magnetic ground states. For the purposes of clarity, oxygen atoms have been excluded from panels (b) and (c).

and 16*c* sites with values of 0.3125 and 0.375 representing perfect (undistorted) octahedral and cubic polyhedra, respectively. Since a single value of x cannot satisfy both ideal coordination polyhedra simultaneously, the value of x assumes an intermediate value correlated to a combination of the ionic radii for both cations with the unit cell's lattice parameter a, resulting in the distortion of both coordination polyhedra.

The presence of such distortions, particularly about the A^{3+} cation where distortions tend be much greater, has been shown to have important consequences in the fundamental properties of the magnetic pyrochlore oxides. One of the most important consequences of the distortion about the A^{3+} cation can be rationalised by employing an alternative view of the local coordination. As illustrated in Fig. 1.5(a), the distorted cube can be thought of consisting of six O ligands forming a puckered or buckled hexagon with two O′ ligands forming a linear O′-A^{3+}-O′ chain that is located orthogonal to the average plane of the buckled hexagon. These short A^{3+}-O′ bond distances, some of which are among the shortest experimentally observed for rare earth oxides, introduce significant axial symmetry directed along the local ⟨111⟩, strongly influencing the local crystal

field configuration that often dictates the low temperature properties for many of these pyrochlores.

As illustrated in Fig. 1.5(b), the three dimensional arrangement of the A^{3+} and B^{4+} cations each form a network of corner-sharing tetrahedra, which in turn interpenetrate one another, forming the quintessential framework for a geometrically frustrated lattice. The propensity of the pyrochlore lattice towards geometric frustration can be further emphasised in Fig. 1.5(c) by viewing the pyrochlore lattice in the [111] crystallographic direction where the A^{3+} and B^{4+} cations each form alternating triangular and Kagomé layers, two prototypical examples of two-dimensional frustrated motifs. Both the interpenetrating network of corner sharing tetrahedra and the stacked triangular and Kagomé motifs along [111], demonstrate that the pyrochlore lattice is highly susceptible to geometric frustration. Corresponding to a situation where the relevant interactions are incompatible with the geometric constraints of the underlying crystal symmetry, geometric frustration, particularly in the case of magnetic systems, has provided the community with many exotic and often novel ground states.

The particular interest in the magnetic pyrochlore oxides, stems from the large number of combinations of diverse elements occupying the A^{3+} and B^{4+} positions, a number that is continuously increasing with rapid advances in material preparation. With such a large variety of exotic and sometimes novel magnetic behaviour stemming from a combination of a large stability field in the presence of a highly frustrated lattice, the magnetic pyrochlore oxides have captured a significant amount of interest in the condensed matter community. The magnetic ground states observed in these oxides vary significantly depending on the specific cation combination, from long-range ordered magnetic states to spin glasses to short-range ordered magnetic states that include spin liquids and spin ices.

α-$\mathbf{CoV_3O_8}$

The α-CoV_3O_8 structure (*Ibam*, S.G. 72/230, $Z = 8$) that is the subject of investigation in Chapter 3 is the least common among the four structures that are encountered in this Thesis. This discussion is based on Oka *et al.* [75], Wallington *et al.* [76], Kim *et al.* [77] and references contained therein. Any additional references will be stated explicitly in the text. In contrast with the vanadium oxide bronzes, members of the M−V−O family where M=alkali or alkali earth metal, the orthorhombic unit cell of α-CoV_3O_8 exhibits a framework

consisting of both V−O and M−O polyhedra.

Just as is the case for other members of the M−V−O family where M is a *d*-block metal such as Zn^{2+}, there are three distinct polyhedra in the α-CoV_3O_8 structure: MO_6 octahedra, where M=Co^{2+} or V^{4+}(1), each with $\frac{1}{2}$ occupancy, $V^{5+}(2)O_4$ tetrahedra and $V^{5+}(3)O_5$ trigonal bipyramids. As illustrated in Fig. 1.6(a), the MO_6 octahedra are edge sharing, employing two different pairs of oxygens, O(2)-O(3) and O(6)-O(6), respectively. The alternating use of the two different edges results in zig-zag chains running along the crystallographic *c* axis that are connected along *b* *via* oxygen O(5) vertices. Within these chains, there are no restrictions on the distribution of metal cations M, in contrast to its *Iba*2 counterpart where M^{2+}, such as Zn^{2+}, and V^{4+} cations alternate. Although the distribution within an individual chain may be effectively considered as random, adjacent chains behave as "mirror images" of one another with one M^{2+} and one V^{4+} being located on the opposite metal sites of the O(5) vertex, as summarised by Fig. 1.6(b). Such a local selection rule exists for both *Ibam* and its *Iba*2 counterpart and results in a relative occupancy of $\frac{1}{2}$ for both magnetic cations in the metal site and an overall chemical formula of MV_3O_8.

Within the *ab* plane (Fig. 1.6(c)), dimers of $V(3)O_5$ trigonal bipyramids are connected *via* the O(4)−O(4) edge with two $V(2)O_4$ tetrahedra attached to each O(4) oxygen on opposite sides. The combined $V(2)O_4$−$V(3)O_5$−$V(3)O_5$−$V(2)O_4$ unit connects the octahedral slab defined by the MO_6 octahedra in the *ab* plane. The zig-zag arrangement of the MO_6 octahedra along *c*, combined with the $V(2)O_4$−$V(3)O_5$−$V(3)O_5$−$V(2)O_4$ connectivity in the *ab* plane defines large hexagonal shaped tunnels running along *c* with potential electrochemical applications. It should be noted that Casalot & Hagenmuller [78] reported that CoV_3O_8 crystallised in a high temperature β-structure above 650^{o}C with a monoclinic $C2/m$ (S.G. 12/230) unit cell similar to that exhibited by MgV_3O_8. Both follow-up studies reported in the literature and the investigation comprising Chapter 3 failed to reproduce such a high temperature β-phase and thus shall not be discussed any further.

As is the case for many Cobaltates, the magnetic Co^{2+} cations in the α-CoV_3O_8 structure are arranged in pseudo-one dimensional chains. Cobaltates with lower dimensionality, particularly those containing a one dimensional chain structure (*e.g.* $CoNb_2O_6$ [63]), exhibit a plethora of exotic behaviour including: quantum criticality, large anisotropy, magnetisation plateaus and field-induced spin order-disorder transitions. Although the physical origins for such rich physics is still under investigation, a recent investigation on the cobalt vanadates α-

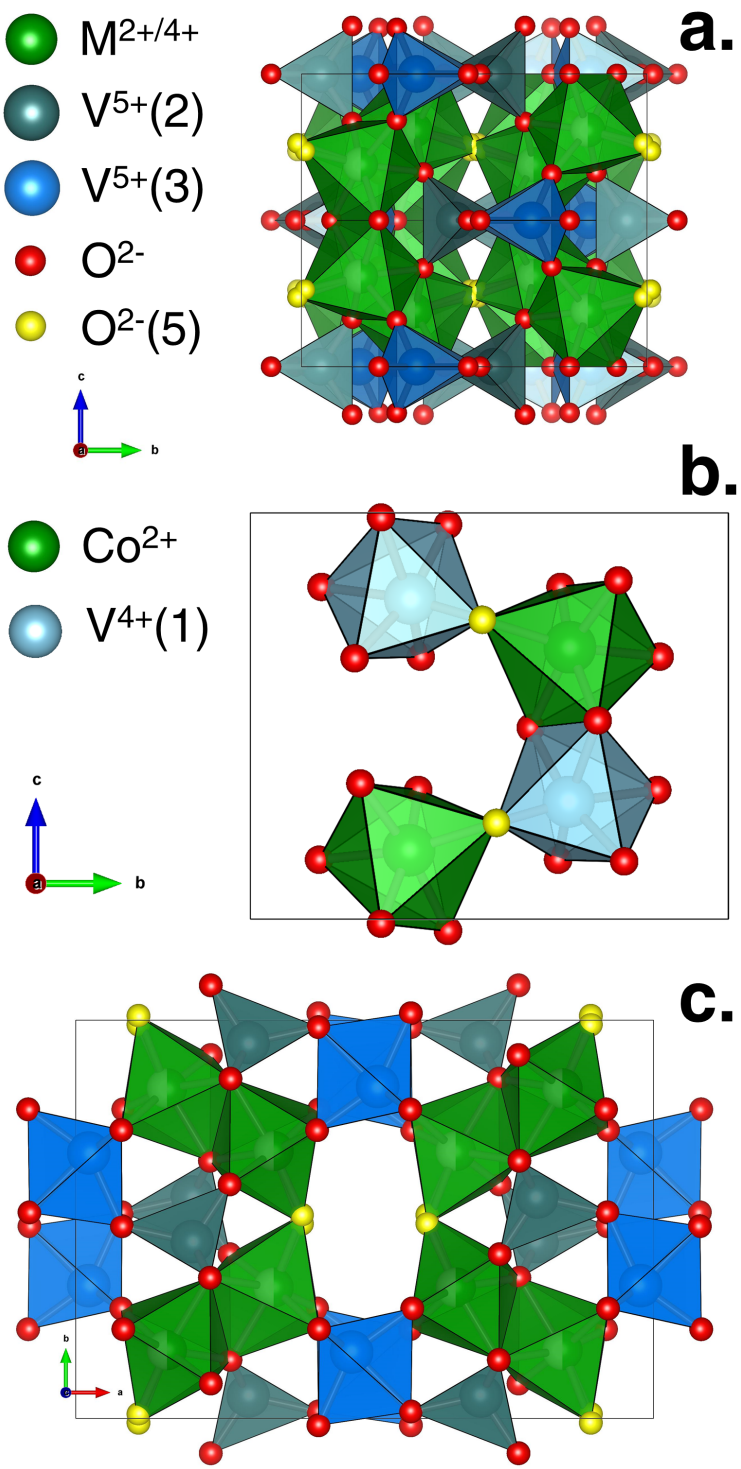

Figure 1.6 (a) Proposed crystal structure of α-CoV_3O_8 (*Ibam*, S.G. 72/230) along the *bc* plane. (b) Local constraint of the *Ibam* structure. Metal sites opposite of the bridging O(5) must be occupied by one Co^{2+} and one V^{4+}, with the O(5) situated closer to the V^{4+} site. (c) Proposed crystal structure of α-CoV_3O_8 along the *ab* plane.

CoV_2O_6 and γ-CoV_2O_6 has revealed the importance of octahedral distortions in the presence of strong spin-orbit coupling. GGA + η DFT calculations confirmed the sensitivity of the crystal field scheme with respect to both the O−Co−O distances and angles. A significant compression along the local z-axis, combined with a deviation of the angle ϕ away from the ideal 90°, led to both an increase in the orbital moment contribution and the introduction of strong Ising anisotropy. Such distinct single-ion anisotropy introduced by axial compression, combined with strong spin orbit coupling, provides a natural explanation for the similarities (*e.g.* missing magnetic entropy) and differences (*e.g.* direction of anisotropic easy axis) in the properties exhibited by α-CoV_2O_6 and its less distorted counterparts such as γ-CoV_2O_6 and $CoNb_2O_6$. In the case of α-CoV_3O_8, the reported structure indicates that the CoO_6 octahedra are not significantly distorted, as illustrated in Fig. 1.7.

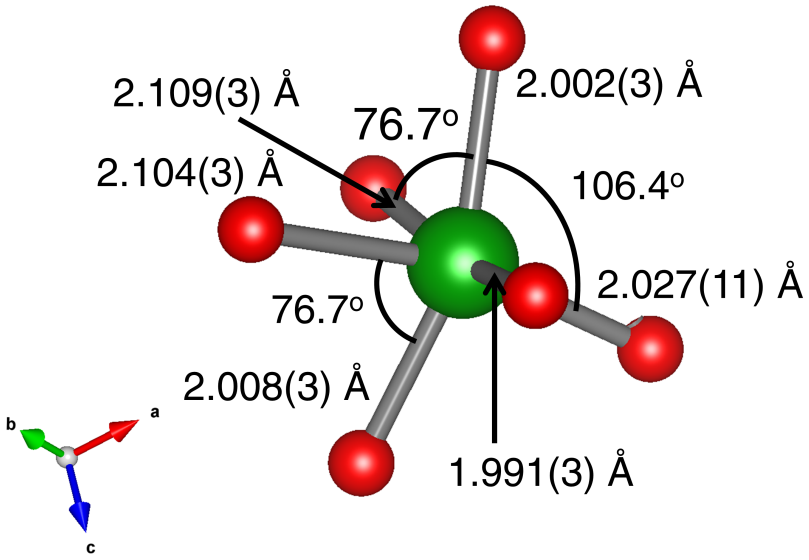

Figure 1.7 Proposed [79] trigonal distortion of CoO_6 octahedra in α-CoV_3O_8.

The distortion of the local octahedra can quantified by the parameter δ defined by

$$\delta = \frac{1}{\mathcal{N}} \sum_i \left\{ \left(\frac{d_i - \langle d \rangle}{\langle d \rangle} \right)^2 \times 10^4 \right\}, \tag{1.75}$$

where $\mathcal{N} = 6$ and $\langle d \rangle$ denotes the average distance [76, 80]. With a minor trigonal

distortion, combined with angular deviations of ±15°, resulting in an octahedral distortion parameter $\delta \sim 6$, α-CoV_3O_8 appears to belong to the weakly distorted regime that includes γ-CoV_2O_6 with $\delta = 2.1$ and 4.8, opposite to that of α-CoV_2O_6 with a $\delta = 55$. As discussed in Chapter 3, the refined structure obtained from single crystal and x-ray diffraction confirms that α-CoV_3O_8 possesses slightly distorted CoO_6 octahedra with a $\delta = 11$, placing it within the γ-CoV_2O_6 regime. The absence of significant octahedral distortions for this particular sample is supported by (i) an ordered moment of $3.5\mu_B$, a value that is much closer to the spin-only moment of $3\mu_B$, (ii) the anisotropic easy axis being directed along the chain, and (iii) the excitation spectrum being described as pure j_{eff} states that are consistent with a $^4T_{1g}$ ground state configuration, all properties exhibited by the γ-polymorph and other less distorted 1D Cobaltates.

CoO

The transition metal monoxide CoO and its magnetically diluted analogue $Co_{0.03}Mg_{0.97}O$ that are investigated in Chapters 4 and 5, respectively, both crystallise in the NaCl structure at room temperature. This discussion is based on a combination of Smart & Moore [81], Jauch *et al.* [82], Tomiyasu [83], Tombs & Rooksby [84] and the references contained therein. Any additional references will be stated explicitly in the text. Commonly referred to as rock salt, the cubic NaCl structure ($Fm\bar{3}m$, S.G. 225/230, Z=4) presented in Fig. 1.8 consists of atoms A and B occupying two unique special crystallographic positions 4*a* and 4*b*, respectively. The three dimensional atomic arrangement of atoms A and B is completely specified with no variable position parameters. The structure may be regarded as two inter-penetrating face-centered cubic lattices with each lattice composed of atoms occupying a particular crystallographic site. Alternatively, the NaCl structure can be described as a cubic closed-packed array of atom B with the atom A site filling all the octahedral holes or *vice versa*. With both atoms A and B being in octahedral coordination, the NaCl structure is commonly regarded as being composed of a three dimensional network of edge-sharing AB_6 or BA_6 octahedra, a subtle observation that will prove to play a key role in Chapters 5 and 6. Despite its simplicity, many compounds assume the NaCl structure including: most alkali halides, all alkali hydrides and many divalent metal oxides and sulphides. With the combination of its structural simplicity and its ability to host a large number of possible combinations of diverse elements, the NaCl structure has played, and continues to play a significant role in fundamental

and applied scientific research, in addition to its unique pedagogical value in the classroom.

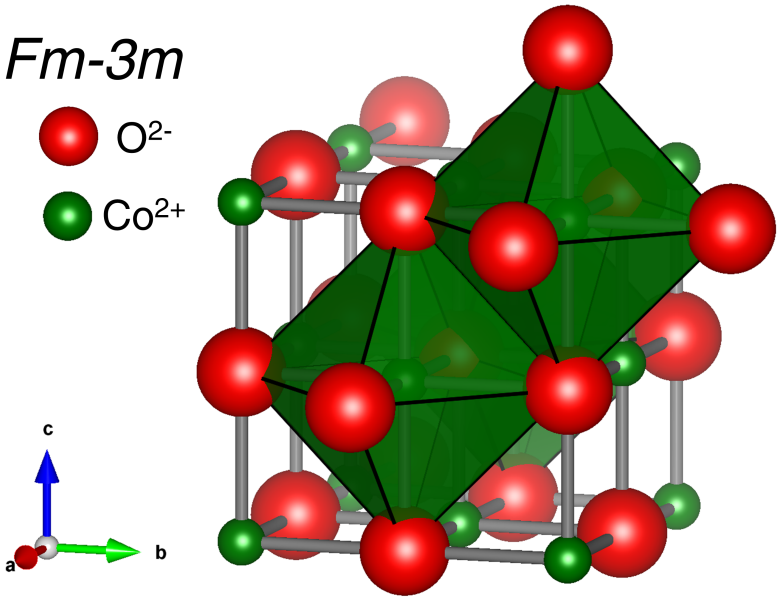

Figure 1.8 Isometric view of the high temperature rocksalt unit cell of CoO with an emphasis on the edge-sharing CoO_6 octahedra.

In the 1950's, the first neutron diffraction experiments on CoO revealed a significant tetragonal distortion ($\frac{c}{a} < 1$) accompanying long range antiferromagnetic order. Such a distortion is not only expected for the Jahn-Teller active high spin d^7 Co^{2+} but is consistent with a refined crystal field theory that was established by Goodenough [85]. Incorporating spin-orbit effects, Goodenough demonstrated that for systems with triple degeneracy in the t_{2g} channel, there was a competition between a pure static Jahn-Teller distortion and a magnetostrictive static distortion. In the case of T_{1g} configurations with spin-orbit coupling constants $\lambda < 0$, such as high spin Co^{2+}, a tetragonal ($\frac{a}{c} < 1$) distortion at a temperature $T \approx T_N$ is preferred, corresponding to an axial distortion parameter $\Gamma_z < 0$, opposite to what is observed in thin films. The negative distortion parameter results in the stabilisation of the $m = \pm 1$ states, whose degeneracy is ultimately lifted by spin-orbit coupling. The tetragonal distortion at $\sim T_N$ is a cooperative effect that is mediated by the orbital ordering as determined by spin-orbit coupling and thus its presence has important consequences on the magnetism of these triply degenerate systems such as the introduction of single-ion anisotropy and magnetostriction to any spin order.

Throughout the following decades, multiple studies suggested that the low

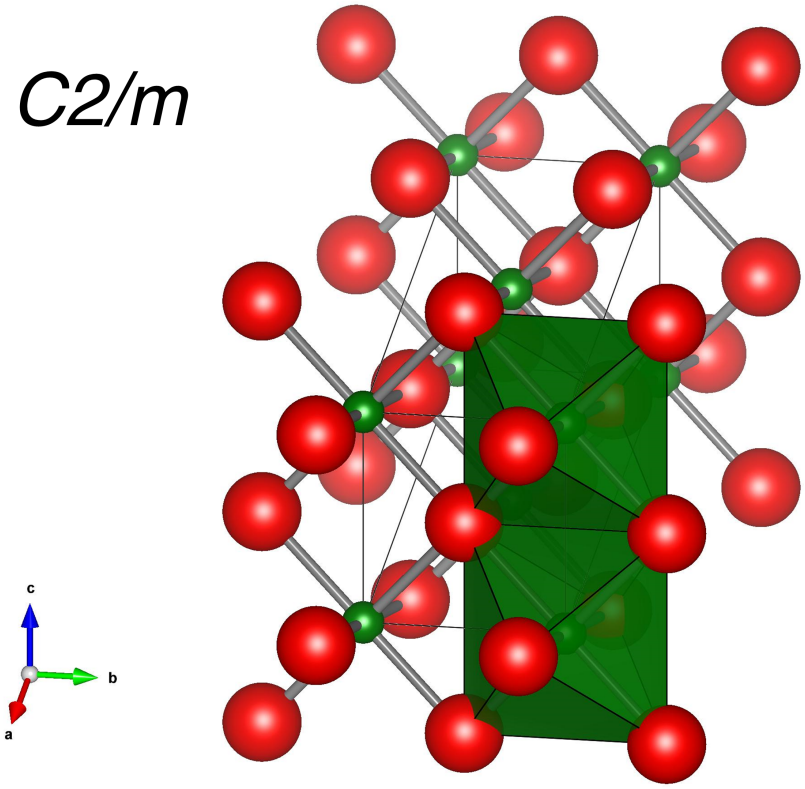

Figure 1.9 Isometric view of the low temperature monoclinic $C2/m$ unit cell of CoO with an emphasis on the edge-sharing CoO_6 octahedra.

temperature unit cell was not purely tetragonal but rather monoclinic. It was not until 2001 that high-resolution synchrotron and neutron powder diffraction confirmed that CoO crystallises in the monoclinic $C2/m$ space group (S.G. 12/230) below T_N, in agreement with the original suspicions of Saito *et al.* [86]. As illustrated in Fig. 1.9, the low temperature monoclinic unit cell consists of Co^{2+} and O^{2-} occupying two unique special Wyckoff positions $2a$ and $2d$, respectively. Although the formal description of the unit cell is the monoclinic structure ($C2/m$, $Z = 2$), a common approach is to describe the unit cell in terms of a deformed NaCl structure type ($Fm\bar{3}m$, $Z = 4$). In a similar manner to the high temperature NaCl structure, the Co^{2+} cations are still in octahedral coordination with the overall three dimensional structure composed of a three dimensional network of edge-sharing octahedra exhibiting rhombic distortions, predominately along the axial direction. Although the cubic-to-monoclinic transition and the accompanying rhombic octahedral distortion do contribute to the rich magnetic behaviour of CoO in the Néel state, it will be shown that such distortions do not have a significant effect on the final conclusions of the two investigations involving CoO. In the case of $Co_{0.03}Mg_{0.97}O$ in Chapter 4, chemical dilution results in the

absence of magnetic ordering and thus a lack of a crystallographic distortion away from the cubic rocksalt structure. In Chapter 5, the low energy magnetic excitations are shown to be fully captured using a multi-level spin wave theory employing a cubic unit cell. Such observations do not imply that the distortions present in CoO have no influence on its properties in the Néel state, in fact there is some evidence that such distortions may play a key role in the refinement of the calculated models, possibly comprising future investigations. As is the case for α-CoV_3O_8, the experimental data suggests that perhaps other energy scales such as the exchange and spin-orbit coupling may be more relevant and thus enough for a fundamental description of the low temperature magnetic properties, as has been shown to be the case for many Cobaltates.

1.2.4 Sample Preparation

Having introduced the three crystal structures of interest, the experimental techniques involved in their preparation will now be discussed. In this Thesis, both polycrystalline and single crystal samples have been prepared. Whereas both are composed of crystallites, regions where constituent atoms are arranged in an ordered pattern based on one of the unit cells described above, the spatial extent for the former is limited to the scale of μm, whilst the latter extends to mm or larger [81]. Both polycrystalline and single crystal samples play central key roles in materials science. Polycrystalline samples are traditionally much easier to synthesise in large quantities with high purity, which is particularly advantageous when employing experimental probes with limited flux, such as is the case for inelastic neutron scattering [87]. Although useful for initial exploratory investigations, the random orientation of the crystallites in polycrystalline samples often obscure the rich physics through "powder averaging" and other effects such as grain boundaries, whilst preventing the ability to probe the properties of the microscopic interactions that underlie complex and often emergent behaviours [88]. In contrast, single crystals, with their extended spatial array of ordered atomic arrangement, have been responsible for not only establishing a much deeper understanding of previously probed physics (*e.g.* high-temperature superconductivity), but has also opened completely new avenues for future research (*e.g.* magnetocrystalline anisotropy, predicted novel emergent correlated electronic states) [89]. In this final subsection, the experimental techniques involved in the preparation of both polycrystalline and single crystal samples investigated in this Thesis are discussed.

Polycrystalline Samples

All experimental investigations comprising Chapters 2-5 involved the synthesis of both polycrystalline precursors and final products. These samples were synthesised using either the ceramic or sol-gel method. This discussion is based on Rao [90], Rao & Biswas [91], Danks [92] and Smart & Moore [81].

Involving the heating of a mixture of the relevant reagents, the ceramic method is based on the physical principle that given enough energy, two materials in contact with the correct orientation will react and form the desired product at the contact interface. The simple physical principle, combined with its amenability towards experimentation, has made the ceramic method arguably the most common method of synthesis in the solid state and has been used to produce a plethora of oxides, sulfides, phosphides, chalcogenides and many others.

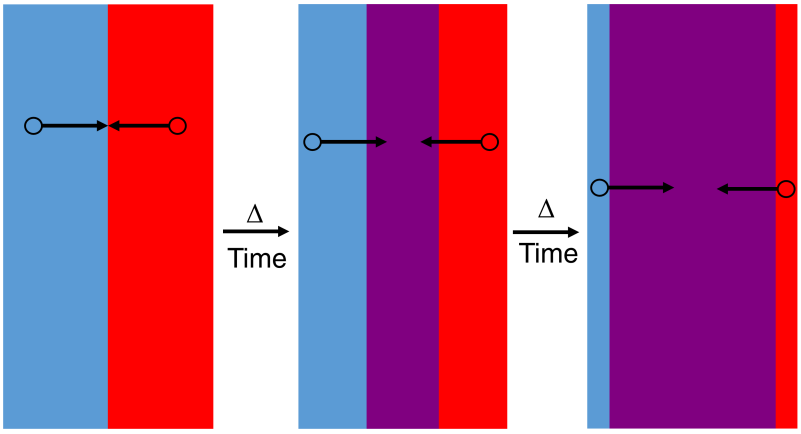

Figure 1.10 Pictorial representation of the physical mechanism underlying the ceramic method. In presence of high temperatures over time, the constituents' components, labelled by blue and red, respectively, react with one another at the contact interface forming the desired product (purple). As the reaction proceeds, its individual components continue to diffuse and react, resulting in an increase in the product's size. The increase in size results in the product behaving as an effective "buffer", slowing the reaction down due to an increase in average diffusion lengths.

Despite its ubiquity and far reaching applicability, the ceramic method does suffer from significant disadvantages, mostly stemming from the requirements of physical contact with sufficient kinetic energy. In the case when no melt is formed, the reaction must occur entirely in the solid state, beginning at the contact interface and proceeding by the diffusion of the constituent components.

As the reaction proceeds, the product phase increases in size. As illustrated in Fig. 1.10, the product phase behaves as a type of "buffer", and its growth results in a longer diffusion path for the constituents, and thus slowing the rate of reaction. The reduction of the reaction rate may result in an incomplete reaction, corresponding to the concurrent presence of both product and unreacted reagents or compositional inhomogeneity, problems that may be further exacerbated by secondary reactions with the container (*e.g.* crucibles, quartz tubes).

In order to address the limiting step of diffusion, the procedure constituting the ceramic method has been adapted to include multiple repetitions of thorough grinding, pelleting and heating in a variety of containers. The process of grinding, accomplished by either a mortar and pestle or a ball mill, not only increases chemical homogeneity, but also decreases particle size, thus maximising the surface area available for reaction. The process of pelleting, accomplished by a hydraulic press, reduces the distance between the constituent components and maximises the number of crystallite faces in direct contact. Heating, accomplished by resistance, laser, electric arc or skull techniques, is used to increase the kinetic and thermodynamic favourability of the reaction, whilst the choice of container (*e.g.* chemical composition of crucibles) prevents the occurrence of any secondary reactions. Finally, by repeating the three aforementioned processes, fresh crystallite faces are brought into direct contact, thus significantly increasing the rate of reaction, whilst minimising chemical inhomogeneity.

So far, the ceramic method discussed above involve heating reagents in air, *i.e.* under ambient atmospheric conditions. With its rich O_2 content, air often prevents the formation (or retention) of lower oxidation states such as +4 in the case of vanadium, particularly at high temperatures. As discussed in Chapter 3, the oxidation of V^{4+} to the preferred V^{5+} was accomplished by performing the ceramic method *in vacuo*. The experimental setup is summarised in Fig. 1.11 and involves the placement of a mixture of reagents in an evacuated quartz ampoule. By establishing an airtight seal, the heat treatment constituting the last step of the ceramic method may be performed in the absence of any significant amount of oxygen. An additional advantage of performing the reaction *in vacuo* is that the chemical system behaves as if it is closed. Such behaviour is particularly beneficial when volatile reagents are involved, a common concern for many solid state reactions due to the need for high synthesis temperatures.

The use of high temperatures in the ceramic method, an experimental necessity due to the large lattice energies of ionic compounds, for some reactions can often be reduced by the use of reagents that decompose whilst heating

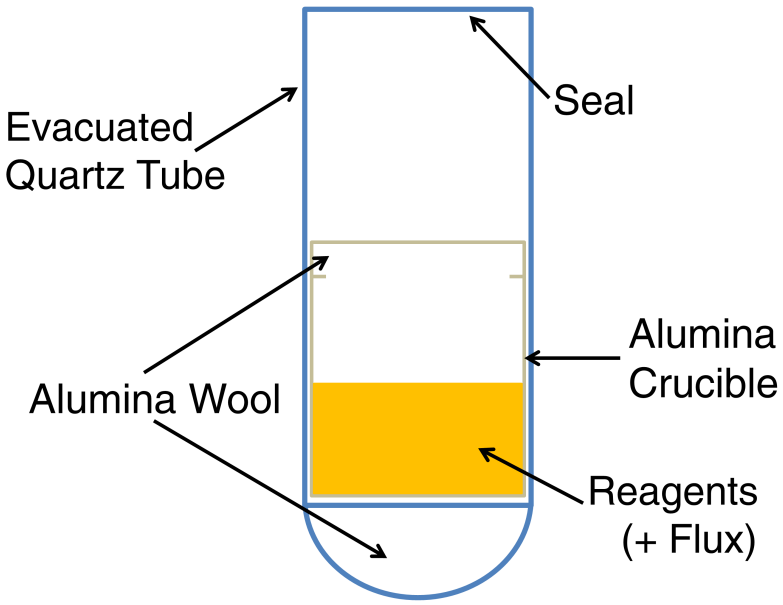

Figure 1.11 Schematic of a chemical reaction performed *in vacuo*. In this Thesis, all reagents (and flux) were placed in an alumina crucible. The crucible was placed inside a quartz tube that was evacuated using a combination of a mechanical and a turbo pump. After evacuating the tube for 24 h to a pressure of 0.07 mTorr, the tube was sealed using a blow torch of propane and oxygen. Alumina wool was used as a buffer on the bottom as compensation for the different thermal expansion coefficients for the quartz tube and alumina crucible. Extra wool was placed over the top as compensation for higher volatility of some reagents (*e.g.* V_2O_5). In the case where reagents have significant volatility, an extra crucible may be placed over the alumina wool, behaving as an effective "cap".

or following topotactic synthesis routes. A commonly used solution-based alternative to the solid state ceramic method is called sol-gel. Playing a key role in Chapter 4, the sol-gel technique requires much lower synthesis temperatures compared to the traditional ceramic method. The depression of the synthesis temperature is accomplished by the reduction of the average particle size. In some cases, the reduction of size corresponds to two orders of magnitude, resulting in a depression of hundreds of degrees relative to those observed for traditional solid state methods.

The particular variation of the sol-gel technique used in this Thesis is composed of three main steps that are summarised in Fig. 1.12. The first step consists of the addition of metal salts to a solvent (*e.g.* ethanol) providing the metal cations and oxide anions, respectively, in the final desired product. The choice of solvent, temperature and pH is crucial as to prevent any precipitation. In the presence of constant stirring, a reaction between the metal salts and the solvent constituting the original homogeneous solution results in the formation of

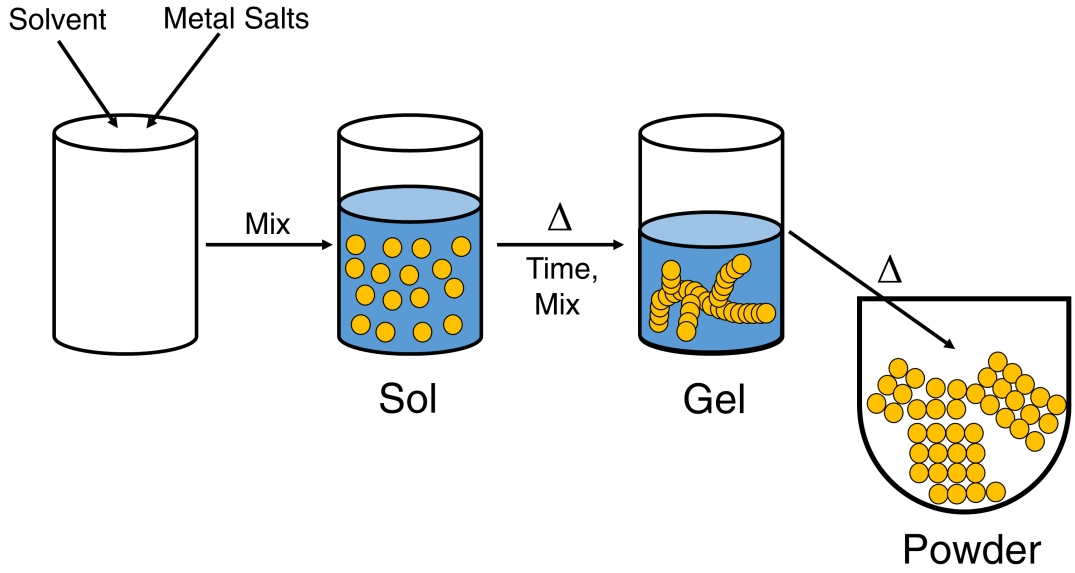

Figure 1.12 Schematic of the three main experimental steps constituting the sol-gel process. The creation of the sol from a combination of metal salts and solvent is followed by a heat treatment under moderate temperatures to create the gel. Constituting a continuous and porous metal oxide network covered by liquid co-products, the sol is sintered to collapse the gel network into a dense ceramic.

metal hydroxides. The solution of metal hydroxide products, organic co-products and remaining solvent is called the *sol*. The sol is either left alone (termed *ageing*) or is heated under moderate temperatures. Through ageing or heat treatment, the sol is converted to the *gel*, consisting of a continuous and porous metal oxide network covered by a liquid phase containing organic co-products and any remaining solvent. Finally, by sintering the gel at high temperatures, both the undesired volatile co-products and solvent are removed, whilst densification and decomposition of the gel results in the collapse of the gel inorganic network into a glass or a dense ceramic. The benefits of the sol-gel is that the technique does not rely on precipitation which may leave select ions remaining in solution. Instead the technique enables mixing at the atomic level, whilst yielding smaller particles that are easily sinterable, implying greater control in chemical stoichiometry and propensity for chemical homogeneity.

Single Crystal Samples

For the experimental investigations outlined in Chapters 3 and 5, single crystals of α-CoV_3O_8 and CoO were grown using flux growth and optical float

zone techniques, respectively. The discussion is based on Fisk [93], Canfield & Fisk [94], Scheel [95], Schmehr & Wilson [89], and references contained therein. Any additional references will be stated explicitly in the text.

Flux growth is a high temperature solution-based crystal growth technique consisting of the dissolution of the constituents of the desired crystal (solutes) in a suitable solvent (*flux*). In this Thesis, as is the case for many flux growths reported in the literature, the flux consists of a single or combination of molten salts or oxides. The choice of the word flux is a reflection of the depression of the solutes' melting temperature due to the presence of the solvent. Crystallisation occurs as the mixture of the solute(s) and the flux becomes critically supersaturated. In this Thesis, supersaturation was accomplished by reducing the temperature in a controlled manner. As the solutes begin to crystallise either by spontaneous nucleation or *via* a seed crystal, the solute concentration in the solution and correspondingly the saturation temperature decreases. In this Thesis, the crystallisation process was continuously repeated as the system was cooled and artificially terminated by quenching.

As a consequence of the relative "simplicity" of the physical principles underlying the crystallisation process, the flux growth technique has widespread applicability. With the exception of compounds that decompose at relatively low temperatures (*e.g.* organics, hydrates), the flux growth technique, in principle, could be used to grow single crystals, assuming the use of a proper solvent and optimised experimental conditions. Crystals grown using the flux growth technique are particularly widespread in industry with applications varying from communications to semi-conductors to non-linear optics. The widespread applicability of the flux technique ultimately reflects its numerous advantages over other crystallisation techniques. The majority of which stem from the use of lower temperatures and the lack of stark temperature gradients resulting in the crystal growth that is not bound by thermal and mechanical constraints, yielding better crystal quality with respect to equilibrium defects including: point defects, dislocation densities and low-angle grain boundaries, particularly for materials composed of volatile constituents, materials with very high vapour pressures near their melting temperature and those materials that melt incongruently.

Despite the clear advantages of flux growth, it has been considered traditionally a secondary alternative to other techniques, particularly to those that are melt-based, thus hindering the spread of its use in both academia and industry. A driving force for such attitudes is a combination of the numerous disadvantages posed by the technique. These disadvantages include:

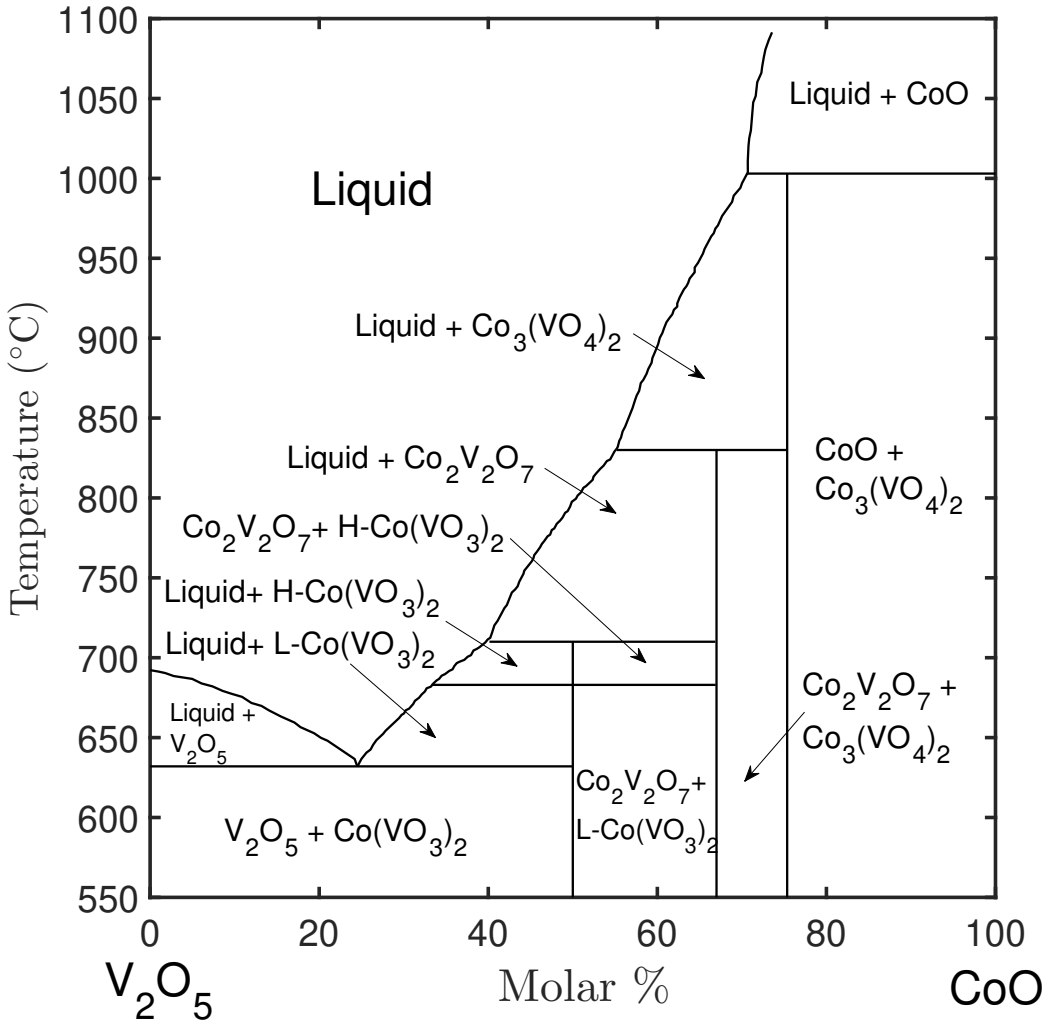

Figure 1.13 Binary V_2O_5-CoO phase diagram [96]. L-CoV_2O_6 and H-CoV_2O_6 denote low temperature γ-CoV_2O_6 and high temperature α-CoV_2O_6 polymorphs, respectively [76].

substitutional or interstitial substitution of the solvent ions into the crystal, microscopic and macroscopic inclusions of the solvent, secondary reactions with the container, slow growth rate, small crystal size and the need for precise and detailed phase diagrams such as the one illustrated in Fig. 1.13. As is the case for all other crystal growth techniques, all these disadvantages may be remedied by a combination of experience, cost and time, resulting in a combination of optimised choices for flux, container and cooling routine. In the case of α-CoV_3O_8 in Chapter 3, a V_2O_5 flux was chosen due to a combination of high solute solubility at moderate temperatures ($T \leq 800$°C), and the fact that V_2O_5 being one of the solutes minimises any issues with chemical composition. The use of moderate temperatures not only permitted the use of quartz ampoules but also reduced the

amount of solvent evaporation and secondary reactions with the alumina crucible. A slow cooling rate of $1°C \cdot hr^{-1}$ was chosen to reduce the supersaturation ratio resulting in a slower growth rate from fewer nucleation centres, resulting in larger single crystals that contain fewer solvent inclusions.

One of the techniques that often supersedes flux growth in terms of preference is a particular variant of zone melting, called the optical floating zone (OFZ) technique. As illustrated in Fig. 1.14, the melt-based technique consists of melting a translatable section of a precursor which is usually the desired crystal, but in polycrystalline form, and compressed into cylindrical rods. In the case of the OFZ technique, the feed polycrystalline rod is vertically suspended over either a seed polycrystalline rod or a seed crystal of the desired final product. Ellipsoidal mirrors focus light from optically-based heating sources, typically halogen lamps, onto a small volume constituting the bottom of the feed rod, creating a localised molten zone. The feed rod and seed rod/crystal are subsequently joined, thus creating the "working" molten zone. Both the feed rod and seed rod or crystal are counter-rotated to facilitate thorough mixing of the melt, whilst minimising non-uniformities in the transverse optical plane. By translating the feed rod and seed rod or crystal through the optical focal plane, the molten zone translates up the feed rod, melting more polycrystalline precursor at the melt edge, whilst the material left behind at the growth edge cools, crystallising into the desired single crystal.

Despite the clear disadvantages associated with the use of high temperatures such as the need for expensive equipment, propensity for thermal and mechanical strain, and concentration gradients, its numerous and often unique advantages have made the OFZ technique one of the leading and most widely used single crystal growth techniques in the modern laboratory. One of the main advantages is that the vertically suspended molten zone is maintained by surface tension alone, eliminating the need of a container and with it, the undesired possibilities of contamination and secondary reactions. Other advantages of the OFZ technique include: relatively fast growth rates, the ability to incorporate a flux within the growth process *via* a travelling solvent; while the reaction conditions such as temperature, temperature gradients, growth atmospheres and pressures, can be readily optimised *in situ*, often yielding high purity crystals with dimensions on the order of centimetres for certain systems.

Despite the ability of other techniques to grow much larger crystals, the crystal sizes and sample quality commonly grown using the OFZ technique are well-suited for materials research, naturally compatible with a myriad of experimental

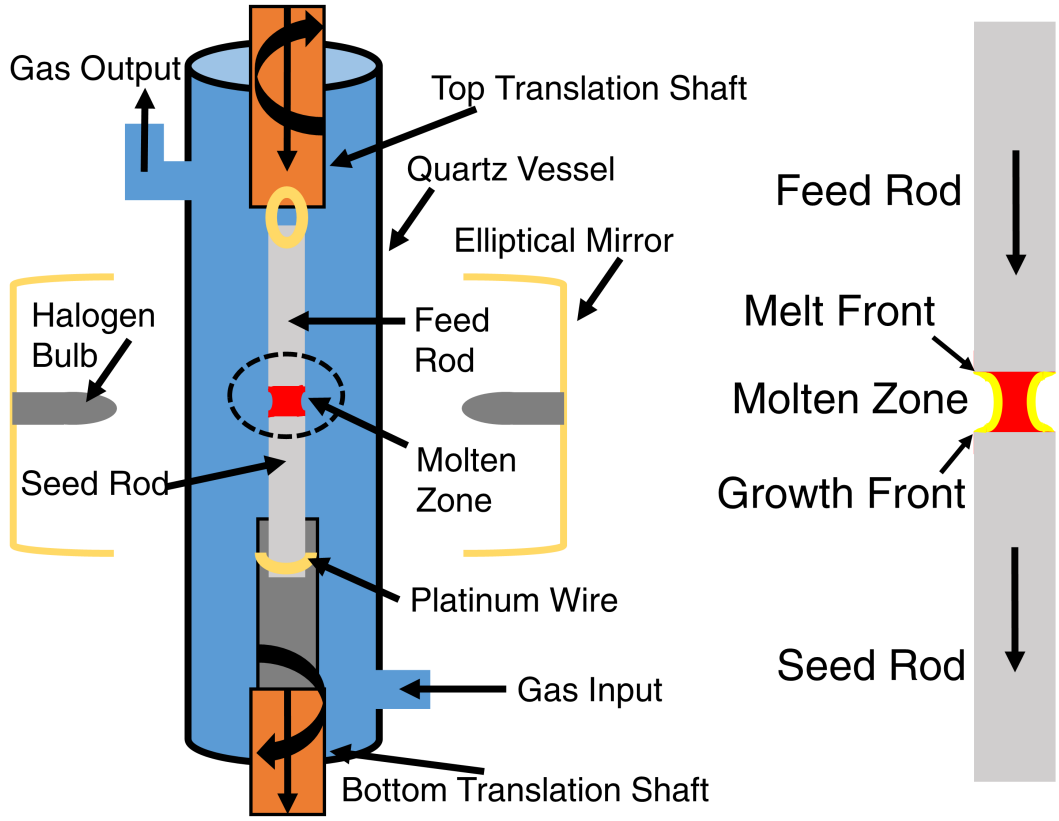

Figure 1.14 (left) Schematic of a conventional optical mirror furnace setup. (right) Illustration of the molten zone that is held between the feed and seed rods *via* surface tension [89].

techniques used to probe structural, electronic and magnetic properties. As a result, crystals grown using the OFZ technique have played an important role in the discovery and characterisation of novel quantum materials. A key role exemplified by a large variety of systems ranging from the ruthenates $Sr_3Ru_2O_7$ and Sr_2RuO_4 to multiferroic oxides $YMnO_3$ and $BiFeO_3$ and the titanate and zirconate pyrochlores $Yb_2Ti_2O_7$ [97] and $Pr_2Zr_2O_7$ [98]. Recent advances include the development of laser heating providing higher temperatures, whilst high pressure growth chambers allow for the incorporation of volatile elements such as the light alkali metals. The inclusion of traditionally problematic reagents combined with higher synthesis temperatures will continue the expansion of the accessible chemical compositional space spanned by crystals that could be grown by OFZ, thus insuring that the technique will remain at the frontier of materials science for many years to come.

1.3 Neutron Scattering

Having described how the four magnetic oxides of interest were synthesised, the discussion now proceeds to neutron scattering, the primary experimental technique employed in the characterisation of their low temperature magnetic properties. The purpose of this particular section is to simply provide the reader with a general introduction to the technique with a particular emphasis on neutron inelastic scattering. For the purposes of brevity, important results are stated without proof, as they are discussed elsewhere in detail. This section is based on Squires [99], Shirane [100], Scherm & Fåk [87], Zaliznyak & Lee [101] and references contained therein. Any additional references will be stated explicitly in the text.

1.3.1 Introduction & Motivation

"If the neutron did not exist, it would need to be invented!"
— Bertram Brockhouse, 1994 Nobel Laureate in Physics

As summarised by the 1982 quote from the Nobel Laureate Bert Brockhouse (1918-2003), the technique of neutron scattering has proven to be one of the most versatile techniques for the study of structural and dynamic properties of materials. After its discovery in 1932, the possibility and importance of the neutron as an important probe in the study of materials was quickly recognised, as exemplified by its use for diffraction only four years later. Despite being limited by the low flux of the first Ra-Be sources, the use of neutron scattering as an experimental technique experienced rapid development in the decades immediately following its inception. Such rapid development was driven by the availability of sources with ever increasing flux, made possible by the knowledge gained from the Manhattan project and the birth of the Atomic age. With the availability of greater flux through the development of high flux reactors and spallation sources, different types of neutron scattering such as neutron inelastic scattering were now made possible, thus expanding our ability to probe an ever increasing range of length and timescales.

As an experimental probe for the properties of materials, the neutron being an electrically neutral subatomic particle with significant mass possesses several advantages over other probes such as x-rays and electrons. With its electrical

neutrality, neutrons are a bulk probe, possessing large penetration depths $l \sim$ cm. This weak interaction with matter removes many of the restrictions on sample geometry and sample environments inherent to highly attenuated probes such as x-rays and electrons. When the neutron does scatter from matter, it can do so in two different ways: the nuclear interaction and the dipole-dipole interaction *via* the strong force and (electro-)magnetic force, respectively, with both interactions possessing cross sections with the same order of magnitude. The former describes the interaction of the neutron with the nuclei of the material. Such an interaction can be modelled very well by scattering from point particles, corresponding to a model much simpler than other probes such as the interaction of x-rays and the electron cloud. The dipole-dipole interaction particularly emphasises the importance of the neutron. Possessing a magnetic moment μ_n of $-1.9\ \mu_N$, the neutron can directly interact with atomic electrons, "seeing" the magnetic moments from unpaired electrons. This ability of neutrons to probe magnetism is in stark contrast with x-rays and electrons, where information from the former is limited due to weak coupling *via* the magnetic field, whilst the latter suffers from being subject to the Lorentz force due to internal magnetic fields.

It can be argued that the greatest advantage of the neutron is the range of its energies available at typical sources. From the de Broglie hypothesis, it can be readily shown that the energies of the neutron, given by

$$E = \frac{p^2}{2m_n} = \frac{h^2}{2m_n\lambda^2}, \tag{1.76}$$

span several orders of magnitude, ranging from MeV to meV, corresponding to length scales varying from the nucleus to large biological macromolecules. With energy scales of $\sim$meV available, corresponding to energies and wavelengths on the order of $k_\mathrm{B}T$ and Å, respectively, neutrons possess the ability to measure both dynamic and structural properties, while avoiding any damage or inducing any changes to the samples under investigation. This is in stark contrast with conventional x-ray sources where energies are on the order of several thousand eV and thus limited mainly to measuring static (structural) properties or dynamics near the zone centre.

Despite the clear disadvantages of neutron scattering including larger costs, limited flux, and the need for larger samples compared to other probes, the ability to effectively transfer arbitrary momentum and energy to a sample ensures that neutron scattering will continue to play a central role in the study of materials.

1.3.2 Reactor & Spallation Sources

At the present, there are two types of neutron sources available for scientific research: reactor and spallation, both of which were employed for experiments in this Thesis. The main difference between the two types is based on the nuclear process by which bound neutrons are freed from nuclei and made available for experimentation. As summarised by Fig. 1.15, whereas reactor sources produce neutrons by the spontaneous nuclear fission of ^{235}U, providing a continuous flux of neutrons, spallation sources produce neutrons by the bombardment of a heavy target (*e.g.* W, Hg) with high-energy protons, providing a pulsed flux.

The reactor source was the first and is historically the most widely used type out of the two. Older reactor sources typically consisted of a sealed vessel containing the reactor, auxiliary equipment and experimental facilities. Neutrons from the reactor would be thermalised by a D_2O moderator and reached the experimental floor through horizontal beam tubes. Modern reactor sources have additional moderators, called cold sources, usually consisting of liquid H_2 or CH_4 that are held at cryogenic temperatures ($\sim$20 K). These cold sources down shifts the Maxwellian velocity distribution, optimising experimental access to lower energies.

As an attempt to increase both the effective thermal neutron flux beyond practical engineering-power density limits and avoiding the environmental risks of nuclear contamination inherent to the use of reactor sources, interest in the development of spallation sources grew rapidly in the mid-1970's. Beginning with the successful operation of ZING-P and ZING-P′ at Argonne National Laboratory (ANL), the desire for the use of neutrons produced by the process of spallation culminated in the introduction of the Intense Pulsed Neutron Source (IPNS) with its full user programme in the early 1980's that formed the basis of modern sources such as the spallation neutron source (SNS) at Oak Ridge National Laboratory (ORNL). Despite its time-averaged flux being considerably lower than continuous sources, spallation sources do provide many advantages over their reactor counterparts. The background is lower, the resolution $\frac{\Delta E_o}{E_o}$ is relatively constant, the source pulse defines one part of the resolution function, and unlike the pure Maxwellian distribution from reactor sources, spallation sources are naturally rich in epithermal neutrons (E>100 meV) and don't require an additional "hot" source such as hot graphite. The significant gains in peak flux and more efficient use of the time structure through both technological and infrastructure improvement has resulted in the rapid decrease in the difference

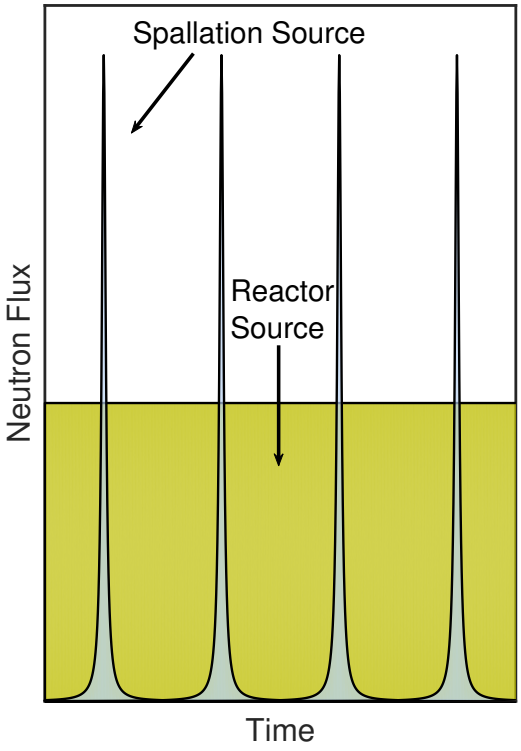

Figure 1.15 Pictorial representation of the time structures for reactor (continuous) and spallation (pulsed) sources.

between the time-averaged flux of reactor and spallation sources, making the latter even more attractive, exemplified by the development of the European Spallation Source (ESS) currently under construction in Sweden.

1.3.3 Time-of-Flight & Triple Axis Spectrometers

Having described how neutrons are produced at research sources, the discussion now proceeds to the instruments that utilise such neutrons in the study of materials. Since this Thesis focusses on the measurement of magnetic excitations, the current discussion will be limited to neutron spectrometers, instruments designed to measure changes in the energy of the neutron upon scattering. For the sake of brevity, other types of instruments such as diffractometers and reflectometers are excluded. In this Thesis, both time-of-flight (TOF) and triple axis (TAX) spectrometers were employed. As alluded to by their names, the two types of spectrometers essentially differ in their specific

choice of technique that is used to specify and measure the initial and scattered wavevectors $\mathbf{k}_i$ and $\mathbf{k}_f$, respectively.

All key elements of a triple axis spectrometer are presented in Fig. 1.16. First developed by Brockhouse at Chalk River, the triple axis spectrometer selects $\mathbf{k}_i$, $\mathbf{k}_f$ and the momentum transfer $\mathbf{Q} = \mathbf{k}_i - \mathbf{k}_f$ by the interaction of the neutron with three crystals along its path from source to detector, with each of the three crystals: the monochromator, the sample and the analyser, having the ability to rotate independently about a particular vertical axis centred about the crystal. In triple axis spectroscopy, a polychromatic beam of neutrons from the neutron source is monochromatised by the monochromator crystal. Monochromatisation, referring to the selection of a specific wavelength, is accomplished by Bragg diffraction. The rotation of the monochromator crystal such that a specific set of its atomic Bragg planes with an inter-planar spacing d is oriented θ_M relative to the incoming (or scattered) neutron beam, will result in neutrons satisfying the Bragg condition,

$$n\lambda = 2d \sin \theta_M, \tag{1.77}$$

to be scattered at an angle of $2\theta_M$ relative to the incident neutron beam. In this Thesis, the monochromator was highly oriented pyrolytic graphic (HOPG), a low Z material, possessing negigible incoherent and absorption cross section. HOPG is also commonly used as a wavelength filter for thermal neutrons (Be or BeO for cold neutrons) since it consists of stacked graphite layers randomly oriented about the c-axis, making HOPG behave as a single crystal along [001] but polycrystalline in the two orthogonal directions. Such a configuration ensures that neutrons of undesired wavelengths (energies) will be scattered out of the beam, significantly reducing the background.

In order for the monochromatised beam of neutrons with a wavelength λ to strike the sample, all downstream elements (sample, analyser and detector) must be rotated $2\theta_M$ about the monochromator axis. The following description of the monochromatisation process is instructive since it introduces the concept of a Bragg angle θ_ξ and a scattering angle $2\theta_\xi$, where ξ denotes the particular axis of interest. The Bragg angle refers to the rotation of the crystal itself, whilst the scattering angle refers to the rotation of the downstream elements in order to be coincident with the scattered beam. It should be noted that the labels θ_ξ and $2\theta_\xi$ are simply labels derived from Bragg scattering. The Bragg and scattered angles are not necessarily related to one another by a factor of two, as is the situation for many inelastic processes about the sample axis.

As the monochromatised neutron beam interacts with the sample, its

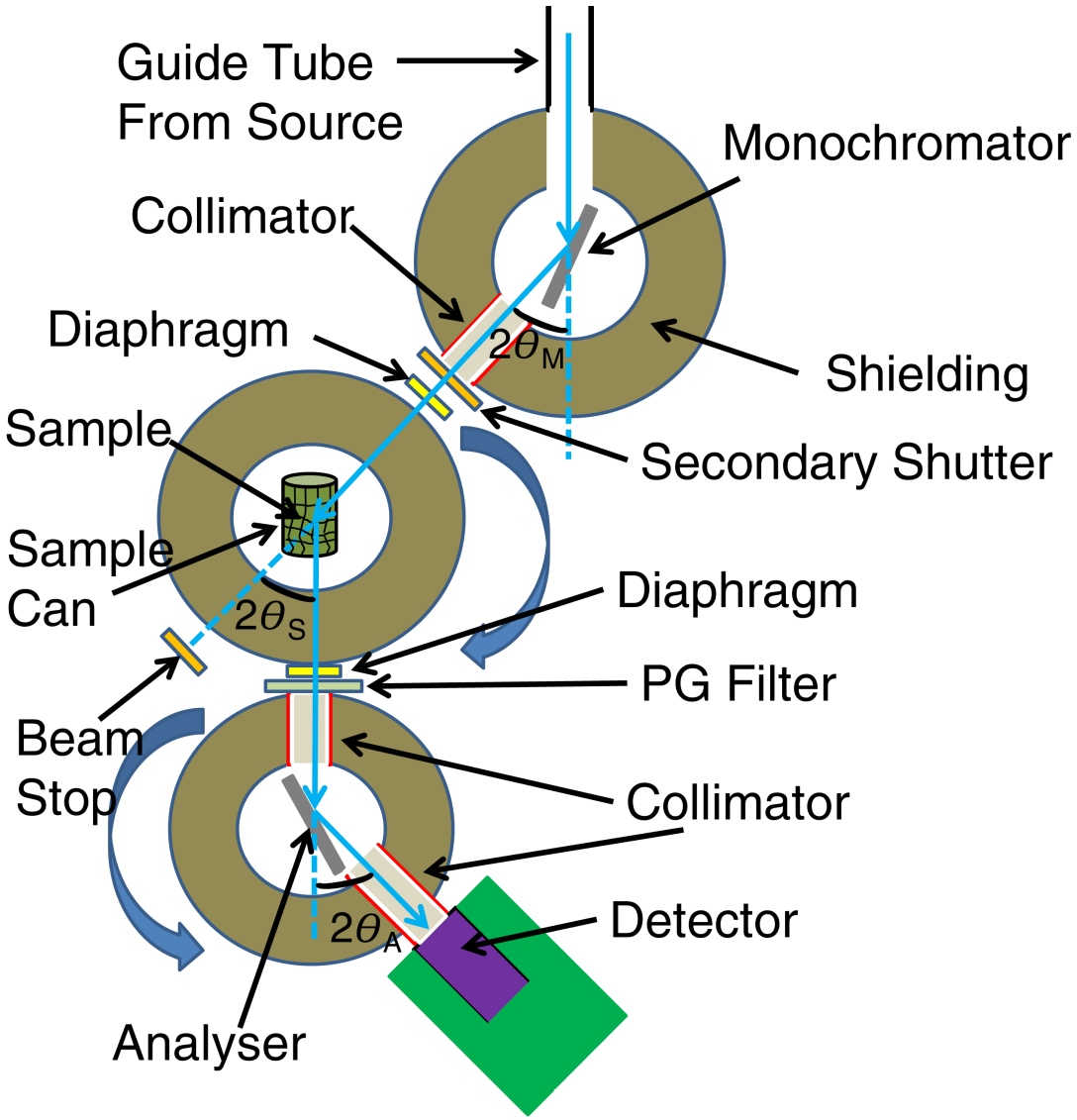

Figure 1.16 Schematic of the IN20 spectrometer (ILL) displaying all key elements of a triple axis spectrometer. The spectrometer is in W-configuration with an alternating sense of scattering from monochromator, sample and analyser [88].

energy may or may not change, and is scattered by an angle $2\theta_S$, relative to the incident monochromatised beam. The scattered beam then proceeds to the analyser crystal that selects a particular wavelength (energy) by a Bragg diffraction process. The energy selection is accomplished by orienting a particular Bragg plane of the analyser crystal such that is forms an angle θ_A with the neutron beam scattered from the sample. The neutron detector is located at an angle $2\theta_A$ relative to the incident beam which ensures that only energies (wavelengths) satisfying the Bragg condition (Eq. 1.77) will fall onto the detector and be detected.

Since θ_M and θ_A specify the incident and final energies, respectively, by combining Eqs. 1.76 and 1.77, it can be shown that the measured energy transfer ΔE, usually denoted by simply E or $\hbar\omega$, is given by

$$E = E_i - E_f = \frac{h^2}{8m_n}\left(\frac{1}{d_M^2 \sin\theta_M} - \frac{1}{d_A^2 \sin\theta_A}\right). \tag{1.78}$$

In addition to the values of θ_M and θ_A that specify the moduli of the incident and final wavevectors $|\mathbf{k}_i|$ and $|\mathbf{k}_f|$, respectively, the modulus and direction of the momentum difference $\mathbf{Q}$, is also dependent on the scattering angle $2\theta_S$. By applying the law of cosines to the scattering triangle (Fig. 1.17), it can be shown that the modulus of the momentum transfer is given by

$$Q = \sqrt{k_i^2 + k_f^2 - 2k_i k_f \cos 2\theta_S}, \tag{1.79}$$

where Q, k_i and k_f denote the moduli $|\mathbf{Q}|$, $|\mathbf{k}_i|$ and $|\mathbf{k}_f|$, respectively. It is important to note that the modulus of the momentum transfer is a function of the scattered angle $2\theta_S$ and not the Bragg angle θ_S. The value of θ_S, representing the internal degree of rotation of the crystal itself, is used to specify the orientation axis and thus specifying the orientation of specific crystallographic axes relative to $\mathbf{Q}$. This is particularly important when probing dynamics in a particular direction but since all measurements performed with triple axis instruments in this Thesis employed polycrystalline samples, the role of θ_S was rendered moot. Despite significant improvements in robotics, construction materials and detectors, the fundamental design underlying triple axis neutron spectrometers has remained unchanged from the first instruments used to measure the phonon and magnon dispersion relations of simple materials in the 1950's.

In contrast with the triple axis spectrometer where monochromatisation and energy discrimination is accomplished *via* Bragg optics, time-of-flight (ToF) spectrometers instead utilise neutron velocities in either monochromatisation, energy discrimination or both. There are two classes of ToF spectrometers: direct (Fig. 1.18) and indirect geometry (Fig. 1.19). Within each class, subclassifications are made based on if and where crystal analysers or crystal monochromators are used. Some examples include: hybrid ToF spectrometers that have a direct geometry setup but employ a crystal monochromator to select $\mathbf{k}_i$, whilst in the case that the ToF is used for the selection of $\mathbf{k}_i$ and determination of $\mathbf{k}_f$ in a direct geometry setup, the instrument is called a chopper spectrometer.

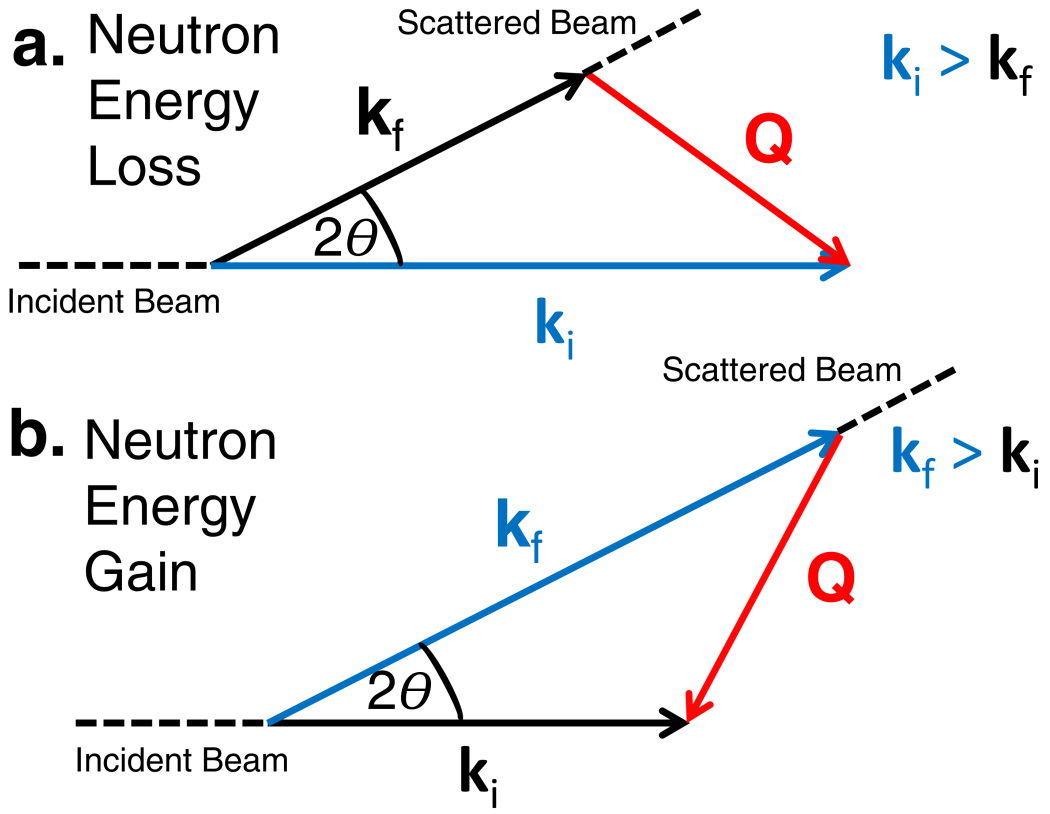

Figure 1.17 Scattering triangle for (a) creation and (b) annihilation of an excitation, corresponding to the neutron losing and gain energy, respectively. In an elastic scattering process, $|\mathbf{k}_i| = |\mathbf{k}_f|$, otherwise, the process is termed inelastic.

For direct geometry ToF spectrometers, the incident energy is defined before the sample and the final energy is determined by the time required for the neutron to travel the distance from the sample to the detector. For indrect geometry ToF spectrometers, a polychromatic beam is incident on the sample. The incident energy of the neutron is determined by the time required for the neutron to travel the distance from the pulsed source to the sample, whilst the final energy is fixed by analyser crystals located before the detectors.

Since both classes of ToF spectrometers employ the time-of-flight technique consisting of determining the velocity (and energy) *via* time travelled, a pulse incident beam is required since the neutrons are indistinguishable particles and cannot be individually labelled. Such pulsing in theory could be accomplished by simply utilising a pulsed source (*i.e.* spallation) without the need for any additional treatment. In this Thesis, such a situation is not the case for both reactor and spallation sources, where disc choppers are placed after the moderator to create the pulsed beam. Disc choppers are discs composed of highly neutron absorbing materials (*e.g.* Gd) with transparent slits rotating about an axis parallel

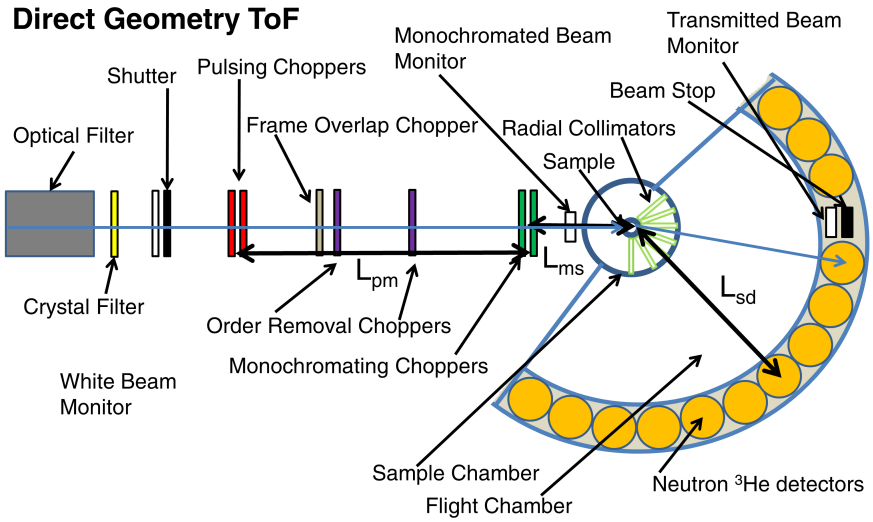

Figure 1.18 Schematic of the DCS spectrometer (NIST NCNR) displaying all key elements of a direct time-of-flight spectrometer [102].

to the incident beam. For direct geometry, the pulsed beam is monochromatised by a Fermi-disc chopper located just before the sample. Fermi choppers are essentially multiple collimators composed of highly neutron absorbing materials rotating about an axis perpendicular to the incident beam. Based on the rotation frequency ω, the Fermi-disc chopper will only allow neutrons with a specific velocity (energy) to pass through, thus defining the incident energy. It should be noted that a pulsed monochromator beam could also be created by a single crystal monochromator followed by a Fermi-disc chopper. In this Thesis, the ToF spectrometers are optimised for cold neutrons and thus do not employ crystal monochromators due to the lack of necessary d-spacings. In some cases, particularly when employing very cold neutrons, multiple disc choppers are placed just before the sample. The cascade of disc choppers removes contamination from other pulsed sources including the problem of frame overlap where the fastest neutrons of a pulse take over the slowest neutrons of the previous pulse. After being scattered from the sample, the final energy of the neutron is determined by measuring the time to travel the known distance from the sample to the neutron detector. Utilising simple geometric arguments in the classical (ballistic) treatment, it can be shown that the final energy for a direct ToF spectrometer is given by

$$E_f = \frac{1}{2} m_n \left(\frac{L_{sd}}{t - \frac{L_{ms}}{v_i}}, \right)^2 \tag{1.80}$$

for a neutron detected at a distance L_{sd} from the sample after a time t after monochromatisation with a monochromator located at a distance L_{ms} from the sample giving an initial velocity v_i. The uncertainty in E_f corresponds to the width of the pulsed beam incident on the detectors and is given by

$$\Delta E_f[\text{in meV}] = 0.6472 \frac{\sqrt{\Delta t_p^2 + \Delta t_m^2 + \Delta t_l^2}}{\lambda_f^3 L_{pm} L_{sd}}, \tag{1.81}$$

where

$$\Delta t_p = \tau_p \left(L_{ms} + L_{sd} \frac{\lambda_f^3}{\lambda_i^3} \right), \tag{1.82}$$

$$\Delta t_m = \tau_m \left(L_{pm} + L_{ms} L_{sd} \frac{\lambda_f^3}{\lambda_i^3} \right), \tag{1.83}$$

$$\Delta t_l = L_{pm} \lambda_f \frac{m_n}{h} \Delta L, \tag{1.84}$$

where L_{pm}, L_{ms}, L_{sd}, τ_p, τ_m and ΔL corresponds to the pulsing-monochromating chopper distance, monochromating chopper-sample, sample-detector distances and spread (in time) of the initial pulse, opening time of the monochromator and flight path length uncertainties, respectively. Eqs. 1.82-1.84 represent contributions to the uncertainty from the creation of the pulse, monochromatisation of the pulse and the determination of the arrival times, respectively.

For indirect ToF spectrometers, a finite range of neutron energies is selected from the initial beam originating from the moderator by a sequence of disc choppers located before the sample. The incident beam is polychromatic, possessing a spread in the time required for the neutrons to travel the distance L_{ms} from the moderator to the sample, thus defining a spread of incident energies. Due to the presence of analyser crystals (*e.g.* pyrolytic grapite), after the neutrons are scattered by the sample, only those with the appropriate final energy (wavelength) will be Bragg scattered into the detectors. An equivalent statement would be that only those neutrons that require a characteristic time t_2 to travel the distance between the sample and detector L_{sd} will be detected. The value of t_2 given by

$$t_2 = \frac{2 m_n L_{sd} d_A \sin\theta}{h}, \tag{1.85}$$

where d_A and θ is the inter-planar spacing of the analyser crystal and the Bragg

angle. It is important to note that the time t_2 is only dependent on the specific analyser crystal and its geometric arrangement relative to the detector.

Since the interaction between the neutron and the sample may or may not result in a change of energy, there will be a distribution of different arrival times at the detector with the energy transfer being a function of the total flight time t given by

$$\Delta E = E_i - E_f = \frac{1}{2} m_n \left[\left(\frac{L_{ms}}{t - t_2} \right)^2 - \left(\frac{L_{sd}}{t_2} \right)^2 \right], \tag{1.86}$$

where t is the sum of the time required to travel from moderate to the sample t_1 and the time required to travel from the sample to detector t_2 given by Eq. 1.85 above.

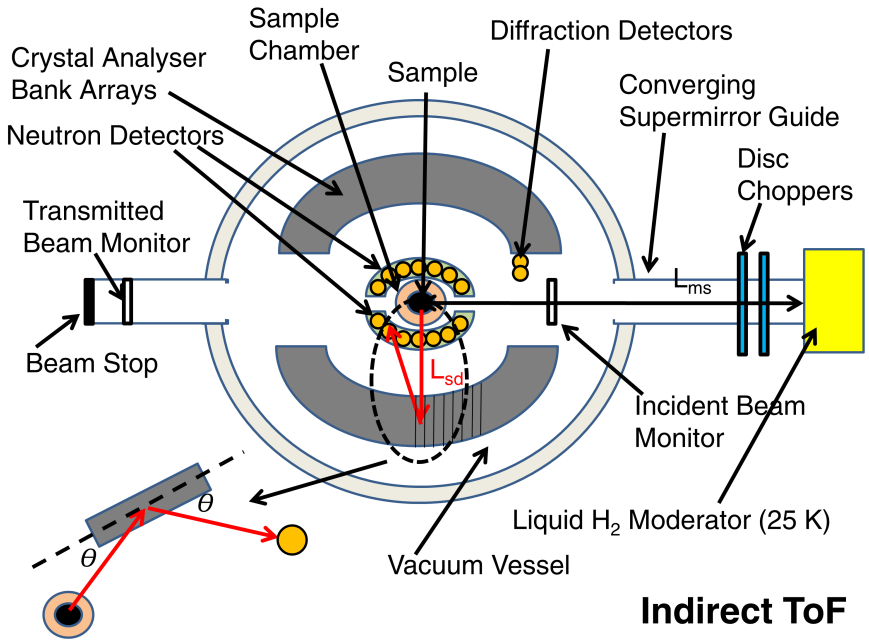

Figure 1.19 Schematic of the IRIS spectrometer (ISIS) displaying all key elements of an indirect time-of-flight spectrometer [103, 104].

It should be emphasised that triple axis and ToF spectrometers represent complementary techniques. The former is very well suited for measurements over a limited range in $(\mathbf{Q}, E)$ space or if the direction of $\mathbf{Q}$ is important. On the other hand, ToF is best suited for polycrystalline samples where the direction of $\mathbf{Q}$ is not relevant or for measurements requiring a large region of $(\mathbf{Q}, E)$ to be probed simultaneously, such as is the case for exploratory investigations and for

systems that exhibit weak dispersions.

Table 1.4 Summary of the neutron spectrometers employed in this Thesis. Spectrometers are organised by facility and technique. Relevant chapters are labelled for reference.

Type of Source	Source Name	TAX	Direct ToF	Indirect ToF	Chapter
Reactor	HFIR	HB-1A			2
	NCNR	BT4			3
			DCS		2
Spallation	SNS		CNCS		2
			SEQUOIA		2
	ISIS		MARI		3,4
			MERLIN		5
				IRIS	3,4

1.3.4 Neutron Inelastic Scattering

Introduction: Cross Section & Kinematics

To conclude this chapter, having discussed how spectrometers measure the energy change of neutrons scattered by samples, the discussion now shifts to a general introduction of how such an energy change can be used to infer a wealth of information concerning a sample's dynamics.

Such a discussion begins by the introduction of the double differential scattering neutron cross section $\frac{d^2\sigma}{d\Omega dE}$. The double differential scattering cross section, sometimes written as $\frac{d^2\sigma}{d\Omega dE_\mathrm{f}}$, is directly proportional to the number of neutrons that are scattered into a particular solid angle element $d\Omega$ with a particular final energy lying in the range dE_f from E_f. This definition is the most generic and is defined more strictly in actual experiments as a function of incoming energy E_i and direction (θ, ϕ) as illustrated in Fig. 1.20. Although beyond the scope of the current discussion, it should be noted that the interaction between incident neutrons and the sample is not limited to simply scattering but includes the possibilities of absorption and transmittance, with each process providing some information about the sample (*e.g.* real space imaging).

Two (out of the three) possibilities of the scattering process are illustrated in Fig. 1.17 above. A neutron with an initial wavevector $\mathbf{k}_i$ which specifies its

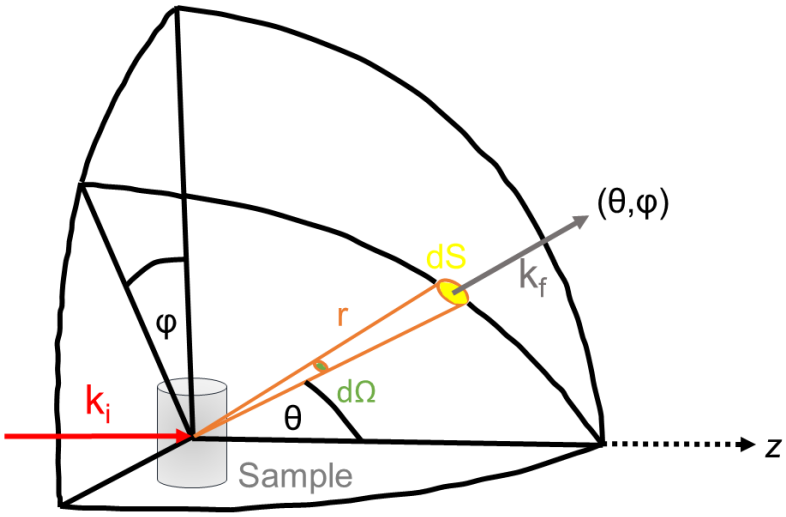

Figure 1.20 Classical description of the scattering geometry for a neutron scattering experiment. The double differential cross section $\frac{d^2\sigma}{d\Omega dE_f}$ provides the probability that for a normalised flux of neutrons with an incident wavevector $\mathbf{k}_i$ are scattering into a solid angle element $d\Omega$ at (θ, ϕ) with a final energy lying between $E_f = \frac{\hbar^2 k_f^2}{2m}$ and $E_f + dE_f$.

momentum *via*

$$\mathbf{p} = \hbar\mathbf{k}, \tag{1.87}$$

scatters from a sample with a final wavevector $\mathbf{k}_f$ resulting in either a gain ($k_i < k_f$) or a loss in energy ($k_i > k_f$). The third possibility is elastic scattering corresponding to a situation where the neutron neither gains nor loses energy ($k_i = k_f$). All three scattering possibilities correspond to physical processes and are thus subject to energy and momentum conservation given by:

$$\Delta E = E_i - E_f = \frac{\hbar^2}{2m}\left(k_i^2 - k_f^2\right) \tag{1.88}$$

and

$$\mathbf{Q} = \mathbf{k}_i - \mathbf{k}_f. \tag{1.89}$$

By employing Eq. 1.89, one obtains the scattering triangle (Fig. 1.17) which can

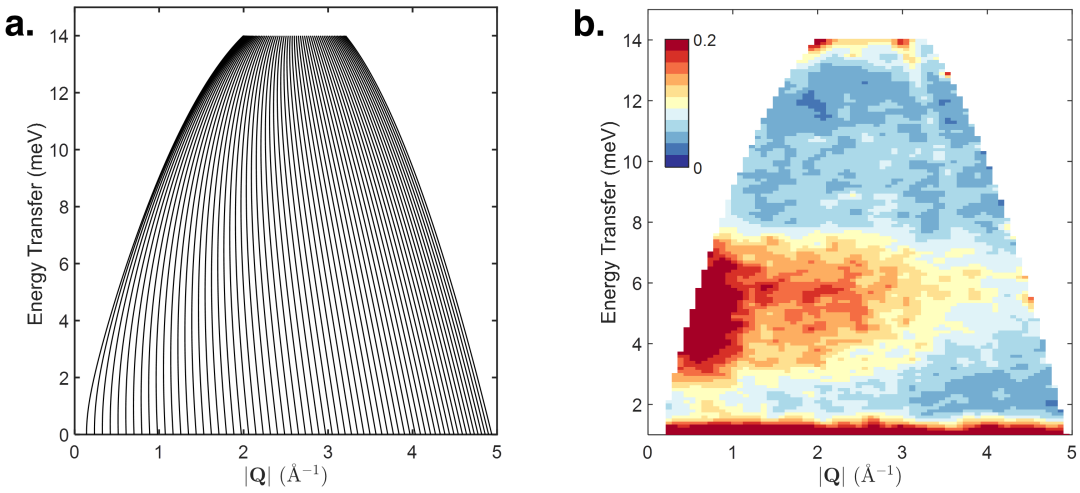

Figure 1.21 Comparison of (a) the calculated dynamic range and (b) experimental data for α-CoV_3O_8 at 5 K with an E_i =15 meV on the direct spectrometer MARI spanning $2\theta = 3°$-$134°$. Calculations in (a) were performed in $2\theta = 1°$ steps for the down-scattering energy range exclusively.

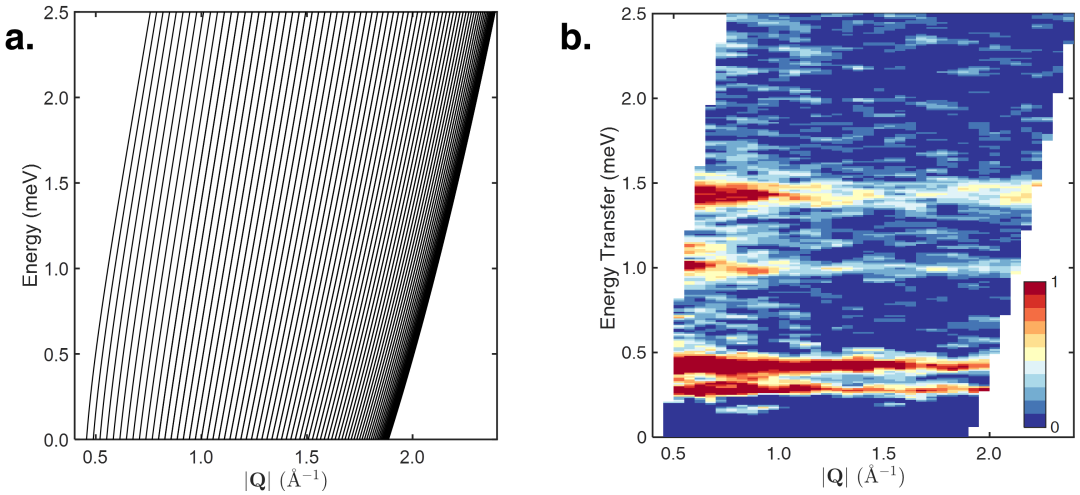

Figure 1.22 Comparison of (a) the calculated dynamic range and (b) experimental data for $Co_{0.03}Mg_{0.97}O$ at 11 K on the indirect spectrometer IRIS spanning $2\theta = 25°$-$160°$ for the down-scattering energy range. Despite the final energy E_f of IRIS being fixed to 1.84 meV, E_f in (a) was set to 2.5 meV. The larger E_f reflects the increased bandwidth that is achievable by the selection of mutliple time windows *via* IRIS' array of disc choppers located along its long path length.

be used to derive Eq. 1.79 given by

$$Q = \sqrt{k_i^2 + k_f^2 - 2k_i k_f \cos 2\theta}. \tag{1.90}$$

By applying the constraints of energy conservation defined by Eq. 1.88 on the

scattering triangle, it can be shown that

$$\frac{\hbar^2 Q^2}{2m} = 2E_i - \Delta E - 2\cos 2\theta \sqrt{E_i(E_i - \Delta E)} \tag{1.91}$$

and

$$\frac{\hbar^2 Q^2}{2m} = 2E_f + \Delta E - 2\cos 2\theta \sqrt{E_f(E_f + \Delta E)} \tag{1.92}$$

for direct and indirect geometry spectrometers, respectively. Both Eqs. 1.91 and 1.92 correspond to kinematic contraints that define the accessible range in $(\mathbf{Q}, \Delta E)$ (also commonly stated as $(\mathbf{Q}, E)$) space, given a scattered angle 2θ and either an incident or final energy for a direct or indirect spectrometer, respectively. Examples of accessible ranges in $(\mathbf{Q}, E)$) space for direct and indirect time-of-flight spectrometers are illustrated in Figs. 1.21 and 1.22, respectively.

Nuclear Scattering

Having described both the double differential scattering neutron cross section and its constraints in $(\mathbf{Q}, E)$ space, the discussion now proceeds to the relationship between $\frac{d^2\sigma}{d\Omega dE}(\mathbf{Q}, E)$ which is the quantity measured in an neutron inelastic scattering experiment and the dynamic structure factor $S(\mathbf{Q}, E)$ which contains the desired information about the dynamics of the system under investigation. Following the logic of Squires [99], the discussion will first begin by introducing the reader to nuclear scattering.

Corresponding to the weak interaction between the neutron and the nucleus of a sample *via* the strong nuclear force, such an interaction can be approximated as a perturbation. Such an approximation allows one to employ time-dependent perturbation theory and Fermi's golden rule. Through some algebraic manipulation, it can be shown that the double differential scattering neutron cross section assumes the form

$$\frac{d^2\sigma}{d\Omega dE} = \left(\frac{m_n}{2\pi\hbar^2}\right)^2 \frac{k_f}{k_i} \sum_{n_0} p(n_0) \sum_{n_1} |\langle k_f \sigma_f n_1 | V | k_i \sigma_i n_0 \rangle|^2 \delta(\epsilon(n_1) - \epsilon(n_0) - \Delta E). \tag{1.93}$$

Commonly referred to as the "Master equation" or "Master formula", Eq. 1.93 summarises the mathematical relationship between the scattering cross section and the perturbative potential from which the neutrons are scattering from. The equation contains two sets of indices. The first set, denoted by i and f, refers to the neutron with energy E, whilst the second set, denoted by 0 and 1, refers to the system with energy ϵ under investigation. The "Master equation" contains two sums. The first sum is over all initial states of the system n_0, each thermally weighted by

$$p(n_o) = \frac{e^{-\frac{\epsilon(n_0)}{k_B T}}}{\sum_{n_0} e^{-\frac{\epsilon(n_0)}{k_B T}}}, \tag{1.94}$$

for a given temperature T. The second sum is over all final states of the system n_1. The matrix element describing the probability associated with the transition from an initial total state (neutron and system) $|k_i \sigma_i n_0\rangle$ to a final total state $|k_f \sigma_f n_1\rangle$ is calculated over both sums with the delta function $\delta(\epsilon(n_1) - \epsilon(n_0) - \Delta E)$ selecting only those final states of the system that satisfy energy conservation. The prefactor $\frac{k_f}{k_i}$ is a consequence of the definition of the cross section. In most cases, this prefactor is reduced to a constant and is either compensated for by data reduction algorithms or ultimately absorbed in either the normalisation or overall scale constant.

Although originally motivated by the relatively weak neutron-nucleus interaction, Eq. 1.93 is a general mathematical relationship valid for any weak perturbative potential, a generalisation that will be exploited when discussing magnetic neutron scattering. In the case of nuclear scattering, the perturbative potential V is conventionally approximated by the Fermi pseudo-potential

$$V(\mathbf{r}) = \frac{2\pi\hbar^2}{m} \sum_j b_j \delta(\mathbf{r} - \mathbf{R}_j), \tag{1.95}$$

where $\mathbf{R}_j$ is the position of nucleus j with a scattering length b_j. The potential in Eq. 1.95 is spherically symmetric, as one would expect for s-wave scattering, a reflection of the fact that the neutron is not sensitive to the internal structure of the nucleus. By inserting Eq. 1.95 into Eq. 1.93, it can be shown that the cross

section becomes

$$\frac{d^2\sigma}{d\Omega dE} = \frac{k_f}{k_i}\sum_{n_0} p(n_0)\sum_{n_1}|\langle n_1|\sum_j b_j e^{i\mathbf{Q}\cdot\mathbf{R}_j}|n_0\rangle|^2\delta(\epsilon(n_1)-\epsilon(n_0)-\Delta E), \quad (1.96)$$

for unpolarised neutron scattering, as will be the case for the rest of the chapter since no polarised instruments were employed in this Thesis. For many introductory treatments of neutron scattering, Eq. 1.96 serves as a natural motivation for a discussion of coherent and incoherent scattering. Such a discussion begins by focussing on the square modulus of the matrix element in Eq. 1.96. By extracting $\sum_j b_j$ and relabelling $\langle n_1|e^{i\mathbf{Q}\cdot\mathbf{R}_j}|n_0\rangle$ as $\langle j\rangle$, then one obtains the following relationship

$$|\langle n_1|\sum_j b_j e^{i\mathbf{Q}\cdot\mathbf{R}_j}|n_0\rangle|^2 = |\sum_j b_j\langle j\rangle|^2 \quad (1.97)$$

Assuming that the scattering lengths for all j are real, a valid assumption for the particular nuclei investigated in this Thesis since none are particularly well-absorbing, then the RHS of Eq. 1.97 can be simplified further to

$$|\sum_j b_j\langle j\rangle|^2 = \sum_{jj'} b_{j'}b_j\langle j'\rangle^*\langle j\rangle. \quad (1.98)$$

In the case that all the nuclei have the same scattering lengths, then the labels on b are rendered moot and the square of the scattering length b^2 can be extracted from the sum. In the case that the scattering lengths are different, as is the case for a sample containing various isotopes of an element, then one must average over b_j. The evaluation of the average results in two terms:

$$\overline{b_{j'}b_j} = \overline{b_{j'}}\,\overline{b_j} = \overline{b}^2 \quad \text{for} \quad j \neq j' \quad (1.99)$$

and

$$\overline{b_{j'}b_j} = \overline{b^2} \quad \text{for} \quad j = j', \quad (1.100)$$

both valid under the assumption that the values of b_j follow a random distribution, a valid assumption for the systems under investigation. Eqs. 1.99 and 1.100 implies that Eq. 1.98 averaged over b_j becomes a sum of two terms

$$|\sum_j b_j\langle j\rangle|^2 = \overline{b}^2\sum_{j\neq j'}\langle j'\rangle^*\langle j\rangle + \overline{b^2}\sum_j\langle j'\rangle^*\langle j\rangle. \tag{1.101}$$

The second term is a self-correlation function that describes the motion of one particle. The first term, usually referred to as the "distinct" term, cannot be experimentally measured because the neutrons behave as indistinguishable particles, *i.e.* they cannot be labelled. To overcome this fundamental limitation, it can be shown that if one adds and subtracts a term where $j = j'$, then one obtains

$$|\sum_j b_j\langle j\rangle|^2 = \overline{b}^2\sum_{jj'}\langle j'\rangle^*\langle j\rangle + \left(\overline{b^2} - \overline{b}^2\right)\sum_j\langle j'\rangle^*\langle j\rangle, \tag{1.102}$$

By employing Eq. 1.96 above, it can be shown that the two quantities in Eq. 1.102 correspond to two experimentally measurable quantities. The first corresponds to the coherent cross section, describing correlations between all atoms in the sample, whilst the second term corresponds to the incoherent cross section, describing self-correlations. Although the coherent cross section will be of primary interest for the remainder of this Thesis, it is worth mentioning that the incoherent cross section does play an important role in the normalisation procedure that is described in Appendix I.

Having introduced the coherent and incoherent cross section, the discussion will now proceed to the dynamic structure factor. With the introduction of Heisenberg operators, it can be shown that Eq. 1.96 becomes

$$\frac{d^2\sigma}{d\Omega dE} = \frac{k_f}{k_i}\overline{b^2}S(\mathbf{Q},E) \tag{1.103}$$

or equivalently

$$\frac{d^2\sigma}{d\Omega dE} = \frac{k_f}{k_i}b_{coh}^2S_{coh}(\mathbf{Q},E) + \frac{k_f}{k_i}b_{inc}^2S_{inc}(\mathbf{Q},E), \tag{1.104}$$

by employing the logic of Eq. 1.102, where $b_{coh} \equiv \bar{b}$ and $b_{inc} \equiv \overline{b^2} - \overline{b}^2$. Both

Eqs. 1.103 and 1.104 correspond to the separation of information regarding how the neutron interacts with the sample, given by $\frac{k_f}{k_i}b^2$ and information about the system itself, as summarised by $S(\mathbf{Q}, E)$. It should be noted that neutron spectroscopy data is conventionally reported with respect to the change in energy of the system and thus the E in $S(\mathbf{Q}, E)$ denotes $\Delta\epsilon$ in the convention set by Eq. 1.93.

The significance of the dynamic structure factor $S(\mathbf{Q}, E)$ can be illustrated by recognising that its double Fourier transform from $(\mathbf{Q}, E)$ into $(\mathbf{r}, t)$ corresponds to the time-dependent pair-correlation function, as summarised by

$$G(\mathbf{r}, t) = \frac{1}{8\hbar\pi^3} \int d\mathbf{Q} e^{i\mathbf{Q}\cdot\mathbf{r}} \int dE e^{\frac{iEt}{\hbar}} S(\mathbf{Q}, E). \tag{1.105}$$

The significance of the relationship described by Eq. 1.105 can be deduced by noting that the time-dependent pair-correlation function can be shown to be a density-density correlation function given by

$$G(\mathbf{r}, t) = \int d\mathbf{r}' \langle \rho(\mathbf{r}', 0)\rho(\mathbf{r}', t)\rangle_T, \tag{1.106}$$

where ρ is the density operator defined as

$$\rho(\mathbf{r}, t) = \sum_j \delta(\mathbf{r} - \mathbf{R}_j(t)), \tag{1.107}$$

where each nucleus is defined as a delta function. The notation $\langle \dots \rangle_T$ denotes the average over all initial states at a temperature T, *i.e.* $\frac{\sum_{jj'}}{N}$. The appearance of an average in Eq. 1.106 also suggests that one must choose arbitrarily a reference $\mathbf{r}$ that is set as the origin $\mathbf{0}$ at $t = 0$.

Eqs. 1.106-1.107 imply that given an atom is found at $\mathbf{r} = 0$ at $t = 0$, the probability of another atom (either the same or different) to be found at a position $\mathbf{r}$ at a time t is given by $G(\mathbf{r}, t)$[‖]. This observation, combined with Eq. 1.105 demonstrates that $S(\mathbf{Q}, E)$ through its $\mathbf{Q}$ and E-dependence or $G(\mathbf{r}, t)$ through its $\mathbf{r}$ and t-dependence determines where to and how atoms move, thus

[‖] It should be noted that technically such an interpretation of $G(\mathbf{r}, t)$ is strictly valid when the function is real which occurs in the classical limit of $T \gg \frac{\Delta E}{k_B}$. In fact, the function $G(\mathbf{r}, t)$ need not be real, but may be complex, a consequence of the fact that the Heisenberg operators $\mathbf{R}_{j'}(0)$ and $\mathbf{R}_j(t)$ do not commute since the Hamiltonian contains momentum and position operators for all nuclei in the system.

providing important information concerning both structure and dynamics.

Dynamic Structure Factor

Having introduced the dynamic structure factor, the discussion now proceeds to a description of its properties, many of which will prove critical in the investigations comprising this Thesis.

Employing dimensional analysis in either Eq. 1.103 or Eq. 1.104, it can be deduced that $S(\mathbf{Q}, E)$ is always positive, behaving as a distribution function in E (and not $\mathbf{Q}$) with units of [energy]$^{-1}$.

A second crucial property is that $S(\mathbf{Q}, E)$ obeys the principle of detailed balance

$$S(-\mathbf{Q}, -E) = e^{-\frac{E}{k_B T}} S(\mathbf{Q}, E), \tag{1.108}$$

providing a mathematical relationship between the intensity for up-scattering and down-scattering, corresponding to $E < 0$ and $E > 0$ energy transfers, respectively. The principle of detailed balance corresponds to the thermodynamic limitations imposed on the transition probabilities, stemming from the $\sum_{n_0} p(n_0)$ prefactor in Eq. 1.93. The thermodynamic limitations being the thermal populations of the two energy levels involved in the transition. Such limitations can be deduced by observing that as $T \ll E$ in Eq. 1.108, then the value of $S(-\mathbf{Q}, -E) \to 0$, as is expected for a system whose ground state is exclusively populated and thus minimal probability to transfer energy to the incident neutron. In contrast, as $T \gg E$, then $S(-\mathbf{Q}, -E) \to S(\mathbf{Q}, E)$, reflecting the fact that all energy levels are equally populated in the high temperature limit and thus equally as likely to excite than receive energy from an incident neutron.

Since the origins of detailed balance lies in the $\sum_{n_0} p(n_0)$ prefactor, its validity is based on the assumption of thermal equilibrium and thus any deviation of the ratio of the respective energy gain-loss intensities can be used as a direct measure for the non-equilibrium thermal populations.

Finally, as discussed in Appendix F, the fluctuation-dissipation theorem allows one to relate the imaginary component of the susceptibility $\chi(\mathbf{Q}, E)$ to $S(\mathbf{Q}, E)$

via

$$S(\mathbf{Q},E)=\frac{1}{\pi}\frac{1}{1-e^{-\frac{E}{k_BT}}}\chi''(\mathbf{Q},E)\equiv\frac{1}{\pi}[n(E)+1]\chi''(\mathbf{Q},E), \tag{1.109}$$

where $n(E)$ is the Bose factor. It is important to emphasise the importance of the fluctuation-dissipation theorem. Following directly from the Langevin equation and a hallmark in linear response theory, this theorem allows for the description of a microscopic quantity, the correlation function *via* the dynamic structure factor S, in terms of a macroscopic quantity such as the dynamic susceptibility χ''. The restrictions imposed by detailed balance means that $\chi''(\mathbf{Q},E)$ must be an odd function in E. In Appendix F, the converse is also shown, such that the definition of χ'' in Eq. 1.109 with the assumption of the function being odd with respect to E produces the limitations of detailed balance. As will be discussed later, the susceptibility and more precisely, the dynamic spin susceptibility $\chi''(\mathbf{Q},E)$ will prove to be a particularly useful quantity in magnetic neutron scattering, where the removal of the trivial temperature dependence related to the thermal population assists in probing the underlying physics.

Finally, by utilising the definition of $S(\mathbf{Q},E)$ as the double (inverse) Fourier transform of the time-dependent pair-correlation function

$$S(\mathbf{Q},E)=\frac{1}{2\pi}\int d\mathbf{r}e^{i\mathbf{Q}\cdot\mathbf{r}}\int dte^{-\frac{iEt}{\hbar}}G(\mathbf{r},t), \tag{1.110}$$

and fixing E to be 0, one obtains

$$S(\mathbf{Q},E=0)=\frac{1}{2\pi}\int d\mathbf{r}e^{i\mathbf{Q}\cdot\mathbf{r}}\int dtG(\mathbf{r},t), \tag{1.111}$$

demonstrating that elastic scattering provides information about the time-averaged structure. This is in contrast with fixing $t=0$ for $G(\mathbf{r},t)$ (Eq. 1.105) which yields

$$G(\mathbf{r},t=0)=\frac{1}{8\hbar\pi}\int d\mathbf{r}e^{-i\mathbf{Q}\cdot\mathbf{r}}\int dES(\mathbf{Q},E), \tag{1.112}$$

which demonstrates that total scattering is a measure of the instantaneous structure. In the case of solids, as is the case for this Thesis, the difference between

the instantaneous and time-averaged structures is minimal since the atoms are vibrating about their equilibrium positions in the case of nuclear scattering. Such a statement is not necessarily true for magnetic scattering, as is the case for the systems of interest in this Thesis. Such an observation is very important since the information obtained from a diffractometer with no energy discrimination, and thus the benefits of increased flux, will yield a structure that is a close approximation to the desired time-averaged structure.

It is worth noting that the terms "time averaged" and "instantaneous" possess an inherent ambiguity. Such ambiguity is based on the fact that each instrument has a finite energy resolution δE which determines a finite coherence time that is probed by the neutron. This is significant because fluctuations with time scales $\tau \gg \frac{\hbar}{\delta E}$ will appear quasi-static. In other words, only fluctuations with a shorter time scale (higher frequency) compared to the coherence time of the neutron will actually appear dynamic. This implies that if one desires to probe slower fluctuations with $\tau \ll 10^9\ s$, other techniques such as neutron spin echo, μSR or nuclear magnetic resonance (NMR) spectroscopy will need to be employed. A comparison of the accessible time scales for various experimental techniques are summarised in Fig. 1.23.

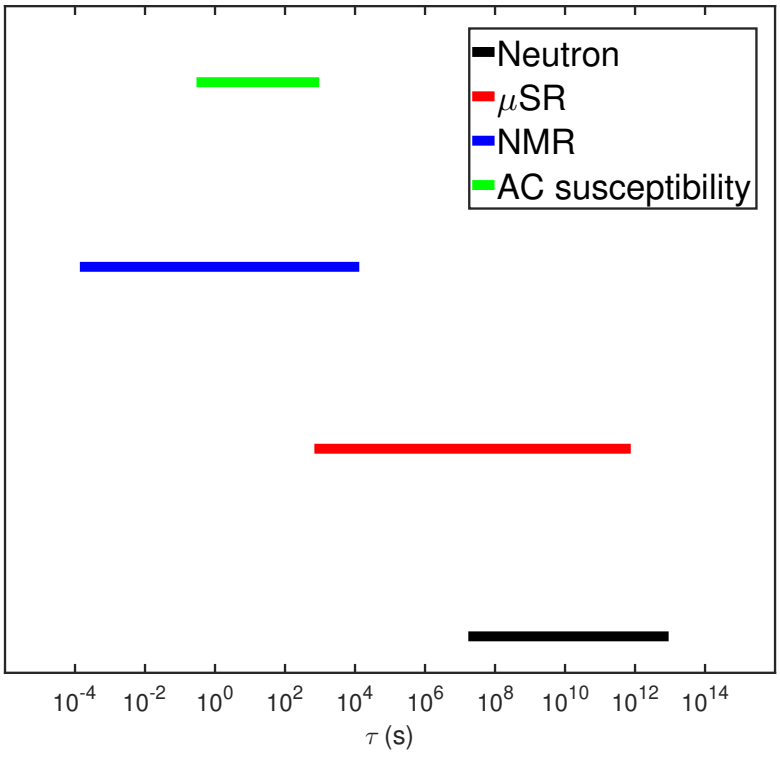

Figure 1.23 Comparison of time scales that are accessed by various experimental techniques [87].

Magnetic Scattering

Utilising key conclusions deduced from nuclear scattering, this discussion will now address magnetic scattering and the added complexities involved when describing the interaction between the magnetic dipole moment of the neutron and the dipolar magnetic field of the unpaired electrons. The discussion begins with the observation that such an interaction is relatively weak, suggesting a perturbative approach. As was the case for nuclear scattering, such an approach allows for the use of the "Master equation" (Eq. 1.93). *In lieu* of the Fermi pseudo-potential that was employed for the case of nuclear scattering, the magnetic double differential scattering cross section requires a potential U of the form

$$U = \mu \cdot \mathbf{H} = -\gamma \mu_N \sigma \cdot \mathbf{H}, \tag{1.113}$$

where μ and σ are the magnetic moment and Pauli spin operators, respectively, whilst γ, the gyromagnetic ratio of the neutron, and μ_N, the nuclear magneton, are tabulated constants. $\mathbf{H}$ denotes the total dipolar magnetic field produced by the unpaired electrons. Consisting of two terms, corresponding to the contributions to the dipolar field from the neutron's intrinsic spin and orbital motion around the nucleus, respectively, $\mathbf{H}$ is defined by

$$\mathbf{H} = \nabla \times \left\{ \frac{\mu_e \times \mathbf{R}}{|\mathbf{R}|^3} \right\} - \frac{e}{c} \left\{ \frac{\mathbf{v}_e \times \mathbf{R}}{|\mathbf{R}|^3} \right\}, \tag{1.114}$$

where $\mu_e = -2\mu_B \mathbf{S}$, $\mathbf{v}_e$, $\mathbf{R}$ are the electronic moment operator, the velocity of the electron and the displacement vector of the electron relative to the point of interest, respectively, whilst e, the elementary electric charge, and c, the speed of light (in a vacuum), are tabulated constants.

First calculated by Halpern & Johnson in 1939 [105], by subtituting Eqs. 1.113 and 1.114 into Eq. 1.93, the magnetic double differential scattering cross section is given by

$$\left(\frac{d^2\sigma}{d\Omega dE} \right)_{\text{mag}} = \frac{k_f}{k_i} (\gamma r_o)^2 S_{\text{mag}}(\mathbf{Q}, E), \tag{1.115}$$

where r_o is the classical electron radius and the scattering length in Eq. 1.103 has been replaced by the strength of the dipolar neutron-electron interaction γr_o,

which is taken to be 5.391 fm sr^{-1} in this Thesis. The magnetic dynamic structure factor $S_{\text{mag}}(\mathbf{Q}, E)$ in Eq. 1.115 is defined as

$$S_{\text{mag}}(\mathbf{Q}, E) = \frac{1}{2\pi} \int dt e^{-\frac{iEt}{\hbar}} \langle \mathbf{M}_{\perp}^{\dagger}(-\mathbf{Q}, 0) \cdot \mathbf{M}_{\perp}(\mathbf{Q}, t) \rangle, \tag{1.116}$$

where $\mathbf{M}(\mathbf{Q}, t)$ is the magnetisation operator, corresponding to the Fourier transform of the total magnetisation density $\mathbf{M}(\mathbf{r}, t)$. The perpendicular subscript $\perp$ on $\mathbf{M}$ is a reflection that only magnetic moments and magneic fluctuations that are orthogonal to $\mathbf{Q}$ can be measured. It should be noted that is common in the literature to replace $\mathbf{M}_{\perp}$ in Eq. 1.116 with the equivalent expression $\hat{\mathbf{Q}} \times (\mathbf{M} \times \hat{\mathbf{Q}})$. A comparison of Eq. 1.116 to Eqs. 1.106 and 1.107 reveals that the magnetic dynamic structure factor contains information about correlations in both time and space between magnetic moments instead of the nuclei, as was the case of nuclear scattering.

If one assumes that the magnetisation density is carried by electrons that are localised on the magnetic ions that are arranged in a lattice, as is the case for the insulators in this Thesis, then the dynamic structure factor and ultimately the cross section can be parameterised by the correlation between the lattice and the total (atomic and orbital) spin variables. Such a re-paramaterisation allows one to write a modified magnetic dynamic structure factor

$$S_{\text{mag}}(\mathbf{Q}, E) = \left(\frac{1}{2} g\right)^2 |f(\mathbf{Q})|^2 \sum_{\alpha,\beta} (\delta_{\alpha\beta} - \hat{Q}_{\alpha} \hat{Q}_{\beta}) S^{\alpha\beta}(\mathbf{Q}, E), \tag{1.117}$$

where g is the Landé g-factor, $f(\mathbf{Q})$ is the magnetic form factor, $\delta_{\alpha\beta} - \hat{Q}_{\alpha} \hat{Q}_{\beta}$ is the orientation factor, whilst

$$S_{\text{mag}}^{\alpha\beta}(\mathbf{Q}, E) = \frac{1}{2N\pi} \int dt e^{-\frac{iEt}{\hbar}} \sum_{j} e^{i\mathbf{Q} \cdot \mathbf{r}_j} \langle S_0^{\alpha}(0) S_l^{\beta}(t) \rangle, \tag{1.118}$$

where α, β denotes the Cartesian components x, y, z of an effective spin operator S_j at site $\mathbf{r}_j$. As is common in the literature, the prefactor of $\frac{N}{\hbar}$ and the Debye-Waller factor e^{-2W_Q} were both excluded from Eq. 1.117. The numerator N in the former factor is conventionally excluded since it will be cancelled by the $\frac{1}{N}$ prefactor in Eq. 1.118, whilst $\hbar$ is conventionally excluded since all relevant quantities, in particular the susceptibility is understood to be normalised by $\hbar$.

The Debye-Waller factor, which describes the movement of the atoms constituting the scattering system, is approximately one in the low temperature-energy regime that is investigated in this Thesis.

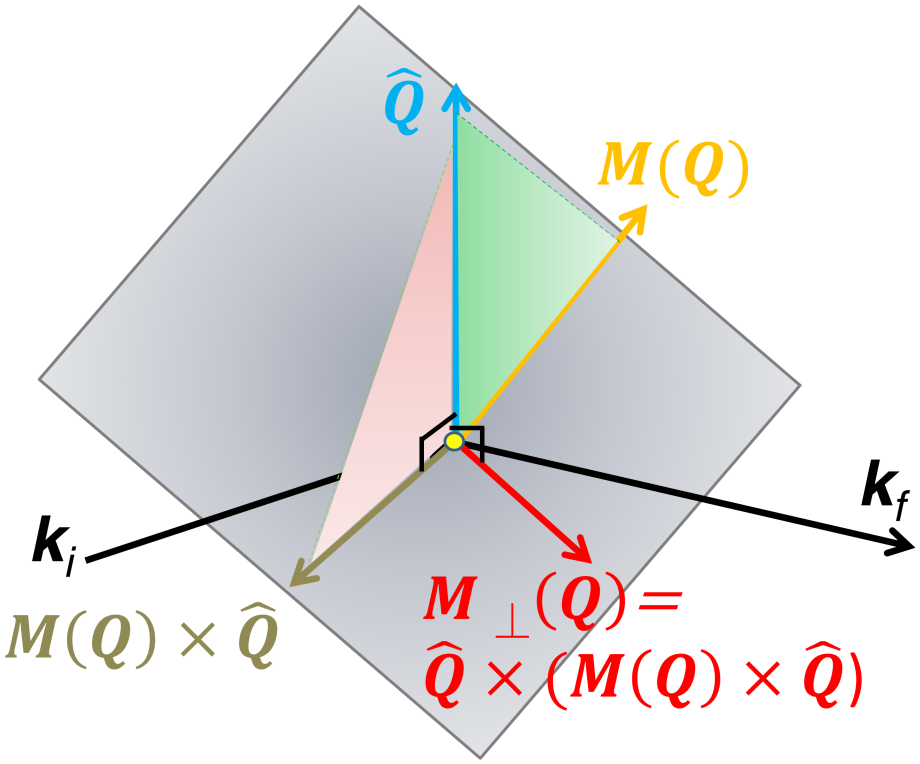

Figure 1.24 Scattering geometry for magnetic neutron scattering. Neutrons are only sensitive to the components of the magnetisation density $M(\mathbf{Q})$ that are perpendicular to $\mathbf{Q}$, denoted by $M_\perp(\mathbf{Q})$ [101].

A comparison of the magnetic and nuclear dynamic structure factor reveals two key differences. The first is the inclusion of the orientation factor reflecting that the neutron can only probe magnetism, both static and dynamic, that is orthogonal to $\mathbf{Q}$ (Fig. 1.24). This can be seen as a consequence of the fact that the dipole-dipole interaction of the spin and orbital contributions to the dipolar field experienced by the incoming neutron are not central forces. The second is the inclusion of the magnetic form factor which reflects the fact that magnetic neutron scattering involves the interaction of the neutron and the unpaired atomic electrons and thus must take into consideration the extension of the electron clouds in real space. This is stark contrast with nuclear scattering where the nuclei are considered point scatters and thus no explicit $\mathbf{Q}$ was required in $S(\mathbf{Q}, E)$.

By inserting Eq. 1.117 into Eq. 1.115, the magnetic double differential neutron

scattering cross section becomes

$$\left(\frac{d^2\sigma}{d\Omega dE}\right)_{\text{mag}} = \frac{k_f}{k_i}\left(\frac{\gamma r_o}{2}\right)^2 |f(\mathbf{Q})|^2 g^2 \sum_{\alpha,\beta}(\delta_{\alpha\beta} - \hat{Q}_\alpha \hat{Q}_\beta) S^{\alpha\beta}_{\text{mag}}(\mathbf{Q}, E), \quad (1.119)$$

where $\left(\frac{\gamma r_o}{2}\right)^2$ is conventionally taken to be 73 mb sr^{-1} [106]. In this Thesis, a simplified expression of $\left(\frac{d^2\sigma}{d\Omega dE}\right)_{\text{mag}}$ is employed. As discussed in Appendix A, by utilising the dipole approximation, the magnetic form factor $f(\mathbf{Q})$ was approximated to be $f(|\mathbf{Q}|)$. Secondly, as was mentioned above, since the prefactor $\frac{k_f}{k_i}$ in most cases is reduced to a constant that is either accounted for or absorbed into a normalisation constant, it is omitted for convenience. Thirdly, the paramagnetic approximation was utilised [107]. Such an approximation corresponds to the assumption that only isotropic spin excitations are being measured. Since all magnetic anisotropy is assumed to be absent, the system must be rotationally invariant and thus,

$$S^{zz}_{\text{mag}}(\mathbf{Q}, E) = S^{yy}_{\text{mag}}(\mathbf{Q}, E) = S^{xx}_{\text{mag}}(\mathbf{Q}, E). \quad (1.120)$$

Since the polarisation factor implies sensitivity to only orthogonal components, then the summation in Eq. 1.119 may be simplified to

$$\sum_{\alpha\beta}(\delta_{\alpha\beta} - \hat{Q}_\alpha \hat{Q}_\beta) S^{\alpha\beta}(\mathbf{Q}, E) = \frac{2}{3} Tr(S^{\alpha\beta}_{\text{mag}}(\mathbf{Q}, E)). \quad (1.121)$$

By omitting the $\frac{k_i}{k_f}$ prefactor and applying both dipole and paramagnetic approximations to Eq. 1.119, one obtains

$$\left(\frac{d^2\sigma}{d\Omega dE}\right)_{\text{mag}} = \left(\frac{\gamma r_o}{2}\right)^2 |f(|\mathbf{Q}|)|^2 g^2 2 S_{\text{mag}}(\mathbf{Q}, E), \quad (1.122)$$

where $S_{\text{mag}}(\mathbf{Q}, E)$ is understood to be $S^{zz}_{\text{mag}}(\mathbf{Q}, E) \equiv \frac{Tr(S^{\alpha\beta}_{\text{mag}})}{3}(\mathbf{Q}, E))$ [108]. As discussed in Appendices H and I, this factor is directly accounted for by either multiplying the integrated intensity by a factor of three as was the case of the total moment sum rule or by multiplying the expression for the particular sum rule of interest by a factor of $\frac{1}{3}$, as was the case for the first moment sum rule. It

should be noted that the paramagnetic approximation, as its name suggests, is only an approximation. Its validity relies on the condition that the energy scales of interest are much larger than the anisotropy, as is the case for many Co^{2+}-based magnets, including many of the members of the Co-V phase diagram [76] that are summarised in Fig. 1.13.

Finally, by employing the fluctuation-dissipation theorem, it can be shown that the magnetic dynamic structure factor is related to the imaginary part of the spin susceptibility by

$$S^{\alpha\beta}_{\text{mag}}(\mathbf{Q}, E) = \frac{1}{\pi}[n(E) + 1]\frac{\chi''(\mathbf{Q}, E)}{g^2\mu_B^2}, \tag{1.123}$$

where the factors g and μ_B ensure dimensionality consistency with the bulk spin susceptibility. By inserting Eq. 1.123 into Eq. 1.122, one obtains

$$\left(\frac{d^2\sigma}{d\Omega dE}\right)_{\text{mag}} = \left(\frac{\gamma r_o}{2}\right)^2 |f(|\mathbf{Q}|)|^2 \frac{2}{\pi}[n(E) + 1]\frac{\chi''(\mathbf{Q}, E)}{\mu_B^2}, \tag{1.124}$$

where once again $\chi''(\mathbf{Q}, E)$ is understood to be $\chi''_{zz}(\mathbf{Q}, E) \equiv \frac{Tr(\chi''_{\alpha\beta})}{3}(\mathbf{Q}, E))$. The importance of Eq. 1.124 is that it allows one to compare magnetic neutron inelastic scattering data with other measurements of the spin susceptibility, such as those performed with a SQUID magnetometer**.

Excitations: Types, Experimental Considerations & Lineshapes

Having provided a general overview of the technique of neutron inelastic scattering, the discussion will conclude with a brief overview of three important topics concerning the excitations that will be observed in this Thesis. First, the reader will be introduced to the three types of excitations that are observed. Secondly, the discussion will shift to the experimental considerations required to detect these excitations. The chapter will then conclude with a discussion on the lineshapes that were used to model and infer information from these excitations.

** The static spin susceptibility χ is measured on a SQUID magnetometer. It can be related to the dynamic spin susceptibility by

$$\chi = \lim_{Q\to 0}\chi'(Q) = \lim_{Q\to 0}\int dE\frac{\chi''(\mathbf{Q}, E)}{E}. \tag{1.125}$$

In this Thesis, there are two, possibly three types of excitations that will be observed with neutron inelastic scattering. The first type is a single particle excitation where the excitation energy does not exhibit any $\mathbf{Q}$-dependence, *i.e.* is non-dispersive. Whilst these single particle excitations may lack dispersion, their intensity may exhibit a strong $\mathbf{Q}$-dependence. The underlying physical mechanisms for such $\mathbf{Q}$-dependence vary widely with one example being the electron cloud structure intrinsic to single-ion physics for the case of crystal fields, such as those probed in this Thesis. The second type of excitations is called collective excitations, examples of which include phonons and magnons. Involving the simultaneous motion of numerous atoms or moments, these excitations are dispersive with excitation energies that are $\mathbf{Q}$-dependent. In the case of crystalline materials, the energies themselves are periodic in $\mathbf{Q}$, where the periodicity is based on the Brillouin zone. Consequently, the excitations depend only on the reduced wavevector $\mathbf{q} = \mathbf{Q} - \Gamma$, where Γ denotes the zone centre. Although the dispersion is periodic and relies on $\mathbf{q}$, its intensity depends on $\mathbf{Q}$. Thus, it is commonly instructive to measure these excitations in various Brillouin zones over a variety of $\mathbf{Q}$ values. As will be discussed below, the energy width of these collective excitations depends on the damping of the mode describing the collective motion with the strength of such damping having important consequences in data modelling. There exists a third type excitation called multi-excitations [109]. Depending on the interpretation of the experimental data, one may argue that there is evidence that this type of excitation may be key in understanding the magnetic excitation spectrum of CoO and is thus discussed in more detail in Chapter 5. As the name suggests, multi-excitations describe the interactions between individual excitations such as phonons or magnons. Such interactions may be harmonic, whereby the energy of the multi-excitations are $n\Delta E$, where ΔE denotes the energy of the original excitation. Another possibility is that the interactions may be anharmonic, resulting in a non-uniform spacing between the energies. Both harmonic and anharmonic coupling processes are bound[††] by the conservation of energy and momentum with such limitations defining kinematically accessible regions in $(\mathbf{Q}, E)$ space [111]. Combined with other key characteristics, such as the observed $\mathbf{Q}$-dependence of the intensity over several Brillouin zones, these kinematic constraints have proven key in some studies for identifying such excitations.

[††]This is not always the case, particularly in the presence of defects [110]. Examples include disordered crystals of ferrospinels, crystals with surface imperfections, and impurities in polycrystalline samples. For this Thesis, in particular for the case of the CoO single crystal that is investigated in Chapter 5, the effects of any such defects was assumed to be negligible.

It is important to distinguish between multi-excitations and multi-scattering processes [112]. For the former case, these are several excitations that are created by a single scattering event, whilst the latter describes multiple single excitations that are created by distinct scattering events that are separated in both space and time. Examples of multi-scattering processes involve the neutron scattering from different atoms or moments along its path through the sample under investigation or it may involve scattering contributions from a component of the sample environment such as a cryostat. Whilst the former is often a source of rich physics, the latter is generally undesired and commonly labelled as *spurious* scattering. Note that the term spurious scattering is used *in lieu* of *parasitic* scattering which is conventionally used to describe scattering that occurs whilst the sample is not present in the beam and is often caused by, but not limited to, scattering off the edges of collimators. The prevention (or minimisation) of multi-scattering processes is generally accomplished by either reducing the sample thickness such that no more than 10% of the neutrons are scattered by the sample or by employing higher incident energies (*i.e.* shorter wavelengths) to increase the mean free path $\Lambda(\lambda)$ of the neutron or sometimes a combination of both. While the elimination of all multi-scattering events may not be possible in some cases, such as secondary scattering by the sample environment, such spurious processes can be accounted for by employing a variety of analysis techniques such as verifying that the excitations obey the principle of detailed balance.

Sample thickness and incident energy selection are only two of the mryiad of experimental parameters that one must be consider and attempt to optimise when performing neutron inelastic spectroscopy. Although numerous and often technically demanding, the experimental parameters and the process of optimisation are ultimately dictated by the type of information that is desired to be extracted for a particular sample of a system of interest. For example, throughout the evolution of neutron scattering, different neutron spectrometers at different facilities have been optimised for particular ranges (Fig. 1.25), with no one instrument capable of adequately probing the over six orders of magnitude spanned by inelastic spectroscopy. So inevitably the first question corresponds to which instrument should be employed. The choice of instrument fundamentally stems from the delicate balance for the need of a sufficiently high incident (final) energy to both provide an adequate $(\mathbf{Q}, E)$ range and minimise neutron absorption, whilst satisfying the need for a sufficiently low incident (final) energy to provide an adequate resolution. An additional consideration that one is faced with when choosing a spectrometer is the choice of triple-axis or time-of-flight.

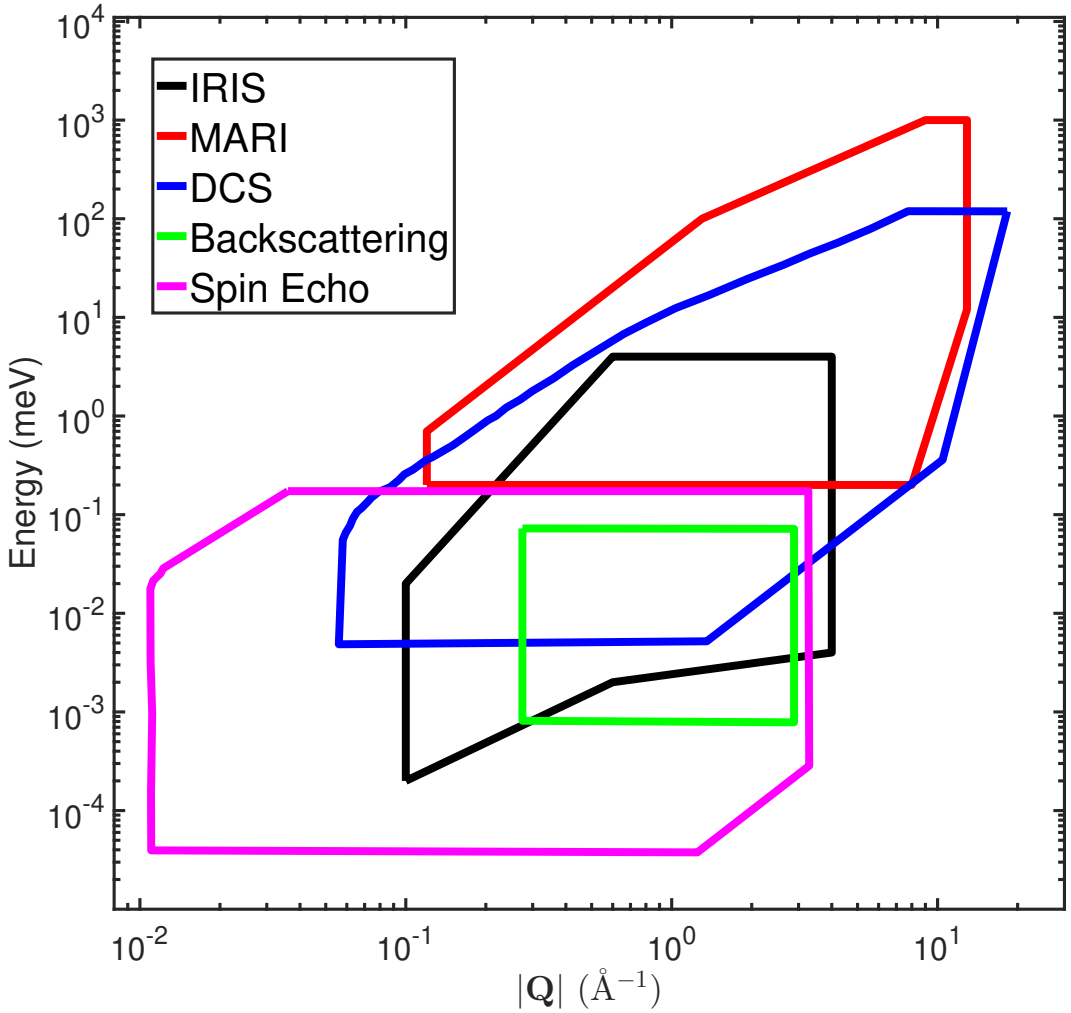

Figure 1.25 Comparison of the dynamic ranges accessed by various spectrometers and techniques [87, 88, 102].

As described above, such a choice depends on the nature of the sample (*e.g.* polycrystalline or single crystal, composition), on the nature of the investigation (*e.g.* exploratory or focussed regions in $(\mathbf{Q}, E)$ space) and the nature of the excitations (*e.g.* dispersive or flat modes). In addition of the need for both an adequate experimentally accessible $(\mathbf{Q}, E)$ range and adequate instrumental resolution, an experimental parameter that is of particular concern is the neutron flux Φ. The importance of the neutron flux is that it ultimately determines the time required for performing a measurement, *i.e.* counting times. The flux is a complicated parameter that is dependent on the particular source and instrument that is employed in the measurement. When choosing an instrument and the values for its instrumental parameters (*e.g.* incident energy, chopper frequency), one must always consider the delicate balance between flux and resolution. Although an instrument may be capable of providing extremely fine

resolution in the desired $(\mathbf{Q}, E)$ range, the resolution may need to be reduced when performing the actual measurement. Since the flux goes as $\sim (\delta E)^n$, where δE is the instrumental resolution and $n \sim$ 2-4, an increase in the resolution results in significant decreases in flux and thus longer counting times. The increase in counting times may be a significant experimental limitation, particularly for weakly scattering samples such as is the case for the effective spin-$\frac{1}{2}$ magnets investigated in this Thesis. To overcome this particular experimental limitation, a coarser instrumental resolution may be chosen such that the higher available flux provides adequate counting statistics in order to provide a level of precision that allows one to distinguish individual excitations with the chosen resolution in the available measurement time. For both practical (*e.g.* data acquisition) and statistical reasons (*e.g.* systematic errors), achieving the necessary counting statistics by performing multiple measurements, each with shorter counting times, is generally preferred over simply performing a single long measurement. An example of the balance between all experimental considerations considered so far is presented pictorially in Fig. 1.26. These experimental considerations are by no means limited to those presented so far, although too numerous to be listed here, the interested reader may refer to some comprehensive reviews on the subject matter.

Having described both the types of excitations and some of the parameters one must consider when experimentally measuring these excitations, the discussion and this chapter will conclude with a brief description of some select lineshapes that were used in this Thesis to model such excitations. This discussion is based on Appendix A of Cowley *et al.* [21] and references contained therein. In the simplest case, an excitation with a given energy E_o has an infinite lifetime τ. Such an excitation is represented by a delta function in energy and centred at $E = E_{\mathbf{q}}$, *i.e.* $\delta(E - E_{\mathbf{q}})$ and the dynamic structure factor for this particular excitation would correspond to

$$S(\mathbf{Q}, E) = [n(E) + 1] Z_{\mathbf{Q}} [\delta(E - E_{\mathbf{q}}) - \delta(E + E_{\mathbf{q}})], \tag{1.126}$$

where $Z_{\mathbf{Q}}$ is a dimensionless structure factor. Utilising the logic outlined by Eq. 1.124, the $[\dots]$ term corresponds to χ''. There are two important observations that should be noted here. First, a second δ-function but now centred at $E = -E_{\mathbf{q}}$ is present. This second term is called the anti-Stokes term and represents the possibility for the annihilation of an excitation, *i.e.* the system transfers energy to the incident neutron. Secondly, χ'' is given by an anti-symmetrised linear

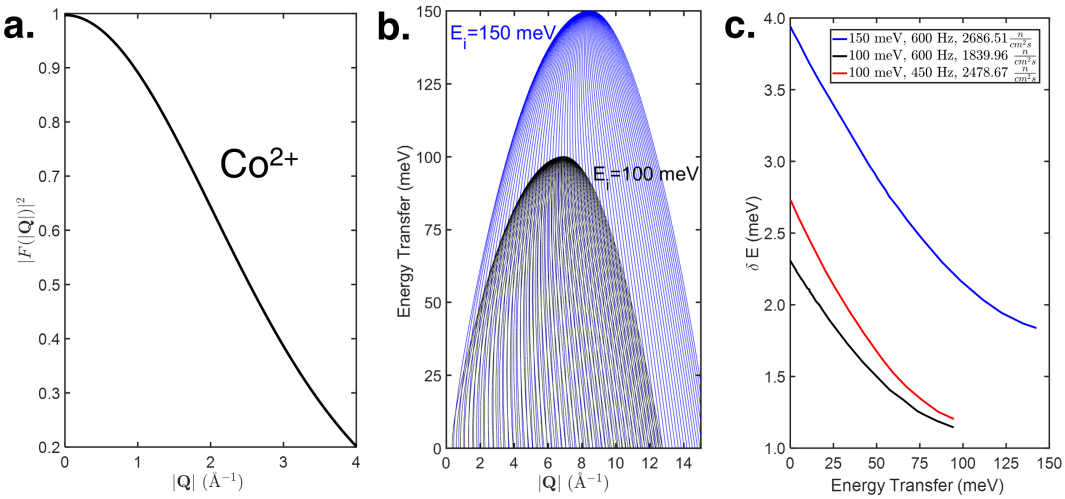

Figure 1.26 (a) The $|\mathbf{Q}|$-dependence of the square modulus of the magnetic form factor $|f_{\text{mag}}(|\mathbf{Q}|)|$ for Co^{2+}. (b) Calculated dynamic range on the direct geometry time-of-flight spectrometer MARI with incident energies of 150 meV and 100 meV for the down scattering range. (c) Calculated energy dependence of the instrumental resolution in energy for MARI employing various incident energies and chopper frequencies with the gadolinium or G-chopper. This figure summarises all key experimental considerations when performing a magnetic neutron inelastic scattering experiment on a polycrystalline sample. Panel (a) determines which $|\mathbf{Q}|$-range is of interest. Panel (b) determines the dynamic range that is experimentally accessible with a particular instrumental configuration. Panel (c) provides a quantitative measure of the subtle balance between flux and resolution.

combination of the two δ-functions. The negative sign in Eq. 1.127 ensures that χ'' is odd with respect to energy, an essential requirement based on the principle of detailed balance as discussed in Appendix F.

In the case that the excitation has a finite lifetime, both δ-functions in Eq. 1.126 may be replaced by Lorentzians, yielding a new dynamic structure factor given by

$$S(\mathbf{Q},E) = \frac{1}{\pi}[n(E)+1]Z_{\mathbf{Q}}\left[\frac{\Gamma_{\mathbf{q}}}{(E-E_{\mathbf{q}})^2+\Gamma_{\mathbf{q}}^2} - \frac{\Gamma_{\mathbf{q}}}{(E+E_{\mathbf{q}})^2+\Gamma_{\mathbf{q}}^2}\right], \qquad (1.127)$$

where $\frac{1}{\pi}$ is a normalisation constant and $\Gamma_{\mathbf{q}}$ is the $\mathbf{q}$-dependent linewidth corresponding to the half-width-half-maximum. In contrast to Eq. 1.126, where the Fourier transform of the δ-function corresponds to a complex sine wave propagating indefinitely in time, the Fourier transform of both Lorentzians in Eq. 1.127 corresponds to an expontential decay in time that will prove

particularly useful for modelling excitations in Chapter 2. Such time dependence is reminiscent of a damped sine wave; thus, it is common in the literature to rewrite Eq. 1.127 in the form of a damped harmonic oscillator given by

$$S(\mathbf{Q},E) = \frac{1}{\pi}[n(E)+1]Z_{\mathbf{Q}}\left\{\frac{4EE_{\mathbf{q}}\Gamma_{\mathbf{q}}}{(E^2-\Omega_{\mathbf{q}}^2)^2+4E_{\mathbf{q}}^2\Gamma_{\mathbf{q}}^2}\right\}, \tag{1.128}$$

where $\Omega_{\mathbf{q}}^2 = E_{\mathbf{q}}^2 + \Gamma_{\mathbf{q}}^2$. It is important to note that both Eqs. 1.127 and 1.128 are commonly used to model underdamped modes. In contrast, overdamped modes, corresponding to excitations that are much broader in energy and thus exhibit much faster rates of decay in time, are often modelled by

$$S(\mathbf{Q},E) = \frac{1}{\pi}[n(E)+1]\frac{Z_{\mathbf{Q}}}{\Omega_{\mathbf{q}}}\frac{E\Gamma_{\mathbf{Q}}}{E^2+\Gamma_{\mathbf{Q}}^2}, \tag{1.129}$$

where $\frac{\Omega_{\mathbf{q}}}{\Gamma_{\mathbf{q}}}$ is taken to be zero in Eq. 1.128 that is evaluated in the limit of $E \to 0$. The lineshape given by Eq. 1.129 will be employed in Chapter 3 and describes a quasi-elastic Lorentzian, being only valid for low energy transfers, with its Fourier transform exponentially decaying in time. Since all excitations modelled in this Thesis are magnetic in origin, the structure factor $Z_{\mathbf{q}}$ or $Z_{\mathbf{Q}}$ in both Eqs. 1.127 and 1.129 was taken to be the real part of the susceptibility χ'.

Chapter 2

Evidence for the confinement of magnetic monopoles in quantum spin ice

2.1 Introduction

2.1.1 Motivation

Magnetic monopoles remained at the periphery of physics until Dirac published his quantum theory of magnetic charge in which he envisioned a monopole as the end of an infinitesimally thin solenoid construct known as a Dirac string [113]. Dirac proposed that not only were magnetic monopoles consistent with quantum theory, but their existence would result in the quantisation of electrical charge [113, 114]. While the latter has been verified experimentally [115], the identification of magnetic monopoles has remained challenging. Establishing the existence of this elusive elementary particle would lead to a beautiful symmetrisation of Maxwell's equations and validate several modern physical theories [116].

Recently, the discovery of a class of magnets known as spin ices has made the study of magnetic monopole quasiparticles viable [114, 118, 119]. Spin ices are found in a series of magnetic pyrochlore oxides $A_2^{3+}B_2^{4+}O_7$ [120], which have moments residing on the A-site [74], corner-sharing tetrahedra sublattice

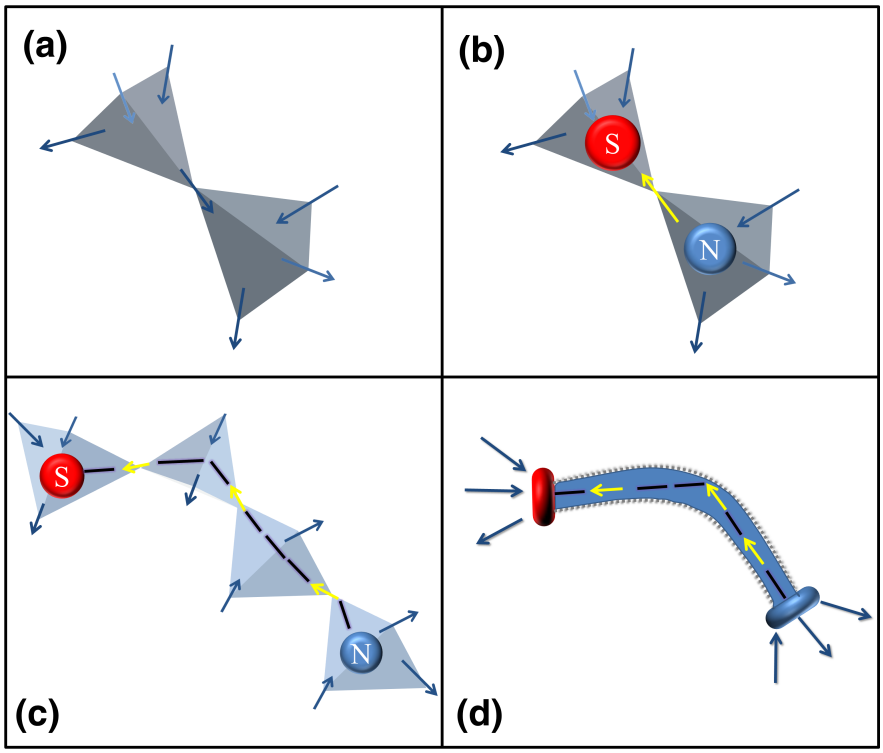

Figure 2.1 (a) Schematic of one possible two-in/two-out spin ice configuration [117] in adjacent tetrahedra of the pyrochlore lattice illustrated in Fig. 1.5(b). (b) A defect spin ice state is created by the flipping of a spin labelled in yellow and results in the creation of a magnetic monopole pair labelled **N** and **S** [118]. (c) The monopole pair can separate further *via* adjacent spin flips [119]. (d) A schematic of an effective "Dirac string", which consists of an infinitesimally thin solenoid (one unit of flux width) connecting the monopole pair [113].

as illustrated in Fig. 1.5(b). At low temperatures, the moments assume a two-in/two-out short-ranged magnetically ordered state as shown in Figure 2.1(a), possessing Pauling's configurational entropy [73, 121]. Castelnovo *et al.* [118] first proposed that dipolar spin ices (DSIs) may host mobile magnetic monopole quasiparticles as illustrated in Figure 2.1(b). These monopoles are expected to interact *via* a magnetic Coulomb law suggesting deconfinement [114, 118], and the strings connecting them in pairs (see Figures 2.1(c) and (d)) have not been easily measurable. Consequently, although there is mounting experimental evidence [114, 122] supporting the existence of monopoles in the DSIs, the exact nature of the interaction between these monopoles is still under active investigation [123].

In an attempt to measure interactions between magnetic monopoles, the attention of the community has shifted to quantum spin ices (QSIs) [23, 124–129]. This family of materials differs from dipolar spin ices in the nature of the interactions between the magnetic moments [23], as their magnetic Hamiltonians

consist of transverse coupling terms leading to significant fluctuations of the moments away from the local [111] quantisation axes. As a result, although monopole quasiparticles are deconfined in dipolar spin ices, such deconfinement may not be the case for quantum spin ices [19, 130, 131]. Possessing enhanced quantum effects and shorter correlation times [132], the interactions between monopole quasiparticles in quantum spin ices remains an issue of central interest to the community [133].

2.1.2 Pr^{3+}-based Quantum Spin Ices

Among the numerous quantum spin ice candidates reported in the literature [23], Pr^{3+}-based quantum spin ice candidates, as summarised in Tab. 2.1, have recently captured a significant amount interest from the frustrated magnetism community [129]. Although investigated much later than their Tb^{3+} and Yb^{3+} counterparts [45], the possibility of a quantum spin ice state in Pr^{3+}-based pyrochlore oxides was first inspired by the discovery of the *dynamic spin ice* state in $Pr_2Sn_2O_7$ [17]. This discovery of a highly dynamic ground state, possessing a spin ice-like scattering profile, identified the importance of the balance between the three dominant energy scales in magnetic pyrochlore oxides: the crystalline electric field (CEF), nearest neighbour dipolar (D_{NN}) and exchange (J_{NN}) interactions [134]. In contrast with dipolar spin ices possessing large moments such that $D_{\mathrm{NN}} \gg \mathrm{J_{NN}}$ [135–137], and the quantum spin liquid candidate $Tb_2Ti_2O_7$ where CEF $\sim D_{\mathrm{NN}} \sim \mathrm{J_{NN}}$ [138–140], the strong single-ion anisotropy from crystal field effects combined with the significantly reduced moment and enhanced superexchange resulting from the low f-electron count of Pr^{3+} placed $Pr_2Sn_2O_7$ in what was then the relatively unexplored CEF$\gg J_{\mathrm{NN}} \gg \mathrm{D_{NN}}$ regime, corresponding to a spin ice-like system where quantum effects played a much more influential role [125].

Motivated by the significant influence of quantum fluctuations in $Pr_2Sn_2O_7$, Onoda & Tanaka published two seminal theoretical papers [19, 141] on the so-called *quantum melting* of spin ice between 2010 and 2011. As alluded to by its name, *quantum melting* is a process by which strong quantum effects *via* quantum entanglement, *in lieu* of thermal heating, lifts the ground state manifold degeneracy, thereby suppressing freezing that is characteristic of the dipolar spin ice state. Such a model was shown to not only account for a plethora of experimental data for $Pr_2Sn_2O_7$ [17] but also many of the exotic magnetic and physical properties of the chiral spin liquid $Pr_2Ir_2O_7$ [142–145] that were just being

discovered during the same time period. The influence of the *quantum melting* model was profound and stems from its simplicity, and ultimately its generality. Consisting of the well-characterised dipolar spin ice Hamiltonian [120, 146] that was now subject to strong anisotropic superexchange interactions, the model that was based on fourth order strong-coupling perturbation theory was further generalised to any magnet based on non-Kramers atomic doublets, in particular those based on Pr^{3+}, a subtle but key observation further elaborated in another key theoretical study by Lee, Onoda & Balents [126]. The subtle dichotomy of generality of non-Kramers doublets and specificity for the Pr^{3+} cation, was particularly significant because the vast majority of the community's resources at the time were allocated towards Yb^{3+}-based pyrochlores, particularly motivated by the exotic magnetism that was being observed in $Yb_2Ti_2O_7$ at the time [147–149].

The concrete predictions by Onoda & Tanaka [19, 141] for key experimental signatures that are indicative of the quantum spin ice state, such as the smearing of the much-celebrated pinch-points at (111) and (002) in $S(\mathbf{Q})$ [150, 151], combined with the explicit proposal that Pr^{3+} was key in achieving such an exotic magnetic state, have significantly contributed to the resurgence of intense interest in Pr^{3+}-based pyrochlores that continues to this day [129]. No longer were Pr^{3+}-based pyrochlores ignored and relegated to footnotes in literature reviews [45, 74] focussing on their Yb^{3+} and Tb^{3+} counterparts, rather the community quickly recognised the Pr^{3+} cation as a unique and unexplored avenue for achieving a quantum spin ice state. At the same time of the work by Onoda & Tanaka [19, 141], interest in achieving such a novel magnetic state was gaining significant attention [23]. Interest in quantum spin ices already existed, going back as far as the early 2000's; but such attention was largely driven by the desire for the discovery of a spin liquid phase in 3D magnets, where quantum effects would prevent long range magnetic ordering, as was already experimentally observed in low dimensional systems [152–156]. The explosion of interest in quantum spin ices in the early 2010's stemmed from a large collection of theoretical studies that proposed that spin ice systems that were subject to enhanced quantum fluctuations could host a U(1) quantum spin liquid state with emergent photons [127, 157–162]. Fuelled by their potential role in achieving a completely novel magnetic state that not only has the ability to host emergent gauge fields, but also fractional excitations and large-scale quantum entanglement, the experimental realisation of quantum spin ices became and remains to this day a central point of interest for both the experimental and

theoretical communities in condensed matter [153, 163].

The recognition of the importance of Pr^{3+} in achieving the coveted quantum spin ice state is particularly evident with the recent explosion of experimental studies on all six members of the $Pr_2B_2O_7$ (B=Pb^{4+}, Hf^{4+}, Zr^{4+}, Sn^{4+}, Ir^{4+} and Ru^{4+}) family, a family of compounds that were the subject of only a handful of papers one decade earlier [23, 45, 129, 153]. As is the case for many systems, the amount of studies on a particular member of the $Pr_2B_2O_7$ family is directly correlated with the ability to synthesise high quality single crystal samples. Consequently, $Pr_2Pb_2O_7$, requiring a synthesis pressure of 2 GPa at 900°C using a multi-anvil press [164], is the least studied member of the Pr^{3+}-based pyrochlores. DC magnetic susceptibility and isobaric heat capacity confirmed strong $\langle 111 \rangle$ single-ion anisotropy, evidence for monopole dynamics (*e.g.* non-Schottky behaviour in the heat capacity [165]), and a lack of long-range magnetic order down to 400 mK, providing evidence that $Pr_2Pb_2O_7$ is a quantum spin ice candidate [164]. Despite the aforementioned importance of $Pr_2Sn_2O_7$ in the resurgence of interest in the Pr^{3+}-based pyrochlores, the stannate member remains relatively unexplored, a result of the unavailability of large single crystals due to SnO_2 volatility [45]. In addition to the original studies by Subramanian [74], Matsuhira [166] and Zhou [17], very few studies have been reported in the literature [16, 134], but this will likely not be the case in the near future due to a recent report of the successful growth of large single crystals of multiple stannate pyrochlores, including $Pr_2Sn_2O_7$, using a $Na_2B_4O_7$-NaF flux [167]. Finally, isobaric heat capacity studies on polycrystalline samples of $Pr_2Ru_2O_7$ revealed that the Pr^{3+} moments do not assume a long range magnetic order down to 400 mK, despite strong Pr^{3+} spin-spin correlations [168], whilst DC magnetometry confirms dominant $\langle 111 \rangle$ single-ion anisotropy [169]. In contrast with the plumbate [164] and stannate [17], the non-Kramers doublet of $Pr_2Ru_2O_7$ exhibits inhomogeneous splitting that was previously observed in Bi^{3+}-doped $Pr_{2-x}Bi_xRu_2O_7$ [170]. The unknown origin of the inhomogeneous splitting, combined with the Ru^{4+} sublattice assuming long range magnetic order [171], and the lack of availability of high quality single crystals, had limited the interest in this particular member, despite evidence for quantum spin ice-like behaviour [45, 172]. Although largely disregarded for almost five years, a recent study by van Duijin *et al.* [173] proposing a quantum spin ice state in the $Pr_2Ru_2O_7$ is accomplished *via* a disordered-induced mechanism similar to that of $Pr_2Zr_2O_7$ [125] will likely encourage further studies in the future.

Among the Pr^{3+}-based pyrochlores with large single crystals available,

$Pr_2Ir_2O_7$ was the first to be successfully grown with minimal structural defects using a KF flux [45, 174]. Sitting at the intersection of two fields of recent interest in condensed matter physics: spin ices and the iridates, preliminary physical property measurements of $Pr_2Ir_2O_7$ confirmed dominant $\langle 111 \rangle$ single anisotropy [175], where the in-plane components were strictly quadrupolar and the RKKY interaction yields ferromagnetic coupling between Pr^{3+} moments [142, 144, 176–178], despite a negative θ_{CW} [143]. Magnetisation data provided substantial evidence for spin ice correlations, in particular the well-documented metamagnetic transition for external fields aligned along the [111] direction [142]. However, sharp pinch points in $S(\mathbf{Q})$ and the Pauling residual entropy are both absent in the iridate, and remains an open question to this day [143, 176]. Contextually, $Pr_2Ir_2O_7$ among all rare earth-based irriate pyrochlores was of particular interest since both theoretical and experiental studies deduced that the metallic $Pr_2Ir_2O_7$ was located close to a metal-to-insulator transition [179, 180]. Further attention was directed towards $Pr_2Ir_2O_7$ because for such a heavy fermion material, either long range magnetic order or heavy Fermi liquid behaviour was originally expected, yet neither was observed [176]. In the case of $Pr_2Ir_2O_7$, it was later suggested that the Pr^{3+} and Ir^{4+} moments were coupled *via* the two-channel and not the ordinary Kondo effect, and thus a lack of heavy Fermi liquid behaviour is in fact consistent with the lack of a phase transition as shown in both physical property and muon spin relaxation spectroscopic measurements [145, 181]. Ultimately $Pr_2Ir_2O_7$ gained significant attention after Machida *et al.* [142] proposed the iridate was the long sought after chiral spin liquid [156, 182, 183]. The presence of a chiral state was deduced from an anomalous Hall effect that persists in the absence of both an external magnetic field and any observable magnetisation [142, 184–186]. Flint & Senthil [176] later proposed that the chiral state was selected from the spin ice manifold *via* a mechanism corresponding to a chiral analogue of the RKKY interaction that is based on the chiral fluctuations of the Ir^{4+} moments that induces ferrochiral coupling between Pr^{3+} moments.

In contrast to its iridate counterpart, early investigations on $Pr_2Zr_2O_7$ were significantly hampered by the lack of availability of high quality large single crystals [45, 165, 187, 188]. The lack of a suitable flux, praseodymium volatility, and the similar Shannon radii of six coordinate Pr^{4+} and Zr^{4+} resulted in single crystals exhibiting both significant strain and off-stoichiometry *via* anti-site disorder, where the latter was already shown to have significant influence on the low temperature physical properties of other quantum spin ice candidates

$Yb_2Ti_2O_7$ [97, 189, 190] and $Tb_2Ti_2O_7$ [45, 191]. Motivated by preliminary physical property and neutron inelastic scattering measurements providing strong evidence for quantum spin ice-like behaviour in $Pr_2Zr_2O_7$ [45, 165, 187], there was a concerted effort in the community to grow defect-free fully stoichiometric single crystals of the zirconate. Through an optimisation of the OFZ growth conditions (*e.g.* static argon atmosphere, intermediate rotation rate, additional sintering just below the melting temperature), Koohpayeh *et al.* [98] finally grew a fully stoichiometric large single crystal of the zirconate. Despite the success of achieving the desired stoichiometry, structural defects were still present in the form of local Pr^{3+} off-centering from the ideal pyrochlore sites, a type of local structural defect seen in the trivalent sites for both $Bi_2Ti_2O_7$ [192] and $La_2Zr_2O_7$ [193]. Motivated by both the availability of fully stoichiometric large single crystals and the bold suggestion by Savary & Balents [194] that weak structural disorder would promote a quantum spin liquid state in pyrochlores based on non-Kramers ions, Wen *et al.* [125] revisited the low energy magnetic dynamics of the single crystals of $Pr_2Zr_2O_7$ containing weak quenched local structural disorder. Low energy neutron inelastic scattering measurements were highly reminiscent of the aforementioned $Pr_2Ru_2O_7$ [170, 172], and consistent with structural disorder behaving as transverse fields acting on effective spin-$\frac{1}{2}$ moments. Utilising the original proposal by Savary & Balents [194], Wen *et al.* [125] argued that the transverse fields observed in the zirconate induced quantum tunnelling between degenerate classical spin ice ground states, resulting in the stabilisation of a U(1) quantum spin liquid.

Despite the success of the so-called disorder-induced random transverse Ising model to account for the low energy magnetism of $Pr_2Zr_2O_7$ [125, 129], the suggestion that the zirconate does host a U(1) quantum spin liquid has still not been experimentally proven [23]. In particular, despite the tremendous amount of effort throughout the community, there was a clear absence of any experimental evidence for the key prediction of a gapped linear photon-like dispersion that is indicative of low energy electrodynamics in not only the zirconate, but all other quantum spin ice candidates at the time [23, 125, 127, 129, 159, 195]. In the same year as Wen *et al.* [125] published their work on the zirconate, two key experimental studies by Sibille *et al.* [124] and Anand *et al.* [196] brought considerable attention onto $Pr_2Hf_2O_7$. Albeit relatively untouched and disregarded by experimentalists until 2016, a combination of physical property and neutron inelastic spectroscopy measurements on the hafnate quickly revealed its importance to the search of the U(1) quantum spin liquid

behaviour [128, 197]. Preliminary measurements [124, 196] confirmed the absence of long range magnetic order down to 90 mK in the cubic hafnate pyrochlore, possessing (i) weak net ferromagnetic nearest neighbour coupling between (ii) well-separated (isolated) non-Kramers doublets such that (iii) its low energy magnetic dynamics can be described by an effective spin-$\frac{1}{2}$ Hamiltonian with (iv) a highly anisotropic Ising g tensor, all consistent with spin ice-like physics. Despite the relatively large crystal field gap of $\Delta \sim 9$ meV, similar to that of the aforementioned plumbate [164], an analysis of the crystal field scheme indicated significant admixture of non-Ising and higher energy multiplets contributions to the ground state doublet, providing strong evidence for the presence of enhanced quantum fluctuations. Motivated by the evidence for quantum spin ice behaviour in $Pr_2Hf_2O_7$, both groups dedicated the next year towards the optimisation of single crystal growth conditions using the OFZ method [198, 199]. Ultimately, these efforts came to fruition, when in late 2018, single crystal neutron inelastic scattering revealed low energy spin excitations that resemble fractionalised, topological exciations that are characteristic of emergent quantum electrodynamics that were predicted for the U(1) QSL hosted by quantum spin ice [128]. This report by Sibille *et al.* [128], although unverified*, represents a significant step in the study of both quantum spin ices and liquids, and will most likely assure Pr^{3+}-based pyrochlores will remain at the forefront of condensed matter physics for the immediate future [19, 23, 141, 152, 153, 194, 197, 200].

Despite the significant progress in both the search and characterisation of quantum spin ice candidates among the Pr^{3+}-based pyrochlores, such progress has been effectively limited to a select number of systems [23]. In contrast to those systems that have high quality single crystals readily available, *i.e.* the irridates, zirconates and hafnates, very few neutron inelastic studies [16, 170, 173] have been reported for their polycrystalline counterparts after the original work by Zhou *et al.* [17], despite being a key source of motivation for the earlier work of Onoda & Tanaka [19, 141] that began the recent resurgence of interest in Pr^{3+}-based pyrochlores. Furthermore, despite a large body of theoretical studies (*e.g.* [130, 131]) that suggest non-negligible interactions between monopole quasiparticles, a comprehensive understanding of the properties of monopoles in quantum spin ices has remained elusive [19, 160–162, 201, 202]. Motivated by both key limitations in the literature, the low energy magnetic dynamics of the first, and still relatively unexplored Pr^{3+}-based quantum spin ice candidate $Pr_2Sn_2O_7$ [17] have been revisited. In this chapter, evidence is presented for the

*At the time of the writing of this Thesis.

direct observation of interacting magnetic monopole quasiparticles in $Pr_2Sn_2O_7$ using neutron inelastic spectroscopy. Measurements allowed for both an estimate of the monopole pair creation energy $2\hbar\omega_o$ and a lower bound of the effective tension λ between monopoles.

2.2 Experimental Details

2.2.1 Solid State Synthesis of the $Pr_2Sn_{2-x}Ti_xO_7$ Series

Polycrystalline samples of $Pr_2Sn_{2-x}Ti_xO_7$ (x = 0.00, 0.05, 0.10, 0.30, 0.40, 0.50 and 0.60) were prepared by a standard solid state reaction of stoichiometric amounts of Pr_6O_{11} (99.99 %, Alfa Aesar), SnO_2 (99.99 %, Alfa Aesar) and TiO_2 (99.99 %, Alfa Aesar) and summarised as

$$Pr_6O_{11(s)} + (6-3x)SnO_{2(s)} + (3x)TiO_{2(s)} \longrightarrow 3Pr_2Sn_{2-x}Ti_xO_{7(s)} + O_{2(g)}. \quad (2.1)$$

As outlined by Kennedy, Hunter & Howard [203], the powder reagents were mixed together, finely ground and pressed into a pellet using a uniaxial press. The pellets were placed in an alumina crucible and were pre-reacted by heating in air at 1000°C for 24 h. The pellets were then reground, repelletised and heated in air at 1400°C for approximately 48 h with intermittent grindings until room temperature powder x-ray diffraction measurements with a Bruker D2 phaser laboratory diffractometer using a Cu $K_{\alpha 1,2}$ source confirmed no discernable impurities.

2.2.2 High Resolution Powder Neutron Diffraction

Room temperature neutron powder diffraction experiments were performed on the high resolution powder diffractometer HB-2A [204] at the High Flux Isotope Reactor (HFIR) at Oak Ridge National Laboratory (ORNL). Approximately five grams of polycrystalline $Pr_2Sn_2O_7$ and all members of the disordered $Pr_2Sn_{2-x}Ti_xO_7$ series were sealed in aluminium ($x = 0$) and vanadium ($x \neq 0$) cans, respectively, under a helium atmosphere and mounted on the HB-2A multi-sample changer. A vertically focussing Ge(115) monochromator was utilised to provide a neutron wavelength λ of 1.54 Å. The collimation settings were open-

21'-12' for the pre-monochromator, monochromator-sample and sample-detector positions respectively, providing a high resolution mode of operation with a $\frac{\Delta d}{d} \approx 2$ x 10^{-3}.

2.2.3 DC Magnetometry

The temperature dependence of the DC magnetisation was measured using the VSM (vibrating sample magnetometry) option on the Quantum Design Dynacool PPMS. The DC magnetisation of a 51.1(1) mg polycrystalline sample of $Pr_2Sn_2O_7$ placed in a polypropylene holder was measured in an applied field $\mu_o H_{ext} = 0.1$ T between 1.8 K and 300 K in 87 steps with a logarithmic distribution.

2.2.4 Magnetic Diffuse Neutron Scattering

Magnetic diffuse neutron scattering experiments were performed on the fixed-incident-energy triple-axis spectrometer HB-1A [205] at the High Flux Isotope Reactor (HFIR) at ORNL. Approximately five grams of polycrystalline $Pr_2Sn_2O_7$ and all members of the disordered $Pr_2Sn_{2-x}Ti_xO_7$ series were placed in aluminium cans and loaded in an orange cryostat (CRYO-C). A series of two PG(002) crystal monochromators provided the fixed incident energy $\hbar\omega_i$ of 14.64 meV and two-highly oriented pyrolytic graphic (HOPG) filters were placed in the incident beam to remove higher order contamination. A PG(002) analyser crystal was located before the detector for energy discrimination. This setup resulted in an energy resolution at the elastic line of approximately 1 meV. The diffuse scattering was measured over a $|\mathbf{Q}|$-range of [0.46, 2.00] Å^{-1} in 0.009 Å^{-1} steps at 1.5 K. A high temperature background (250 K) was measured over the same $|\mathbf{Q}|$-range with identical statistics.

2.2.5 Low Energy Transfer Neutron Inelastic Scattering

Low energy transfer neutron inelastic scattering experiments were performed on the direct-geometry time-of-flight cold neutron chopper spectrometer CNCS [206] at the spallation neutron source (SNS) at Oak Ridge National Laboratory (ORNL). Approximately five grams of polycrystalline $Pr_2Sn_2O_7$ and all members of the disordered $Pr_2Sn_{2-x}Ti_xO_7$ series were sealed in aluminium cans

under a helium atmosphere for the experiment. The sample cans were mounted on the CNCS automatic three sample rotator stick (SS-003) with a boron nitride (BN) spacer adapted for a top loading 100 mm orange cryostat (CRYO-006). Measurements utilised incident energies $\hbar\omega_{\mathrm{i}}$ of 3.32 meV and 25 meV in high flux mode, providing an energy resolution at the elastic line of approximately 0.01 and 2 meV, respectively. Additional measurements were collected with an incident energy of 4.1 meV in medium resolution mode, providing an energy resolution at the elastic line of approximately 0.08 meV. An empty aluminium can was also measured for approximately half the counting time at identical experimental conditions, and the resulting spectra were subtracted from the corresponding sample spectra. The high flux and medium resolution modes were accomplished by spinning the high speed double disk chopper located just before the sample at a frequency of 300 Hz and 240 Hz, respectively

2.2.6 High Energy Neutron Inelastic Scattering

Higher energy transfer neutron inelastic scattering experiments were performed on the direct-geometry time-of-flight chopper spectrometer SEQUOIA [207] at the SNS at ORNL. A 5 g polycrystalline sample of $Pr_2Sn_2O_7$ was placed in an aluminium can and loaded in an orange cryostat (CRYO-007). Spectra were collected with an incident energy $\hbar\omega_{\mathrm{i}}$ of 170 meV, operating in fine energy resolution mode providing an elastic resolution of $\sim$ 2 % the incident energy, to measure crystal field excitations. The empty aluminium can was measured in identical experimental conditions for approximately one fifth of the sample counting time, and the resulting spectra were subtracted from the corresponding sample spectra. Fine energy resolution mode was achieved using a Fermi chopper operating at 600 Hz, and the background from the prompt pulse was removed with a T_o chopper operating at 120 Hz.

2.3 Experimental Results & Analysis

2.3.1 Sample Characterisation

As illustrated in Figs. 2.2(a) and (b), Rietveld refinement of the room temperature neutron diffraction patterns of the $Pr_2Sn_{2-x}Ti_xO_7$ series confirmed

the presence of a single phase, possessing $Fd\bar{3}m$ symmetry with no discernible impurities. In particular, the refined lattice parameter of 10.6038(3) Å for the undoped member $Pr_2Sn_2O_7$ (*i.e.* $x = 0$) agrees with previously reported values in the literature [17, 203, 208]. The chemical substitution of Sn^{4+} by the significantly smaller Ti^{4+} results in a linear decrease in the lattice parameter a with respect to the Ti^{4+} content x, in agreement with the predictions of Vegard's law [209]. Since this chapter constitutes the first successful synthesis of the $Pr_2Sn_{2-x}Ti_xO_7$ series, a direct comparison between the experimentally determined lattice parameters and those in the literature is not possible. Instead, a quantitative comparison between the experimentally determined lattice parameters and the expected lattice parameters was performed. The calculation of the expected lattice parameters for the $Pr_2Sn_{2-x}Ti_xO_7$ series was accomplished by first obtaining a relationship between the lattice parameter a of various praseodymium-based pyrochlores (i.e. $Pr_2B_2O_7$) and their corresponding Shannon-Prewitt ionic radius for the various B^{4+} cations summarised in Tab. 2.1. A linear regression was subsequently performed on the data summarised in Tab. 2.1, providing a quantitative relationship between the value of a and the Shannon-Prewitt ionic radius of the B^{4+} cation. Since the $Pr_2Sn_{2-x}Ti_xO_7$ series is essentially a binary solid state mixture of two different tetravalent cations, an effective B^{4+} radius can be calculated with respect to x by a linear combination of the individual Shannon-Prewitt ionic radii of Sn^{4+} and Ti^{4+} given by

$$R_{\mathrm{B,eff}} = (1 - \xi)R_B + \xi R_{B'}, \tag{2.2}$$

where $\xi = \frac{x}{2}$, R_B and $R_{B'}$ are the Shannon-Prewitt ionic radii for six-coordinate Sn^{4+} and Ti^{4+}, respectively. As summarised by both Fig. 2.2(c) and Tab. 2.2, the linear decrease in a with respect to x agrees both with the behaviour predicted by a linear extrapolation of the reported lattice parameters, providing strong experimental support for the homogeneous incorporation of particular nominal concentrations of Ti^{4+} cations into the B-site of the pyrochlore structure.

Table 2.1 Reported lattice constants and magnetic ground states for the $Pr_2B_2O_7$ pyrochlore series employed to calculate the expected lattice parameter for the newly synthesised $Pr_2Sn_{2-x}Ti_xO_7$ pyrochlore series.

B	B^{4+} radius (Å)	Lattice Constant (Å)	Magnetic Ground State
Pb	0.775	10.872(3)	Quantum Spin Ice [71, 164]
Hf	0.71	10.715(3)	Quantum Spin Ice [124, 196]
Zr	0.72	10.71(4)	Quantum Spin Ice [165]
Sn	0.69	10.603(4)	Quantum Spin Ice [17]
Ir	0.625	10.394(6)	Metallic Quantum Spin Ice [152, 210] or Chiral Spin Liquid [142, 176]
Ru	0.62	10.377(4)	Spin Liquid [168, 172]

Table 2.2 A comparison between the refined and predicted lattice parameters for polycrystalline samples of the $Pr_2Sn_{2-x}Ti_xO_7$ series at room temperature. All Rietveld refinements were performed using the FUllPRoF software suite [211]. All refined parameters and corresponding goodness-of-fit metrics are summarised in Tab. B.1 in Appendix B. The predicted lattice constants were calculated from a linear regression of the reported lattice constants for the $Pr_2B_2O_7$ pyrochlore series [17, 74, 164, 165, 168, 172, 176]. Numbers in parentheses indicate statistical errors.

Sample Label x	Refined x	Refined a (Å)	Predicted a (Å)
0	0	10.6038(3)	10.6034(6)
0.05	0.048(1)	10.5950(2)	10.5969(5)
0.10	0.120(2)	10.5845(2)	10.5872(5)
0.20	0.220(2)	10.5733(2)	10.5736(4)
0.30	0.310(2)	10.5625(3)	10.5614(4)
0.40	0.400(3)	10.5499(3)	10.5492(4)
0.50	0.504(2)	10.5348(3)	10.5351(3)
0.60	0.558(4)	10.5269(4)	10.5278(3)

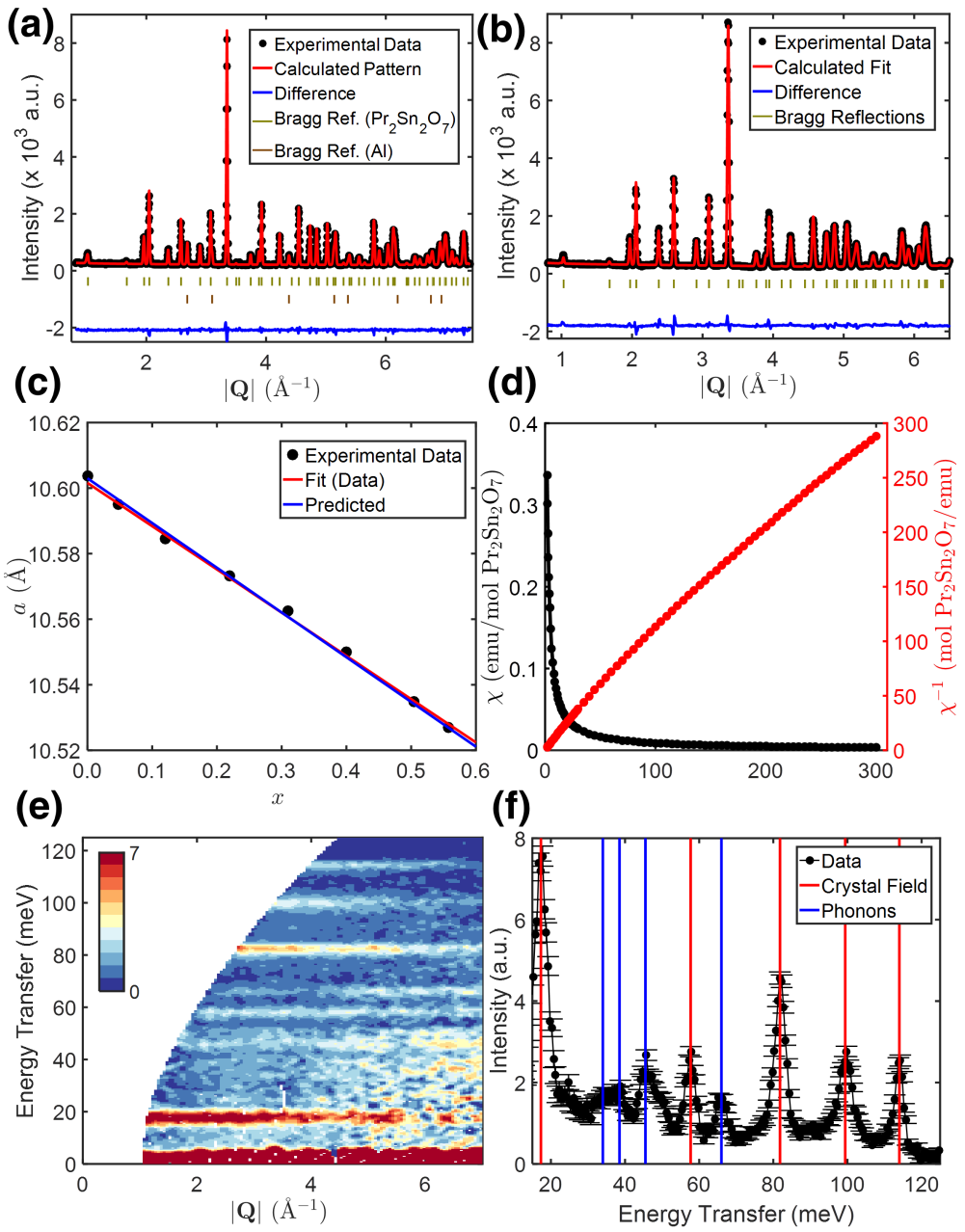

Figure 2.2 Measured, calculated and difference room temperature neutron powder diffraction profiles for (a) $Pr_2Sn_2O_7$ and (b) $Pr_2Sn_{1.4}Ti_{0.6}O_7$ measured on HB-2A with $\lambda = 1.54$ Å. (c) Dependence of the refined lattice parameter, a on the Ti^{4+} content, x. The observed linear decrease of a with respect to x implies Vegard's law [209] is obeyed and agrees with the behaviour as predicted from the literature [17, 74, 164, 165, 168, 172, 176], and summarised in Tab. 2.2. (d) Temperature dependence of the DC magnetic susceptibility and its inverse of $Pr_2Sn_2O_7$ in $\mu_o H_{ext} = 0.1$ T. (e) Background-subtracted $S(|\mathbf{Q}|, \hbar\omega)$ of $Pr_2Sn_2O_7$ measured on SEQUOIA at 1.65 K with an $\hbar\omega_i = 170$ meV. (f) A $|\mathbf{Q}|$-integrated cut ($|\mathbf{Q}| = [0,5]$ Å^{-1}) of (e). The energies assigned to the crystal field excitations are summarised in Table 2.3.

Focussing on the confirmation of sample quality concerning the undoped member $Pr_2Sn_2O_7$, DC magnetic susceptibility data (Fig. 2.2(d)) confirmed the lack of long range magnetic ordering down to 1.8 K. A Curie-Weiss fit between 4 K and 15 K yielded an effective paramagnetic moment μ_{eff} and a Weiss temperature θ_{CW} of 2.61(1) μ_{B} and 0.26(3) K respectively, in agreement with Zhou *et al.* [17]. The use of a low temperature range for the Curie-Weiss fit was an attempt to minimise the effects of the low lying crystal field excitation at $\Delta \sim$ 18 meV [16, 17]. The experimentally determined effective paramagnetic moment is less than the expected value of the free Pr^{3+} moment ($\mu_{Pr^{3+}} \sim 3.6\ \mu_{\text{B}}$), possibly indicating the presence of frustration, whilst a Weiss temperature of 0.26(3) K indicates the presence of weak net ferromagnetic interactions between Pr^{3+} moments, all in agreement with previous characterisation studies [17, 166, 208].

A final confirmation of the phase purity of the undoped $Pr_2Sn_2O_7$ sample consisted of a measurement of the crystal field excitations on the direct geometry time-of-flight chopper spectrometer SEQUOIA [207]. As illustrated in Figs. 2.2(e) and (f), all five excited crystal field levels, including the thermally isolated ground state doublet ($\Delta \sim 18$ meV), of the $^3H_4$ ground state multiplet previously reported by Princep *et al.* [16] were observed at 1.8 K on SEQUOIA with an $\hbar\omega_i = 170$ meV. Individual crystal field excitations were determined by first performing a $|\mathbf{Q}|$-integrated cut ($|\mathbf{Q}| = [0,5]$ Å^{-1}) and then fitting the individual excitations to Gaussians. Next, $\hbar\omega$-integrated cuts with energy integration ranges centered about the different modes were examined to distinguish between phonons and crystal field excitations *via* their $|\mathbf{Q}|$-dependence. The determination of the crystal field levels, as illustrated in Fig. 2.2(f) and Tab. 2.3, indicate that all six crystal field levels agree within experimental error to the values reported by Princep *et al.* [16]. Since the refined lattice parameter, Curie-Weiss parameters, and crystal field levels for the current study all agree well with their respective literature values, there is reason for confidence in the current sample's quality.

Table 2.3 A comparison between the observed crystal field levels of $Pr_2Sn_2O_7$ reported by Princep *et al.* [16] as measured on MERLIN [212] with an incident energy $\hbar\omega_i$ of 170 meV at 5 K with the observed crystal field levels measured on SEQUOIA [207] in high resolution mode with an $\hbar\omega_i$ of 170 meV at 1.8 K. The crystal field levels were determined by fitting the observed excitations to Gaussians and distinguished from phonons based on their $|\mathbf{Q}|$-dependence. Numbers in parentheses indicate statistical errors.

MERLIN (meV)	SEQUOIA (meV)
0	0
0	0
17.8(4)	17.3(1)
57.8(4)	57.7(1)
57.8(4)	57.7(1)
82.2(4)	81.8(2)
100.0(5)	99.4(1)
100.0(5)	99.4(1)
115.0(5)	114.0(5)

2.3.2 Neutron Inelastic Scattering

Motivated by the confirmation for both the aforementioned sample quality and the presence of key ingredients [23, 197, 201, 216] of the quantum spin ice state (*e.g.* frustration, $\mu_{\text{eff}} \ll 10\mu_{\text{B}}$), the low-energy spin fluctuations of polycrystalline $Pr_2Sn_2O_7$ have been remeasured on the cold neutron chopper spectrometer (CNCS). Broad, quasielastic scattering previously measured [17] was confirmed in the current sample at 1.65 K. However, the high resolution and time-integrated flux of the CNCS also enabled the observation of a discernible fine structure to the scattering, as illustrated in Fig 2.3(a). A hierarchy of nearly-dispersionless excitations was identified and measured up to $\hbar\omega \sim 2$ meV. These excitations are also visible with different incident energies (Fig. 2.3(b)), decrease in intensity with increasing temperature while obeying detailed balance (Fig. 2.3(c)), confirming these excitations are magnetic and not spurious in origin [99, 100].

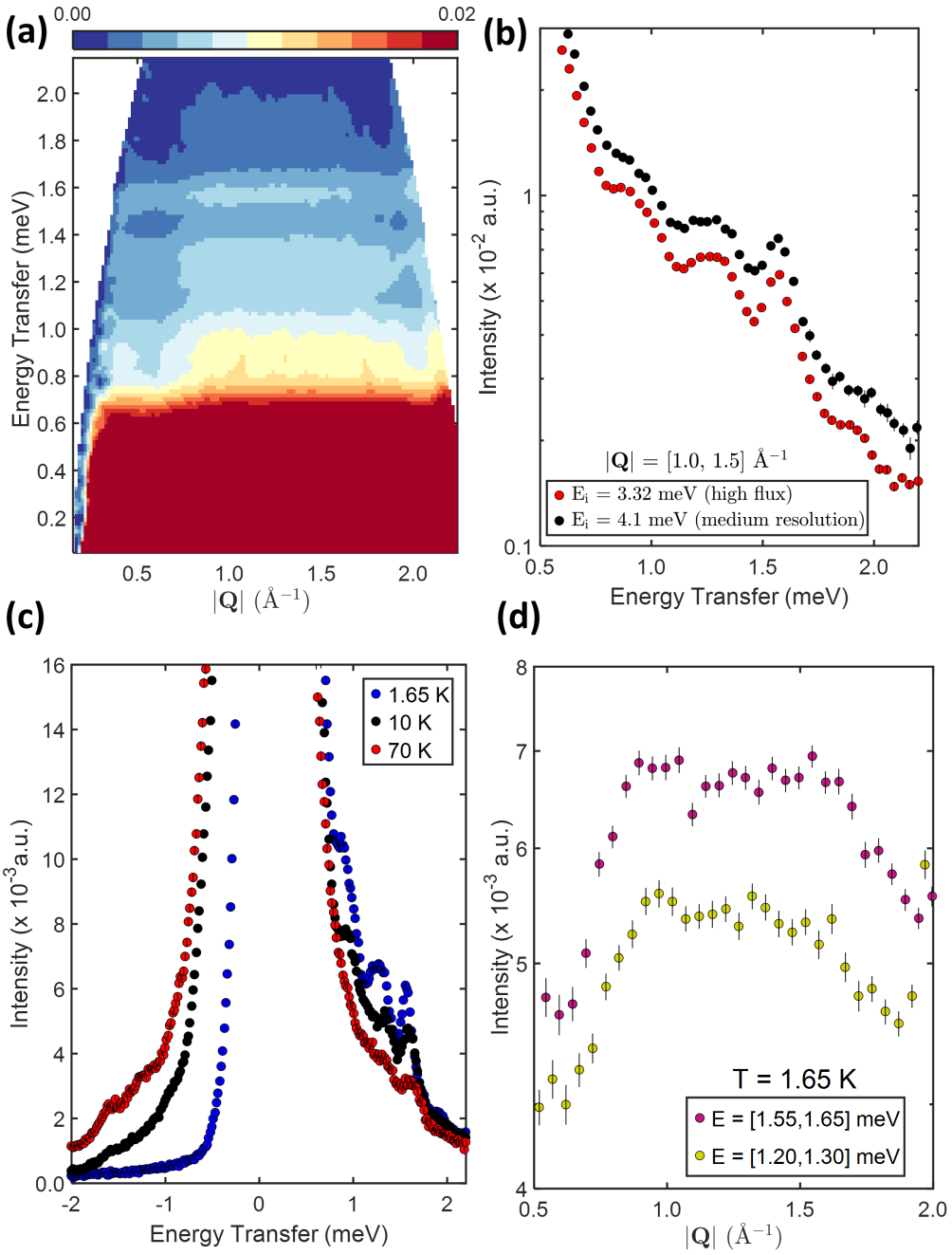

Figure 2.3 (a) Background-subtracted $S(|\mathbf{Q}|, \hbar\omega)$ of polycrystalline $Pr_2Sn_2O_7$ at 1.65 K with an $\hbar\omega_i = 3.32$ meV on the CNCS, displaying unequally-spaced nearly-dispersionless excitations. (b) A comparison of $|\mathbf{Q}|$-integrated cuts ($|\mathbf{Q}| = [1.0,1.5]$ Å^{-1}) of background-subtracted $S(|\mathbf{Q}|, \hbar\omega)$ measured on the CNCS at 1.65 K with $\hbar\omega_i$ of 3.32 and 4.1 meV. (c) $|\mathbf{Q}|$-integrated cut ($|\mathbf{Q}| = [1.0, 1.5]$ Å^{-1}) of background-subtracted $S(|\mathbf{Q}|, \hbar\omega)$ at various temperatures on the CNCS with an incident energy $\hbar\omega_i = 3.32$ meV, suggesting that these excitations are magnetic, and confirming detailed balance [99, 100] is obeyed. (d) $\hbar\omega$-integrated cuts for two of the low energy excitations with the highest relative intensity. The non-monotonic behaviour contrasts the behaviour predicted for both vibrational [213] and single-ion excitations [214, 215].

2.4 Discussion

2.4.1 Potential Physical Origins of the Low Energy Excitations

The observation of a hierarchy of low energy magnetic excitations, previously unreported in a well-characterised system, naturally raises suspicion concerning the physical origin of such excitations. The primary initial concern that the low energy magnetic excitations were spurious in nature has been addressed by measuring the excitations' dependence on incident energy and temperature.

A second concern was that the current sample possessed significant cationic disorder or oxygen non-stoichiometry. Such a concern stems from the observation that Pr^{3+} is a non-Kramers doublet [218]. With the lack of protection by time-reversal symmetry, the ground state crystal field doublet could potentially split and the observed excitations could simply originate from singlet-singlet single-ion transitions [170]. Such a concern can be addressed by first noting that the preliminary sample characterisation outlined in §2.3.1, including neutron powder diffraction, DC magnetometry and high energy neutron inelastic spectroscopy, indicates that the current sample's magnetic properties are in agreement with those samples reported in the literature [17, 74, 166, 203, 208]. Secondly, the temperature and $|\mathbf{Q}|$-dependence of the magnetic excitations are inconsistent with the behaviour expected for crystal fields [170]. As illustrated in Fig. 2.3(c), the centre-of-masses for all excitations shift towards higher energy transfers as the temperature is increased, an observation that will be later addressed in §2.4.3. Whilst the excitations exhibit a modulated $|\mathbf{Q}|$-dependence, as illustrated in Fig. 2.3(d), in contrast with the Pr^{3+} form factor (Fig. A.1) describing the behaviour predicted for single-ion physics [214, 215].

A final argument against the role of disorder consists of the intentional introduction of disorder in $Pr_2Sn_2O_7$. As summarised by Figs. 2.4(a) and (b), disorder, accomplished by the random chemical substitution of Sn^{4+} by Ti^{4+}, effectively broadens the crystal field features present in the parent compound. Such broadening is a consequence of disorder *via* the random distribution of Ti^{4+}/Sn^{4+} along the six coordinate ring around the Pr^{3+} [45]. More specifically, the broadening arises from a statistical distribution of possible local environments for the Pr^{3+}, which splits the non-Kramers doublet and therefore generates many different single ion singlet-singlet transitions [170, 197, 219]. Such a mechanism

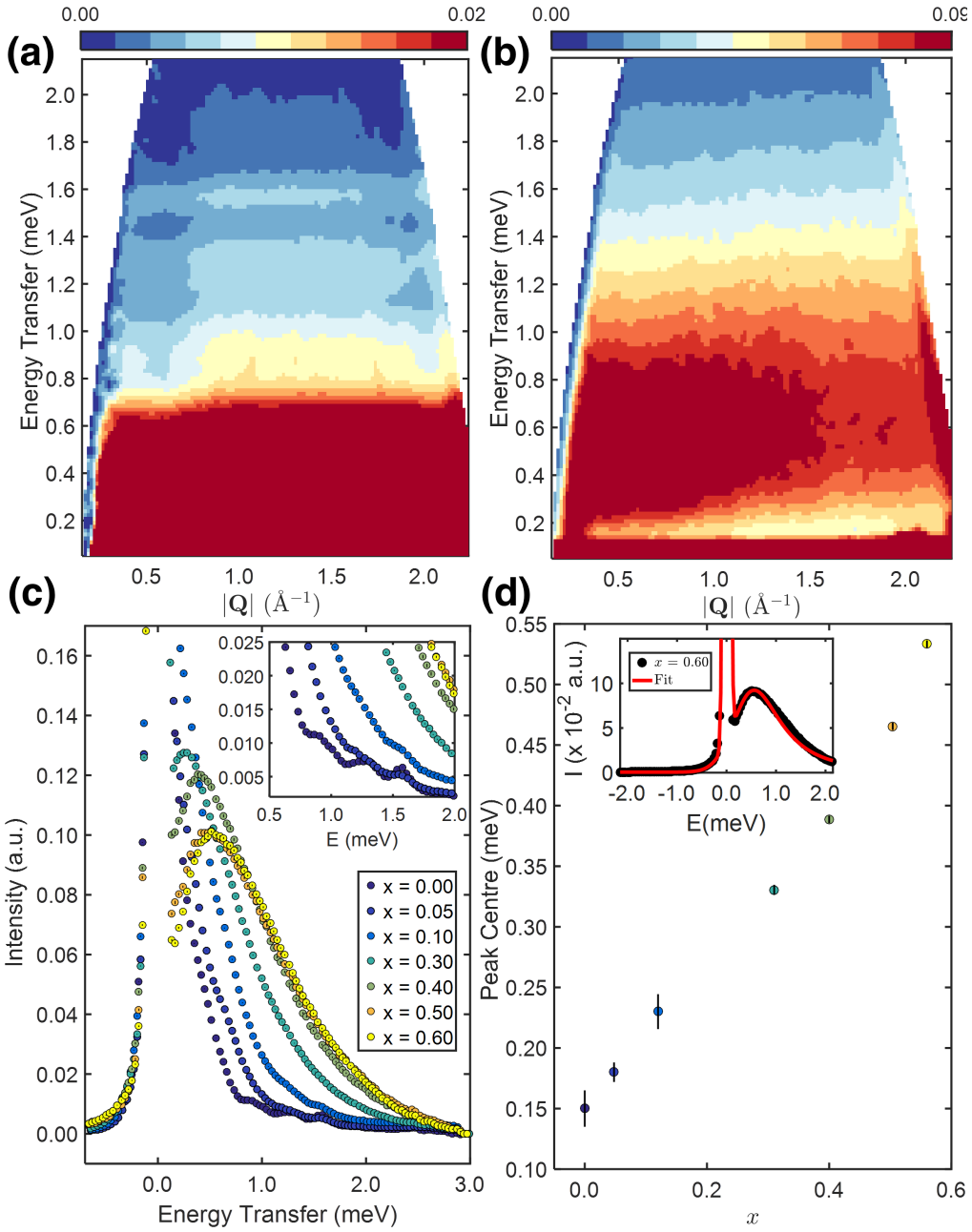

Figure 2.4 Background-subtracted $S(|\mathbf{Q}|, \hbar\omega)$ of (a) $Pr_2Sn_2O_7$ and (b) $Pr_2Sn_{1.4}Ti_{0.6}O_7$ measured at 1.65 K with an $\hbar\omega_i = 3.32$ meV on the CNCS. (c) $|\mathbf{Q}|$-integrated cuts ($|\mathbf{Q}| = [1.0, 1.5]$ Å^{-1}) of background-subtracted $S(|\mathbf{Q}|, \hbar\omega)$ of the $Pr_2Sn_{2-x}Ti_xO_7$ series at 1.65 K with an $\hbar\omega_i = 3.32$ meV on the CNCS, revealing that (inset) the low energy excitations are quickly replaced by a prominent inelastic signal with minimal values of Ti^{4+} content, x. (d) Dependence of the centre-of-mass of the inelastic signal on x, where for each member of the $Pr_2Sn_{2-x}Ti_xO_7$ series, the centre-of-mass was determined by (inset) fitting $|\mathbf{Q}|$-integrated cuts ($|\mathbf{Q}| = [1.0, 1.5]$ Å^{-1}) presented in (c) to a sum of a Gaussian and an antisymmetrised linear combination of two Lorentzians given by Eq. 2.3 [21, 217].

is consistent with the shift of the centre-of-mass of the inelastic feature with increasing Ti^{4+} content x and has been observed in other pyrochlores with B-site disorder [220]. To parametrise the dependence of the centre-of-mass on x, a fit of $|\mathbf{Q}|$-integrated cut ($|\mathbf{Q}|$=[1.0,1.5] Å^{-1}) to a sum of a Gaussian and an antisymmetrised linear combination of two Lorenztians, corresponding to the elastic and inelastic components, respectively, was performed for each member of the $Pr_2Sn_{2-x}Ti_xO_7$. Such a fitting function has been used extensively in the literature (*e.g.* lattice dynamics of $BaTiO_3$ [217]) in various equivalent forms. The equivalence between the various forms is discussed by Cowley *et al.* [21]. The particular form of the lineshape chosen in this study is given by

$$S(\hbar\omega) = \mathcal{A}e^{-\frac{1}{2}\left(\frac{\hbar\omega-\hbar\omega_{o,1}}{\sigma}\right)^2} + \mathcal{B}[n(\hbar\omega)+1]\left(\frac{\Gamma}{\Gamma^2+(\hbar\omega-\hbar\omega_{o,2})^2} - \frac{\Gamma}{\Gamma^2+(\hbar\omega+\hbar\omega_{o,2})^2}\right) + \mathcal{C}, \quad (2.3)$$

where $n(\hbar\omega)$ is the Bose factor, $\mathcal{A}$ and $\mathcal{B}$ are scale factors, $\mathcal{C}$ is a constant vertical background, σ, $\hbar\omega_{0,1}$ and Γ, $\hbar\omega_{0,2}$ are width parameters and centre-of-masses for the Gaussian and Lorenztian, respectively. The values of $\hbar\omega_{0,1}$ and σ for the Gaussian (*i.e.* the elastic peak) were allowed to vary and was refined to 0.005(1) to 0.046(3) meV, respectively, for $x = 0.60$. The refined values are similar to the expected values of zero and 0.043 meV, where the latter corresponds to instrumental elastic resolution (FWHM) of 0.1 meV for the CNCS with an $\hbar\omega_i = 3.32$ meV operating in high flux mode [206]. As summarised in Fig. 2.4(d), fits of all members of the $Pr_2Sn_{2-x}Ti_xO_7$ to Eq. 2.3 demonstrated a linear dependence of the centre-of-mass on the value of x. Such analogous behaviour was observed by Gaulin *et al.* [220] in another disordered quantum spin ice system $Tb_2Sn_{2-x}Ti_xO_7$ and by Wen *et al.* [125] in $Pr_2Zr_2O_7$, a pyrochlore known for anti-site mixing [165]. Since the effect of cationic disorder is the broadening of crystal field excitations, sharp features are not expected to arise in the inelastic spectra from this mechanism. Similar broadening of the crystal field levels should also arise in non-stoichiometric samples, since the Pr^{3+} ions would again be subjected to many different local environments.

Finally, a third potential origin of these low energy excitations could be low energy spin waves. Such a suggestion is based on the detection of similar low energy modes in $Yb_2Ti_2O_7$ by Peçanha-Antonio *et al.* [221] that exhibit similar temperature and $|\mathbf{Q}|$-dependence. Although such an analogy is tempting, one key difference between both systems is that the particular $Yb_2Ti_2O_7$ sample measured by Peçanha-Antonio *et al.* assumes long range magnetic order below

280 mK [221], whilst $Pr_2Sn_2O_7$ does not down to 90 mK [166]. In contrast, the relatively low intensity of the low energy excitations relative to the quasi-elastic signal is highly reminiscent of another Pr^{3+}-based quantum spin ice candidate $Pr_2Zr_2O_7$ [165]. The similar behaviour between both the stannate and zirconate may suggest that the origins of these low energy excitations may lie with the quantum spin ice state, a claim that will be central theme for the rest of this investigation.

2.4.2 Physical Model for Low Energy Magnetic Excitations

Extraction of Centre-of-Masses of the Five Magnetic Excitations

With counterarguments presented for both natural concerns: spurions and chemical disorder, the centre-of-masses for each of the five low energy magnetic excitations presented in Fig. 2.4(a) were extracted using a convolution of a fixed-width Gaussian, denoted as G and a free-width Lorentzian, denoted as L. The convolution of a Gaussian with its peak centre at $x = 0$ and a Lorentzian, commonly referred to as the Voigt profile $V(x;\sigma,\gamma)$ [222] is defined as

$$V(x;\sigma,\gamma) = G(x;\sigma) * L(x;\gamma) = \int_{-\infty}^{\infty} G(x';\sigma)L(x-x';\gamma)dx'. \tag{2.4}$$

To model such a convolution, an analytical expression for Equation 2.4 was used. The analytical expression for the Voigt profile is defined as

$$V(x;\sigma,\gamma) = \frac{1}{\sigma\sqrt{2\pi}}\Re[w(z)], \tag{2.5}$$

where $\Re[w(z)]$ denotes the real part of the Faddeeva function evaluated for $z = \frac{x+i\gamma}{\sigma\sqrt{2}}$ (refer to expression 7.4.13 in §7.4 in Abramowitz & Stegun [223]).

The fixed width of the Gaussians was calculated from first principles using the instrumental energy resolution function (see Ehlers *et al.* [206]) and subsequently verified at the elastic line with empty aluminium can measurements.

For each of the five low energy magnetic excitations, in addition to the aforementioned convolution of a fixed-width Gaussian and a free-width Lorentzian, two additional contributions constituting a baseline background were included. These two contributions were:

- A Gaussian function to model the elastic line and nuclear incoherent scattering. The Gaussian's peak centre and relative intensity were fixed since they are known instrumental parameters [206].
- Another convolution of a fixed-width Gaussian and free-width Lorentzian, multiplied by the Bose factor to introduce asymmetry, to model the prominent quasielastic signal around the elastic line, centered at 0.2 meV that was previously attributed to quantum tunnelling between degenerate spin ice configurations [17]. The relative intensity of the Gaussian and the Bose factor were fixed to assure convergence since only positive energy transfers ($\hbar\omega > 0$) were modelled.

It should be noted that the fitting of the five low energy excitation peaks did not include the Bose factor because the relative ratio of $\frac{\hbar\omega}{k_B T}$ reduces the Bose factor to approximately one in the dynamic range of interest at all measured temperatures. Furthermore, it was also observed that at both 1.65 K and 10 K, the peak centre for the first low energy excitation ($\hbar\omega \approx 0.5$ meV) could shift freely between 0.2 meV and 0.5 meV without any significant change in χ^2, representing a large systematic error of ± 0.15 meV. The results of each convolution and the sum of all convolutions at base temperature are shown in Fig. 2.5(a). The shaded areas below the fitted curve represent an illustration of how the fitted lineshape is deconstructed. Although other parameterisations may also be possible, the only meaningful parameter extracted from the fits is an estimate of the excitations' centre-of-mass.

The error bars were calculated by $\sqrt{[\delta(\hbar\omega)]^2 + (0.2 \cdot \mathrm{FWHM})^2}$, where $\delta(\hbar\omega)$ and FWHM are the errors in the peak position and the full-width-at-half-maximum of the free-width Lorentzian, respectively. The addition of 20 % of the fitted FWHM in quadrature to the error in the fitted peak position is an *ad hoc* method of including the FWHM in the error of the peak position, which is particularly relevant when the error in the fitted peak location is significantly smaller than the FWHM of the peak itself [224].

Confinement of Magnetic Monopoles, Quantum Harmonic Oscillator and Soliton Models

As illustrated in Fig. 2.5(b), the analysis reveals that these modes are not evenly-spaced. The lack of even spacing, together with the observed decrease in relative intensity with increasing temperature (Fig. 2.3(c)), rule out a possible

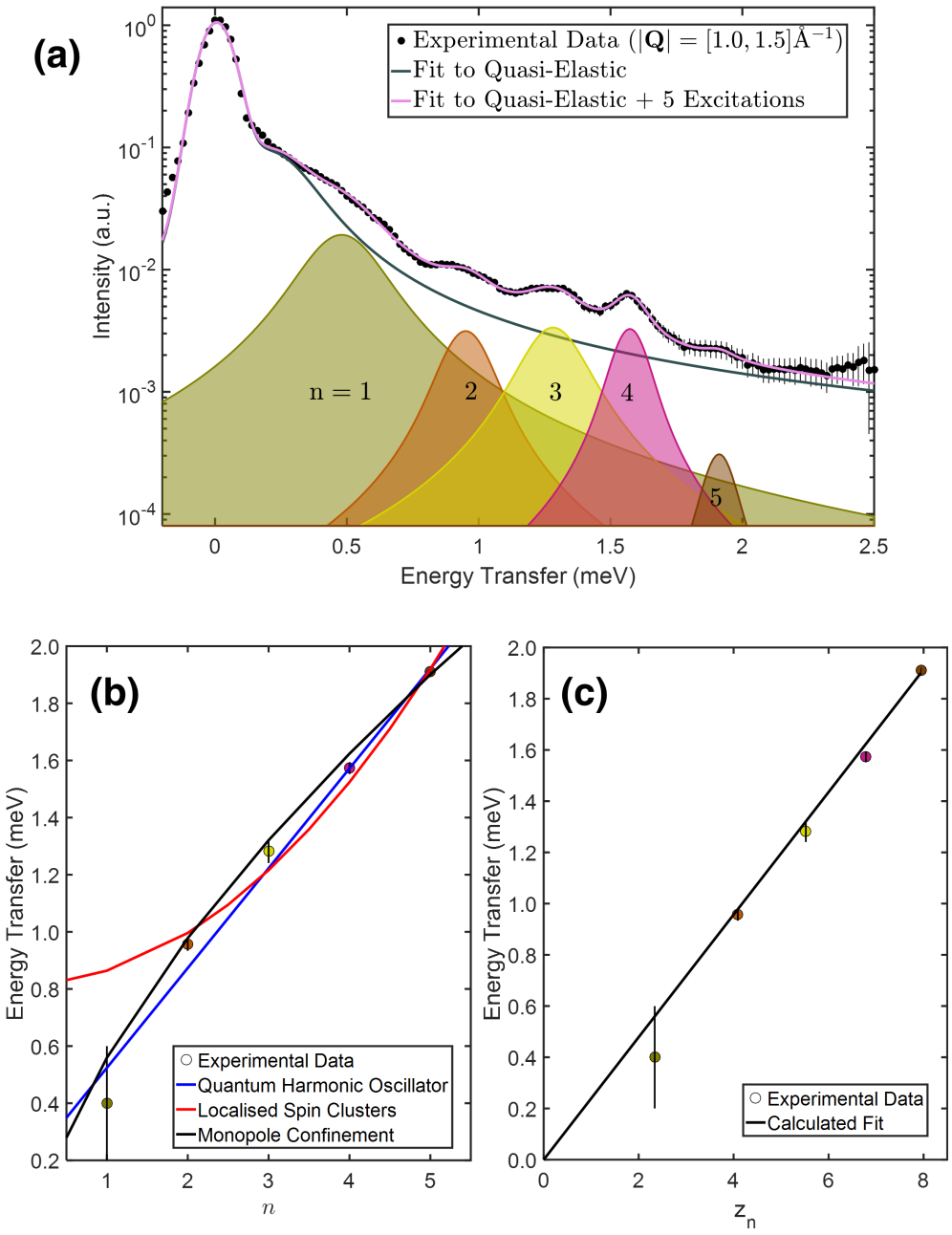

Figure 2.5 (a) $|\mathbf{Q}|$-integrated ($|\mathbf{Q}| = [1.0,\ 1.5]$ Å^{-1}) cut of background-subtracted $S(|\mathbf{Q}|, \hbar\omega)$ of $Pr_2Sn_2O_7$ at 1.65 K with an $\hbar\omega_i = 3.32$ meV on the CNCS. A fitting routine, as described in the main text, was applied exclusively to $\hbar\omega > 0$ with the fit to each excitation labelled by its quantum number n. (b) Comparison between the observed low energy excitations at 1.65 K and the predicted behaviour from three competing models [63, 213, 225]. The predicted values for each model were obtained by fitting the observed values to each model's fitting function as described in the main text, and are connected by interpolated lines as a guide to the eye. (c) The plot of excitation energies against the negative zeros of the Airy function z_n exhibits linear behaviour as predicted by the monopole confinement model [63]. A least squares fit with Eq. 2.6 (shown by red lines in both panels (b) and (c)) yielded a lower bound for the effective tension λ of 0.642(8) K $\cdot$Å^{-1} and a monopole pair creation energy $2\hbar\omega_o$ of 0 meV at 1.65 K.

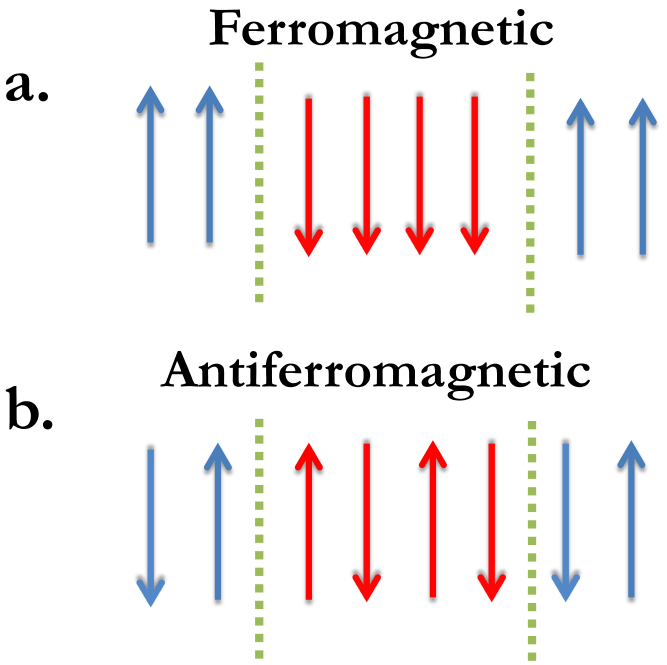

Figure 2.6 A pictorial representation of the propagation of spin defects in a one-dimensional (a) ferromagnetic and (b) antiferromagnetic spin-$\frac{1}{2}$ chain. Blue and red arrows represent non-flipped and flipped spin-$\frac{1}{2}$ moments, respectively. When one spin is flipped, two domain walls are created indicated by the dashed vertical olive green lines. These domain walls may be regarded as effective spin-$\frac{1}{2}$ defects [63, 226–233].

quantum harmonic oscillator (QHO) interpretation such as what is observed in uranium nitride [213] and thus imply a magnetic origin instead. Furthermore, the QHO possibility can be ruled out even more definitively by investigating the $|\mathbf{Q}|$-dependence of the excitations. As shown in Fig. 2.3(d), the scattering intensity does not increase with $|\mathbf{Q}|^{2n}$, as expected for the n^{th} mode of a QHO in the low $|\mathbf{Q}|$ limit [99, 100]. The experimental data suggests that there is an absence of a vibrational contribution to these low energy excitations and consequently, there is strong evidence in favour of ruling out a QHO interpretation.

With the QHO interpretation effectively discarded, other possible mechanisms that lead to quantised, unevenly-spaced magnetic excitations must be considered. The dynamic response for the spin defects of a quasi-one-dimensional Ising $S = \frac{1}{2}$ spin chain such as $CoNb_2O_6$ [63] below the magnetic ordering temperature has the desired characteristics. As illustrated in Fig. 2.6, spin defects in quasi-one dimensional quantum Ising chains such as $CoNb_2O_6$ correspond to domain walls [230, 231]. Two domain walls are created by flipping one spin, effectively creating two spin-$\frac{1}{2}$ defects. In the absence of a longitudinal magnetic

field (either applied or molecular), flipping N adjacent spins results in a magnetic state that still possesses two domain walls with an identical energy as the magnetic state created by one spin flip. In other words, these effective spin-$\frac{1}{2}$ defects can move freely with no energy cost *via* quantum exchange, resulting in a continuum spectrum [232]. Only once the spin chain is subjected to a longitudinal magnetic field, a linear confining potential is introduced [234, 235]. This linear potential effectively leads to bound states reflected in the appearance of a spectrum of sharp modes *in lieu* of the aforementioned continuum spectrum [227–229, 233]. The appearance of these sharp modes has been seen experimentally in both ferromagnetic [63] and antiferromagnetic chains [226, 227]. A similar spin defect confinement model may apply to $Pr_2Sn_2O_7$, under the assumption that the relevant defects in this case are magnetic monopole quasiparticles and not solitons, while the tension in the "Dirac string" provides the linear confining potential. Just as is the case for the quantum confinement in $CoNb_2O_6$ [63], while the monopole quasiparticles are created in pairs, they are ultimately bound together in the ordered state due to an attractive linear potential, the origins of which are discussed further in §2.4.3. Note that the analogy between spin defects and monopoles in a spin ice has been discussed previously [114, 118, 119, 236, 237]. If the monopole confinement model is valid for $Pr_2Sn_2O_7$, then the energies of the excitations should be described by

$$\hbar\omega_n = 2\hbar\omega_o + z_n\lambda^{\frac{2}{3}}\left(\frac{\hbar^2}{\mu}\right)^{\frac{1}{3}}, \tag{2.6}$$

where n is a positive integer, μ is the reduced mass, $\hbar\omega_n$ is the n^{th} excitation energy, $2\hbar\omega_o$ is the energy cost to produce a pair of monopoles, λ is an effective tension and z_n are the negative zeros of the Airy function [63, 229, 232, 238, 239]. Furthermore, using the observation that Equation 2.6 yields a linear relation between $\hbar\omega_n$ and z_n, the slope of a linear fit would be

$$\frac{d(\hbar\omega)}{dz} = \lambda^{\frac{2}{3}}\left(\frac{\hbar^2}{\mu}\right)^{\frac{1}{3}}. \tag{2.7}$$

An estimate of the monopole mass m in the limit of low $|\mathbf{Q}|$ has been derived by Pan *et al.* [202] as

$$m \approx \frac{4\hbar^2}{\alpha J_\perp a^2}, \tag{2.8}$$

where α is a constant (usually set to the value of 1), a is the lattice parameter

and $J_\perp$ is the dominant transverse coupling term for the QSI candidate being considered. By setting $\mu = \frac{m}{2}$ and solving for λ, one obtains a relationship between the slope and the tension given by

$$\lambda = \sqrt{\left(\frac{d(\hbar\omega)}{dz}\right)^3 \left(\frac{2}{\alpha \cdot J_\perp \cdot a^2}\right)}. \tag{2.9}$$

Before proceeding, it must be noted that only a lower bound and not the exact value for λ can be reported for the current study. This limitation is a consequence of the fact that the transverse term of the magnetic exchange $J_\perp$ in Eq. 2.9, which appears due to the estimation of the effective monopole mass (Eq. 2.8) for $Pr_2Sn_2O_7$, is currently unknown. Zhou *et al.* [17], using the broad peak in the heat capacity and the dipolar spin ice model [146], estimated the value of the magnetic exchange J as approximately 0.92 K. Consequently, since it is assumed in the preceding calculations that $J = J_\perp$ as a first approximation, then λ in Eq. 2.9 is minimised.

Figure 2.5(b) plots the observed energy levels versus the excitation number to facilitate a direct comparison between three different candidate scenarios. Two possibilities, the monopole confinement [63] and QHO [213] models, have already been discussed in detail above. A third model is considered here, based on localised high S clusters [225]. The magnetic excitation spectrum for an isolated spin cluster also consists of a series of quantised energy levels [240–242], and the spacing between the modes can be non-trivial or follow the simple relationship $\hbar\omega_n \propto n^2$ depending on the specific details of the magnetic Hamiltonian [225, 243]. Fits of the centre-of-masses of the five excitations were performed to each of these models with the phenomenological expression $\hbar\omega_n = A + Bx_n$, where A and B are constants and x_n is n, n^2, or z_n for the QHO [213], localised spin cluster [225] or monopole confinement [63] models, respectively. The solid curves in Figure 2.5(b) represent the best fit to each of the models and they clearly illustrate that the monopole confinement model provides the best agreement. Additional details are presented in Table 2.4. Furthermore, a plot of $\hbar\omega_n$ vs. z_n, as shown in Figure 2.5(c), produces a linear relationship in agreement with the predictions of this model [63, 229, 232, 238]. Therefore, the data suggests that these excitations may be interpreted as direct spectroscopic evidence of interacting magnetic monopoles within the pyrochlore lattice.

By restricting the value of the y-intercept $b \geq 0$ for the fit shown in Figure 2.5(b), a value for the slope $\frac{d(\hbar\omega)}{dz}$ as 0.239(2) meV is obtained. Utilising the values for α, $J_\perp$ and a of 1, 0.0793 meV and 10.6038(3) Å respectively [17,

Table 2.4 Comparison between the observed and predicted values of the energy transfer $\hbar\omega$ for the quantum harmonic oscillator [213], localised spin cluster [225] and monopole confinement [63] models at 1.65 K. The calculated values were obtained by fitting the five observed low energy excitations to the functional form of the individual models, with further details of the fitting described in the main text. Numbers in parentheses indicate statistical errors. The goodness-of-fit metric χ^2_ν for each model is provided for a quantitative comparison.

Model / Mode	$n=1$	$n=2$	$n=3$	$n=4$	$n=5$	χ^2_ν
Observed (1.65 K)	0.4(2)	0.96(2)	1.28(4)	1.57(2)	1.912(9)	
Monopole Confinement	0.559(5)	0.978(8)	1.32(1)	1.62(1)	1.90(2)	3.5
QHO	0.524(5)	0.873(9)	1.22(1)	1.57(2)	1.92(2)	5.6
Localised Spin Clusters	0.86(6)	1.00(7)	1.22(9)	1.5(1)	1.9(1)	8.5

202, 203], a lower bound of an effective tension $\lambda = 0.0553(7)$ meV $\cdot$ Å^{-1} or 0.642(8) K $\cdot$ Å^{-1} is obtained for 1.65 K.

Some physical insights can be made from the measurement of these two parameters. Firstly, the value of the tension is positive and non-negligible, implying that the monopoles are confined unlike in DSIs [114, 118, 119, 202]. Secondly, the value of $\lambda \sim 0.6$ K$\cdot$ Å^{-1} is surprisingly large for the expected energy scale with $J \sim 1$ K [17]. In fact, the energy cost to separate two monopoles by the distance between the centers of adjacent Pr^{3+} tetrahedra corresponds to approximately a temperature scale of 3 K. This strong tension prevents the propagation of monopoles over long distances. The confinement of these monopoles can be roughly quantified, since exact analytical solutions for the Schrödinger equation with an $|x|$-potential are known [238, 244]. Utilising the solutions determined by Hohlfeld & Sandri [238], one may obtain the expectation value $\langle|x|\rangle$ for a bound monopole pair as

$$\langle|x|\rangle = \frac{2}{3}\left(\frac{\hbar^2}{\mu\lambda}\right)^{\frac{1}{3}} \cdot z_n. \tag{2.10}$$

By combining Eq. 2.10 with the definition of λ (Eq. 2.9), one obtains an equivalent expression for $\langle|x|\rangle$ as

$$\langle|x|\rangle = \left(\frac{2}{3}\right)\left(\frac{\alpha \cdot J_\perp \cdot a^2}{2 \cdot \sqrt{\left(\frac{d(\hbar\omega)}{dz}\right)^3 \cdot \left(\frac{2}{\alpha \cdot J_\perp \cdot a^2}\right)}}\right)^{\frac{1}{3}} \cdot z_n. \tag{2.11}$$

With $a \approx 10.6$ Å, $\frac{d(\hbar\omega)}{dz} \approx 0.24$ meV, a transverse coupling term of $J_\perp \approx 0.0793$ meV and setting the value for z_n to 7.94 which corresponds to the $n = 5$ excitation [17, 63, 203, 229, 238], one obtains the value for a relatively short distance $\langle|x|\rangle \approx 20$ Å for 1.65 K, corresponding to approximately five nearest neighbour distances or two unit cells. It should be noted that the linear fit yields a value of zero (within error) as an estimate of $2\hbar\omega_o$. The value of zero implies that $Pr_2Sn_2O_7$ is far removed from the regime where monopoles are considered in quantum spin ice models [245], which is not unexpected since previous neutron inelastic scattering measurements have determined that the ground state doublet wavefunctions contain large terms with $m_J \neq \pm 4$ [16]. Although refined to be zero, the absolute value of $2\hbar\omega_o$ is extremely sensitive to the energy of the first excitation and thus should be interpreted with caution.

As summarised by both Fig. 2.5(b) and Tab. 2.4, the various models considered provide comparable fits to the experimental data. At first glance, one may argue that the only significant difference between the fits arises from the lowest magnetic excitation ($n = 1$), which itself possesses a large uncertainty due to the difficulty of extracting the energy of this mode. In order to prove that the monopole confinement model [63, 229, 232] provides the best description of the experimental data, two additional checks were performed for the analysis of data collected at 1.65 K:

- The original $n = 1$ magnetic excitation was assumed to still exist but was excluded from the fitting routine outlined in §2.4.2. The results are summarised in Fig. 2.7(a) and in Tab. 2.5 below and demonstrate that the monopole confinement model [63, 229, 232] best describes the experimental data in this case.

- The original $n = 1$ magnetic excitation was assumed to be an artefact of the prominent quasi-elastic signal [17] and consequently, the originally labelled $n = 2$ was relabelled as $n = 1$ and all higher excitations were correspondingly relabelled. The fitting routine outlined in §2.4.2 was then performed and the results are summarised in both Fig. 2.7(b) and Tab. 2.6, demonstrating that the monopole confinement model [63, 229, 232] best describes the experimental data in this case as well.

A final physical insight pertains to the excitations' temperature dependence. As illustrated in Fig. 2.7 and summarised in Tab. 2.7, all excitations, with the exception of the first, increase in energy transfer as the temperature is increased to

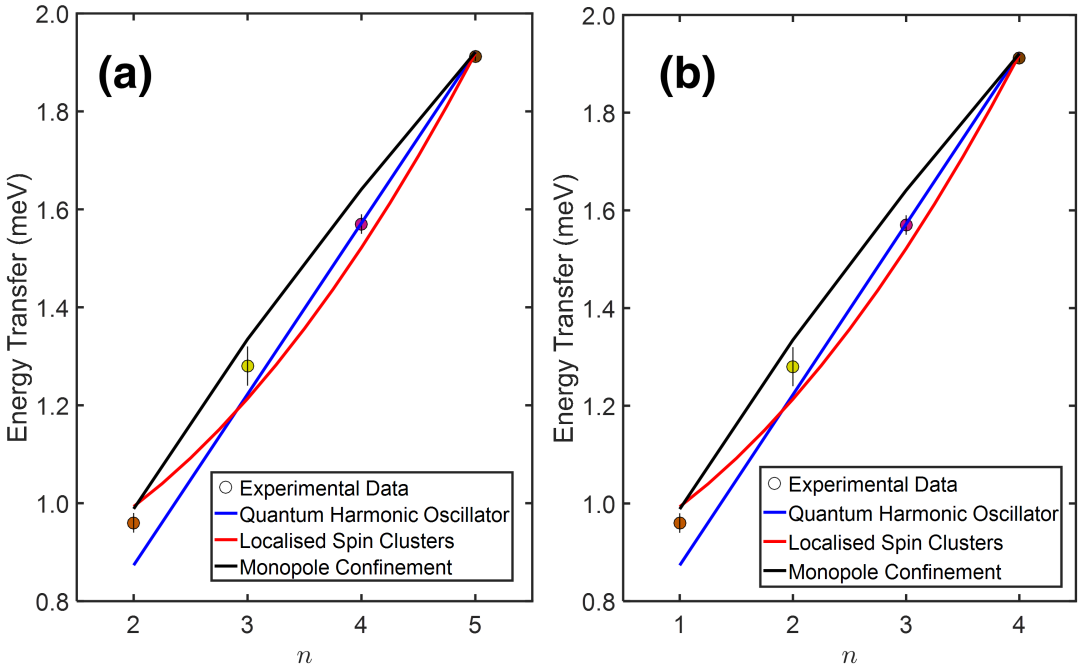

Figure 2.7 The direct comparison between the observed low energy magnetic excitations at 1.65 K and the predicted behaviour from three competing models [63, 213, 225] assuming (a) the n = 1 mode does exist but is excluded from the fit and (b) the n = 1 mode is assumed not to exist (*i.e.* it is an artefact of the prominent quasi-elastic signal [17]). The predicted values of $\hbar\omega$ for each model were obtained by fitting the corresponding observed values to each model's fitting function as described in the main text, and they are connected by solid curves as a guide to the eye.

Table 2.5 Comparison between the observed and predicted values of the energy transfer $\hbar\omega$ for the quantum harmonic oscillator [213], localised spin cluster [225] and the monopole confinement [63] models. The calculated values were obtained by fitting the highest four out of the five observed low energy excitations to the functional form of the individual models, with further details of the fitting described in the main text. Numbers in parentheses indicate statistical errors. The goodness-of-fit metric χ^2_ν for each model is provided for a quantitative comparison.

Model / Mode	$n = 2$	$n = 3$	$n = 4$	$n = 5$	χ^2_ν
Observed (1.65 K)	0.96(2)	1.28(4)	1.57(2)	1.912(9)	
Monopole Confinement	0.99(7)	1.33(9)	1.6(1)	1.9(1)	3.9
QHO	0.87(1)	1.22(1)	1.57(2)	1.92(2)	7.8
Localised Spin Clusters	1.0(1)	1.2(1)	1.5(2)	1.9(2)	11

Table 2.6 Comparison between the observed and predicted values of the energy transfer $\hbar\omega$ for the quantum harmonic oscillator [213], localised spin cluster [225] and the monopole confinement [63] models. The calculated values were obtained by first assuming that the originally labelled $n = 1$ excitation was simply an artefact of the prominent quasi-elastic signal [17] and all higher excitations were relabelled accordingly as $n = 1 \ldots 4$. These four excitations were fitted to the functional form of the individual models, with further details of the fitting described in the main text. Numbers in parentheses indicate statistical errors. The goodness-of-fit metric χ^2_ν for each model is provided for a quantitative comparison.

Model / Mode	$n = 1$	$n = 2$	$n = 3$	$n = 4$	χ^2_ν
Observed (1.65 K)	0.96(2)	1.28(4)	1.57(2)	1.912(9)	
Monopole Confinement	0.94(2)	1.32(3)	1.63(4)	1.90(4)	6.4
QHO	0.65(5)	1.08(9)	1.5(1)	1.9(2)	93
Localised Spin Clusters	1.0(1)	1.2(2)	1.5(2)	1.9(3)	11

Table 2.7 Comparison between the observed and predicted values of the energy transfer $\hbar\omega$ for the monopole confinement model [63, 229, 232] at 1.65 K and 10 K. The calculated values were obtained by fitting the five observed low energy excitations to the functional form of the monopole confinement model described in the main text. Numbers in parentheses indicate statistical errors.

Model (Temp.) / Mode	$n = 1$	$n = 2$	$n = 3$	$n = 4$	$n = 5$
Observed (1.65 K)	0.4(2)	0.96(2)	1.28(4)	1.57(2)	1.912(9)
Calculated (1.65 K)	0.559(5)	0.978(8)	1.32(1)	1.62(1)	1.90(2)
Observed (10 K)	0.4(2)	1.01(1)	1.36(2)	1.65(2)	1.94(3)
Calculated (10 K)	0.573(5)	1.001(8)	1.35(1)	1.66(1)	1.95(2)

10 K. Applying an identical analysis algorithm outlined in §2.4.2 to data collected at 10 K, yields a larger lower bound of 0.667(8) K $\cdot$ Å^{-1} for the effective tension compared to the value of 0.642(8) K $\cdot$ Å^{-1} at 1.65 K. Such behaviour is important for two reasons. Firstly, such a large systematic increase in the excitations' centre-of-masses is unexpected for crystal fields, where minimal shifts would be expected due to thermal contraction/expansion [246–248]. Secondly and in contrast to crystal fields, an increase would be expected if the confining potential was attributed — to some extent — to the spin ice state. Such an increase can be rationalised by recognising that with increasing temperature, the monopole (defect) density would increase [249–251], and thus the propogation of defects would be hindered, resulting in a larger effective tension λ.

2.4.3 Physical Origin of the Linear Potential

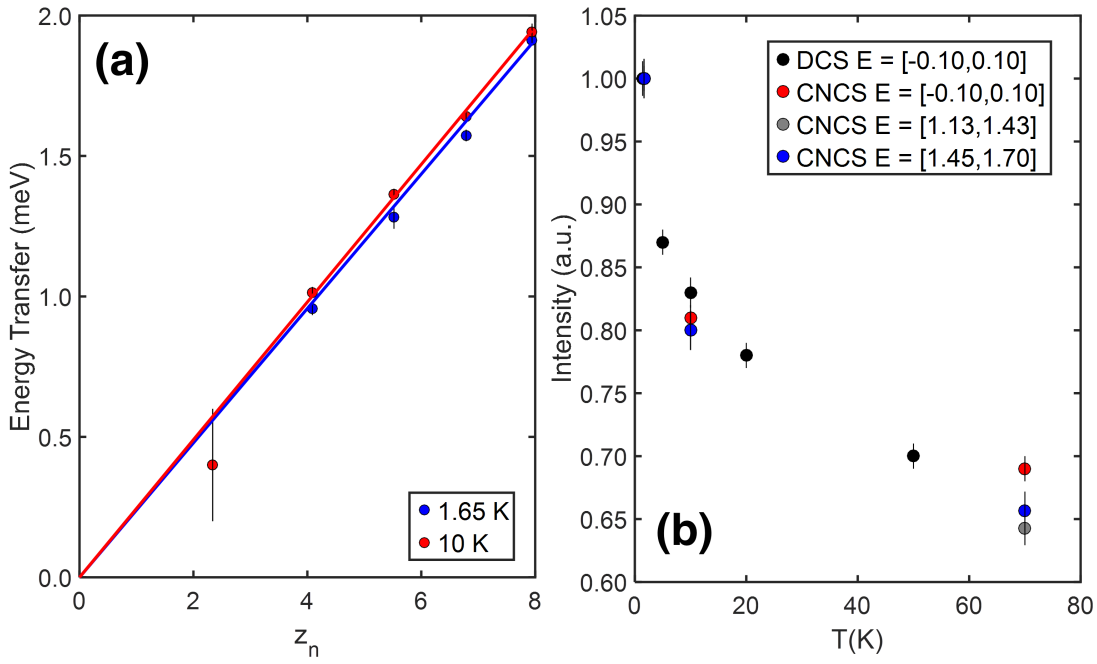

Figure 2.8 (a) Plot of excitation energies at 1.65 K and 10 K against the negative zeros of the Airy function z_n both exhibits linear behaviour as predicted by the monopole confinement model [63, 229, 238]. A least squares fit with Eq. 2.6 in the main text yielded a lower bound for the effective tension λ of 0.642(8) K $\cdot$ Å^{-1} and 0.667(8) K $\cdot$ Å^{-1} at 1.65 K and 10 K, respectively, whilst yielding a monopole pair creation energy $2\hbar\omega_o$ of 0 meV (within error) for both temperatures. (b) Comparison of the temperature dependence of the normalised integrated intensity of the magnetic diffuse scattering and the two lowest energy magnetic excitations observed for $Pr_2Sn_2O_7$ on the CNCS. For the purposes of comparison, the temperature dependence of the integrated intensity of the magnetic diffuse scattering from previous DCS data [17] with an $\hbar\omega_i = 3.27$ meV is also shown. Both data sets are integrated over identical ranges in $|\mathbf{Q}|$= [0.35, 1.75] Å^{-1}. The similar temperature dependence of all four data sets suggests that the low energy magnetic excitations may be attributed to the quantum spin ice state.

Despite the success of the monopole confinement model [63, 229, 238] to account for the experimental data, there remains one crucial unanswered question. What is the physical origin of the linear potential between the monopole quasiparticles? To address the linear potential, the temperature dependence of the excitations were investigated in further detail. As illustrated in Fig. 2.8(b), the excitations exhibit a remarkably similar temperature dependence to the magnetic diffuse scattering observed in the elastic channel on the CNCS, which was later confirmed by additional measurements on the triple-axis spectrometer HB-1A (Fig. 2.9). For additional analysis, the temperature dependence of the

magnetic diffuse scattering of another sample of polycrystalline $Pr_2Sn_2O_7$ was investigated. The second sample was measured on another cold time-of-flight chopper spectrometer, the DCS [102] at the NIST NCNR 10 years prior [17]. The advantages of comparing the previous DCS data to the current CNCS data are:

- the second sample is completely independent of the sample characterised on the CNCS. Although the sample was made with the same heating routine, every chemist and every reaction is slightly different from one another with slight variabilities.

- The second measurement on the DCS used a different experimental set-up (dilution fridge, copper can, detectors, *etc.*) and a different incident wavelength ($\lambda = 5.0$ Å corresponding to a slightly different $\hbar\omega_{\rm i} = 3.27$ meV) and consequently, the second measurement allows for the identification of spurious features, whilst having almost identical resolution about the elastic line with $\delta\hbar\omega \sim 0.1$ meV [102].

- The measurement of the second sample on the DCS did not show any low energy magnetic excitations [17], and thus if there existed any difference between the behaviour of the elastic channel of the two different samples, this difference in behaviour may help to explain the presence of the excitations in one sample and not the other.

As shown illustrated in Fig. 2.7(b), the temperature dependence of the magnetic diffuse scattering from the DCS exhibits similar behaviour as the temperature-dependence of both the magnetic diffuse scattering and low-energy magnetic excitations measured on the CNCS. The similar temperature dependence suggests that the excitations are associated with the quantum spin ice state.

The implication that these low energy magnetic excitations are in some way associated with the quantum spin ice state raises two important questions that must be addressed. Firstly, since the quantum spin ice state is three dimensional (*vis* à *vis* the pyrochlore lattice), how can a one-dimensional potential $V(x) = \lambda|x|$ account for the experimental data? The answer stems from the observation that the Hamiltonian describing the interactions between monopoles (*i.e.* magnetic charges) are angular independent and only depend on the distance r between the monopoles [118, 250]. As a consequence, the original three-dimensional problem

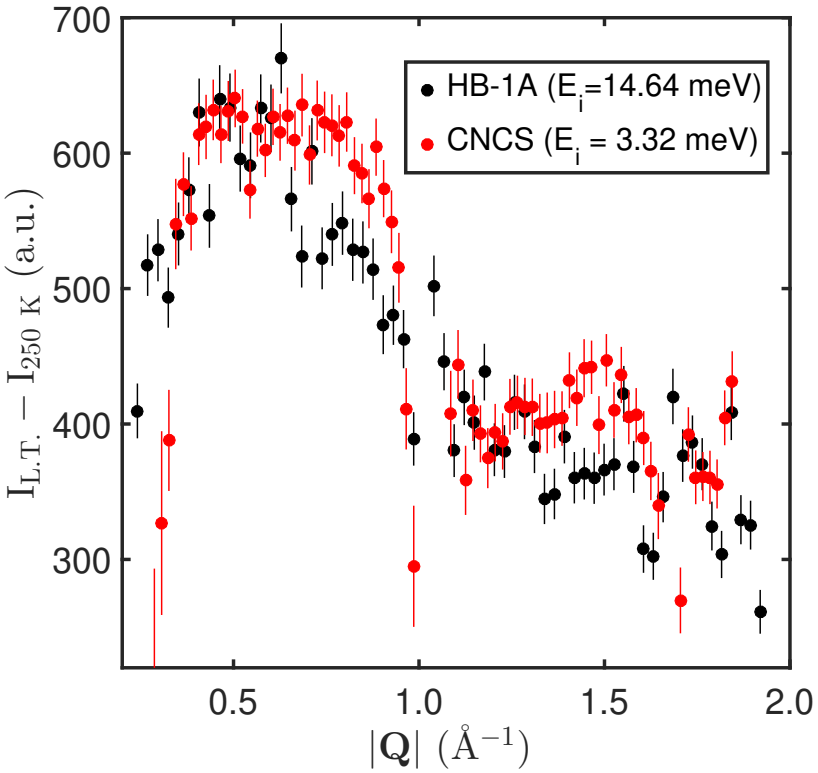

Figure 2.9 Magnetic diffuse scattering of polycrystalline $Pr_2Sn_2O_7$ measured on HB-1A with an $\hbar\omega_i = 14.64$ meV at 1.5 K and the CNCS at 1.65 K with an $\hbar\omega_i = 3.32$ meV. The diffuse scattering measured on the CNCS was isolated by performing a constant-$\hbar\omega$ cut along the elastic line ($\hbar\omega$ = [-0.1, 0.1] meV). The magnetic component of the diffuse scattering for both data sets were isolated by subtracting a high temperature (250 K) background. In contrast to the monotonic decrease of the Pr^{3+} form factor [215] (Fig. A.1), the periodic modulations are in agreement with the behaviour predicted for spin-ice correlations [252, 253], and as was previously observed by Zhou *et al.* [17].

can be reduced to a one dimensional problem with appropriate relabelling, as is the case for the potential energy U between electric charges in classical electromagnetism [254].

The second and related question is why the potential linear in character? One possible solution [255] can be derived by treating the monopole quasiparticles as electrolytes in Debye-Hückel theory, a common approach taken in the literature [71, 114, 250, 256, 257]. If one assumes that the constitutent monopoles of a monopole pair, corresponding to charges q_1 and q_2 originally separated by a

distance r_o, are further separated to a new distance $r_2 = r_o + x$, then by Debye-Hückel theory, the potential difference ΔU between the monopole pair is given by

$$\Delta U(x) = \frac{kq_1q_2}{r_2} e^{-\frac{r_2}{r_D}} - \frac{kq_1q_2}{r_o}, \tag{2.12}$$

where k is Coulomb constant, $r_2 = r_o + x$, and r_D corresponds to a fundamental/characteristic length scale called the Debye length [258]. The exponential factor in Eq. 2.12 represents an effective screening term and approaches its minimum as $r_2 \to r_o$, *i.e.* the shortest possible distance between the monopoles. By expanding ΔU in the limit of small distances, *i.e.* $r_2 \ll r_D$, and replacing r_2 by its definition of $r_o + x$, then Eq. 2.12 can be rewritten as

$$\Delta U = kq_1q_2 \left[\frac{1 - \left(\frac{r_o + x}{r_D} \right)}{r_o + x} - \frac{1}{r_o} \right], \tag{2.13}$$

or equivalently,

$$\Delta U(x) = -\frac{kq_1q_2}{r_D} + kq_1q_2 \left[\frac{1}{r_o + x} - \frac{1}{r_o} \right]. \tag{2.14}$$

Eq. 2.14 effectively states that in the limit of small distances, *i.e.* $r_2 \ll r_D$, the effect of the screening term in Eq. 2.12 is a constant shift in the potential. Thus, by setting the first term in Eq. 2.14 to a constant $\mathcal{C}$ and focussing on the last two terms, through some algebraic manipulation Eq. 2.14 reduces to

$$\Delta U(x) = \mathcal{C} + kq_1q_2 \left[\frac{r_o - (r_o + x)}{r_o(r_o + x)} \right] \equiv \mathcal{C} - \frac{kq_1q_2}{r_o} \left[\frac{x}{(r_o + x)} \right]. \tag{2.15}$$

Taking the limit of small x, *i.e.* $r_o + x \sim r_o$, and recognising that x can only assume positive values (*i.e.* $x = |x|, \forall\ x$), then Eq. 2.15 becomes

$$\Delta U(x) = \mathcal{C} - \frac{kq_1q_2}{r_o} \left[\frac{x}{r_o} \right] \equiv \mathcal{C} - \frac{kq_1q_2}{r_o^2} |x|, \tag{2.16}$$

where the second and only non-constant term corresponds to the desired linear

potential. Taking the limit of large x, *i.e.* $r_o+x \sim x$, then Eq. 2.15 becomes

$$\Delta U(x) = \mathcal{C} - \frac{kq_1q_2}{r_o}\left[\frac{x}{x}\right] \equiv \mathcal{C} - \frac{kq_1q_2}{r_o}, \tag{2.17}$$

which is simply a constant.

The two limits of Eq. 2.15 provide a natural explanation as to why distinct magnetic excitations are only observed up to energy transfers of approximately 2 meV. Since the energy transfer of an excitation may be regarded as corresponding to a particular distance between monopoles, with increasing energy corresponding to increasing distance, then by utilising the logic of Eqs. 2.16 and 2.17, the linear potential should describe the actual potential very well at low energy transfers and failing at high energy transfers, both of which are observed experimentally.

2.4.4 The $j_{\text{eff}} = \frac{1}{2}$ Approximation

Before concluding this chapter, the subtle but very important issue of the $j_{\text{eff}} = \frac{1}{2}$ approximation must be addressed. In various instances in the literature [16, 19, 23, 141, 197], it has been suggested that the magnetic ground state of the non-Kramers Pr^{3+} in $Pr_2Sn_2O_7$ could be approximated as a $j_{\text{eff}} = \frac{1}{2}$ system. Such an approximation is based on the observation that the crystal field configuration of Pr^{3+} in $Pr_2Sn_2O_7$ consists of a thermally isolated ground state doublet with a $\Delta \sim 18$ meV [16, 17]. Such logic and terminology has also been applied to the Kramers Yb^{3+}-based pyrochlores [259], ultimately driven by the necessity to address the most studied quantum spin ice candidate $Yb_2Ti_2O_7$, whose $\Delta \sim 53$ meV [260].

Although the application of the $j_{\text{eff}} = \frac{1}{2}$ approximation for Pr^{3+} in $Pr_2Sn_2O_7$ is tempting due to the significant simplification of any theoretical treatment that would follow, such an approximation is ultimately not correct. The failure of an approximation can be immediately rationalised by recognising that the spherical symmetry [47] of a $j_{\text{eff}} = \frac{1}{2}$ manfiold is incompatible with the highly anisotropic (Ising) nature of Pr^{3+} in $Pr_2Sn_2O_7$ with a $g_{\|}$=5.17 [16]. Such strong anisotropy is a consequence of the heavily distorted coordination polyhedra in the pyrochlore structure and is immediately reflected in the six term crystal field

Table 2.8 Stevens parameters B_k^q for $Pr_2Sn_2O_7$ calculated by Princep *et al.* [16] from experimental neutron inelastic scattering data collected on MERLIN [212]. The values of B_k^q were calculated using the program `SPECTRE` [269] with the assumption of pure LS coupling exclusively within the $^3H_4$ ground state multiplet.

B_k^q	Calculated Value (meV)
B_2^0	-0.733
B_4^0	-0.0365
B_4^3	-0.383
B_6^0	2.78×10^{-4}
B_6^3	3.28×10^{-5}
B_6^6	-0.00459

Hamiltonian [260–264]

$$\hat{\mathcal{H}}_{\mathrm{CF}} = \mathrm{B}_2^0\hat{\mathrm{O}}_2^0 + \mathrm{B}_4^0\hat{\mathrm{O}}_4^0 + \mathrm{B}_4^3\hat{\mathrm{O}}_4^3 + \mathrm{B}_6^0\hat{\mathrm{O}}_6^0 + \mathrm{B}_6^3\hat{\mathrm{O}}_6^3 + \mathrm{B}_6^6\hat{\mathrm{O}}_6^6, \tag{2.18}$$

describing the $\bar{3}m$ (D_{3d}) point-group symmetry of the $16d$ (rare-earth) site [45, 74]. The influence of such strong anisotropy is made even more evident by contrasting such a Hamiltonian given by Eq. 2.18 to

$$\hat{\mathcal{H}}_{\mathrm{CF}} = \mathrm{B}_4\left(\hat{\mathrm{O}}_4^0 + 5\hat{\mathrm{O}}_4^4\right), \tag{2.19}$$

corresponding to a crystal field Hamiltonian describing the isotropic $m\bar{3}m$ (O_h) point-group symmetry of ideal octahedral coordination at the $4a$ site of the $Fm\bar{3}m$ (rock-salt) lattice [18, 47, 261, 265].

Another, but ultimately related argument against the $j_{\mathrm{eff}} = \frac{1}{2}$ approximation consists of employing the fundamental definition of the angular momentum operators. As discussed in Appendix G, angular momentum operators are the generators of rotations in three dimensions corresponding to the Lie group SO(3) with Lie algebra $\mathfrak{so}(3)$ [266, 267]. The identification of the Lie bracket that defines the Lie algebra $\mathfrak{so}(3)$ as simply the canonical commutation relations [268]

$$[\hat{J}_i, \hat{J}_j] = \epsilon_{ijk}\hat{J}_k, \tag{2.20}$$

Table 2.9 A comparison between the observed crystal field levels of $Pr_2Sn_2O_7$ as measured on SEQUOIA [207] in high resolution mode with an $\hbar\omega_i$ of 170 meV at 1.8 K with the corresponding energy eigenvalues of the crystal field Hamiltonian $\hat{\mathcal{H}}_{\text{CF}}$ utilising the Stevens parameters [16] in Tab. 2.8.

SEQUOIA (meV)	Calculated (meV)
0	0
0	0
17.3(1)	17.7
57.7(1)	57.9
57.7(1)	57.9
81.8(2)	82.3
99.4(1)	99.9
99.4(1)	99.9
114.0(5)	114.9

provides an equivalent definition of what constitutes an angular momentum operator. To be more precise, the Lie algebra that is both more relevant for the case of the $j_{\text{eff}} = \frac{1}{2}$ approximation and more general, due to its double cover of $\mathfrak{so}(3)$, is $\mathfrak{su}(2)$, which is defined by the same Lie bracket as Eq. 2.20 [270]. In other words, the canonical commutation relations identifies a clear property that determines what does and does not constitute an angular momentum operator and is considered a central/fundamental theme in quantum mechanics.

In order to use property summarised by Eq. 2.20, one must project all the angular momentum operators onto the ground state crystal field doublet manifold. Such a projection is necessary since the $j_{\text{eff}} = \frac{1}{2}$ approximation refers exclusively to the ground state doublet and is accomplished by an algorithm derived in Appendix C:

- Combining the Stevens parameters from Princep *et al.* [16] as summarised in Tab. 2.8 and the Stevens operators as defined in Appendix D [264], the crystal field Hamiltonian $\hat{\mathcal{H}}_{\text{CF}}$ [261] can be defined in the $|J = 4, m_J\rangle$ basis. As summarised by Tab. 2.9, diagonalising $\hat{\mathcal{H}}_{\text{CF}}$ yielded eigenvalues in close agreement with the crystal fields measured on SEQUOIA.

- A transformation matrix $\mathcal{C}$ is constructed from the eigenvectors of $\hat{\mathcal{H}}_{\text{CF}}$ since the projection of particular linear operators (*i.e.* components of angular

momentum) onto individual crystal field manifolds is desired. The existence of such a transformation matrix $\mathcal{C}$ is guaranteed by the observation that $\hat{\mathcal{H}}_{\mathrm{CF}}$ is diagonalisable since a square matrix is diagonalisable if and only if there exists a basis of eigenvectors [47].

- The projection of the components of the angular momentum operator is accomplished by the general relation

$$\hat{O}_{[\mathcal{B}]} = \mathcal{C}^{-1}\hat{O}_{[\mathcal{A}]}\mathcal{C}, \tag{2.21}$$

where $\hat{O}$ is a general linear operator and the bases $\mathcal{A}$ and $\mathcal{B}$ correspond to the original $|J = 4, m_J\rangle$ and new crystal field bases, respectively [271].

- After the projection of each component of the angular momentum, the operator in the ground state crystal field doublet manifold is extracted by isolating the top 2 x 2 block matrix and follows from the definition of the matrix representation of operators [272].

- Once all components are extracted in ground state crystal field doublet manifold, if the commutation relations (Eq. 2.20) are satisfied, then the ground state manifold can be approximated as $j_{\mathrm{eff}} = \frac{1}{2}$, otherwise such an approximation is not valid [266–268, 270].

As summarised in Appendix E, the three components of the angular momentum operator projected onto the ground state crystal field doublet manifold are given by

$$\widetilde{\hat{J}}_z = \begin{pmatrix} 3.5648 & 0 \\ 0.0102 & -3.5648 \end{pmatrix} \tag{2.22}$$

$$\widetilde{\hat{J}}_x = \begin{pmatrix} 0 & 0 \\ 0 & 0 \end{pmatrix} \tag{2.23}$$

$$\widetilde{\hat{J}}_y = i\begin{pmatrix} 0 & 0 \\ 0 & 0 \end{pmatrix} \tag{2.24}$$

Inserting the projected components $\hat{J}_x$ and $\hat{J}_y$ into the commutator,

$$[\widetilde{\hat{J}}_x, \widetilde{\hat{J}}_y] = i \begin{pmatrix} 0 & 0 \\ 0 & 0 \end{pmatrix}, \tag{2.25}$$

yields a matrix that is not equal to $i\widetilde{\hat{J}}_z$. The observation that one of the commutation relations is not satisfied is sufficient to conclude that the ground state crystal field doublet manifold of Pr^{3+} in $Pr_2Sn_2O_7$ cannot be approximated as a $j_{\text{eff}} = \frac{1}{2}$. As will be discussed in the next two chapters, such an approximation is in fact valid for two Co^{2+}-based systems α-CoV_3O_8 [75] and $Co_{0.03}Mg_{0.97}O$ [18], systems whose coordination polyhedra are minimally distorted.

2.5 Concluding Remarks & Future Directions

Despite the success of the monopole confinement model utilising a linear potential, it must be conceded that, as described in §2.4.3, the linear potential is only valid for short distances and consequently, the exact potential and the corresponding Hamiltonian's eigenvalues must differ from z_n, albeit possibly smaller than experimental error. Therefore, future investigations involving the modification of the form of the relevant potential in Hamiltonian may present a fruitful avenue for future research. One approach is to apply an effective screening term to the potential [273], corresponding to

$$V(x) = \lambda|x|e^{-\frac{|x|}{l}}, \tag{2.26}$$

where l is a characteristic length scale. Another, but possibly more relevant potential [255] is one that obeys the behaviour at the limits of Eq. 2.15 defined by both Eqs. 2.16 and 2.17 such as

$$V(x) = \lambda\frac{|x|}{\frac{|x|}{h}+1}, \tag{2.27}$$

where h denotes the height of the potential. In contrast to Eq. 2.26 where the potential disappears at large distances, the potential described by Eq. 2.27 behaves as a screened Coulomb potential [274], approaching a linear $\lambda|x|$ and a

constant λh potential in the limits of small and large values of $|x|$, respectively. In terms of experimental work, one extension of this work would be to remeasure the low energy dynamics of other QSI candidates (*e.g.* $Pr_2Zr_2O_7$ [165, 197]) to determine if these systems exhibit similar non-negligible monopole tensions, while another future avenue consists of exploring the effects of external perturbations on the tension such as the application of external magnetic fields and pressure [250].

To summarise, high resolution cold neutron inelastic scattering measurements on polycrystalline $Pr_2Sn_2O_7$ have revealed a previously unreported fine structure to the low energy excitation spectrum consisting of a series of unevenly spaced nearly-dispersionless magnetic excitations. A quantum confinement model with a linear potential $\lambda|x|$ accounts for the fine structure suggesting these magnetic excitations are a direct spectroscopic observation of interacting magnetic monopole quasiparticles resulting from a finite tension between them. The success of the monopole confinement model for $Pr_2Sn_2O_7$ encourages future studies on QSIs with the ultimate goal of understanding exactly how monopole confinement affects other physical properties of QSIs.

Chapter 3

Ordered magnetism in the intrinsically decorated $j_{\text{eff}} = \frac{1}{2}$ α-CoV_3O_8

3.1 Introduction

Introducing disorder into condensed matter systems often suppresses common mean-field phases and transitions in favour of states that exhibit unusual critical properties [44, 194, 197, 275–283]. Examples of such exotic behaviour in insulating systems include the study of quenched disorder through doping in both model magnets [284, 285] and liquid crystal systems [286–288]. While the presence of strong disorder disrupts translational symmetry, often resulting in a glassy phase [289] with long range order destroyed for all length scales, the presence of weak disorder can give rise to phases displaying distinct responses for differing length scales. For example, in model random field systems near a phase transition, critical thermal fluctuations dominate until the length scale of the order parameter becomes large enough where static terms originating from the induced disorder dominate [290, 291]. Examples of new disordered-induced phases include the concept of "Bragg glass" [292–296] that were first postulated in the context of flux lattices in superconductors [297–299] where Bragg peaks exist,

however other properties reflect a glass type response. A further example of unusual phases in the presence of disorder is the Griffiths phase [300–302] that were first suggested in the context of Ising ferromagnets, where an ordered local region co-exists within a globally disordered phase. So far, the search for new disordered-induced phases have been limited to introducing disorder by doping in the case of solid state materials, or porous media for liquid crystals [287, 303–305] and quantum fluids [306–310].

One example of theoretical efforts to understand the effects of quenched disorder on the order parameter near a phase transition is random field theory which relates disorder to the lowering of the dimensionality of the underlying universality class [311, 312]. Model random magnets [284, 285, 313, 314] have played a significant role in the development and validation of such theories with an important example being the dilute Ising antiferromagnets such as $Fe_xZn_{1-x}F_2$ [278, 315–317] (Fe^{2+}, $L = 2$ and $S = 2$) and $Mn_xZn_{1-x}F_2$ [318, 319] (Mn^{2+}, $L = 0$ and $S = \frac{5}{2}$). In these magnets, the random occupancy introduced through doping combined with a magnetic field results in a tunable random field. While these systems show a competition between static and thermal fluctuations driving magnetic order, the dynamics are largely unaltered by the introduction of weak disorder [320, 321] and therefore the magnets with weak quenched disorder have collective dynamics very similar to the parent compounds. Despite significant interest in the community [322], the amount of systems that have been shown to host such exotic phases as described above have been limited, in particular, there are few examples of definitive "Bragg glass" and Griffiths phases. In this chapter, the search for these exotic phases has shifted towards α-CoV_3O_8, a system where disorder is not introduced through doping, but rather is inherit to the crystallographic symmetry and therefore is a situation where magnetic disorder is introduced despite the presence of structural order.

In contrast to the disordered systems described above, where the disorder is a consequence of an addition external to the original system (*e.g.* doping [278, 315–319], porous media [303, 308, 309], *etc.*), and thus can be finely tuned [323], the disorder in α-CoV_3O_8 is simply inherent to its *Ibam* crystal structure. As illustrated in Figs. 3.1(a) and (b), the proposed crystal structure of α-CoV_3O_8 consists of zig-zag chains of edge-sharing MO_6 octahedra (M = Co^{2+} and V^{4+}) running along c [79]. With the exception of a single crystallographic constraint corresponding to a local selection rule requiring that one Co^{2+} and one V^{4+} reside on opposite sides of the O(5) bridging oxygen (Fig. 3.1(c)), the *Ibam* structure of α-CoV_3O_8 consists of a random distribution of metal cations

along the zig-zag chains. A combination of the proposed random metal cation distribution with both evidence [79] for dominant antiferromagnetic exchange coupling from DC susceptibility and Ising anisotropy due to local axial octahedral distortions and spin-orbit coupling, suggests that α-CoV_3O_8 may represent a potential alternative route for the investigation of disordered-induced physics.

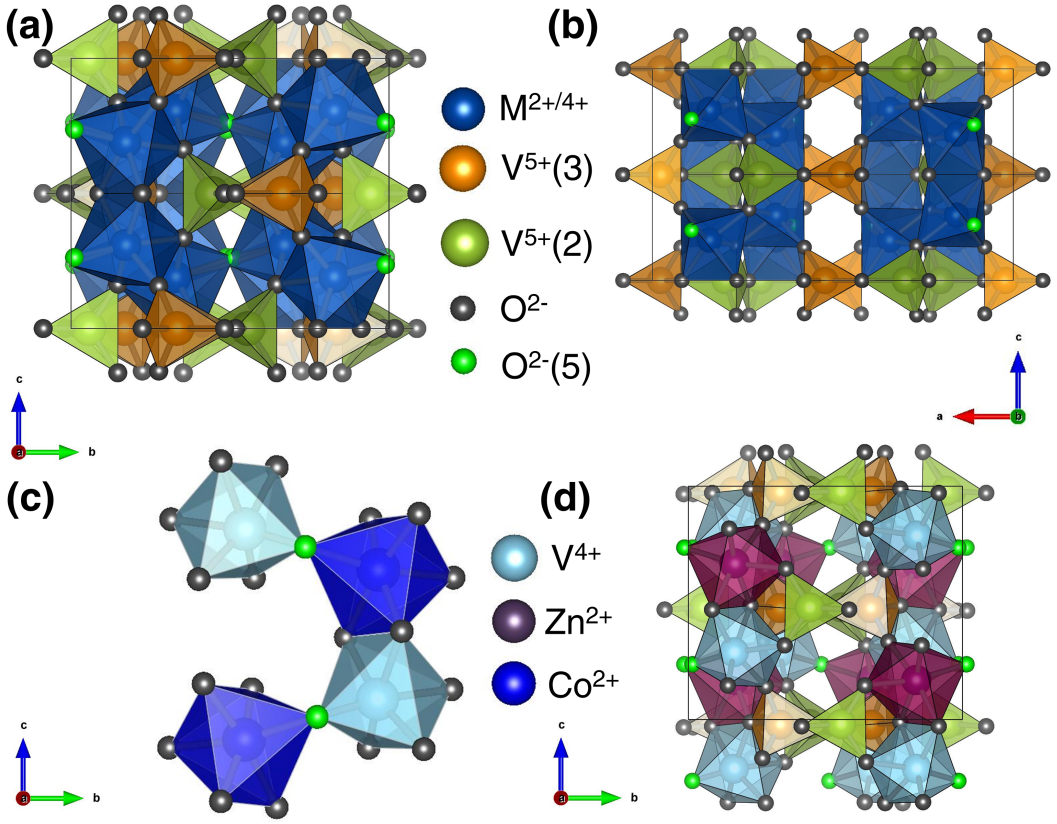

Figure 3.1 Proposed [79] crystal structure of α-CoV_3O_8 (*Ibam*, #72) along the (a) *bc* and (b) *ac* planes, consisting of zigzag chains of edge-sharing MO_6 (M = Co^{2+}, V^{4+}) octahedra running parallel to *c*. (c) Local constraint of the *Ibam* structure. Metal sites opposite of the bridging O(5) must be occupied by one Co^{2+} and one V^{4+}, with the O(5) situated closer to the V^{4+} site. (d) Crystal structure of α-ZnV_3O_8 (*Iba*2, #45). In contrast to *Ibam*, the *Iba*2 structure consists of an ordered alternating distribution of Zn^{2+} and V^{4+} along the zigzag chains [324].

In this chapter, both the crystal-magnetic structure and fluctuations of α-CoV_3O_8 are characterised. This chapter consists of five sections discussing our results including this introduction and a subsequent section on experimental details. The characterisation of the static nuclear-magnetic structure are first presented. High resolution single crystal x-ray and neutron diffraction data confirmed both the disordered *Ibam* crystal structure and the presence

of local octahedral distortions. A combination of single crystal magnetic neutron diffraction and single crystal DC susceptibility identified the presence of ferromagnetic correlations between Co^{2+} cations within the *ab* plane, in addition to a dominant antiferromagnetic coupling along *c*. Low energy critical scattering is consistent with 3D Ising behaviour attributable to the $j_{\text{eff}} = \frac{1}{2}$ Co^{2+} ions. However, in contrast to the intrinsically disordered *Ibam* crystal structure, by applying the first moment sum rule of neutron scattering, it was determined that the excitations are well described by an ordered Co^{2+} arrangement. This chapter concludes with a section discussing the experimental results in the context of models for disordered magnets and the role of spin-orbit coupling through a comparison of model magnets in a random field.

3.2 Experimental Details

3.2.1 Sample Preparation

Single crystals of α-CoV_3O_8 were grown using a modified "self-flux" heating routine for α-CoV_2O_6 [325]. Precursor polycrystalline samples of α-CoV_2O_6 were first synthesised by a standard solid-state reaction consisting of heating a stoichiometric mixture of $Co(CH_3CO_2)_2 \cdot 4\ H_2O$ (Sigma-Aldrich, 98%) and V_2O_5 (Alfa Aesar, 99.6%) in air for 12 h at 650°C, then for 48 h at 725°C, followed by quenching in liquid nitrogen [76, 326]. A mixture of the α-CoV_2O_6 polycrystalline precursor and V_2O_5 in a 3:2 ratio in the presence of approximately 0.01% (w/w) of B_2O_3 (Alfa Aesar, 98.5%) was heated in a vacuum sealed quartz tube at 780°C for 24 h and subsequently cooled to 700°C at a rate of 1°C hr^{-1}. After 24 h of heating at 700°C, the sample was cooled to 600°C at a rate of 1°C hr^{-1} and subsequently quenched to room temperature.

Polycrystalline samples of α-CoV_3O_8 and α-ZnV_3O_8 were synthesised by a standard solid-state reaction consisting of heating a stoichiometric mixture of CoO (Alfa Aesar, 95%) or ZnO (Alfa Aesar, 99.99%), VO_2 (Alfa Aesar, 99%) and V_2O_5 for 96 h at 650°C under static vacuum in a sealed quartz tube with intermittent grindings until laboratory powder x-ray diffraction confirmed no discernable impurities [324, 327]. All stoichiometric mixtures of polycrystalline precursors were first mixed thoroughly together and finely ground to homogeneity with acetone using an agate mortar and pestle. The mixtures were pressed into $\sim$ 2 g pellets using a uniaxial press and subsequently placed in alumina crucibles

or directly in quartz ampoules for reactions performed in air and in vacuum, respectively. Unless otherwise stated, all heating routines involved a ramping rate of 5°C min^{-1} and samples were furnace cooled back to room temperature.

3.2.2 Laboratory X-ray Diffraction

Single crystal x-ray diffraction was performed at 120 K on a 0.011 mg single crystal of α-CoV_3O_8 with dimensions of 0.40 × 0.11 × 0.09 mm^3 using monochromated Mo K_α radiation on an Oxford Diffraction SuperNova dual wavelength diffractometer equipped with an Atlas CCD detector and an Oxford Cryostream-*Plus* low-temperature device. Data collection, integration, scaling, multiscan absorption corrections and indexing were performed using the CrysAlisPro v1.171.37.35e software package [328]. The structure solution was performed using a direct approach method with the SHELXS-97 program in Olex2 [329].

Room temperature powder diffraction patterns of α-CoV_2O_6, α-CoV_3O_8 and α-ZnV_3O_8 were collected over 2θ = [5, 70]° in 0.0365° steps on a Bruker D2 Phaser laboratory x-ray diffractometer using monochromated Cu K_α radiation.

All structural refinements for single crystal and polycrystalline measurements were performed using the JANA2006 [330] and GSAS [331] Rietveld refinement program packages, respectively, and are summarised in Appendix B. For the single-crystal refinement, the solved structure was refined by a full-matrix least squares against F^2 using only data $I > 3\sigma(I)$.

3.2.3 DC Magnetic Susceptibility

A 7.7 mg single crystal of α-CoV_3O_8 with dimensions of 2 × 1 × 1 mm^3 was aligned along the three principal axes. All crystal alignments were performed with polychromatic Laue backscattering diffraction employing adapted photostimulable plates using the Fujifilm FCR Capsula XL II system [332]. The temperature dependence of ZFC magnetisation for all three principal axes was measured on a Quantum Design MPMS in an external DC field $\mu_o H_{ext}$ = 0.5 T applied parallel to the particular axis of interest. Measurements were performed in 2 K steps spaced linearly from 2 K to 300 K.

3.2.4 Neutron Single Crystal Diffraction

Neutron single crystal diffraction experiments were performed on the SXD [333, 334] time-of-flight instrument at the ISIS spallation source. The SXD diffractometer employs the time-of-flight Laue technique. The combination of a polychromatic incident beam falling on a stationary sample surrounded by 11 ZnS scintillator PSDs covering $\Omega \sim 2\pi$ sr enables quick access to a large amount of reciprocal space with minimal sample movement during data collection. A 0.4312 g single crystal of α-CoV_3O_8 with dimensions of $13.2 \times 4.1 \times 2.1$ mm^3 as illustrated in Fig. 3.2(d) was mounted on the end of a 6 mm aluminium pin with aluminium tape, vertically suspended from a liquid helium 50 mm bore Orange cryostat providing ω-motion in an accessible temperature range of 1.5 to 300 K. Diffraction data was collected at both 5 K and 50 K for three different single crystal frames with an accumulated charge of 1300 μA·h ($\sim$ 8 h). After each temperature change, the sample was allowed to thermalise for 15 minutes. Reflection intensities were extracted, reduced and integrated to structure factors using standard SXD procedures, as implemented in `SXD2001` [333–335].

3.2.5 Inelastic Neutron Time-of-Flight Scattering Spectroscopy

All inelastic neutron scattering experiments were performed on the direct geometry MARI [336, 337] and indirect geometry IRIS [103] time-of-flight spectrometers located at ISIS. Neutron spectroscopic measurements were performed on powders as preliminary measurements found the signal from single crystals to be weak. High-energy measurements (> 2 meV) on 32.6 g of α-CoV_3O_8 and 31.9 g of α-ZnV_3O_8 were performed on the direct geometry MARI spectrometer. The t_o chopper was operated at 50 Hz in parallel with a Gd chopper spun at 350, 300 and 250 Hz with incident energies $E_i = 150$, 60 and 15 meV, respectively, providing an elastic resolution of 5.87, 1.82 and 0.321 meV, respectively. A thick disk chopper spun at $f = 50$ Hz reduced the background from high-energy neutrons. A top loading Displex CCR provided an accessible temperature range of 5 to 600 K.

For lower energies, measurements on 15.1 g of α-CoV_3O_8 were performed on the indirect geometry IRIS spectrometer. As an indirect geometry spectrometer, the final energy E_f was fixed at 1.84 meV by cooled PG002 analyser crystals in near backscattering geometry. The graphite analysers were cooled to reduce

thermal diffuse scattering [104], providing an elastic resolution of 17.5 μeV. A top loading Displex CCR provided an accessible temperature range of 5 to 580 K.

3.2.6 Neutron Powder Diffraction

Neutron diffraction measurements on 1.8 g of polycrystalline α-CoV_3O_8 were performed on the BT-4 thermal triple axis spectrometer [338] at the NIST Center for Neutron Research (NCNR). Incident and scattering neutron energies were set to 14.7 meV (λ=2.3592 Å), selected by vertically focussing PG002 monochromator and analyser crystals with PG filters located before and after the sample to reduce higher-order neutron contamination. The Söller horizontal collimator configuration downstream order was 60′-monochromator-80′-sample-80′-analyser-60′-detector. A top loading liquid helium 50 mm bore Orange cryostat provided an accessible temperature range of 1.5 to 300 K. θ-2θ measurements were collected at both 3 K and 300 K over 2θ = [15, 90]° in 0.2° steps ($|\mathbf{Q}|$ = [0.695,3.766] Å^{-1} in 0.009 Å^{-1} steps). Magnetic order parameter measurements were performed at 2θ = 41.6° ($|\mathbf{Q}|$ = 1.89 Å^{-1}) over T=[3, 32] K in 0.1 K steps.

3.3 Results & Analysis

3.3.1 Crystal Structure

As illustrated in Fig. 3.2(a) and summarised in Tabs. B.2-B.4, single crystal x-ray diffraction at 120 K confirmed an orthorhombic unit cell (a = 14.29344(4) Å, b = 9.8740(3) Å, c = 8.34000(3) Å) with a volume of 1185.60(6) Å^3, corresponding to Z = 8. Systematic extinctions provided *Ibam* (#72, Fig. 3.1(a,b)) and *Iba*2 (#45, Fig. 3.1(d)) as possible space groups, with statistical analysis of the intensity data favouring the centrosymmetric *Ibam*. In a procedure analogous to previous studies on hydrothermally grown single crystals, the structure was solved using direct methods [79]. The corresponding unit cell was found to consist of three metal sites with octahedral (16k), tetrahedral (8j) and trigonal bipyramidal (8j) coordination, with Co^{2+} and V^{4+} with half occupancies independently distributed over the 16k site and V^{5+} with full occupancies in the latter two 8j sites. Structural refinements utilising 910 out of a total of 985 measured

reflections confirmed two important conclusions from previous studies [79, 327]. Firstly, Co^{2+} and V^{4+} are both randomly and equally distributed over the $16k$ site with refined occupancies of 0.506(6) and 0.494(4), respectively. Secondly, the large refined anisotropic displacements resulting from placing the O(5) oxygen in the $8f$ position with full occupancy support the local selection rule consisting of Co^{2+} and V^{4+} occupying respective positions on opposite sides of the O(5) bridging oxygen ligand, as illustrated in Fig. 3.1(c).

3.3.2 DC Magnetic Susceptibility

As summarised by Tab. 3.1 and Fig. 3.2(a), DC susceptibility measurements along all three principal axes indicates that α-CoV_3O_8 behaves as a Curie-Weiss paramagnet at high temperatures and undergoes an antiferromagnetic transition at 19.5(5) K, corresponding to a T_N much greater than previously reported T_N of 8.2 K for crystals grown hydrothermally [79]. Fig. 3.2*b* presents a fit of the high temperature data (T=[200,300] K) to the Curie-Weiss law, yielding Curie-Weiss temperatures θ_{CW} of 9.5(7), 2(1), −21.3(2) K for $\mu_o H_{ext}$ applied along a, b and c, respectively. The small θ_{CW} with an average $\theta_{CW} = 3.2(4)$ K is suggestive of either weak exchange interactions or the presence of multiple and nearly cancelling ferro/antiferromagneic interactions resulting in the experimentally observed small average. The differences in the constants measured along different directions is also indicative of an anisotropy in the system likely originating from the distortion of the local octahedra [20, 76].

Table 3.1 Curie-Weiss parameters for α-CoV_3O_8 in an external DC field $\mu_o H_{ext} = 0.5$ T applied parallel to the three principal axes. Numbers in parentheses indicate statistical errors.

Crystallographic Axis	C (emu K/mol)	p_{eff} (μ_B)	θ_{CW} (K)
a	3.525(9)	5.310(7)	9.5(7)
b	3.31(2)	5.15(2)	2(1)
c	3.354(2)	5.180(2)	−21.3(2)
Average	3.396(7)	5.213(7)	−3.2(4)

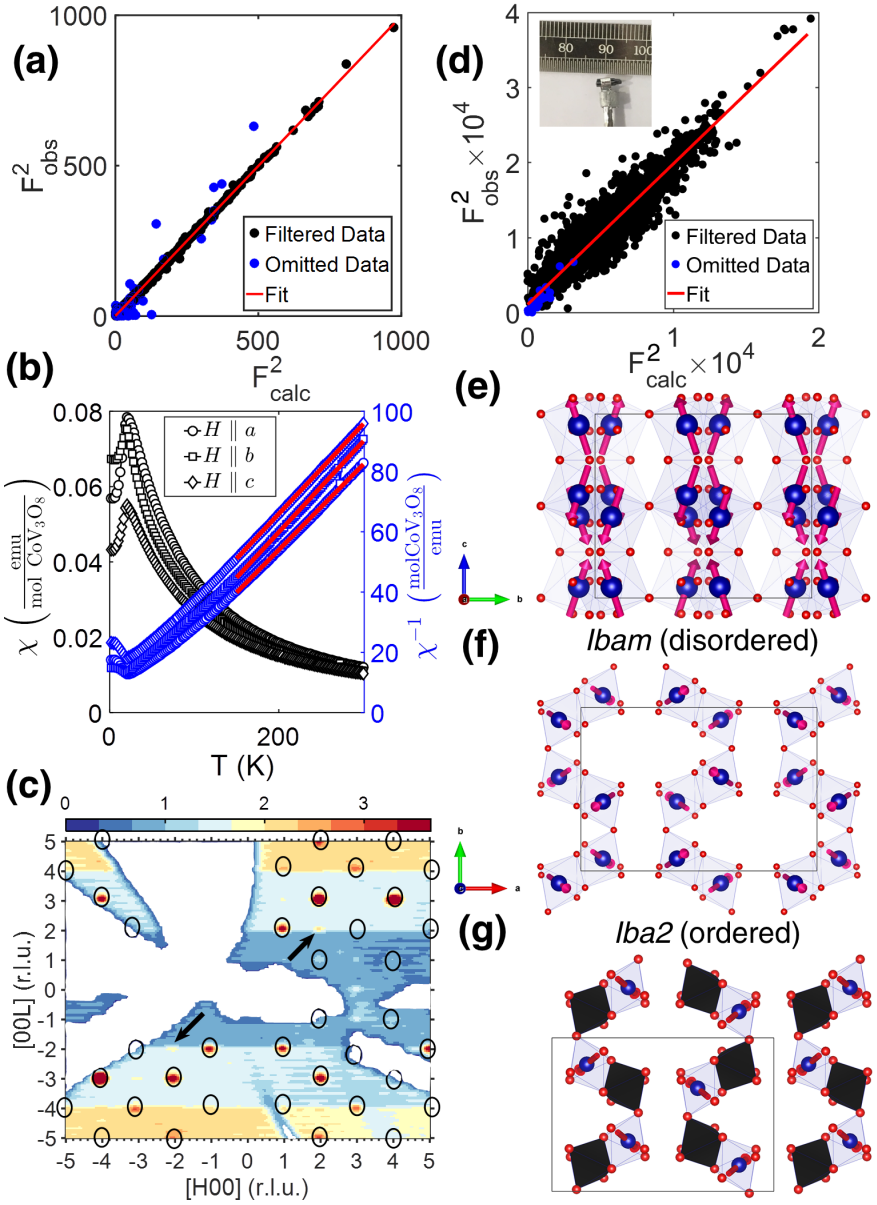

Figure 3.2 (a) F^2_{obs}-F^2_{calc} plot for the refinement of single crystal x-ray diffraction data collected at 120 K (R_{F^2}=1.65%, R_{wF^2}=2.38% and χ^2=1.47), yielding a refined *Ibam* unit cell (a=14.29344(4) Å, b=9.8740(3) Å, c= 8.34000(3) Å). (b) Temperature dependence of the DC magnetic susceptibility in $\mu_o H_{ext}$ = 0.5 T applied parallel to the three principal axes. Red lines indicate Curie-Weiss fits. (c) Single crystal neutron diffraction intensity pattern collected at 5 K in the ($H0L$) scattering plane. Black ellipses indicate nuclear Bragg reflections. Arrows indicate strong magnetic Bragg reflections. (d) F^2_{obs}-F^2_{calc} for the joint nuclear-magnetic refinement of single crystal neutron diffraction data on a (inset) single crystal of α-CoV_3O_8 collected at 5 K (R_{F^2}=8.34%, R_{wF^2}=8.98%, $R_{F^2_{mag}}$=23.44% and χ^2=3.18), utilising a propagation vector **k**=(1,1,1) with the P_Iccn Shubnikov magnetic space group. Schematic illustration of the refined magnetic structure of α-CoV_3O_8 along the (e) bc and (f) ab planes with the Co^{2+} having a 50% occupancy. The orientation of the refined magnetic moments on Co^{2+} are indicated by red arrows. (g) illustrates the ordered *Iba*2 space group with each Co^{2+} site fully occupied and the black octahedra representing non-magnetic V^{4+} sites.

As illustrated in Fig. 3.2(b), the magnetisation does not approach zero in the low temperature limit after the antiferromagnetic transition. Instead, its value for all three principal axes plateaus at 2 K which indicates the possibility for the presence of paramagnetism at lower temperatures, although no measurements were conducted below 2 K. In contrast to the d^7 Co^{2+} moments that can couple *via* e_g orbitals, coupling between the d^1 V^{4+} moments are exclusively *via* t_{2g} orbitals which is predicted to be much weaker [53, 54, 56] and thus more likely to exhibit paramagnetic behaviour. In fact, V^{4+} paramagnetism is supported by the observation that the saturated moment in the low temperature limit corresponds to 0.150(2) μ_B, a value consistent with a strongly reduced V^{4+} effective paramagnetic moment predicted to occur in the presence of strong spin-orbit coupling and octahedral distortions as has been previously observed experimentally in $Na_2V_3O_7$ [339, 340]. Finally, the average effective paramagnetic moment of 5.213(7) μ_B is smaller than the predicted moment of 5.6 μ_B, for Co^{2+} in an octahedral environment as studied in CoO [341] and assuming a 1:1 ratio of high spin Co^{2+} and V^{4+}, confirming that both spin-orbit and distortion effects play a significant role [326] in the magnetism of α-CoV_3O_8, a topic that will be later addressed with inelastic neutron scattering in §3.3.4.

3.3.3 Magnetic Structure

As shown in Fig. 3.2(c) and summarised in Tabs. B.5-B.7, single crystal neutron diffraction confirmed both an absence of any structural distortion away from the *Ibam* space group down to 5 K and the appearance of additional Bragg reflections confirming long range magnetic ordering as measured by previous DC susceptibility measurements [79]. Since DC susceptibility measurements suggested that V^{4+} remained paramagnetic down to at least 2 K, the refinement of single crystal neutron diffraction data collected at 5 K assumed that the magnetic Bragg reflections were exclusively due to Co^{2+} that were randomly distributed throughout the 16k metal sites. The random distribution of Co^{2+} was accomplished by constraining the occupancy of each metal site to a value of $\frac{1}{2}$. The additional magnetic Bragg reflections were successfully indexed using a propagation vector $\mathbf{k}$ = (1, 1, 1) with the P_Iccn (#56.376) Shubnikov space group [342]. The propagation vector $\mathbf{k}$ = (1, 1, 1) was initially chosen as it corresponds to the first point of symmetry reduction by removing body-centering symmetry with the same structural unit cell [343]. Subsequently, utilising the aforementioned value of $\mathbf{k}$, a symmetry analysis was performed in

JANA2006 [330]. With a $\mathbf{k} = (1, 1, 1)$, the symmetry analysis considers which models were compatible — following the symmetry operations of the group, but excluding body-centering — with the restriction that moments at (x, y, z) are antiferromagnetically aligned with those moments at ($x + \frac{1}{2}$, $y + \frac{1}{2}$, $z + \frac{1}{2}$). Four models were found to be compatible, with the P_Iccn (#56.376) Shubnikov space group yielding the best match.

Tab. 3.2 summarises the results of a joint nuclear and magnetic refinement utilising 5086 out of a total of 5120 measured reflections at 5 K (Fig. 3.2(d)), confirming a strong preference for the P_Iccn Shubnikov space group of $Ibam$ over P_Icc2 of $Iba2$. The refined magnetic moment for Co^{2+} was found to be $\mu = 3.53(2)$ μ_B with μ_a, μ_b and μ_c as 1.35(5) μ_B, 1.16(5) μ_B and 3.05(5) μ_B, respectively. α-CoV_3O_8 adopts a magnetic structure consisting of effective pairs of 2D layers in the ab plane, separated from one another by a non-magnetic layer consisting of tetrahedrally coordinated V^{5+}, as illustrated in Fig. 3.2(f). Within these 2D layers, Co^{2+} spins are ferromagnetically coupled along both a and b, corresponding to inter-chain superexchange interactions. These 2D layers come in pairs with each offset from one another by [0.1858a, 0.1508b and 0.1194c] with the pair being antiferromagnetically coupled to the adjacent pair along c, corresponding to intra-chain superexchange interactions.

Table 3.2 Comparison of the refined magnetic moment's components assuming random ($Ibam$) and ordered ($Iba2$) distribution of Co^{2+} and V^{4+} on the metal sites of α-CoV_3O_8. The goodness-of-fit metric χ^2 and residuals from the magnetic refinement of neutron single crystal diffraction data collected at 5 K suggests that Co^{2+} and V^{4+} are randomly distributed. Numbers in parentheses indicate statistical errors.

Parameter	Value ($Ibam$)	Value ($Iba2$)
μ_a	1.35(5) μ_B	1.30(6) μ_B
μ_b	1.16(5) μ_B	1.09(8) μ_B
μ_c	3.05(4) μ_B	2.32(5) μ_B
χ^2	3.18	5.15
R_{F^2}	8.38%	10.59%
R_{wF^2}	8.99%	14.57%
$R_{F^2_{mag}}$	24.13%	32.28%

3.3.4 Inelastic Neutron Scattering

Motivated by the random distribution of Co^{2+} and V^{4+}, multiple ferro-/antiferromagnetic interactions and the presence of strong spin-orbit coupling, the

spin dynamics of α-CoV_3O_8 was investigated with neutron inelastic scattering. All inelastic scattering intensities were normalised to absolute units using the paramagnetic approximation [107]. As discussed in Appendix I, the normalisation procedure consists of using both Co and V as internal incoherent standards [106, 344] to calculate an absolute calibration constant $\mathcal{A}$ converting vanadium-corrected scattering intensities $\widetilde{I}(\mathbf{Q}, E)$ to the differential scattering cross section $\frac{d^2\sigma}{dEd\Omega}$ which was then converted to the dynamic structure factor $S(\mathbf{Q}, E)$ by

$$\mathcal{A}\widetilde{I}(\mathbf{Q}, E) \equiv \frac{d^2\sigma}{dEd\Omega} = \left(\frac{\gamma r_o}{2}\right)^2 g_J^2 2|f(\mathbf{Q})|^2 S(\mathbf{Q}, E), \tag{3.1}$$

where it is understood that $S(\mathbf{Q}, E)$ is $S^{zz}(\mathbf{Q}, E) = \frac{Tr\left\{S^{\alpha\beta}(\mathbf{Q},E)\right\}}{3}$, $\left(\frac{\gamma r_o}{2}\right)^2$ and g_J^2 equals to 73 mb sr^{-1} and the Landé g-factor, respectively, while the factor of 2 corresponds to the paramagnetic cross section [99, 106, 107, 345]. The value for the Landé g-factor is discussed in Appendix E. Hereafter, all neutron scattering quantities with a tilde (for example $\widetilde{S}(|\mathbf{Q}|, E)$), denote the inclusion of the magnetic form factor squared $|f(\mathbf{Q})|^2$.

Spin-Orbit Transitions

As will be discussed in much further detail in both Appendix E and Chapter 4, Co^{2+} ($L = 3$ and $S = \frac{3}{2}$) in an octahedral crystal field environment can be projected onto a ground state with an effective orbital angular momentum [20] of $l = 1$. As a consequence of the projection of $\hat{\mathbf{L}}$ with $L = 3$ onto $\hat{\mathbf{l}}$ with $l = 1$, a projection factor [76, 341] α of $-\frac{3}{2}$ is introduced, yielding a new projected spin-orbital Hamiltonian $\hat{\mathcal{H}}_{S.O.} = \alpha\lambda\hat{\mathbf{l}} \cdot \hat{\mathbf{S}}$. Diagonalising the projected spin-orbit Hamiltonian results in three spin-orbit split Kramers doublets [18, 47, 346] characterised by an effective angular momentum $\hat{\mathbf{j}} = \hat{\mathbf{l}} + \hat{\mathbf{S}}$ with eigenvalues $j \equiv j_{\text{eff}}$ of $\frac{1}{2}$, $\frac{3}{2}$, and $\frac{5}{2}$. The $j_{\text{eff}} = \frac{3}{2}$ and $\frac{5}{2}$ manifolds are separated in energy from the $j_{\text{eff}} = \frac{1}{2}$ ground state doublet manifold by $\frac{3}{2}\alpha\lambda$ and $\frac{5}{2}\alpha\lambda$, respectively [20]. Based on the work performed on $Co_{0.03}Mg_{0.97}O$ [18], it can be assumed that for pure CoO [18], $|\alpha\lambda| \sim 24$ meV, in contrast to the theoretical single-ion value of $\sim$35 meV, possibly indicative of coupling to the ^4P excited state. Therefore for an undistorted octahedra, using the value as determined for $Co_{0.03}Mg_{0.97}O$, one would expect a crystal field excitation at $\sim$36 meV. In this section, the magnetic excitations in α-CoV_3O_8 are investigated using neutron spectroscopy in order to determine if its ground state can be considered as a $j_{\text{eff}} = \frac{1}{2}$.

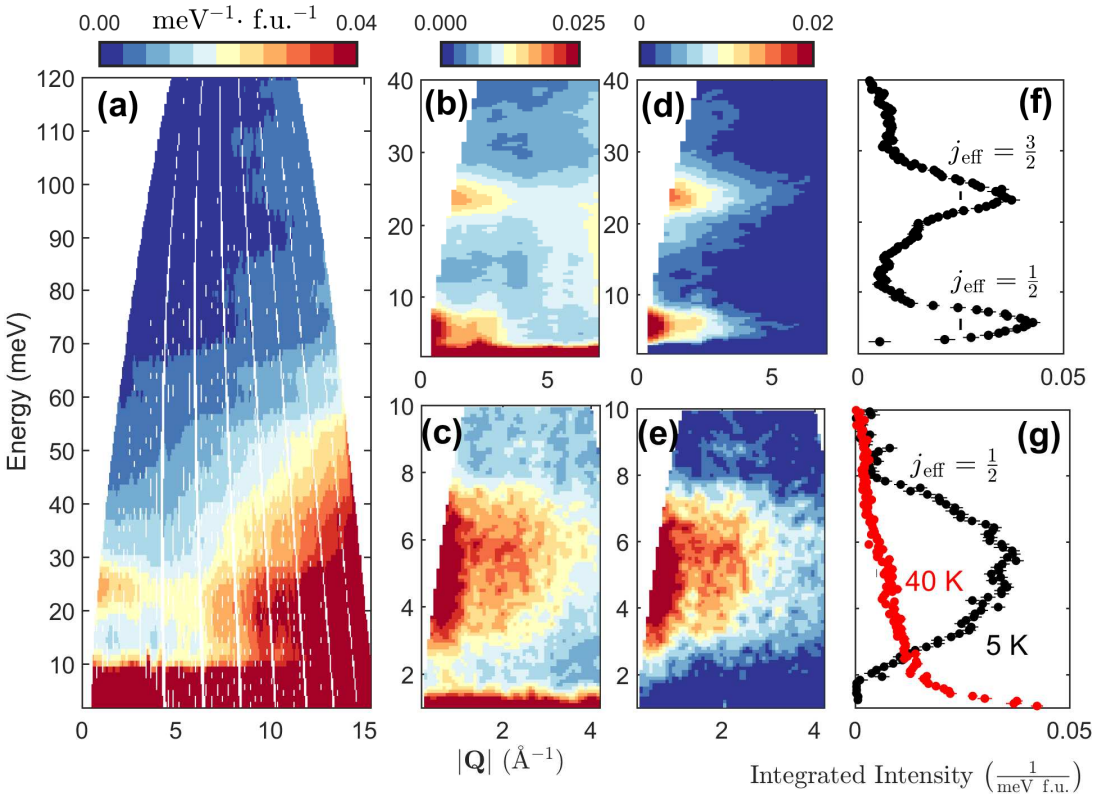

Figure 3.3 $\widetilde{S}(|\mathbf{Q}|, E)$ measured on MARI at T = 5 K with an E_i of (a) 150 meV, (b) 60 meV and (c) 15 meV. (d,e) Magnetic scattering $\widetilde{S}_M(|\mathbf{Q}|, E)$ and (f,g) corresponding $|\mathbf{Q}|$-integrated cuts ($|\mathbf{Q}|$=[0,3] Å^{-1}). Vertical lines in (f,g) indicate instrumental resolution. $\widetilde{S}_M(|\mathbf{Q}|, E)$ was calculated by the subtraction of corresponding $\widetilde{S}(|\mathbf{Q}|, E)$ for α-ZnV_3O_8 measured at identical experimental conditions. All inelastic scattering intensities have been normalised to absolute units.

Neutron inelastic scattering measurements (Figs. 3.3(a)-(c)) on polycrystalline α-CoV_3O_8 with an $E_i = 150$, 60 and 15 meV, respectively at 5 K revealed two clear low $|\mathbf{Q}|$ excitations at $\sim$ 5 meV and $\sim$ 25 meV. To prevent any weak magnetic signal of interest from being masked by strong phonon bands, a scaled inelastic scattering spectrum $\widetilde{\gamma}\widetilde{S}(|\mathbf{Q}|, E)$ of an approximate isostructural compound α-ZnV_3O_8 [324] collected with identical experimental conditions was subtracted as a background [3]. Neutron inelastic scattering investigations of α-ZnV_3O_8 on MARI found no evidence of correlated V^{4+} moments over the energy range reported here. The scaling factor $\widetilde{\gamma}$ for the background was calculated from the ratio between energy-integrated cuts of $\widetilde{S}(|\mathbf{Q}|, E)$ of α-CoV_3O_8 and α-ZnV_3O_8 along $|\mathbf{Q}|$ at high $|\mathbf{Q}|$, thereby normalising by the phonon scattering. The use of α-ZnV_3O_8 as a background not only removes the constant and $|\mathbf{Q}|^2$-dependent background contributions but the presence of V^{4+} in both compounds allows for

the isolation of magnetic fluctuations solely attributable to Co^{2+}. As illustrated in Figs. 3.3(d)-(g), the use of α-ZnV_3O_8 as an effective background revealed that the origin of the low-$|\mathbf{Q}|$ excitations must be due to Co^{2+} exclusively, excluding the possibility of any contribution from V^{4+}.

Following the analysis of inelastic scattering measurements on monoclinic and triclinic polymorphs of CoV_2O_6 [76], the low-$|\mathbf{Q}|$ excitations in α-CoV_3O_8 can be understood as transitions between different spin-orbit manifolds. A comparison between the inelastic spectra of CoV_2O_6 and α-CoV_3O_8 suggests that the excitations at ~ 5 meV and ~ 25 meV are due to transitions within the $j_{\text{eff}} = \frac{1}{2}$ manifold and between the $j_{\text{eff}} = \frac{1}{2}$ and $j_{\text{eff}} = \frac{3}{2}$ manifolds, respectively. In α-CoV_3O_8, these modes appear much broader than in CoV_2O_6; this will be discussed later. Such an assignment is supported by the observation that the transition at ~ 5 meV is gapped at 5 K in the magnetically ordered regime, as illustrated in Figs. 3.3(g). Such a gap would be a consequence of the Zeeman splitting of the $j_{\text{eff}} = \frac{1}{2}$ manifold due to the internal molecular field caused by long range ordering in the Néel phase [76]. Once the temperature is raised above T_N, the molecular field would be significantly reduced due to the loss of magnetic order, resulting in the disappearance of a gap, as is experimentally observed in Fig. 3.3(g).

In the context of this assignment in terms of j_{eff} spin-orbit split manifolds, a difference between α-CoV_3O_8 and monoclinic α-CoV_2O_6 is the absence of an observable $\sim$110 meV magnetic excitation (Fig. 3.3(a)). As was previously calculated for CoV_2O_6 [76], in addition to the strong excitations for the intra-$j_{\text{eff}} = \frac{1}{2}$ and the $j_{\text{eff}} = \frac{1}{2}$ to $j_{\text{eff}} = \frac{3}{2}$ transitions, the intensity of the $j_{\text{eff}} = \frac{1}{2}$ to $j_{\text{eff}} = \frac{5}{2}$ transition scales with the distortion of the local coordination octahedra [21, 347] with the transition being absent for a perfect octahedra like in rocksalt and cubic CoO [18]. α-CoV_3O_8 exhibits a much weaker octahedral distortion ($\delta = 11.106(8)$) than α-CoV_2O_6 ($\delta = 55$) and is thus expected to have a significantly weaker intensity. This is also in agreement with previous results on triclinic γ-CoV_2O_6 (with $\delta = 2.1$ and 4.8 for the two different Co^{2+} sites) which failed to observe a $j_{\text{eff}} = \frac{5}{2}$ transition [76]. A distortion of the local octahedra around the Co^{2+} site should result in an anisotropic term in the magnetic Hamiltonian [265, 347, 348]. Given the powder average nature of the dynamics (discussed below), this particular study is not sensitive to this term. However, the consistency of the inelastic response with the j_{eff} description discussed above in terms of the energy response is also consistent with other Co^{2+} where a local distortions of the octahedra exists [21, 76]. In the next subsection, it will be shown that by applying the sum rules of neutron scattering,

the lowest magnetic excitation corresponds to a $j_{\text{eff}} = \frac{1}{2}$ manifold, thus providing further evidence for the interpretation outlined above of the low energy magnetic excitations in terms of pure j_{eff} levels.

Total Moment Sum Rule

To confirm the assignment of the 5 meV signal as excitations within the ground state $j_{\text{eff}} = \frac{1}{2}$ manifold, the total integrated spectral weight at 5 K of the lowest lying excitation was calculated. As derived in Appendix H, the total moment sum rule of neutron scattering [106, 349–352] states that the sum of all spectral weight is defined by

$$\frac{3\int d^3\mathbf{Q}\int dES(\mathbf{Q},E)}{\int d^3\mathbf{Q}} = j(j+1), \tag{3.2}$$

where $S(\mathbf{Q},E) \equiv S^{zz}(\mathbf{Q},E)$ denotes the magnetic component of the dynamic structure factor $\widetilde{S}^{zz}_{M}(\mathbf{Q},E)$ that has been further renormalized by $|f(\mathbf{Q})|^2$. The extra factor of 3 has been included to assure consistency with the definition of $S(\mathbf{Q},E) \equiv S^{zz}(\mathbf{Q},E)$ given by Eq. J.7 in the paramagnetic approximation. A measurement of the integrated intensity is therefore sensitive to the effective j of the manifold of levels being integrated over. Eq. 3.2 can be simplified by integrating out the angular dependence and cancelling common terms resulting in an integral $\mathcal{L}$ defined by

$$\mathcal{L}(|\mathbf{Q}|) = \frac{3\int d|\mathbf{Q}|\mathbf{Q}|^2\int dES(|\mathbf{Q}|,E)}{\int d|\mathbf{Q}||\mathbf{Q}|^2}. \tag{3.3}$$

The total integral $\mathcal{L}$ is uniquely a function of $|\mathbf{Q}|$ and represents an integration of the magnetic density of states over all energies including both elastic and inelastic channels in the cross section [106]. With $j_{\text{eff}} = \frac{1}{2}$, the total moment sum rule (Eq. 3.2) would predict a value of 0.75 for the total integrated intensity.

Since the assignment discussed above based on spin-orbit transitions assumes that the $\sim$5 meV excitation and the elastic cross section is exclusively due to excitations within the $j_{\text{eff}} = \frac{1}{2}$ manifold, all quantities in Eq. 3.2 were projected onto the ground state doublet manifold by the projection theorem of angular momentum [3, 47]. As discussed in Appendix E, the projection onto the ground state doublet required defining the projected value of the Landé g-factor g_J as

$g'_J = \frac{13}{3}$ and the effective angular momentum j_{eff} as $\frac{1}{2}$ [20, 353].

Before proceeding, although one may be tempted to project the individual eigenvalues of S in Eq. H.11 utilising the logic outlined in Appendices C and E, such a projection is ultimately incorrect. The projection onto the $j_{\text{eff}} = \frac{1}{2}$ is completely accounted for by the use of a projected Landé g-factor g'_J. As described in Appendix E, the Landé g-factor is a projection factor, as deduced from the projection theorem (Appendix C) accompanying a projection from the effective magnetic moment $\hat{\mathbf{M}} = g_L\hat{\mathbf{L}} + g_S\hat{\mathbf{S}}$ onto a total angular momentum $\hat{\mathbf{J}}$. In the current investigation, the projection performed is from $\hat{\mathbf{M}}$ onto an effective total angular momentum $\hat{\mathbf{j}} = \hat{\mathbf{l}} + \hat{\mathbf{S}}$, where the effective label reflects the initial projection of the orbital angular momentum operator $\hat{\mathbf{L}}$ onto an effective $\hat{\mathbf{l}}$ with eigenvalue l=1. To differentiate the projection of $\hat{\mathbf{M}}$ onto $\hat{\mathbf{J}}$ and $\hat{\mathbf{M}}$ onto $\hat{\mathbf{j}}$, a prime is placed on g_J for the latter case, as will be the convention for the remainder of this Thesis.

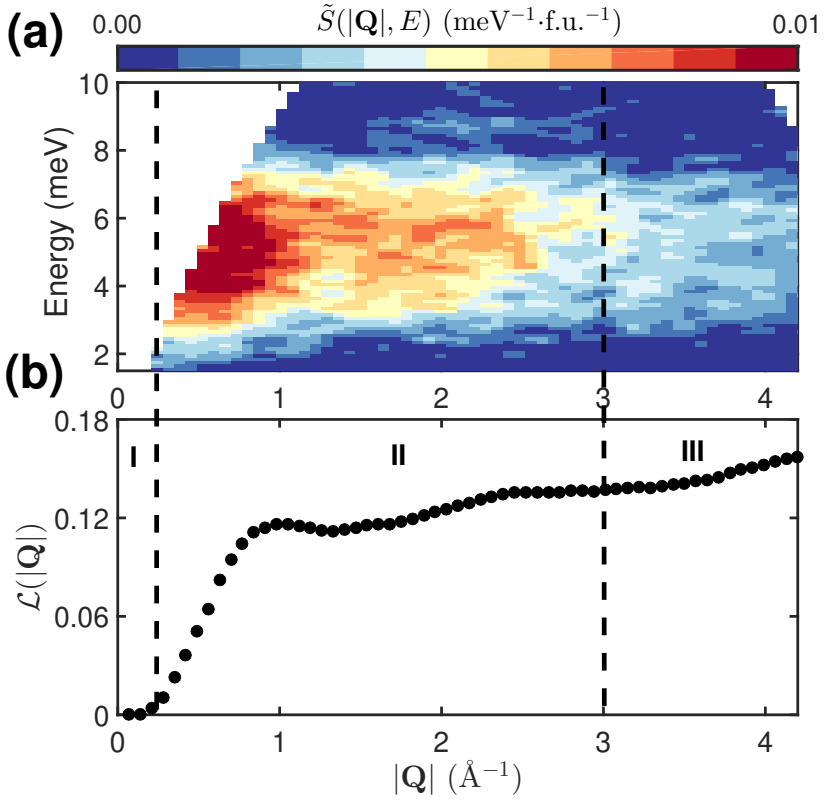

Figure 3.4 (a) Magnetic scattering $\widetilde{S}_M(|\mathbf{Q}|, E)$ of α-CoV_3O_8 measured on MARI at T = 5 K with an E_i of 15 meV and the corresponding (b) $|\mathbf{Q}|$-dependence of the total integrated inelastic (E=[2,8] meV) magnetic scattering intensity $\mathcal{L}$. Regions I, II and III denote "get-lost" tube-, magnetic- and phonon/form factor-dominated regions, respectively.

As illustrated in Fig. 3.4, the total integrated inelastic intensity of $S(|\mathbf{Q}|, E) \equiv S^{zz}(|\mathbf{Q}|, E)$ given by $\mathcal{L}(|\mathbf{Q}|)$ (Eq. 3.3) saturates at 0.15(1). Combining the integral of the inelastic contribution and an elastic contribution of $\left(\frac{\mu}{g'_J \mu_B}\right)^2 = 0.66$, yields a total integral of 0.81±0.14, in good agreement with the total moment predictions for $j_{\text{eff}} = \frac{1}{2}$ of 0.75. The agreement further confirms the assignment of the low energy excitations to transitions within the ground state $j_{\text{eff}} = \frac{1}{2}$ spin-orbit doublet manifold.

With the low energy excitations being successfully approximated by pure j_{eff} manifolds, the effective paramagnetic moment p_{eff} of 5.213(7) μ_{B} that was calculated from DC susceptibility may be addressed. Given that the $j_{\text{eff}} = \frac{1}{2}$ and $j_{\text{eff}} = \frac{3}{2}$ manifolds are separated by ∼24 meV (∼278 K), both are significantly thermally populated at the high temperatures used for the Curie-Weiss fit. In such a high temperature regime, one would expect a p_{eff} of $g_s\sqrt{S(S+1)} = 3.9\ \mu_B$, which is significantly less than the measured value as has been commonly observed for other magnets based on Co^{2+} in octahedral coordination [76, 326, 346, 354]. The extra component measured with susceptibility may be accounted for by noting that V^{4+} contributes $g_s\sqrt{S(S+1)} = 1.7\ \mu_{\text{B}}$. Therefore the addition of the contributions to p_{eff} from both Co^{2+} and V^{4+} corresponds to a total predicted $p_{\text{eff}} = 5.6\ \mu_{\text{B}}$, in close agreement with the experimental data, with the small discrepancy potentially attributable to the fact that the $j_{\text{eff}} = \frac{5}{2}$ manifold is still not significantly populated at T∼300 K. Although it is worth noting that an additional and distinct possibility for a much larger measured effective paramagnetic moment may be a strong orbital contribution as has been observed for the case of CoO [355, 356], where the orbital contribution is significant, corresponding to approximately $\frac{1}{3}$ of the total ordered moment.

3.3.5 Critical Exponents

Despite the similarities between the inelastic spectra of α-CoV_3O_8 and CoV_2O_6, one difference is the bandwidth of the low energy excitation that has been assigned to the $j_{\text{eff}} = \frac{1}{2}$ manifold. As illustrated in Fig. 3.3(g), in contrast to both polymorphs of CoV_2O_6, α-CoV_3O_8 exhibits a broad peak in energy whose bandwidth is approximately 20 times that of instrumental resolution. Such a large bandwidth could be accounted for by magnetic exchange coupling between spins [76, 357, 358]. However, an alternative explanation may lie in the intrinsic cationic disorder inherent to the disordered *Ibam* structure of α-CoV_3O_8 [79]. Such large cationic disorder would result in a distribution of cationic sites and

correspondingly a spread of spin-orbit transitions as has been shown for multiple doped systems [170, 220, 317, 320, 359–361], and thus perhaps such disorder may also explain the large bandwidth in α-CoV_3O_8 due to a distribution of molecular fields splitting the $j_{\text{eff}} = \frac{1}{2}$ manifold. In this subsection, such a possibility is investigated using a critical scaling analysis.

Scaling Analysis

The presence of such disorder would result in temperature being the dominant energy scale. To investigate this possibility, the temperature dependence of the Co^{2+} spin fluctuations was analysed using a scaling analysis previously employed for the charge-doped cuprates [362–366]. For paramagnetic fluctuations, critical scattering theory assumes a single energy scale, the relaxation rate Γ is dominant [64]. If Γ is driven by temperature, then it can be shown that the energy-temperature dependence of the uniform dynamic susceptibility $\chi''(E,T)$, follows $\frac{E}{T}$ scaling [362, 363] given by

$$\frac{\chi''(T,E)}{\chi''(T=0\ K,E)} = \arctan\left\{\sum_{i=0} a_i \left(\frac{E}{T}\right)^{2i+1}\right\}, \tag{3.4}$$

where $\chi''(T = 0\ K, E)$ denotes the value of χ'' in the limit of T = 0 K and all even powers are excluded in the sum to satisfy detailed balance, requiring χ'' to be an odd function of energy [365]. For this particular analysis, the value of $\chi''(T,E)$ was calculated by first subtracting a temperature independent background from the measured $S(T,|\mathbf{Q}|,E)$. The contribution of the background was determined by an algorithm previously employed for $Fe_{1+x}Te_{0.7}Se_{0.3}$ [367] and polymer quantum magnets [368]. The algorithm is based on the requirement that all inelastic scattering must obey detailed balance accounting for both sample environment and other temperature-independent scattering contributions and thus isolating the fluctuations exclusively due to Co^{2+}. The background-subtracted dynamic structure factor was then converted to $\chi''(T,|\mathbf{Q}|,E)$ *via* the fluctuation-dissipation theorem [369]

$$\chi''(T,|\mathbf{Q}|,E) \ = \ g^2\mu_B^2\pi\left\{\frac{1}{n(E,T)+1}\right\}S(T,|\mathbf{Q}|,E), \tag{3.5}$$

where $n(E,T)$ is the Bose factor. Finally, $\chi''(T,|\mathbf{Q}|,E)$ was integrated over

$|\mathbf{Q}| = [0, 3]$ and $[0, 2]$ Å^{-1} for measurements on MARI and IRIS, respectively. As illustrated in Fig. 3.5(c), $\frac{E}{T}$ scaling adequately accounts for the experimental data with the need for only two refined constants of 3.2(1) and 0.8(2) for a_o and a_2, respectively, since the inclusion of higher order terms in Eq. 3.4 did not improve the fit. The success of $\frac{E}{T}$ scaling suggests that $\Gamma \propto T^{\nu}$ and the larger value of a_o over all other terms suggests $\nu \leq 1$.

The value of ν was refined using a modified scaling algorithm previously employed to detect anomalous scaling in the vicinity of a quantum critical point for $CeCu_2Si_2$ and $CeCu_{6-x}Au_x$ [370–372]. Utilising the single relational energy mode approximation and the Kramers-Kronig relations [254], the uniform dynamic susceptibility can be approximated as a Lorentzian-like response [21, 362, 373–378] given by

$$\chi'' = \chi' \left\{ \frac{E\Gamma}{E^2 + \Gamma^2} \right\}, \tag{3.6}$$

where χ' is the static susceptibility and $\Gamma \propto \xi^{-1}$ where ξ is the correlation length [379]. If one assumes both the single energy scale $\Gamma = \gamma(\mathrm{T} - \mathrm{T_N})^{\nu}$ and the static susceptibility $\chi' = \frac{C}{\Gamma}$, where γ and C are constants of proportionality, then Eq. 3.6 assumes the form

$$\chi'' = \frac{C}{\gamma(T - T_N)^{\nu}} \left\{ \frac{\frac{E}{\gamma(T-T_N)^{\nu}}}{1 + \left(\frac{E}{\gamma(T-T_N)^{\nu}}\right)^2} \right\}. \tag{3.7}$$

The first assumption leading to Eq. 3.7 stems from the fact that the scaling properties of the dynamics are being investigated near the vicinity of an ordering transition at $\mathrm{T_N} \sim 19$ K and not a quantum critical point as in the cuprates and heavy fermion systems [372, 380, 381], a fact that was reflected in Fig. 3.5(c) by defining $\chi''(T = 0, E)$ as the value at 24 K. The second assumption is based on the paramagnetic behaviour observed with DC susceptibility at high temperatures, suggesting χ' should adopt a Curie-Weiss form [362, 380]. As illustrated in Fig. 3.5(d), the scaling relation (Eq. 3.7) provides a good description of the experimental data over four orders of magnitude in $\frac{E}{T}$, yielding a refined ν of 0.636(10). It is important to note that the refined value of ν is not consistent with random dilute 3D Ising behaviour where $\nu = 0.683(2)$, but instead is consistent with the ordered 3D Ising universality class with a $\nu = 0.6312(3)$ [64, 382–386]. While scaling and critical scattering typically only applies near the

phase transition, work on other transition metal based compounds has found critical scattering that scales up to high temperatures in the paramagnetic regime [357, 387].

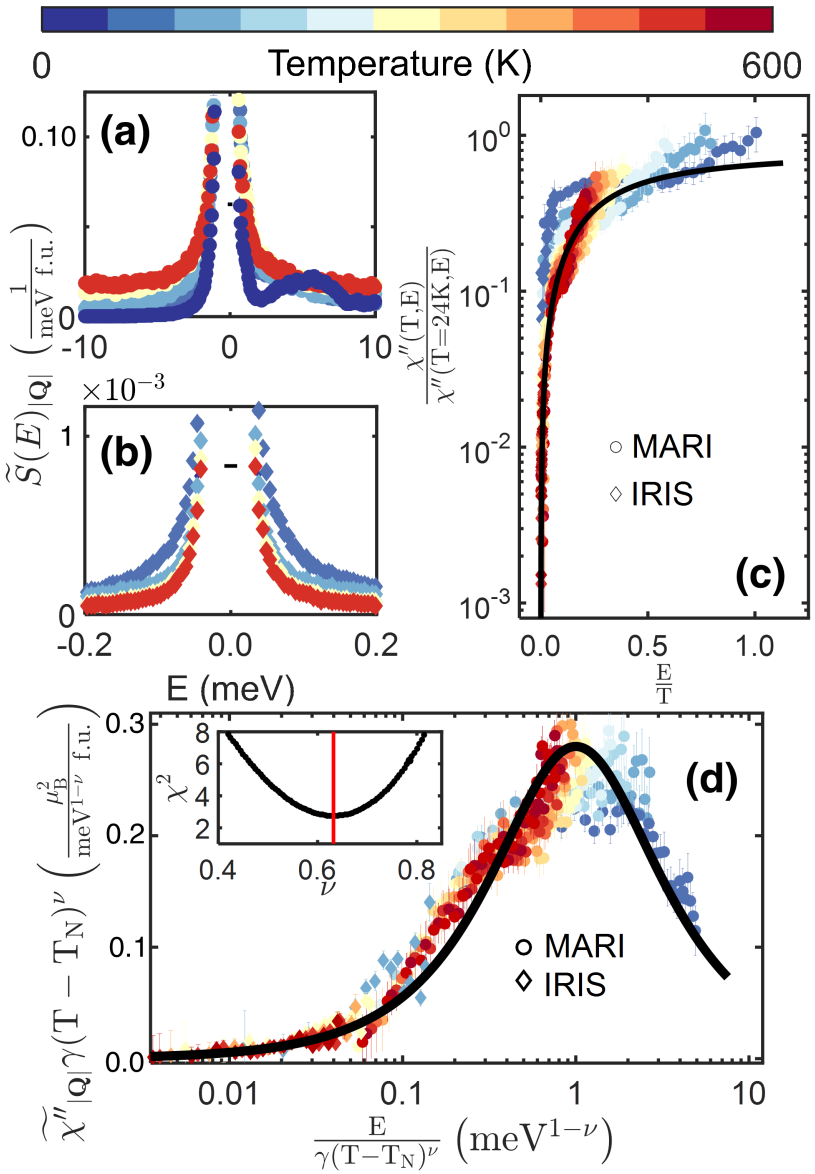

Figure 3.5 $|\mathbf{Q}|$-integrated cuts of $\widetilde{S}(|\mathbf{Q}|, E)$ measured on (a) MARI and (b) IRIS at various temperatures. Horizontal lines indicate instrumental resolution. (c) Energy and temperature dependence of the normalised χ'' calculated from $|\mathbf{Q}|$-integrated cuts of $\widetilde{S}_M(|\mathbf{Q}|, E)$ measured on both IRIS at MARI. (d) Compilation of the energy-temperature dependence of $|\mathbf{Q}|$-integrated χ'' as calculated in (c). As discussed in the main text, the data is described by a Lorentzian relaxational form (Eq. 3.7), revealing scaling behaviour consistent with $\Gamma \propto (T - T_N)^\nu$. The line of best fit yields $\nu = 0.636(10)$, corresponding to a global minimum of χ^2 as illustrated in the inset. All panels share the same temperature scale (top horizontal intensity bar). All $|\mathbf{Q}|$-integrated cuts on MARI and IRIS are from $|\mathbf{Q}|$=[0,3] Å^{-1} for E_i=15 meV and from $|\mathbf{Q}|$=[0,2] Å^{-1} for E_f=1.84 meV, respectively.

Magnetic Order Parameter

The scaling analysis in the previous subsubsection found that the critical fluctuations are consistent with an ordered three dimensional Ising universality class and is consistent with the DC susceptibility data presented above. Consequently, while the excitations are separated into distinct j_{eff} manifolds, the scaling analysis indicates that the distortion does introduce an anisotropy term in the magnetic Hamiltonian influencing the critical dynamics outlined in the previous subsubsection. In an attempt to further deduce the universality class of CoV_3O_8, neutron diffraction measurements were performed on polycrystalline α-CoV_3O_8 to extract further critical exponents. As illustrated in Fig. 3.6(a), polycrystalline α-CoV_3O_8 exhibits long range magnetic ordering at 3 K, in agreement with both single crystal DC susceptibility (Fig. 3.2(b)) and single crystal neutron diffraction (Fig. 3.2(c)) measurements. The temperature dependence of the scattering intensity of the (212) magnetic Bragg reflection is displayed in Fig. 3.6(b), corresponding to the square of the magnetic order parameter [388] ϕ, given by the power-law dependence

$$I(T) \equiv \phi^2(T) \propto (T_{\text{N}} - T)^{2\beta}, \tag{3.8}$$

yields a refined T_N of 18.8(6) K in agreement with DC susceptibility measurements and a refined β of 0.28(7). Although the value of β is in agreement with the predicted value of 0.326 for the ordered 3D Ising universality class [64], the large statistical error also implies agreement with the predicted value for the random dilute 3D Ising model of 0.35 [382–385]. Therefore, the critical magnetic fluctuations are in agreement with expectations from both ordered and disordered 3D Ising behaviour.

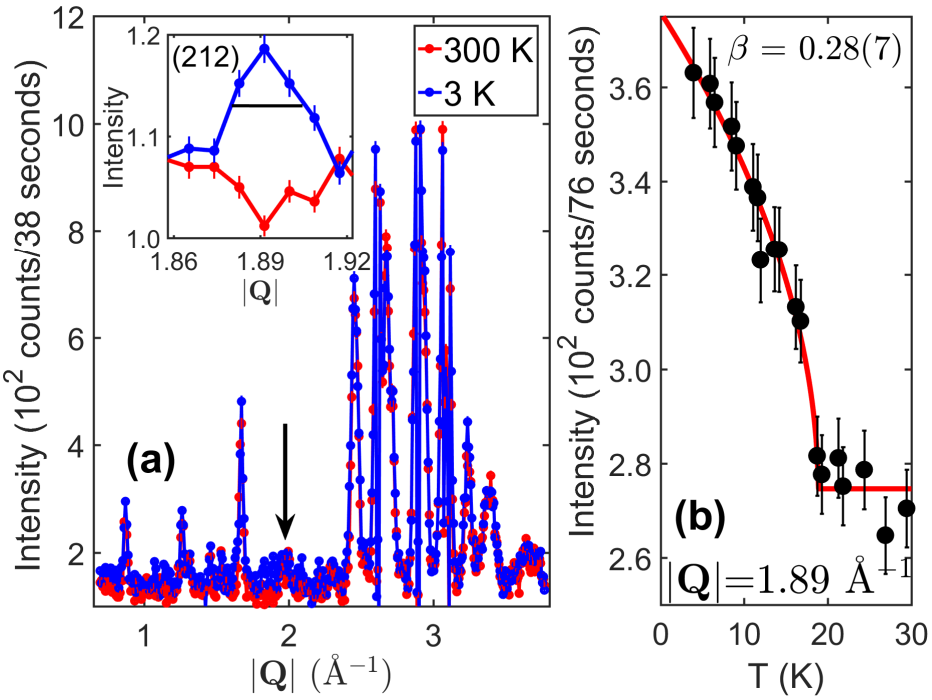

Figure 3.6 (a) Neutron diffraction profiles of polycrystalline α-CoV_3O_8 collected at 3 and 300 K on BT4. (inset) Additional scattering intensity on the (212) magnetic Bragg reflection at 3 K confirms long range magnetic order. The horizontal line indicates instrumental resolution. (b) Temperature dependence of the elastic intensity at $|\mathbf{Q}| = 1.89$ Å^{-1} ($2\theta = 41.6°$), corresponding to the maximum of the (212) magnetic Bragg reflection as indicated by the arrow in (a). A fit to $(T_N - T)^{2\beta}$ yields T_N=18.8(6) K and β=0.28(7).

3.3.6 First Moment Sum Rule, Local Cation Ordering & Single Mode Approximation

In order to deduce further information concerning both the dimensionality d and the microscopic exchange constants J, a combination of the first moment sum rule of neutron scattering and the single mode approximation was employed. The determination of the values for J and d begin with the Hohenberg-Brinkman first moment sum rule [389] given by

$$\begin{aligned}\langle E\rangle(\mathbf{Q}) &= \int dEES(\mathbf{Q},E) \\ &= -\frac{2}{3}\sum_{i,j} n_{ij}J_{ij}\langle\hat{\mathbf{S}}_i\cdot\hat{\mathbf{S}}_j\rangle(1-\cos(\mathbf{Q}\cdot\mathbf{d}_{ij}))\end{aligned} \tag{3.9}$$

and its powder-average

$$\langle E\rangle(|\mathbf{Q}|) = -\frac{2}{3}\sum_{i,j} n_{ij}J_{ij}\langle\hat{\mathbf{S}}_i\cdot\hat{\mathbf{S}}_j\rangle\left\{1-\frac{\sin(|\mathbf{Q}||\mathbf{d}_{ij}|)}{|\mathbf{Q}||\mathbf{d}_{ij}|}\right\}, \tag{3.10}$$

as derived in Appendix H, where n_{ij}, J_{ij}, $\langle\hat{\mathbf{S}}_i\cdot\hat{\mathbf{S}}_j\rangle$ and $\mathbf{d}_{ij}$ denote the number of individual exchange interactions, the exchange constant, the spin-spin correlator and the displacement vector between spins at sites i and j, respectively [76, 351, 390].

Since all of the inelastic intensity measured at 5 K on MARI with an $E_{\mathrm{i}} = 15$ meV shown in Fig. 3.3(g) corresponds to excitations within the ground state $j_{\mathrm{eff}} = \frac{1}{2}$, proven by the total moment sum rule, then the single mode approximation (SMA) can be applied [351, 391]. The single mode approximation, applicable to a situation where the excitation spectrum is dominated a single coherent mode, allows for the dynamic structure factor to be written as $S(\mathbf{Q},E) = S(\mathbf{Q})\delta[\epsilon(\mathbf{Q})-E]$, where $\delta[\epsilon(\mathbf{Q})-E]$ assures energy conservation [76, 106, 349, 368, 392]. Applying the single mode approximation to the first moment sum rule yields

$$\begin{aligned} S(\mathbf{Q},E) = -\frac{2}{3}\frac{1}{\epsilon(\mathbf{Q})}\sum_{i,j} n_{ij}J_{ij}\langle\hat{\mathbf{S}}_i\cdot\hat{\mathbf{S}}_j\rangle\cdot \\ \{1-\cos(\mathbf{Q}\cdot\mathbf{d}_{ij})\}\,\delta[\epsilon(\mathbf{Q})-E], \end{aligned} \tag{3.11}$$

providing a quantitative relationship between $S(\mathbf{Q},E)$ and the dispersion $\epsilon(\mathbf{Q})$ and by extension, a measure of the dimensionality [76, 106, 393, 394]. For numerical purposes, the delta function was approximated as a Lorentzian with a FWHM equal to that of the calculated experimental resolution width of 0.24 meV at 5 meV transfer on MARI. Eqs. 3.9-3.11 assume the presence of Heisenberg exchange and thus excludes exchange anisotropy [76, 349, 351, 391]. It is important to note that the exclusion of any anisotropy terms is simply a first approximation based on the success of the isotropic exchange model to account for experimental data in a variety of other Co^{2+}-based systems such as CoV_2O_6, $KMn_{1-x}Co_xF_3$ and $Mn_{1-x}Co_xF_2$ [76, 284, 346, 353, 395]. In fact, there is evidence that anisotropic exchange is not negligible in α-CoV_3O_8. Such experimental evidence includes equal intensities for transitions within the ground state manifold and between the ground state and first excited state

manifolds [20, 346], as illustrated in Fig. 3.3(f). Another piece of evidence is the presence of a weak signal at ~ 1 meV at low energy transfer measurements, as illustrated in Fig. 3.3(g) that may be indicative of anisotropic breakdown of magnetic excitations [20, 76, 106, 349, 396]. The non-negligible value of anisotropic exchange in α-CoV_3O_8 is indeed expected due to the distorted coordination octahedra around Co^{2+} ($\delta \sim 11$) and has been observed in α, γ-CoV_2O_6 with similar distortion parameters [76, 77] but will be excluded in the context of the current discussion.

First Moment Sum Rule & Cation Order

This section utilises the first moment sum rule of neutron scattering to provide an estimate of the exchange constants in α-CoV_3O_8. Fig. 3.7(a) shows the background subtracted first moment $\widetilde{\langle E \rangle}(|\mathbf{Q}|)$ at 5 K was successfully described by the powder averaged first moment sum rule (Eq. 3.10) incorporating all possible 15 Co^{2+}−Co^{2+} distances in the α-CoV_3O_8 unit cell from $|\mathbf{d}_{ij}| = [3.209, 7.669]$ Å. As summarised by Tab. 3.3, a least squares optimisation revealed that only six unique distances possess non-negligible $-n_{ij}J_{ij}\langle \hat{\mathbf{j}}_i \cdot \hat{\mathbf{j}}_j \rangle$ values. Before proceeding, it is important to note that the use of $\hat{\mathbf{j}}$ in the correlator instead of $\hat{\mathbf{S}}$ was because all scattering intensities were normalised by g'_J. Two particular distances with negligible $-n_{ij}J_{ij}\langle \hat{\mathbf{j}}_i \cdot \hat{\mathbf{j}}_j \rangle$ contributions are 3.209 Å and 3.540 Å corresponding to the nearest neighbour and metal site distances across the O(5) bridging ligand, respectively. The absence of the latter is expected due to the local selection rule [79] as illustrated in Fig. 3.1(c), but the absence of the nearest neighbour distance is inconsistent with a random distribution of Co^{2+} inherent to the disordered *Ibam* structure previously deduced by diffraction measurements (Fig. 3.2). Upon closer inspection of the α-CoV_3O_8 unit cell, these six distances were shown to correspond to the unique distances found exclusively in the ordered *Iba*2 structure [324] as illustrated in Figs. 3.7(c) and (d), confirming an ordered arrangement of Co^{2+}.

While this analysis indicates the distances are consistent with the ordered *Iba*2 structure, there are two potential caveats. Because the product $-n_{ij}J_{ij}\langle \hat{\mathbf{j}}_i \cdot \hat{\mathbf{j}}_j \rangle$ is measured, (i) the value of n_{ij} may not be negligible but instead the correlator $\langle \hat{\mathbf{j}}_i \cdot \hat{\mathbf{j}}_j \rangle$ can; (ii) and/or the exchange constants J_{ij} may themselves be negligible. To address issue (i), the correlator $\langle \hat{\mathbf{j}}_i \cdot \hat{\mathbf{j}}_j \rangle$ has been calculated based on energy-integrated magnetic diffraction data (Tab. 3.3) and found it to be substantial for all distances. Argument (ii) may be addressed by pointing out that some distances

with negligible $n_{ij}J_{ij}$ have a Co^{2+}-O^{2-}-Co^{2+} angle close to 180°, predicted by the Goodenough-Kanamori-Anderson rules to yield strong antiferromagnetic exchange [53, 54, 56].

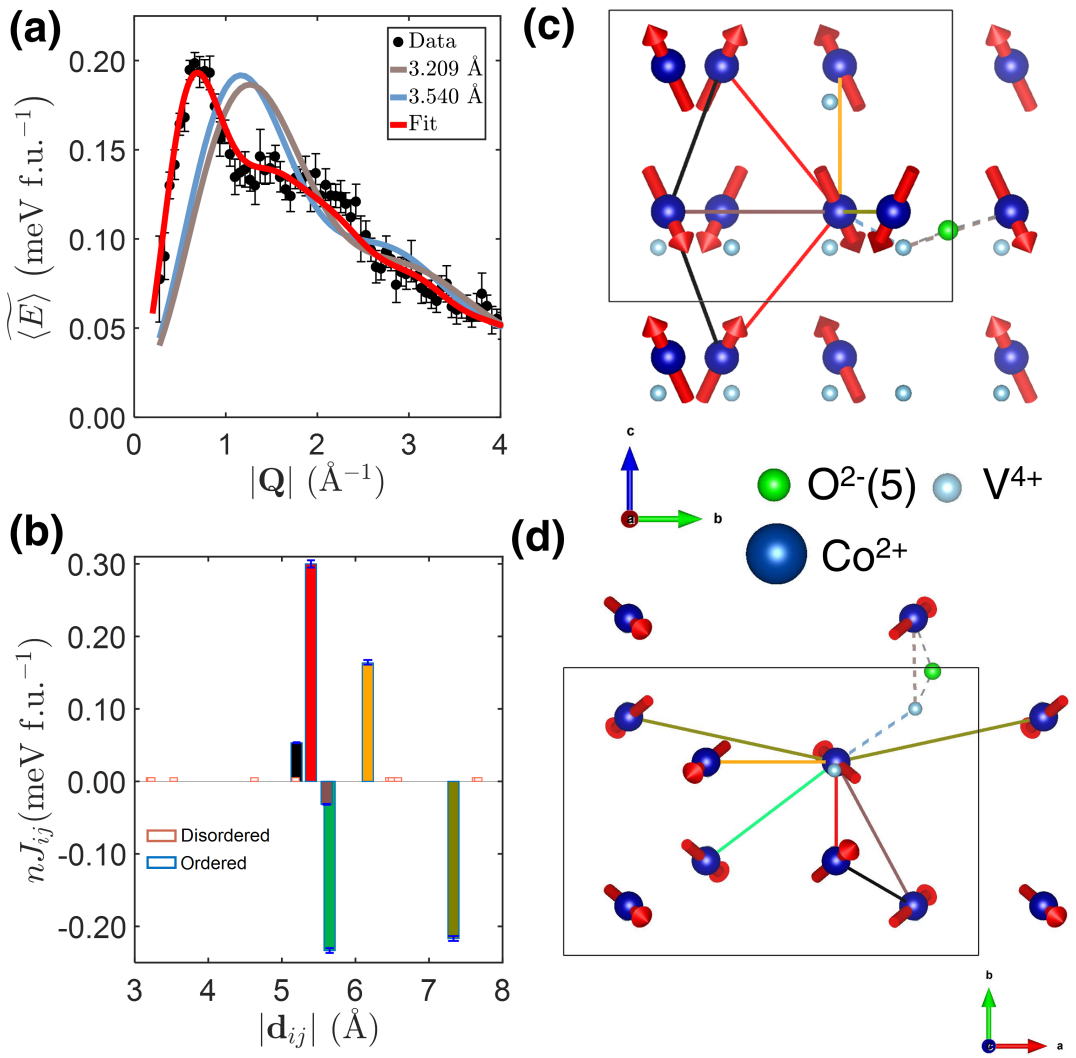

Figure 3.7 (a) $|\mathbf{Q}|$-dependence of the first moment $\langle E \rangle$ as measured on MARI at T=5 K with an E_i=15 meV integrated over E=[2,8] meV. A fit to the first moment sum rule (Eq. 3.10) reveals that only six distances $|\mathbf{d}_{ij}|$ out to 7.5 Å possess non-negligible nJ_{ij} values as illustrated in (b), and summarised in Tab. 3.3. For the purposes of comparison, distances present only in the ordered and disordered atomic arrangements are distinguished by purple and dark pink outline colours, respectively. Distances with non-negligible nJ_{ij} contributions have a face colour corresponding to the illustration of the corresponding six interactions along the (c) *bc* and (d) *ac* planes of the α-CoV_3O_8 unit cell. Both non-bridging oxygen atoms have been excluded and V^{4+} ions have been reduced in size for the purposes of clarity. Two particular distances: 3.209 Å and 3.540 Å are absent as noted in (a), corresponding to nearest neighbour and bridging metal site distances, respectively.

Table 3.3 Distances $|\mathbf{d}_{ij}|$ with corresponding non-negligible refined values of $-n_{ij}J_{ij}\langle\hat{\mathbf{j}}_i \cdot \hat{\mathbf{j}}_j\rangle$ and nJ_{ij} from the fit of the first moment $\langle E\rangle(|\mathbf{Q}|)$ (E=[2,8] meV) at 5 K to the first moment sum rule [389]. The corresponding calculated spin-orbit corrected Curie-Weiss constant $\widetilde{\theta}_{CW}$ (Eq. 3.12) is in close agreement with the experimentally determined Curie-Weiss constant averaged over all three principal directions $\bar{\theta}_{\mathrm{CW,exp}}$. Numbers in parentheses indicate statistical errors.

$\lvert\mathbf{d}_{ij}\rvert$ (Å)	$-n_{ij}J_{ij}\langle\hat{\mathbf{j}}_i \cdot \hat{\mathbf{j}}_j\rangle$ (meV f.u.$^{-1}$)	$\langle\hat{\mathbf{j}}_i \cdot \hat{\mathbf{j}}_j\rangle$	$n_{ij}J_{ij}$ (meV f.u.$^{-1}$)
5.200(2)	0.023(1)	−0.420(2)	0.055(1)
5.395(3)	0.17(1)	−0.594(3)	0.30(1)
5.6083(14)	0.016(2)	0.484(2)	−0.033(1)
5.649(4)	0.098(2)	0.417(3)	−0.24(1)
6.168(3)	0.08(1)	−0.483(3)	0.17(1)
7.3321(9)	0.13(1)	0.595(4)	−0.22(1)
$\bar{\theta}_{\mathrm{CW,exp}}$	−3.2(4) K		
$\widetilde{\theta}_{\mathrm{CW}}$	−0.24(15) K		

The exchange constants J_{ij} can now be extracted by dividing out the correlator from the $-n_{ij}J_{ij}\langle\hat{\mathbf{j}}_i \cdot \hat{\mathbf{j}}_j\rangle$. Inserting the 6 values of $n_{ij}J_{ij}$ in the mean field expression for the Curie-Weiss temperature [37, 397]

$$\widetilde{\theta}_{\mathrm{CW}} = -\frac{S(S+1)\sum_{i,j} n_{ij}J_{ij}}{3\zeta}, \tag{3.12}$$

where ζ is a scale factor of 1.9 calculated by Kanamori [341], one obtains −0.24(15) K, a value that is both small and negative, in agreement with the experimentally determined value of −3.2(4) K. The close similarity between the calculated and experimentally determined values of θ_{CW} suggests that all relevant exchange interactions have been accounted for by the *Iba*2 structure. It is important to emphasise that this analysis assumes isotropic exchange and thus assumes the isotropic part of the magnetic Hamiltonian is dominant. While susceptibility data indicates some anisotropy, the similarity between the extracted exchange constants and the θ_{CW} lends support for the isotropic approximation. Future advances in both single crystal growth of this material and also higher flux neutron instrumentation will allow single crystal data to be obtained and the parameters refined.

Single Mode Approximation & Dimensionality

Since the first moment sum rule indicates the presence of multiple unique interactions spanning all three crystallographic directions in the $Iba2$ structure [324], it was suspected that a more intriciate dispersion relation should be chosen for Eq. 3.11, such as the expression given by

$$\begin{aligned}\epsilon(\mathbf{Q}) = (&B_o + B_h\cos(2\pi h) + B_k\cos(2\pi k) + B_l\cos(2\pi l)\\ &+ B_{hk}\{\cos[2\pi(h+k)] + \cos[2\pi(h-k)]\}\\ &+ B_{hl}\{\cos[2\pi(h+l)] + \cos[2\pi(h-l)]\}\\ &+ B_{kl}\{\cos[2\pi(k+l)] + \cos[2\pi(k-l)]\}\\ &+ B_{2h}\cos(4\pi h) + \beta_{2k}\cos(4\pi k) + B_{2l}\cos(4\pi l))^{\frac{1}{2}}\,, \end{aligned} \tag{3.13}$$

where B_i are the dispersion parameters. The dispersion relation $\epsilon(\mathbf{Q})$ in Eq. 3.13 satisfies Bloch's theorem [99] and has been previously used to parametrise the dispersion for more complex systems involving multiple exchange interaction pathways such as PHCC [349], whose large dispersions could not be adequately described with the heuristic model $\epsilon(\mathbf{Q}) = \beta_o + \sum_i \beta_i \cos(\mathbf{Q}\cdot\mathbf{d}_{ij})$ [76, 368, 398].

As a first approximation, the parameters in Eq. 3.13 involving interactions between the principal axes were set to zero and each parameter along a particular principal axis was set to be equal (e.g. $B_h = B_{2h}$). This simple model effectively reduces Eq. 3.13 to the aforementioned simple heuristic model [76, 368, 398] and treats every exchange interaction as a combination of interactions along the three principal axes. As illustrated in Fig. 3.8, all major features of $\widetilde{S}_M(|\mathbf{Q}|, E)$ collected at 5 K, including the large bandwidth, was successfully accounted for by a least squares optimisation of the dispersion parameters. As summarised in Tab. 3.4, the refined dispersion parameters indicate the presence of three dimensional magnetism, consistent with the lack of significant asymmetry in the $|\mathbf{Q}|$-integrated cut $\widetilde{S}_M(E)_{|\mathbf{Q}|}$ displayed in Fig. 3.8(c), as would be expected for both 1D and 2D magnetic fluctuations [106, 399, 400] . As summarised by Tab. 3.4, the dispersion parameters along h and l are both negative whilst the dispersion parameters along k are positive with a larger magnitude. Both the signs and relative magnitudes of the dispersion parameters can be reconciled using the spin-flip hopping model [76, 401], where B_i for a particular direction i is interpreted as a hopping term whose value is proportional to the energy

cost of a spin-flip $t \sim SJ$ along that particular direction. The negative h and k dispersion parameters correspond to ferromagnetic coupling along a and b, respectively, while the larger positive l dispersion parameters correspond to stronger antiferromagnetic coupling along c, all consistent with both DC susceptibility and the refined magnetic structure presented in Fig. 3.2. The ability to describe the powder average magnetic dynamic response in terms of a coherent sharp mode is further evidence that the broadening of the magnetic excitations is due to powder averaging and not due to the underlying disorder.

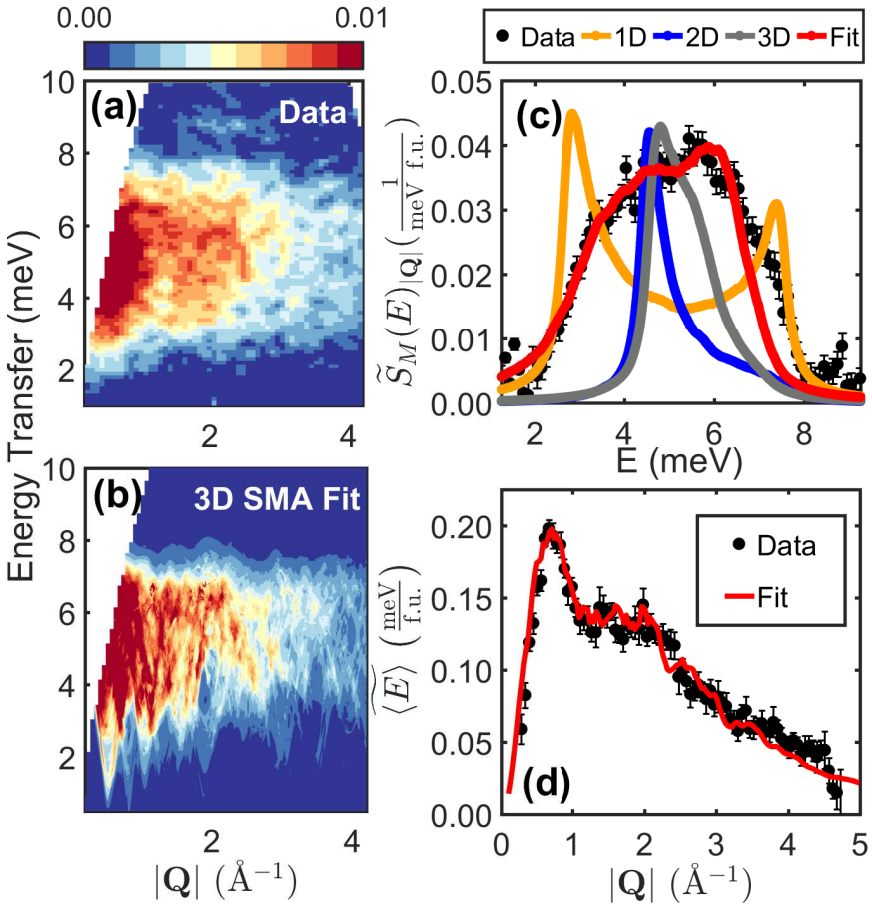

Figure 3.8 (a) $\widetilde{S}_M(|\mathbf{Q}|, E)$ measured on MARI at T=5 K with an E_i=15 meV. (b) $\widetilde{S}_M(|\mathbf{Q}|, E)$ calculated by the optimisation of all parameters B_i in the heuristic model of $\epsilon(\mathbf{Q})$ in the single mode approximation of $\widetilde{S}(\mathbf{Q}, E)$ utilising the refined values of $-nJ_{ij}\langle \mathbf{S}_i \cdot \mathbf{S}_j \rangle$ from the first moment sum rule. (c) Comparison of $|\mathbf{Q}|$-integrated cuts ($|\mathbf{Q}|$=[0,3] Å^{-1}) of measured and calculated $\widetilde{S}_M(|\mathbf{Q}|, E)$. For the purposes of comparison, non-optimised $|\mathbf{Q}|$-integrated cuts for all three types of dimensionality d are also presented. These cuts assume both $\epsilon(\mathbf{Q})$ possesses the same gap parameter B_o obtained from the 3D SMA fit in (b) and each permissible set of parameters is equally weighted. (d) Comparison of the measured and calculated $|\mathbf{Q}|$-dependence of the first moment $\langle E \rangle$ integrated over E=[2,8] meV.

Table 3.4 Refined parameters of the heuristic dispersion relation in the single mode approximation of $\widetilde{S}(|\mathbf{Q}|, E)$ utilising the refined values of $-n_{ij}J_{ij}\langle\hat{\mathbf{S}}_i \cdot \hat{\mathbf{S}}_j\rangle$ at 5 K summarised in Tab. 3.3. As a first approximation, the intra-plane dispersion parameters were fixed to zero. Numbers in parentheses indicate statistical errors.

Dispersion Parameter	Refined Value (meV^2)
B_o	28.2(3)
B_h	−1.13(2)
B_k	−4.63(4)
B_l	6.8(7)
B_{hk}	0
B_{hl}	0
B_{kl}	0
B_{2h}	−1.13(2)
B_{2k}	−4.63(4)
B_{2l}	6.8(7)

3.4 Discussion

3.4.1 Experimental limitations

There are several limitations to the analysis presented in this paper. The first is the use of α-ZnV_3O_8 as a background for the analysis of the low temperature inelastic spectrum of α-CoV_3O_8. As shown in Fig. 3.1(d), α-ZnV_3O_8 crystallises in the cation ordered $Iba2$ space group [324] and is thus not completely isostructural to α-CoV_3O_8. It can be argued that the local cation ordering deduced is an artefact of the $Iba2$ structure of the α-ZnV_3O_8 background. To counter such a claim, it is worth pointing out that the scaling analysis as outlined in §3.3.5 utilised the same inelastic neutron scattering data, but only after the subtraction of an independently calculated temperature-independent background derived from detailed balance [367, 368], did the data provide a critical exponent ν consistent with pure 3D Ising behaviour. Such pure 3D Ising behaviour would be unexpected if Co^{2+} was locally disordered.

Another limitation is the observation that the low temperature cooperative magnetism of α-CoV_3O_8 can be treated as exclusively due to coupling between Co^{2+} moments. The presence of a second magnetic disordered counter-cation is in contrast to the model dilute 3D Ising antiferromagnets where the counter-cations are non-magnetic and thus interactions between magnetic ions of one type (e.g. Fe^{2+}) are exclusively considered [278, 284, 318, 319, 402]. Such a situation was assumed to apply to α-CoV_3O_8 in the analysis presented so far as a first approximation since there is evidence that V^{4+} behaves paramagnetically; although it is highly unlikely that coupling between V^{4+} and other V^{4+} or Co^{2+} plays no role in the low temperature magnetism and thus the analogy to the dilute antiferromagnets such as $Fe_xZn_{1-x}F_2$ should be approached with caution. It is important to note that the apparent lack of influence of V^{4+} coupling, relative to coupling between Co^{2+} cations, may be due to the exclusive use of t_{2g} orbitals by V^{4+}, in contrast to the e_g orbitals utilised by Co^{2+} which is predicted to give much stronger coupling [47, 53, 54, 56, 272].

A further limitation concerns the nature of the competing ferromagnetic and antiferromagnetic interactions in α-CoV_3O_8. In contrast to the $Fe_xZn_{1-x}F_2$ series [284, 320, 403], α-CoV_3O_8 exhibits both distinct ferromagnetic inter-chain and antiferromagnetic intra-chain coupling along the ab plane and along c, respectively. Both ferromagnetic and antiferromagnetic coupling possess similar magnitudes as proven by their near cancellation corresponding to a Weiss temperature near zero. It is interesting to note that with an average Weiss temperature near zero combined with a $T_{\mathrm{N}} \sim 19$ K, the frustration index $f = \left|\frac{\theta_{CW}}{T_N}\right| \lesssim 1$, implying an absence of frustration, a key contributor to the rich phase diagram of the dilute 3D Ising antiferromagnets [278] and a phenomneon one may expect to be present with the concurrent presence of both strong ferromagnetic and antiferromagnetic couplings. To address the concurrent presence of both ferromagnetic and antiferromagnetic couplings, it is worth noting that such a situation is reminiscent of another random dilute 3D Ising magnet system $Fe_xMg_{1-x}Cl_2$ where $x > 0.55$, a series of compounds whose magnetic properties have been shown consistently to be qualitatively similar to that of $Fe_xZn_{1-x}F_2$ [404, 405]. To address the absence of frustration, it is worth noting that in contrast to the current study, previous work [79] on smaller hydrothermally grown crystals of α-CoV_3O_8 reported a $T_{\mathrm{N}} = 8.2$ K and a Weiss temperature of -32.1 K, corresponding to a frustration index $f \sim 4$, indicating evidence for significant frustration. Such contrasting behaviour provides strong evidence that sample dependence may play a significant role in determining the

magnetic properties of α-CoV_3O_8, as has been consistently observed for the dilute antiferromagnets, whose response functions are significantly influenced by both sample quality and non-equilibrium physics [44, 284, 403]. The particular dependence on sample quality can be partially rationalised using recent work on α-ZnV_3O_8 [406]. Numerical simulations indicated that although the ordered-$Iba2$ arrangement was predicted to exhibit minimal frustration, if one instead assumed a disordered-$Ibam$ arrangement, significant magnetic frustration was predicted to manifest itself as competing inter-chain couplings of similar magnitudes in the presence of a dominant antiferromagnetic intra-chain coupling. The contrasting behaviour between $Iba2$ and $Ibam$ cationic arrangement may provide an explanation for the aforementioned difference in the experimentally determined frustration indices with samples possessing more disorder exhibiting a larger value of f.

3.4.2 Disordered Ibam versus ordered Iba2?

An important contradiction arises from a combined analysis of x-ray and neutron diffraction, DC susceptibility and inelastic neutron spectroscopy measurements in that the disordered-$Ibam$ structure is derived from diffraction measurements, however the dynamics are more consistent with an ordered-$Iba2$ arrangement of Co^{2+} ions. Such a contradiction may suggest that one of the models is in fact incorrect. Since the ordered-$Iba2$ arrangement was deduced from multiple experimental probes using multiple analysis techniques, one would be tempted to re-investigate the model deduced from single crystal diffraction. This particular re-investigation is further motivated by the observation that although one would expect diffuse scattering to appear for a disordered $Ibam$, no diffuse scattering is clearly visible in both x-ray and neutron diffraction data sets. The lack of diffuse scattering could readily be accounted for by the $Iba2$ structure where the spectral weight of the diffuse scattering would be incorporated into Bragg peaks. As summarised by Tabs. B.10-B.12 and Fig. B.1, structural refinements utilising 1638 out of a total of 1802 measured reflections and employing a $Iba2$ unit cell, yielded a negative anisotropic thermal factor for $V(1)$, which was was not observed in the disordered-$Ibam$ model, whilst all three goodness-of-fit metrics were of poorer quality compared to the refinement utilising an ordered-$Ibam$ as previously presented in §3.3.1. The conclusion that the ordered-$Ibam$ unit cell is the correct structure was confirmed employing single crystal neutron diffraction data from SXD. Assuming an ordered-$Iba2$

nuclear unit cell, the additional Bragg reflections appearing below T_{N} were successfully indexed with a propagation vector $\mathbf{k} = (1, 1, 1)$ with the $P_I cc2$ (#27.86) Shubnikov space group. As summarised by Tabs. 3.2, B.13, B.14 and Fig. B.2, a joint nuclear-magnetic refinement utilising 5086 out of 5120 measured reflections at 5 K, produced significantly poorer goodness-of-fit metrics compared to the ordered-*Ibam* model. Despite both x-ray and neutron single crystal diffraction strongly favouring the disordered-*Ibam* over the ordered-*Iba*2 model, the lack of diffuse scattering remains an open question. One likely possibility is that the diffraction data was collected over short collection times resulting in poor statistics, particularly for the single crystal neutron diffraction data collected on SXD, the data one would expect to see the diffuse scattering due to the stark contrast of coherent cross sections of cobalt and vanadium. Upon closer inspection Fig. 3.2(c), there appears to be some evidence for weak diffuse scattering around the (40-1) Bragg peak and thus suggests that with longer counting times, single crystal neutron diffraction may detect the diffuse scattering one would expect from the disordered-*Ibam* model. Consequently, with the additional analysis outlined in above, diffraction strongly indicates that statically the arrangement of Co^{2+} ions is disordered, however the collective long wavelength fluctuations, as deduced from neutron inelastic scattering, seem to average out this disorder. α-CoV_3O_8 therefore appears to be magnetically ordered for longer lengthscales. The apparent robustness of α-CoV_3O_8 to disorder is discussed below in the context of spin-orbit coupling and comparison to other model magnets in a random field.

3.4.3 Universality class of α-CoV_3O_8

Ising anisotropy is experimentally supported by several observations discussed above: the presence of a significant octahedral distortion ($\delta \sim 11$) as deduced from a combination of single crystal x-ray and neutron diffraction data, the presence of 3D Ising fluctuations as deduced from both critical exponents ν and β, and the presence of strong spin-orbit coupling supported by neutron spectroscopy. 3D dimensionality ($d = 3$) is suggested based on the following: the values of the critical exponents ν and β, the non-zero refined values of all h, k and l dispersion parameters in $\epsilon(\mathbf{Q})$ reflecting both strong coupling in both the ab plane and along c, in combination with the relatively weak anisotropy of the DC susceptibility.

The random magnetic cation distribution is supported by the refined *Ibam* structure from both single crystal x-ray and neutron diffraction and the value of β. An additional observation is the intrinsic width of the AFM transition

as measured with DC susceptibility, reflected by the large experimental error of β caused by the rounding of the order parameter measurement, as has been experimentally observed in other dilute 3D Ising antiferromagnets such as $Co_xZn_{1-x}F_2$ [22]. The dilution of 3D Ising magnetism can be rationalised by the key observation that V^{4+} appears to remain purely paramagnetic down to 2 K and thus has no significant influence on the low temperature cooperative magnetic properties of α-CoV_3O_8, as proven by a combination of inelastic neutron scattering and DC susceptibility measurements.

3.4.4 Comparison between α-CoV_3O_8 and Random Field Ising magnets

If one disregards the magnetic influence of V^{4+}, effectively treating the cation as a counter-ion such as Zn^{2+} in $Fe_xZn_{1-x}F_2$ or $Mn_xZn_{1-x}F_2$, then the magnetism due to Co^{2+} in α-CoV_3O_8 may be regarded as being magnetically diluted by 50%. Additionally, it is important to note that the failure to observe strong structural diffuse scattering with x-ray and neutron diffraction measurements is suggestive of a lack of local cation ordering or gradients. These concentration gradients were noted in dilute model antiferromagnets [44, 402, 403, 407–409]. Such a combination of significant dilution and disorder would be expected to have a significant effect on the dynamics [44, 282, 283, 291, 320, 322, 361, 410–412]. In this sense, it is surprising that there seems to be little effect on the magnetic dynamics in α-CoV_3O_8, where the magnetic excitations are consistent with a fully ordered cation arrangement. Such behaviour is suggestive that hydrodynamic and long wavelength fluctuations are not strongly sensitive to the disorder in α-CoV_3O_8, in contrast with expectations based on theory [413, 414]. The robust nature of the dynamics to dilution and in particular disorder is analogous to several observations in dilute random field magnets and in particular the $Fe_xZn_{1-x}F_2$ series [317, 415, 416], where sharp excitations are still observable for large amount of doping [320]. Unlike members of the $Fe_xZn_{1-x}F_2$ series closer to the percolation threshold ($x_p \sim 0.24$) that exhibit spin glass behaviour [278, 316, 320, 410], $Fe_{0.5}Zn_{0.5}F_2$ assumes long range antiferromagnetic order in zero field with a T_N corresponding to half of that of FeF_2 [417, 418]. The appearance of long range antiferromagnetic order as measured by DC susceptibility with a $\mu_o H_{ext} = 0.5$ T supports the claim that α-CoV_3O_8 is not close to the percolation threshold, where even the smallest external field destroys

long range order, as is the case for $M_xZn_{1-x}F_2$, where M = Co^{2+} and Fe^{2+} [374]. However, the random field Ising magnet $Mn_xZn_{1-x}F_2$ [419, 420] does show strong effects of the disorder on the dynamics. Such behaviour is consistent with cases of random fields introduced through confinement where when the critical fluctuations have a similar length scale to the underlying disorder, the phase transition is strongly altered [44, 282, 291, 412, 421].

A key difference between MnF_2 and both α-CoV_3O_8 and FeF_2 is the presence of strong crystal field effects and spin-orbit coupling in the latter two compounds [376, 415]. It is also worth noting that unlike the case of pure CoO [3, 18, 341, 422–425] where the large and far reaching exchange constants result in a significant and ultimately problematic entanglement of spin-orbit levels, in the case of α-CoV_3O_8, the exchange constants are weak and the Weiss temperature is near 0 K. Both observations suggest that the presence of both strong crystal field effects and spin-orbit coupling with well-separated j_{eff} manifolds, as is the case for α-CoV_3O_8, may be central to making the dynamics robust against strong disorder.

3.5 Concluding Remarks & Future Directions

Despite the successful description of the low temperature magnetic excitations of α-CoV_3O_8 as collective excitations from an ordered-$Iba2$ arrangement of $j_{\text{eff}} = \frac{1}{2}$ Co^{2+} moments coupled through a 3D network, there still remains numerous unanswered questions. Many of these unanswered questions stem from the experimental limitations of the current study as outlined in §3.4.1. These questions include determining the role of synthesis conditions, sample quality and non-equilibrium effects on the magnetic properties and intrinsic physics of α-CoV_3O_8. Perhaps the most interesting questions stem from the strong analogy that was established between α-CoV_3O_8 and the other random 3D Ising magnets in §3.4. Despite possessing different routes towards disorder: chemical dopants versus intrinsic crystallographic constraints (or lack thereof) in the case of $Fe_xZn_{1-x}F_2$ and α-CoV_3O_8, respectively, the current data suggests a strong similarity between the systems' low temperature magnetic properties. Such a strong similarity suggests that α-CoV_3O_8 may exhibit random dilute 3D Ising behaviour or at the very least suggests that α-CoV_3O_8 has the potential to exhibit such behaviour with optimised synthesis conditions. The possibility that random dilute Ising behaviour may be present in α-CoV_3O_8 suggests that the

particularly contentious random field Ising model (RFIM) state may be induced in α-CoV_3O_8 with the application of an external field [311, 426–431].

As alluded to in the concluding remarks of §3.4, perhaps the questions that may garner the most interest in the community may lie in the role of the chemical composition on the low temperature magnetism of these intrinsically disordered compounds. These questions include the effect of increasing/decreasing disorder and the choice of which elements (and oxidation states) are present. Not only are these questions extremely pertinent in the context of recent literature [32], but furthermore these questions can be addressed in a relatively straightforward and quickly parametrisable experimental method of chemical doping.

In summary, a combination of zero field diffraction, DC susceptibility and neutron spectroscopy measurements have indicated that the low temperature cooperative magnetism of α-CoV_3O_8 is dominated by $j_{\text{eff}} = \frac{1}{2}$ Co^{2+} cations randomly distributed over the $16k$ metal site of the $Ibam$ structure, thus corresponding to an intrinsically disordered magnet without the need for any external influences such as chemical dopants or porous media. Despite the intrinsic disorder, by employing the sum rules of neutron scattering, the collective excitations have been shown to not be significantly affected by the disorder, displaying behaviour consistent with an ordered-$Iba2$ arrangement of $j_{\text{eff}} = \frac{1}{2}$ Co^{2+} moments over a macroscopic scale. These Co^{2+} moments are coupled *via* a 3D network of competing ferromagnetic and stronger antiferromagnetic superexchange interactions within the ab plane and along c, respectively, resulting in long range antiferromagnetic order of the Co^{2+} moments at $T_{\text{N}} \sim$19 K, despite a Weiss temperature near 0 K. A comparison of the current experimental results to the random 3D Ising magnets and other compounds where spin-orbit coupling is present indicate that both the presence of an orbital degree of freedom, in combination with strong crystal field effects and well-separated j_{eff} manifolds may be key in making the dynamics robust against disorder.

Chapter 4

Disentangling orbital and spin exchange interactions for Co^{2+} on a rocksalt lattice

4.1 Introduction

Magnetic interactions in the presence of an orbital degeneracy have provided the basis for understanding a variety of topics in materials science including metal-insulator transitions, high temperature superconductors, colossal magnetoresistance [432–434], and more recently Kitaev interactions [435–437]. Rocksalt CoO was the first orbitally degenerate compound to have its magnetic structure investigated using neutron diffraction, but the underlying exchange interactions are still not understood [438–441]. Despite decades of persistent research, calculations and experiment have been hindered by the complex electronic and orbital ground state of Co^{2+}.

4.1.1 Spin-Orbital Hamiltonian for Co^{2+} in CoO

As first alluded to in §3.3.4, the starting point for understanding the spin-orbital Hamiltonian for Co^{2+} ions is crystal field theory based on octahedral coordination [47, 261, 442, 443], as illustrated in Fig. 4.1 for rocksalt CoO [18, 341, 444]. As schematically shown in Fig. 4.2, the octahedral crystal field splits

the 5 degenerate d-orbitals (^4F) such that the d^7 electronic structure consists of five electrons occupying the lower energy t_{2g} states and two electrons in the higher energy e_g orbitals. This constitutes two orbital triplets ($^4T_{1,2}$) levels separated by $10Dq \sim 900$ meV [18], whose degeneracy and magnetic exchange are both based in the t_{2g} channel. In contrast to systems based on e_g mediated magnetic exchange and whose magnetic properties have been well understood (*e.g.* $KCuF_3$ [445]), the case of exchange involving degenerate t_{2g} orbitals has proven more difficult [446].

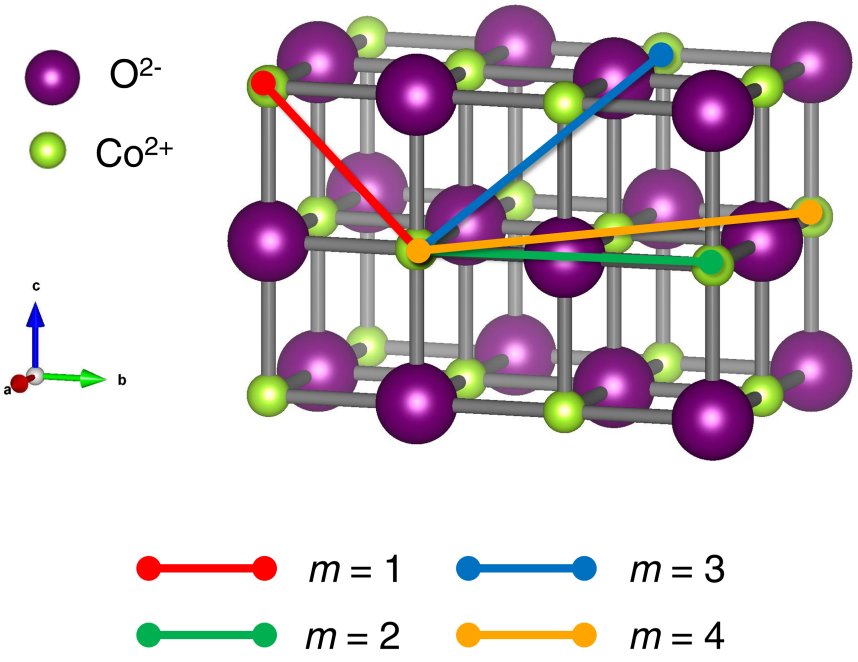

Figure 4.1 Isometric projection of the room-temperature cubic rocksalt ($Fm\bar{3}m$, SG: 225/230) crystal structure of CoO [82, 440, 441]. The pair distances between first shell (nearest) neighbours, second shell (next-nearest) neighbours, *etc.* are denoted by $m = 1$, 2, *etc.*, respectively.

As illustrated in Appendix E, the one hole occupying one of the three t_{2g} orbitals means that the orbital degenerate $^4T_1$ level can be approximated to have an effective orbital angular momentum of $l = 1$ with a corresponding projection factor $\alpha = -\frac{3}{2}$ [18, 20, 21, 47, 76, 341, 447, 448]. Applying spin-orbit coupling, defined by $\alpha\lambda\hat{\mathbf{l}}\cdot\hat{\mathbf{S}}$ with $S = \frac{3}{2}$, to this orbital ground state results in three effective spin-orbit manifolds classified by an effective angular momentum of $j_{\text{eff}} = \frac{1}{2}$, $\frac{3}{2}$ and $\frac{5}{2}$, with $\hat{\mathbf{j}}_{\text{eff}} = \hat{\mathbf{l}} + \hat{\mathbf{S}}$. The ground state is separated from the higher energy $j_{\text{eff}} = \frac{3}{2}$ states by $\frac{3}{2}\alpha\lambda \sim 36$ meV in the case of $Co_{0.03}Mg_{0.97}O$ [18, 21].

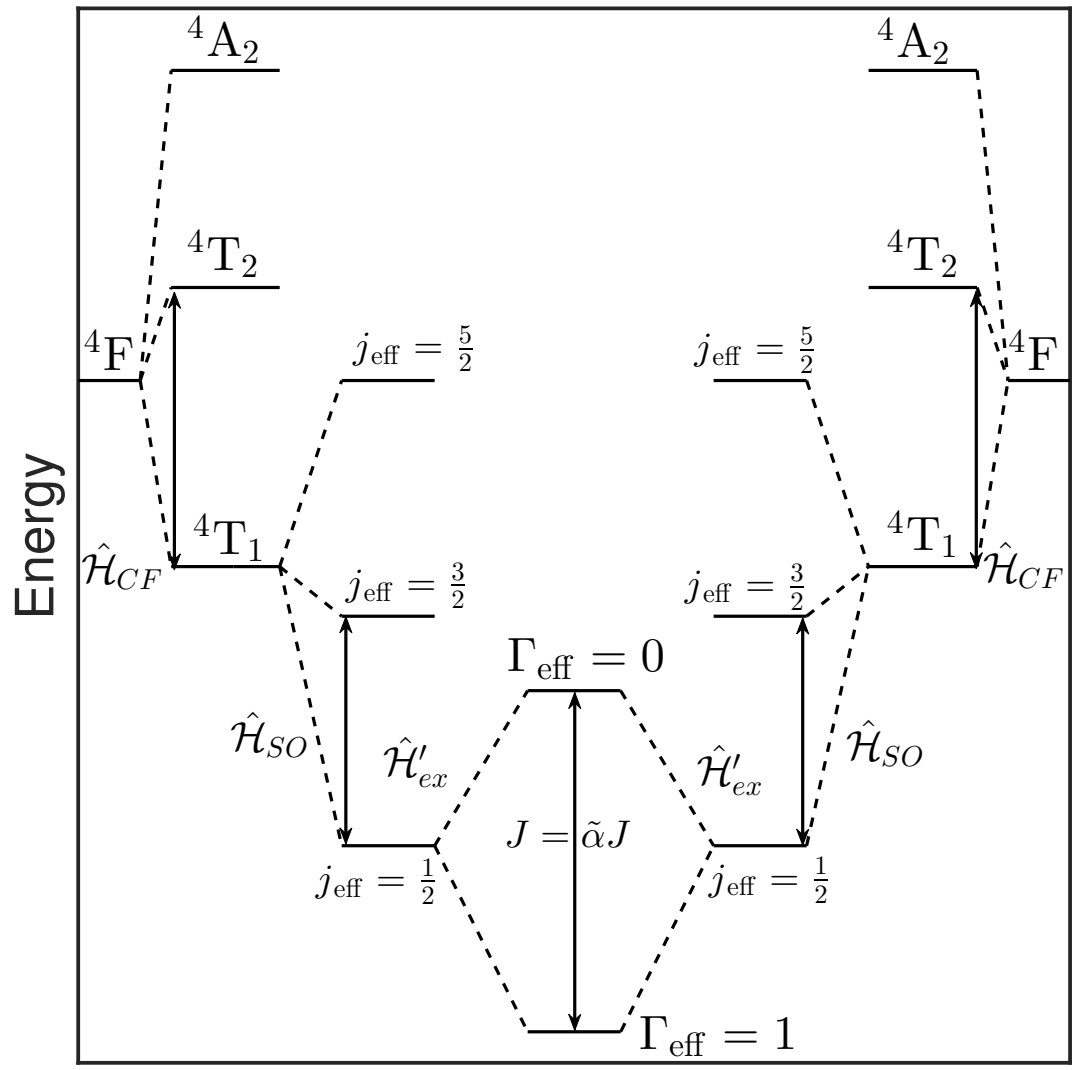

Figure 4.2 Illustration of each contribution to the effective pair Hamiltonian $\hat{\mathcal{H}}_{pair}$ (Eq. 4.4) for $Co_{0.03}Mg_{0.97}O$ with ferromagnetic ($J < 0$) coupling. The left and right hand side correspond to Co^{2+} ions 1 and 2, respectively, whose interaction is described by the effective exchange Hamiltonian $\hat{\mathcal{H}}'_{ex}$ (4.3).

The total single-ion Hamiltonian for Co^{2+} in magnetically ordered CoO [82–84, 424, 449, 450] can then be summarised by the single ion Hamiltonian

$$\hat{\mathcal{H}}_{SI} = \hat{\mathcal{H}}_{CF} + \hat{\mathcal{H}}_{SO} + \hat{\mathcal{H}}_{MF}, \tag{4.1}$$

where $\hat{\mathcal{H}}_{CF}$, $\hat{\mathcal{H}}_{SO}$ and $\hat{\mathcal{H}}_{MF}$ are the octahedral crystal field, spin-orbit, and molecular field contributions, respectively [18, 76, 422, 448]. The effect of

magnetic ordering on the three spin-orbit manifolds can be illustrated by considering a single dominant next nearest neighbour 180° Co^{2+}-O^{2-}-Co^{2+} superexchange J_2 [341] with

$$\hat{\mathcal{H}}_{MF} = 2J_2 z_2 \langle \hat{\mathbf{S}} \rangle_{av} \hat{S}_z, \tag{4.2}$$

where z_2 and $\hat{S}_z$ denote the number of Co^{2+} neighbours and the z-axis of the spin operator, respectively [444]. As illustrated in Fig. 4.3, by considering only the predicted value of J_2 by Kanamori [341] in the mean field expression for $\hat{\mathcal{H}}_{MF}$, a complex admixture of different molecular field split Co^{2+} spin-orbit manifolds occurs in the presence of magnetic order [20, 341, 424, 444, 447].

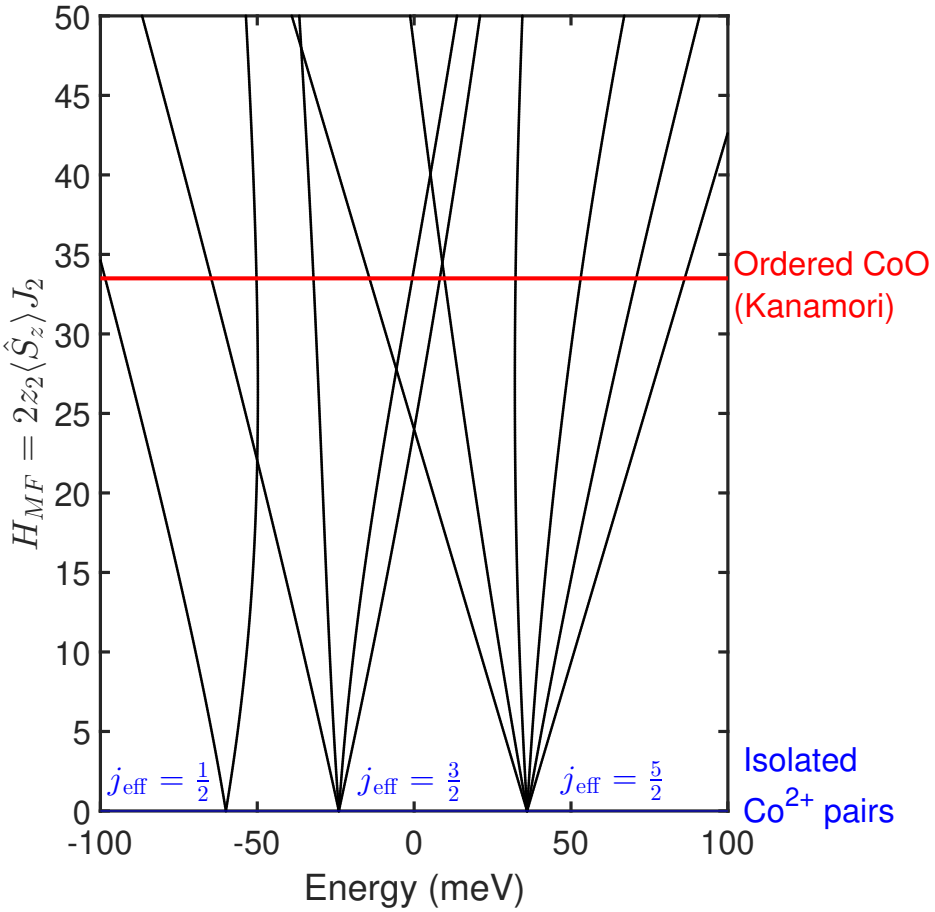

Figure 4.3 Illustration of molecular field-induced entanglement of the Co^{2+} spin-orbit manifolds. The black lines denote the energy eigenvalues of the single-ion Hamiltonian $\hat{\mathcal{H}}_{SI}$ in the presence of a molecular field H_{MF}. As reference, the mean field value of H_{MF} using Kanamori's original estimate of J_2 [341] in the Néel state of CoO is shown by the solid red line.

The strong magnetic ordered induced mixing of multiple j_{eff} manifolds in CoO is in contrast to many other Co^{2+} based magnets [63, 76, 451, 452] that have both weak exchange and molecular fields and thus exhibit weak mixing, such as was the case for α-CoV_3O_8 in the preceding chapter. CoO is further complicated by the presence of significant spin-spin couplings over several shells of neighbours [341, 424, 425, 453, 454]. The extraction of the multiple spin exchanges in CoO is thus experimentally very difficult despite the simplicity of the rocksalt crystal structure (Fig. 4.1).

4.1.2 Spin-Orbital Hamiltonian for Co^{2+} in $Co_xMg_{1-x}O$

To extract individual J constants for Co^{2+}, inspired by the pioneering work on dilute Mn^{2+} [455–458] and Co^{2+} [18, 20] compounds, the dilute monoxide $Co_{0.03}Mg_{0.97}O$ was measured using neutron inelastic spectroscopy. The high magnetic dilution prevents the system from assuming long range magnetic order [18]. The absence of long rang magnetic order removes both the problematic molecular field discussed above and accompanying magnetoelastic distortions [82, 449, 459], thus suppressing strong mixing between the j_{eff} manifolds.

In addition to reducing the problematic H_{MF} contribution to effectively zero, such high magnetic dilution allows for the cooperative magnetism in $Co_{0.03}Mg_{0.97}O$ to dominated by pairwise interactions between isolated Co^{2+} pairs. Such dominance of pairwise interactions can be rationalised from probabilistic arguments based on the observation that for a given random distribution of x Co^{2+} and $(1-x)$ Mg^{2+} ions, the number of Co^{2+} pairs and the number of pairwise interactions for a given geometry present in the lattice far outweighs the number of Co^{2+} triplets and corresponding interactions between three Co^{2+} cations. For example, if there are N ways that a cluster with a particular geometry of three sites XYZ can occur in a given crystal, the relative probabilities of an arrangement of 3 Mg^{2+}, 1 Co^{2+}, and 2 Mg^{2+} (and its permutations), 2 Co^{2+} and 1 Mg^{2+} (and its permutations), and 3 Co^{2+} occupying the three sites XYZ are $(1-x)^3$, $x(1-x)^2$, $x^2(1-x)$, and x^3, respectively. Hence the ratio of numbers of spin pairs with XY, XZ, and YZ geometry to spin triplets with XYZ geometry in the lattice is $\frac{1-x}{x}$, and thus for small x, as is the case for $Co_{0.03}Mg_{0.97}O$, the number and hence neutron inelastic scattering intensities of Co^{2+} pair excitations far outweigh those from larger Co^{2+} clusters.

By approximating the cooperative magnetism in $Co_{0.03}Mg_{0.97}O$ as being

determined exclusively by Co^{2+} pair interactions and in particular, low-energy excitations within the lowest $j_{\text{eff}} = \frac{1}{2}$ doublet manifold with $\alpha'\hat{\mathbf{j}} = \hat{\mathbf{S}}$, the interaction energy $\hat{\mathcal{H}}_{ex}$ in the diluted monoxide $Co_{0.03}Mg_{0.97}O$ can be approximated by

$$\hat{\mathcal{H}}_{ex} = 2J\hat{\mathbf{S}}_1 \cdot \hat{\mathbf{S}}_2 \sim \widetilde{\alpha} J\, \hat{\mathbf{j}}_1 \cdot \hat{\mathbf{j}}_2, \tag{4.3}$$

where $\hat{\mathbf{j}}$ and $\widetilde{\alpha} = 2(\alpha')^2$ denote an effective total angular momentum operator with $j = \frac{1}{2}$ and a projection factor, respectively. As illustrated in Fig. 4.2, $\hat{\mathcal{H}}_{ex}$ describes individual $j_{\text{eff}} = \frac{1}{2}$ pair excitations as transitions between triplet ($\Gamma_{\text{eff}} = 1$) and singlet ($\Gamma_{\text{eff}} = 0$) levels separated by an energy of $\hbar\omega = \widetilde{\alpha}J$ [270, 390, 457]. The projection factor $\widetilde{\alpha}$, in this low energy approximation, can be calculated by diagonalising $\hat{\mathcal{H}}_{SI} + \hat{\mathcal{H}}_{ex}$, with $\hat{\mathcal{H}}_{MF} = 0$ owing to the lack of long range magnetic order in $Co_{0.03}Mg_{0.97}O$ [18]. Such a Hamiltonian is equivalent to the Hamiltonian for two (labelled 1 and 2) interacting Co^{2+} ions given by

$$\hat{\mathcal{H}}_{pair} = \alpha\lambda\hat{\mathbf{l}}_1 \cdot \hat{\mathbf{S}}_1 + \alpha\lambda\hat{\mathbf{l}}_2 \cdot \hat{\mathbf{S}}_2 + 2J\hat{\mathbf{S}}_1 \cdot \hat{\mathbf{S}}_2, \tag{4.4}$$

where the first two terms corresponds to the spin-orbit manifolds of individual Co^{2+} ions, whilst the third term introduces interaction between their individual manifolds. As described in Appendix E, by considering $l = 1$ and $S = \frac{3}{2}$, this amounts to 144 basis states and a 144×144 matrix for this particular Hamiltonian in terms of the two-particle basis of $|l_1, m_{l,1}, s_1, m_{s,1}\rangle \otimes |l_2, m_{l,2}, s_2, m_{s,2}\rangle$, where l_i, $m_{l,i}$, s_i, and $m_{s,i}$ denote the eigenvalues corresponding to the $\hat{\mathbf{l}}_i$, $\hat{l}_{z,i}$, $\hat{\mathbf{S}}_i$, and $\hat{S}_{z,i}$ operators, respectively, for the i^{th} particle. As illustrated in Fig. 4.4, in the limit of $J \ll \lambda$, the energy splitting within the $j_{\text{eff}} = \frac{1}{2}$ manifold $\Delta E\left(\left|\frac{J}{\lambda}\right|\right)$ is linear with $\widetilde{\alpha} = \frac{50}{9}$ in agreement with the projection theorem of angular momentum [47, 270] as shown in Appendix G. Therefore, a neutron spectroscopy measurement of the pair excitations in dilute $Co_{0.03}Mg_{0.97}O$ with low incident energies at base temperatures provides a value for the magnitude of exchange constant $|J|$ between a pair of Co^{2+} ions.

While the excitation energy provides the magnitude $|J|$ [390], the neutron spectroscopic momentum dependence can be used to extract the corresponding intra-pair distance $\mathbf{R}_m$, where m denotes the coordination shell. By applying the powder-averaged Hohenberg-Brinkman first moment sum rule [389] and the single mode approximation [106, 351, 368, 391, 460] for an isolated pair as derived

in Appendix H, excitations from a Co^{2+} pair have the following $|\mathbf{Q}|$ dependence

$$S(|\mathbf{Q}|) \propto \frac{|F(|\mathbf{Q}|)|^2}{\hbar\omega_o}\left(1 - \frac{\sin(|\mathbf{Q}||\mathbf{R}_m|)}{|\mathbf{Q}||\mathbf{R}_m|}\right), \tag{4.5}$$

where $|F(|\mathbf{Q}|)|^2$ is the magnetic form factor. Since the modulation is solely dependent on the intra-pair distance $\mathbf{R}_m$, an excitation can be assigned to a particular pair and corresponding coordination shell in the $Fm\bar{3}m$ structure as illustrated in Fig. 4.1.

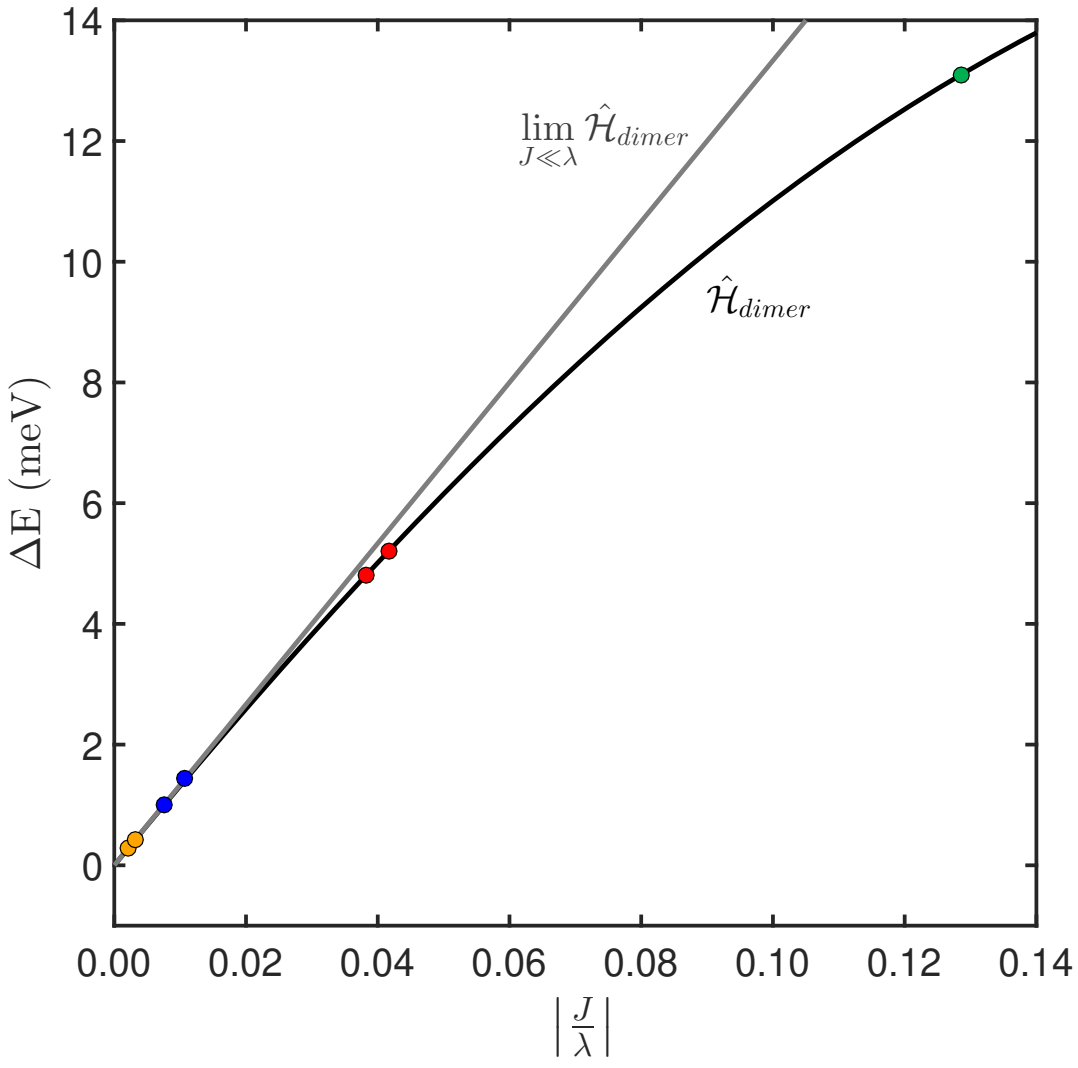

Figure 4.4 The black curve denotes the pair energy splitting as a function of the normalised exchange $\Delta E\left(\left|\frac{J}{\lambda}\right|\right)$. The points are measured energy positions from Fig. 4.7. The grey line is the same relationship derived using the projection theorem (Appendix G) in the large-λ limit [47, 270].

4.2 Experimental Details

4.2.1 Materials Preparation

Two polycrystalline samples of $Co_{0.03}Mg_{0.97}O$ were synthesised for this particular investigation. The first was synthesised by traditional solid-state methods as outlined by Cowley *et al.* [18]. A second sample of $Co_{0.03}Mg_{0.97}O$ was made using solution techniques by mixing stoichiometric amounts of $Mg(NO_3)_2 \cdot 6H_2O$ and $Co(NO_3)_2 \cdot 6H_2O$. The solid mixture was dissolved in CH_3CH_2OH and stirred for 1 h and heated to 70°C for 12 h, yielding a pink gel. The gel was heated in air to 600°C with a heating rate of 20°C/h, reacted for 24 h, subsequently heated to 1000°C with a heating rate of 150°C/h, held for an additional 48 h, and finally cooled to room temperature by switching off the furnace. The gel was reground, remixed and reheated until room temperature powder x-ray diffraction measurements with a Bruker D2 phase laboratory diffractometer using a Cu $K_{\alpha,1,2}$ source confirmed no discernible impurities. Details concerning the synthesis and treatment of MgO and CoO samples are outlined by Cowley *et al.* [18].

4.2.2 Energy-Dispersive X-ray Analysis

Microscopic images and their elemental compositions were determined by scanning electron and energy-dispersive x-ray spectroscopy, respectively, both performed using a Hitachi SU-70 Schottky field-emission gun SEM equipped with a Bruker Quantax energy-dispersive x-ray detector. Energy-dispersive x-ray spectroscopy (EDS) was carried out at 15 keV.

4.2.3 DC Magnetic Susceptibility

Temperature dependence of magnetisation was measured on a Quantum Design MPMS for a 32.5(1) mg of polycrystalline $Co_{0.03}Mg_{0.97}O$ synthesised by sol-gel in an external DC field $\mu_o H_{\text{ext}}$=0.1 T. Zero-field cooling (ZFC) measurements were performed in 2 K steps spaced linearly from 2 to 300 K, while FC measurements were performed in 5 K steps spaced linearly from 2 to 170 K.

4.2.4 Neutron Inelastic Scattering Details

45.8, 45.2, 32.5, and 15.7 g of $Co_{0.03}Mg_{0.97}O$ synthesised by the standard solid-state and sol-gel methods, annealed MgO and CoO, respectively, were placed in separate airtight aluminium cans under helium. The high-energy measurements were made on the direct geometry MARI spectrometer [336, 337]. For measurements concerning the $Co_{0.03}Mg_{0.97}O$ sample synthesised by traditional solid-state methods, MgO and CoO powders, the t_o chopper was operated at 50 Hz in parallel with a Gd chopper spun at frequencies $f = 350$, 250 and 150 Hz with incident energies $\hbar\omega_i = 30$, 10, and 5 meV, respectively, providing an elastic resolution of 0.7, 0.2, and 0.1 meV, respectively. For measurements concerning the $Co_{0.03}Mg_{0.97}O$ sample synthesised by sol-gel, the Gd chopper was spun at $f = 350$ and 250 Hz with an $\hbar\omega_i$ of 29.50 and 14.50 meV, providing an elastic resolution of 0.7 and 0.2 meV, respectively. For both $Co_{0.03}Mg_{0.97}O$ samples, a thick disk chopper with f = 50 Hz reduced the background from high-energy neutrons. A top-loading Displex CCR cooled the samples to a base temperature of approximately 5 K.

For lower energies, measurements were made on the indirect geometry IRIS spectrometer [103]. The final energy was fixed at 1.84 meV by PG002 analyser crystals in near backscattering geometry. The graphite analysers are cooled to reduce thermal diffuse scattering, providing an elastic resolution of 17.5 μeV [104]. A combination of IRIS' long path length and its array of disk choppers allows for the selection of multiple time windows, resulting in the measured bandwidth being selectively increased to include energy transfers up to $\sim$2 meV [76]. A top-loading Displex CCR was used to cool the sample to a base temperature of approximately 11 K. For all samples, identical instrumental and environmental parameters were employed on IRIS.

4.3 Results & Discussion

4.3.1 Determination of the Sample Quality

As discussed in §4.1.2, both the presence and prevalence of Co^{2+} pairs in $Co_xMg_{1-x}O$ constitutes the foundation for the strategy of chemical dilution [18, 457] used to disentangle individual spin-orbit manifolds, and thus allow for the extraction of multiple magnetic exchange constants. Utilising the probabilistic

arguments outlined in §4.1.2, the concurrent requirement of both presence and prevalence of Co^{2+} pairs in $Co_xMg_{1-x}O$ emphasises the importance of the value of x. As outlined in §4.2.1, the value of $x \sim 0.03$ was chosen due to the requirement for the value of $x \to 0$ to prevent the prevalence of larger clusters of Co^{2+} ions, whilst providing enough Co^{2+} pairs in the bulk sample as to be detected with neutron inelastic spectroscopy. In order to confirm the value of $x \sim 0.03$, its value was experimentally determined using two independent measurement techniques: x-ray diffraction and DC magnetometry.

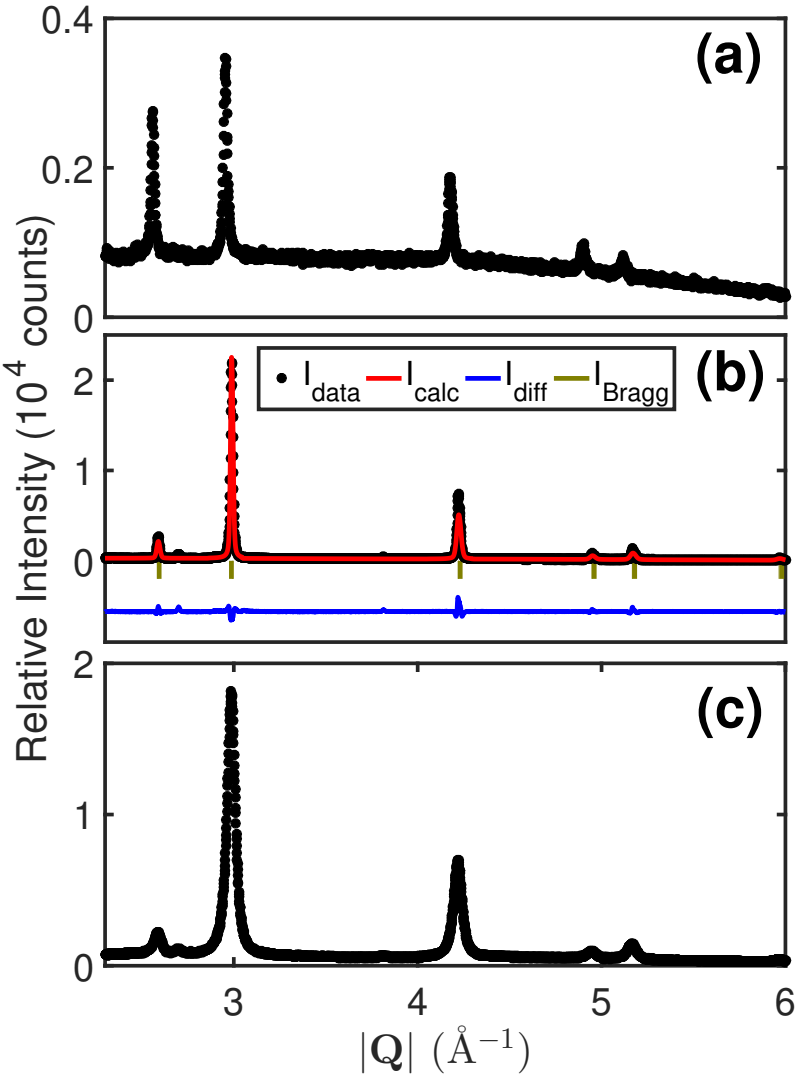

Figure 4.5 Room temperature diffraction profiles for CoO, $Co_xMg_{1-x}O$ (synthesised by sol-gel) and MgO collected on a Bruker D2 Phaser x-ray diffractometer utilising a monochromated Cu $K_{\alpha,1,2}$ source. Rietveld refinement ($\chi^2 = 6.91$, $R_p = 10.12\%$ and $R_{wp} = 13.25\%$) of $Co_xMg_{1-x}O$ indicates that the solid solution assumes a rock-salt structure ($Fm\bar{3}m$) with a unit cell parameter $a = 4.2131(2)$ Å, corresponding to an $x = 0.025(5)$ according to Vegard's law [209].

As illustrated in Fig. 4.5, the Rietveld refinement of $Co_{0.03}Mg_{0.97}O$ indicates that the solid solution assumes a rocksalt structure ($Fm\bar{3}m$) with a unit cell parameter a = 4.2131(2) Å. Utilising the measured values of the end members CoO (4.2594(4) Å) and MgO (4.2118(1) Å), both in agreement with values in the literature [461–465], the unit cell parameter of 4.2131(2) Å corresponds to an x = 0.025(5) according to Vegard's law [209], confirming that approximately 3% of the Mg^{2+} sites contain Co^{2+}.

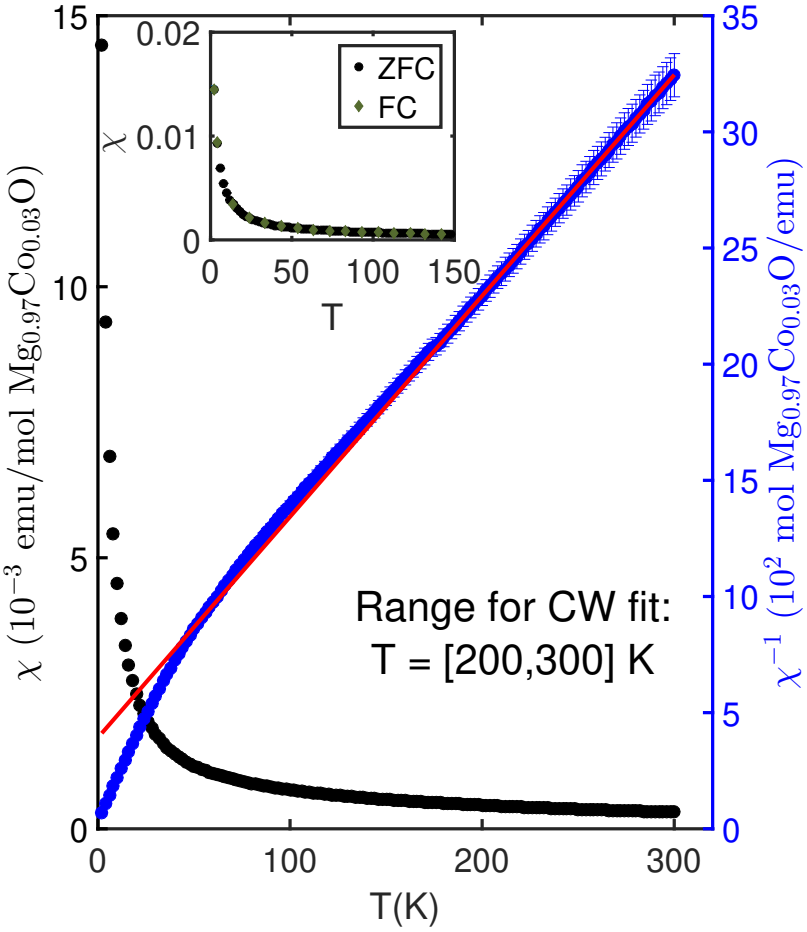

Figure 4.6 Temperature dependence of ZFC molar magnetic susceptibility ($\mu_o H_{\text{ext}}$ = 0.1 T) and its inverse for the polycrystalline $Co_xMg_{1-x}O$ sample synthesised by sol-gel. (inset) A comparison of the temperature dependence of the FC and ZFC molar magnetic susceptibility. The high temperature portion of the ZFC data (T = [200,300] K) exhibits Curie-Weiss behaviour [37], shown by the red line, corresponding to a Curie constant C and Curie-Weiss temperature θ_{CW} of 0.105(8) emu·K/mol and−41(6) K, respectively. The apparent "shift" at T≈ 180 K is an instrumental artifact and is not experimentally reproducible.

As illustrated in Fig. 4.6, there is an absence of magnetic ordering between 2

and 300 K, in contrast to CoO which assumes long range antiferromagnetic order at $T_{\rm N} \sim 290$ K [82, 341, 424, 425]. The high temperature portion of the data (T =[200, 300] K) exhibits Curie-Weiss behaviour with a Curie constant C and Curie-Weiss temperature $\theta_{\rm CW}$ of 0.105(8) emu·K/mol and−41(6) K, respectively. As established in the mean field derivation of the Curie-Weiss law, the Curie constant C is assumed to account for all Co^{2+} in $Co_xMg_{1-x}O$, and thus its value is directly proportional to x [37, 397].

The determination of the value of x from the Curie constant C begins by first recalling that the effective paramagnetic moment is defined as [397]

$$\mu_{\rm eff} = g_J\sqrt{S(S+1)} \tag{4.6}$$

where g_J is the Landé g-factor. Since the $j_{\rm eff} = \frac{1}{2}$ and $j_{\rm eff} = \frac{3}{2}$ manifolds are separated by 36 meV ($\sim$ 420 K) [18, 20, 444], a first approximation consists of treating the doublet ground state manifold as thermally isolated in the temperature range probed. It is important to note that the claim of the ground state spin-orbit manifold as being characterised as $j_{\rm eff} = \frac{1}{2}$ has been confirmed explicitly in Appendix E, in contrast to the previously discussed case of Pr^{3+} in $Pr_2Sn_2O_7$ in Chapter 2. Consequently, it is necessary to project all quantities in Eq. 4.6 to the ground state manifold

$$\mu_{\rm eff} = g'_J\sqrt{j_{\rm eff}(j_{\rm eff}+1)}, \tag{4.7}$$

where g'_J denotes the projected Landé g-factor [20, 47, 270] as described in Appendix E and previously discussed in §3.3.4. Inserting the values for g'_J and $j_{\rm eff}$ as $\frac{13}{3}$ and $\frac{1}{2}$, respectively, as derived in Appendix E, Eq. 4.7 becomes

$$\mu_{\rm eff} = \frac{13}{3}\cdot\sqrt{\frac{1}{2}\cdot\left(\frac{1}{2}+1\right)} = 3.75\ \mu_B. \tag{4.8}$$

A comparison of the expected value of $\mu_{\rm eff}$ in Eq. 4.8 to the its experimentally determined value first requires utilising the definition of the Curie constant [37, 397]

$$C = \frac{N\mu_{eff}^2}{3k_B}. \tag{4.9}$$

It should be noted that χ in Fig. 4.6 was normalised by moles and thus N in

Eq. 4.9 must be set to N_{A}. By solving for μ_{eff}, inserting the value of 0.105(8) emu/K mol, and utilising the fact that EDS measurements (later presented in §4.3.3 as Fig. 4.11) indicate that only 4(1)% of the Co^{2+} sites are in fact magnetic, an effective paramagnetic moment of

$$\mu_{eff} = \sqrt{\frac{3k_B}{N_A} \cdot \frac{1}{0.04(1)} \cdot 0.105(8)} = 4.6(8)\ \mu_B \tag{4.10}$$

is obtained, in excellent agreement with the predicted value given by Eq. 4.8, and thus confirming that approximately 3% of the Co^{2+} sites contain Co^{2+}.

4.3.2 Neutron Inelastic Spectroscopy

Assignments of the relative coordination shell m via |Q|-dependence

Having confirmed the concentration x of Co^{2+} in $Co_xMg_{1-x}O$, the experimental data is now presented. As illustrated in Fig. 4.7, low-temperature/incident-energy inelastic neutron spectroscopic measurements on powder $Co_{0.03}Mg_{0.97}O$ display a hierarchy of dispersionless excitations up to $\hbar\omega \sim 15$ meV. Upon closer inspection, intensities for some excitations exhibit a modulated $|\mathbf{Q}|$-dependence, characteristic of pairwise interactions [351, 390, 391, 460], and thus distinguishing them from single-ion dispersionless crystal-field excitations. It is important to recall from §4.1.2, that the period of modulation in the measured $|\mathbf{Q}|$-dependence of the $S(|\mathbf{Q}|)$ for a particular pair excitation as described by Eq. 4.5, is uniquely determined by the intra-pair distance $|\mathbf{R}_m|$ [390], thus may be used as a method for the identification of the corresponding coordination shell m. The following algorithm was developed to assign m labels to the excitations summarised in Fig. 4.7:

- To prevent the inundation of magnetic dimer excitations by strong phonon bands, a scaled inelastic neutron scattering intensity $S_\gamma(|\mathbf{Q}|, \hbar\omega)$ of a non-magnetic isostructural lattice MgO, collected at identical experimental conditions, was subtracted as a background. The scaling factor γ, such that $S_\gamma(|\mathbf{Q}|, \hbar\omega) = \gamma \cdot S(|\mathbf{Q}|, \hbar\omega)$, was calculated from the ratio between constant-$\hbar\omega$ cuts of $S(|\mathbf{Q}|, \hbar\omega)$ of MgO and $Co_{0.03}Mg_{0.97}O$ along $|\mathbf{Q}|$ at high $|\mathbf{Q}|$ for a dynamic range $\hbar\omega$ exhibiting no strong low-$|\mathbf{Q}|$ scattering. Since the intensity of a non-magnetic isostructural lattice was subtracted,

the resulting inelastic neutron scattering intensity $S'(|\mathbf{Q}|, \hbar\omega)$ should be exclusively magnetic.

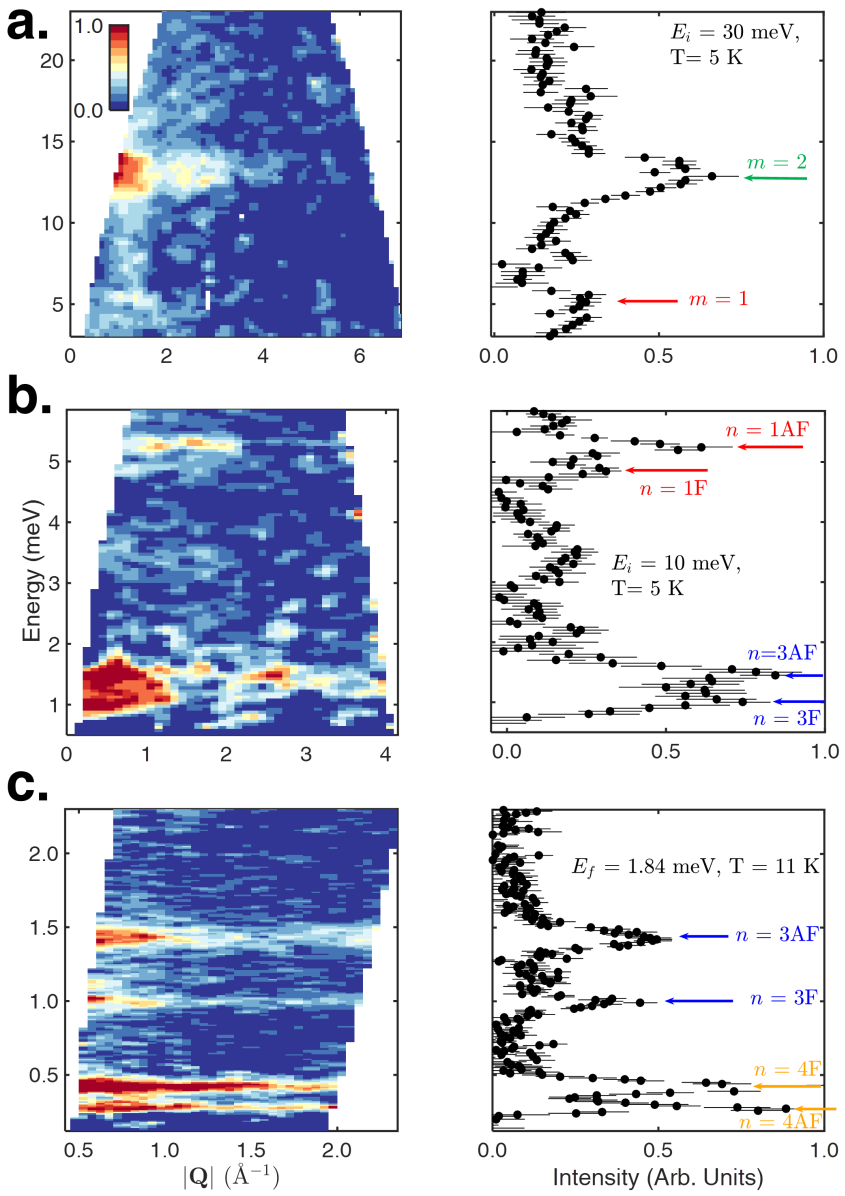

Figure 4.7 Background-subtracted powder-averaged neutron-scattering intensity maps of $Co_{0.03}Mg_{0.97}O$ measured on (a) MARI at 5 K with an $\hbar\omega_i = 30$ meV, (b) MARI at 5 K with an $\hbar\omega_i = 10$ meV and (c) IRIS at 11 K with an $\hbar\omega_f = 1.84$ meV, revealing seven low-energy bands of dispersionless magnetic excitations. The right column shows $|\mathbf{Q}|$-integrated cuts. Labels denote the coordination shell m and the type of coupling present with label n, as determined in Figs. 4.8 and 4.9, respectively.

- Potential dimer excitations were first identified by peaks present in $|\mathbf{Q}|$-integrated cuts (integrated over all $|\mathbf{Q}|$) along $\hbar\omega$ of $S'(|\mathbf{Q}|, \hbar\omega)$ at base

temperature. Each distinct peak was fitted to a Gaussian of the form

$$[S'_{|\mathbf{Q}|}(\hbar\omega)]_i = A_i \left(e^{-\frac{(\hbar\omega - \hbar\omega_{o,i})^2}{2\sigma_i}} \right) + B_i, \tag{4.11}$$

where $[S'_{|\mathbf{Q}|}(\hbar\omega)]_i$, A_i, $\Delta E_{o,i}$, σ_i and B_i denote $|\mathbf{Q}|$-integrated cuts along $\hbar\omega$, scale factor, peak centre, standard deviation and vertical background terms, respectively, for the i^{th} peak.

- $\hbar\omega$-integrated cuts along $|\mathbf{Q}|$ were performed on $\hbar\omega S'(|\mathbf{Q}|, \hbar\omega)$ where the range of integration was from $\hbar\omega_{o,i} \pm 2\sigma_i$ for each i^{th} peak. An integration range of $\pm 2\sigma$, accounting for 95% of the integrated intensity of an ideal Gaussian, was chosen as an attempt to account for all the intensity corresponding to the i^{th} excitation since all experimentally observed excitations were broader than instrumental resolution [103, 337]. The need to account for all the intensity corresponds to the fundamental assumption that the $S(|\mathbf{Q}|, \hbar\omega)$ of a particular m dimer in the current study may be approximated by a delta function [76, 106, 391]. Such an assumption is crucial since it allows for the significant simplification of the first moment sum rule [389] (Eq. H.56) into Eq. 4.5 *via* the single mode approximation [351] as derived in Appendix H.

- Possible dimer excitations were then identified by the presence of modulation in the $|\mathbf{Q}|$-dependence of the aforementioned $\hbar\omega$-integrated cuts along $|\mathbf{Q}|$. As illustrated in Fig. 4.8, seven of the low energy excitations exhibited a modulated $|\mathbf{Q}|$-dependence and their peak centres are summarised in Tab. 4.1.

Table 4.1 Summary of the calculated parameters from each of the three sequential procedures constituting the analysis algorithm that is described in the main text.

$\hbar\omega_o$ (meV)	$\lvert\mathbf{R}\rvert$ (Å)	m	Coupling Type	J (meV)
13.1(2)	4.2(3)	2	AF	3.09(5)
5.256(4)	3.1(5)	1	AF	1.000(8)
4.857(3)	3.4(3)	1	F	−0.918(6)
1.434(3)	5.5(5)	3	AF	0.258(1)
0.998(4)	5.4(6)	3	F	−0.182(1)
0.420(2)	6.3(7)	4	AF	0.0759(4)
0.279(2)	5.8(5)	4	F	−0.0504(4)

- For the seven $\hbar\omega$-integrated cuts along $|\mathbf{Q}|$ exhibiting a modulated $|\mathbf{Q}|$-dependence, the intensity was fitted to a function of the form [106, 351, 368, 390, 391, 460]

$$[\hbar\omega S'_{\hbar\omega}(|\mathbf{Q}|)]_i = A_i|F(|\mathbf{Q}|)|^2\left(1-\frac{\sin(|\mathbf{Q}||\mathbf{R}_i|)}{(|\mathbf{Q}||\mathbf{R}_i|)}\right), \tag{4.12}$$

where $[\hbar\omega S'_{\hbar\omega}(|\mathbf{Q}|)]_i$, A_i, $F(|\mathbf{Q}|)$ and $|\mathbf{R}_i|$ denote $\hbar\omega$-integrated cuts along $|\mathbf{Q}|$ of $\hbar\omega S'(|\mathbf{Q}|,\hbar\omega)$, scale factor, Co^{2+} magnetic form factor and the intra-dimer distance of the i^{th} peak, respectively. It should be noted that the vertical offset B was excluded in Eq. 4.12 due to the use of MgO as a non-magnetic background.

Table 4.2 Select summary of crystallographic parameters of the diluted monoxide $Co_{0.03}Mg_{0.97}O$. The number of neighbours in a relative coordination shell m was determined by assuming a collinear type-II antiferromagnetic structure analogous to the magnetic structure assumed by undiluted CoO [84, 422, 449, 454].

m	$\lvert\mathbf{R}_m\rvert$ at 298 K (Å)	Neighbours in m	AF	F
1	2.983(1)	12	6	6
2	4.218(2)	6	6	0
3	5.166(2)	24	12	12
4	5.966(2)	12	0	12

- By comparing the refined values of $|\mathbf{R}_i|$ (Tab. 4.1) to the intra-dimer distances $|\mathbf{R}_m|$ (Tab. 4.2) for the relative coordination shell m calculated from the crystallographic unit cell of $Co_{0.03}Mg_{0.97}O$, the value of m was assigned to the i^{th} peak. As summarised in Tab. 4.1, the seven low energy magnetic excitations in Fig. 4.7 correspond to pair excitations with values of m ranging from 1 to 4.

Finally, to concisely present all calculated fits of the $|\mathbf{Q}|$-dependence of $[\hbar\omega S'_{\hbar\omega}(|\mathbf{Q}|)]$ to Eq. 4.12, each $[\hbar\omega S'_{\hbar\omega}(|\mathbf{Q}|)]_i$ was first normalised by its calculated scale factor A_i and then plotted with respect to $|\mathbf{Q}||\mathbf{R}_i|$, representing a re-scaled version of $|\mathbf{Q}|$, as shown in Fig. 4.8.

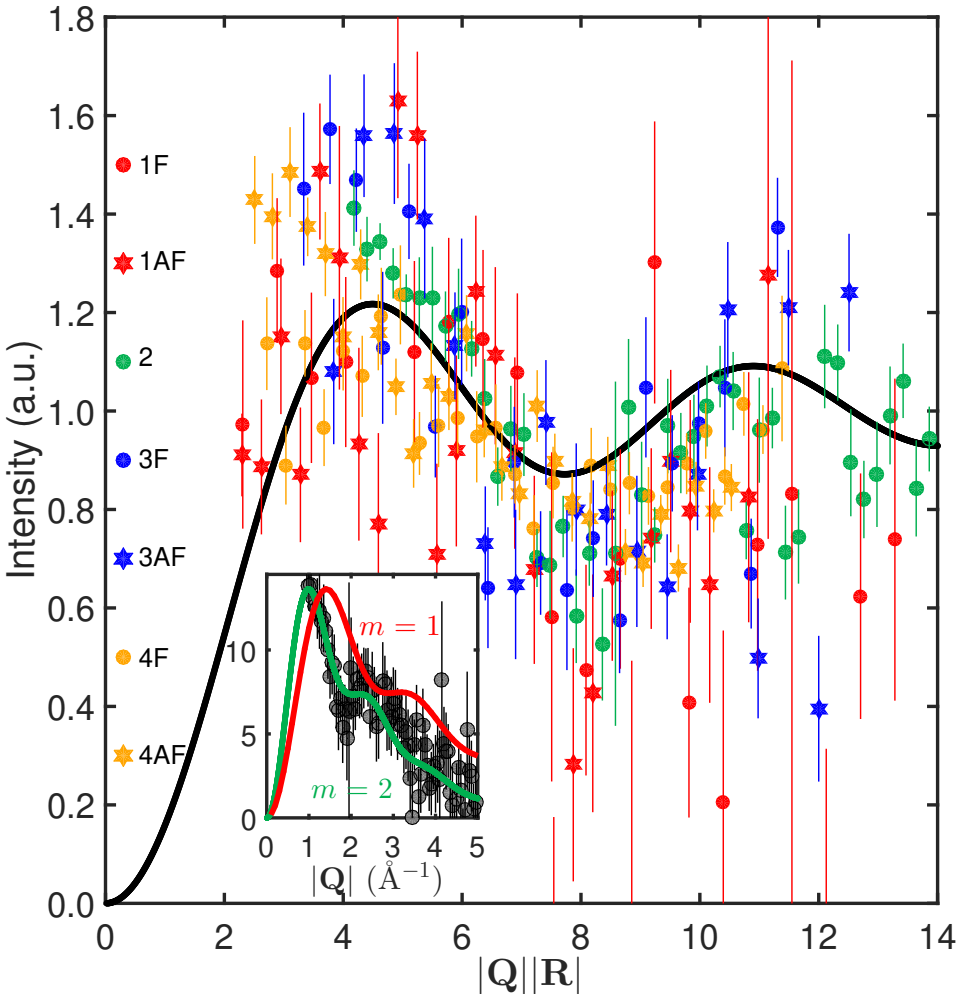

Figure 4.8 Scaled and form factor-corrected $|\mathbf{Q}|$ dependence of the intensities for all magnetic excitations with $|\mathbf{R}|$ calculated from fits to Eq. 4.5 as illustrated in the inset. The solid black curve denotes $1 - \frac{\sin(|\mathbf{Q}||\mathbf{R}|)}{|\mathbf{Q}||\mathbf{R}|}$. (inset) Constant-energy cut (ΔE = [12,14] meV) from MARI at 5 K with an $\hbar\omega_i = 30$ meV. The green curve is a fit to Eq. 4.5 with $|\mathbf{R}| = 4.2(3)$ Å, corresponding to $m = 2$ pairs. The red curve is with $|\mathbf{R}|$ fixed as 2.98 Å, corresponding to $m = 1$ pairs.

Determination of the modulus of the magnetic exchange constant $|J|$ via measured energy transfer ΔE

Having identified seven excitations from Co^{2+} pairs for various relative coordination shells, the determination of the magnetic exchange constants between the Co^{2+} ions constituting the pairs is now presented. Before proceeding, it is important to recall that as discussed in §4.1.2, the excitation energies $\hbar\omega$ for a particular Co^{2+} pair provides a direct experimental measurement of the modulus of the exchange constant $|J|$ between the two Co^{2+} ions of interest. As illustrated in Fig. 4.2, the correspondence between $\hbar\omega$ and $|J|$ is attributed to the observation that the energy gap ΔE, or equivalently $\hbar\omega$ as measured by neutron inelastic spectroscopy, between $\Gamma_{\text{eff}} = 1$ and $\Gamma_{\text{eff}} = 0$ is proportional to $|J|$ [390, 456–458].

As discussed in Appendix G, by assuming $\lambda \gg J$, it can be shown that the energy splitting of the ground state $j_{\text{eff}} = \frac{1}{2}$ doublet manifold is linear with respect to $|J|$, with a proportionality constant $\alpha' = \frac{50}{9}$ [47, 270]. Although tempting due to its simplicity, this linearity was based on an assumption that is not valid for all J for CoO, in particular, the dominant 180° antiferromagnetic superexchange J_2 [341]. As illustrated in Fig. 4.3, failure to meet the condition $\lambda \gg J$ implies that different spin-orbit manifolds couple to one another, introducing non-linearity in the J-dependence of ΔE. To compensate for non-linearity, the energy splitting ΔE as a function of J, or more precisely $|J|$ was determined numerically by the following procedure:

- Each operator in Eq. 4.4 was expressed as a 144×144 matrix in the two particle basis of $|l_1, m_{l,1}, s_1, m_{s,1}\rangle \otimes |l_2, m_{l,2}, s_2, m_{s,2}\rangle$.
- The validity of all expressions for both orbital and spin angular momentum operators in the two particle basis was verified by confirming that all angular momenta operators satisfy the canonical commutation relations of angular momentum [37, 266, 267, 270]

$$[\hat{\mathcal{O}}_x, \hat{\mathcal{O}}_y] = i\hbar\epsilon_{xyz}\hat{\mathcal{O}}_z, \tag{4.13}$$

  where $\hat{\mathcal{O}}$ and ϵ_{xyz} denote an angular momentum operator, either spin or orbital, and the Levi-Civita symbol, respectively.
- Utilising the projection factor $\alpha = -\frac{3}{2}$ [18, 20, 341, 444] as calculated in Appendix E, and the experimentally determined value of $\lambda = -16(3)$ meV

as determined for the case of $Co_{0.03}Mg_{0.97}O$ by Cowley *et al.* [18], the magnitude of the exchange constant $|J|$ in Eq. 4.4 was varied linearly from [0, 3.2] meV in steps of $1 \cdot 10^{-4}$ meV. For each value of $|J|$, the 144×144 matrix corresponding to $\hat{\mathcal{H}}_{pair}$ was diagonalised and its energy eigenvalues retrieved. The energy splitting ΔE for each $|J|$ was then determined by calculating the difference between the two energy eigenvalues of the $j_{\text{eff}} = \frac{1}{2}$ manifold.

- Once the calculation of ΔE for all $|J| = [0, 3.2]$ meV was completed, for each $\hbar\omega_{\text{o}}$ that was experimentally determined in § 4.3.2, the `find` function in MATLAB [466] was used to determine the corresponding value of $|J|$. A summary of the conversion of $\hbar\omega_{\text{o}}$ into values of $|J|$ is presented in Tab. 4.1 and Fig. 4.3.

- Finally, the validity of the numerically calculated $|J|$-dependence of the energy splitting ΔE of the $j_{\text{eff}} = \frac{1}{2}$ manifold was verified by confirming two conditions: (i) as $\left|\frac{J}{\lambda}\right| \rightarrow 0$, the J-dependence of ΔE became linear with a slope of $\frac{50}{9}$, whilst (ii) at $|J| = 0$, the value of ΔE was uniquely zero. Both conditions are shown to be satisfied in Fig. 4.3.

Assignments of ferromagnetism or antiferromagnetism via temperature dependence

Although the proportionality constants for all seven Co^{2+} pair excitations have been determined, it must be emphasised that only $|J|$ and not the actual value of J may be determined using the numerical calculations so far. Such a limitation is due to observation that ΔE, as measured by neutron inelastic spectroscopy, is simply an energy difference between the two eigenvalues of the $j_{\text{eff}} = \frac{1}{2}$ ground state manifold, corresponding to either a transition from the triplet $\Gamma = 1$ to the singlet $\Gamma = 0$ state or *vice versa* [390]. Consequently, the experimentally determined value of $\hbar\omega$ is independent of the sign of J. To address such a limitation, an analysis of the temperature dependence of the low energy excitations is presented, with the goal of extracting of the sign of J.

Antiferromagnetically coupled ($J > 0$) pairs of $j_{\text{eff}} = \frac{1}{2}$ spins consist of a singlet ground state ($\Gamma_{\text{eff}} = 0$) and a triplet ($\Gamma_{\text{eff}} = 1$) excited state, whilst ferromagnetic coupling ($J < 0$) corresponds to a triplet ground state and a singlet excited state [37, 390, 467]. These two different coupling scenarios give distinct temperature dependences of the integrated intensity that scales as the thermal

population difference between the ground and excited states [460, 468], with antiferromagnetic pairs following

$$S_{AF}(T) \propto \frac{1 - e^{-\Delta E/k_B T}}{1 + 3e^{-\Delta E/k_B T}}, \tag{4.14}$$

and ferromagnetic pairs following

$$S_F(T) \propto \frac{1 - e^{-\Delta E/k_B T}}{3 + e^{-\Delta E/k_B T}}, \tag{4.15}$$

such that as $T \to 0$ K, the ratio

$$\frac{S_{AF}}{S_F} = \frac{3 + e^{-\Delta E/k_B T}}{1 + 3e^{-\Delta E/k_B T}} \to 3. \tag{4.16}$$

As illustrated in Fig. 4.9(a), all coordination shells, with the exception of $m = 2$, display two closely spaced excitations. The ratio described by Eq. 4.16 proved to be the key observation used to identify the type of coupling for each excitation, with the exception of the $m = 2$. Since all pairs of magnetic excitations exhibited the 1:3 ratio at base temperatures, AF or F labels were assigned to the excitations with higher and lower relative intensities, respectively, as summarised in Tab 4.1. Once a magnetic excitation was assigned AF or F, the corresponding value of $|J|$ was assigned either a positive or negative sign, respectively. The presence of dual ferro- and antiferromagnetic interactions for $m = 1$, 3, and 4 is consistent with the GKA rules [53, 54, 56, 57] since each of these exchange pathways consists of at least one 90° Co^{2+}-Co^{2+} interaction involving the overlap of half and completely filled t_{2g} orbitals as shown in Fig. 4.1. Indeed, the GKA rules predict that the combination of the orbital degree of freedom for each Co^{2+} and a lack of orbital ordering (or anisotropy) would manifest itself as either a direct antiferromagnetic $t_{2g}^1 - t_{2g}^1$ or a weaker ferromagnetic $t_{2g}^1 - t_{2g}^2$ exchange interaction as illustrated schematically in Fig. 4.9(b). As summarised in Fig. 4.7 and Tab. 4.1, the experimental results are consistent with the GKA rules, as the antiferromagnetic interaction is stronger than the ferromagnetic alternative for all the $m \neq 2$ excitations, while the 180° Co^{2+}-O^{2-}-Co^{2+} $m = 2$ coupling leads to only a strong antiferromagnetic interaction [341, 422, 425, 444].

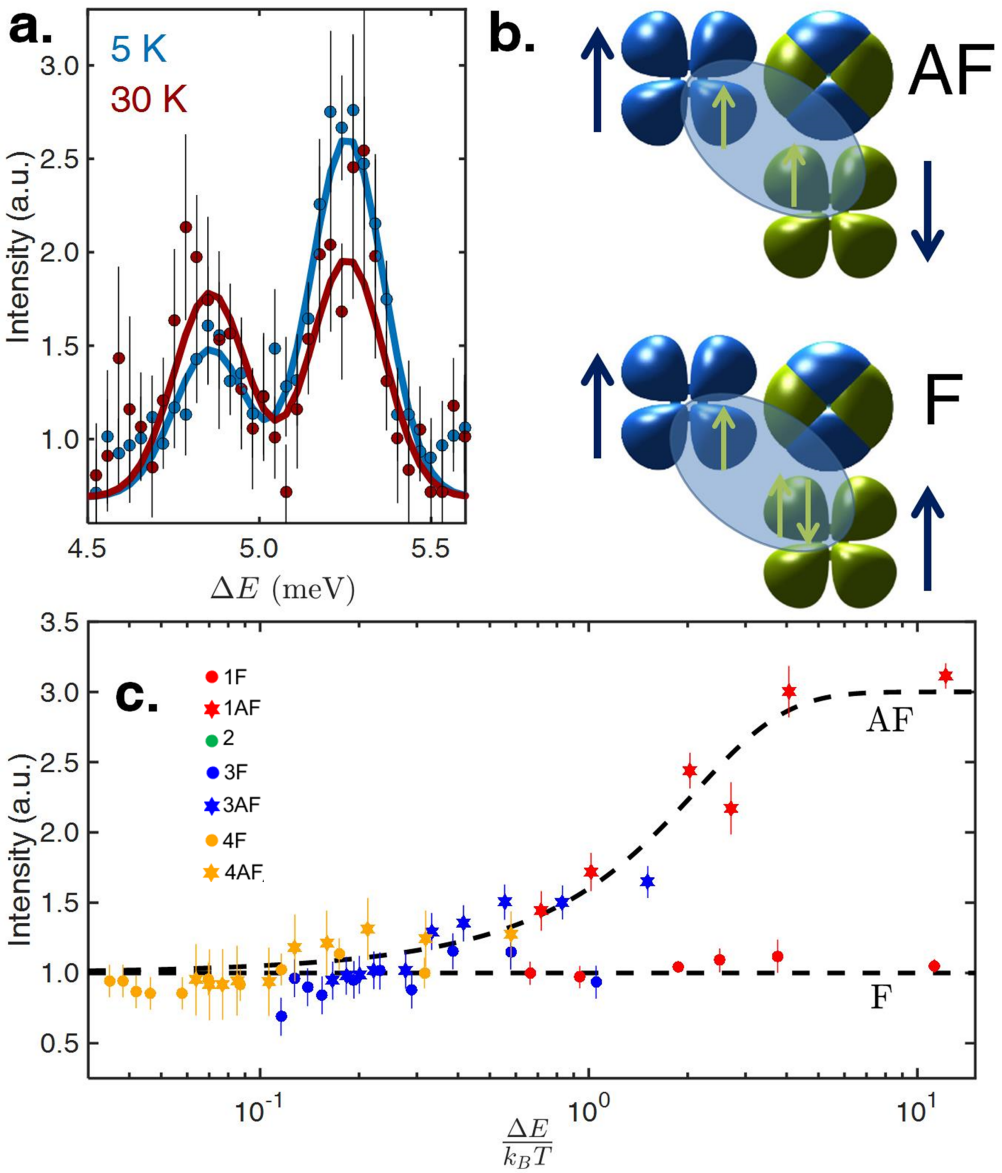

Figure 4.9 (a) Constant-$|\mathbf{Q}|$ cut (MARI, $\hbar\omega_i = 10$ meV) showing a different temperature dependence for the two peaks despite both corresponding to $m = 1$ pairs. (b) Pictorial representation of the sign of J as predicted by the GKA rules [53, 54, 56, 57]. Antiferromagnetism (top) is a result of exchange between two half-filled t_{2g} orbitals, while weaker ferromagnetism (bottom) is a result of exchange between a half-filled and completely filled t_{2g} orbitals. Yellow arrows denote local t_{2g} spin configurations and teal arrows denote total spin configurations on each Co^{2+}. (c) Normalised temperature dependence of the Bose factor-corrected integrated intensity for all seven excitations (Fig. 4.7) showing two universal curves calculated (dashed lines) for antiferromagnetic and ferromagnetic coupling [460, 468]. Both the integrated intensities and the calculated behaviour of antiferromagnetic or ferromagnetically coupled pairs were normalised by $S_F(T)$, as described in the main text.

In order to confirm the assignment of labels AF or F to a particular excitation

identified in Fig. 4.7 and Tab. 4.1, a fit to either:

$$\mathcal{A}\left(\frac{1-e^{\frac{-\Delta E}{k_B T}}}{1+3e^{\frac{-|\Delta E|}{k_B T}}}\right), \tag{4.17}$$

or

$$\mathcal{B}\left(\frac{1-e^{\frac{-\Delta E}{k_B T}}}{3+e^{\frac{-|\Delta E|}{k_B T}}}\right), \tag{4.18}$$

where $\mathcal{A}$ and $\mathcal{B}$ are scale factors, was applied to the temperature dependence of the Bose-corrected integrated relative intensity for that particular excitation originally identified as AF or F, respectively [460, 468]. The value of ΔE in Eqs. 4.17 and 4.18 to a particular excitation was fixed as the excitation's centre-of-mass $\hbar\omega_o$ that was calculated from $|\mathbf{Q}|$-integrated cuts along $\hbar\omega$ and summarised in Tab. 4.1. The integrated intensity of a particular excitation at a specific temperature was determined by fitting the peak in the $|\mathbf{Q}|$-integrated cut of $S(|\mathbf{Q}|, \hbar\omega)$ corresponding to that particular excitation and specified temperature to a Gaussian. It should be noted that the fit parameters ΔE and vertical offset B were fixed to their refined values at base temperature. Finally, in order to present the data concisely, the Bose-corrected integrated relative intensities were then normalised by both the calculated scale factor and the analytical form describing ferromagnetism (Eq. 14 excluding $\mathbf{B}$). As illustrated in Fig. 4.9(c), a plot of the normalised intensities were with respect to $\frac{\Delta E}{k_B T}$ for the entire dynamic range of interest, reveals that all integrated intensities fall onto either one of two universal curves describing antiferromagnetism or ferromagnetism, thus confirming the original assignments based on intensity ratios at base temperature.

Comparison to bulk thermodynamic data

Having assigned the signs of the seven exchange constants for dilute monoxide $Co_{0.03}Mg_{0.97}O$, a comparison with thermodynamic data and previously measured and calculated exchange constants for bulk CoO is now presented. The additional complication of dual ferro- and antiferromagnetic interactions for most m exchange pathways in combination with the entanglement of individual spin-orbit manifolds in the presence of magnetic order provides a possible explanation for the large range of J values reported for CoO in the literature [423–425, 469–473]. As summarised in Tab. 4.3, the experimentally determined values of J for the current study exhibit excellent agreement with three general trends reported by

experiment [425]: (i) a dominant $J_2 > 0$, (ii) a $J_1 < 0$, and (iii) a significantly smaller but non-negligible value for J_3, all in broad agreement with the trends concluded from a recent generalised gradient approximation (GGA)+U density functional theory (DFT) calculation on CoO [454], though it is worth noting that no such dual exchange was predicted.

Table 4.3 Magnetic exchange constants for $Co_{0.03}Mg_{0.97}O$ determined by the current study, magnetic exchange constants for CoO as cited in literature [423–425, 469–473] and calculated for CoO by Deng *et al.* [454] using $GGA + U$ DFT. The values from $GGA + U$ DFT have been renormalised such that J_2 is equal to the value from this current study. The values of T_N, θ_{CW} and λ reported in literature [18, 82, 341, 474, 475] for CoO have been included for the purposes of a comparison to the mean field value [37, 397] of θ_{CW} corresponding to the J values determined by the current study.

Quan. / Source	Current Study (meV)	Literature (meV)	Calc. [454] (meV)
λ	−16(3) [18]	−12 to −23.4 [47]	
J_{1AF} J_{1F}	1.000(8) −0.918(6)	0.60 to −0.31 [341, 425]	−0.97(2)
J_2 or J_{2AF}	3.09(5)	2.8 to 0.0013 [425]	3.09(5)
J_{3AF} J_{3F}	0.258(1) −0.182(1)	−0.67 [424]	−0.461(8)
J_{4AF} J_{4F}	0.0759(4) −0.0504(4)		−0.0085(1)
T_{N}	24.4(3)	25.1(4) [82, 341]	
θ_{CW}	−25.4(5)	−28.4(4) [474, 475]	

The interpretation of the magnetic excitations illustrated in Fig. 4.7 as distinct pair-wise interactions due to a combination of chemical dilution and an intrinsic assumption of physical homogeneity in $Co_{0.03}Mg_{0.97}O$ corresponds to a direct analogue of the physical model [37, 397] underlying the mean field estimate of the Curie-Weiss temperature given by

$$\theta_{\mathrm{CW}} = -\frac{2}{3}S(S+1)\sum_i z_i J_i, \tag{4.19}$$

where the spin value $S = \frac{3}{2}$ and z_i is the number of neighbours for each i^{th} exchange interaction with exchange constant J_i. Before θ_{CW} can be estimated with Eq. 8, it is important to note that while the value of $S = \frac{3}{2}$ is well-established

as determined by Hund's rules [18, 76, 266, 267], the value of z_i possesses an inherent ambiguity in $Co_{0.03}Mg_{0.97}O$. Since $Co_{0.03}Mg_{0.97}O$ itself does not magnetically order down to 2 K [18], as confirmed by DC magnetometry (Fig. 4.6), the number of Co^{2+} exhibiting each type of coupling J_i as measured by inelastic neutron spectroscopy cannot be determined by referring to its magnetic structure. Instead, it was assumed that the interactions in $Co_{0.03}Mg_{0.97}O$ are approximately analogous to those in CoO and thus the values of z_i may be inferred by investigating the number of couplings between different coordination shells in the collinear type-II antiferromagnetic structure proposed for CoO [84, 422, 449, 454]. The determination of the value of z_i for coordination shells $m = 1 \ldots 4$ was accomplished by first applying a transformation of the cubic $Fm\bar{3}m$ space group into its rhombohedral maximal subgroup $R\bar{3}m$ of the hexagonal crystal family [476]. This transformation results in the stacking of (111) planes along c in the $R\bar{3}m$ representation. Since Co^{2+} in 0, -2, ... and -1, -3, ... layers relative the $\langle 111 \rangle$ layer of reference are coupled F and AF, respectively, in a collinear type-II antiferromagnet, then the c coordinate of each Co^{2+} in a particular m coordination shell determined the type of coupling each Co^{2+} was predicted to exhibit. It should be noted that this analysis suggests only ferromagnetic correlations should exist in $m = 4$ coordination shell, in contradiction with the AF assignment to the magnetic excitation at $\hbar\omega = 0.0759(2)$ meV, which may indicate the presence of magnetic frustration [422]. The number of Co^{2+} in each coordination shell exhibiting F or AF coupling is summarised in Tab. 4.2.

By inserting the values of $S = \frac{3}{2}$, as determined from Hund's rules, J_i as determined from the measured energy transfers and z_i as determined from the aforementioned rhombohedral transformation analysis, into the mean field estimate of the Curie-Weiss temperature with Kanamori's correction factor for strong spin-orbit coupling in Co^{2+}-based oxides [341], Eq. 4.19 yields

$$\tilde{\theta}_{\mathrm{CW}} = \left(\frac{-5}{2 \cdot 1.9}\right) \{-0.918(6) \cdot 6 + 1.000(8) \cdot 6 + 3.09(5) \cdot 6$$
$$-0.182(1) \cdot 12 + 0.258(1) \cdot 12 - 0.0504(4) \cdot 12\} = -295(5)\ \mathrm{K}, \qquad (4.20)$$

corresponding to a value very similar to the experimental value of θ_{CW} of -330 K [474, 475] and in particular, $T_{\mathrm{N}} = 291$ K [82, 341]. The excellent agreement results from the near perfect cancellation of antiferromagnetic and ferromagnetic interactions for all coordinations with the exception of $m = 2$ (the

180° interaction).

4.3.3 Addressing the Possibility of Co^{2+}-Clustering

Before concluding this chapter, a subtle but very important assumption of the strategy used to disentangle individual spin-orbit manifolds must be addressed. As discussed in §4.1.2, the significant chemical dilution of the Co^{2+} magnetism in $Co_{0.03}Mg_{0.97}O$ simplifies the cooperative magnetism such that individual Co^{2+} pair excitations can be probed directly with neutron inelastic spectroscopy, utilising a combination of low temperatures and incident energies. Such a claim employs probabilistic arguments based on the fundamental assumption that Co^{2+} ions are homogeneously distributed throughout the rocksalt ($Fm\bar{3}m$) lattice. In other words, the strategy that forms the basis of the analysis presented above would be invalidated if Co^{2+} (or alternative Mg^{2+}) exhibited some form of preferential clustering. To refute such a possibility of cation clustering, a series of counterarguments are presented:

- as described in §4.2, measurements were performed on a polycrystalline sample of $Co_{0.03}Mg_{0.97}O$ synthesised *via* traditional solid state methods involving high temperatures well above 1000°C. The use of high synthesis temperatures would encourage a random distribution of Co^{2+} in the $Fm\bar{3}m$ structure [81].

- Supposing that Co^{2+} did exhibit clustering, then regions exhibiting an excess or deficiency of Co^{2+} relative to the average concentration would exist. Regions with excess Co^{2+} would behave as CoO, while correspondingly deficient regions would behave as MgO. Such a coexistence of CoO and MgO can be refuted by contrasting $S(|\mathbf{Q}|, \hbar\omega)$ of $Co_{0.03}Mg_{0.97}O$ with those from both CoO and MgO, as illustrated in Fig. 4.10. The contrast between $Co_{0.03}Mg_{0.97}O$ and MgO is made particularly evident by noting that the seven low energy excitations in Fig. 4.7 represents excess scattering after the subtraction of the $S(|\mathbf{Q}|, \hbar\omega)$ of MgO. The effectiveness of MgO as a non-magnetic background, yielding a $S(|\mathbf{Q}|, \hbar\omega)$ completely different than that of pure CoO, further suggests the absence of Co^{2+} clustering. Furthermore, utilising the same $Co_{0.03}Mg_{0.97}O$ powder sample, Cowley *et al.* [18] successfully measured the spin-coupling constant λ as $-16(3)$

meV, in close agreement with the listed experimental single ion value of −22.1 meV [47]. An agreement only made possible by disentangling coupling between spin-orbit manifolds, a process that would hindered by any type of clustering.

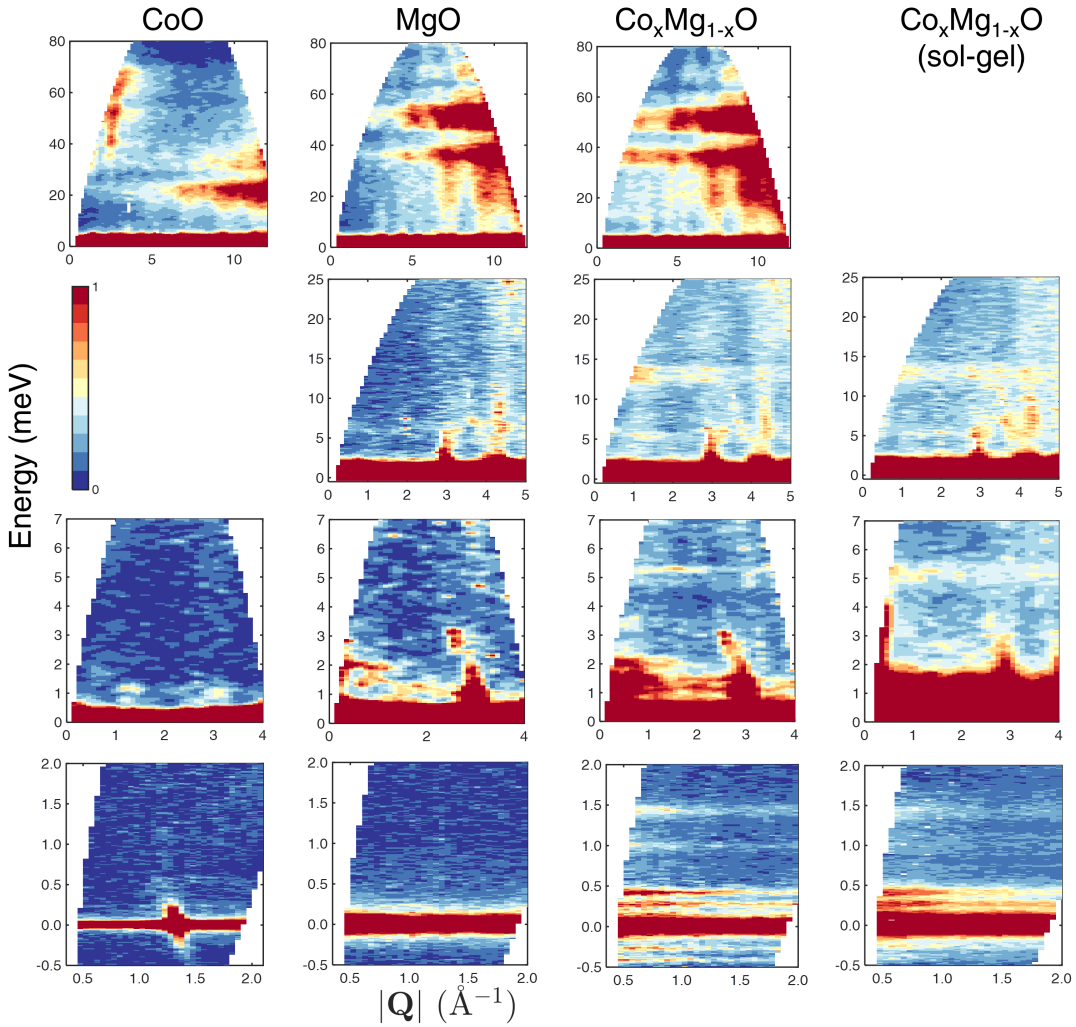

Figure 4.10 A comparison of raw (non-background subtracted) neutron-scattering intensity maps at 5 K for CoO, MgO, $Co_{0.03}Mg_{0.97}O$ synthesised by standard solid state methods and $Co_{0.03}Mg_{0.97}O$ synthesised by sol-gel. Each column corresponds to a particular compound as labelled from above. Rows 1 to 3 correspond to an $\hbar\omega_i$ of 85 meV (f = 300 Hz), 30 meV (f = 350 Hz), 10 meV (f = 250 Hz) measured on MARI, respectively, whilst row 4 corresponds to an $\hbar\omega_f$ of 1.84 meV measured on IRIS. Three exceptions include: CoO in row 1 corresponding to an $\hbar\omega_i$ of 100 meV (f = 350 Hz), $Co_{0.03}Mg_{0.97}O$ (sol-gel) in rows 2 and 3 correspond to an $\hbar\omega_i$ of 29.5 meV (f = 350 Hz) and 14.5 meV (f = 250 Hz), respectively. All $S(|\mathbf{Q}|, E)$ maps have been renormalised to a common intensity scale.

- As summarised in §4.2 and illustrated in Fig. 4.10, neutron inelastic

spectroscopic measurements with slightly different incident energies on both IRIS and MARI were performed on a second polycrystalline sample of $Co_{0.03}Mg_{0.97}O$ at identical temperatures. In contrast to the first sample, the second was synthesised *via* a solution-based technique (sol-gel). The additional measurement of a second $Co_{0.03}Mg_{0.97}O$ sample was motivated by two key reasons: (1) the use of a solution-based synthesis technique represents a completely different synthetic route, and thus would exhibit a different propensity for clustering compared to the traditional solid state route. In particular, the sol-gel method was chosen because previously reported EPR studies on $Co_xMg_{1-x}O$ samples that have been synthesised *via* the sol-gel method, have provided no evidence of Co^{2+} clustering, even for values of $x \gg 0.03$ [477]. (2) The use of a slightly different incident energy, although measuring essentially the same dynamic range, would identify any incident energy dependence, and thus determine if the excitations were spurious. As illustrated in Fig. 4.10, $S(|\mathbf{Q}|, \hbar\omega)$ for both $Co_{0.03}Mg_{0.97}O$ samples are identical, and thus casts doubt on the claim that the magnetic excitations illustrated in Fig. 4.7 can be attributed to either Co^{2+} clustering or are themselves spurious artifacts. It is important to note that the similarities between both $Co_{0.03}Mg_{0.97}O$ samples suggests that the conclusions deduced from measurements performed on the sample synthesised by sol-gel (*e.g.* §4.3.1) are also applicable to the sample synthesised by standard solid state methods.

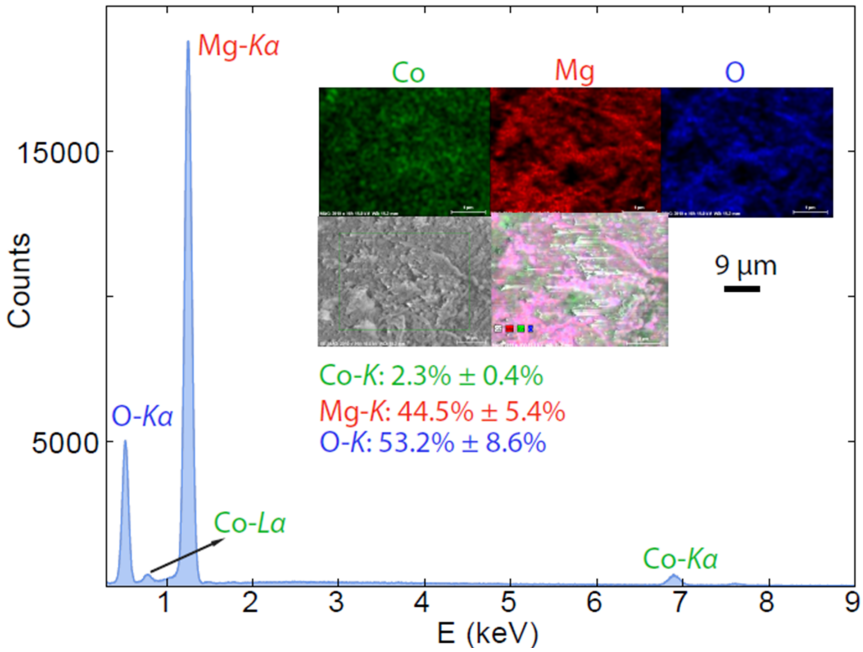

Figure 4.11 Energy dispersive spectroscopy (EDS) analysis for the polycrystalline $Co_xMg_{1-x}O$ sample synthesised by sol-gel. Percentages denote atomic composition (at. %). The resulting elemental analysis yields an x=0.04(1), a value that is consistent with x-ray diffraction and DC susceptibility measurements. (inset) Distribution of Co^{2+}, Mg^{2+}, and O^{2-}, providing no indication of significant clustering.

- As summarised in the inset of Fig. 4.11, EDS-SEM measurements confirmed the uniform distribution of Co^{2+}, Mg^{2+} and O^{2-}, with no evidence for significant clustering. The resulting elemental analysis confirmed that the Co^{2+} concentration of $x = 0.04(1)$ was within experimental error to the values deduced by both DC magnetometry and x-ray diffraction measurements presented in §4.3.1.

- A final argument against Co^{2+} clustering consists of a comparison of the experimentally determined value for the Curie-Weiss temperature of $Co_{0.03}Mg_{0.97}O$ and its value obtained from mean field theory [37, 397]. As summarised in Tab. 4.3, every coordination shell, with the exception of $m = 2$, exhibits two closely spaced magnetic exchange constants, reflecting the concurrent presence of anti- and ferromagnetic behaviour, respectively. Utilising the mean field definition of the Curie-Weiss temperature (Eq. 4.19), the concurrent presence of anti- and ferromagnetic behaviour in each coordination shell, with the exception of the second, implies that the contribution of each coordination shell to θ_{CW} would be dominated by the second coordination shell. By inserting the values of $S = \frac{3}{2}$, $J_2 = 35.9(6)$ K

(3.09(5) meV), setting the value of z as 1 since individual Co^{2+} pairs are of interest, and dividing by the correction factor of 1.9 [341], Eq. 4.19 yields a value of

$$\theta_{CW} = -\left(\frac{\frac{3}{2}\left(\frac{3}{2}+1\right)}{2 \cdot 1.9}\right)(1 \cdot 35.9(6)) = -44.9(7)\ \text{K}, \tag{4.21}$$

in excellent agreement with the experimentally determined value of $-41(6)$ K. The success in accounting for the Curie-Weiss temperature implies that $Co_{0.03}Mg_{0.97}O$ may be regarded as consisting of Co^{2+} pairs since the θ_{CW} is a measure of effective spin-spin interactions. It is worthwhile to note that the magnetic susceptibility exhibits no difference between ZFC/FC as illustrated in the inset of Fig. 4.6, implying an absence of glassy behaviour down to 2 K. Such an observation supports the claim that larger molecular clusters are absent, since these clusters would be expected to yield glassy behaviour and thus a ZFC/FC split [390].

4.4 Concluding Remarks & Future Directions

Despite the success of the chemical dilution approach in the extraction of magnetic exchange constants J in $Co_{0.03}Mg_{0.97}O$, it must be conceded that the values of J extracted in the current study are limited to approximations of their true values in pure CoO. Such a limitation stems from the presence of the non-magnetic Mg^{2+} in the MgO host lattice and its influence on the superexchange pathways between individual Co^{2+} pairs. It is worth noting that although the $Co_{0.03}Mg_{0.97}O$ lattice (a = 4.21 Å) is contracted relative to that of pure CoO (a = 4.26 Å [478]), the agreements of energy scales between the current study and those reported in the literature [424, 425] demonstrate that the Co^{2+}-Co^{2+} exchange interactions are not greatly changed, or at least any changes are smaller than systematic errors introduced by attempting to simplify the scheme in pure CoO. Hence not only does the present results represent a comprehensive set of interaction energy estimates for CoO, the chemical dilution technique outlined in this chapter represents a possible fruitful avenue for future research. The extraction of J by measuring pairwise excitations in a magnetically diluted isostructural analogue, corresponds to an experimental approach that has only been applied to a handful of systems [456–458]. Despite its limited use in the literature, the approach outlined in this chapter has potential widespread

applicability, especially for extracting individual J constants in systems that have proven to be either problematic or impossible so far.

A second avenue for future research would stem from the fact that the dual anti- and ferromagnetic interactions measured in $Co_{0.03}Mg_{0.97}O$ have never been experimentally observed or predicted before this study, and represents a stark contrast to the behaviour when the degeneracy lies in the e_g channel [445]. To confirm such dual anti- and ferromagnetic interactions are a consequence of the t_{2g} degeneracy, future possible studies may consist of performing analogous measurements on other Co^{2+}-based magnets, while possibly extending into other magnets based on cations with a high spin d^7 configuration and possibly $4d$ cations exhibiting strong spin-orbit coupling, such as the low spin d^5 Ru^{3+}, a cation currently of particular interest in community for its potential ability to host Kitaev physics [271, 479–482].

In summary, the exchange and spin-orbit interactions have been disentangled for Co^{2+} on a rocksalt lattice by employing the technique of chemical dilution [448, 456–458]. Through a combined analysis of the energy, momentum, and temperature dependence, seven exchange constants have been measured out to the fourth coordination shell. Both anti- and ferromagnetic interactions are observed, with the exception of second neighbor interactions through linear Co^{2+}-O^{2-}-Co^{2+} bridges, in agreement with both the GKA rules [53, 54, 56, 57] and thermodynamic data [82, 341, 474, 475]. The results demonstrate that in the case of an orbital degeneracy in the t_{2g} channel, dual anti- and ferromagnetic interactions occur with comparable magnitudes.

Chapter 5

Deterioration of spin-orbit transitions in the Mott insulator CoO

5.1 Introduction

Mott insulators are materials where conventional band theory fails, predicting metallic behaviour owing to half-filled bands with the origin of the insulating response indicative of strong electronic correlations [483, 484]. Spurred by the discovery of high temperature superconductivity in the hole-doped cuprates [43, 485, 486], there has been a resurgence of interest in the Mott insulators. In addition to being the parent materials for high temperature cuprate, and possibly pnictide superconductivity [392, 487, 488], Mott insulator hosts have provided the materials research community with a wealth of exotic physical phenomena ranging from metal-to-insulator transitions to quantum criticality to colossal magneto-resistance [489, 490]. Driven by significant advances in both instrumentation and sample preparation, Mott insulators continue to remain at the forefront of materials research which include studies on pressure-induced superconductivity [491–495] and most recently, the search for physical realisations of the Kitaev quantum spin liquid state [30, 33, 437, 496].

5.1.1 The Enigmatic Monoxide, CoO

CoO is arguably one of the oldest known and most extensively studied Mott insulators and one of the first orbitally ordered materials to be studied with neutron diffraction [440, 441, 497, 498]. Its primitive unit cell consists of one Co^{2+} and one O^{2-}, corresponding to 15 valence electrons. With an odd number of electrons, conventional band theory [454, 499] would predict CoO to be metallic, however, CoO is a very strong insulator with a room temperature resistivity of 10^8 Ω·cm [500] and an optical band gap of 2.5 eV [501–503], with evidence for metallic behaviour being found only under extremely high pressures of $\sim$100 GPa [504].

Possessing a cubic $Fm\bar{3}m$ structure at room temperature (Fig. 5.1(a)), CoO assumes long range antiferromagnetic order at $T_N \sim 290$ K [83, 341, 447], in contrast to the long range ferromagnetism predicted by general band coupling models assuming a dominant direct exchange [454, 505–507]. Despite being the subject of numerous neutron diffraction studies stretching over seven decades, revealing a proposed frustration relief-driven cubic-to-monoclinic distortion accompanying magnetic order [82], its magnetic structure has proven to be particularly controversial and has yet to be solved unambiguously with both collinear and non-collinear models describing diffraction patterns equally as well [82, 83, 423, 440, 441, 449, 508].

As described in Chapter 4 and Appendix E, the magnetism of CoO is based on Co^{2+} in octahedral coordination, corresponding to a high spin d^7 configuration with one hole in the t_{2g} orbital manifold [3, 18, 47, 341, 447]. The resulting orbital degeneracy, coupled with various significant and far-reaching superexchange spin-spin interactions, results in a complex magnetic excitation spectrum with multiple spin-orbit levels intertwined as illustrated in Fig. 5.1(b). The resulting multi-parameter spin-orbital Hamlitonian incorporating both exchange and spin-orbit coupling of similar magnitude, combined with complex magnetic ordering, has made the modelling of the magnetic excitations in this deceptively simple material intractable using conventional spin wave approaches [320, 424, 425, 444]. Consequently, despite decades of spectroscopic measurements [18, 422, 424, 444, 471–473, 508, 509], there still remains a lack of a comprehensive theoretical framework to account for a complete and coherent understanding of the magnetic excitations in CoO.

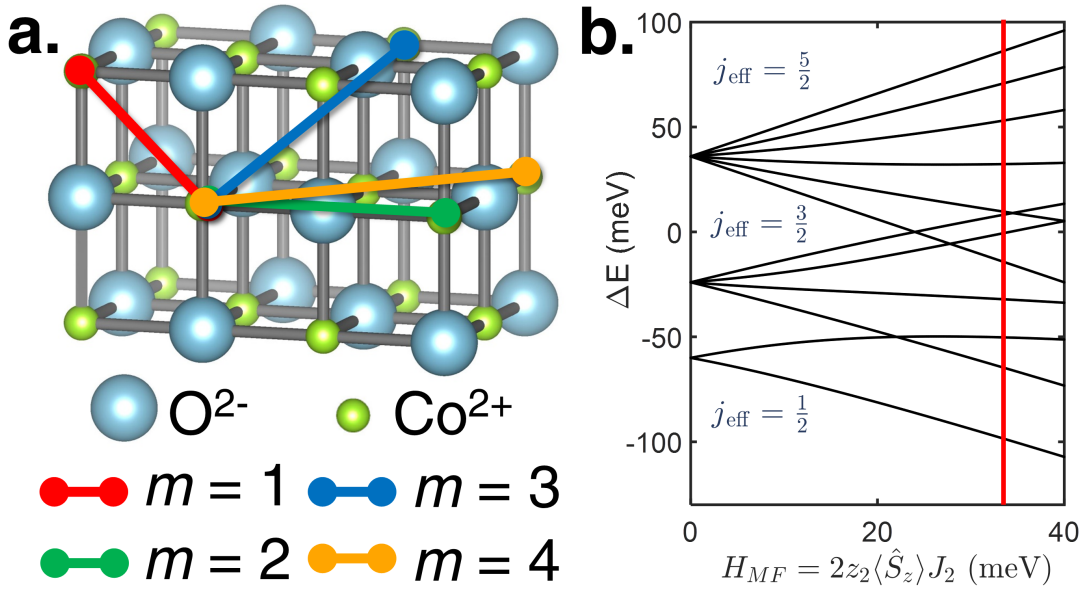

Figure 5.1 (a) First four coordination shells of the high temperature CoO rocksalt structure [478]. (b) Molecular field-induced entanglement of the spin-orbit manifolds. The red line indicates Kanamori's estimate of the molecular field [341, 447].

5.1.2 Equations-of-Motion for Green's Functions in the Random Phase Approximation Approach to Multi-Level Spin Wave Theory

In order to circumvent both the complexity of assigning an individual boson to each of the numerous spin-orbit levels, and the intrinsic restriction to excitations in the limit of $T = 0$ K (*i.e.* $|0\rangle \rightarrow |m\rangle$) associated with conventional pseudo-bosonic approaches based on Holstein-Primakov transformations [20, 510–512], an alternative approach based on Green's functions was employed to model the magnetic excitations of CoO.

Motivated by both the failure of the singlet-singlet [513] and singlet-triplet models [514] to capture the behaviour of the magnetic excitations of singlet-ground-state systems (*e.g.* TbSb [510]) and the limitations of conventional pseudo-bosonic approaches, Buyers, Holden & Perreault [515] established a novel approach describing the temperature dependence of the spin wave spectrum of both singlet- and degenerate-ground state magnetic systems. Abandoning the pseudo-bosonic concept, the approach is instead based on the use of operators that create or annihilate a given single-ion eigenstate that is defined by a single-ion Hamiltonian $\hat{\mathcal{H}}_{S.I.}$ [18, 20, 76, 444]. By utilising these single-ion creation/annihilation operators, transitions between all single-ion eigenstates of

the ground state multiplet are considered, describing the system as a set of spin waves from each level coupled together by an exchange interaction $J(\mathbf{Q})$, if the levels possess the same symmetry [516]. Such an approach is unique as it includes the possibility of mode-mode interactions at finite temperatures with such interactions proving key to understanding the energy gap at $\mathbf{q}$=0 in the case of Pr_3Tl [512, 515, 517, 518]. As derived in Appendix J, by employing a Fock-like decoupling random phase approximation (RPA) in the equation-of-motion-Green's function method [515, 519–522], the equation-of-motion is reduced to a set of coupled linear equations given by

$$G_{ij}^{\alpha\beta}(\mathbf{Q},E) = \delta_{ij} g_i^{\alpha\beta}(E) + \sum_k g_i^{\alpha\beta}(E)\Phi^{\alpha\beta} J_{i,i+k}(\mathbf{Q}) G_{i+k,j}^{\alpha\beta}(\mathbf{Q},E), \tag{5.1}$$

where the indices i, j denote sites and α, β denote $+$, $-$ or z. $g^{\alpha\beta}$ is the single-site susceptibility defined by

$$g^{\alpha\beta}(E) = \sum_{mn} \frac{S_{\alpha mn} S_{\beta nm}(f_m - f_n)}{E - E_n + E_m}, \tag{5.2}$$

where $S_{\alpha nm}$ denotes the matrix element $\langle n|\hat{S}_\alpha|m\rangle$, $|m\rangle$ is an eigenstate of the single-ion Hamiltonian $\hat{\mathcal{H}}_{S.I.}$ with eigenvalue E_m and thermal weighting factor f_m defined by

$$f_m = \frac{e^{\frac{-E_m}{k_B T}}}{\sum\limits_n \frac{-E_n}{k_B T}}, \tag{5.3}$$

while the prefactor $\Phi^{\alpha\beta}$ is defined as

$$\Phi^{\alpha\beta} = \begin{cases} 1 & \text{when } \alpha = + \text{ or } - \\ 2 & \text{when } \alpha = z. \end{cases}$$

It is worth noting that the form of the equation-of-motion as expressed in Eq. 5.1 is only a valid approximation if one assumes the only α, β combinations that yield non-negligible values for $g^{\alpha\beta}$ are $+-$, $-+$ and zz [20, 515, 523], as discussed in §J.3.5. Finally, $J(\mathbf{Q})$ is the Fourier transform of the exchange interaction [516],

given by

$$J(\mathbf{Q}) = \sum_{i \neq j} J_{ij} e^{i\mathbf{Q}\cdot\mathbf{d}_{ij}}, \tag{5.4}$$

where J_{ij} and $\mathbf{d}_{ij}$ denote the exchange constant and displacement vector, respectively, between sites i and j. The use of subscripts for $J(\mathbf{Q})$ is relatively unorthodox but will be discussed in §5.3 below.

In this chapter, an investigation of the spin-orbit transitions with high resolution neutron spectroscopic measurements of the magnetic excitations in CoO below T_{N} is presented. It will be shown that well-defined spin excitations present at low energies break down into a momentum and energy broadened continuum at higher energy transfers, reminiscent of the behaviour in the cuprates when charge-doped towards superconductivity [524–528]. The results are compared against a mean-field-RPA multi-level spin wave model based on Green's functions. While excellent agreement is found near the magnetic zone centre at low energies, the model fails to capture the high energy continuum. The failures of the model and the breakdown of the spin-orbit transitions at high energy transfers are discussed in terms of coupling to higher energy processes including itinerant excitations and multi-magnon decay.

5.2 Experimental Details

5.2.1 Sample Preparation

The neutron inelastic scattering measurements forming the basis of this study were performed on a 5 g single crystal of CoO ($l = 50$ mm, $\phi = 8$ mm) originally grown at Oxford University. The synthesis route is described by Cowley *et al.* [18] and consists of the following experimental procedure:

- polycrystalline samples of CoO were synthesised by annealing high purity Co_3O_4 ($> 99.99\%$) under flowing Ar at 1200°C for 36 h with intermittent grinding until laboratory x-ray diffraction confirmed the absence of the Co_3O_4 precursor ($\lesssim 1\%$ to 2%).

- The phase pure CoO powder was compressed into cylindrical rods using a

hydraulic press and subsequently annealed under flowing Ar at 1275°C for 24 h in a horizontal annealing furnace.

- Crystal growth was performed using the floating zone technique with a four-mirror optical floating zone halogen furnace (CSI system Inc.) at the Clarendon Laboratory, Oxford. The feed and seed rods were counter-rotated at 35 rpm with a vertical translation of 2 to 4 mm hr^{-1} in a pure Ar atmosphere. The initial polycrystalline seed rod was replaced for subsequent runs by single crystal seeds previously grown from earlier growths.

5.2.2 Neutron Inelastic Scattering Details

The neutron inelastic scattering measurements described in this study were performed on the MERLIN direct geometry chopper spectrometer [212] at the ISIS neutron spallation source (Didcot, U.K.). The t_0 (nimonic) chopper was spun at 50 Hz in parallel with the "sloppy" Fermi chopper package. To access a large dynamic range, three fixed incident energies E_i of 110 meV, 75 meV and 45 meV were selected with Fermi chopper frequencies of 350, 300 and 250 Hz, providing a resolution at the elastic line of 7.3, 4.8 and 2.7 meV, respectively.

The 5 g single crystal was mounted in a top loading closed cycle refrigerator (ISIS CCR 62) such that the [110] and [001] axes laid within the scattering plane. A tomographic reconstruction in momentum-space was accomplished by rotating the single crystal about the [1-10] axis over 120° in 0.5° steps.

The four dimensional $(\mathbf{Q}, E)$ experimental data at each angle Ψ and E_i was collected at 5 K for a fixed amount of accumulated charge (30 $\mu A \cdot s \sim 15$ minutes) on the spallation target. The raw experimental data was normalised by accumulated proton charge, corrected for detector-efficiency using a vanadium reference sample and reduced by the Mantid data analysis software [529]. Visualisation and manipulation of reduced experimental data including rebinning and projections were performed using the HORACE software package [530] distributed by ISIS.

5.3 Details of Analysis Algorithm

Equation-of-Motion & Additional Approximations

As discussed in §4.3.2, the proposed type-II antiferromagnetic magnetic structure of CoO in the low temperature limit can be approximated as (111) ferromagnetic sheets stacked antiferromagnetically along [111] [82, 422, 438, 440, 441]. Such an approximation implies that CoO can be reduced to two unique magnetic sublattices, and thus the value of the site indices i and j can assume the values of either 1 or 2. The restriction of the values of i and j reduces Eq. 5.1 to four coupled linear equations given by:

$$G_{11}^{\alpha\beta}(\mathbf{Q},E) = g_1^{\alpha\beta}(E) + g_1^{\alpha\beta}(E)\Phi^{\alpha\beta}J_s(\mathbf{Q})G_{11}^{\alpha\beta}(\mathbf{Q},E) + g_1^{\alpha\beta}(E)\Phi^{\alpha\beta}J_d(\mathbf{Q})G_{21}^{\alpha\beta}(\mathbf{Q},E) \tag{5.5}$$

$$G_{21}^{\alpha\beta}(\mathbf{Q},E) = g_2^{\alpha\beta}(E)\Phi^{\alpha\beta}J_s(\mathbf{Q})G_{21}^{\alpha\beta}(\mathbf{Q},E) + g_2^{\alpha\beta}(E)\Phi^{\alpha\beta}J_d(\mathbf{Q})G_{11}^{\alpha\beta}(\mathbf{Q},E) \tag{5.6}$$

$$G_{12}^{\alpha\beta}(\mathbf{Q},E) = g_1^{\alpha\beta}(E)\Phi^{\alpha\beta}J_s(\mathbf{Q})G_{12}^{\alpha\beta}(\mathbf{Q},E) + g_1^{\alpha\beta}(E)\Phi^{\alpha\beta}J_d(\mathbf{Q})G_{22}^{\alpha\beta}(\mathbf{Q},E) \tag{5.7}$$

$$G_{22}^{\alpha\beta}(\mathbf{Q},E) = g_2^{\alpha\beta}(E) + g_2^{\alpha\beta}(E)\Phi^{\alpha\beta}J_s(\mathbf{Q})G_{22}^{\alpha\beta}(\mathbf{Q},E) + g_2^{\alpha\beta}(E)\Phi^{\alpha\beta}J_d(\mathbf{Q})G_{12}^{\alpha\beta}(\mathbf{Q},E), \tag{5.8}$$

where J_s and J_d denotes $J(\mathbf{Q})$ on the same ($i = j$) and different ($i \neq j$) sublattices, respectively. Combining Eqs. 5.5 to 5.8, the four coupled linear equations are reduced to

$$\begin{aligned} G^{\alpha\beta}(\mathbf{Q},E) &\equiv \sum_{ij} G_{ij}^{\alpha\beta}(\mathbf{Q},E) \\ &= \frac{g_1^{\alpha\beta}(E) + g_2^{\alpha\beta}(E) + 2g_1^{\alpha\beta}(E)g_2^{\alpha\beta}(E)[\Phi^{\alpha\beta}J_d(\mathbf{Q}) - \Phi^{\alpha\beta}J_s(\mathbf{Q})]}{[1 - g_1^{\alpha\beta}(E)\Phi^{\alpha\beta}J_s(\mathbf{Q})][1 - g_2^{\alpha\beta}(E)\Phi^{\alpha\beta}J_s(\mathbf{Q})] - g_1^{\alpha\beta}(E)g_2^{\alpha\beta}(E)[\Phi^{\alpha\beta}J_d(\mathbf{Q})]^2}. \end{aligned} \tag{5.9}$$

As Eq. 5.9 is written, the equation-of-motion is explicitly a function of two variables: the single-site susceptibility $g^{\alpha\beta}$ and the Fourier transform of the exchange interaction $J(\mathbf{Q})$. The single-site susceptibility will now be addressed. Since the energy transfers ΔE under consideration (≥ 20 meV) are much larger

than the sample temperature ($\sim$ 0.5 meV) in this particular experiment, the single-site susceptibility given by Eq. 5.2 can be simplified to

$$g^{\alpha\beta}(E) = \sum_{n} \left\{ \frac{S_{\alpha 0n} S_{\beta n0}}{E - E_{n0}} - \frac{S_{\alpha n0} S_{\beta 0n}}{E + E_{n0}} \right\}, \tag{5.10}$$

corresponding to its definition in the $T = 0$ K limit, as used in the pseudo-bosonic approach [20, 511, 515]. The value of E corresponds to $E + i\Delta$, where E and Δ represent an input energy and a positive infinitesimal to ensure causality/analyticality *via* the Cauchy residual theorem [531, 532], respectively. For numerical purposes, Δ was set to 50% of the calculated experimental resolution width on MERLIN [212], *i.e.* the calculated half-width-at-half-maximum (HWHM) at the incident energy of interest. The eigenstates $|n\rangle$ and their corresponding eigenvalues E_n were calculated by diagonalising the single-ion Hamiltonian [76] given by

$$\hat{\mathcal{H}}_{S.I.} = \alpha\lambda\hat{\mathbf{l}} \cdot \hat{\mathbf{S}} + H_{MF}\hat{S}_z + \Gamma_z \left(\hat{L}_z^2 - \frac{2}{3} \right) + \Gamma_x(\hat{L}_x^2 - \hat{L}_y^2), \tag{5.11}$$

corresponding to spin-orbit coupling, Zeeman splitting due to a molecular field, axial and planar distortion contributions, respectively; with each contribution to $\hat{\mathcal{H}}_{S.I.}$ being parametrised by the spin-orbit coupling constant λ, the molecular field strength parameter $H_{MF}(i) = 2\sum_{j} J(ij)\langle\hat{S}_z(j)\rangle$ and distortion parameters Γ_z and Γ_x, respectively. It was originally assumed that the spin-orbit coupling constant λ was equal to the experimental value of $-16(3)$ meV as measured by Cowley *et al.* [18]. With the high symmetry approximation [422] which is required for Eq. 5.1 to be valid, the values of Γ_z and Γ_x were originally assumed to be zero.

The Fourier transform of the exchange interactions will now be addressed. Recall that the approximation [82, 422, 438, 440, 441] of the magnetic structure as (111) ferromagnetic sheets stacked antiferromagnetically resulted in the restriction of the site indices i and j in Eq. 5.1 to the values of either 1 or 2 and the relabelling of $J(\mathbf{Q})$ to either $J_s(\mathbf{Q})$ or $J_d(\mathbf{Q})$. Such relabelling suggests that $J(\mathbf{Q})$ given by Eq. 5.4 may be redefined as

$$J_\xi(\mathbf{Q}) = \sum_{\eta} J_{\xi,\eta} e^{i\mathbf{Q}\cdot\mathbf{d}_{\xi,\eta}}, \tag{5.12}$$

where the indices ξ and η denote a particular sublattice (either s or d) and a particular ij pair, respectively. The analytical form of J_ξ for both $\xi = s$ and d was derived for the four coordination shells for CoO, assuming a cubic rocksalt ($Fm\bar{3}m$) structure, by the following method:

- Eq. 5.12 was first redefined in terms of coordination shells that are summarised in Tab. 5.1. The new $J(\mathbf{Q})$ is given by

$$J_\xi(\mathbf{Q}) = \sum_m \sum_\eta J_{\xi,m,\eta} e^{i\mathbf{Q}\cdot\mathbf{d}_{\xi,m,\eta}}, \tag{5.13}$$

  where the sum over all distances in a particular ξ sublattice in Eq. 5.12 has been replaced by a summation of distances in a particular coordination shell m, followed by a summation over all coordination shells.

Table 5.1 Select summary of crystallographic parameters [461–463] of CoO. The number of neighbors in a relative coordination shell m was determined with the assumption that CoO assumes a collinear type-II antiferromagnetic structure [82, 422, 438, 440, 441]. Numbers in parentheses indicate statistical errors.

m	$\lvert\mathbf{d}_m\rvert$ (Å)	Neighbours in m	d-Sublattice	s-Sublattice
1	3.0144(8)	12	6	6
2	4.2630(11)	6	6	0
3	5.2211(13)	24	12	12
4	6.0288(15)	12	0	12

- As summarised by Tab. 5.1 and illustrated in Fig. 5.2, the number of Co^{2+} in the d- and s-sublattices for a particular coordination shell m was determined by first arbitrarily selecting a reference Co^{2+}, thus defining a reference (111) plane. Once a reference (111) plane was selected, for each Co^{2+} in the coordination shell m, the relative location of its particular (111) plane to the reference (111) plane was identified. By definition [440, 441], Co^{2+} located on odd integer number of (111) planes away from the reference (111) plane are defined as being located on d sublattice. While Co^{2+} located in the same or an even integer number of (111) planes away are defined as being located on the s sublattice. The process was repeated for all coordination shells and the numbers of Co^{2+} in each sublattice are summarised in Tab. 5.1.

- For a particular coordination shell m in a particular sublattice, the displacement vectors $\mathbf{d}_{m,ij}$ between the particular Co^{2+} of interest and the reference Co^{2+} was determined by VESTA [533]. The process was repeated

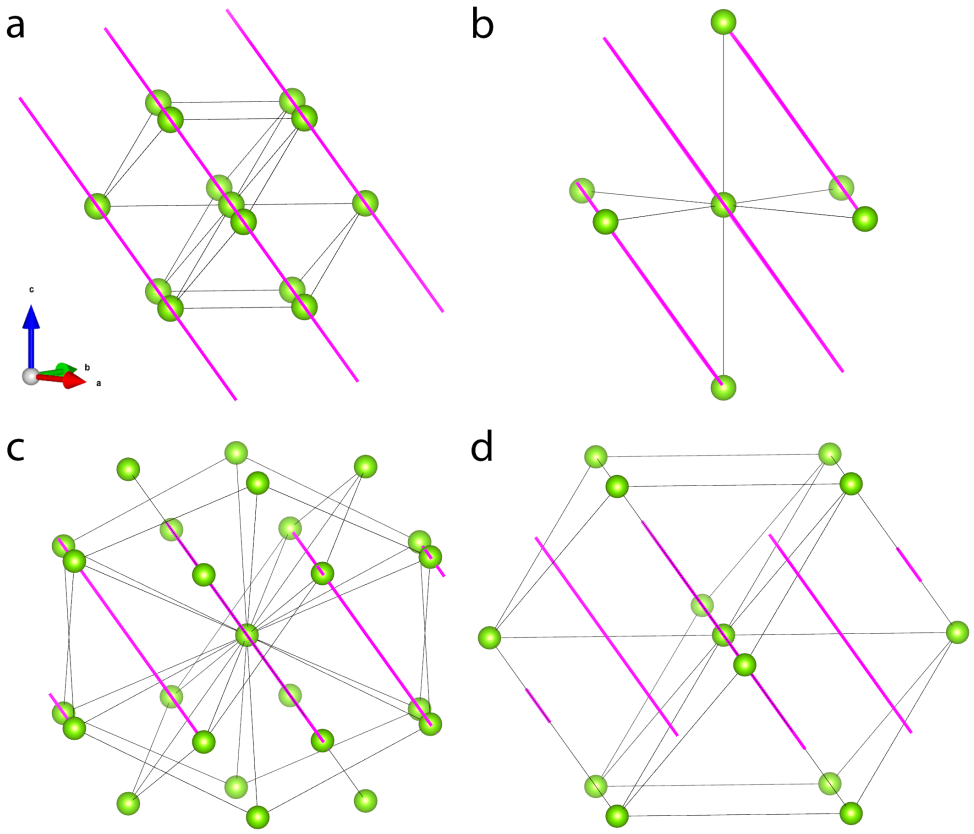

Figure 5.2 Isometric view of all Co^{2+} cations contained in the (a) first, (b) second, (c) third and (d) fourth coordination shell of the CoO rocksalt structure. For the purposes of reference, (111) planes are indicated by solid blue lines. All displacement vectors $\mathbf{d}_{m,ij}$ are listed in Tab. 5.2.

for all Co^{2+} in each coordination shell, then repeated for all coordination shells and finally repeated for both s and d sublattices. All displacement vectors $\mathbf{d}_{m,ij}$ are summarised in Tab. 5.2.

- For each coordination shell m, the calculated displacement vectors $\mathbf{d}_{m,ij}$ and its corresponding exchange constant J_m for a particular sublattice were inserted into the modified definition of $J(\mathbf{Q})$ given by Eq. 5.13, yielding:

$$\begin{aligned} J_s(\mathbf{Q}) = {} & 2J_{1F}\{\cos(\pi(H-K)) + \cos(\pi(K-L)) + \cos(\pi(L-H))\} \\ & + 2J_{3F}\{\cos(\pi(2H-K-L)) + \cos(\pi(2H+K+L)) \\ & + \cos(\pi(H-2K+L)) + \cos(\pi(-H-2K-L)) \\ & + \cos(\pi(H-K+2L)) + \cos(\pi(-H-K+2L))\} \\ & + 2J_{4F}\{\cos(2\pi(H-L)) + \cos(2\pi(H-K)) + \cos(\pi(L-K)) \\ & + \cos(\pi(H+L)) + \cos(\pi(H+K)) + \cos(\pi(K+L))\} \end{aligned} \quad (5.14)$$

Table 5.2 Summary of displacement vectors $\mathbf{d}_{m,ij}$ for each coordination shell m in each magnetic sublattice in CoO. All vectors were calculated using the VESTA visualisation software package [533]. Numbers in parentheses indicate statistical errors.

m	$\lvert\mathbf{d}_{m,ij}\rvert$ (Å)	Neighbours	$\mathbf{d}_{m,ij}$ in d-Sublattice (a)	$\mathbf{d}_{m,ij}$ in s-Sublattice (a)
1	3.0144(8)	12	$\left(-\frac{1}{2}\ -\frac{1}{2}\ 0\right)$ $\left(-\frac{1}{2} 0\ -\frac{1}{2}\right)$ $\left(0\ -\frac{1}{2}\ -\frac{1}{2}\right)$ $\left(0\ \frac{1}{2}\ \frac{1}{2}\right)$ $\left(\frac{1}{2}\ 0\ \frac{1}{2}\right)$ $\left(\frac{1}{2}\ \frac{1}{2}\ 0\right)$	$\left(0\ -\frac{1}{2}\ \frac{1}{2}\right)$ $\left(\frac{1}{2}\ -\frac{1}{2}\ 0\right)$ $\left(\frac{1}{2}\ 0\ -\frac{1}{2}\right)$ $\left(0\ \frac{1}{2}\ -\frac{1}{2}\right)$ $\left(-\frac{1}{2}\ \frac{1}{2}\ 0\right)$ $\left(-\frac{1}{2}\ 0\ \frac{1}{2}\right)$
2	4.2630(11)	6	$(-1\ 0\ 0)$ $(\ 0\ 0-1)$ $(\ 0-1\ 0)$ $(\ 1\ 0\ 0)$ $(\ 0\ 0\ 1)$ $(\ 0\ 1\ 0)$	
3	5.2211(13)	24	$\left(1\ -\frac{1}{2}\ \frac{1}{2}\right)$ $\left(1\ \frac{1}{2}\ -\frac{1}{2}\right)$ $\left(-1\ -\frac{1}{2}\ \frac{1}{2}\right)$ $\left(-1\ \frac{1}{2}\ -\frac{1}{2}\right)$ $\left(-\frac{1}{2}\ -1\ \frac{1}{2}\right)$ $\left(\frac{1}{2}\ -1\ -\frac{1}{2}\right)$ $\left(-\frac{1}{2}\ 1\ \frac{1}{2}\right)$ $\left(\frac{1}{2}\ 1\ -\frac{1}{2}\right)$ $\left(-\frac{1}{2}\ \frac{1}{2}\ 1\right)$ $\left(\frac{1}{2}\ -\frac{1}{2}\ 1\right)$ $\left(-\frac{1}{2}\ \frac{1}{2}\ -1\right)$ $\left(\frac{1}{2}\ -\frac{1}{2}\ -1\right)$	$\left(1\ -\frac{1}{2}\ -\frac{1}{2}\right)$ $\left(1\ \frac{1}{2}\ \frac{1}{2}\right)$ $\left(-1\ \frac{1}{2}\ \frac{1}{2}\right)$ $\left(-1\ -\frac{1}{2}\ -\frac{1}{2}\right)$ $\left(\frac{1}{2}\ -1\ \frac{1}{2}\right)$ $\left(-\frac{1}{2}\ -1\ -\frac{1}{2}\right)$ $\left(-\frac{1}{2}\ 1\ -\frac{1}{2}\right)$ $\left(\frac{1}{2}\ 1\ \frac{1}{2}\right)$ $\left(-\frac{1}{2}\ -\frac{1}{2}\ 1\right)$ $\left(\frac{1}{2}\ \frac{1}{2}\ 1\right)$ $\left(\frac{1}{2}\ \frac{1}{2}\ -1\right)$ $\left(-\frac{1}{2}\ -\frac{1}{2}\ -1\right)$
4	6.0288(15)	12		$(\ 1\ 0\ 1)$ $(\ 1\ 0-1)$ $(\ 1-1\ 0)$ $(\ 0-1\ 1)$ $(\ 0\ 1-1)$ $(-1\ 0\ 1)$ $(-1\ 1\ 0)$ $(\ 1\ 1\ 0)$ $(\ 0\ 1\ 1)$ $(\ 0-1-1)$ $(-1-1\ 0)$ $(-1\ 0-1)$

and

$$\begin{aligned} J_d(\mathbf{Q}) = 2J_{1AF}\{&\cos(\pi(H+K)) + \cos(\pi(K+L)) + \cos(\pi(L+H))\} \\ &+ 2J_{2AF}\left\{\cos(2\pi H) + \cos(2\pi K) + \cos(2\pi L)\right\} \\ &+ 2J_{3AF}\left\{\cos\left(\pi\left(2H-K+L\right)\right) + \cos\left(\pi\left(2H+K-L\right)\right)\right. \\ &+ \cos\left(\pi\left(-H-2K+L\right)\right) + \cos\left(\pi\left(H-2K-L\right)\right) \\ &\left.+ \cos\left(\pi\left(-H+K+2L\right)\right) + \cos\left(\pi\left(H-K+2L\right)\right)\right\}, \end{aligned} \quad (5.15)$$

for the s and d-sublattices, respectively. As an approximation, the exchange constants J_m used in this particular analysis were assumed to equal the experimentally determined exchange constants for $Co_{0.03}Mg_{0.97}O$ [3] as summarised in Tab. 5.3. It is also worth noting that the exclusive use of ferromagnetic and antiferromagnetic exchange constants in J_s and J_d, respectively, corresponds to the aforementioned approximation of the magnetic structure of CoO [82, 422, 438, 440, 441].

Table 5.3 Experimentally determined magnetic exchange constants $J_{m,n}$ for $Co_{0.03}Mg_{0.97}O$ [3]. Indices m and n denote the relative coordination shell and type of spin coupling, respectively. Labels AF and F for the index n denote antiferromagnetic ($J > 0$) and ferromagnetic ($J < 0$) coupling, respectively. Numbers in parentheses indicate statistical errors.

Exchange Constant	Experimental Value (meV)
J_{1AF}	1.000(8)
J_{1F}	−0.918(6)
J_2 or J_{2AF}	3.09(5)
J_{3AF}	0.258(1)
J_{3F}	−0.182(1)
J_{4AF}	0.0759(4)
J_{4F}	−0.0504(4)

After both the single-site susceptibility $g^{\alpha\beta}$ and the Fourier transform of the exchange interaction $J(\mathbf{Q})$ are calculated, one can utilise the definition [100, 515, 531, 534] that the sum of the Green's functions is proportional to the generalised susceptibility χ, given by

$$\chi(\mathbf{Q}, E) = -g_J^2 \mu_B^2 G(\mathbf{Q}, E), \quad (5.16)$$

where g_J and μ_B is the Landé g-factor and Bohr magneton, respectively, and

$$G(\mathbf{Q}, E) \equiv \sum_{ij} G_{ij}(\mathbf{Q}, E) = G_{11}(\mathbf{Q}, E) + G_{12}(\mathbf{Q}, E) + G_{21}(\mathbf{Q}, E) + G_{22}(\mathbf{Q}, E). \tag{5.17}$$

It should be noted that the negative sign in Eq. 5.16 is due to the definition of $E = E + i\Delta$ in Eq. 5.10. The presence of $+i\Delta$ in the denominator for both terms of Eq. 5.10 corresponds to the retarded response function, implying that all poles for both excitations and their corresponding holes lie within the lower half of the complex plane [531, 532, 535, 536].

Finally, by the fluctuation-dissipation theorem [107], one can convert the Green's functions *via* Eq. 5.16 to the dynamic structure factor $S(\mathbf{Q}, E)$ by

$$S(\mathbf{Q}, E) \propto -|f(\mathbf{Q})|^2 Im\left\{G(\mathbf{Q}, E)\right\}, \tag{5.18}$$

since the Bose factor $[n(E)+1]$ is set to 1 in the limit of 0 K [100].

Transverse & Longitudinal Mode Coupling

Despite several decades of investigation, the magnetic structure of CoO remains controversial [82, 440, 537–539], with some claiming that CoO may assume a non-collinear magnetic structure [83, 441] instead of the initially proposed type-II collinear antiferromagnetic structure [422, 438]. The presence of non-collinear magnetic ordering would suggest the possibility of coupling between longitudinal and transverse modes [540–543], a possibility that will be later employed to address the high energy continuum at the magnetic zone boundaries. Before proceeding, two important assumptions must be made clear. Firstly, the analysis presented so far is based on the assumption that CoO exhibits type-II collinear antiferromagnetic order and thus assumes a lack of non-collinearity. Consequently, any coupling applied to the modes calculated using Eq. 5.9 must be treated as simply an approximation, and ultimately speculative. Secondly, the longitudinal-transverse coupling was assumed to be applicable to single-quasiparticle modes, instead of coupling between single and multi-quasiparticle modes [542–546]. A subtle, but very important distinction that will be later addressed. Inspired by the work of Wehner on coupled phonons [547, 548], such

longitudinal-transverse mode coupling was approximated by

$$\widetilde{G}_{ij}(\mathbf{Q},E) = \delta_{ij}G_i(\mathbf{Q},E) + \sum_{k=\pm1} G_i(\mathbf{Q},E)\Pi_{i,i+k}\widetilde{G}_{i+k,j}(\mathbf{Q},E), \tag{5.19}$$

where G_i, $\widetilde{G}_{ij}$ and Π_{ij} denote the Green's functions derived from coupling single-site response functions in Eq. 5.9, the Green's function coupling i^{th} and j^{th} Green's functions and the coupling constant between i^{th} and j^{th} Green's functions, respectively. As a first approximation, all coupling constants Π_{ij} were fixed to be a positive real value equal to $J_2 \sim 4.1$ meV [3] which specifies the maximum energy scale in CoO. Indices i and j assume either values 1 to 3 corresponding to

$$G_1(\mathbf{Q},E) = G^{+-}(\mathbf{Q},E) \tag{5.20a}$$
$$G_2(\mathbf{Q},E) = G^{zz}(\mathbf{Q},E) \tag{5.20b}$$
$$G_3(\mathbf{Q},E) = G^{-+}(\mathbf{Q},E). \tag{5.20c}$$

The sum in Eq. 5.19 was limited to indices $k = \pm1$ to ensure coupling up to first order was between only longitudinal and transverse Green's functions exclusively [531], yielding nine coupled linear equations:

$$\widetilde{G}_{11}(\mathbf{Q},E) = G_1(\mathbf{Q},E) + G_1(\mathbf{Q},E)\Pi_{12}\widetilde{G}_{21}(\mathbf{Q},E) \tag{5.21a}$$
$$\widetilde{G}_{21}(\mathbf{Q},E) = G_2(\mathbf{Q},E)\Pi_{21}\widetilde{G}_{11}(\mathbf{Q},E) \tag{5.21b}$$
$$\widetilde{G}_{22}(\mathbf{Q},E) = G_2(\mathbf{Q},E) + G_2\Pi_{21}\widetilde{G}_{12}(\mathbf{Q},E) \tag{5.21c}$$
$$\widetilde{G}_{12}(\mathbf{Q},E) = G_1(\mathbf{Q},E)\Pi_{12}\widetilde{G}_{22}(\mathbf{Q},E), \tag{5.21d}$$
$$\widetilde{G}_{33}(\mathbf{Q},E) = G_3(\mathbf{Q},E) + G_3(\mathbf{Q},E)\Pi_{32}\widetilde{G}_{23}(\mathbf{Q},E) \tag{5.21e}$$
$$\widetilde{G}_{31}(\mathbf{Q},E) = G_3(\mathbf{Q},E)\Pi_{32}\widetilde{G}_{21}(\mathbf{Q},E) \tag{5.21f}$$
$$\widetilde{G}_{32}(\mathbf{Q},E) = G_3(\mathbf{Q},E)\Pi_{32}\widetilde{G}_{22}(\mathbf{Q},E) \tag{5.21g}$$
$$\widetilde{G}_{13}(\mathbf{Q},E) = G_1(\mathbf{Q},E)\Pi_{12}\widetilde{G}_{23}(\mathbf{Q},E) \tag{5.21h}$$
$$\widetilde{G}_{23}(\mathbf{Q},E) = G_2(\mathbf{Q},E)\Pi_{23}\widetilde{G}_{33}(\mathbf{Q},E) + G_2(\mathbf{Q},E)\Pi_{21}\widetilde{G}_{13}(\mathbf{Q},E). \tag{5.21i}$$

Through some algebraic manipulation, the coupled Green's functions $\tilde{G}_{ij}$ can be rewritten in terms of the G_i derived from the single-site response functions, as

summarised by:

$$\widetilde{G}_{11}(\mathbf{Q},E) = \frac{G_1(\mathbf{Q},E)}{1 - G_1(\mathbf{Q},E)G_2(\mathbf{Q},E)\Pi_{12}\Pi_{21}} \tag{5.22a}$$

$$\widetilde{G}_{22}(\mathbf{Q},E) = \frac{G_2(\mathbf{Q},E)}{1 - G_2(\mathbf{Q},E)G_1(\mathbf{Q},E)\Pi_{12}\Pi_{21}}, \tag{5.22b}$$

$$\widetilde{G}_{23}(\mathbf{Q},E) = \frac{G_2(\mathbf{Q},E)\Pi_{23}G_3(\mathbf{Q},E)}{1 - G_2(\mathbf{Q},E)\Pi_{23}G_3(\mathbf{Q},E)\Pi_{32} - G_2(\mathbf{Q},E)\Pi_{21}G_1(\mathbf{Q},E)\Pi_{12}}. \tag{5.22c}$$

After mode coupling is performed, one can once again utilise Eq. 5.16 with

$$\begin{aligned} G(\mathbf{Q},E) \equiv \sum_{ij} \widetilde{G}_{ij}(\mathbf{Q},E) = \widetilde{G}_{11}(\mathbf{Q},E) + \widetilde{G}_{12}(\mathbf{Q},E) + \widetilde{G}_{22}(\mathbf{Q},E) \\ + \widetilde{G}_{21}(\mathbf{Q},E) + \widetilde{G}_{33}(\mathbf{Q},E) + \widetilde{G}_{31}(\mathbf{Q},E) \\ + \widetilde{G}_{32}(\mathbf{Q},E) + \widetilde{G}_{13}(\mathbf{Q},E) + \widetilde{G}_{23}(\mathbf{Q},E), \end{aligned} \tag{5.23}$$

and Eq. 5.18 to calculate the dynamic structure factor $S(\mathbf{Q},E)$ [100, 107, 515, 536].

Analysis Algorithm

The total analysis algorithm is presented in Fig. 5.3 and consists of two (or three) connected sections: (i) statement of parameters defining the coupling of $g^{\alpha\beta}$, (ii, optional) the coupling of $G^{\alpha\beta}$, and (iii) the calculation of $S(\mathbf{Q},E)$.

The first portion of the analysis is centred on the calculation of $G^{\alpha\beta}(\mathbf{Q},E)$, quantifying the coupling of the single-site susceptibility terms. As summarised by Eq. 5.9, $G^{\alpha\beta}(\mathbf{Q},E)$ is a function of the single-site susceptibility $g^{\alpha\beta}(E)$ and the Fourier transform of the exchange interactions $J_\xi(\mathbf{Q})$, providing the E and $\mathbf{Q}$-dependence, respectively. With the combination of the $T = 0$ K and cubic approximations, the single-ion Hamiltonian $\hat{\mathcal{H}}_{S.I.}$ (Eq. 5.11), and thus $g^{\alpha\beta}$ (Eq. 5.10) has only one free parameter, the molecular field strength H_{MF}. While the aforementioned approximation of the magnetic structure as (111) sheets [82, 422, 438, 440, 441], combined with the approximation that the

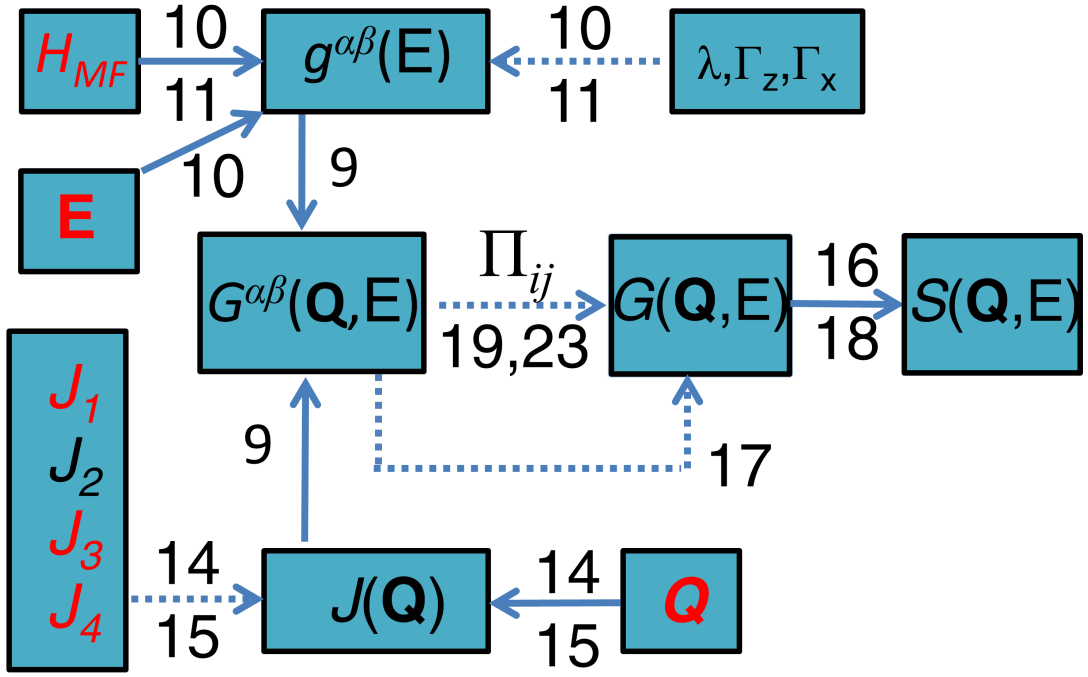

Figure 5.3 Pictorial schematic of the analysis algorithm. Input variables are denoted by red, whilst each number corresponds to the relevant equation in the text. Dashed lines indicate alternative routes in the analysis algorithm.

exchange constants are equal to those measured for $Co_xMg_{1-x}O$ [3] in Chapter 4, results in $J_\xi(\mathbf{Q})$ possessing no free parameters.

In the event that such restrictions on both $g^{\alpha\beta}$ and $J_\xi(\mathbf{Q})$ would result in the failure of the model to capture the magnetic excitations, an alternative algorithm was simultaneously developed. The modified algorithm defined the parameters λ, Γ_z and Γ_x as input variables, and thus allowed to vary. Secondly, the alternative algorithm defined $J_\xi(\mathbf{Q})$ in terms of four free parameters J_m corresponding to the four respective coordination shells for a particular sublattice ξ. Such a definition is the simplest deviation away from the intrinsic restrictions of the aforementioned approximation of the magnetic structure [82, 422, 438, 440, 441], and consists of $J(\mathbf{Q})$ being a function of the same four exchange constants J for both ξ=s or d. In other words, for a particular coordination shell m, the exchange constant was assumed to be identical in both sub-lattices. As summarised by Figs. 4.4 and 4.9 in Chapter 4, neutron spectroscopic measurements on $Co_{0.03}Mg_{0.97}O$ [3] revealed that each coordination shell, with the exception of the second, exhibits both antiferromagnetic and a weaker ferromagnetic exchange coupling. Such dual behaviour is a reflection of the t_{2g} degeneracy of the high spin d^7 configuration of Co^{2+}, and thus a particular choice of J, be it antiferromagnetic or ferromagnetic, corresponds to a specific local orbital arrangement. Consequently, the calculation

of $G^{\alpha\beta}$ *via* Eq. 5.9 was performed eight times, corresponding to the number of different combinations for the values of J in the definition of $J(\mathbf{Q})$ in Eq. 5.13, since three out of the four J_m parameters was free to assume either the ferromagnetic or antiferromagnetic values measured for $Co_{0.03}Mg_{0.97}O$ [3]. Since each particular combination corresponds to a particular orbital arrangement and each arrangement can be physically interpreted as a particular physical pathway in the lattice, it was expected that the molecular field for each orbital arrangement would differ from one another. To reflect different physical pathways, the molecular field strength given by H_{MF} for each combination of J was allowed to vary from its mean field estimate of 64.8(9) meV, a value derived from the experimentally determined Curie-Weiss temperature of -330 K [474, 475]. Consequently, by specifying a particular combination of J and its corresponding molecular field strength H_{MF}, $G^{\alpha\beta}$ was calculated *via* Eq. 5.9 for a particular $\alpha\beta = +-$, $-+$ and zz.

The second optional portion of the analysis algorithm consists of coupling $G^{\alpha\beta}$ as a speculative attempt to address the breakdown of sharp spin waves at high energy transfers. For each combination of exchange constants J, the Green's functions $G^{\alpha\beta}$ were coupled utilising Eq. 5.19 [547, 548]. Consequently, for a particular J combination and its corresponding H_{MF} value, the sum of $\widetilde{G}_{ij}$ or G_{ij} over all ij combinations was calculated *via* Eqs. 5.22 or 5.17 for the case when coupling was included or excluded, respectively, both yielding $G(\mathbf{Q}, E)$ which is directly proportional to the generalised susceptibility χ *via* Eq. 5.16 [515, 536].

The third and final portion consists of converting $G(\mathbf{Q}, E)$ for a particular combination of J and corresponding H_{MF} to the dynamic structure factor $S(\mathbf{Q}, E)$ *via* Eq. 5.18 [100, 107]. All three portions of the analysis algorithm outlined above were repeated for all eight combinations of exchange constants and their corresponding values for H_{MF}. The algorithm was performed repeatedly for a least squares refinement of the H_{MF} values.

5.4 Results & Discussion

5.4.1 Experimental Data

Having described the analysis algorithm, a summary of the experimental data is now presented in Fig. 5.4. As illustrated in Figs. 5.4(a) and (b), ($\mathbf{Q}$,E) slices in the $\left(\frac{3}{2}, \frac{3}{2}, L\right)$ and $(2, 2, L)$ planes exhibit contrasting low energy

profiles in the Néel state. The former exhibits a complex fine structure at the magnetic zone centres consisting of four (or more) excitations (Figs. 5.4(c,d)) that are replaced by energy and momentum broadened excitations at higher energy transfers. In contrast, no such structure exists for the latter, which exhibits strong magnetic scattering consisting of multiple energy and momentum broadened excitations over the entire dynamic range centred at the zone boundaries (Fig. 5.4(e)), both in agreement with a myriad of spectroscopy measurements spanning decades [422, 424, 444, 469, 472, 473, 508, 509]. Whereas the broad excitations at the zone boundaries have been well-documented since the first neutron spectroscopy measurements by Sakurai [444], the fine structure at the zone-centres was only recently fully characterised by Yamani, Buyers, Cowley & Prabhakaran [422], while its replacement by energy and momentum broadened excitations has yet to be reported.

Although there are key similarities between the current data and previous measurements in the literature, it is important to note two key differences at the magnetic zone centres. The first difference pertains to the physical origin of the lowest energy excitation centred at ∼18 meV. Whereas previous measurements [422] claimed that the majority, if not all of the intensity of the lowest energy excitation could be attributed to coherent phonon scattering, the **Q**-dependence of the fine structure presented in Fig. 5.4(c) suggests that the excitation in question possesses a significant magnetic contribution with only minor phonon contributions from the aluminium sample can. The second difference pertains to the width of the highest energy mode. Whereas previous studies [422] measured an excitation centred at ∼41 meV that was much broader than both instrumental resolution and the widths of all the other excitations constituting the fine structure, the current data instead consists of one resolution-limited excitation centred at ∼37 meV. Both differences in peak width and centre can be quickly accounted for by noting the energy-transfer of the particular peak of interest overlaps a region of spurious signal on $C5$ due to $\frac{\lambda}{2}$ contamination [100]. Such a spurious contribution in previous measurements would provide a natural explanation for both the absence of such broadness in the current data and the shift in the peak centre to a lower energy value in agreement with optical measurements [469, 509], thus casting significant doubt on the previous assignment [422] of a spin-orbiton excitation to the highest energy excitation.

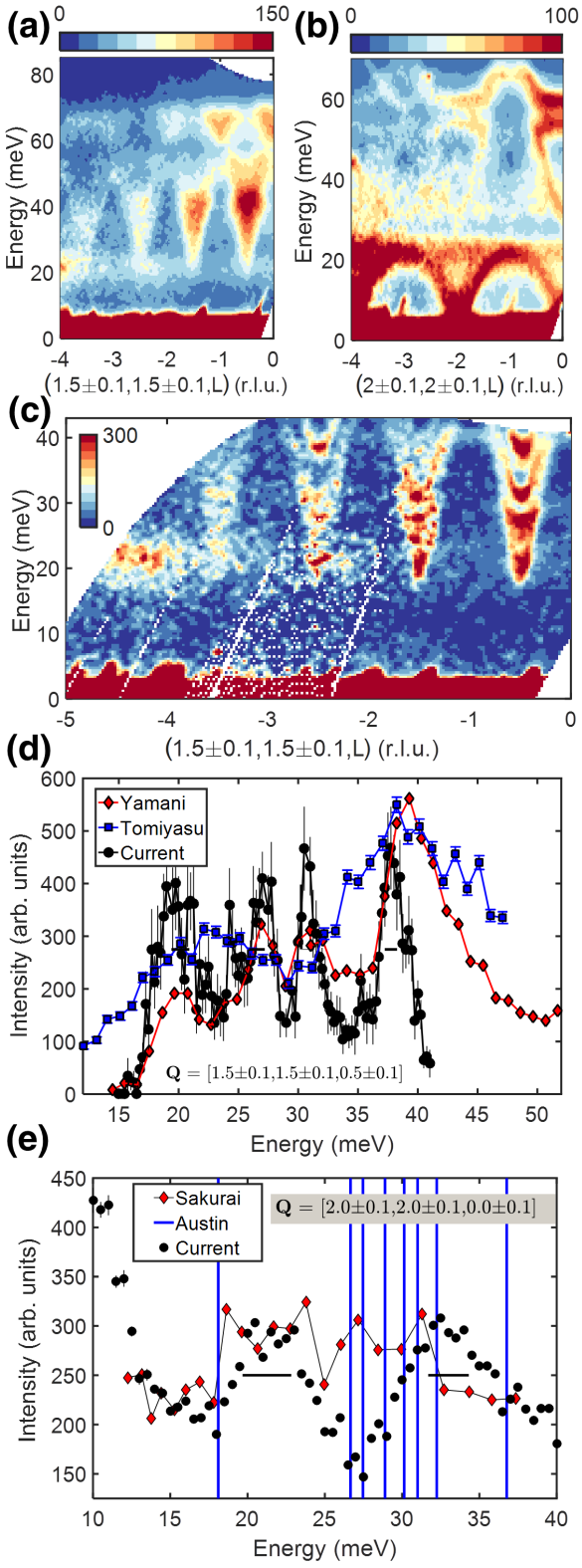

Figure 5.4 (**Q**,E) slices of CoO measured on MERLIN at 5 K with an E_i of (a) 110 meV, (b) 75 meV and (c) 45 meV. All (**Q**,E) slices have been folded along [001]. A comparison of constant-**Q** cuts of (c) and (b) with previous measurements in the literature at the (d) magnetic zone centres [422, 424] and (e) magnetic zone boundaries [444], respectively. Solid lines in (e) indicate the location of excitations previously determined by IR spectroscopy [509]. Horizontal bars indicate instrumental resolution.

The rich low energy excitation spectrum below T_N is in stark contrast with the behaviour of other Co^{2+}-based magnets such as CoF_2 [549] and $KCoF_3$ [20] that exhibit multiple sharp magnon branches. As alluded to in the introductory remarks, such contrasting behaviour from the latter Co^{2+}-based compounds is a consequence of the comparable energy scales of far reaching magnetic exchange and spin-orbit coupling in CoO [18, 20, 47, 76, 341, 422, 424, 444]. The combination of these two distinct contributions, possibly further compounded by significant structural distortions [82, 424, 440, 441], has resulted in confusion as to the choice of the proper Hamiltonian and thus ultimately a poor understanding of the low energy dynamics in the Néel state.

5.4.2 Comparison of Experimental Data and Calculated Models

Having presented the experimental data, a comparison is now presented to the calculated model assuming: (i) the magnetic exchange constants for each coordination shell were equal to the values obtained for $Co_{0.03}Mg_{0.97}O$ [3] (Tab. 5.3), (ii) $J_s(\mathbf{Q})$ (Eq. 5.14) and $J_d(\mathbf{Q})$ (Eq. 5.15) utilised exclusively ferromagnetic and antiferromagnetic exchange constants, respectively, and (iii) the mean field strength parameter H_{MF} was fixed to 65 meV. The value of 65 meV for H_{MF} was determined by noting that the mean field expression $H_{MF} = 2\langle \hat{S}_z \rangle zJ$, corresponding to Eq. J.4 reduced over one coordination shell. Since the product zJ in H_{MF} also parametrises the mean-field definition of the Curie-Weiss temperature $\theta_{\mathrm{CW}} = \frac{-2S(S+1)zJ}{3\xi}$, the value of H_{MF} was determined directly from the experimentally determined θ_{CW} of -330 K [474, 475].

As summarised by Figs. 5.5(a) and (b), the calculated model fails to capture all major features of the experimental data at both the zone centres and boundaries. Whereas the former exhibits only one magnetic excitation at select zone centres (*e.g.* $\left(\frac{3}{2}, \frac{3}{2}, \frac{3}{2}\right)$) *in lieu* of four (or more) as described in Figs. 5.4(a) and (c), the latter exhibits no magnetic excitations whatsoever instead of the multiple peaks that are observed experimentally, as shown in Figs. 5.4(b) and 5.5(f). In fact, the lack of intensity at particular zone centres (*e.g.* $\left(\frac{3}{2}, \frac{3}{2}, \frac{1}{2}\right)$) suggests that the initial estimate of H_{MF} used in the single-ion Hamiltonian $\hat{\mathcal{H}}_{S.I.}$ (Eq. 5.11) is not large enough to allow the magnon branches to connect in a dynamic range of positive energy transfers, thus causing a clear instability. As illustrated in Fig. 5.5(c), the value of H_{MF} must be significantly greater than 100 meV to have

a magnetic excitation in the desired dynamic range at the zone centres originally lacking intensity. Figs. 5.5(c,e) and (d,f) demonstrate that despite the use of a physically unrealisable value of H_{MF}, the model once again fails in a similar manner as the original calculations in Figs. 5.5(a) and (b). Whereas the calculated model once again predicts no intensity at the zone boundaries, the location of the magnetic modes at the zone centres depend on the value of L, in contrast to what is experimentally observed [422, 424, 444, 509]. The failure of such a model presented above is not particularly surprising. Such a conclusion can be readily obtained by noting that the spin-spin interactions are based on orbital overlap, must possess time reversal symmetry or T-symmetry. By noting that the reversal of time would essentially flip which spins belong to the s and d sublattices, then it must hold that $J_{s,m} = J_{d,m}$, for all coordination shells m.

As an attempt to account for the clear discrepancies between the calculated model and the data, the definitions of both $J_s(\mathbf{Q})$ and $J_d(\mathbf{Q})$ were modified. As discussed in §5.3, instead of utilising the common approximation of the magnetic structure of CoO as antiferromagnetically coupled ferromagnetic (111) sheets [82, 422, 438, 440, 441], it was assumed that for each coordination shell m, the exchange constants were equal in the expressions for both $J_s(\mathbf{Q})$ and $J_d(\mathbf{Q})$. A consequence of the removal of both restrictions of $J_{s,m} < 0$ and $J_{d,m} > 0$ for all m is an inherent ambiguity in which exchange constants of $Co_{0.03}Mg_{0.97}O$ from Tab. 5.3 should be used in $J(\mathbf{Q})$. Such an ambiguity follows from the observation that, with the exception of the $m = 2$, each coordination shell has both an antiferromagnetic and weaker ferromagnetic option available [3], yielding $2^3 = 8$ unique arrangements of exchange constants over four coordination shells. Another, albeit related consequence of the removal of the aforementioned restrictions on $J(\mathbf{Q})$ is an inherent ambiguity of the value of the mean field strength parameter H_{MF}. Such ambiguity stems from the deduction that the presence of both antiferromagnetic and ferromagnetic exchange couplings is a direct consequence of the orbital degree of freedom of Co^{2+}, with each choice of J, be it ferromagnetic or antiferromagnetic, corresponding to a particular t_{2g}-t_{2g} configuration, and thus a particular orbital arrangement [3, 53, 54, 56, 57]. Such individual arrangements could be physically interpreted as particular physical pathways in the CoO lattice and thus it would be expected that the molecular field would differ from one unique arrangement to another. Consequently, as discussed in §5.3, the molecular field strength parameter H_{MF} for all eight arrangements was allowed to deviate from the original estimate of 64.8(9) meV as deduced from the experimental value of θ_{CW} [474, 475].

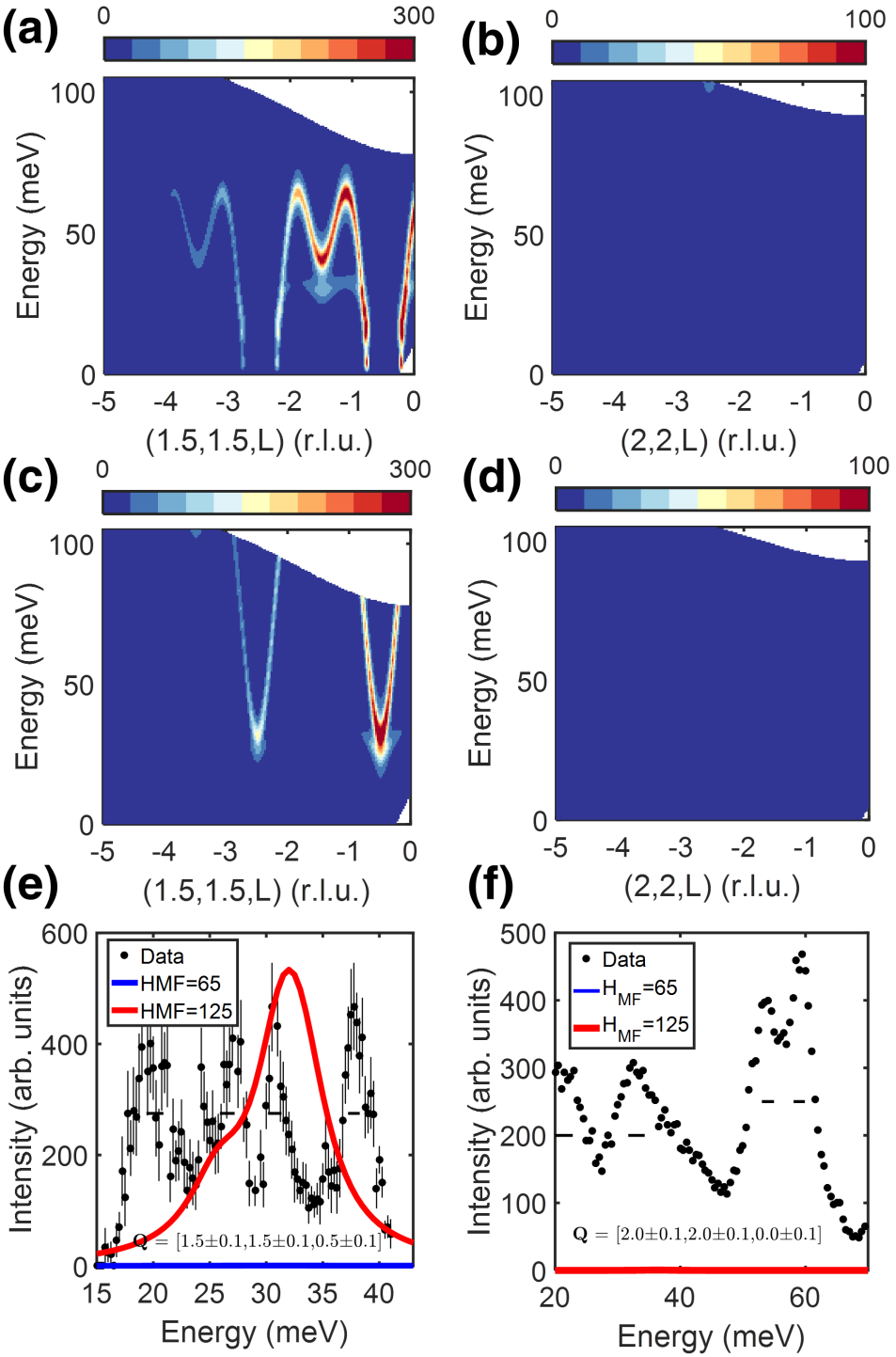

Figure 5.5 Calculated (**Q**,E) slices for an E_i=110 meV with a molecular field contribution H_{MF} of (a,b) 65 meV and (c,d) 125 meV in Eq. 5.11. (e,f) A comparison of measured and calculated constant-**Q** cuts. All calculations assumed the exclusive use of ferromagnetic and antiferromagnetic exchange constants (Tab. 5.3) in J_s (Eq. 5.14) and J_d (Eq. 5.15), respectively. Horizontal bars for constant-**Q** cuts indicate experimental resolution.

As illustrated in Fig. 5.6, a least squares optimisation of the H_{MF} parameter in Eq. 5.9 at the zone centre $\left(\frac{3}{2}, \frac{3}{2}, \frac{1}{2}\right)$ incorporating all eight possible arrangements of exchange constants from Tab. 5.3 in $J(\mathbf{Q})$ (Eqs. 5.14 and 5.15) successfully captured the fine structure at low energy transfers at the zone centres, with only minor deviations being caused by an overestimation of the transverse G^{+-} mode. The refined values for H_{MF} are summarised in Tab. 5.4. The eight values vary from 64.3(1) to 75.5(1) meV, representing a maximum deviation of 8.6(1)% from the average H_{MF} value of 69.53(4) meV, a value within 7.3(1)% to the mean field estimate of 64.8(9) meV [474, 475]. The discrepancy between the average of the refined H_{MF} values and the mean field estimate may be accounted for by noting that the mean field treatment assumes a collinear arrangement of magnetic moments [37]. Recall that the removal of the restrictions on $J(\mathbf{Q})$ in both Eqs. 5.14 and 5.15 corresponds to the removal of the assumption of collinearity in the Néel state. Therefore, a small deviation in the calculated model from the mean field estimate is not completely unexpected, but instead may support the numerous suggestions in the literature that CoO assumes a non-collinear magnetic structure [83, 441, 537, 538, 550].

Table 5.4 Refined mean field strength parameter H_{MF} in the single-ion Hamiltonian $\hat{\mathcal{H}}_{S.I.}$ for eight different orbital arrangements in CoO. Each arrangement corresponds to a different combination of magnetic exchange constants $J_{m,n}$ and is denoted by four letters. Each letter represents the type of coupling n, either antiferromagnetic (A) or ferromagnetic (F), present in each coordination shell m, from the first (far left) to the fourth (far right). Numbers in parentheses indicate statistical errors.

Combination of Exchange Constants	Refined/Calculated Value (meV)
AAAA	74.9(1)
AAFA	75.5(1)
FAFA	69.0(1)
FAAA	69.4(1)
AAAF	66.4(1)
AAFF	65.2(1)
FAAF	71.5(1)
FAFF	64.3(1)
Average	69.53(4)
Mean field estimate	64.8(9)

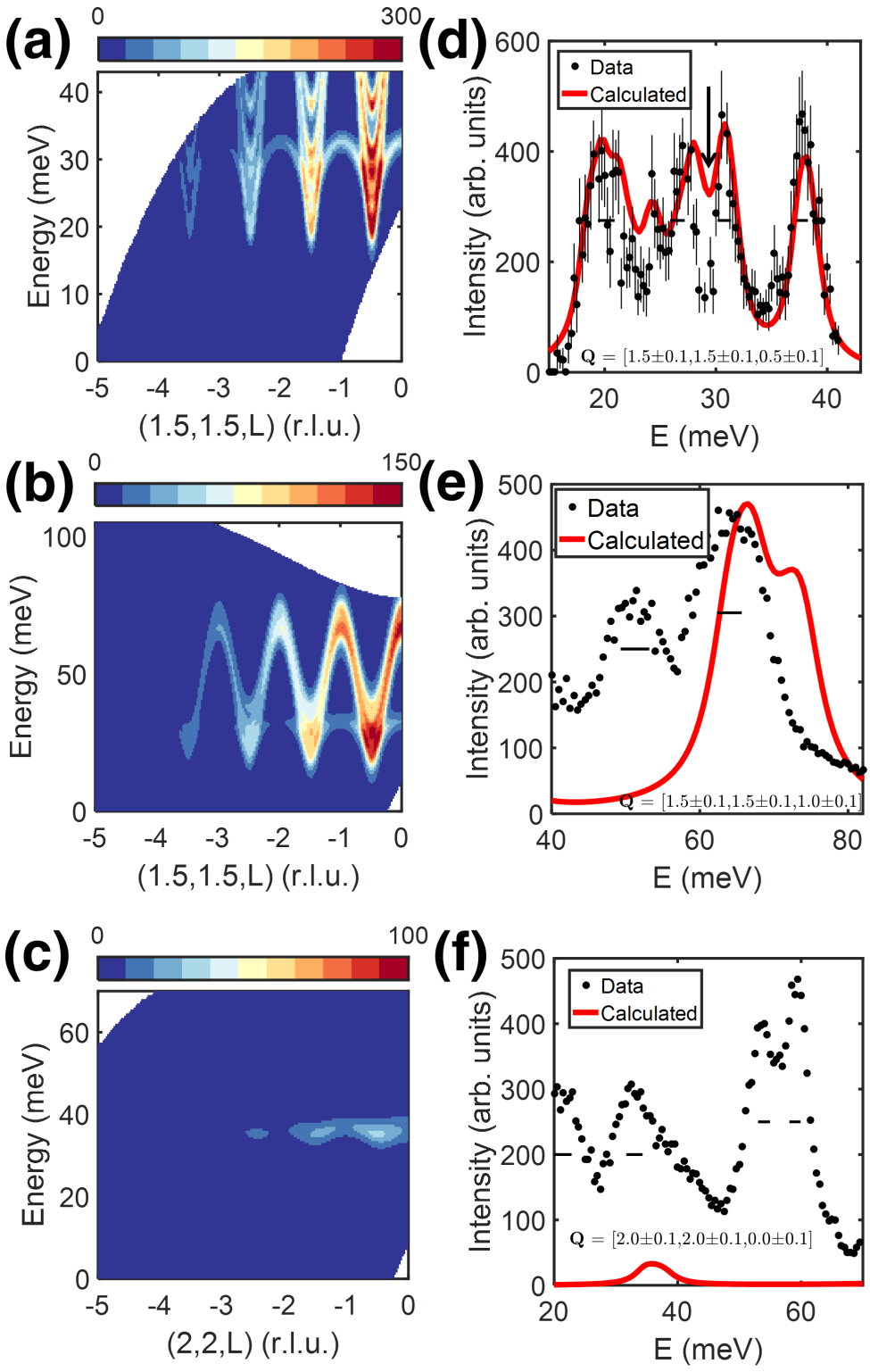

Figure 5.6 Calculated (**Q**,E) slices for an E_i of (a) 45 meV, (b) 110 meV and (c) 70 meV. (d-f) Comparison of measured (5 K) and calculated constant-**Q** cuts of (a-c). The corresponding exchange constants for a particular coordination shell m in both J_s and J_d were assumed to be equal to one another and equal to the values summarised in Tab. 5.3. Horizontal bars for constant-**Q** cuts indicate experimental resolution. Arrow in panel (d) indicates the overestimated G^{+-} mode.

Despite the success of the calculated model to capture the fine structure at the zone centres (Figs. 5.6 (a) and (d)), the calculated model ultimately fails at magnetic zone boundaries. Constant-**Q** cuts at the zone boundaries (Figs. 5.6 (e) and (f)) reveal that while the calculated model does successfully predict the presence of two peaks at $\left(\frac{3}{2}, \frac{3}{2}, 1\right)$, both peaks are much sharper and their centre-of-masses are shifted to much higher energy transfers than what is experimentally observed. In contrast, the calculated model predicts no significant intensity, with an exception of a weak mode at ∼30 meV [18, 422, 424] corresponding to the G^{+-} mode in Eq. 5.9, for all energy transfers in the $(2, 2, L)$ plane.

The discrepancies between the experimental data and the calculated model at the $\left(\frac{3}{2}, \frac{3}{2}, L\right)$ zone boundaries will now be addressed. As illustrated in Fig. 5.6, the calculated model describes the magnetic scattering at the zone boundaries in the $\left(\frac{3}{2}, \frac{3}{2}, L\right)$ plane as a sum of resolution-limited spin waves, whose centre-of-masses are determined by the mean field strength parameter H_{MF}. Utilising the algorithm described in §5.3, the value of the H_{MF} parameter is determined by the dispersion of the spin waves into the zone centres. In other words, since the calculated model predicts a trough at the zone boundaries, the values of H_{MF} are ultimately determined by any parameter that affects the location in energy of the trough. Perhaps the most natural dispersion parameter is the magnetic exchange constant J in Eqs. 5.14 and 5.15. Inserting exchange constants with larger magnitudes results in sharper spin waves with troughs located at lower energy transfers, thus requiring larger H_{MF} values to position the magnetic excitations in the dynamic range overlapping the fine structure introduced in Fig. 3.5. As illustrated in Figs. 5.5(a) and (b), if the value of H_{MF} is smaller than a particular value for a specific set of magnetic exchange constants, a trough may be completely absent due to the inability of the calculated spin waves to connect at positive energy transfers leading an instability.

The significant shift of the centre-of-masses at the zone boundaries in the $\left(\frac{3}{2}, \frac{3}{2}, L\right)$ plane towards higher energy transfers with a correspondingly larger value of H_{MF} relative to mean field predictions both suggest that the magnetic exchange constants used in the original calculations are overestimated and cannot simply be attributed to normalisation effects for the breakdown of spin waves into multiparticle states [551–553] that will be discussed later. In an attempt to investigate such a possibility, all magnetic exchange constants in Tab. 5.3 were reduced by 20%. It could be argued that such a deviation is a consequence of the fact that the exchange constants in Tab. 5.3 correspond to those in $Co_{0.03}Mg_{0.97}O$ and are simply estimates of those in CoO. As illustrated in

Fig. 5.7, a least squares optimisation of Eq. 5.9 at the zone centre $\left(\frac{3}{2}, \frac{3}{2}, \frac{1}{2}\right)$ incorporating all eight possible arrangements of the reduced exchange constants in $J(\mathbf{Q})$ (Eqs. 5.14 and 5.15) successfully captured the fine structure at low energy transfers at the zone centres but once again, the G^{+-} mode is overestimated. The refined values for H_{MF} are summarised in Tab. 5.5. As predicted, the eight values exhibited a significant decrease from those H_{MF} values calculated in Tab. 5.4 utilising the original model. The decreased values vary from 53.1(1) to 65.55(3) meV, representing a maximum deviation of 11.8(1)% from the average H_{MF} value of 60.16(2) meV, a value within 7.2(1)% to the mean field estimate of 64.8(9) meV [474, 475]. Despite the shift of the centre-of-masses of the two peaks at $\left(\frac{3}{2}, \frac{3}{2}, 1\right)$ (Fig. 5.7(f)) to lower energy transfers, the calculated model once again fails to account both for the large broadness in $\left(\frac{3}{2}, \frac{3}{2}, L\right)$ plane and the magnetic scattering intensity in the $(2, 2, L)$ plane.

Table 5.5 Refined mean field strength parameter H_{MF} in the single-ion Hamiltonian $\hat{\mathcal{H}}_{S.I.}$ for eight different orbital arrangements in CoO utilising exchange constants J that are 80% of the values reported for $Co_{0.03}Mg_{0.97}O$ [3]. Each arrangement corresponds to a different combination of magnetic exchange constants $J_{m,n}$ and is denoted by four letters. Each letter represents the type of coupling n, either antiferromagnetic (A) or ferromagnetic (F), present in each coordination shell m, from the first (far left) to the fourth (far right). Numbers in parentheses indicate statistical errors.

Combination of Exchange Constants	Refined/Calculated Value (meV)
AAAA	65.55(3)
AAFA	64.45(5)
FAFA	63.85(4)
FAAA	58.88(6)
AAAF	61.75(4)
AAFF	59.15(5)
FAAF	54.55(4)
FAFF	53.1(1)
Average	60.16(2)
Mean field estimate	64.8(9)

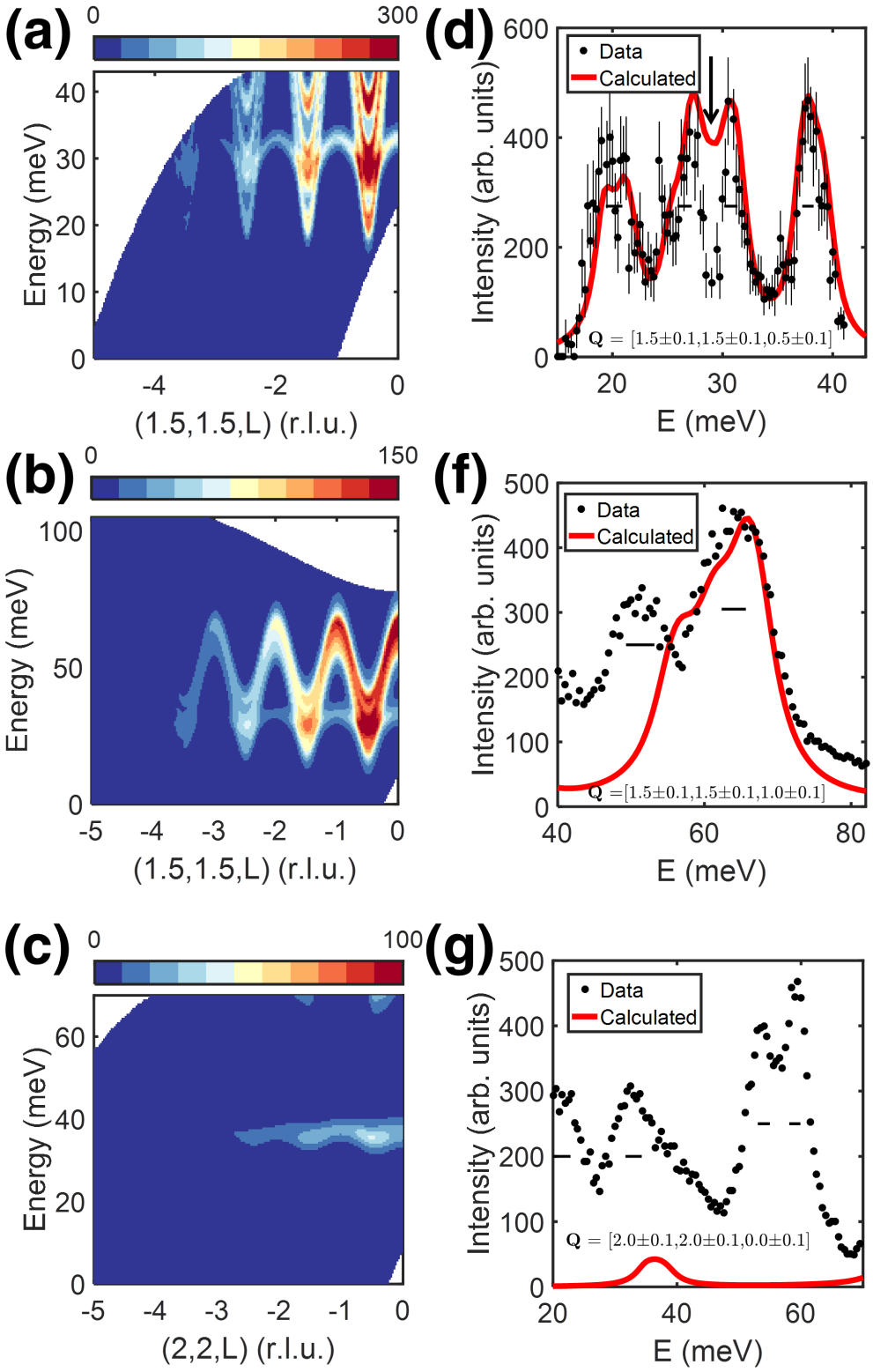

Figure 5.7 Calculated (**Q**,E) slices for an E_i of (a) 45 meV, (b) 110 meV and (c) 70 meV. (d-f) Comparison of measured (5 K) and calculated constant-**Q** cuts of (a-c). The corresponding exchange constants for a particular coordination shell m in both J_s (Eq. 5.14) and J_d (Eq. 5.15) were assumed to be equal to one another and equal to 80% of the values summarised in Tab. 5.3. Horizontal bars for constant-**Q** cuts indicate experimental resolution. Arrow in panel (d) indicates the overestimated G^{+-} mode.

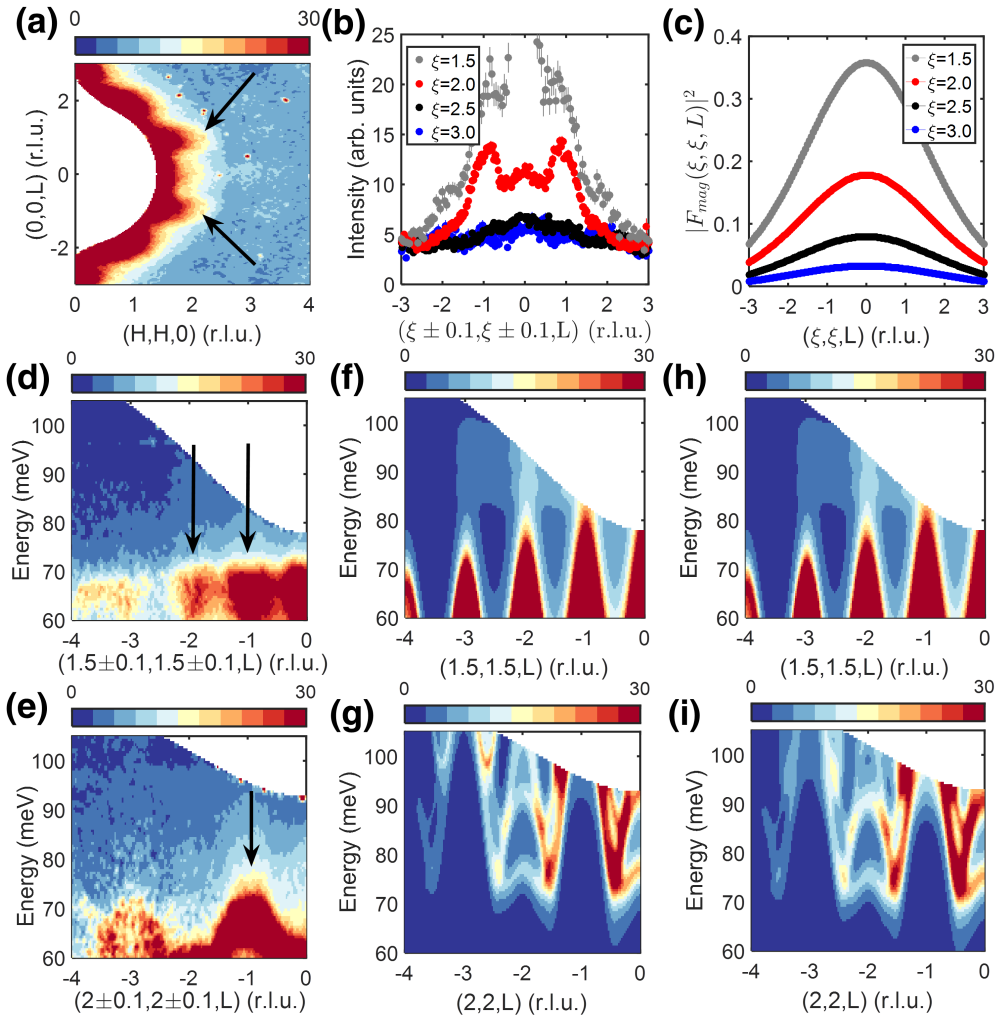

Figure 5.8 (a) Constant-energy (E=[70,105] meV) slice at 5 K with an E_i=110 meV. (b) Constant-energy cuts of (a) revealing a strong magnetic response at $L = \pm 1$. (c) **Q**-dependence of the Co^{2+} magnetic form factor squared. A comparison of (d,e) measured (E_i=110 meV, 5 K) and their corresponding calculated (**Q**,E) slices (f,g) excluding and (h,i) including longitudinal-transverse mode coupling. Arrows in (d,e) indicate steeply dispersive energy and momentum broadened excitations.

Motivated by the failure of the model to account for the replacement of sharp spin waves by energy and momentum broadened excitations at high energy transfers at the zone boundaries of the $\left(\frac{3}{2},\frac{3}{2},L\right)$ plane, the (H,H,L) plane was energy-integrated at high energy transfers (E=[70,105] meV). As illustrated in Fig. 5.8(a), there exists a distinct signal at $L = \pm 1$ that was confirmed by constant-**Q** cuts (Fig. 5.8(b)) to exhibit a form factor-like **Q**-dependence (Fig. 5.8(c)). (**Q**,E) slices in both the $\left(\frac{3}{2},\frac{3}{2},L\right)$ (Fig. 5.8(d)) and $(2,2,L)$ (Fig. 5.8(e)) planes, revealed that the strong magnetic signal corresponds to steeply dispersive energy and momentum broadened excitations, confirming

previous measurements on polycrystalline samples [18]. While the calculated model successfully predicts both the presence and location of the columns of magnetic scattering in the $\left(\frac{3}{2},\frac{3}{2},L\right)$ plane (Figs. 5.8(f)), it ultimately fails to account for the large broadening in both momentum and energy (Fig. 5.7(f)). In contrast, the model completely fails to capture the experimental data in the $(2,2,L)$ plane (Figs. 5.8(g)), predicting intensity at $L=-2$, while significantly overestimating the dynamic range spanned by the columns of scattering at $L=-1,-3$.

As summarised in Figs. 5.8(h,i), the failure of the calculated model in both the $\left(\frac{3}{2},\frac{3}{2},L\right)$ and $(2,2,L)$ planes cannot be accounted for by coupling of the longitudinal G^{zz} and transverse G^{+-} and G^{-+} modes [547, 548, 554]. Such mode coupling *via* Eq. 5.19 was speculative and investigated as a possibility due to three key observations: (1) the overestimation of the energy transfer for the longitudinal G^{zz} mode, (2) the overlap of the G^{zz} and transverse G^{-+} modes at high energy transfers, while (3) it has been proposed that such coupling is supported in non-collinear magnetic structures such as some possibilities proposed for CoO [540–542, 544, 555–557]. The inclusion of longitudinal-transverse mode coupling is illustrated in Figs. 5.8(h,i) and 5.9. While such coupling does not address the aforementioned discrepancies between experimental data and the calculated model in both $\left(\frac{3}{2},\frac{3}{2},L\right)$ and $(2,2,L)$ planes, its inclusion results in the enhancement of both the G^{zz} mode at higher energy transfers and the flat G^{+-} mode at ∼30 meV [18, 422, 424], a mode that has been consistently overestimated in all calculations presented so far in Figs. 5.5(d) and 5.5(e). As will be shown below, the failure of the current approach for longitudinal-transverse mode coupling may possibly stem from the use of two *single*-particle modes.

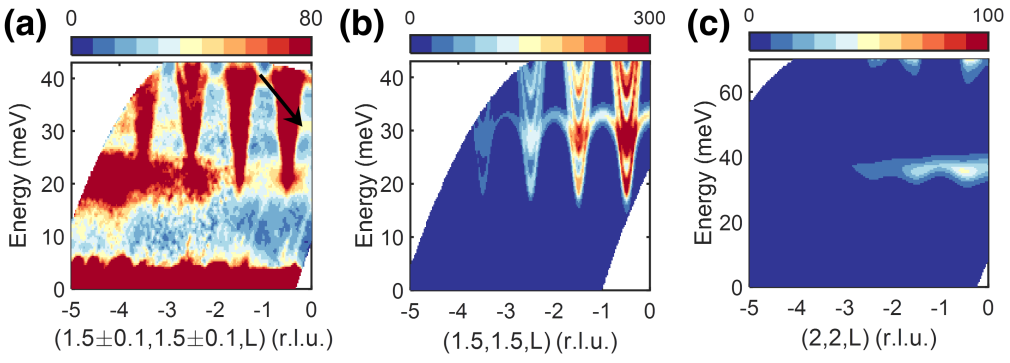

Figure 5.9 A comparison of (a) measured (E_i=45 meV, 5 K) and (b,c) calculated (**Q**,E) slices. Calculations included longitudinal-transverse mode coupling. Arrow in (b) indicates the presence of a weak magnetic mode at approximately 30 meV.

The replacement of well-defined spin waves corresponding to long-lived single-quasiparticle excitations into steeply dispersive broadened excitations is somewhat unexpected for CoO, since unlike other low dimensional Co-based systems that were previously discussed in Chapter 2 [230, 231, 558] that exhibit broad scattering at high energy transfers, CoO is neither low dimensional, nor is its magnetic ground state is not a pure $j_{\text{eff}} = \frac{1}{2}$ due to the strong entanglement induced by the molecular field. Although unexpected, such behaviour is highly reminiscent of the itinerant helical magnet $CeRhIn_5$ [544]. In the case of $CeRhIn_5$, its broad excitations were successfully accounted for by the "1+2" multimagnon model [545, 546]. These short-lived energy-dampened excitations corresponded to anharmonic multiparticle decay processes attributed to the coupling of single-magnon transverse fluctuations with longitudinal multiparticle fluctuations [540–543]. Such a process has been unaccounted for in the calculated model so far and may provide an explanation for observed failure of previous attempts to couple of longitudinal and transverse modes in Fig. 5.7(h) and (i), since the coupled modes were all single-particle or -magnon modes.

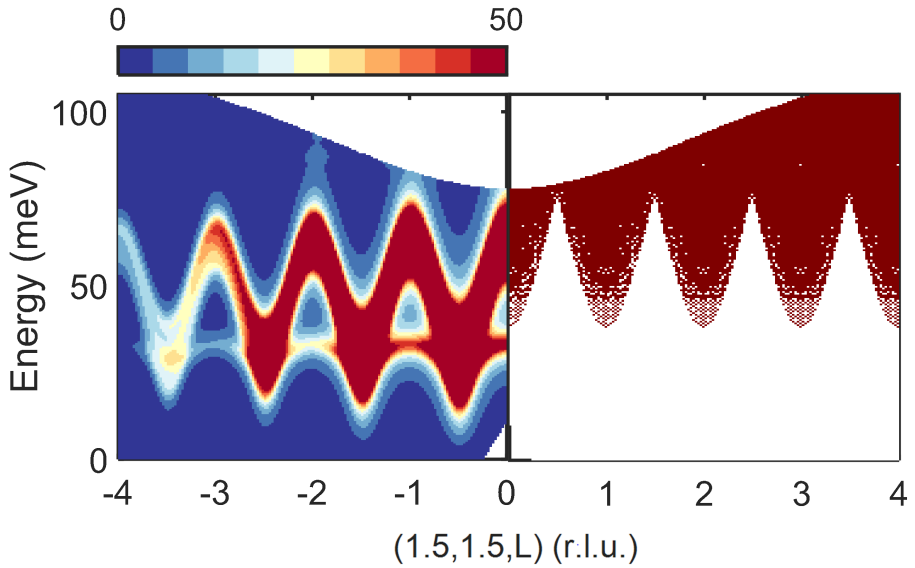

Figure 5.10 Constant-energy (E=[20,45] meV) slice at 5 K with an E_i=45 meV.

Although speculative, the possibility of such coupling was investigated by calculating the kinematically permissible region in $(\mathbf{Q}, E)$ for multimagnon scattering. The calculation was accomplished by employing the constraints of both the conservation of energy and momentum [111, 545, 559, 560] summarisedby

$$G(\mathbf{Q}, E) = \sum_{\mathbf{Q}_1, \mathbf{Q}_2} \delta(\mathbf{Q} - \mathbf{Q}_1 - \mathbf{Q}_2)\delta(E - E_{\mathbf{Q}_1} - E_{\mathbf{Q}_2}). \tag{5.24}$$

As illustrated in Fig. 5.10, the combined kinematically permissible region for all 36 unique couplings between two transverse (*i.e.* G^{-+} or G^{+-}) modes spans a large region in $(\mathbf{Q}, E)$ space and accounts for many of the calculated model's discrepancies in the $\left(\frac{3}{2}, \frac{3}{2}, L\right)$ plane, including both the sharp vertical dispersion, and in particular, the broadness in $(\mathbf{Q}, E)$ at the zone boundaries at high energy transfers, where instrumental resolution is at its best [212, 529]. The overlap of the large dynamic range predicted for the multimagnon continuum at the zone boundaries with the dynamic range where the calculated model fails to account for the large bandwidth (Fig. 5.7(f)) suggests the possibility of a common origin; and such multi-quasiparticle processes would provide a natural explanation for the observed failure of the single magnon-based calculations that have been presented so far. Upon closer investigation, the failures of the calculated model at the zone boundaries, including the increased bandwidth and potential decrease in intensity are consistent with mode damping [111, 559, 561]. Such damping could be accounted for by the mode coupling underlying the multimagnon process, as is the case for $CeRhIn_5$ [544], where the longitudinal fluctuations comprising the longitudinal multimagnon continuum dampen the well-defined single-magnon transverse fluctuations [545, 546, 555]. Such a mechanism may be present in CoO as illustrated in Fig. 5.7, where the longitudinal G^{zz} mode appears to be a source of spectral weight into the steeply disperive columns of scattering that are emanating from the G^{-+} transverse mode, reminiscent of the high energy excitations in $CeRhIn_5$ [544].

One aspect of the discussion that has not been addressed is the underlying energy scale for the proposed strong mode coupling and resulting multimagnon processes. For the case of $CeRhIn_5$ [544], it was suggested that the coupling was not due to localised effects but instead was due to either single magnon coupling with electronic excitations [562] or collective itinerant magnetism [563–565]. The former is unlikely in the case of CoO due to a combination of the high energy scales of the crystal field excitations [18, 501, 502] and the observation that such magneto-electronic coupling strongly dampens the magnon modes, up to the point of disappearance [566]. The mechanism based on itinerant magnetism in CoO may be disputed from three key arguments. Firstly, the steep vertical dispersion that is both reminiscent of high velocity excitations off the Fermi surface and characteristic of itinerant magnetism [567–569] is accounted for by

the multimagnon continuum at the zone boundaries as illustrated in Fig. 5.10. Secondly, the failure of the model to account for the intensity and energy transfer of the longitudinal G^{zz} mode in Fig. 5.8, a mode that is expected to be most affected by itinerant effects [570, 571], may be a consequence of the random phase approximation-mean field (RPA-MF) approach employed in the model instead of evidence for itinerant effects. The failure of RPA-MF-based models to account for G^{zz} mode has been well-documented in various other antiferromagnets [572, 573]. In contrast with the RPA-MF predictions for both sharp and broad modes with longitudinal polarisation [574–576], only the latter is observed for CoO, as is the case for $KCuF_3$ [573]. Thirdly, as illustrated in Fig. 5.8, the $\mathbf{Q}$-dependence of the columns of scattering agrees very well with the $|F_{mag}(\mathbf{Q})|^2$, contrary to what is expected for itinerant magnetism [577]. The aforementioned discrepancies between the possibilities of the underlying energy scales for CoO and $CeRhIn_5$ is in fact not entirely unexpected with such discrepancies can be attributed to the fact that the former is a Mott insulator, whilst the latter is a heavy fermion metal, and thus although the comparison outlined above between both systems has been instructive, its use should be approached with caution.

The agreement between the experimental data and the $|F_{mag}(\mathbf{Q})|^2$ summarised in Fig. 5.8 presents an interesting contradiction. The multimagnon continuum is a multiparticle process [555, 559, 578] and thus is not based on localised magnetism in contrast to underlying physics of the magnetic form factor. The suggestion that localised magnetism is the basis for the columns of scattering can be further disputed by the failure of the calculated localised model to fully capture the dispersion at high energy transfers. Furthermore, the observation that the vertical columns are both purely inelastic and possess >10% of the intensity of the transverse fluctuations also contrasts the behaviour of other classical and insulating magnets where the signal is expected to be almost purely elastic and on the order of 1-2% [544]. One possible solution to this apparent contradiction is to note that Rb_2MnF_4 [545], despite its higher value of $S = \frac{5}{2}$ did exhibit a multicontinuum contribution with a slightly higher contribution of ∼4% of that of the single-magnon mode. Such an observation suggests that, although beyond the scope of this study, the possibility of a two multi-magnon continuum represents a possible avenue for future investigation. Another possible avenue for further investigation stems from a comparison between the behaviour of CoO with that of the Kitaev quantum spin liquid candidate α-$RuCl_3$ [29]. As is the case for CoO, the single quasiparticle approach for α-$RuCl_3$ at low energy transfers at the magnetic zone centres deteroriates into a continuum at the zone

boundaries. The similarities between the high energy excitations for CoO and both α-$RuCl_3$ [579–581] and other Ir^{4+}-based systems [582–584] suggests that strong spin-orbit coupling in the presence of strong exchange anisotropy and frustration may play a significant role in the deteroiation of the sharp excitations in CoO at high energy transfers [32, 33].

5.5 Concluding Remarks & Future Directions

Although the calculated model successfully described the fine structure at the magnetic zone centres with great accuracy, such a description required the reduction of the exchange constants in $J(\mathbf{Q})$ by 20% from their original estimates measured in $Co_{0.03}Mg_{0.97}O$ [3]. Despite the success of the calculated model to shift the centre-of-masses of the two peaks at the zone boundaries to lower energy transfers (Fig. 5.6(f)), the required reduction of the exchange constants resulted in a significant underestimation of H_{MF} that was equal in magnitude to the original overestimation when using the exchange constants for $Co_{0.03}Mg_{0.97}O$. Such a significant underestimation suggests that the underlying physics cannot be completely described by a simple reduction of the values of J, and thus other contributions must be considered.

One such possible contribution may be distortions parallel and orthogonal to the main octahedral axis due to their presence in the single-ion Hamiltonian $\hat{\mathcal{H}}_{S.I.}$ (Eq. 5.11) as the parameters Γ_z and Γ_z, respectively [21, 76, 265, 347]. As described in §5.1, in the case of pure CoO, a large structural distortion accompanies the assumption of long range magnetic order [82–84, 440, 441], and thus one would expect the necessity for the inclusion of distortions in order for the calculated model to capture the essential physics. An additional and related possible contribution may be the spin-orbit coupling, once again due to its presence in $\hat{\mathcal{H}}_{S.I.}$ in the form of the parameter λ [18, 76]. Although attempts to measure λ has spanned decades, consisting of measurements employing a variety of spectroscopic techniques, the value of λ in pure CoO still remains a source of controversy with experimental values ranging from -22.1 meV to -12 meV [18, 47, 83, 469, 585]. Despite the large variety of reported values in the literature, all values are consistently smaller in magnitude compared to the free-ion value of -23.4 meV [47]. Such behaviour has been attributed to either coupling between the ground ^4F and first excited ^4P single ion states or

covalency effects [18, 20, 341, 509, 586], albeit the latter is not supported by previous neutron studies on other transition metal oxides [587].

The inclusion of the effects of distortions and spin-orbit coupling was accomplished by fixing the distortion parameters $\Gamma_z = \Gamma_x$ in Eq. 5.11 to -5 meV, whilst defining λ as a free parameter that was allowed to vary from its free-ion value [47] to -12 meV [83]. It should be noted that setting $\Gamma_z = \Gamma_x$ correponds to the simplest approximation concerning distortions, whilst its value is approximately five times larger than the value reported for $KCoF_3$ [20, 348] reflecting the significantly larger distortion for CoO than what has been reported for $KCoF_3$ [20, 588]. As illustrated in Figs. 5.11(a,d), a least squares optimisation of the modified model still captures the fine structure at the magnetic zone centres with great accuracy, whilst maintaining the correct dynamic range for the two peaks at the zone boundaries (Figs. 5.11(b,e)). The refinement of the value of λ yielded the upper limit value of -12 meV, whilst the values of J were only required to be reduced by 15% instead of the original 20%. Furthermore, as is summarised in Tab. 5.6, the refined H_{MF} varied from 58.15(4) to 71.29(3) meV, corresponding to an average of 65.18(2) meV, in agreement (within error) to the mean field estimate derived from the experimental θ_{CW} [474, 475].

Table 5.6 Refined mean field strength parameter H_{MF} for eight different orbital arrangements in CoO utilising a single-ion Hamiltonian $\hat{\mathcal{H}}_{S.I.}$ with distortions parameters $\Gamma_z = \Gamma_x = -5$ meV, a reduced spin-orbit coupling constant $\lambda = -12$ meV and exchange constants J that are 85% of the values reported for $Co_{0.03}Mg_{0.97}O$ [3]. Each arrangement corresponds to a different combination of magnetic exchange constants $J_{m,n}$ and is denoted by four letters. Each letter represents the type of coupling n, either antiferromagnetic (A) or ferromagnetic (F), present in each coordination shell m, from the first (far left) to the fourth (far right). Numbers in parentheses indicate statistical errors.

Combination of Exchange Constants	Refined/Calculated Value (meV)
AAAA	71.29(3)
AAFA	69.31(6)
FAFA	69.62(7)
FAAA	63.57(5)
AAAF	65.92(4)
AAFF	63.36(6)
FAAF	60.2(1)
FAFF	58.15(4)
Average	65.18(2)
Mean field estimate	64.8(9)

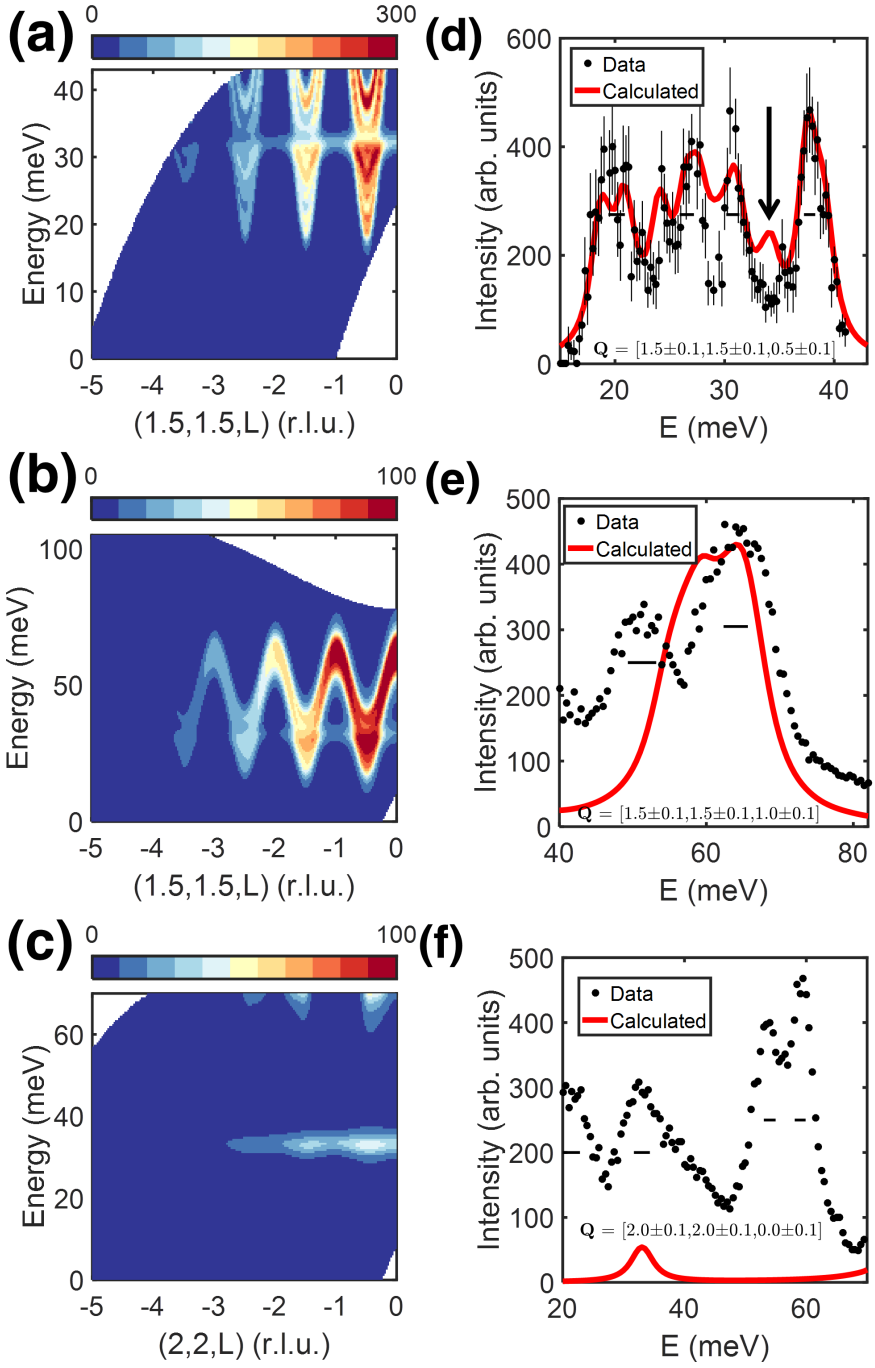

Figure 5.11 Calculated (**Q**,E) slices for an E_i of (a) 45 meV, (b) 110 meV and (c) 70 meV. (d-f) Comparison of measured (5 K) and calculated constant-**Q** cuts of (a-c). Calculations assumed the presence of distortions parallel and orthogonal to the main octahedral axis with equal magnitudes ($\Gamma_z = \Gamma_x = -5$ meV) with a reduced value of the spin-orbit coupling constant λ of -12 meV in Eq. 5.11. The corresponding exchange constants for a particular coordination shell m in both J_s (Eq. 5.14) and J_d (Eq. 5.15) were assumed to be equal to one another and equal to 85% of the values summarised in Tab. 5.3. Horizontal bars for constant-**Q** cuts indicate experimental resolution. Arrow in panel (d) indicates an additional contribution from the G^{+-} mode at higher energy transfers.

Despite the statistical agreement between the refined and predicted values for H_{MF} and concomitant increase in the exchange constants, there still remains discrepancies between the experimental data and the modified model. The first refers to the observation that the inclusion of the distortion and spin-orbit contributions results in an additional contribution from the already overestimated flat transverse G^{+-} mode at higher energy transfers as emphasised in Fig. 5.11(d). Secondly, despite the inclusion of the aforementioned additional contributions, the exchange constants were still required to be reduced by 15%, thus the question concerning the true values for the exchange constants still remains and represents an avenue for future studies. A question made even more difficult by noting that the exchange constants previously measured for $Co_{0.03}Mg_{0.97}O$ [3] are technically only applicable in the $j_{\text{eff}} = \frac{1}{2}$ manifold [589], whilst the equation-of-motions summarised in Eq. 5.1 considers coupling between all j_{eff} manifolds [515].

So far, the limitations of the calculated model in the $\left(\frac{3}{2}, \frac{3}{2}, L\right)$ plane have been addressed. An explanation for the failure of our model to capture features over all energy transfers in the $(2, 2, L)$ plane, in particular, the low energy modes, may also lie with non-localised magnetism. As summarised in Fig. 5.12, energy-integrating the (H, H, L) plane within a dynamic range (E=[20,45] meV) that includes the fine structure [422] illustrated in Figs. 5.4(a,c), reveals that half-integer positions along $[H, H, 0]$ exhibit much stronger intensities compared to their integer counterparts and thus suggests a physical mechanism that is different than a localised model. Although beyond the scope of this study, it is worthwhile to note the particular $\mathbf{Q}$-dependence of the mode between 20 and 50 meV. As illustrated in Fig. 5.4(b), although the mode appears to initially decrease with increasing $\mathbf{Q}$, an increase is observed at $\mathbf{Q} \sim 4$ Å^{-1} with both extrema in $\mathbf{Q}$ exhibiting identical dispersion relations. Such behaviour suggests the possibility that these excitations may be magnetoelastic [590, 591] in origin, similar to what is observed in the pyrochlore $Tb_2Ti_2O_7$ [592, 593], and most recently with NaFeAs [594], the parent compound of an iron-pnictide superconductor. Such a suggestion is supported by the presence of much more prominent acoustic phonons in the $(2, 2, L)$ plane and may present another avenue for future investigation.

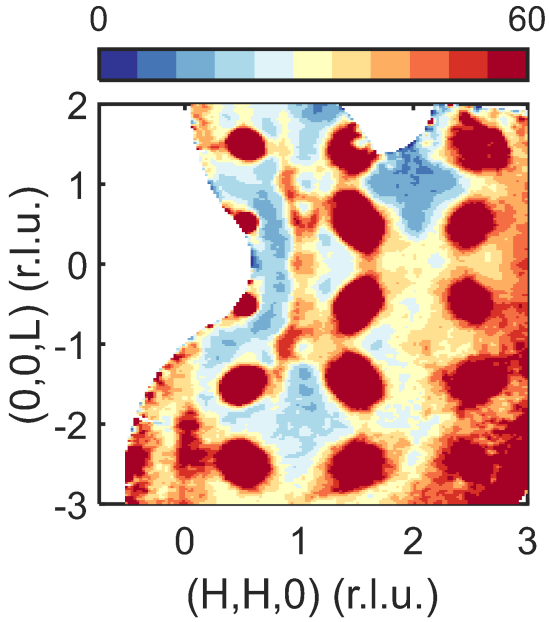

Figure 5.12 Constant-energy (E=[20,45] meV) slice at 5 K with an E_i=45 meV.

In summary, the low temperature magnetic excitations of CoO in the Néel regime have been investigated using high resolution neutron inelastic spectroscopy. Utilising a mean-field multilevel spin wave model based on the equation-of-motion-Green's functions technique with a Fock-like decoupling random phase approximation [515], the fine structure at the magnetic zone centre has been successfully described with great accuracy. At higher energy transfers, the replacement of the sharp resolution-limited spin waves at the zone centre by energy and momentum broadened excitations at the zone boundaries coincides with the deterioration of the calculated model. Upon closer comparison to $CeRhIn_5$ [544], the breakdown of the localised approach appears to suggest the presence of the coupling of transverse fluctuations and longitudinal multimagnon fluctuations [540, 541]. Despite the similarities between the multimagnon continuum of $CeRhIn_5$ and the vertical columns of scattering observed for CoO, the proposed itinerant effects [563–565] underlying the coupling mechanism in $CeRhIn_5$ does not appear to be likely in the present case of CoO, and thus remains an open question for future investigation.

Chapter 6

Conclusions

This Thesis has investigated the low energy magnetic properties of systems constructed from the magnetic cations Pr^{3+} and Co^{2+} with neutron inelastic spectroscopy. Although both cations are commonly treated as effective spin-$\frac{1}{2}$ in the literature [19, 20, 23, 141, 595, 596], the work contained in this Thesis has demonstrated that such an approximation is only valid under certain circumstances; with such circumstances being ultimately dictated by the complex and often subtle interplay of the interactions between spin, orbital and electronic degrees of freedom [597].

In Chapter 2, the low energy magnetic fluctuations of the dynamic spin ice $Pr_2Sn_2O_7$ were investigated. The strong single-ion anisotropy and frustration induced by the pyrochlore structure [45], combined with the weaker magnetism of Pr^{3+} [17, 166], suggested that $Pr_2Sn_2O_7$, with its increased monopole density, was a promising route for the investigation of the exact nature of the interaction between magnetic monopoles [114, 122, 126, 130–132]. High resolution neutron inelastic spectroscopy revealed the presence of a hierarchy of unequally-spaced magnetic excitations. These minimally dispersive excitations are well-described by a simple model of monopole pairs bound by a linear potential [63, 229, 232] with an effective tension of $0.642(8)\ \mathrm{K} \cdot \mathrm{\AA}^{-1}$ at 1.65 K. Despite the success of the confinement model employing a linear potential, such a potential was shown to represent only an approximation, whose validity holds only in the limit of short distances. The determination of the true potential, its presence in other quantum spin ice candidates [165, 197], and how such a potential is influenced by external perturbations including external magnetic fields and pressure [250], represents multiple fruitful avenues for future research.

Consisting of Chapters 3-5, the second portion of this Thesis attempted to establish a complete description of the low energy magnetic excitation spectrum of the enigmatic Mott insulator CoO by investigating the low temperature magnetic properties of three different magnets constructed from high spin d^7 Co^{2+} in octahedral coordination.

The zero field structural and dynamic properties of the first magnet, α-CoV_3O_8, are presented in Chapter 3. Although both x-ray and neutron diffraction provided evidence for significant macroscopic disorder inherent to its *Ibam* structure [75], the dynamics of the mixed ternary oxide α-CoV_3O_8 appear largely unaffected, with the low energy magnetic excitations parametrisable using an ordered *Iba*2-like Co^{2+} arrangement and critical scattering consistent with a three dimensional Ising universality class [64, 382–386]. A crystal field analysis determined the presence of two broad bands of excitations separated in energy at 5 meV and 25 meV, consistent with a $j_{\text{eff}} = \frac{1}{2}$ ground state with little mixing between spin-orbit split Kramers doublets. A comparison of α-CoV_3O_8 to the 3D Ising magnets and other compounds where spin-orbit coupling is present [44, 278, 317, 402, 403, 407–409, 415, 416] indicate that the presence of an orbital degree of freedom, in combination with strong crystal field effects and well-separated j_{eff} manifolds may play a key role in making the dynamics largely insensitive to disorder; a role which may be potentially determined experimentally through the careful selection of both chemical composition and synthesis conditions [44, 284, 405].

Despite the magnetism in CoO and α-CoV_3O_8 being both based on high spin d^7 Co^{2+} in octahedral coordination, their low energy excitation spectra differ significantly from one another. The rich excitation spectrum of CoO stems from the comparable strength of J and λ [3, 18, 424, 444]. The resulting complex entanglement between spin-orbit and spin-exchange interactions is further compounded by structural distortions accompanying orbital order [82, 83, 440, 441]. In contrast, α-CoV_3O_8 being located in the $\lambda \gg J$ regime with minimal octahedral distortions [79], exhibits no such entanglement with a much simpler spectrum consisting of distinct bands corresponding to pure j_{eff} manifolds [76]. The simplification of the excitation spectrum of CoO to one similar to that of α-CoV_3O_8 was accomplished in Chapter 4 through the placement of the orbitally degenerate Co^{2+} on a non-magnetic host MgO rocksalt lattice. The paramagnetic nature of the substituted monoxide $Co_{0.03}Mg_{0.97}O$ [18], where no long range spin or orbital order exists, places the system deep within the $\lambda \gg J$ regime, resulting in the desired disentanglement of spin-

orbit and spin-exchange interactions [456–458]. By considering the prevalent excitations from Co^{2+} spin pairs [390], seven exchange constants J out to the fourth coordination shell were extracted. An antiferromagnetic next nearest neighbour 180° exchange interaction was shown to be dominant, however, dual ferromagnetic and antiferromagnetic interactions were observed for pairings with other pathways. As a consequence of the t_{2g} orbital degeneracy of Co^{2+}, these dual interactions were shown to be understood in terms the Goodenough-Kanamori rules [53, 54, 56, 57] and consistent with thermodynamic measurements [474, 475]. With its basic requirement of an isostructural non-magnetic host lattice, the use of the chemical dilution technique employed in Chapter 4 has widespread applicability in extracting individual magnetic exchange constants in a variety of magnets spanning both chemical composition and lattice geometries [456–458], while also providing an experimental avenue for the exploration of the contrasting effects of e_g and t_{2g} degeneracy [445, 446].

Having extracted estimates for the magnetic exchange constants spanning four coordination shells, the low energy magnetic excitations of CoO were reinvestigated in Chapter 5. A mean-field multilevel spin wave model based on the equation-of-motion-Green's functions technique with a Fock-like decoupling random phase approximation [515, 519–522] successfully captured the fine structure at the magnetic zone centres [422, 424] with great accuracy. In contrast, its failure at high energy transfers identified the replacement of resolution-limited spin waves at the zone centres to energy and momentum broadened excitations at the zone boundaries. Upon closer comparison to the itinerant magnet $CeRhIn_5$ [544] and other non-collinear magnets [540, 541], the observed breakdown of the localised model suggests the possibility of coupling between the transverse single magnon and longitudinal multimagnon fluctuations. Despite the similarities between the multimagnon continuum of $CeRhIn_5$ and the vertical columns of scattering observed for CoO, the proposed itinerant effects [563–565] underlying the coupling mechanism in $CeRhIn_5$ does not appear to be applicable in the case of CoO, and the identity of the underlying energy scale remains an open question for future investigation.

Despite the $j_{\text{eff}} = \frac{1}{2}$ description being invalid for two out of the four compounds ($Pr_2Sn_2O_7$ and CoO) investigated in this Thesis, the rich variety of magnetic properties exhibited for all four oxides exemplifies the subtle, yet profound influence of spin-orbit coupling in the determination of magnetic ground states [489, 490, 598–603]. A relativistic effect originating from the interaction of an electron's spin with the magnetic field generated by its motion, spin-orbit

coupling provides the cornerstone for coupling structural and spin degrees of freedom [270, 436, 604, 605]. In addition to its central historic role in the theoretical treatment of magnetism in the solid state (*e.g.* the Dzyaloshinskii-Moriya interaction [606, 607]), the importance of spin-orbit coupling has been at the forefront of contemporary materials science, driven in large part, but not limited to the pursuit of physical realisations of Kitaev physics [27, 28]. Possessing not only the potential to revolutionise quantum computing [608–612], the Kitaev model represents a unique experimental platform for the discovery of novel spin liquid phases [152, 153], Majorana fermions [613, 614], and direct experimental evidence for gauge physics in the solid state [615, 616].

Despite the search for Kitaev physics being largely focused on the so-called "spin-orbit assisted Mott insulators" [437, 617] constructed from heavier low spin d^5 cations such as Ru^{3+} [30, 581] and Ir^{4+} [489, 496, 583, 618], two recent independent theoretical studies [32, 33] have provided clear arguments that Mott insulators constructed from high spin d^7 cations such as Co^{2+} may host Kitaev physics with a much richer phase diagram than their d^5 counterparts. In fact, the suggestion that Co^{2+}-based magnets have the potential to exhibit Kitaev physics may be key in addressing the broad continuum observed at high energy transfers in CoO. Broad continua corresponding to the breakdown of magnons has been observed in the majority of Kitaev spin liquid candidates at high energy transfers [29, 30, 579, 581–584, 613]. Once postulated to be a consequence of the Kitaev state, a recent investigation of α-$RuCl_3$ has suggested the necessary ingredients to yield such a continuum goes beyond the Kitaev state [29]. Calculations argue that the continuum may be in fact incoherent excitations arising from strong magnetic anharmonic effects that are the result of a combination of anisotropic magnetic exchange, deviation magnetic moments away from high symmetry axes and an overlap of the multimagnon continuum with transverse magnon excitations [31, 542, 555, 619, 620], and as shown in this Thesis, all ingredients present in the edge-sharing octahedrally coordinated Co^{2+} comprising CoO. The suggestion that high spin d^7 cations constitute an alternative route for experimental realisations of Kitaev physics represents the possibility of a renaissance in the study of Co^{2+}-based magnetism, and with such increased attention comes the potential for the discovery of a large variety of exotic and novel magnetic ground states.

Bibliography

[1] P. M. Sarte, A. A. Aczel, G. Ehlers, C. Stock, B. D. Gaulin, C. Mauws, M. B. Stone, S. Calder, S. E. Nagler, J. W. Hollett, et al., J. Phys.: Condens. Matter **29**, 45LT01 (2017).

[2] P. M. Sarte, A. M. Arévalo-López, M. Songvilay, D. Le, T. Guidi, V. García-Sakai, S. Mukhopadhyay, S. C. Capelli, W. D. Ratcliff, K. H. Hong, et al., Phys. Rev. B **98**, 224410 (2018).

[3] P. M. Sarte, R. A. Cowley, E. E. Rodriguez, E. Pachoud, D. Le, V. García-Sakai, J. W. Taylor, C. D. Frost, D. Prabhakaran, C. MacEwen, et al., Phys. Rev. B **98**, 024415 (2018).

[4] P. A. Cox, *Transition Metal Oxides* (Clarendo Press, Oxford, 1992).

[5] J. Greedan, *Introduction to the Crystal Chemistry of Transition Metal Oxides* (American Cancer Society, 2017), chap. 5, pp. 161–220.

[6] J. M. D. Coey, M. Venkatesan, and H. Xu, *Introduction to Magnetic Oxides* (Wiley-Blackwell, 2013), chap. 1, pp. 1–49, ISBN 9783527654864.

[7] J. B. Goodenough, Annual Review of Materials Science **28**, 1 (1998).

[8] S. M. A. Tabei, F. Vernay, and M. J. P. Gingras, Phys. Rev. B **77**, 014432 (2008).

[9] S. M. A. Tabei, M. J. P. Gingras, Y.-J. Kao, P. Stasiak, and J.-Y. Fortin, Phys. Rev. Lett. **97**, 237203 (2006).

[10] A. H. MacDonald, S. M. Girvin, and D. Yoshioka, Phys. Rev. B **37**, 9753 (1988).

[11] A. L. Chernyshev, D. Galanakis, P. Phillips, A. V. Rozhkov, and A.-M. S. Tremblay, Phys. Rev. B **70**, 235111 (2004).

[12] A. M. Hallas, J. Gaudet, and B. D. Gaulin, Annual Review of Condensed Matter Physics **9**, 105 (2018).

[13] S. H. Curnoe, Phys. Rev. B **88**, 014429 (2013).

[14] R. Schmied, J. H. Wesenberg, and D. Leibfried, New Journal of Physics **13**, 115011 (2011).

[15] V. M. Katukuri, S. Nishimoto, V. Yushankhai, A. Stoyanova, H. Kandpal, S. Choi, R. Coldea, I. Rousochatzakis, L. Hozoi, and J. van den Brink, New Journal of Physics **16**, 013056 (2014).

[16] A. J. Princep, D. Prabhakaran, A. T. Boothroyd, and D. T. Adroja, Phys. Rev. B **88**, 104421 (2013).

[17] H. D. Zhou, C. R. Wiebe, J. A. Janik, L. Balicas, Y. J. Yo, Y. Qiu, J. R. D. Copley, and J. S. Gardner, Phys. Rev. Lett. **101**, 227204 (2008).

[18] R. A. Cowley, W. J. L. Buyers, C. Stock, Z. Yamani, C. Frost, J. W. Taylor, and D. Prabhakaran, Phys. Rev. B **88**, 205117 (2013).

[19] S. Onoda and Y. Tanaka, Phys. Rev. B **83**, 094411 (2011).

[20] W. J. L. Buyers, T. M. Holden, E. C. Svensson, R. A. Cowley, and M. T. Hutchings, J. Phys. C Solid State Phys. **4**, 2139 (1971).

[21] R. A. Cowley, W. J. L. Buyers, P. Martel, and R. W. H. Stevenson, J. Phys. C Solid State Phys. **6**, 2997 (1973).

[22] R. S. Cowley and K. Carneiro, J. Phys. C: Solid State Phys. **13**, 3281 (1980).

[23] M. J. P. Gingras and P. A. McClarty, Rep. Prog. Phys. **77**, 056501 (2014).

[24] A. Vasiliev, O. Volkova, E. Zvereva, and M. Markina, npj Quantum Materials **3**, 18 (2018).

[25] N. Majlis, in *Surface Science*, edited by F. A. Ponce and M. Cardona (Springer Berlin Heidelberg, Berlin, Heidelberg, 1991), pp. 443–451.

[26] K. Katsumata, Current Opinion in Solid State and Materials Science **2**, 226 (1997).

[27] A. Kitaev, Ann. Phys. **321**, 2 (2006).

[28] A. Kitaev, Ann. Phys. **303**, 2 (2003).

[29] S. M. Winter, K. Riedl, P. A. Maksimov, A. L. Chernyshev, A. Honecker, and R. Valentí, Nat. Commun. **8**, 1152 (2017).

[30] A. Banerjee, C. Bridges, J.-Q. Yan, A. Aczel, L. Li, M. Stone, G. Granroth, M. Lumsden, Y. Yiu, J. Knolle, et al., Nat. Mater. **15**, 733 (2016).

[31] S. M. Winter, Y. Li, H. O. Jeschke, and R. Valentí, Phys. Rev. B **93**, 214431 (2016).

[32] H. Liu and G. Khaliullin, Phys. Rev. B **97**, 014407 (2018).

[33] R. Sano, Y. Kato, and Y. Motome, Phys. Rev. B **97**, 014408 (2018).

[34] J. P. Mercier, G. Zambelli, and W. Kurz, in *Introduction to Materials Science*, edited by J. P. Mercier, G. Zambelli, and W. Kurz (Elsevier, Oxford, 2002), pp. 1 – 16.

[35] C. N. R. Rao, Annual Review of Physical Chemistry **40**, 291 (1989).

[36] S. Pumfrey, in *Cambridge Scientific Minds*, edited by P. Harman and S. Mitton (Cambridge University Press, Cambridge, 2002), pp. 6 – 20.

[37] C. Kittel, *Introduction to Solid State Physics* (Wiley, New York, 2005), 8th ed.

[38] L. Landau and E. Lifshitz, *Quantum Mechanics: Non-Relativistic Theory*, vol. 3 of *Course of Theoretical Physics* (Elsevier Butterworth-Heinemann, New York, 1977), 3rd ed.

[39] N. W. Ashcroft and N. D. Mermin, *Solid State Physics* (Saunders College, 6277 Sea Harbor Drive, Orlando, L,, 1976).

[40] J. E. Greedan, *Magnetic Oxides* (American Cancer Society, 2017), pp. 1–45.

[41] A. P. Ramirez, Journal of Physics: Condensed Matter **9**, 8171 (1997).

[42] G. Jonker and J. V. Santen, Physica **16**, 337 (1950).

[43] J. G. Bednorz and K. A. Müller, Z. Phys. B **64**, 189 (1986).

[44] D. S. Fisher and A. Khurana, Phys. Today **41**, 56 (1988).

[45] J. S. Gardner, M. J. P. Gingras, and J. E. Greedan, Rev. Mod. Phys. **82**, 53 (2010).

[46] V. V. Srdi, Z. Cveji, M. Milanovi, G. Stojanovi, and S. Raki, in *Magnetic, Ferroelectric, and Multiferroic Metal Oxides*, edited by B. D. Stojanovic (Elsevier, 2018), Metal Oxides, pp. 313 – 332.

[47] A. Abragam and B. Bleaney, *Electron paramagnetic resonance of transition ions* (Clarendon Press, Great Clarendon Street, Oxford, 1970).

[48] C. Cohen-Tannoudji, D. Diu, and F. Laloe, *Quantum Mechanics* (France, 1973).

[49] L. Pauling and E. B. Wilson, *Introduction to Quantum Mechanics with Applications to Chemistry* (Dover, New York, 1935).

[50] M. A. Morrison, T. L. Estle, and N. F. Lane, *Quantum States of Atoms, Molecules and Solids* (Prentice-Hill, New Jersey, 1976).

[51] B. R. Judd, *Operator Techniques in Atomic Spectroscopy* (Princeton University Press, New Jersey, 1998).

[52] K. W. Stevens, *Magnetic Ions in Crystals* (Princeton University Press, New Jersey, 1997).

[53] J. B. Goodenough, Phys. Rev. **100**, 564 (1955).

[54] J. B. Goodenough, J. Phys. Chem. Solids **6**, 287 (1958).

[55] J. B. Goodenough, *Magnetism and the Chemical Bond* (John Wiley & Sons, New York, 1963).

[56] J. Kanamori, J. Phys. Chem. Solids **10**, 87 (1959).

[57] P. W. Anderson, Phys. Rev. **79**, 350 (1950).

[58] W. Heisenberg, Zeitschrift für Physik **38**, 411 (1926).

[59] P. Dirac, Proc. Royal Soc. Lond. A **112**, 661 (1926).

[60] H. Kramers, Physica **1**, 182 (1934).

[61] H. Meislich, Journal of Chemical Education **44**, 118 (1967).

[62] Néel, M. Louis, Ann. Phys. **12**, 137 (1948).

[63] R. Coldea, D. A. Tennant, E. M. Wheeler, E. Wawrzynska, D. Prabhakaran, M. Telling, K. Habicht, P. Smeibidl, and K. Kiefer, Science **327**, 177 (2010).

[64] M. F. Collins, *Magnetic Critical Scattering*, Oxford series on neutron scattering in condensed matter (Oxford University Press, 200 Madison Avenue, New York, NY, 1989).

[65] M. Reehuis, M. Tovar, D. M. Többens, P. Pattison, A. Hoser, and B. Lake, Phys. Rev. B **91**, 024407 (2015).

[66] A. Bhattacharya and S. J. May, Annu. Rev. Mater. Res. **44**, 65 (2014).

[67] N. Terada, Y. Narumi, Y. Sawai, K. Katsumata, U. Staub, Y. Tanaka, A. Kikkawa, T. Fukui, K. Kindo, T. Yamamoto, et al., Phys. Rev. B **75**, 224411 (2007).

[68] A. D. Huxley, Physica C: Superconductivity and its Applications **514**, 368 (2015).

[69] J. Hamlin, Physica C: Superconductivity and its Applications **514**, 59 (2015).

[70] K. Miyoshi, Y. Takamatsu, and J. Takeuchi, J. Phys. Soc. Jpn. **75**, 065001 (2006).

[71] C. R. Wiebe and A. M. Hallas, APL Mater. **3**, 041519 (2015).

[72] R. E. Cohen, I. I. Mazin, and D. G. Isaak, Science **275**, 654 (1997).

[73] A. P. Ramirez, A. Hayashi, R. J. Cava, R. Siddharthan, and B. S. Shastry, Nature **399**, 333 (1999).

[74] M. Subramanian, G. Aravamudan, and G. S. Rao, Prog. Solid State Chem. **15**, 55 (1983).

[75] Y. Oka, T. Yao, N. Yamamoto, and Y. Ueda, J. Solid State Chem. **141**, 133 (1998).

[76] F. Wallington, A. M. Arévalo-Lopez, J. W. Taylor, J. R. Stewart, V. García-Sakai, J. P. Attfield, and C. Stock, Phys. Rev. B **92**, 125116 (2015).

[77] B. Kim, B. H. Kim, K. Kim, H. C. Choi, S.-Y. Park, Y. H. Jeong, and B. I. Min, Phys. Rev. B **85**, 220407 (2012).

[78] A. Casalot and P. Hagenmuller, J. Inorg. Nucl. Chem. **31**, 3049 (1969).

[79] Y. Oka, T. Yao, N. Yamamoto, and Y. Ueda, J. Solid State Chem. **141**, 133 (1998).

[80] A. M. Abakumov, R. Erni, A. A. Tsirlin, M. D. Rossell, D. Batuk, G. Nenert, and G. V. Tendeloo, Chemistry of Materials **25**, 2670 (2013).

[81] L. E. Smart and E. A. Moore, *Solid State Chemistry: An Introduction* (CRC Press, Boca Raton, FL, 2012), 4th ed.

[82] W. Jauch, M. Reehuis, H. J. Bleif, F. Kubanek, and P. Pattison, Phys. Rev. B **64**, 052102 (2001).

[83] K. Tomiyasu, T. Inami, and N. Ikeda, Phys. Rev. B **70**, 184411 (2004).

[84] N. C. Tombs and H. P. Rooksby, Nature **165**, 442 (1950).

[85] J. B. Goodenough, Phys. Rev. **171**, 466 (1968).

[86] S. Saito, K. Nakahigashi, and Y. Shimomura, J. Phys. Soc. Jpn. **21**, 850 (1966).

[87] R. Scherm and B. Fåk, *Inelastic Neutron Scattering: Introduction* (Springer Netherlands, Dordrecht, 2006), pp. 361–381.

[88] H. Schober, *Neutron Scattering Instrumentation* (Springer US, Boston, MA, 2009), pp. 37–104.

[89] J. L. Schmehr and S. D. Wilson, Annu. Rev. Mater. Sci. **47**, 153 (2017).

[90] C. Rao, Mater. Sci. Eng., B **18**, 1 (1993).

[91] C. Rao and K. Biswas, *Ceramic Methods* (Wiley-Blackwell, 2015), chap. 3, pp. 17–21, ISBN 9781118892671.

[92] A. E. Danks, S. R. Hall, and Z. Schnepp, Mater. Horiz. **3**, 91 (2016).

[93] Z. Fisk and J. Remeika, in *Handbook on the Physics and Chemistry of Rare Earths* (Elsevier, 1989), vol. 12, pp. 53 – 70.

[94] P. C. Canfield and Z. Fisk, Philosophical Magazine B **65**, 1117 (1992).

[95] H. J. Scheel, Prog. Cryst. Growth & Charact. **5**, 277 (1982).

[96] C. Brisi, Ann. Chim. **47**, 815 (1957).

[97] K. A. Ross, T. Proffen, H. A. Dabkowska, J. A. Quilliam, L. R. Yaraskavitch, J. B. Kycia, and B. D. Gaulin, Phys. Rev. B **86**, 174424 (2012).

[98] S. Koohpayeh, J.-J. Wen, B. Trump, C. Broholm, and T. McQueen, J. Cryst. Growth **402**, 291 (2014).

[99] G. L. Squires, *Introduction to the Theory of Thermal Neutron Scattering* (Cambridge University Press, Cambridge, U.K., 2012).

[100] G. Shirane, S. Shapiro, and J. Tranquada, *Neutron Scattering with a Triple-Axis Spectrometer: Basic Techniques* (Cambridge University Press, Cambridge, U.K., 2002).

[101] I. A. Zaliznyak and S.-H. Lee, in *Modern Techniques for Characterizing Magnetic Materials*, edited by Y. Zhu (Kluwer Academic, London, 2005), chap. 1, pp. 3–62.

[102] J. R. D. Copley and J. C. Cook, Chem. Phys. **292**, 477 (2003).

[103] F. Hippert, E. Geissler, J. L. Hodeau, E. Lelièvre-Berna, and J.-R. Regnard, *Neutron and X-ray Spectroscopy* (Springer Science & Business Media, Berlin, 2006).

[104] C. J. Carlile, M. A. Adams, P. S. R. Krishna, M. Prager, K. Shibata, and P. Westerhuijs, Nucl. Instr. Meth. Phys. Res. A **338**, 78 (1994).

[105] O. Halpern and M. H. Johnson, Phys. Rev. **55**, 898 (1939).

[106] C. Stock, L. C. Chapon, O. Adamopoulos, A. Lappas, M. Giot, J. W. Taylor, M. A. Green, C. M. Brown, and P. G. Radaelli, Phys. Rev. Lett. **103**, 077202 (2009).

[107] G. Xu, Z. Xu, and J. Tranquada, Rev. Sci. Instrum. **84**, 083906 (2013).

[108] H. F. Fong, P. Bourges, Y. Sidis, L. P. Regnault, J. Bossy, A. Ivanov, D. L. Milius, I. A. Aksay, and B. Keimer, Phys. Rev. B **61**, 14773 (2000).

[109] R. Currat, *Three-Axis Inelastic Neutron Scattering* (Springer Netherlands, Dordrecht, 2006), pp. 383–425.

[110] L. Walker, in *Magnetism*, edited by G. T. Rado and H. Suhl (Academic Press, 1963), pp. 299 – 381.

[111] C. Stock, P. M. Gehring, R. A. Ewings, G. Xu, J. Li, D. Viehland, and H. Luo, Phys. Rev. Materials **2**, 024404 (2018).

[112] I. Grillo, *Small-Angle Neutron Scattering and Applications in Soft Condensed Matter* (Springer Netherlands, Dordrecht, 2008), pp. 723–782.

[113] P. A. M. Dirac, Proc. Roy Soc. A **133**, 60 (1931).

[114] D. J. P. Morris, D. A. Tennant, S. A. Grigera, B. Klemke, C. Castelnovo, R. Moessner, C. Czternasty, M. Meissner, K. C. Rule, J-U. Hoffmann, et al., Science **326**, 411 (2009).

[115] R. A. Millikan, Phys. Rev. **2**, 109 (1913).

[116] B. Acharya, J. Alexandre, J. Bernabéu, M. Campbell, S. Cecchini, J. Chwastowski, M. De Montigny, D. Derendarz, A. De Roeck, J. R. Ellis, et al., Int. J. Mod. Phys. B **29**, 1430050 (2014).

[117] M. J. P. Gingras, *Spin Ice* (Springer Berlin Heidelberg, Berlin, Heidelberg, 2011), pp. 293–329.

[118] C. Castelnovo, R. Moessner, and S. Sondhi, Nature **451**, 42 (2008).

[119] S. T. Bramwell, , S. R. Giblin, S. Calder, R. Aldus, D. Prabhakaran, and T. Fennell, Nature **461**, 956 (2009).

[120] S. T. Bramwell and M. J. P. Gingras, Science **294**, 1495 (2001).

[121] L. Pauling, J. Am. Chem. Soc. **57**, 2680 (1935).

[122] T. Fennell, P. P. Deen, A. R. Wildes, K. Schmalzl, D. Prabhakaran, A. T. Boothroyd, R. J. Aldus, D. F. McMorrow, and S. T. Bramwell, Science **326**, 415 (2009).

[123] C. Paulsen, S. R. Giblin, E. Lhotel, D. Prabhakaran, K. Matsuhira, and S. T. Bramwell, Nat. Phys. **12**, 661 (2016).

[124] R. Sibille, E. Lhotel, M. C. Hatnean, G. Balakrishnan, B. Fåk, N. Gauthier, T. Fennell, and M. Kenzelmann, Phys. Rev. B **94**, 024436 (2016).

[125] J-J. Wen, S. M. Koohpayeh, K. A. Ross, B. A. Trump, T. M. McQueen, K. Kimura, S. Nakatsuji, Y. Qiu, D. M. Pajerowski, J. R. D. Copley, et al., Phys. Rev. Lett. **118**, 107206 (2017).

[126] S. Lee, S. Onoda, and L. Balents, Phys. Rev. B. **86**, 104412 (2012).

[127] O. Benton, O. Sikora, and N. Shannon, Phys. Rev. B. **86**, 075154 (2012).

[128] R. Sibille, N. Gauthier, H. Yan, M. C. Hatnean, J. Ollivier, B. Winn, G. Balakrishnan, M. Kenzelmann, N. Shannon, and T. Fennell, Nat. Phys. **14**, 711 (2018).

[129] O. Benton, Phys. Rev. Lett. **121**, 037203 (2018).

[130] B. Lian, Phys. Rev. A **91**, 053605 (2015).

[131] Y. Wan and O. Tchernyshyov, Phys. Rev. Lett. **108**, 247210 (2012).

[132] G. Ehlers, A. L. Cornelius, M. Orendac, M. Kajnakova, T. Fennell, S. T. Bramwell, and J. S. Gardner, Phys. Rev. B **73**, 174429 (2006).

[133] G. Chen, Phys. Rev. B **96**, 195127 (2017).

[134] S. Saha, S. Prusty, S. Singh, R. Suryanarayanan, A. Revcolevschi, and A. Sood, J. Solid State Chem. **184**, 2204 (2011).

[135] S. T. Bramwell, M. J. Harris, B. C. den Hertog, M. J. P. Gingras, J. S. Gardner, D. F. McMorrow, A. R. Wildes, A. L. Cornelius, J. D. M. Champion, R. G. Melko, et al., Phys. Rev. Lett. **87**, 047205 (2001).

[136] M. J. Harris, S. T. Bramwell, D. F. McMorrow, T. Zeiske, and K. W. Godfrey, Phys. Rev. Lett. **79**, 2554 (1997).

[137] T. Fennell, O. A. Petrenko, B. Fåk, S. T. Bramwell, M. Enjalran, T. Yavors'kii, M. J. P. Gingras, R. G. Melko, and G. Balakrishnan, Phys. Rev. B **70**, 134408 (2004).

[138] J. S. Gardner, S. R. Dunsiger, B. D. Gaulin, M. J. P. Gingras, J. E. Greedan, R. F. Kiefl, M. D. Lumsden, W. A. MacFarlane, N. P. Raju, J. E. Sonier, et al., Phys. Rev. Lett. **82**, 1012 (1999).

[139] J. S. Gardner, B. D. Gaulin, A. J. Berlinsky, P. Waldron, S. R. Dunsiger, N. P. Raju, and J. E. Greedan, Phys. Rev. B **64**, 224416 (2001).

[140] S.-W. Han, J. S. Gardner, and C. H. Booth, Phys. Rev. B **69**, 024416 (2004).

[141] S. Onoda and Y. Tanaka, Phys. Rev. Lett. **105**, 047201 (2010).

[142] Y. Machida, S. Nakatsuji, S. Onoda, T. Tayama, and T. Sakakibara, Nature **463**, 210 (2010).

[143] S. Nakatsuji, Y. Machida, Y. Maeno, T. Tayama, T. Sakakibara, J. v. Duijn, L. Balicas, J. N. Millican, R. T. Macaluso, and J. Y. Chan, Phys. Rev. Lett. **96**, 087204 (2006).

[144] D. MacLaughlin, Y. Ohta, Y. Machida, S. Nakatsuji, G. Luke, K. Ishida, R. Heffner, L. Shu, and O. Bernal, Physica B Condens. Matter **404**, 667 (2009).

[145] D. L. Cox and A. Zawadowski, Adv. Phys. **47**, 599 (1998).

[146] B. C. den Hertog and M. J. P. Gingras, Phys. Rev. Lett. **84**, 3430 (2000).

[147] K. A. Ross, L. Savary, B. D. Gaulin, and L. Balents, Phys. Rev. X **1**, 021002 (2011).

[148] K. A. Ross, J. P. C. Ruff, C. P. Adams, J. S. Gardner, H. A. Dabkowska, Y. Qiu, J. R. D. Copley, and B. D. Gaulin, Phys. Rev. Lett. **103**, 227202 (2009).

[149] J. S. Gardner, G. Ehlers, N. Rosov, R. W. Erwin, and C. Petrovic, Phys. Rev. B **70**, 180404 (2004).

[150] S. V. Isakov, K. Gregor, R. Moessner, and S. L. Sondhi, Phys. Rev. Lett. **93**, 167204 (2004).

[151] C. L. Henley, Phys. Rev. B **71**, 014424 (2005).

[152] L. Balents, Nature **464**, 199 (2010).

[153] L. Savary and L. Balents, Rep. Prog. Phys. **80**, 016502 (2017).

[154] P. A. Lee, Science **321**, 1306 (2008).

[155] P. W. Anderson, Phys. Rev. **102**, 1008 (1956).

[156] X. G. Wen, F. Wilczek, and A. Zee, Phys. Rev. B **39**, 11413 (1989).

[157] M. Hermele, M. P. A. Fisher, and L. Balents, Phys. Rev. B **69**, 064404 (2004).

[158] A. Banerjee, S. V. Isakov, K. Damle, and Y. B. Kim, Phys. Rev. Lett. **100**, 047208 (2008).

[159] L. Savary and L. Balents, Phys. Rev. Lett. **108**, 037202 (2012).

[160] N. Shannon, O. Sikora, F. Pollmann, K. Penc, and P. Fulde, Phys. Rev. Lett. **108**, 067204 (2012).

[161] Z. Hao, A. G. R. Day, and M. J. P. Gingras, Phys. Rev. B **90**, 214430 (2014).

[162] G. Chen, Phys. Rev. B **94**, 205107 (2016).

[163] Y. Zhou, K. Kanoda, and T.-K. Ng, Rev. Mod. Phys. **89**, 025003 (2017).

[164] A. M. Hallas, A. M. Arevalo-Lopez, A. Z. Sharma, T. Munsie, J. P. Attfield, C. R. Wiebe, and G. M. Luke, Phys. Rev. B **91**, 104417 (2015).

[165] K. Kimura, S. Nakatsuji, J. J. Wen, C. Broholm, M. B. Stone, E. Nishibori, and H. Sawa, Nat. Commun. **4**, 1934 (2013).

[166] K. Matsuhira, C. Sekine, C. Paulsen, and Y. Hinatsu, J. Magn. Magn. Mater. **272-276**, E981 (2004).

[167] D. Prabhakaran, S. Wang, and A. Boothroyd, J. Cryst. Growth **468**, 335 (2017).

[168] M. Tachibana, Y. Kohama, T. Atake, and E. Takayama-Muromachi, J. Appl. Phys. **101**, 09D502 (2007).

[169] N. Taira, M. Wakeshima, and Y. Hinatsu, J. Phys.: Condens. Matter **11**, 6983 (1999).

[170] J. van Duijn, K. H. Kim, N. Hur, D. Adroja, M. A. Adams, Q. Z. Huang, M. Jaime, S.-W. Cheong, C. Broholm, and T. G. Perring, Phys. Rev. Lett. **94**, 177201 (2005).

[171] M. Ito, Y. Yasui, M. Kanada, H. Harashina, S. Yoshii, K. Murata, M. Sato, H. Okumura, and K. Kakurai, J. Phys. Soc. Jpn. **69**, 888 (2000).

[172] S. Zouari, R. Ballou, A. Cheikhrouhou, and P. Strobel, J. Alloys Compd. **476**, 43 (2009).

[173] J. van Duijn, K. H. Kim, N. Hur, R. Ruiz-Bustos, D. T. Adroja, F. Bridges, A. Daoud-Aladine, F. Fernandez-Alonso, J. J. Wen, V. Kearney, et al., Phys. Rev. B **96**, 094409 (2017).

[174] J. N. Millican, R. T. Mascaluso, S. Nakatsuji, Y. Yachida, Y. Maeno, and C. J. Y., Mater. Res. Bull. **42**, 928 (2007).

[175] Y. Machida, S. Nakatsuji, H. Tonomura, T. Tayama, T. Sakakibara, J. van Duijn, C. Broholm, and Y. Maeno, J. Phys. Chem. Solids **66**, 1435 (2005).

[176] R. Flint and T. Senthil, Phys. Rev. B **87**, 125147 (2013).

[177] Y. Machida, S. Nakatsuji, Y. Maeno, T. Tayama, T. Sakakibara, and S. Onoda, Phys. Rev. Lett. **98**, 057203 (2007).

[178] M. Udagawa, H. Ishizuka, and Y. Motome, Phys. Rev. Lett. **108**, 066406 (2012).

[179] X. Wan, A. M. Turner, A. Vishwanath, and S. Y. Savrasov, Phys. Rev. B **83**, 205101 (2011).

[180] D. Yanagishima and Y. Maeno, J. Phys. Soc. Jpn. **70**, 2880 (2001).

[181] P. Chandra, P. Coleman, and R. Flint, Nature **493**, 621 (2013).

[182] G. Baskaran and P. W. Anderson, Phys. Rev. B **37**, 580 (1988).

[183] R. B. Laughin, Science **242**, 525 (1988).

[184] J. Ye, Y. B. Kim, A. J. Millis, B. I. Shraiman, P. Majumdar, and Z. Tešanović, Phys. Rev. Lett. **83**, 3737 (1999).

[185] H. Kawamura, Phys. Rev. Lett. **90**, 047202 (2003).

[186] N. Nagaosa, J. Sinova, S. Onoda, A. H. MacDonald, and N. P. Ong, Rev. Mod. Phys. **82**, 1539 (2010).

[187] K. Matsuhira, C. Sekine, C. Paulsen, M. Wakeshima, Y. Hinatsu, T. Kitazawa, Y. Kiuchi, Z. Hiroi, and S. Takagi, J. Phys. Conf. Ser. **145**, 012031 (2009).

[188] M. C. Hatnean, C. Decorse, M. R. Lees, O. A. Petrenko, D. S. Keeble, and G. Balakrishnan, Mater. Res. Express **1**, 026109 (2014).

[189] K. A. Ross, L. R. Yaraskavitch, M. Laver, J. S. Gardner, J. A. Quilliam, S. Meng, J. B. Kycia, D. K. Singh, T. Proffen, H. A. Dabkowska, et al., Phys. Rev. B **84**, 174442 (2011).

[190] E. Lhotel, S. R. Giblin, M. R. Lees, G. Balakrishnan, L. J. Chang, and Y. Yasui, Phys. Rev. B **89**, 224419 (2014).

[191] H. Takatsu, H. Kadowaki, T. J. Sato, J. W. Lynn, Y. Tabata, T. Yamazaki, and K. Matsuhira, J. Phys.: Condens. Matter **24**, 052201 (2012).

[192] D. P. Shoemaker, R. Seshadri, A. L. Hector, A. Llobet, T. Proffen, and C. J. Fennie, Phys. Rev. B **81**, 144113 (2010).

[193] Y. Tabira, R. Withers, J. Thompson, and S. Schmid, Journal of Solid State Chemistry **142**, 393 (1999).

[194] L. Savary and L. Balents, Phys. Rev. Lett. **118**, 087203 (2017).

[195] M. Taillefumier, O. Benton, H. Yan, L. D. C. Jaubert, and N. Shannon, Phys. Rev. X **7**, 041057 (2017).

[196] V. K. Anand, L. Opherden, J. Xu, D. T. Adroja, A. T. M. N. Islam, T. Herrmannsdörfer, J. Hornung, R. Schönemann, M. Uhlarz, H. C. Walker, et al., Phys. Rev. B **94**, 144415 (2016).

[197] N. Martin, P. Bonville, E. Lhotel, S. Guitteny, A. Wildes, C. Decorse, M. Ciomaga Hatnean, G. Balakrishnan, I. Mirebeau, and S. Petit, Phys. Rev. X **7**, 041028 (2017).

[198] V. Anand, A. Islam, A. Samartzis, J. Xu, N. Casati, and B. Lake, Journal of Crystal Growth **498**, 124 (2018).

[199] M. C. Hatnean, R. Sibille, M. R. Lees, M. Kenzelmann, V. Ban, V. Pomjakushin, and G. Balakrishnan, J. Phys.: Condens. Matter **29**, 075902 (2017).

[200] Y. Kato and S. Onoda, Phys. Rev. Lett. **115**, 077202 (2015).

[201] T. A. Bojesen and S. Onoda, Phys. Rev. Lett. **119**, 227204 (2017).

[202] L. D. Pan, N. J. Laurita, K. A. Ross, B. D. Gaulin, and N. P. Armitage, Nat. Phys. **12**, 361 (2016).

[203] B. J. Kennedy, B. A. Hunter, and C. J. Howard, J. Solid State Chem. **130**, 58 (1997).

[204] V. O. Garlea, B. C. Chakoumakos, S. A. Moore, G. B. Taylor, T. Chae, R. G. Maples, R. A. Riedel, G. W. Lynn, and D. L. Selby, Appl. Phys. A **99**, 531 (2010).

[205] J. M. Carpenter and C.-K. Loong, *Elements of Slow-Neutron Scattering: Basics, Techniques, and Applications* (Cambridge University Press, 2015), pp. 204–236.

[206] G. Ehlers, A. A. Podlesnyak, J. L. Niedziela, E. B. Iverson, and P. E. Sokol, Rev. Sci. Instrum. **82**, 085108 (2011).

[207] G. E. Granroth, D. H. Vandergriff, and S. E. Nagler, Physica B Condens. Matter **385-386**, 1104 (2006).

[208] D. L. Price and F. Fernandez-Alonso, *Neutron Scattering - Magnetic and Quantum Phenomena*, vol. 48 (Elsevier, 125 London Wall, London, 2015).

[209] L. Vegard, Z. Phys. **5**, 17 (1921).

[210] Y. Tokiwa, J. Ishikawa, S. Nakatsuji, and P. Gegenwart, Nat. Mater. **13**, 356 (2014).

[211] J. Rodrguez-Carvajal, Physica B Condens. Matter. **192**, 55 (1993).

[212] R. I. Bewley, R. S. Eccleston, K. A. McEwen, S. M. Hayden, M. T. Dove, S. M. Bennington, J. R. Treadgold, and R. L. S. Coleman, Physica B Condens. Matter **385-386**, 1029 (2006).

[213] A. A. Aczel, G. E. Granroth, G. J. MacDougall, W. J. L. Buyers, D. L. Abernathy, G. D. Samolyuk, G. M. Stocks, and S. E. Nagler, Nat. Commun. **3**, 1124 (2012).

[214] N. G. Parkinson, P. D. Hatton, J. A. K. Howard, S. R. Giblin, I. Terry, C. Ritter, B.-H. Mok, and M.-K. Wu, J. Mater. Chem. **15**, 1375 (2005).

[215] E. Balcar, S. W. Lovesey, and F. A. Wedgwood, J. Phys. C Solid State Phys. **3**, 1292 (1970).

[216] R. Applegate, N. R. Hayre, R. R. P. Singh, T. Lin, A. G. R. Day, and M. J. P. Gingras, Phys. Rev. Lett. **109**, 097205 (2012).

[217] J. Harada, J. D. Axe, and G. Shirane, Phys. Rev. B **4**, 155 (1971).

[218] H. A. Kramers, Proc. Amsterdam Acad. **33**, 959 (1930).

[219] L. Minervini, R. W. Grimes, and K. E. Sickafus, J. Am. Ceram. Soc. **83**, 1873 (2004).

[220] B. D. Gaulin, E. Kermarrec, M. L. Dahlberg, M. J. Matthews, F. Bert, J. Zhang, P. Mendels, K. Fritsch, G. E. Granroth, P. Jiramongkolchai, et al., Phys. Rev. B **91**, 245141 (2015).

[221] V. Pe çanha Antonio, E. Feng, Y. Su, V. Pomjakushin, F. Demmel, L.-J. Chang, R. J. Aldus, Y. Xiao, M. R. Lees, and T. Brückel, Phys. Rev. B **96**, 214415 (2017).

[222] P. R. Bevington, D. K. Robinson, J. M. Blair, A. J. Mallinckrodt, and S. McKay, Comp. Phys. **7**, 415 (1993).

[223] M. Abramowitz and I. A. Stegun, Appl. Mat. Ser. **55**, 62 (1966).

[224] M. B. Stone, Private Communication.

[225] C. Stock, E. E. Rodriguez, N. Lee, M. A. Green, F. Demmel, R. A. Ewings, P. Fouquet, M. Laver, Ch. Niedermayer, Y. Su, et al., Phys. Rev. Lett. **117**, 017201 (2016).

[226] J. P. Goff, D. A. Tennant, and S. E. Nagler, Phys. Rev. B **52**, 15992 (1995).

[227] S. E. Nagler, W. J. L. Buyers, R. L. Armstrong, and B. Briat, Phys. Rev. B **27**, 1784 (1983).

[228] S. E. Nagler, W. J. L. Buyers, R. L. Armstrong, and B. Briat, Phys. Rev. B **28**, 3873 (1983).

[229] B. McCoy and T. Wu, Phys. Rev. D **18**, 1259 (1978).

[230] J. Torrance and M. Tinkham, Phys. Rev. **187**, 587 (1969).

[231] J. Torrance and M. Tinkham, Phys. Rev. **187**, 595 (1969).

[232] C. M. Morris, R. Valdés Aguilar, A. Ghosh, S. M. Koohpayeh, J. Krizan, R. J. Cava, O. Tchernyshyov, T. M. McQueen, and N. P. Armitage, Phys. Rev. Lett. **112**, 137403 (2014).

[233] H. Shiba, Progr. Theor. Phys. **64**, 466 (1980).

[234] W. Breitling, W. Lehmann, and R. Weber, J. Magn. Magn. Mater. **10**, 25 (1979).

[235] I. Johnstone and D. Lockwood, Solid State Commun. **32**, 285 (1979).

[236] S. Ladak, D. E. Read, G. K. Perkins, L. F. Cohen, and W. R. Branford, Nat. Phys. **6**, 359 (2010).

[237] L. D. C. Jaubert and P. C. W. Holdsworth, Nat. Phys. **5**, 258 (2009).

[238] R. G. Hohlfeld and G. Sandri, Wavelet Technologies White Paper **11**, 1 (2011).

[239] S. B. Rutkevich, J. Stat. Phys. **131**, 917 (2008).

[240] D. I. Pushkarov and K. I. Pushkarov, Phys. Status Solidi B **81**, 703 (1977).

[241] D. I. Pushkarov and K. I. Pushkarov, Phys. Status Solidi B **85**, K89 (1978).

[242] K. I. Pushkarov and D. I. Pushkarov, physica status solidi (b) **93**, 735 (1979).

[243] J. G. Rau, L. S. Wu, A. F. May, L. Poudel, B. Winn, V. O. Garlea, A. Huq, P. Whitfield, A. E. Taylor, M. D. Lumsden, et al., Phys. Rev. Lett. **116**, 257204 (2016).

[244] W. W. Lui and M. Fukuma, J. Appl. Phys. **60**, 1555 (1986).

[245] Y. Tokiwa, T. Yamashita, M. Udagawa, S. Kittaka, T. Sakakibara, D. Terazawa, Y. Shimoyama, T. Terashima, Y. Yasui, T. Shibauchi, et al., Nat. Commun. **7** (2016).

[246] W. M. Walsh, J. Jeener, and N. Bloembergen, Phys. Rev. **139**, A1338 (1965).

[247] J. Joyce, A. Arko, J. Lawrence, J. Tang, P. Canfield, R. Bartlett, Z. Fisk, J. Thompson, and P. Riseborough, Solid State Commun. **83**, 551 (1992).

[248] M. S. S. Brooks, D. A. Goodings, and H. I. Ralph, J. Phys. C: Sol. State Phys. **1**, 132 (1968).

[249] C. Castellano, G. Berti, F. Rubio-Marcos, G. Lamura, S. Sanna, E. Salas-Colera, A. Brambilla, . Muoz-Noval, L. Du, and F. Demartin, J. Alloys Compd. **723**, 327 (2017).

[250] H. D. Zhou, S. T. Bramwell, J. G. Cheng, C. R. Wiebe, G. Li, L. Balicas, J. A. Bloxsom, H. J. Silverstein, J. S. Zhou, J. B. Goodenough, et al., Nat. Commun. **2**, 478 (2011).

[251] C. Paulsen, M. J. Jackson, E. Lhotel, B. Canals, D. Prabhakaran, K. Matsuhira, S. Giblin, and S. Bramwell, Nat. Phys. **10**, 135 (2014).

[252] H. Kadowaki, Y. Ishii, K. Matsuhira, and Y. Hinatsu, Phys. Rev. B **65**, 144421 (2002).

[253] A. M. Hallas, J. A. M. Paddison, H. J. Silverstein, A. L. Goodwin, J. R. Stewart, A. R. Wildes, J. G. Cheng, J. S. Zhou, J. B. Goodenough, E. S. Choi, et al., Phys. Rev. B **86**, 134431 (2012).

[254] J. D. Jackson, *Classical electrodynamics* (Wiley, New York, New York, 1975).

[255] C. R. Wiebe, Private Communication.

[256] N. Bjerrum, Kgl. Dan. Vidensk. Selsk. Mat.-Fys. Medd. **7**, 1 (1926).

[257] C. Castelnovo, R. Moessner, and S. L. Sondhi, Phys. Rev. B **84**, 144435 (2011).

[258] P. Debye and E. Hückel, Phys. Z. **24**, 185 (1923).

[259] A. M. Hallas, J. Gaudet, and B. D. Gaulin, Annu. Rev. Condens. Matter Phys. **9**, 105 (2018).

[260] J. A. Hodges, P. Bonville, A. Forget, M. Rams, K. Królas, and G. Dhalenne, J Phys Condens Matter. **13**, 9301 (2001).

[261] M. T. Hutchings, *Solid State Physics: Advances in Research and Applications*, vol. 16 (Academic Press, Berkeley Square House, London, 1965).

[262] J. Gaudet, A. M. Hallas, A. I. Kolesnikov, and B. D. Gaulin, Phys. Rev. B **97**, 024415 (2018).

[263] A. M. Hallas, J. Gaudet, M. N. Wilson, T. J. Munsie, A. A. Aczel, M. B. Stone, R. S. Freitas, A. M. Arevalo-Lopez, J. P. Attfield, M. Tachibana, et al., Phys. Rev. B **93**, 104405 (2016).

[264] K. W. H. Stevens, Proc. Phys. Soc. London, Sect. A **65**, 209 (1952).

[265] U. Walter, J. Phys. Chem. Solids. **45**, 401 (1984).

[266] R. Shankar, *Principles of Quantum Mechanics* (Springer, New York, New York, 1994).

[267] D. Griffiths, *Introduction to Quantum Mechanics* (Cambridge University Press, Cambridge, U.K., 2016).

[268] W. Greiner and B. Müller, *Angular Momentum Algebra Representation of Angular Momentum Operators — Generators of SO(3)* (Springer Berlin Heidelberg, Berlin, Heidelberg, 1994), pp. 57–85.

[269] A. T. Boothroyd, SPECTRE, a program for calculating spectroscopic properties of rare earth ions in crystals (1990-2018).

[270] M. E. Rose, *Elementary theory of angular momentum*, Structure of matter series (Wiley, New York, New York, 1957).

[271] D. I. Khomskii, K. I. Kugel, A. O. Sboychakov, and S. V. Streltsov, J. Exp. Theor. Phys. **122**, 484 (2016).

[272] G. L. Stamokostas and G. A. Fiete, Phys. Rev. B **97**, 085150 (2018).

[273] Y. Li, X. Luo, and H. Kröger, Science in China Series G **49**, 60 (2006).

[274] A. das Arulsamy, Pramana **74**, 615 (2010).

[275] R. Sibille, E. Lhotel, M. C. Hatnean, G. J. Nilsen, G. Ehlers, A. Cervellino, E. Ressouche, M. Frontzek, O. Zaharko, V. Pomjakushin, et al., Nat. Commun. **8**, 892 (2017).

[276] S. F. Edwards and P. W. Anderson, J. Phys. F: Met. Phys. **5**, 965 (1975).

[277] S. F. Edwards and P. W. Anderson, J. Phys. F: Met. Phys. **6**, 1927 (1976).

[278] E. P. Raposo and M. D. Coutinho-Filho, Phys. Rev. B **57**, 3495 (1998).

[279] O. Narayan and D. S. Fisher, Phys. Rev. B **42**, 7869 (1990).

[280] E. Altman, Y. Kafri, A. Polkovnikov, and G. Refael, Phys. Rev. Lett. **93**, 150402 (2004).

[281] P. B. Weichman, Mod. Phys. Lett. B **22**, 2623 (2008).

[282] J. A. Hoyos and T. Vojta, Phys. Rev. Lett. **100**, 240601 (2008).

[283] T. Vojta, Journal of Physics A: Mathematical and General **39**, R143 (2006).

[284] R. A. Cowley and W. J. L. Buyers, Rev. Mod. Phys. **44**, 406 (1972).

[285] T. M. Nieuwenhuizen and C. N. A. van Duin, Eur. Phys. J. B **7**, 191 (1999).

[286] L. Radzihovsky and J. Toner, Phys. Rev. B **60**, 206 (1999).

[287] T. Bellini, L. Radzihovsky, J. Toner, and N. A. Clark, Science **294**, 1074 (2001).

[288] J. Toner and D. P. DiVincenzo, Phys. Rev. B **41**, 632 (1990).

[289] K. Binder and A. P. Young, Rev. Mod. Phys. **58**, 801 (1986).

[290] H. Barghathi and T. Vojta, Phys. Rev. Lett. **109**, 170603 (2012).

[291] T. Vojta, *Computing Quantum Phase Transitions* (Wiley-Blackwell, 2009), chap. 4, pp. 167–221.

[292] T. Giamarchi and P. Le Doussal, Phys. Rev. B **52**, 1242 (1995).

[293] T. Klein, I. Joumard, S. Blanchard, J. Marcus, R. Cubitt, T. Giamarchi, and P. Le Doussal, Nature **413**, 404 (2001).

[294] A. D. Hernández and D. Domínguez, Phys. Rev. Lett. **92**, 117002 (2004).

[295] P. Olsson, Phys. Rev. Lett. **98**, 097001 (2007).

[296] D. Li and B. Rosenstein, Phys. Rev. Lett. **90**, 167004 (2003).

[297] M. J. P. Gingras and D. A. Huse, Phys. Rev. B **53**, 15193 (1996).

[298] D. S. Fisher, Phys. Rev. Lett. **78**, 1964 (1997).

[299] T. Giamarchi and P. Le Doussal, Phys. Rev. Lett. **72**, 1530 (1994).

[300] R. B. Griffiths, Phys. Rev. Lett. **23**, 17 (1969).

[301] A. J. Bray, Phys. Rev. Lett. **59**, 586 (1987).

[302] B. M. McCoy, Phys. Rev. Lett. **23**, 383 (1969).

[303] S. Park, R. L. Leheny, R. J. Birgeneau, J.-L. Gallani, C. W. Garland, and G. S. Iannacchione, Phys. Rev. E **65**, 050703 (2002).

[304] R. L. Leheny, S. Park, R. J. Birgeneau, J.-L. Gallani, C. W. Garland, and G. S. Iannacchione, Phys. Rev. E **67**, 011708 (2003).

[305] P. S. Clegg, C. Stock, R. J. Birgeneau, C. W. Garland, A. Roshi, and G. S. Iannacchione, Phys. Rev. E **67**, 021703 (2003).

[306] H. R. Glyde, Rep. Prog. Phys. **81**, 014501 (2018).

[307] H. R. Glyde, O. Plantevin, B. Fåk, G. Coddens, P. S. Danielson, and H. Schober, Phys. Rev. Lett. **84**, 2646 (2000).

[308] J. V. Porto and J. M. Parpia, Phys. Rev. Lett. **74**, 4667 (1995).

[309] D. T. Sprague, T. M. Haard, J. B. Kycia, M. R. Rand, Y. Lee, P. J. Hamot, and W. P. Halperin, Phys. Rev. Lett. **75**, 661 (1995).

[310] N. Mulders, J. Reppy, M. Chan, N. Mulders, and J. Reppy, Physics Today **49**, 30 (1996).

[311] Y. Imry and S.-k. Ma, Phys. Rev. Lett. **35**, 1399 (1975).

[312] A. Aharony, Y. Imry, and S.-k. Ma, Phys. Rev. Lett. **37**, 1364 (1976).

[313] S. M. A. Tabei, M. J. P. Gingras, Y.-J. Kao, P. Stasiak, and J.-Y. Fortin, Phys. Rev. Lett. **97**, 237203 (2006).

[314] D. Silevitch, D. Bitko, J. Brooke, S. Ghosh, G. Aeppli, and T. Rosenbaum, Nature **448**, 567 (2007).

[315] Z. Slanič, D. P. Belanger, and J. A. Fernandez-Baca, Phys. Rev. Lett. **82**, 426 (1999).

[316] G. Álvarez, N. Aso, D. P. Belanger, A. M. Durand, V. Martín-Mayor, K. Motoya, and Y. Muro, Phys. Rev. B **86**, 024416 (2012).

[317] Y. W. Rodriguez, I. E. Anderson, D. P. Belanger, H. Nojiri, F. Ye, and J. A. Fernandez-Baca, J. Magn. Magn. Mater. **310**, 1546 (2007).

[318] R. A. Cowley, H. Yoshizawa, G. Shirane, and R. J. Birgeneau, Z Phys. B Con. Mat. **58**, 15 (1984).

[319] R. J. Birgeneau and Y. J. Uemura, Journal of Applied Physics **61**, 3692 (1987).

[320] C. Paduani, D. P. Belanger, J. Wang, S.-J. Han, and R. M. Nicklow, Phys. Rev. B **50**, 193 (1994).

[321] Leheny, R. L., Lee, Y. S., Shirane, G., and Birgeneau, R. J., Eur. Phys. J. B **32**, 287 (2003).

[322] T. Vojta, AIP Conf. Proc. **1550**, 188 (2013).

[323] S. Fishman and A. Aharony, J. Phys. C: Solid State Phys. **12**, L729 (1979).

[324] D. J. Lloyd and J. Galy, Cryst. Struct. Commun. **2**, 209 (1973).

[325] Z. He, J.-I. Yamaura, Y. Ueda, and W. Cheng, J. Am. Chem. Soc. **131**, 7554 (2009).

[326] M. Markkula, A. M. Arévalo-López, and J. P. Attfield, J. Solid State Chem. **192**, 390 (2012).

[327] S. Ichikawa, M. Hibino, and T. Yao, Asian J. Energy Environ. **8**, 33 (2007).

[328] Agilent-CrysAlisPRO, Yarnton, Oxfordshire, England (2013).

[329] O. V. Dolomanov, L. J. Bourhis, R. J. Gildea, J. A. Howard, and H. Puschmann, J. Appl. Crystallogr. **42**, 339 (2009).

[330] V. Petříček, M. Dušek, and L. Palatinus, Z. Kristallogr. Cryst. Mater. **229**, 345 (2014).

[331] B. H. Toby, J. Appl. Crystallogr. **34**, 210 (2001).

[332] W. Whitley, C. Stock, and A. D. Huxley, J. Appl. Crystallogr. **48**, 1342 (2015).

[333] C. L. Bull, M. W. Johnson, H. Hamidov, K. Komatsu, M. Guthrie, M. J. Gutmann, J. S. Loveday, and R. J. Nelmes, J. Appl. Crystallogr. **47**, 974 (2014).

[334] M. J. Gutmann, V. Petříček, M. A. Daoud-Aladine, and C. Y. Martin, Meas. Sci. Technol. **19**, 034005 (2008).

[335] M. Gutmann, Acta Cryst. A **61**, c164 (2005).

[336] C. Stock, R. A. Cowley, J. W. Taylor, and S. M. Bennington, Phys. Rev. B **81**, 024303 (2010).

[337] K. H. Andersen, Nucl. Instr. Meth. Phys. Res. A **371**, 472 (1996).

[338] National Institute of Standards and Technology, *NIST Center for Neutron Research Accomplishments and Opportunities*, vol. 962 of *ASTM Special Technical Publication* (Department of Commerce, United States of America, 2001).

[339] Z. Ropka and R. J. Radwanski, Czech J. Phys. **54**, 427 (2004).

[340] J. L. Gavilano, D. Rau, S. Mushkolaj, H. R. Ott, P. Millet, and F. Mila, Phys. Rev. Lett. **90**, 167202 (2003).

[341] J. Kanamori, Progr. Theor. Phys. **17**, 177 (1957).

[342] D. B. Litvin, *Magnetic Group Tables: 1-, 2- and 3-Dimensional Magnetic Subperiodic Groups and Magnetic Space Groups* (International Union of Crystallography, Chester, U.K., 2013).

[343] M. De Graef, Metall. Mater. Trans. A **41**, 1321 (2010).

[344] Z. Xu, J. Wen, T. Berlijn, P. M. Gehring, C. Stock, M. B. Stone, W. Ku, G. Gu, S. M. Shapiro, R. J. Birgeneau, et al., Phys. Rev. B **86**, 174419 (2012).

[345] C. Stock, W. J. L. Buyers, R. Liang, D. Peets, Z. Tun, D. Bonn, W. N. Hardy, and R. J. Birgeneau, Phys. Rev. B **69**, 014502 (2004).

[346] W. J. L. Buyers, R. A. Cowley, T. M. Holden, and R. W. H. Stevenson, J. Appl. Phys. **39**, 1118 (1968).

[347] P. Martel, R. A. Cowley, and R. W. H. Stevenson, Can. J. Phys. **46**, 1355 (1968).

[348] H. M. Gladney, Phys. Rev. **146**, 253 (1966).

[349] M. B. Stone, I. Zaliznyak, D. H. Reich, and C. Broholm, Phys. Rev. B **64**, 144405 (2001).

[350] J. Lorenzana, G. Seibold, and R. Coldea, Phys. Rev. B **72**, 224511 (2005).

[351] K. W. Plumb, J. R. Morey, J. A. Rodriguez-Rivera, H. Wu, A. A. Podlesnyak, T. M. McQueen, and C. L. Broholm, Phys. Rev. X **6**, 041055 (2016).

[352] P. R. Hammar, D. H. Reich, C. Broholm, and F. Trouw, Phys. Rev. B **57**, 7846 (1998).

[353] T. Holden, W. Buyers, E. Svensson, R. Cowley, M. Hutchings, D. Hukin, and R. Stevenson, J. Phys. C Solid State Phys. **4**, 2127 (1971).

[354] S. A. J. Kimber, H. Mutka, T. Chatterji, T. Hofmann, P. F. Henry, H. N. Bordallo, D. N. Argyriou, and J. P. Attfield, Phys. Rev. B **84**, 104425 (2011).

[355] R. Radwanski and Z. Ropka, Physica B Condens. Matter **345**, 107 (2004), proceedings of the Conference on Polarised Neutron and Synchrotron X-rays for Magnetism.

[356] W. Neubeck, C. Vettier, F. de Bergevin, F. Yakhou, D. Mannix, L. Ranno, and T. Chatterji, J. Phys. Chem. Solids **62**, 2173 (2001).

[357] R. Birgeneau, A. Aharony, N. Belk, F. Chou, Y. Endoh, M. Greven, S. Hosoya, M. Kastner, C. Lee, Y. Lee, et al., J. Phys. Chem. Solids **56**, 1913 (1995).

[358] M. Greven, R. J. Birgeneau, Y. Endoh, M. A. Kastner, M. Matsuda, and G. Shirane, Z. Phys. B Con. Mat. **96**, 465 (1995).

[359] M. Songvilay, S. Petit, V. Hardy, J. P. Castellan, G. André, C. Martin, and F. Damay, Phys. Rev. B **91**, 054408 (2015).

[360] J. Gaudet, D. D. Maharaj, G. Sala, E. Kermarrec, K. A. Ross, H. A. Dabkowska, A. I. Kolesnikov, G. E. Granroth, and B. D. Gaulin, Phys. Rev. B **92**, 134420 (2015).

[361] Y. J. Uemura and R. J. Birgeneau, Phys. Rev. B **36**, 7024 (1987).

[362] C. Stock, W. J. L. Buyers, Z. Yamani, Z. Tun, R. J. Birgeneau, R. Liang, D. Bonn, and W. N. Hardy, Phys. Rev. B **77**, 104513 (2008).

[363] R. J. Birgeneau, R. W. Erwin, P. M. Gehring, M. A. Kastner, B. Keimer, M. Sato, S. Shamoto, G. Shirane, and J. Tranquada, Z. Phys. B Con. Mat. **87**, 15 (1992).

[364] W. Bao, Y. Chen, Y. Qiu, and J. L. Sarrao, Phys. Rev. Lett. **91**, 127005 (2003).

[365] B. Keimer, R. J. Birgeneau, A. Cassanho, Y. Endoh, R. W. Erwin, M. A. Kastner, and G. Shirane, Phys. Rev. Lett. **67**, 1930 (1991).

[366] S. D. Wilson, S. Li, P. Dai, W. Bao, J.-H. Chung, H. J. Kang, S.-H. Lee, S. Komiya, Y. Ando, and Q. Si, Phys. Rev. B **74**, 144514 (2006).

[367] C. Stock, E. E. Rodriguez, and M. A. Green, Phys. Rev. B **85**, 094507 (2012).

[368] T. Hong, M. Kenzelmann, M. M. Turnbull, C. P. Landee, B. D. Lewis, K. P. Schmidt, G. S. Uhrig, Y. Qiu, C. Broholm, and D. Reich, Phys. Rev. B **74**, 094434 (2006).

[369] T. E. Mason, in *High-Temperature Superconductors — II* (Elsevier, 2001), vol. 31 of *Handbook on the Physics and Chemistry of Rare Earths*, pp. 281 – 314.

[370] A. Schröder, G. Aeppli, R. Coldea, M. Adams, O. Stockert, H. Löhneysen, E. Bucher, R. Ramazashvili, and P. Coleman, Nature **407**, 351 (2000).

[371] O. Stockert, M. Enderle, and H. v. Löhneysen, Phys. Rev. Lett. **99**, 237203 (2007).

[372] A. J. Millis, Phys. Rev. B **48**, 7183 (1993).

[373] B. L. Bean and J. R. Izatt, J. Opt. Soc. Am. **63**, 832 (1973).

[374] M. Hagen, R. A. Cowley, S. K. Satija, H. Yoshizawa, G. Shirane, R. J. Birgeneau, and H. J. Guggenheim, Phys. Rev. B **28**, 2602 (1983).

[375] W. Bao, C. Broholm, G. Aeppli, S. A. Carter, P. Dai, T. F. Rosenbaum, J. M. Honig, P. Metcalf, and S. F. Trevino, Phys. Rev. B **58**, 12727 (1998).

[376] M. T. Hutchings, M. P. Schulhof, and H. J. Guggenheim, Phys. Rev. B **5**, 154 (1972).

[377] M. F. Collins, V. J. Minkiewicz, R. Nathans, L. Passell, and G. Shirane, Phys. Rev. **179**, 417 (1969).

[378] M. P. Schulhof, R. Nathans, P. Heller, and A. Linz, Phys. Rev. B **4**, 2254 (1971).

[379] H. Chou, J. M. Tranquada, G. Shirane, T. E. Mason, W. J. L. Buyers, S. Shamoto, and M. Sato, Phys. Rev. B **43**, 5554 (1991).

[380] C. Stock, C. Broholm, F. Demmel, J. Van Duijn, J. W. Taylor, H. J. Kang, R. Hu, and C. Petrovic, Phys. Rev. Lett. **109**, 127201 (2012).

[381] Q. Si, S. Rabello, K. Ingersent, and J. L. Smith, Nature **413**, 804 (2001).

[382] M. Hasenbusch, F. P. Toldin, A. Pelissetto, and E. Vicari, J. Stat. Mech. **2007**, P02016 (2007).

[383] H. G. Ballesteros, L. A. Fernández, V. Martín-Mayor, A. Muñoz Sudupe, G. Parisi, and J. J. Ruiz-Lorenzo, Phys. Rev. B **58**, 2740 (1998).

[384] P. Calabrese, V. Martín-Mayor, A. Pelissetto, and E. Vicari, Phys. Rev. E **68**, 036136 (2003).

[385] P. Calabrese, A. Pelissetto, and E. Vicari, Phys. Rev. B **68**, 092409 (2003).

[386] M. J. George and J. J. Rehr, Phys. Rev. Lett. **53**, 2063 (1984).

[387] C. Stock, L. C. Chapon, A. Schneidewind, Y. Su, P. G. Radaelli, D. F. McMorrow, A. Bombardi, N. Lee, and S.-W. Cheong, Phys. Rev. B **83**, 104426 (2011).

[388] S. D. Wilson, Z. Yamani, C. R. Rotundu, B. Freelon, E. Bourret-Courchesne, and R. J. Birgeneau, Phys. Rev. B **79**, 184519 (2009).

[389] P. C. Hohenberg and W. F. Brinkman, Phys. Rev. B **10**, 128 (1974).

[390] J. T. Haraldsen, T. Barnes, and J. L. Musfeldt, Phys. Rev. B **71**, 064403 (2005).

[391] G. Xu, C. Broholm, D. H. Reich, and M. A. Adams, Phys. Rev. Lett. **84**, 4465 (2000).

[392] E. E. McCabe, C. Stock, E. E. Rodriguez, A. S. Wills, J. W. Taylor, and J. S. O. Evans, Phys. Rev. B **89**, 100402 (2014).

[393] S. Ma, C. Broholm, D. H. Reich, B. J. Sternlieb, and R. W. Erwin, Phys. Rev. Lett. **69**, 3571 (1992).

[394] S. M. Girvin, A. H. MacDonald, and P. M. Platzman, Phys. Rev. B **33**, 2481 (1986).

[395] E. C. Svensson, W. J. L. Buyers, T. M. Holden, R. A. Cowley, and R. W. Stevenson, Can. J. Phys. **47**, 1983 (1969).

[396] M. Ramazanoglu, C. P. Adams, J. P. Clancy, A. J. Berlinsky, Z. Yamani, R. Szymczak, H. Szymczak, J. Fink-Finowicki, and B. D. Gaulin, Phys. Rev. B **79**, 024417 (2009).

[397] K. Lee, J. Lee, C. Lee, and M. Whangbo, Bull. Korean Chem. Soc. **35**, 1277 (2014).

[398] M. B. Stone, Y. Chen, J. Rittner, H. Yardimci, D. H. Reich, C. Broholm, D. V. Ferraris, and T. Lectka, Phys. Rev. B **65**, 064423 (2002).

[399] R. J. Birgeneau, Q. Feng, Q. J. Harris, J. P. Hill, A. P. Ramirez, and T. R. Thurston, Phys. Rev. Lett. **75**, 1198 (1995).

[400] Y. J. Kim, R. J. Birgeneau, F. C. Chou, M. Greven, M. A. Kastner, Y. S. Lee, B. O. Wells, A. Aharony, O. Entin-Wohlman, I. Y. Korenblit, et al., Phys. Rev. B **64**, 024435 (2001).

[401] I. Cabrera, J. D. Thompson, R. Coldea, D. Prabhakaran, R. I. Bewley, T. Guidi, J. A. Rodriguez-Rivera, and C. Stock, Phys. Rev. B **90**, 014418 (2014).

[402] A. P. Young, *Spin Glasses and Random Fields*, Directions in condensed matter physics (World Scientific, 57 Shelton Street, Covent Garden, London, 1998), 12th ed.

[403] A. R. King and V. Jaccarino, J. Appl. Phys. **52**, 1785 (1981).

[404] J. Mattsson, J. Kushauer, D. Bertrand, J. Ferr, and W. Kleemann, J. Magn. Magn. Mater. **130**, 216 (1994).

[405] N. G. Fytas, V. Martín-Mayor, M. Picco, and N. Sourlas, J. Stat. Phys. (2018).

[406] L. M. Volkova, J. Phys. Condens. Matter **19**, 176208 (2007).

[407] G. D'Ariano and F. Borsa, Phys. Rev. B **26**, 6215 (1982).

[408] C. A. Ramos, A. R. King, and V. Jaccarino, Phys. Rev. B **37**, 5483 (1988).

[409] D. P. Belanger, A. R. King, I. B. Ferreira, and V. Jaccarino, Phys. Rev. B **37**, 226 (1988).

[410] D. P. Belanger and H. Yoshizawa, Phys. Rev. B **47**, 5051 (1993).

[411] T. Terao, K. Yakubo, and T. Nakayama, Phys. Rev. E **50**, 566 (1994).

[412] M. Vojta, Phys. Rev. Lett. **111**, 097202 (2013).

[413] I. Y. Korenblit and E. F. Shender, Phys. Rev. B **48**, 9478 (1993).

[414] C. C. Wan, A. B. Harris, and D. Kumar, Phys. Rev. B **48**, 1036 (1993).

[415] M. T. Hutchings, B. D. Rainford, and H. J. Guggenheim, J. Phys. C: Solid State Phys. **3**, 307 (1970).

[416] C. B. de Araujo, Phys. Rev. B **22**, 266 (1980).

[417] R. J. Birgeneau, R. A. Cowley, G. Shirane, H. Yoshizawa, D. P. Belanger, A. R. King, and V. Jaccarino, Phys. Rev. B **27**, 6747 (1983).

[418] J. P. Hill, Q. Feng, Q. J. Harris, R. J. Birgeneau, A. P. Ramirez, and A. Cassanho, Phys. Rev. B **55**, 356 (1997).

[419] P. W. Mitchell, R. A. Cowley, H. Yoshizawa, P. Böni, Y. J. Uemura, and R. J. Birgeneau, Phys. Rev. B **34**, 4719 (1986).

[420] G. J. Coombs, R. A. Cowley, W. J. L. Buyers, E. C. Svensson, T. M. Holden, and D. A. Jones, J. Phys. C: Solid State Phys. **9**, 2167 (1976).

[421] M. Chan, N. Mulders, and J. Reppy, Phys. Today **49**, 30 (2018).

[422] Z. Yamani, W. J. L. Buyers, R. A. Cowley, and D. Prabhakaran, Physica B **403**, 1406 (2008).

[423] T. Satoh, R. Iida, T. Higuchi, Y. Fujii, A. Koreeda, H. Ueda, T. Shimura, K. Kuroda, V. I. Butrim, and B. A. Ivanov, Nat. Commun. **8**, 638 (2017).

[424] K. Tomiyasu and S. Itoh, J. Phys. Soc. Jpn. **75**, 084708 (2006).

[425] M. Feygenson, X. Teng, S. E. Inderhees, Y. Yiu, W. Du, W. Han, J. Wen, Z. Xu, A. A. Podlesnyak, J. L. Niedziela, et al., Phys. Rev. B **83**, 174414 (2011).

[426] G. Grinstein, J. Appl. Phys. **55**, 2371 (1984).

[427] Y. Imry, J. Stat. Phys. **34**, 849 (1984).

[428] T. Senthil, Phys. Rev. B **57**, 8375 (1998).

[429] J. Villain, B. Semeria, F. Lancon, and L. Billard, J. Phys. C: Solid State **16**, 6153 (1983).

[430] A. Aharony, Phys. Rev. B **18**, 3318 (1978).

[431] J. L. Cardy, Phys. Rev. B **29**, 505 (1984).

[432] Y. Tokura and N. Nagaosa, Science **288**, 462 (2000).

[433] E. Dagotto, Science **309**, 257 (2005).

[434] K. I. Kugel and D. I. Khomskii, Sov. Phys. JETP **36**, 725 (1973).

[435] Y. Okamoto, M. Nohara, H. A. Katori, and H. Takagi, Phys. Rev. Lett. **99**, 137207 (2007).

[436] R. Wang, A. Go, and A. J. Millis, Phys. Rev. B **95**, 045133 (2017).

[437] G. Jackeli and G. Khaliullin, Phys. Rev. Lett. **102**, 017205 (2009).

[438] C. G. Shull, W. A. Strauser, and E. O. Wollan, Phys. Rev. **83**, 333 (1951).

[439] Y. Y. Li, Phys. Rev. **100**, 627 (1955).

[440] W. L. Roth, Phys. Rev. **110**, 1333 (1958).

[441] B. van Laar, Phys. Rev. **138**, A584 (1965).

[442] M. W. Haverkort, A. Tanaka, L. H. Tjeng, and G. A. Sawatzky, Physical Rev. Lett. **99**, 257401 (2007).

[443] B. C. Larson, W. Ku, J. Z. Tischler, C.-C. Lee, O. D. Restrepo, A. G. Eguiluz, P. Zschack, and K. D. Finkelstein, Phys. Rev. Lett. **99**, 026401 (2007).

[444] J. Sakurai, W. J. L. Buyers, R. A. Cowley, and G. Dolling, Phys. Rev. **167**, 510 (1968).

[445] S. K. Satija, J. D. Axe, G. Shirane, H. Yoshizawa, and K. Hirakawa, Phys. Rev. B **21**, 2001 (1980).

[446] A. M. Oles, P. Horsch, L. F. Feiner, and G. Khaliullin, Phys. Rev. Lett. **96**, 147205 (2006).

[447] J. Kanamori, Progr. Theor. Phys. **17**, 197 (1957).

[448] W. J. L. Buyers, T. M. Holden, E. C. Svensson, and D. J. Lockwood, Phys. Rev. B **30**, 6521 (1984).

[449] D. Herrmann-Ronzaud, P. Burlet, and J. Rossat-Mignod, J. Phys. Condens. Matter **11**, 2123 (1978).

[450] S. Greenwald, Acta Crystallogr. **6**, 396 (1953).

[451] B. Grenier, S. Petit, V. Simonet, E. Canévet, L.-P. Regnault, S. Raymond, B. Canals, C. Berthier, and P. Lejay, Phys. Rev. Lett. **114**, 017201 (2015).

[452] H. D. Zhou, C. Xu, A. M. Hallas, H. J. Silverstein, C. R. Wiebe, I. Umegaki, J. Q. Yan, T. P. Murphy, J.-H. Park, Y. Qiu, et al., Phys. Rev. Lett. **109**, 267206 (2012).

[453] A. L. Dalverny, J. S. Filhol, F. Lemoigno, and M. L. Doublet, J. Phys. Chem. C **114**, 21750 (2010).

[454] H.-X. Deng, J. Li, S.-S. Li, J.-B. Xia, A. Walsh, and S.-H. Wei, Appl. Phys. Lett. **96**, 162508 (2010).

[455] E. C. Svensson, M. Harvey, W. J. L. Buyers, and T. M. Holden, J. Appl. Phys. **49**, 2150 (1978).

[456] A. Furrer, E. Pomjakushina, V. Pomjakushin, J. P. Embs, and T. Strässle, Phys. Rev. B **83**, 174442 (2011).

[457] A. Furrer and O. Waldmann, Rev. Mod. Phys. **85**, 367 (2013).

[458] A. Furrer, A. Podlesnyak, and K. W. Krämer, Phys. Rev. B **92**, 104415 (2015).

[459] A. Schrön, C. Rödl, and F. Bechstedt, Phys. Rev. B **86**, 115134 (2012).

[460] M. B. Stone, M. D. Lumsden, S. Chang, E. C. Samulon, C. D. Batista, and I. R. Fisher, Phys. Rev. Lett. **100**, 237201 (2008).

[461] M. J. Redman and E. G. Steward, Nature **193**, 867 (1962).

[462] R. Kannan and M. S. Seehra, Phys. Rev. B **35**, 6847 (1987).

[463] H. N. Ok and J. G. Mullen, Phys. Rev. **168**, 550 (1968).

[464] V. G. Tsirelson, A. S. Avilov, Y. A. Abramov, E. L. Belokoneva, R. Kitaneh, and D. Feil, Acta Crystallogr. Sect. B **54**, 8 (1998).

[465] R. M. Hazen, Am. Mineral. **62**, 280 (1977).

[466] MATLAB and Statistics Toolbox Release 2016b, The MathWorks, Inc., Natick, MA, USA.

[467] C. Kittel and H. Kroemer, *Thermal Physics* (W. H. Freeman, New York, New York, 1980), 2nd ed.

[468] Y. Zhu, *Modern techniques for characterizing magnetic materials* (Springer Science & Business Media, Berlin-Heidelberg, 2005).

[469] C. Kant, T. Rudolf, F. Schrettle, F. Mayr, J. Deisenhofer, P. Lunkenheimer, M. V. Eremin, and A. Loidl, Phys. Rev. B **78**, 245103 (2008).

[470] M. Tachiki, J. Phys. Soc. Jpn. **19**, 454 (1964).

[471] M. El-Batanouny, J. Phys.: Condens. Matter **14**, 6281 (2002).

[472] H.-h. Chou and H. Y. Fan, Phys. Rev. B **13**, 3924 (1976).

[473] R. R. Hayes and C. H. Perry, Solid State Commun. **13**, 1915 (1973).

[474] J. R. Singer, Phys. Rev. **104**, 929 (1956).

[475] T. Nagamiya, K. Yosida, and R. F. Kubo, Adv. Phys. **4**, 1 (1955).

[476] W. Bollmann, *Some Special Crystal Structures* (Springer Berlin Heidelberg, Berlin, Heidelberg, 1970), pp. 13–36.

[477] D. Gazzoli, M. Occhiuzzi, A. Cimino, D. Cordischi, G. Minelli, and F. Pinzari, J. Chem. Soc. Faraday Trans. **92**, 4567 (1996).

[478] S. Sasaki, K. Fujino, and Y. TakÉchi, Proc. Jpn. Acad. Ser. B Phys. Biol. Sci. **55**, 43 (1979).

[479] I. Kimchi and A. Vishwanath, Phys. Rev. B **89**, 014414 (2014).

[480] G. Baskaran, S. Mandal, and R. Shankar, Phys. Rev. Lett. **98**, 247201 (2007).

[481] J. Knolle, D. L. Kovrizhin, J. T. Chalker, and R. Moessner, Phys. Rev. Lett. **112**, 207203 (2014).

[482] J. Knolle, D. L. Kovrizhin, J. T. Chalker, and R. Moessner, Phys. Rev. B **92**, 115127 (2015).

[483] N. F. Mott, Proc. Phys. Soc., London, Sect. A **62**, 416 (1949).

[484] V. I. Anisimov, J. Zaanen, and O. K. Andersen, Phys. Rev. B **44**, 943 (1991).

[485] P. A. Lee, N. Nagaosa, and X.-G. Wen, Rev. Mod. Phys. **78**, 17 (2006).

[486] M. A. Kastner, R. J. Birgeneau, G. Shirane, and Y. Endoh, Rev. Mod. Phys. **70**, 897 (1998).

[487] Q. Si and E. Abrahams, Phys. Rev. Lett. **101**, 076401 (2008).

[488] J.-X. Zhu, R. Yu, H. Wang, L. L. Zhao, M. D. Jones, J. Dai, E. Abrahams, E. Morosan, M. Fang, and Q. Si, Phys. Rev. Lett. **104**, 216405 (2010).

[489] B. J. Kim, H. Jin, S. J. Moon, J.-Y. Kim, B.-G. Park, C. S. Leem, J. Yu, T. W. Noh, C. Kim, S.-J. Oh, et al., Phys. Rev. Lett. **101**, 076402 (2008).

[490] F. Ming, S. Johnston, D. Mulugeta, T. S. Smith, P. Vilmercati, G. Lee, T. A. Maier, P. C. Snijders, and H. H. Weitering, Phys. Rev. Lett. **119**, 266802 (2017).

[491] T. Yamauchi, Y. Hirata, Y. Ueda, and K. Ohgushi, Phys. Rev. Lett. **115**, 246402 (2015).

[492] R. Arita, A. Yamasaki, K. Held, J. Matsuno, and K. Kuroki, Phys. Rev. B **75**, 174521 (2007).

[493] S. Lefebvre, P. Wzietek, S. Brown, C. Bourbonnais, D. Jérome, C. Mézière, M. Fourmigué, and P. Batail, Phys. Rev. Lett. **85**, 5420 (2000).

[494] F. Kagawa, T. Itou, K. Miyagawa, and K. Kanoda, Phys. Rev. B **69**, 064511 (2004).

[495] V. Balédent, F. Rullier-Albenque, D. Colson, J. M. Ablett, and J.-P. Rueff, Phys. Rev. Lett. **114**, 177001 (2015).

[496] J. c. v. Chaloupka, G. Jackeli, and G. Khaliullin, Phys. Rev. Lett. **105**, 027204 (2010).

[497] C. Rödl, F. Fuchs, J. Furthmüller, and F. Bechstedt, Phys. Rev. B **79**, 235114 (2009).

[498] B. Brandow, Advances in Physics **26**, 651 (1977).

[499] E. Engel and R. N. Schmid, Phys. Rev. Lett. **103**, 036404 (2009).

[500] J. T. Cox and C. M. Quinn, J. Mater. Sci. **4**, 33 (1969).

[501] J. van Elp, J. L. Wieland, H. Eskes, P. Kuiper, G. A. Sawatzky, F. M. F. de Groot, and T. S. Turner, Phys. Rev. B **44**, 6090 (1991).

[502] C. de Graaf, W. de Jong, R. Broer, and W. Nieuwpoort, Chem. Phys. **237**, 59 (1998).

[503] G. W. Pratt and R. Coelho, Phys. Rev. **116**, 281 (1959).

[504] R. E. Cohen, I. I. Mazin, and D. G. Isaak, Science **275**, 654 (1997).

[505] A. Walsh, J. L. F. Da Silva, and S.-H. Wei, Phys. Rev. Lett. **100**, 256401 (2008).

[506] G. M. Dalpian, S.-H. Wei, X. Gong, A. J. da Silva, and A. Fazzio, Solid State Commun. **138**, 353 (2006).

[507] J. Coey, M. Venkatesan, and C. Fitzgerald, Nature Mater. **4**, 173 (2005).

[508] M. R. Daniel and A. P. Cracknell, Phys. Rev. **177**, 932 (1969).

[509] I. G. Austin and E. S. Garbett, J. Phys. C: Solid State Phys. **3**, 1605 (1970).

[510] T. M. Holden, E. C. Svensson, W. J. L. Buyers, and O. Vogt, Phys. Rev. B **10**, 3864 (1974).

[511] B. Grover, Phys. Rev. **140**, A1944 (1965).

[512] B. R. Cooper, Phys. Rev. B **6**, 2730 (1972).

[513] Y.-L. Wang and B. R. Cooper, Phys. Rev. **185**, 696 (1969).

[514] D. A. Pink, J. Phys. C **1**, 1246 (1968).

[515] W. J. L. Buyers, T. M. Holden, and A. Perreault, Phys. Rev. B **11**, 266 (1975).

[516] I. Turek, J. Kudrnovský, V. Drchal, and P. Bruno, Philos. Mag. **86**, 1713 (2006).

[517] R. J. Birgeneau, J. Als-Nielsen, and E. Bucher, Phys. Rev. B **6**, 2724 (1972).

[518] R. J. Birgeneau, J. Als-Nielsen, and E. Bucher, Phys. Rev. Lett. **27**, 1530 (1971).

[519] H. Yamada and M. Shimizu, J. Phys. Soc. Jpn. **21**, 1517 (1966).

[520] H. Yamada and M. Shimizu, J. Phys. Soc. Jpn. **22**, 1404 (1967).

[521] P. A. Wolff, Phys. Rev. **120**, 814 (1960).

[522] J. F. Cooke, Phys. Rev. B **7**, 1108 (1973).

[523] T. M. Holden and W. J. L. Buyers, Phys. Rev. B **9**, 3797 (1974).

[524] K. W. Plumb, A. T. Savici, G. E. Granroth, F. C. Chou, and Y.-J. Kim, Phys. Rev. B **89**, 180410 (2014).

[525] N. S. Headings, S. M. Hayden, R. Coldea, and T. G. Perring, Phys. Rev. Lett. **105**, 247001 (2010).

[526] C. Stock, R. A. Cowley, W. J. L. Buyers, C. D. Frost, J. W. Taylor, D. Peets, R. Liang, D. Bonn, and W. N. Hardy, Phys. Rev. B **82**, 174505 (2010).

[527] C. Stock, R. A. Cowley, W. J. L. Buyers, R. Coldea, C. Broholm, C. D. Frost, R. J. Birgeneau, R. Liang, D. Bonn, and W. N. Hardy, Phys. Rev. B **75**, 172510 (2007).

[528] C.-M. Ho, V. N. Muthukumar, M. Ogata, and P. W. Anderson, Phys. Rev. Lett. **86**, 1626 (2001).

[529] O. Arnold, J. Bilheux, J. Borreguero, A. Buts, S. Campbell, L. Chapon, M. Doucet, N. Draper, R. F. Leal, M. Gigg, et al., Nucl. Instrum. Methods Phys. Res. **764**, 156 (2014).

[530] R. Ewings, A. Buts, M. Le, J. van Duijn, I. Bustinduy, and T. Perring, Nucl Instrum Methods Phys Res A. **834**, 132 (2016).

[531] M. M. Odashima, B. G. Prado, and E. Vernek, Rev. Bras. Ensino Fís. **39**, e1303 (2017).

[532] J. Beck, K. Cole, A. Haji-Sheikh, and B. Litkouhl, *Heat Conduction Using Green's Function* (Taylor & Francis, Milton Park, U.K., 2010).

[533] K. Momma and F. Izumi, J. Appl. Crystallogr. **44**, 1272 (2011).

[534] A. Czachor and H. Al-Wahsh, Phys. Rev. B **63**, 064419 (2001).

[535] G. Baym, Phys. Rev. **121**, 741 (1961).

[536] M. Mourigal, W. T. Fuhrman, A. L. Chernyshev, and M. E. Zhitomirsky, Phys. Rev. B **88**, 094407 (2013).

[537] L. Timm, M. G. Tucker, D. A. Keen, P. M. M. Thygesen, P. J. Saines, and A. L. Goodwin, Phys. Scr. **91**, 114004 (2016).

[538] K. H. Germann, K. Maier, and E. Strauss, Phys. Stat. Sol. B **61**, 449 (1974).

[539] T. Shishidou and T. Jo, J. Phys. Soc. Jpn. **67**, 2637 (1998).

[540] J. Oh, M. D. Le, J. Jeong, J.-h. Lee, H. Woo, W.-Y. Song, T. G. Perring, W. J. L. Buyers, S.-W. Cheong, and J.-G. Park, Phys. Rev. Lett. **111**, 257202 (2013).

[541] J. Oh, M. D. Le, H.-H. Nahm, H. Sim, J. Jeong, T. Perring, H. Woo, K. Nakajima, S. Ohira-Kawamura, Z. Yamani, et al., Nat. Commun. **7**, 13146 (2016).

[542] A. L. Chernyshev and M. E. Zhitomirsky, Phys. Rev. Lett. **97**, 207202 (2006).

[543] A. L. Chernyshev and M. E. Zhitomirsky, Phys. Rev. B **79**, 174402 (2009).

[544] C. Stock, J. A. Rodriguez-Rivera, K. Schmalzl, E. E. Rodriguez, A. Stunault, and C. Petrovic, Phys. Rev. Lett. **114**, 247005 (2015).

[545] T. Huberman, R. Coldea, R. A. Cowley, D. A. Tennant, R. L. Leheny, R. J. Christianson, and C. D. Frost, Phys. Rev. B **72**, 014413 (2005).

[546] I. U. Heilmann, J. K. Kjems, Y. Endoh, G. F. Reiter, G. Shirane, and R. J. Birgeneau, Phys. Rev. B **24**, 3939 (1981).

[547] R. Wehner and E. Steigmeier, RCA Review **36**, 70 (1975).

[548] R. Wehner, Phys. Stat. Sol. B **15**, 725 (1966).

[549] R. A. Cowley, P. Martel, and R. W. H. Stevenson, Phys. Rev. Lett. **18**, 162 (1967).

[550] B. van Laar, J. Schweizer, and R. Lemaire, Phys. Rev. **141**, 538 (1966).

[551] J.-i. Igarashi, Phys. Rev. B **46**, 10763 (1992).

[552] J.-i. Igarashi and T. Nagao, Phys. Rev. B **72**, 014403 (2005).

[553] I. Cabrera, J. D. Thompson, R. Coldea, D. Prabhakaran, R. I. Bewley, T. Guidi, J. A. Rodriguez-Rivera, and C. Stock, Phys. Rev. B **90**, 014418 (2014).

[554] R. K. Wehner, Phys. Stat. Sol. B **22**, 527 (1967).

[555] M. E. Zhitomirsky and A. L. Chernyshev, Rev. Mod. Phys. **85**, 219 (2013).

[556] Villain, J., J. Phys. France **35**, 27 (1974).

[557] S. Toth, B. Lake, K. Hradil, T. Guidi, K. C. Rule, M. B. Stone, and A. T. M. N. Islam, Phys. Rev. Lett. **109**, 127203 (2012).

[558] J. P. Goff, D. A. Tennant, R. A. Cowley, R. C. C. Ward, S. E. Nagler, and T. G. Perring, J. Magn. Magn. Mater. **140**, 1675 (1995).

[559] T. Hong, Y. Qiu, M. Matsumoto, D. A. Tennant, K. Coester, K. P. Schmidt, F. F. Awwadi, M. M. Turnbull, H. Agrawal, and A. L. Chernyshev, Nat. Commun. **8**, 15148 (2017).

[560] M. Songvilay, E. E. Rodriguez, R. Lindsay, M. A. Green, H. C. Walker, J. A. Rodriguez-Rivera, and C. Stock, Phys. Rev. Lett. **121**, 087201 (2018).

[561] K. Zakeri, J. Lindner, I. Barsukov, R. Meckenstock, M. Farle, U. von Hörsten, H. Wende, W. Keune, J. Rocker, S. S. Kalarickal, et al., Phys. Rev. B **76**, 104416 (2007).

[562] D. M. Paul, P. W. Mitchell, H. A. Mook, and U. Steigenberger, Phys. Rev. B **38**, 580 (1988).

[563] A. H. MacDonald, S. M. Girvin, and D. Yoshioka, Phys. Rev. B **37**, 9753 (1988).

[564] A. W. Sandvik and R. R. P. Singh, Phys. Rev. Lett. **86**, 528 (2001).

[565] T. C. Hsu, Phys. Rev. B **41**, 11379 (1990).

[566] Y. Ishikawa, Y. Noda, Y. J. Uemura, C. F. Majkrzak, and G. Shirane, Phys. Rev. B **31**, 5884 (1985).

[567] K. Matan, R. Morinaga, K. Iida, and T. J. Sato, Phys. Rev. B **79**, 054526 (2009).

[568] D. Billington, D. Ernsting, T. E. Millichamp, C. Lester, S. B. Dugdale, D. Kersh, J. A. Duffy, S. R. Giblin, J. W. Taylor, P. Manuel, et al., Sci. Rep. **5**, 12428 (2015).

[569] M. J. Gillan, J. Phys. F. **3**, 1874 (1973).

[570] A. Z. Solontsov, A. N. Vasil'ev, and D. Wagner, J. Phys. Condens. Matter **7**, 1855 (1995).

[571] C. Wang, R. Zhang, F. Wang, H. Luo, L. P. Regnault, P. Dai, and Y. Li, Phys. Rev. X **3**, 041036 (2013).

[572] A. Zheludev, K. Kakurai, T. Masuda, K. Uchinokura, and K. Nakajima, Phys. Rev. Lett. **89**, 197205 (2002).

[573] B. Lake, D. A. Tennant, and S. E. Nagler, Phys. Rev. Lett. **85**, 832 (2000).

[574] D. J. Scalapino, Y. Imry, and P. Pincus, Phys. Rev. B **11**, 2042 (1975).

[575] H. J. Schulz, Phys. Rev. Lett. **77**, 2790 (1996).

[576] F. H. L. Essler, A. M. Tsvelik, and G. Delfino, Phys. Rev. B **56**, 11001 (1997).

[577] T. Moriya, J. Magn. Magn. Mater. **100**, 261 (1991).

[578] S. V. Maleev, Soviet Physics, J. Exp. Theor. Phys. **34**, 1518 (1958).

[579] L. J. Sandilands, Y. Tian, K. W. Plumb, Y.-J. Kim, and K. S. Burch, Phys. Rev. Lett. **114**, 147201 (2015).

[580] J. Nasu, J. Knolle, D. L. Kovrizhin, Y. Motome, and R. Moessner, Nature Physics **12**, 912 (2016).

[581] A. Banerjee, J. Yan, J. Knolle, C. A. Bridges, M. B. Stone, M. D. Lumsden, D. G. Mandrus, D. A. Tennant, R. Moessner, and S. E. Nagler, Science **356**, 1055 (2017).

[582] H. Gretarsson, J. P. Clancy, Y. Singh, P. Gegenwart, J. P. Hill, J. Kim, M. H. Upton, A. H. Said, D. Casa, T. Gog, et al., Phys. Rev. B **87**, 220407 (2013).

[583] S. H. Chun, J.-W. Kim, J. Kim, H. Zheng, C. C. Stoumpos, C. Malliakas, J. Mitchell, K. Mehlawat, Y. Singh, Y. Choi, et al., Nat. Phys. **11**, 462 (2015).

[584] A. Glamazda, P. Lemmens, S.-H. Do, Y. Choi, and K.-Y. Choi, Nat. Commun. **7**, 12286 (2016).

[585] M. M. van Schooneveld, R. Kurian, A. Juhin, K. Zhou, J. Schlappa, V. N. Strocov, T. Schmitt, and F. M. F. de Groot, J. Phys. Chem. C **116**, 15218 (2012).

[586] E. Francisco and L. Pueyo, Phys. Rev. B **37**, 5278 (1988).

[587] B. E. F. Fender, A. J. Jacobson, and F. A. Wedgwood, J. Chem. Phys. **48**, 990 (1968).

[588] A. Okazaki and Y. Suemune, J. Phys. Soc. Jpn. **16**, 671 (1961).

[589] G. Fischer, M. Däne, A. Ernst, P. Bruno, M. Lüders, Z. Szotek, W. Temmerman, and W. Hergert, Phys. Rev. B **80**, 014408 (2009).

[590] G. A. Gehring and K. A. Gehring, Rep. Prog. Phys. **38**, 1 (1975).

[591] V. V. Klekovkina, A. R. Zakirov, B. Z. Malkin, and L. A. Kasatkina, J. Phys.: Conf. Ser. **324**, 012036 (2011).

[592] T. Fennell, M. Kenzelmann, B. Roessli, H. Mutka, J. Ollivier, M. Ruminy, U. Stuhr, O. Zaharko, L. Bovo, A. Cervellino, et al., Phys. Rev. Lett. **112**, 017203 (2014).

[593] S. Guitteny, J. Robert, P. Bonville, J. Ollivier, C. Decorse, P. Steffens, M. Boehm, H. Mutka, I. Mirebeau, and S. Petit, Phys. Rev. Lett. **111**, 087201 (2013).

[594] Y. Li, Z. Yamani, Y. Song, W. Wang, C. Zhang, D. W. Tam, T. Chen, D. Hu, Z. Xu, S. Chi, et al., Phys. Rev. X **8**, 021056 (2018).

[595] K. A. Ross, J. W. Krizan, J. A. Rodriguez-Rivera, R. J. Cava, and C. L. Broholm, Phys. Rev. B **93**, 014433 (2016).

[596] M. Kenzelmann, R. Coldea, D. A. Tennant, D. Visser, M. Hofmann, P. Smeibidl, and Z. Tylczynski, Phys. Rev. B **65**, 144432 (2002).

[597] P. K. Das, J. Sławińska, I. Vobornik, J. Fujii, A. Regoutz, J. M. Kahk, D. O. Scanlon, B. J. Morgan, C. McGuinness, E. Plekhanov, et al., Phys. Rev. Materials **2**, 065001 (2018).

[598] A. S. Cavichini, M. T. Orlando, J. B. Depianti, J. L. Passamai, F. Damay, F. Porcher, and E. Granado, Phys. Rev. B **97**, 054431 (2018).

[599] J. H. Pixley, S. S. Natu, I. B. Spielman, and S. Das Sarma, Phys. Rev. B **93**, 081101 (2016).

[600] Z. Wu, L. Zhang, W. Sun, X.-T. Xu, B.-Z. Wang, S.-C. Ji, Y. Deng, S. Chen, X.-J. Liu, and J.-W. Pan, Science **354**, 83 (2016).

[601] J. D. Koralek, C. P. Weber, J. Orenstein, B. A. Bernevig, S.-C. Zhang, S. Mack, and D. D. Awschalom, Nature **458**, 610 (2009).

[602] D. Hsieh, Y. Xia, L. Wray, D. Qian, A. Pal, J. H. Dil, J. Osterwalder, F. Meier, G. Bihlmayer, C. L. Kane, et al., Science **323**, 919 (2009).

[603] S. Mühlbauer, B. Binz, F. Jonietz, C. Pfleiderer, A. Rosch, A. Neubauer, R. Georgii, and P. Böni, Science **323**, 915 (2009).

[604] J. Krempaskỳ et al., Nat. Comm. **7**, 13071 (2016).

[605] C. Day, Phys. Today **62**, 12 (2009).

[606] I. A. Sergienko and E. Dagotto, Phys. Rev. B **73**, 094434 (2006).

[607] J.-G. Park, M. D. Le, J. Jeong, and S. Lee, J. Phys. Condens. Matter **26**, 433202 (2014).

[608] C. Nayak, S. H. Simon, A. Stern, M. Freedman, and S. Das Sarma, Rev. Mod. Phys. **80**, 1083 (2008).

[609] V. Lahtinen, New J. Phys. **13**, 075009 (2011).

[610] S. Bravyi and A. Kitaev, Phys. Rev. A **71**, 022316 (2005).

[611] P. Bonderson et al., Phys. Rev. Lett. **104**, 180505 (2010).

[612] J. Alicea et al., Nat. Phys. **7**, 412 (2011).

[613] S.-H. Do, S.-Y. Park, J. Yoshitake, J. Nasu, Y. Motome, Y. S. Kwon, D. Adroja, D. Voneshen, K. Kim, T.-H. Jang, et al., Nat. Phys. **13**, 1079 (2017).

[614] S. R. Elliott and M. Franz, Rev. Mod. Phys. **87**, 137 (2015).

[615] T. Senthil and M. P. A. Fisher, Phys. Rev. B **62**, 7850 (2000).

[616] N. Read and S. Sachdev, Phys. Rev. Lett. **66**, 1773 (1991).

[617] W. Witczak-Krempa, G. Chen, Y. B. Kim, and L. Balents, Annual Review of Condensed Matter Physics **5**, 57 (2014).

[618] I. Kimchi, R. Coldea, and A. Vishwanath, Phys. Rev. B **91**, 245134 (2015).

[619] Y. Yamaji, T. Suzuki, T. Yamada, S.-i. Suga, N. Kawashima, and M. Imada, Phys. Rev. B **93**, 174425 (2016).

[620] R. Schaffer, S. Bhattacharjee, and Y. B. Kim, Phys. Rev. B **86**, 224417 (2012).

[621] R. Cywinski, Physica B Condens. Matter **234**, 1239 (1997).

[622] P. J. Brown, *International Tables of Crystallography: Volume C*, vol. 4 (Kluwer Academic Publishers, P.O. Box 17, 3300 AA Dordrecht, The Netherlands, 2004), 3rd ed.

[623] S. Roman, *Advanced Linear Algebra*, vol. 135 of *Graduate Texts in Mathematics* (Springer-Verlag, New York, 2008), 3rd ed.

[624] J. Sakurai and J. Napolitano, *Modern Quantum Mechanics* (Cambridge University Press, Cambridge, 2017), 2nd ed.

[625] K. Sturm, Z. Naturforsch. A **48**, 233 (1993).

[626] E. P. Wigner, *Group Theory and its Application to the Quantum Mechanics of Atomic Spectra*, vol. 5 of *Pure and Applied Physics* (Elsevier, New York, 1959), 1st ed.

[627] J. Rotman, *An Introduction to the Theory of Groups*, vol. 148 of *Graduate Texts in Mathematics* (Springer-Verlag, New York, 1995), 4th ed.

[628] P. Dirac, Proc. R. Soc. Lond. A **114**, 243 (1927).

[629] D. Kay, *Schaum's Outline of Tensor Calculus*, Schaum's Outline Series (McGraw Hill Professional, New York, 2011), 2nd ed.

[630] V. F. Sears, Neutron News **3**, 26 (1992).

[631] L. Cruzeiro-Hansson and S. Takeno, Phys. Rev. E **56**, 894 (1997).

Appendix A

Magnetic Form Factors

This appendix summarises the approximated analytical expressions for the magnetic form factors $F(\mathbf{Q})$ of Pr^{3+} and Co^{2+}. Utilising the dipole approximation [208] for low momentum transfers $\mathbf{Q}$, the magnetic form factor $F(\mathbf{Q})$ may be approximated as

$$F(s) = \langle j_0(s)\rangle + \mathcal{C}\langle j_2(s)\rangle, \tag{A.1}$$

where the constant $\mathcal{C}$ is equal to

$$\mathcal{C} = \begin{cases} 1 - \frac{2}{g} & \text{if } \Delta \gg \lambda \\ \frac{2}{g} - 1 & \text{if } \Delta \ll \lambda, \end{cases}$$

where g is the pertinent Landé g-factor and

$$\langle j_0(s)\rangle = A_0 \exp(-a_0 s^2) + B_0 \exp(-b_0 s^2) + C_0 \exp(-c_0 s^2) + D_0 \tag{A.2a}$$
$$\langle j_2(s)\rangle = s^2 \left\{ A_2 \exp(-a_2 s^2) + B_2 \exp(-b_2 s^2) + C_2 \exp(-c_2 s^2) + D_2 \right\}, \tag{A.2b}$$

where $s = \frac{|\mathbf{Q}|}{4\pi} \equiv \frac{\sin\theta}{\lambda}$ in units of $Å^{-1}$. The values of all $\langle j_0(s)\rangle$ and $\langle j_2(s)\rangle$ magnetic form coefficients for Pr^{3+} and Co^{2+} are given in Tab. A.1 below. As

a first approximation, the magnetic form factor of Co^{2+} was evaluated in the $\Delta \gg \lambda$ limit and g was set to the spin Landé g-factor $g_s \simeq 2$, as is convention for other early d-block metals. Pr^{3+} was evaluated in $\Delta \ll \lambda$ limit and g was set to total Landé g-factor g_J, as is convention for other rare earths and actinides [99, 100, 621].

Table A.1 $\langle j_0(s) \rangle$ and $\langle j_2(s) \rangle$ magnetic form factor coefficients for Pr^{3+} and Co^{2+}, reproduced from the *International Tables of Crystallography: Volume C* [622].

Coefficient	Pr^{3+}	Co^{2+}
A_0	0.0504	0.4332
a_0	24.9989	14.3553
B_0	0.2572	0.5857
b_0	12.0377	4.6077
C_0	0.7142	−0.0382
c_0	5.0039	0.1338
D_0	−0.0219	0.0179
A_2	0.08734	1.9049
a_2	18.9876	11.6444
B_2	1.5594	1.3159
b_2	6.0872	4.3574
C_2	0.8142	0.3146
c_2	2.4150	1.6453
D_2	0.0111	0.0017

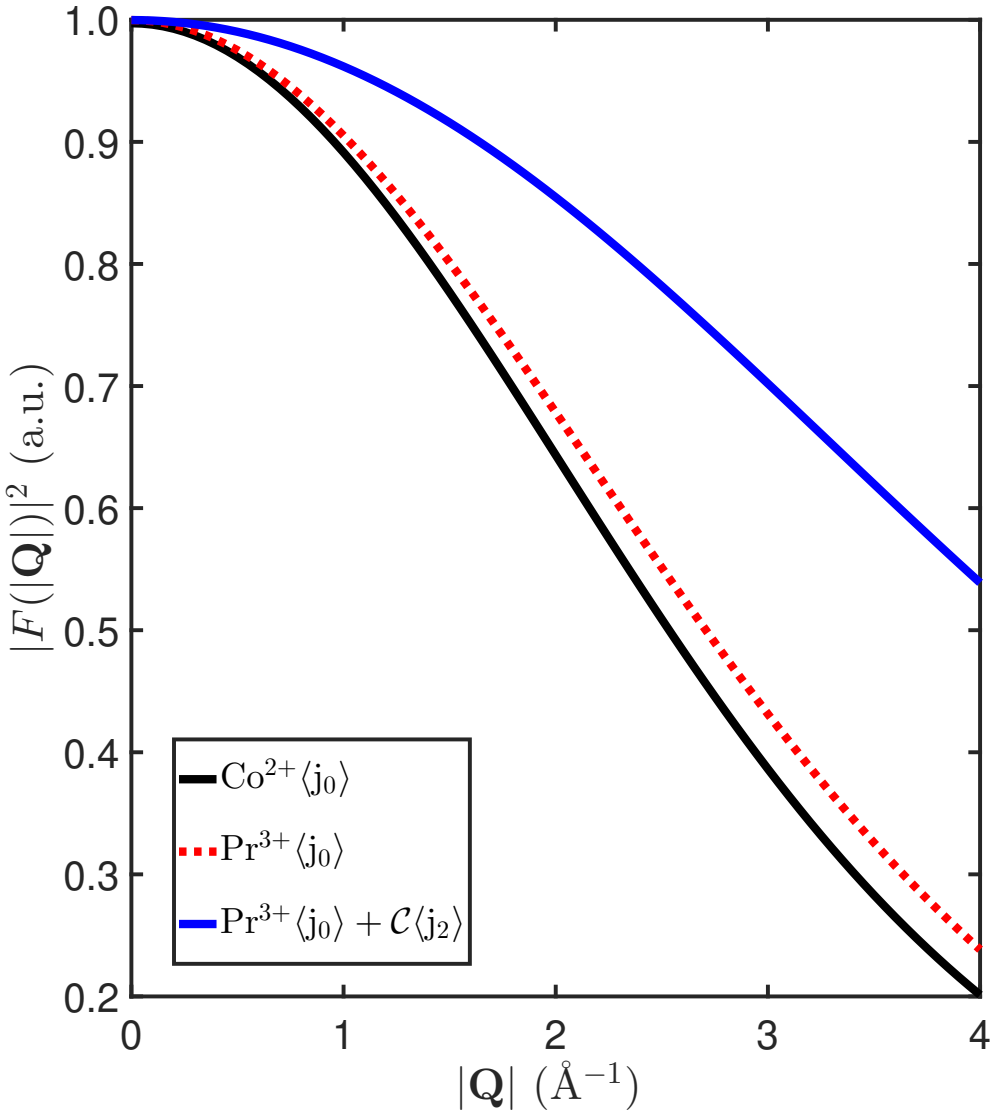

Figure A.1 Calculated $|F(|\mathbf{Q}|)|^2$ for Co^{2+} and Pr^{3+}. For the purposes of comparison, both the calculated $|F(|\mathbf{Q}|)|^2$ for Pr^{3+} including and excluding the $\langle j_2\rangle$ contribution in Eq. A.1 are presented.

Appendix B

Crystallographic Data

B.1 $Pr_2Sn_{2-x}Ti_xO_7$

Table B.1 Refined parameters and corresponding goodness-of-fit metrics for the Rietveld refinements of the room temperature neutron powder diffraction patterns for polycrystalline samples of the $Pr_2Sn_{2-x}Ti_xO_7$ series. The data was collected with the high resolution powder diffractometer HB-2A at the High Flux Isotope Reactor (HFIR) at Oak Ridge National Laboratory (ORNL), using a vertically focussing Ge(115) monochromator providing a neutron wavelength of 1.54 Å. All Rietveld refinements were performed using the FUllPRoF software suite [211]. Numbers in parentheses indicate statistical errors.

Sample / Par.	x	a (Å)	$48f$ x (r.l.u.)	χ^2	R_p(%)	R_{wp}(%)
0	0	10.6038(3)	0.33195(9)	4.51	7.86	9.04
0.05	0.048(1)	10.5950(2)	0.33252(1)	5.96	8.15	10.1
0.10	0.120(2)	10.5845(2)	0.33365(8)	5.16	8.95	9.07
0.20	0.220(2)	10.5733(2)	0.33533(6)	5.82	10.0	9.95
0.30	0.310(2)	10.5625(3)	0.33746(3)	5.25	9.7	9.2
0.40	0.400(3)	10.5499(3)	0.33925(1)	6.04	10.1	10.7
0.50	0.504(2)	10.5348(3)	0.34185(1)	6.15	10.5	11.1
0.60	0.558(4)	10.5269(4)	0.34415(6)	5.87	11.1	10.9

B.2 CoV_3O_8

Table B.2 Crystal data, experimental and structural refinement parameters for single crystal x-ray diffraction measurements on α-CoV_3O_8. Numbers in parentheses indicate statistical errors.

Parameter	Value
Empirical Formula	CoV_3O_8
Formula weight	339.7529 g mol^{-1}
Temperature	120.0(1) K
Crystal Dimensions	$0.398 \times 0.106 \times 0.086$ mm^3
Wavelength	0.71073 Å(Mo K_α)
Crystal System	Orthorhombic
Space Group	*Ibam* (#72)
a	14.29344(4) Å
b	9.8740(3) Å
c	8.34000(3) Å
α,β,γ	90°, 90°, 90°
V	1185.60(6) $Å^3$
Z	8
ρ	3.8069(3) g cm^{-3}
θ range for data collection	$4.13° \leq \theta \leq 30.18°$
Limiting Indices	$-19 \leq h \leq 20$ $-13 \leq k \leq 14$ $-11 \leq l \leq 11$
Number of Reflections $I > 0$	985
Number of Reflections $I > 3\sigma(I)$	910
Absorption Correction Method	Gaussian
Extinction Method	B-C Type 1 Gaussian Isotropic
Extinction Coefficient	2300(100)
Refinement Method	Full matrix least squares on F^2
Number of Parameters(Constraints)	64(9)
R_{F^2} ($I > 3\sigma(I)$, all)	1.65%, 1.90%
R_{wF^2} ($I > 3\sigma(I)$, all)	2.38%, 2.46%
Goodness-of-Fit χ^2 ($I > 3\sigma(I)$, all)	1.47, 1.48

Table B.3 Structural parameters of α-CoV_3O_8 obtained from the refinement of single crystal x-ray diffraction data collected at 120 K.

Atom (Label)	Wyckoff Position	x	y	z	U_{ani} (Å^2)	Fractional Occupancy
Co	16k	0.654760(16)	0.33285(2)	0.81060(3)	0.00496(9)	0.506(6)
V(1)	16k	0.654760(16)	0.33285(2)	0.81060(3)	0.00496(9)	0.494(6)
V(2)	8j	0.52271(2)	0.16672(4)	0.5	0.00407(11)	1
V(3)	8j	0.70168(2)	0.94348(4)	0.5	0.00319(11)	1
O(1)	8j	0.73349(11)	0.41325(16)	0	0.0066(4)	1
O(2)	8j	0.58248(10)	0.27500(16)	0	0.0064(4)	1
O(3)	16k	0.76787(8)	0.35258(11)	0.0067(3)	0.53(2)	1
O(4)	8f	0.61080(11)	0.5	0.75	0.0158(5)	1
O(5)	16k	0.57900(8)	0.22361(12)	0.0100(3)	0.79(3)	1
O(6)	8j	0.57973(10)	0.98272(16)	0.5	0.0061(4)	1

Table B.4 Anisotropic thermal parameters of α-CoV_3O_8 from the refinement of single crystal x-ray diffraction data collected at 120 K.

Atom (Label)	U_{11} (Å^2)	U_{22} (Å^2)	U_{33} (Å^2)	U_{12} (Å^2)	U_{13} (Å^2)	U_{23} (Å^2)
Co	0.00498(14)	0.00631(15)	0.00360(15)	−0.00143(8)	0.00004(8)	0.00035(8)
V(1)	0.00498(14)	0.00631(15)	0.00360(15)	−0.00143(8)	0.00004(8)	0.00035(8)
V(2)	0.00321(19)	0.00386(20)	0.0051(2)	0.00010(12)	0	0
V(3)	0.00293(17)	0.00336(19)	0.0033(2)	−0.00002(12)	0	0
O(1)	0.0048(7)	0.0068(8)	0.0081(8)	−0.0004(6)	0	0
O(2)	0.0059(7)	0.0059(8)	0.0073(8)	−0.0018(6)	0	0
O(3)	0.0077(5)	0.0059(5)	0.0066(6)	0.0017(4)	0.0005(4)	0.0016(4)
O(4)	0.0061(7)	0.0326(11)	0.0086(9)	0	0	−0.0097(8)
O(5)	0.0073(5)	0.0091(6)	0.0135(6)	0.0016(4)	−0.0024(5)	−0.0041(5)
O(6)	0.0038(7)	0.0031(7)	0.0113(8)	−0.0002(6)	0	0

Table B.5 Crystal data, experimental and structural refinement parameters for single crystal neutron diffraction measurements on α-CoV_3O_8. Numbers in parentheses indicate statistical errors.

Parameter	Value
Empirical Formula	CoV_3O_8
Formula weight	339.7529 g mol^{-1}
Temperature	5.00(3) K
Crystal Dimensions	$13.2 \times 4.1 \times 2.1$ mm^3
Wavelength	Polychromatic (time-of-flight)
Crystal System	Orthorhombic
Nuclear Space Group	*Ibam* (#72)
Magnetic Space Group (BNS)	P_Iccn (#56.376) or (I_Pbam' OG 72.10.639)
k	(111)
a	14.3280(4) Å
b	9.9213(3) Å
c	8.4160(3) Å
α,β,γ	90°, 90°, 90°
V	1196.35(7) Å^3
Z	8
ρ	3.773(3) g cm^{-3}
θ range for data collection	$2.94° \leq \theta \leq 76.22°$
Limiting Indices	$-35 \leq h \leq 33$ $-25 \leq k \leq 19$ $-16 \leq l \leq 22$
Number of Reflections $I > 0$	5120
Number of Reflections $I > 3\sigma(I)$	5086
Refinement Method	Full matrix least squares on F^2
Absorption Correction	None
Extinction Method	B-C Type 1 Gaussian Isotropic
Extinction Coefficient	348(8)
Number of Parameters(Constraints)	34(10)
μ_a	1.35(4) μ_B
μ_b	1.16(5) μ_B
μ_c	3.05(4) μ_B
R_{F^2} ($I > 3\sigma(I)$, all)	8.34%, 8.38%
R_{wF^2} ($I > 3\sigma(I)$, all)	8.98%, 8.99%
$R_{F^2_{mag}}$ ($I > 3\sigma(I)$, all)	23.44%, 24.13%
Goodness-of-Fit χ^2 ($I > 3\sigma(I)$, all)	3.18, 3.19

Table B.6 Structural parameters for the nuclear structure of α-CoV_3O_8 obtained from the refinement of single crystal neutron diffraction data collected at 5 K. Numbers in parentheses indicate statistical errors.

Atom (Label)	Wyckoff Position	x	y	z	U_{iso} (Å^2)	Fractional Occupancy
Co	16k	0.9068(3)	0.5765(3)	1.0616(5)	0.0005(5)	0.504(4)
V(1)	16k	0.9068(3)	0.5765(3)	1.0616(5)	0.0005(5)	0.496(4)
V(2)	8j	0.771	0.416	0.75	0.0042	1
V(3)	8j	0.957	1.198	0.75	0.0042	1
O(1)	8j	0.98357(9)	0.66282(11)	0.25	0.00356(16)	1
O(2)	8j	0.83242(8)	0.52523(11)	0.25	0.00388(16)	1
O(3)	16k	1.01787(6)	0.60246(8)	0.91384(10)	0.00392(11)	1
O(4)	8f	0.86076(9)	0.75	1	0.0126(4)[1]	1
O(5)	16k	0.82899(6)	0.47373(8)	0.90801(10)	0.00556(12)	1
O(6)	8j	0.82973(8)	1.23252(10)	0.75	0.00269(15)	1

[1] The anisotropic thermal factor.

Table B.7 Anisotropic thermal parameters of α-CoV_3O_8 obtained from the refinement of single crystal neutron diffraction data collected at 5 K. Numbers in parentheses indicate statistical errors.

Atom (Label)	U_{11} (Å^2)	U_{22} (Å^2)	U_{33} (Å^2)	U_{12} (Å^2)	U_{13} (Å^2)	U_{23} (Å^2)
O(4)	0.0014(5)	0.0290(8)	0.0074(6)	0	0	−0.0080(5)

Table B.8 Cell parameters, fit residuals and agreement factors for α-CoV_3O_8 obtained from the Rietveld refinement of laboratory powder x-ray diffraction data collected at 300 K. Numbers in parentheses indicate statistical errors.

Parameter	Value
a	14.292(1) Å
b	9.8844(9) Å
c	8.3969(8) Å
V	1186.2(3) Å^3
χ^2	1.487
R_p	10.26%
R_{wp}	14.05%

Table B.9 Cobalt-oxygen distances and corresponding octahedral distortion parameter δ for α-CoV_3O_8 at 5 K deduced from the Rietveld refinement of single crystal neutron diffraction data. Numbers in parentheses indicate statistical errors.

Oxygen Label	d (Å)	$\left(\frac{d-\langle d\rangle}{\langle d\rangle}\right)^2 \times 10^4$
O(1)	2.12527(5)	27.79(3)
O(2)	1.98916(5)	2.162(8)
O(3)	2.07872(5)	8.79(2)
O(3)′	2.02358(5)	0.0549(13)
O(4)	1.92213(5)	22.95(3)
O(5)	1.97422(4)	4.89(1)
$\frac{1}{N}\sum\left\{\left(\frac{d-\langle d\rangle}{\langle d\rangle}\right)^2 \times 10^4\right\}$		11.106(8)

Table B.10 Crystal data, experimental and structural refinement parameters for single crystal x-ray diffraction measurements on α-CoV_3O_8 employing $Iba2$ crystallographic symmetry. Numbers in parentheses indicate statistical errors.

Parameter	Value
Empirical Formula	CoV_3O_8
Formula weight	339.7529 g mol^{-1}
Temperature	120.0(1) K
Crystal Dimensions	$0.398 \times 0.106 \times 0.086$ mm^3
Wavelength	0.71073 Å(Mo K_α)
Crystal System	Orthorhombic
Space Group	$Iba2$ (#45)
a	14.2938(4) Å
b	9.8752(3) Å
c	8.3399(3) Å
α,β,γ	90°, 90°, 90°
V	1185.61(6) $Å^3$
Z	8
ρ	3.8069(3) g cm^{-3}
θ range for data collection	$4.13° \leq \theta \leq 30.18°$
Limiting Indices	$-19 \leq h \leq 20$ $-13 \leq k \leq 14$ $-11 \leq l \leq 11$
Number of Reflections $I > 0$	1802
Number of Reflections $I > 3\sigma(I)$	1638
Absorption Correction Method	Gaussian
Extinction Method	B-C Type 1 Gaussian Isotropic
Extinction Coefficient	2070(90)
Refinement Method	Full matrix least squares on F^2
Number of Parameters(Constraints)	110(1)
R_{F^2} ($I > 3\sigma(I)$, all)	2.19%, 2.61%
R_{wF^2} ($I > 3\sigma(I)$, all)	2.86%, 2.94%
Goodness-of-Fit χ^2 ($I > 3\sigma(I)$, all)	1.52, 1.56

Table B.11 Structural parameters of α-CoV_3O_8 obtained from the refinement of single crystal x-ray diffraction data at 120 K. In contrast with Tab. B.3, this refinement employed $Iba2$ symmetry. Numbers in parentheses indicate statistical errors.

Atom (Label)	Wyckoff Position	x	y	z	U_{ani} (Å^2)	Fractional Occupancy
Co	8c	0.15498(7)	0.16799(9)	0.1899(2)	0.0106(3)	1
V(1)	8c	0.15451(8)	0.83359(9)	0.3111(2)	−0.0012(2)	1
V(2)	8c	0.02272(3)	0.66677(4)	−0.0007(3)	0.00405(11)	1
V(3)	8c	0.20169(2)	0.44350(4)	0.0001(3)	0.00309(11)	1
O(1)	8c	0.73354(11)	0.41305(17)	−0.0033(9)	0.0062(5)	1
O(2)	8c	0.58252(11)	0.27542(17)	−0.0017(9)	0.0070(5)	1
O(3)	8c	0.2709(3)	0.8534(5)	0.1641(6)	0.0072(12)	1
O(4)	8c	0.2651(3)	0.1482(5)	0.3363(6)	0.0055(13)	1
O(5)	8c	0.11085(12)	−0.0065(7)	0.2492(9)	0.0147(6)	1
O(6)	8c	0.0776(4)	0.7211(5)	0.1587(6)	0.0100(15)	1
O(7)	8c	0.0800(4)	0.2742(4)	0.3424(6)	0.0095(15)	1
O(8)	8c	0.07987(10)	0.48295(16)	0.0003(10)	0.0066(5)	1

Table B.12 Anisotropic thermal parameters of α-CoV_3O_8 obtained from the refinement of single crystal x-ray diffraction data collected at 120 K. In contrast with Tab. B.4, this refinement employed $Iba2$ symmetry Numbers in parentheses indicate statistical errors.

Atom (Label)	U_{11} (Å^2)	U_{22} (Å^2)	U_{33} (Å^2)	U_{12} (Å^2)	U_{13} (Å^2)	U_{23} (Å^2)
Co	0.0099(4)	0.0143(4)	0.0077(5)	0.0022(4)	0.0003(5)	0.0010(4)
V	−0.0006(4)	−0.0019(3)	−0.0013(5)	−0.0006(4)	0.0004(4)	−0.0003(4)
V(2)	0.00286(18)	0.0040(2)	0.0053(2)	0.00012(12)	0.0005(6)	0.0014(6)
V(3)	0.00294(17)	0.00349(19)	0.00286(19)	0.00009(13)	−0.0001(6)	−0.0005(6)
O(1)	0.0046(6)	0.0067(8)	0.0075(9)	0.0000(6)	−0.001(2)	−0.001(3)
O(2)	0.0061(7)	0.0075(8)	0.0074(9)	−0.0021(6)	−0.008(3)	0.001(2)
O(3)	0.013(2)	0.011(2)	−0.002(2)	−0.0024(16)	−0.0040(16)	0.0044(18)
O(4)	0.0004(16)	0.0007(18)	0.016(3)	−0.0042(14)	−0.0055(16)	−0.0016(18)
O(5)	0.0062(8)	0.0282(14)	0.0097(10)	−0.006(2)	−0.003(3)	−0.0087(10)
O(6)	0.008(2)	0.016(3)	0.006(3)	0.0045(17)	−0.0028(19)	−0.0099(18)
O(7)	0.006(2)	0.001(2)	0.021(3)	0.0010(14)	0.001(2)	0.0016(17)
O(8)	0.0033(7)	0.0040(8)	0.0124(9)	−0.0002(6)	−0.008(2)	−0.002(3)

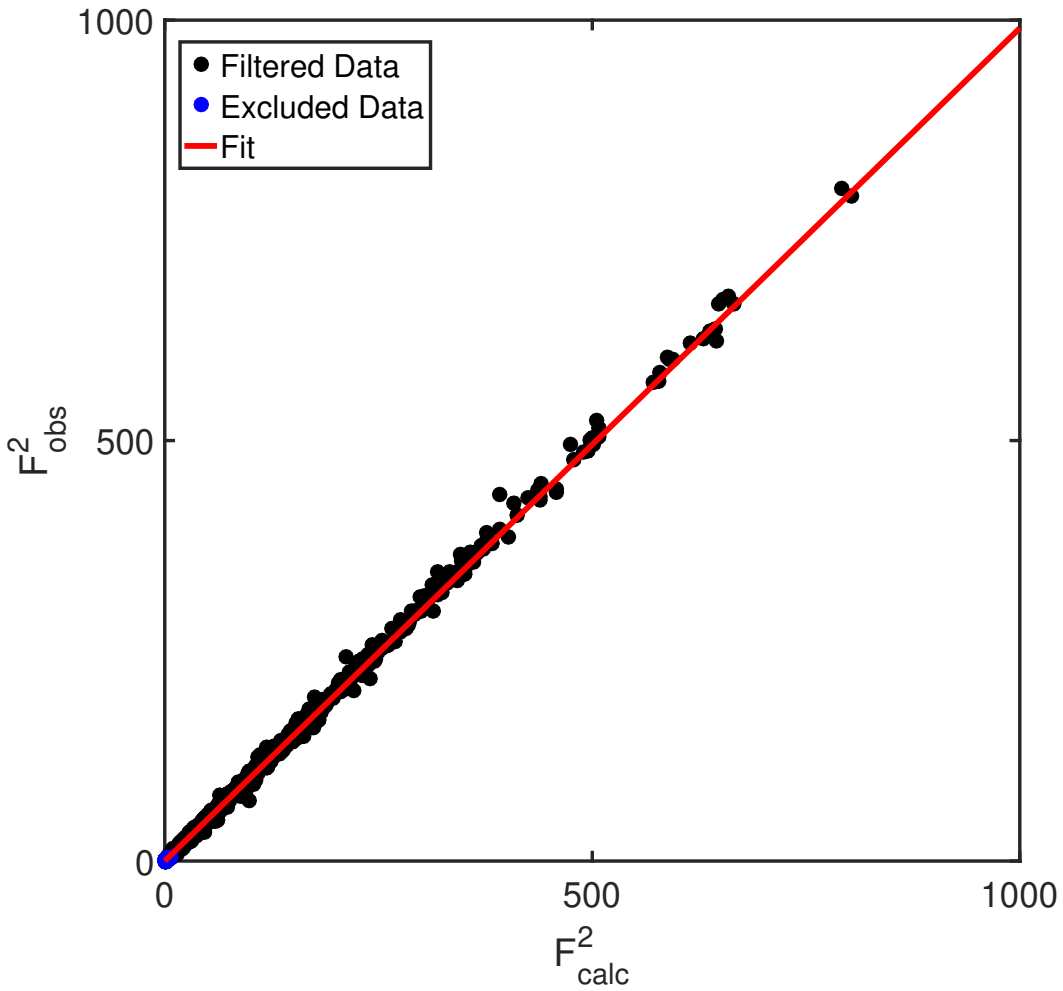

Figure B.1 F^2_{obs}-F^2_{calc} plot for the refinement of single crystal x-ray diffraction data collected at 120 K (R_{F^2}=2.19%, R_{wF^2}=2.86% and χ^2=1.52), yielding a refined $Iba2$ unit cell (a=14.2938(4) Å, b=9.8752(3) Å, c= 8.3399(3) Å).

Table B.13 Crystal data, experimental and structural refinement parameters for single crystal neutron diffraction measurements on α-CoV_3O_8 employing $Iba2$ symmetry for the nuclear unit cell. Numbers in parentheses indicate statistical errors.

Parameter	Value
Empirical Formula	CoV_3O_8
Formula weight	339.7529 g mol^{-1}
Temperature	5.00(3) K
Crystal Dimensions	$13.2 \times 4.1 \times 2.1$ mm^3
Wavelength	Polychromatic (time-of-flight)
Crystal System	Orthorhombic
Nuclear Space Group	$Iba2$ (#45)
Magnetic Space Group (BNS)	P_Icc2 (#27.86) or (I_Pba2 OG 45.5.335)
k	(111)
a	14.3280(4) Å
b	9.9213(3) Å
c	8.4160(3) Å
α,β,γ	90°, 90°, 90°
V	1196.35(7) Å^3
Z	8
ρ	3.773(3) g cm^{-3}
θ range for data collection	$2.94° \leq \theta \leq 76.22°$
Limiting Indices	$-35 \leq h \leq 33$ $-25 \leq k \leq 19$ $-16 \leq l \leq 22$
Number of Reflections $I > 0$	5120
Number of Reflections $I > 3\sigma(I)$	5086
Refinement Method	Full matrix least squares on F^2
Absorption Correction	None
Extinction Method	B-C Type 1 Gaussian Isotropic
Extinction Coefficient	348(8)
Number of Parameters(Constraints)	48(8)
μ_a	1.30(6) μ_B
μ_b	1.09(8) μ_B
μ_c	2.32(5) μ_B
R_{F^2} ($I > 3\sigma(I)$, all)	10.59%, 10.66%
R_{wF^2} ($I > 3\sigma(I)$, all)	14.57%, 14.59%
$R_{F^2_{mag}}$ ($I > 3\sigma(I)$, all)	32.28%, 32.11%
Goodness-of-Fit χ^2 ($I > 3\sigma(I)$, all)	5.15, 5.16

Table B.14 Structural parameters for the nuclear structure of α-CoV_3O_8 obtained from the refinement of single crystal neutron diffraction data collected at 5 K. Numbers in parentheses indicate statistical errors.

Atom (Label)	Wyckoff Position	x	y	z	U^1_{iso} (Å^2)	Fractional Occupancy
Co1	8c	0.6568	0.3283	0.8089	0.00139(9)	1
V2	8c	0.02245	0.667966	0.008917	0.00139(9)	1
V3	8c	0.70196	0.946561	0.49493	0.00139(9)	1
V1	8c	0.652518	0.356973	0.185789	0.00139(9)	1
O1	8c	0.23368	0.91286	0.5026	0.00139(9)	1
O2	8c	0.58254	0.27523	0.0028	0.00139(9)	1
O3	8c	0.767	0.3523	0.6646	0.00139(9)	1
O4	8c	0.7687	0.3528	0.3368	0.00139(9)	1
O5	8c	0.61071	0.51252	0.7451	0.00139(9)	1
O6	8c	0.5806	0.226	0.6548	0.00139(9)	1
O7	8c	0.57752	0.2217	0.3389	0.00139(9)	1
O8	8c	0.57971	0.9827	0.5008	0.00139(9)	1

[1] Simple model where all atoms have some isotropic thermal factors.

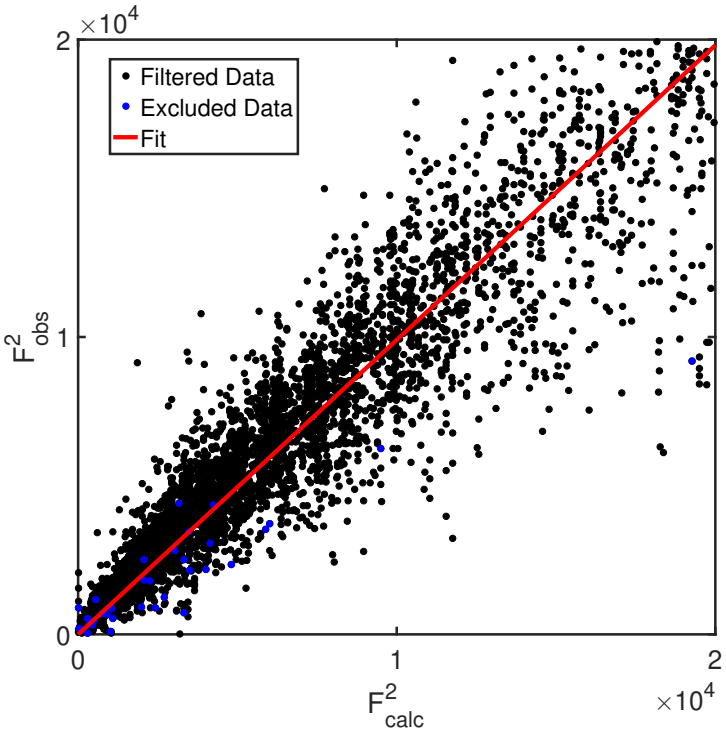

Figure B.2 F^2_{obs}-F^2_{calc} for the joint nuclear-magnetic refinement of single crystal neutron diffraction data on a (inset) single crystal of α-CoV_3O_8 collected at 5 K (R_{F^2}=10.59%, R_{wF^2}=14.57%, $R_{F^2_{mag}}$=32.28% and χ^2=5.15), utilising a propagation vector **k**=(1,1,1) with the P_Icc2 Shubnikov magnetic space group.

B.3 $Co_xMg_{1-x}O$

Table B.15 Cell parameter, fit residuals and agreement factors obtained from the Rietveld refinement of room temperature laboratory powder x-ray diffraction data for CoO, MgO and the $Co_{0.03}Mg_{0.97}O$ sample that was synthesised by sol-gel. Numbers in parentheses indicate statistical errors.

Sample / Parameter	a (Å)	U_{iso} (Å^2)	χ^2	R_p	R_{wp}
CoO	4.2594(4)	0.0090(9)	1.17	3.23%	4.09%
$Co_{0.03}Mg_{0.97}O$	4.2131(2)	0.0377(7)	6.91	10.12%	13.25%
MgO	4.2118(1)	0.0320(4)	3.74	4.75%	6.30%

Appendix C

Representation of Operators in a New Basis

This appendix provides a derivation of the mathematical procedure used for the conversion of an operator $\hat{O}$ from one basis to another. The following derivation is based on Roman's *Advanced Linear Algebra* and references contained therein [623]. Any additional references will be stated in the text explicitly.

Derivation: First, define a quantum mechanical operator $\hat{O}$ as a linear transformation $\mathcal{T} : H \to H$. Since every linear transformation can be represented as a matrix, the linear map $\mathcal{T}$ can be expressed as

$$[\mathcal{T}(\mathbf{x})]_{[\mathcal{A}]} = \mathcal{O}_{[\mathcal{A}]}\mathbf{x}_{[\mathcal{A}]}, \tag{C.1}$$

where $\mathcal{O}$ and $\mathbf{x}$ are the transformation matrix of $\mathcal{T}$ and the coordinate vector, respectively, with respect to a particular basis $\mathcal{A} = \{\mathbf{v}_1, \mathbf{v}_2, \dots\}$, where $\mathbf{v}_i$ denotes basis vectors. Now, suppose one utilises another basis $\mathcal{B} = \{\mathbf{v}'_1, \mathbf{v}'_2, \dots\}$, then Eq. C.1 in the basis $\mathcal{B}$ can be expressed as

$$[\mathcal{T}(\mathbf{x})]_{[\mathcal{B}]} = \mathcal{O}_{[\mathcal{B}]}\mathbf{x}_{[\mathcal{B}]}. \tag{C.2}$$

The relationship between $\mathcal{O}_{[\mathcal{A}]}$ and $\mathcal{O}_{[\mathcal{B}]}$ can be determined by first recalling the relationship between $\mathbf{x}_{[\mathcal{A}]}$ and $\mathbf{x}_{[\mathcal{B}]}$ given by

$$\mathbf{x}_{[\mathcal{A}]} = \mathcal{C}\mathbf{x}_{[\mathcal{B}]}, \tag{C.3}$$

where $\mathcal{C}$ is the change-of-basis matrix, defined by

$$\mathcal{C} = [(\mathbf{v}_1')^T, (\mathbf{v}_2')^T, \dots], \tag{C.4}$$

constituting a matrix whose columns are the basis vectors of the basis $\mathcal{B}$ expressed in the $\mathcal{A}$ basis. Since the columns of $\mathcal{C}$ are linearly independent, $\mathcal{C}$ must be invertible, *i.e.* $\mathcal{C}^{-1}$ does exist. Consequently, it follows from Eq. C.3 that

$$\mathbf{x}_{[\mathcal{B}]} = \mathcal{C}^{-1}\mathbf{x}_{[\mathcal{A}]}. \tag{C.5}$$

Since $\mathcal{O}_{[\mathcal{A}]}\mathbf{x}_{[\mathcal{A}]}$ is a simply vector $[\mathcal{T}(\mathbf{x})]$ in the basis $\mathcal{A}$, then one can utilise Eq. C.5 to convert $[\mathcal{T}(\mathbf{x})]$ into basis $\mathcal{B}$ and thus

$$[\mathcal{T}(\mathbf{x})]_{[\mathcal{B}]} = \mathcal{C}^{-1}\mathcal{O}_{[\mathcal{A}]}\mathbf{x}_{[\mathcal{A}]}. \tag{C.6}$$

Furthermore, the vector $\mathbf{x}_{[\mathcal{A}]}$ can be expressed as $\mathcal{C}\mathbf{x}_{[\mathcal{B}]}$ *via* Eq. C.3 and thus Eq. C.6 can be rewritten as

$$[\mathcal{T}(\mathbf{x})]_{[\mathcal{B}]} = \mathcal{C}^{-1}\mathcal{O}_{[\mathcal{A}]}\mathcal{C}\mathbf{x}_{[\mathcal{B}]}. \tag{C.7}$$

Finally, by replacing $[\mathcal{T}(\mathbf{x})]_{[\mathcal{B}]}$ by its matrix definition in Eq. C.2, one obtains

$$\mathcal{O}_{[\mathcal{B}]}\mathbf{x}_{[\mathcal{B}]} = \mathcal{C}^{-1}\mathcal{O}_{[\mathcal{A}]}\mathcal{C}\mathbf{x}_{[\mathcal{B}]}, \tag{C.8}$$

and thus

$$\mathcal{O}_{[\mathcal{B}]} = \mathcal{C}^{-1}\mathcal{O}_{[\mathcal{A}]}\mathcal{C}, \tag{C.9}$$

must hold true $\forall\ \mathbf{x}_{[\mathcal{B}]}$. For the purposes of consistency, since $\mathcal{O}$ is essentially the matrix representation of the operator $\hat{O}$, Eq. C.9 can be rewritten as

$$\hat{O}_{[\mathcal{B}]} = \mathcal{C}^{-1}\hat{O}_{[\mathcal{A}]}\mathcal{C}. \tag{C.10}$$

Appendix D

Stevens Operators

This appendix provides the operator equivalent definitions [47, 261] of the six Stevens operators $\hat{O}_k^q$ that defined the crystal field Hamiltonian $\hat{\mathcal{H}}_{CF}$. The Stevens operators utilised in this Thesis are:

$$\hat{O}_2^0 = 3\hat{J}_z^2 - \hat{X}, \tag{D.1a}$$

$$\hat{O}_4^0 = 35\hat{J}_z^4 - 30\hat{X}\hat{J}_z^2 + 25\hat{J}_z^2 - 6\hat{X} + 3\hat{X}^2, \tag{D.1b}$$

$$\hat{O}_4^3 = \frac{1}{4}\left\{\hat{J}_z(\hat{J}_+^3 + \hat{J}_-^3) + (\hat{J}_+^3 + \hat{J}_-^3)\hat{J}_z\right\}, \tag{D.1c}$$

$$\hat{O}_4^4 = \frac{1}{2}\left\{\hat{J}_+^4 + \hat{J}_-^4\right\} \tag{D.1d}$$

$$\hat{O}_6^0 = 231\hat{J}_z^6 - 315\hat{X}\hat{J}_z^4 + 735\hat{J}_z^4 + 105\hat{X}^2\hat{J}_z^2 - 525\hat{X}\hat{J}_z^2 + 294\hat{J}_z^2 - 5\hat{X}^3 + 40\hat{X}^2, \tag{D.1e}$$

$$\hat{O}_6^3 = \frac{1}{4}\left\{\left(11\hat{J}_z^3 - 3\hat{X}\hat{J}_z - 59\hat{J}_z\right)\left(\hat{J}_+^3 + \hat{J}_-^3\right) + \left(\hat{J}_+^3 + \hat{J}_-^3\right)\left(11\hat{J}_z^3 - 3\hat{X}\hat{J}_z - 59\hat{J}_z\right)\right\}, \tag{D.1f}$$

$$\hat{O}_6^6 = \frac{1}{2}\left\{\hat{J}_+^6 + \hat{J}_-^6\right\}, \tag{D.1g}$$

in the $|J, m_J\rangle$ basis and where $\hat{X} \equiv J(J+1)$ denotes the $\hat{\mathbf{J}}^2$ operator. It should be noted that the Stevens operators $\hat{O}_k^q$ can be written as a function of $\hat{\mathbf{J}}$ or $\hat{\mathbf{L}}$ in the $|J, m_J\rangle$ or the $|S, L, m_s, m_l\rangle$ basis, respectively, due to the Wigner-Eckart theorem [624].

Appendix E

Projection of Angular Momentum Operators: Calculations

This appendix presents the following projections of angular momentum operators utilising the procedure outlined by Stamokostas & Fiete [272]:

- projection of $\hat{\mathbf{J}}$ for Pr^{3+} in $Pr_2Sn_2O_7$ onto ground state crystal field doublet manifold,

- projection of $\hat{\mathbf{L}}$ Co^{2+} in an ideal octahedral coordination onto ground state crystal field triplet manifold,

- projection of $\hat{\mathbf{S}}$ and $\hat{\mathbf{l}}$ for Co^{2+} in an ideal octahedral coordination onto ground state $j_{\text{eff}} = \frac{1}{2}$ spin-orbit manifold.

An additional section concerning the projection of the Landé g-factor for Co^{2+} onto the $j_{\text{eff}} = \frac{1}{2}$ and $j_{\text{eff}} = \frac{3}{2}$ spin-orbit manifolds is provided at the end of this appendix for reference.

E.1 Projection of $\hat{\mathrm{J}}$ for Pr^{3+} in $Pr_2Sn_2O_7$ onto ground state crystal field doublet manifold

Inserting the Stevens parameters from Princep *et al.* [208] (Tab. 2.8) into the crystal field Hamiltonian

$$\hat{\mathcal{H}}_{\mathrm{CF}} = \mathrm{B}_2^0\hat{\mathrm{O}}_2^0 + \mathrm{B}_4^0\hat{\mathrm{O}}_4^0 + \mathrm{B}_4^3\hat{\mathrm{O}}_4^3 + \mathrm{B}_6^0\hat{\mathrm{O}}_6^0 + \mathrm{B}_6^3\hat{\mathrm{O}}_6^3 + \mathrm{B}_6^6\hat{\mathrm{O}}_6^6, \tag{E.1}$$

yields

$$\hat{\mathcal{H}}_{CF} = \begin{pmatrix} -49.78 & 0 & 0 & 21.45 & 0 & 0 & -8.74 & 0 & 0 \\ 0 & 34.90 & 0 & 0 & 20.43 & 0 & 0 & -11.57 & 0 \\ 0 & 0 & 37.66 & 0 & 0 & 8.15 & 0 & 0 & -8.74 \\ 21.45 & 0 & 0 & -6.90 & 0 & 0 & -8.15 & 0 & 0 \\ 0 & 20.43 & 0 & 0 & -31.77 & 0 & 0 & -20.43 & 0 \\ 0 & 0 & 8.15 & 0 & 0 & -6.90 & 0 & 0 & -21.45 \\ -8.74 & 0 & 0 & -8.15 & 0 & 0 & 37.66 & 0 & 0 \\ 0 & -11.57 & 0 & 0 & -20.43 & 0 & 0 & 34.90 & 0 \\ 0 & 0 & -8.74 & 0 & 0 & -21.45 & 0 & 0 & -49.78 \end{pmatrix}. \tag{E.2}$$

in the one particle $|J = 4, m_J\rangle$ basis. Diagonalising the matrix $\hat{\mathcal{H}}_{CF}$ yields

$$diag(\hat{\mathcal{H}}_{CF}) = \begin{pmatrix} -58.93 & 0 & 0 & 0 & 0 & 0 & 0 & 0 & 0 \\ 0 & -1.04 & 0 & 0 & 0 & 0 & 0 & 0 & 0 \\ 0 & 0 & 40.95 & 0 & 0 & 0 & 0 & 0 & 0 \\ 0 & 0 & 0 & -58.93 & 0 & 0 & 0 & 0 & 0 \\ 0 & 0 & 0 & 0 & -41.23 & 0 & 0 & 0 & 0 \\ 0 & 0 & 0 & 0 & 0 & -1.04 & 0 & 0 & 0 \\ 0 & 0 & 0 & 0 & 0 & 0 & 55.98 & 0 & 0 \\ 0 & 0 & 0 & 0 & 0 & 0 & 0 & 40.95 & 0 \\ 0 & 0 & 0 & 0 & 0 & 0 & 0 & 0 & 23.34 \end{pmatrix}. \tag{E.3}$$

Defining a transformation matrix $\mathcal{C}$ whose columns are the eigenvectors of $\hat{\mathcal{H}}_{CF}$ arranged in order of increasing eigenvalues yields

$$\mathcal{C} = \begin{pmatrix} 0.0013 & -0.93 & 0 & 0.35 & 0.0068 & 0 & 0.15 & -0.016 & 0 \\ 0 & 0 & -0.22 & 0 & 0 & -0.71 & 0 & 0 & 0.67 \\ 0.052 & 0 & 0 & 0 & -0.27 & 0 & 0 & -0.96 & 0 \\ -0.00053 & 0.37 & 0 & 0.90 & 0.018 & 0 & 0.23 & -0.025 & 0 \\ 0 & 0 & 0.95 & 0 & 0 & 0 & 0 & 0 & 0.31 \\ 0.37 & 0 & 0 & 0 & 0.90 & 0 & 0 & -0.23 & 0 \\ 7.48e-05 & -0.052 & 0 & 0.27 & 0.0052 & 0 & -0.96 & 0.11 & 0 \\ 0 & 0 & 0.22 & 0 & 0 & -0.71 & 0 & 0 & -0.67 \\ 0.93 & 0 & 0 & 0 & -0.35 & 0 & 0 & 0.15 & 0 \end{pmatrix}, \tag{E.4}$$

where in the case of degenerate eigenvalues, the eigenvectors are arranged in the order of increasing eigenvalues after the application of a perturbative magnetic field $\hat{\mathcal{H}}_{MF} = H_{MF}\hat{S}_z$. Projecting each component of the angular momentum operator onto the crystal field basis *via* Eq. C.10 in Appendix C yields

$$\mathcal{C}^{-1}\hat{J}_z\mathcal{C} = \left(\begin{array}{cc|ccccccc} 3.56 & 0 & 0 & 0 & -0.92 & 0 & 0 & 0.56 & 0 \\ 0.010 & -3.56 & 0 & 0.92 & 0.017 & 0 & 0.56 & -0.060 & 0 \\ \hline 0 & 0 & 0 & 0 & 0 & -0.94 & 0 & 0 & 0 \\ 0.017 & 0.92 & 0 & -1.15 & -0.045 & 0 & -0.93 & 0.12 & 0 \\ -0.92 & 0 & 0 & 0 & 1.15 & 0 & 0 & -0.92 & 0 \\ 0 & 0 & -0.94 & 0 & 0 & 0 & 0 & 0 & 2.85 \\ 0.061 & 0.56 & 0 & -0.93 & -0.12 & 0 & 1.71 & -0.37 & 0 \\ 0.56 & 0 & 0 & 0 & -0.93 & 0 & 0 & -1.71 & 0 \\ 0 & 0 & 0 & 0 & 0 & 2.85 & 0 & 0 & 0 \end{array}\right) \tag{E.5}$$

$$\mathcal{C}^{-1}\hat{J}_x\mathcal{C} = \left(\begin{array}{cc|cccccccc} 0 & 0 & 1.06 & 0.31 & 0.0061 & -1.00 & -0.74 & 0.080 & -0.55 \\ 0 & 0 & 1.06 & 0.00045 & -0.31 & 0.99 & -0.0011 & -0.73 & -0.55 \\ \hline 1.060 & 1.06 & 0 & 1.91 & 1.95 & 0 & 0.044 & -0.049 & 0 \\ 0.31 & 0.0061 & 1.87 & 0 & 0 & -0.72 & 0.038 & -1.96 & 0.61 \\ 0.00045 & -0.31 & 1.91 & 0 & 0 & 0.70 & -1.96 & 0.21 & 0.62 \\ -1.00 & 0.10 & 0 & -0.70 & 0.69 & 0 & 1.13 & 0.10 & 0 \\ -0.74 & -0.081 & 0.039 & -0.22 & -1.97 & 1.25 & 0 & 0 & 1.34 \\ 0.0011 & -0.74 & -0.045 & -1.98 & -0.039 & 1.13 & 0 & 0 & -1.52 \\ -0.55 & -0.55 & 0 & 0.62 & 0.63 & 0 & 1.51 & -1.67 & 0 \end{array}\right) \tag{E.6}$$

$$\mathcal{C}^{-1}\hat{J}_y\mathcal{C} = i\left(\begin{array}{cc|cccccccc} 0 & 0 & -1.06 & 0.31 & 0.0061 & 1.00 & -0.74 & 0.080 & 0.55 \\ 0 & 0 & 1.060 & 0.00045 & 0.31 & 1.00 & -0.0011 & 0.73 & -0.55 \\ \hline 1.06 & -1.062 & 0 & -1.91 & 1.87 & 0 & -0.044 & -0.039 & 0 \\ -0.31 & 0.0061 & 1.95 & 0 & 0 & -0.69 & 0.038 & 1.95 & 0.63 \\ 0.00045 & -0.31 & -1.91 & 0 & 0 & -0.70 & -1.96 & 0.21 & -0.62 \\ -0.99 & -1.00 & 0 & 0.70 & 0.72 & 0 & -1.13 & 1.24 & 0 \\ 0.74 & -0.081 & 0.049 & -0.22 & 1.96 & 1.0020 & 0 & 0 & 1.68 \\ 0.0011 & -0.74 & 0.045 & -1.98 & -0.039 & -1.13 & 0 & 0 & 1.52 \\ -0.55 & 0.55 & 0 & -0.62 & 0.61 & 0 & -1.51 & -1.34 & 0 \end{array}\right) \tag{E.7}$$

Extraction of the top 2 x 2 block matrices provides the three components of the angular momentum operator projected onto the ground state crystal field doublet manifold:

$$\widetilde{\hat{J}}_z = \begin{pmatrix} 3.5648 & 0 \\ 0.0102 & -3.5648 \end{pmatrix} \tag{E.8}$$

$$\widetilde{\hat{J}}_x = \begin{pmatrix} 0 & 0 \\ 0 & 0 \end{pmatrix} \tag{E.9}$$

$$\widetilde{\hat{J}}_y = i \begin{pmatrix} 0 & 0 \\ 0 & 0 \end{pmatrix}, \tag{E.10}$$

where the tilde denotes particular block matrices of interest. Inserting $\widetilde{\hat{J}}_x$ and $\widetilde{\hat{J}}_y$ into the commutator yields

$$[\widetilde{\hat{J}}_x, \widetilde{\hat{J}}_y] = i \begin{pmatrix} 0 & 0 \\ 0 & 0 \end{pmatrix} \neq i\widetilde{\hat{J}}_z, \tag{E.11}$$

where the final inequality implies the $j_{\text{eff}} = \frac{1}{2}$ approximation is not valid for Pr^{3+} in $Pr_2Sn_2O_7$.

E.2 Projection of $\hat{\mathbf{L}}$ for Co^{2+} in an ideal octahedral coordination onto ground state crystal field triplet manifold

It is important to note that the ground state doublet spin-orbit manifold discussed for the α-CoV_3O_8 and $Co_xMg_{1-x}O$ systems is a consequence of an approach commonly used to address the orbital triplet ground state in Co^{2+} [18, 20, 47, 444]. Such an approach first defines an effective total angular momentum $\hat{\mathbf{j}} = \hat{\mathbf{l}} + \hat{\mathbf{S}}$, where l =1 to reflect an triplet orbital degeneracy. Thus, a projection of any angular momentum operators onto the $j = \frac{1}{2}$ manifold requires a concurrent projection of $\mathbf{L}$ onto $\mathbf{l}$, *via* a projection factor α.

The determination of the projection factor α begins by first defining the crystal

field Hamiltonian $\hat{\mathcal{H}}_{CEF}$ describing the effects of the crystalline electric field on the free ion states of the d^7 Co^{2+} resulting from the symmetry imposed by the crystal lattice. Assuming both negligible distortions away from purely octahedral coordination and negligible admixture between the ^4F ground and first excited ^4P free ion states, a weak crystal field approach can be employed whereby $\hat{\mathcal{H}}_{CEF}$ can be written in terms of the Stevens operators $\hat{O}_4^0$ and $\hat{O}_4^4$ and the numerical coefficient B_4 as

$$\hat{\mathcal{H}}_{CEF} = B_4(\hat{O}_4^0 + 5\hat{O}_4^4). \tag{E.12}$$

The numerical coefficient B_4 is defined as $\beta\langle r^4\rangle$ where β is the Stevens multiplicative factor, while the Stevens operators are defined in terms of the $\hat{L}^2$, $\hat{L}_z$ and $\hat{L}_\pm$ orbital angular momentum operators [47, 261, 264] as

$$\hat{O}_4^0 = 35\hat{L}_z^4 - 30\hat{L}^2\hat{L}_z^2 + 25\hat{L}_z^2 - 6\hat{L}^2 + 3\hat{L}^4, \tag{E.13}$$

and

$$\hat{O}_4^4 = \frac{1}{2}\left[\hat{L}_+^4 + \hat{L}_-^4\right]. \tag{E.14}$$

By combining Eqs. E.12-E.14 and setting B_4 as -1, the crystal field Hamiltonian is given by

$$\hat{\mathcal{H}}_{CF} = \begin{pmatrix} -180 & 0 & 0 & 0 & -232.4 & 0 & 0 \\ 0 & 420 & 0 & 0 & 0 & -300 & 0 \\ 0 & 0 & -60 & 0 & 0 & 0 & -232.4 \\ 0 & 0 & 0 & -360 & 0 & 0 & 0 \\ -232.4 & 0 & 0 & 0 & -60 & 0 & 0 \\ 0 & -300 & 0 & 0 & 0 & 40 & 0 \\ 0 & 0 & -232.4 & 0 & 0 & 0 & -180 \end{pmatrix} \tag{E.15}$$

in the one particle $|L = 3, m_L\rangle$ basis where each operator has been normalised by $\hbar$. Before proceeding, it is worth noting that by setting $|B_4|$ as 1, all energy eigenstates will be in terms of B_4 while the negative sign is due to the d^7 electron configuration of Co^{2+}, producing a triplet and not a singlet ground state like Ni^{2+} [47].

Diagonalising the crystal field Hamiltonian yields

$$diag(\hat{\mathcal{H}}_{CF}) = \begin{pmatrix} -360 & 0 & 0 & 0 & 0 & 0 & 0 \\ 0 & -360 & 0 & 0 & 0 & 0 & 0 \\ 0 & 0 & -360 & 0 & 0 & 0 & 0 \\ 0 & 0 & 0 & 120 & 0 & 0 & 0 \\ 0 & 0 & 0 & 0 & 120 & 0 & 0 \\ 0 & 0 & 0 & 0 & 0 & 120 & 0 \\ 0 & 0 & 0 & 0 & 0 & 0 & 720 \end{pmatrix} \tag{E.16}$$

corresponding to a triply degenerate ground state (Γ_4), a triply degenerate first excited state (Γ_5) and a singlet second excited state (Γ_2), where $\Delta(\Gamma_4 \rightarrow \Gamma_5) = 480B_4$ and $\Delta(\Gamma_5 \rightarrow \Gamma_2) = 600B_4$.

Utilising the diagonalised crystal field Hamiltonian above, a transformation matrix $\mathcal{C}$ can be defined as

$$\mathcal{C} = \begin{pmatrix} 0 & 0 & -0.79 & 0.61 & 0 & 0 & 0 \\ 0 & 0 & 0 & 0 & -0.71 & 0 & -0.71 \\ 0.61 & 0 & 0 & 0 & 0 & -0.79 & 0 \\ 0 & 1.00 & 0 & 0 & 0 & 0 & 0 \\ 0 & 0 & -0.61 & -0.79 & 0 & 0 & 0 \\ 0 & 0 & 0 & 0 & -0.71 & 0 & 0.71 \\ 0.79 & 0 & 0 & 0 & 0 & 0.61 & 0 \end{pmatrix} \tag{E.17}$$

where the columns of $\mathcal{C}$ are the eigenvectors corresponding to the eigenvalues in Eq. E.16 [272]. The eigenvectors are arranged in the order of increasing eigenvalues from left to right. In the case of degenerate eigenvalues, the eigenvectors are arranged in the order of increasing eigenvalues from left to right after the application of a small perturbative magnetic field $\hat{\mathcal{H}}_{MF} = H_{MF}\hat{S}_z$. As derived in Appendix C [623], the transformation matrix $\mathcal{C}$ rotates operators from the $|L = 3, m_L\rangle$ basis to a $|\phi_{\text{CEF}}\rangle$ basis defined by the crystal field eigenvectors by

$$\hat{\mathcal{O}}_{|\phi_{CEF}\rangle} = \mathcal{C}^{-1}\hat{\mathcal{O}}_{|L,m_L\rangle}\mathcal{C}. \tag{E.18}$$

Since the ground state multiplet of the crystal field Hamiltonian corresponds to the triply orbitally degenerate manifold, then the subspace spanned by the

top 3×3 block matrix of any orbital angular momentum operator $\hat{\mathcal{O}}_{|\phi_{CEF}\rangle}$ for a particular irreducible representation [272] will (1) have its matrix entries arranged in a format equivalent to its corresponding angular momentum operator with $l = 1$, whilst (2) the entries in both matrices must be equal up to the projection constant α. Projecting the $\hat{L}_z$ operator from the $|L = 3, m_L\rangle$ basis to the $|\phi_{\text{CEF}}\rangle$ basis *via* Eq. E.18, one obtains

$$\widetilde{\hat{L}_z} = \mathcal{C}^{-1}\hat{L}_z\mathcal{C} = \left(\begin{array}{ccc|ccc|c} 1.50 & 0 & 0 & 0 & 0 & -1.94 & 0 \\ 0 & 0 & 0 & 0 & 0 & 0 & 0 \\ 0 & 0 & -1.50 & -1.94 & 0 & 0 & 0 \\ \hline 0 & 0 & -1.94 & -0.50 & 0 & 0 & 0 \\ 0 & 0 & 0 & 0 & 0 & 0 & 2.00 \\ -1.94 & 0 & 0 & 0 & 0 & 0.50 & 0 \\ \hline 0 & 0 & 0 & 0 & 2.00 & 0 & 0 \end{array}\right) \tag{E.19}$$

A comparison of the top and middle 3×3 block matrices in Eq. E.19 to the $\hat{L}_z$ operator (normalised by $\hbar$) in the $|l = 1, m_l\rangle$ basis given by

$$\hat{L}_z = \begin{pmatrix} -1 & 0 & 0 \\ 0 & 0 & 0 \\ 0 & 0 & 1 \end{pmatrix}, \tag{E.20}$$

reveals that both block matrices have equivalent arrangements of matrix elements to $\hat{L}_z$ in the $|l = 1, m_l\rangle$ basis with projection factors $\alpha = -\frac{3}{2}$ and $\frac{1}{2}$ for the ground and first excited manifolds, respectively, in agreement with previous derivations utilising group theory [47].

As a final confirmation of the validity of the projection described by Eq. E.18, both $\hat{L}_+$ and $\hat{L}_-$ were projected onto the $|\phi_{\text{CEF}}\rangle$ basis:

$$\widetilde{\hat{L}_+} = \mathcal{C}^{-1}\hat{L}_+\mathcal{C} = \left(\begin{array}{ccc|ccc|c} 0 & 2.12 & 0 & 0 & 0 & 0 & 0 \\ 2.12 & 0 & 0 & 0 & 0 & -2.74 & 0 \\ 0 & -2.12 & 0 & 0 & 0 & 0 & 0 \\ \hline 0 & -2.74 & 0 & 0 & 0 & 0 & 0 \\ 0 & 0 & 2.74 & 0.71 & 0 & 0 & 0 \\ 0 & 0 & 0 & 0 & 0.71 & 0 & 2.83 \\ \hline 0 & 0 & 0 & -2.83 & 0 & 0 & 0 \end{array}\right) \tag{E.21}$$

$$\widetilde{\hat{L}_-} = \mathcal{C}^{-1}\hat{L}_-\mathcal{C} = \left(\begin{array}{ccc|ccc|c} 0 & 2.12 & 0 & 0 & 00 & 0 & \\ 0 & 0 & -2.12 & -2.74 & 0 & 0 & 0 \\ 0 & 0 & 0 & 0 & 2.74 & 0 & 0 \\ \hline 0 & 0 & 0 & 0 & 2.74 & 0 & -2.83 \\ -2.74 & 0 & 0 & 0 & 0 & 0.71 & 0 \\ 0 & -2.73 & 0 & 0 & 0 & 0 & 0 \\ \hline 0 & 0 & 0 & -2.83 & 0 & 2.83 & 0 \end{array}\right). \tag{E.22}$$

Both projected x and y-components of the angular momentum $\widetilde{\hat{L}_x}$ and $\widetilde{\hat{L}_y}$ were then calculated using the following identities:

$$\widetilde{\hat{L}_x} = \frac{\widetilde{\hat{L}_+} + \widetilde{\hat{L}_-}}{2} \tag{E.23}$$

$$\widetilde{\hat{L}_y} = \frac{\widetilde{\hat{L}_+} - \widetilde{\hat{L}_-}}{2i}, \tag{E.24}$$

yielding:

$$\widetilde{\hat{L}_x} = \left(\begin{array}{ccc|ccc|c} 0 & 1.06 & 0 & 0 & -1.37 & 0 & 0 \\ 1.06 & 0 & -1.06 & -1.37 & 0 & -1.37 & 0 \\ 0 & -1.06 & 0 & 0 & 1.37 & 0 & 0 \\ \hline 0 & -1.37 & 0 & 0 & 0.35 & 0 & -1.41 \\ -1.37 & 0 & 1.37 & 0.35 & 0 & 0.35 & 0 \\ 0 & -1.37 & 0 & 0 & 0.35 & 0 & 1.41 \\ \hline 0 & 0 & 0 & -1.41 & 0 & 1.41 & 0 \end{array}\right) \tag{E.25}$$

$$\widetilde{\hat{L}_y} = i\left(\begin{array}{ccc|ccc|c} 0 & 1.06 & 0 & 0 & 0 & 0 & 0 \\ -1.06 & 0 & -1.06 & -1.37 & 0 & 1.37 & 0 \\ 0 & 1.06 & 0 & 0 & 1.37 & 0 & 0 \\ \hline 0 & 1.37 & 0 & 0 & 0.35 & 0 & -1.41 \\ -1.37 & 0 & -1.37 & -0.35 & 0 & 0.35 & 0 \\ 0 & -1.37 & 0 & 0 & -0.35 & 0 & -1.41 \\ \hline 0 & 0 & 0 & 1.41 & 0 & 1.41 & 0 \end{array}\right) \tag{E.26}$$

Finally, by extracting the top 3×3 block matrices from the definitions of $\hat{L}_z$ (Eq. E.19), $\hat{L}_x$ (Eq. E.25) and $\hat{L}_y$ (Eq. E.26) and evaluating the commutator $[\widetilde{\hat{L}_x}, \widetilde{\hat{L}_y}]$, one obtains

$$[\widetilde{\hat{L}_x}, \widetilde{\hat{L}_y}] = i \begin{bmatrix} 1.5 & 0 & 0 \\ 0 & 0 & 0 \\ 0 & 0 & -1.5 \end{bmatrix} = i\widetilde{\hat{L}_z}. \tag{E.27}$$

By performing the commutator of all possible permutations of the projected components of the orbital angular momentum operator, it can be shown that the canonical commutation relations of angular momentum normalised by $\hbar$

$$[\widetilde{\hat{L}_x}, \widetilde{\hat{L}_y}] = i\epsilon_{xyz}\widetilde{\hat{L}_z} \tag{E.28}$$

are satisfied for the new $|\phi_{\text{CEF}}\rangle$ basis.

Throughout the analysis presented above, two subtle but key observations must be addressed. The first refers to the arrangement of elements in a particular block matrix. Recall that the arrangement of the matrix elements in the top 3×3 block matrix of $\widetilde{\hat{L}_z}$ (Eq. E.19) was identical to that of the $\hat{L}_z$ operator (normalised by $\hbar$) in the $|l = 1, m_l\rangle$ basis (Eq. E.20). Although the 1:1 correspondence of element arrangement between matrices is particularly useful for the determination of the projection factor α, such a correspondence is not necessarily the case and depends on which particular irreducible representation in the new crystal field basis is chosen. For example, the $\hat{L}_x$ operator (normalised by $\hbar$) in the $|l = 1, m_l\rangle$ basis is given by

$$\hat{L}_x = \frac{1}{\sqrt{2}} \begin{pmatrix} 0 & 1 & 0 \\ 1 & 0 & 1 \\ 0 & 1 & 0 \end{pmatrix}. \tag{E.29}$$

A comparison between Eq. E.29 and the top 3×3 block matrix of $\widetilde{\hat{L}_x}$ (Eq. E.25) reveals that the matrices differ in element arrangement. A similar case occurs for the $\widetilde{\hat{L}_y}$ operator. Consequently, it must be emphasised that the identification of a true angular momentum operator in a particular basis should not be based on a comparison between its elements and the arrangement of matrix elements in the $|l, m_l\rangle$ basis, but rather on the success of satisfying the canonical commutation

relations as summarised in Eq. E.28.

The second observation is that the projection factor α pertains only to the particular manifold of interest such as $\alpha = -\frac{3}{2}$ for the ground state crystal field triplet manifold. In other words, α is not a simple multiplicative factor to project the entire angular momentum operator. A counterargument for such a treatment of α can be rationalised by the following:

- Suppose there are angular momentum operators $\hat{L}_x$, $\hat{L}_y$ and $\hat{L}_z$. It should be noted that such arguments would be equally valid for the total and spin angular momentum operators $\hat{J}_\xi$ and $\hat{S}_\xi$.

- Since the the operators are angular momentum operators, they must satisfy the canonical commutation relations

$$[\hat{L}_x, \hat{L}_y] = i\epsilon_{xyz}\hat{L}_z. \tag{E.30}$$

- Suppose α is treated as a simple multiplicative factor to project the operator for each component of the angular momentum, then Eq. E.30 becomes

$$[\widetilde{\hat{L}_x}, \widetilde{\hat{L}_y}] \equiv [\alpha\hat{L}_x, \alpha\hat{L}_y] = \alpha^2[\hat{L}_x, \hat{L}_y] = i\alpha^2\epsilon_{xyz}\hat{L}_z \equiv i\alpha\epsilon_{xyz}\widetilde{\hat{L}_z}. \tag{E.31}$$

- The second equality results in a clear contradiction, since it was assumed that the projected operator of the z-component of angular momentum was defined as $\alpha\hat{J}_z \neq \alpha^2\hat{J}_z$ as in Eq. E.31.

Such a contradiction emphasises that the projection factors α (and α') that are presented in the context of Co^{2+} magnetism pertains **only** to a particular manifold and not the entire Hilbert space spanned by the angular momentum operators.

E.3 Projection of $\hat{\mathrm{S}}$ and $\hat{\mathrm{l}}$ for Co^{2+} in an ideal octahedral coordination onto ground state $j_{\mathrm{eff}} = \frac{1}{2}$ spin-orbit manifold

As described in the main text, the total single-ion Hamiltonian $\hat{\mathcal{H}}_{SI}$ describing Co^{2+} is

$$\hat{\mathcal{H}}_{SI} = \hat{\mathcal{H}}_{CF} + \hat{\mathcal{H}}_{SO} + \hat{\mathcal{H}}_{MF} + \hat{\mathcal{H}}_{dis}, \tag{E.32}$$

where the spin-orbit, magnetic order induced molecular field and distortions away from ideal octahedral coordination contributions denoted by $\hat{\mathcal{H}}_{SO}$, $\hat{\mathcal{H}}_{MF}$, and $\hat{\mathcal{H}}_{dis}$, respectively, are treated as perturbations to the crystal field Hamiltonian $\hat{\mathcal{H}}_{CF}$ (Eq. E.1) [76]. As a first approximation, if one assumes that the deviation away from ideal octahedral coordination is minimal and that the molecular field-induced Zeeman splitting is small relative to other terms in $\hat{\mathcal{H}}_{SI}$, then the only perturbative term under consideration originates from $\hat{\mathcal{H}}_{SO}$ describing the interaction between the spin and orbital degrees of freedom. In the low temperature limit (*i.e.* $\lambda \gg k_B T$), then it is assumed that the orbital triplet state described above is exclusively populated and thus the effective orbital angular momentum l is set to 1. Thus, the spin-orbit coupling Hamiltonian describing the interaction between an effective angular momentum $\hat{\mathbf{l}}$ and a spin angular momentum $\hat{\mathbf{S}}$, is given by

$$\hat{\mathcal{H}}_{SO} = \widetilde{\lambda}\alpha\hat{\mathbf{l}} \cdot \hat{\mathbf{S}}, \tag{E.33}$$

where $\widetilde{\lambda}$ denotes the spin-orbit coupling constant with a projection factor α after the projection from $\hat{\mathbf{L}}$ to $\hat{\mathbf{l}}$ [20]. By utilising the previously determined value of $\alpha = -\frac{3}{2}$, the value of $\lambda = -16$ meV as determined for $Co_{0.03}Mg_{0.97}O$ [18], $l = 1$ and $S = \frac{3}{2}$ for the high spin d^7 Co^{2+}, then the Hilbert space spanned by $\hat{\mathcal{H}}_{SO}$

consists of 12 basis states and the $\hat{\mathcal{H}}_{SO}$ (Eq. E.33) is given by

$$\hat{\mathcal{H}}_{SO} = \begin{pmatrix} 36 & 0 & 0 & 0 & 0 & 0 & 0 & 0 & 0 & 0 & 0 & 0 \\ 0 & 0 & 0 & 29.39 & 0 & 0 & 0 & 0 & 0 & 0 & 0 & 0 \\ 0 & 0 & -36 & 0 & 29.39 & 0 & 0 & 0 & 0 & 0 & 0 & 0 \\ 0 & 29.39 & 0 & 12 & 0 & 0 & 0 & 0 & 0 & 0 & 0 & 0 \\ 0 & 0 & 29.39 & 0 & 0 & 0 & 33.94 & 0 & 0 & 0 & 0 & 0 \\ 0 & 0 & 0 & 0 & 0 & -12 & 0 & 33.94 & 0 & 0 & 0 & 0 \\ 0 & 0 & 0 & 0 & 33.94 & 0 & -12 & 0 & 0 & 0 & 0 & 0 \\ 0 & 0 & 0 & 0 & 0 & 33.94 & 0 & 0 & 0 & 29.39 & 0 & 0 \\ 0 & 0 & 0 & 0 & 0 & 0 & 0 & 0 & 12 & 0 & 29.39 & 0 \\ 0 & 0 & 0 & 0 & 0 & 0 & 0 & 29.39 & 0 & -36 & 0 & 0 \\ 0 & 0 & 0 & 0 & 0 & 0 & 0 & 0 & 29.39 & 0 & 0 & 0 \\ 0 & 0 & 0 & 0 & 0 & 0 & 0 & 0 & 0 & 0 & 0 & 36 \end{pmatrix}, \tag{E.34}$$

in the one particle basis $|l = 1, m_l, S = \frac{3}{2}, m_s\rangle$. Diagonalising the spin-orbit Hamiltonian yields

$$diag(\hat{\mathcal{H}}_{SO}) = \begin{pmatrix} -60 & 0 & 0 & 0 & 0 & 0 & 0 & 0 & 0 & 0 & 0 & 0 \\ 0 & -60 & 0 & 0 & 0 & 0 & 0 & 0 & 0 & 0 & 0 & 0 \\ 0 & 0 & -24 & 0 & 0 & 0 & 0 & 0 & 0 & 0 & 0 & 0 \\ 0 & 0 & 0 & -24 & 0 & 0 & 0 & 0 & 0 & 0 & 0 & 0 \\ 0 & 0 & 0 & 0 & -24 & 0 & 0 & 0 & 0 & 0 & 0 & 0 \\ 0 & 0 & 0 & 0 & 0 & -24 & 0 & 0 & 0 & 0 & 0 & 0 \\ 0 & 0 & 0 & 0 & 0 & 0 & 36 & 0 & 0 & 0 & 0 & 0 \\ 0 & 0 & 0 & 0 & 0 & 0 & 0 & 36 & 0 & 0 & 0 & 0 \\ 0 & 0 & 0 & 0 & 0 & 0 & 0 & 0 & 36 & 0 & 0 & 0 \\ 0 & 0 & 0 & 0 & 0 & 0 & 0 & 0 & 0 & 36 & 0 & 0 \\ 0 & 0 & 0 & 0 & 0 & 0 & 0 & 0 & 0 & 0 & 36 & 0 \\ 0 & 0 & 0 & 0 & 0 & 0 & 0 & 0 & 0 & 0 & 0 & 36 \end{pmatrix}, \tag{E.35}$$

where the three eigenvalues of -60, -24 and 36 meV (or equivalently 0, 36 and 96 meV) correspond to the $j_{\text{eff}} = \frac{1}{2}$, $\frac{3}{2}$ and $\frac{5}{2}$ spin-orbit manifolds, respectively. Utilising the diagonalised spin-orbit Hamiltonian above, a transformation matrix

$\mathcal{C}$ can be defined as

$$\mathcal{C} = \begin{pmatrix} 0 & 0 & 0 & 0 & 0 & 0 & 1 & 0 & 0 & 0 & 0 & 0 \\ 0 & 0 & -0.77 & 0 & 0 & 0 & 0 & -0.63 & 0 & 0 & 0 & 0 \\ 0.71 & 0 & 0 & -0.63 & 0 & 0 & 0 & 0 & 0.32 & 0 & 0 & 0 \\ 0 & 0 & 0.63 & 0 & 0 & 0 & 0 & -0.77 & 0 & 0 & 0 & 0 \\ -0.58 & 0 & 0 & -0.26 & 0 & 0 & 0 & 0 & 0.77 & 0 & 0 & 0 \\ 0 & -0.41 & 0 & 0 & 0.73 & 0 & 0 & 0 & 0 & 0.55 & 0 & 0 \\ 0.41 & 0 & 0 & 0.73 & 0 & 0 & 0 & 0 & 0.55 & 0 & 0 & 0 \\ 0 & 0.58 & 0 & 0 & -0.26 & 0 & 0 & 0 & 0 & 0.77 & 0 & 0 \\ 0 & 0 & 0 & 0 & 0 & 0.63 & 0 & 0 & 0 & 0 & 0.77 & 0 \\ 0 & -0.71 & 0 & 0 & -0.63 & 0 & 0 & 0 & 0 & 0.32 & 0 & 0 \\ 0 & 0 & 0 & 0 & 0 & -0.77 & 0 & 0 & 0 & 0 & 0.63 & 0 \\ 0 & 0 & 0 & 0 & 0 & 0 & 0 & 0 & 0 & 0 & 0 & 1 \end{pmatrix}. \tag{E.36}$$

where the columns of $\mathcal{C}$ are the eigenvectors corresponding to the eigenvalues in Eq. E.35. The eigenvectors are arranged in the order of increasing eigenvalues from left to right. In the case of degenerate eigenvalues, the eigenvectors are arranged in the order of increasing eigenvalues from left to right after the application of a small perturbative magnetic field $\hat{\mathcal{H}}_{MF} = H_{MF}\hat{S}_z$. As derived in Appendix C [623], the transformation matrix $\mathcal{C}$ rotates operators from the $|l = 1, m_l, S = \frac{3}{2}, m_s\rangle$ basis to a $|\phi_{\mathrm{SO}}\rangle$ basis defined by the spin-orbit eigenvectors. Projecting the $\hat{S}_z$, $\hat{S}_y$ and $\hat{S}_x$ operators from the $|l = 1, m_l, S = \frac{3}{2}, m_s\rangle$ basis to the $|\phi_{\mathrm{SO}}\rangle$ basis *via*

$$\hat{\mathcal{O}}_{|\phi_{SO}\rangle} = \mathcal{C}^{-1}\hat{\mathcal{O}}_{|l=1,m_l,S=\frac{3}{2},m_s\rangle}\mathcal{C}, \tag{E.37}$$

one obtains

$$\mathcal{C}^{-1}\hat{S}_z\mathcal{C} = \left(\begin{array}{cc|cccc|cccccc} -0.83 & 0 & 0 & 0.75 & 0 & 0 & 0 & 0 & 0 & 0 & 0 & 0 \\ 0 & 0.83 & 0 & 0 & 0.75 & 0 & 0 & 0 & 0 & 0 & 0 & 0 \\ \hline 0 & 0 & -1.10 & 0 & 0 & 0 & 0 & -0.49 & 0 & 0 & 0 & 0 \\ 0.75 & 0 & 0 & -0.37 & 0 & 0 & 0 & 0 & 0.6 & 0 & 0 & 0 \\ 0 & 0.75 & 0 & 0 & 0.37 & 0 & 0 & 0 & 0 & -0.6 & 0 & 0 \\ 0 & 0 & 0 & 0 & 0 & 1.10 & 0 & 0 & 0 & 0 & 0.49 & 0 \\ \hline 0 & 0 & -0.49 & 0 & 0 & 0 & -1.50 & 0 & 0 & 0 & 0 & 0 \\ 0 & 0 & 0 & 0 & 0 & -0.49 & 0 & -0.90 & 0 & 0 & 0 & 0 \\ 0 & 0 & 0 & 0 & 0 & 0 & 0 & 0 & -0.30 & 0 & 0 & 0 \\ 0 & 0 & 0 & 0 & 0 & 0 & 0 & 0 & 0 & 0.30 & 0 & 0 \\ 0 & 0 & 0 & 0 & -0.60 & 0 & 0 & 0 & 0 & 0 & 0.90 & 0 \\ 0 & 0 & 0 & 0.60 & 0 & 0 & 0 & 0 & 0 & 0 & 0 & 1.50 \end{array}\right). \tag{E.38}$$

$$\mathcal{C}^{-1}\hat{S}_y\mathcal{C} = i\left(\begin{array}{cc|cccc|cccccc} 0 & -0.83 & -0.65 & 0 & 0.37 & 0 & 0 & 0 & 0 & 0 & 0 & 0 \\ 0.83 & 0 & 0 & 0.37 & 0 & -0.65 & 0 & 0 & 0 & 0 & 0 & 0 \\ \hline 0.65 & 0 & 0 & 0.64 & 0 & 0 & -0.55 & 0 & -0.17 & 0 & 0 & 0 \\ 0 & -0.37 & -0.64 & 0 & -0.73 & 0 & 0 & 0.42 & 0 & -0.30 & 0 & 0 \\ -0.37 & 0 & 0 & 0.73 & 0 & 0.64 & 0 & 0 & 0.30 & 0 & 0.42 & 0 \\ 0 & 0.65 & 0 & 0 & -0.64 & 0 & 0 & 0 & 0 & 0.17 & 0 & 0.55 \\ \hline 0 & 0 & 0.55 & 0 & 0 & 0 & 0 & -0.67 & 0 & 0 & 0 & 0 \\ 0 & 0 & 0 & -0.42 & 0 & 0 & 0.67 & 0 & -0.85 & 0 & 0 & 0 \\ 0 & 0 & 0.17 & 0 & -0.30 & 0 & 0 & 0.85 & 0 & 0.90 & 0 & 0 \\ 0 & 0 & 0 & 0.30 & 0 & -0.17 & 0 & 0 & -0.90 & 0 & 0.85 & 0 \\ 0 & 0 & 0 & 0 & -0.42 & 0 & 0 & 0 & 0 & -0.85 & 0 & 0.67 \\ 0 & 0 & 0 & 0 & 0 & -0.55 & 0 & 0 & 0 & 0 & -0.67 & 0 \end{array}\right). \tag{E.39}$$

$$\mathcal{C}^{-1}\hat{S}_x\mathcal{C} = \left(\begin{array}{cc|cccc|cccccc} 0 & -0.83 & 0.65 & 0 & 0.37 & 0 & 0 & 0 & 0 & 0 & 0 & 0 \\ -0.83 & 0 & 0 & -0.37 & 0 & -0.65 & 0 & 0 & 0 & 0 & 0 & 0 \\ \hline 0.65 & 0 & 0 & 0.64 & 0 & 0 & 0.55 & 0 & -0.17 & 0 & 0 & 0 \\ 0 & -0.37 & 0.64 & 0 & -0.73 & 0 & 0 & -0.42 & 0 & -0.30 & 0 & 0 \\ 0.37 & 0 & 0 & -0.73 & 0 & 0.64 & 0 & 0 & -0.30 & 0.42 & 0 & \\ 0 & -0.65 & 0 & 0 & 0.64 & 0 & 0 & 0 & 0 & -0.17 & 0 & 0.55 \\ \hline 0 & 0 & 0.55 & 0 & 0 & 0 & 0 & -0.67 & 0 & 0 & 0 & 0 \\ 0 & 0 & 0 & -0.42 & 0 & 0 & -0.67 & 0 & -0.85 & 0 & 0 & 0 \\ 0 & 0 & -0.17 & -0.30 & 0 & 0 & 0 & -0.85 & 0 & 0.90 & 0 & 0 \\ 0 & 0 & 0 & -0.30 & 0 & -0.17 & 0 & 0 & 0.90 & 0 & 0.85 & 0 \\ 0 & 0 & 0 & 0 & 0.42 & 0 & 0 & 0 & 0 & 0.85 & 0 & 0.67 \\ 0 & 0 & 0 & 0 & 0 & 0.55 & 0 & 0 & 0 & 0 & 0.67 & 0 \end{array}\right). \tag{E.40}$$

In this Thesis, projections of the components of the spin operator $\hat{\mathbf{S}}$ onto both the ground state $j_{\text{eff}} = \frac{1}{2}$ and the first excited state $j_{\text{eff}} = \frac{3}{2}$ manifolds are of interest. The importance of the latter is due to significant depopulation and population of the ground state and first excited state manifolds, respectively, in the paramagnetic regime (T=[200, 300] K) where fits to the Curie-Weiss law were performed. A comparison of the top 2×2 and middle 3×3 block matrices in Eq. E.38 to the $\hat{S}_z$ operator (normalised by $\hbar$) in the $|S = \frac{1}{2}, m_s\rangle$ and $|S = \frac{3}{2}, m_s\rangle$ bases given by

$$\hat{S}_z = \begin{pmatrix} -\frac{1}{2} & 0 \\ 0 & \frac{1}{2} \end{pmatrix} \tag{E.41}$$

$$\hat{S}_z = \begin{pmatrix} -\frac{3}{2} & 0 & 0 & 0 \\ 0 & -\frac{1}{2} & 0 & 0 \\ 0 & 0 & \frac{1}{2} & 0 \\ 0 & 0 & 0 & \frac{3}{2} \end{pmatrix}, \tag{E.42}$$

respectively, reveals that both block matrices have equivalent arrangements of matrix elements to $\hat{S}_z$ in both $|S = \frac{1}{2}, m_s\rangle$ and $|S = \frac{3}{2}, m_s\rangle$ bases with projection factors $\alpha' = \frac{5}{3}$ and $\frac{22}{30}$ for the ground and first excited manifolds, respectively.

Finally, by extracting the top 2×2 and middle 3×3 block matrices from the definitions of $\widetilde{\hat{S}_z}$ (Eq. E.38), $\widetilde{\hat{S}_y}$ (Eq. E.39) and $\widetilde{\hat{S}_y}$ (Eq. E.40) and evaluating the commutator $[\widetilde{\hat{S}_x}, \widetilde{\hat{S}_y}]$, one obtains

$$[\widetilde{\hat{S}_x}, \widetilde{\hat{S}_y}] = i \begin{pmatrix} -0.83 & 0 \\ 0 & 0.83 \end{pmatrix} = i\widetilde{\hat{S}_z} \tag{E.43}$$

$$[\widetilde{\hat{S}_x}, \widetilde{\hat{S}_y}] = i \begin{pmatrix} -1.1 & 0 & 0 & 0 \\ 0 & -0.37 & 0 & 0 \\ 0 & 0 & 0.37 & 0 \\ 0 & 0 & 0 & 1.1 \end{pmatrix} = i\widetilde{\hat{S}_z}, \tag{E.44}$$

for the ground state and first excited state spin-orbit manifolds. By performing the commutator of all possible permutations of the projected components of the spin angular momentum operator, it can be shown that the canonical

commutation relations of angular momentum normalised by $\hbar$

$$[\widetilde{\hat{S}_x}, \widetilde{\hat{S}_y}] = i\epsilon_{xyz}\widetilde{\hat{S}_z} \tag{E.45}$$

are satisfied for the new $|\phi_{\mathrm{SO}}\rangle$ basis.

A second (and related) projection corresponds to a projection of the components of the angular momentum operator to the $j_{\mathrm{eff}} = \frac{1}{2}$ manifold. The necessity of this particular projection stems for the role of the orbital angular momentum in the spin-orbit coupling contribution to the dimer Hamiltonian [457]

$$\hat{\mathcal{H}}_{dimer} = \alpha\lambda\hat{\mathbf{l}}_1 \cdot \hat{\mathbf{S}}_1 + \alpha\lambda\hat{\mathbf{l}}_2 \cdot \hat{\mathbf{S}}_2 + 2J\hat{\mathbf{S}}_1 \cdot \hat{\mathbf{S}}_2, \tag{E.46}$$

corresponding to the coupling of two different sets of spin-orbit coupling manifolds. As discussed in the main text, as a consequence of experimental conditions (low $\hbar\omega_i$ and low temperatures) and such high chemical dilution, the magnetic properties are determined by ground state doublet $j_{\mathrm{eff}} = \frac{1}{2}$ manifold exclusively. Consequently, all quantities must be projected onto the ground state doublet $j_{\mathrm{eff}} = \frac{1}{2}$ manifold. The projection of the spin operator $\hat{\mathbf{S}}$ has been shown above. Utilising the same transformation matrix $\mathcal{C}$ (Eq. E.36) as was used for the spin operator, projecting the three components of the previously projected orbital angular momentum operator yields

$$\mathcal{C}^{-1}\hat{l}_z\mathcal{C} = \left(\begin{array}{cc|cccc|cccccc} 0.33 & 0 & 0 & -0.75 & 0 & 0 & 0 & 0 & 0 & 0 & 0 & 0 \\ 0 & -0.33 & 0 & 0 & -0.75 & 0 & 0 & 0 & 0 & 0 & 0 & 0 \\ \hline 0 & 0 & -0.40 & 0 & 0 & 0 & 0 & 0.49 & 0 & 0 & 0 & 0 \\ -0.75 & 0 & 0 & -0.13 & 0 & 0 & 0 & 0 & -0.60 & 0 & 0 & 0 \\ 0 & -0.75 & 0 & 0 & 0.13 & 0 & 0 & 0 & 0 & 0.60 & 0 & 0 \\ 0 & 0 & 0 & 0 & 0 & 0.40 & 0 & 0 & 0 & 0 & 0.49 & 0 \\ \hline 0 & 0 & 0 & 0 & 0 & 0 & -1 & 0 & 0 & 0 & 0 & 0 \\ 0 & 0 & 0.49 & 0 & 0 & 0 & 0 & -0.60 & 0 & 0 & 0 & 0 \\ 0 & 0 & 0 & -0.60 & 0 & 0 & 0 & 0 & -0.20 & 0 & 0 & 0 \\ 0 & 0 & 0 & 0 & 0.60 & 0 & 0 & 0 & 0 & 0.20 & 0 & 0 \\ 0 & 0 & 0 & 0 & 0 & 0.49 & 0 & 0 & 0 & 0 & 0.60 & 0 \\ 0 & 0 & 0 & 0 & 0 & 0 & 0 & 0 & 0 & 0 & 0 & 1 \end{array}\right). \tag{E.47}$$

$$\mathcal{C}^{-1}\hat{l}_x\mathcal{C} = \left(\begin{array}{cc|cccc|cccccc} 0 & 0.33 & -0.65 & 0 & -0.37 & 0 & 0 & 0 & 0 & 0 & 0 & 0 \\ 0.33 & 0 & 0 & 0.37 & 0 & 0.65 & 0 & 0 & 0 & 0 & 0 & 0 \\ \hline -0.65 & 0 & 0 & 0.23 & 0 & 0 & -0.55 & 0 & 0.17 & 0 & 0 & 0 \\ 0 & 0.37 & 0.23 & 0 & -0.27 & 0 & 0 & 0.42 & 0 & 0.30 & 0 & 0 \\ -0.37 & 0 & 0 & -0.27 & 0 & 0.23 & 0 & 0 & 0.30 & 0 & -0.42 & 0 \\ 0 & 0.65 & 0 & 0 & 0.23 & 0 & 0 & 0 & 0 & 0.17 & 0 & -0.55 \\ \hline 0 & 0 & -0.55 & 0 & 0 & 0 & 0 & -0.45 & 0 & 0 & 0 & 0 \\ 0 & 0 & 0 & 0.42 & 0 & 0 & -0.45 & 0 & -0.57 & 0 & 0 & 0 \\ 0 & 0 & 0.17 & 0 & 0.30 & 0 & 0 & -0.57 & 0 & 0.60 & 0 & 0 \\ 0 & 0 & 0 & 0.30 & 0 & 0.17 & 0 & 0 & 0.60 & 0 & 0.57 & 0 \\ 0 & 0 & 0 & 0 & -0.42 & 0 & 0 & 0 & 0 & 0.57 & 0 & 0.45 \\ 0 & 0 & 0 & 0 & 0 & -0.55 & 0 & 0 & 0 & 0 & 0.45 & 0 \end{array}\right). \tag{E.48}$$

$$\mathcal{C}^{-1}\hat{l}_y\mathcal{C} = i\left(\begin{array}{cc|cccc|cccccc} 0 & 0.33 & 0.65 & 0 & -0.37 & 0 & 0 & 0 & 0 & 0 & 0 & 0 \\ -0.33 & 0 & 0 & -0.37 & 0 & 0.65 & 0 & 0 & 0 & 0 & 0 & 0 \\ \hline -0.65 & 0 & 0 & 0.23 & 0 & 0 & 0.55 & 0 & 0.17 & 0 & 0 & 0 \\ 0 & 0.37 & -0.23 & 0 & -0.27 & 0 & 0 & -0.42 & 0 & 0.30 & 0 & 0 \\ 0.37 & 0 & 0 & 0.27 & 0 & 0.23 & 0 & 0 & -0.30 & 0 & -0.42 & 0 \\ 0 & -0.65 & 0 & 0 & -0.23 & 0 & 0 & 0 & 0 & -0.17 & 0 & -0.55 \\ \hline 0 & 0 & -0.55 & 0 & 0 & 0 & 0 & -0.45 & 0 & 0 & 0 & 0 \\ 0 & 0 & 0 & 0.42 & 0 & 0 & 0.45 & 0 & -0.57 & 0 & 0 & 0 \\ 0 & 0 & -0.17 & 0 & 0.30 & 0 & 0 & 0.57 & 0 & 0 & 0 & 0 \\ 0 & 0 & 0 & -0.30 & 0 & 0.17 & 0 & 0 & -0.60 & 0 & 0.57 & 0 \\ 0 & 0 & 0 & 0 & 0.42 & 0 & 0 & 0 & 0 & -0.57 & 0 & 0.45 \\ 0 & 0 & 0 & 0 & 0 & 0.55 & 0 & 0 & 0 & 0 & -0.45 & 0 \end{array}\right), \tag{E.49}$$

where the operators $\hat{l}_\xi$ denote the angular momentum operator that has already been projected onto the ground state crystal field triplet manifold. In other words, $\hat{l}_\xi$ refers to $\widetilde{\hat{L}}_\xi$ in the previous subsection. The exclusion of the tilde and the substitution of L for l are both a reflection of the fact that two simultaneous projections of the orbital angular momentum operator are being performed. A comparison of the (top) 2×2 in Eq. E.47 to the $\hat{L}_z$ operator (normalised by $\hbar$) in the $|L = \frac{1}{2}, m_l\rangle$ basis given by

$$\hat{L}_z = \begin{pmatrix} -\frac{1}{2} & 0 \\ 0 & \frac{1}{2} \end{pmatrix} \tag{E.50}$$

reveals that both block matrices have equivalent arrangements of matrix elements to $\hat{L}_z$ in the $|L = \frac{1}{2}, m_l\rangle$ bases with the projection factor $\alpha' = -\frac{2}{3}$. It is important to emphasise that in contrast to α that projects $L = 3$ to $l = 1$, α' projects $l = 1$ to $j_{\text{eff}} = \frac{1}{2}$ or equivalently $j = \frac{1}{2}$.

Finally, by extracting the top 2×2 block matrices from the definitions of $\widetilde{\hat{l}}_z$ (Eq. E.47), $\widetilde{\hat{l}}_x$ (Eq. E.48) and $\widetilde{\hat{l}}_y$ (Eq. E.49) and evaluating the commutator $[\widetilde{\hat{l}}_x, \widetilde{\hat{l}}_y]$, one obtains

$$[\widetilde{\hat{l}}_x, \widetilde{\hat{l}}_y] = i \begin{pmatrix} 0.33 & 0 \\ 0 & -0.33 \end{pmatrix} = i\widetilde{\hat{l}}_z \tag{E.51}$$

By performing the commutator of all possible permutations of the projected components of the orbital angular momentum operator, it can be shown that the canonical commutation relations of angular momentum normalised are satisfied for the new $|\phi_{\text{SO}}\rangle$ basis.

As shown in Appendix G, the projection of the orbital angular momentum operator is not crucial for the determination of the exchange constant J for $\text{Co}_x\text{Mg}_{1-x}\text{O}$. In fact, the projection of the pair Hamiltonian (Eq. E.46) onto the $j_{\text{eff}} = \frac{1}{2}$ manifold reduces to

$$\hat{\mathcal{H}}_{pair} = \frac{50}{9} J \hat{\mathbf{j}}_1 \cdot \hat{\mathbf{j}}_2 + \Phi, \tag{E.52}$$

where $\alpha' \hat{\mathbf{j}}_i \equiv \hat{\mathbf{S}}_i$ for $j_{\text{eff}} = \frac{1}{2}$ and Φ is a constant, in the limit of $\lambda \gg J$. In other words, the spin-orbit and thus the orbital angular momentum contribution is reduced to a constant if the spin-orbit coupling is much stronger than the

magnetic exchange.

To conclude this subsection, despite both the projections of the operators $\hat{\mathbf{S}}$ and $\hat{\mathbf{l}}$ onto the ground state manifold suggesting that the manifold does indeed possess $j_{\text{eff}} = \frac{1}{2}$ character, one can argue that the ultimate confirmation would be the projection of the total angular momentum operator $\hat{\mathbf{j}} = \hat{\mathbf{l}} + \hat{\mathbf{S}}$, since the ratio of the matrix elements between the block matrices and the operators is predicted to be 1 *via* the projection theorem. Utilising the same transformation matrix $\mathcal{C}$ (Eq. E.36) as was used for the spin and orbital angular momentum operators, projecting the three components of the total angular momentum operator, defined by $\hat{\mathbf{j}} = \hat{\mathbf{l}} + \hat{\mathbf{S}}$, yields

$$\mathcal{C}^{-1}\hat{j}_z\mathcal{C} = \left(\begin{array}{cc|cccc|cccccc} -0.50 & 0 & 0 & 00 & 0 & 0 & 0 & 0 & 0 & 0 & 0 & \\ 0 & 0.50 & 0 & 0 & 0 & 0 & 0 & 0 & 0 & 0 & 0 & 0 \\ \hline 0 & 0 & -1.50 & 0 & 0 & 0 & 0 & 0 & 0 & 0 & 0 & 0 \\ 0 & 0 & 0 & -0.50 & 0 & 0 & 0 & 0 & 0 & 0 & 0 & 0 \\ 0 & 0 & 0 & 0 & 0.50 & 0 & 0 & 0 & 0 & 0 & 0 & 0 \\ 0 & 0 & 0 & 0 & 0 & 1.50 & 0 & 0 & 0 & 0 & 0 & 0 \\ \hline 0 & 0 & 0 & 0 & 0 & 0 & -2.50 & 0 & 0 & 0 & 0 & 0 \\ 0 & 0 & 0 & 0 & 0 & 0 & 0 & -1.50 & 0 & 0 & 0 & 0 \\ 0 & 0 & 0 & 0 & 0 & 0 & 0 & 0 & -0.50 & 0 & 0 & 0 \\ 0 & 0 & 0 & 0 & 0 & 0 & 0 & 0 & 0 & 0.50 & 0 & 0 \\ 0 & 0 & 0 & 0 & 0 & 0 & 0 & 0 & 0 & 0 & 1.50 & 0 \\ 0 & 0 & 0 & 0 & 0 & 0 & 0 & 0 & 0 & 0 & 0 & 2.50 \end{array}\right), \tag{E.53}$$

$$\mathcal{C}^{-1}\hat{j}_x\mathcal{C} = \left(\begin{array}{cc|cccc|cccccc} 0 & -0.5 & 0 & 0 & 0 & 0 & 0 & 0 & 0 & 0 & 0 & 0 \\ -0.5 & 0 & 0 & 0 & 0 & 0 & 0 & 0 & 0 & 0 & 0 & 0 \\ \hline 0 & 0 & 0 & 0.9 & 0 & 0 & 0 & 0 & 0 & 0 & 0 & 0 \\ 0 & 0 & 0.9 & 0 & -1.0 & 0 & 0 & 0 & 0 & 0 & 0 & 0 \\ 0 & 0 & 0 & -1.0 & 0 & 0.9 & 0 & 0 & 0 & 0 & 0 & 0 \\ 0 & 0 & 0 & 0 & 0.9 & 0 & 0 & 0 & 0 & 0 & 0 & 0 \\ \hline 0 & 0 & 0 & 0 & 0 & 0 & 0 & -1 & 0 & 0 & 0 & 0 \\ 0 & 0 & 0 & 0 & 0 & 0 & -1 & 0 & -1 & 0 & 0 & 0 \\ 0 & 0 & 0 & 0 & 0 & 0 & 0 & -1 & 0 & 1.5 & 0 & 0 \\ 0 & 0 & 0 & 0 & 0 & 0 & 0 & 0 & 1.5 & 0 & 1 & 0 \\ 0 & 0 & 0 & 0 & 0 & 0 & 0 & 0 & 0 & 1 & 0 & 1 \\ 0 & 0 & 0 & 0 & 0 & 0 & 0 & 0 & 0 & 0 & 1 & 0 \end{array}\right), \tag{E.54}$$

$$\mathcal{C}^{-1}\hat{j}_y\mathcal{C} = i \left(\begin{array}{cc|cccc|cccccc} 0 & -0.5 & 0 & 0 & 0 & 0 & 0 & 0 & 0 & 0 & 0 & 0 \\ 0.5 & 0 & 0 & 0 & 0 & 0 & 0 & 0 & 0 & 0 & 0 & 0 \\ \hline 0 & 0 & 0 & 0.9 & 0 & 0 & 0 & 0 & 0 & 0 & 0 & 0 \\ 0 & 0 & -0.9 & 0 & 1.0 & 0 & 0 & 0 & 0 & 0 & 0 & 0 \\ 0 & 0 & 0 & 0 & 0 & 0.9 & 0 & 0 & 0 & 0 & 0 & 0 \\ 0 & 0 & 0 & 0 & -0.9 & 0 & 0 & 0 & 0 & 0 & 0 & 0 \\ \hline 0 & 0 & 0 & 0 & 0 & 0 & 0 & -1 & 0 & 0 & 0 & 0 \\ 0 & 0 & 0 & 0 & 0 & 0 & 1 & 0 & -1.4 & 0 & 0 & 0 \\ 0 & 0 & 0 & 0 & 0 & 0 & 0 & 1.4 & 0 & 1.5 & 0 & 0 \\ 0 & 0 & 0 & 0 & 0 & 0 & 0 & 0 & -1.5 & 0 & 1.4 & 0 \\ 0 & 0 & 0 & 0 & 0 & 0 & 0 & 0 & 0 & -1.4 & 0 & 1 \\ 0 & 0 & 0 & 0 & 0 & 0 & 0 & 0 & 0 & 0 & -1 & 0 \end{array}\right). \tag{E.55}$$

A comparison of the top 2×2 in Eq. E.53 to the $\hat{J}_z$ operator (normalised by $\hbar$) in the $|J = \frac{1}{2}, m_J\rangle$ basis given by

$$\hat{J}_z = \begin{pmatrix} -\frac{1}{2} & 0 \\ 0 & \frac{1}{2} \end{pmatrix} \tag{E.56}$$

reveals that both block matrices have equivalent arrangements of matrix elements to $\hat{J}_z$ in the $|J = \frac{1}{2}, m_J\rangle$ bases with the projection factor $\alpha' = 1$, in agreement with the projection theorem. It is worth noting that the calculations presented above as Eqs. E.53-E.55 were shown for the purposes of completeness and could have been equally deduced from the observation that the projection factors α' of $\hat{\mathbf{S}}$ and $\hat{\mathbf{l}}$ being $\frac{5}{3}$ and $-\frac{2}{3}$, respectively, add up to a value of 1.

Finally, by extracting the top 2×2 block matrices from the definitions of $\widetilde{\hat{j}_z}$ (Eq. E.53), $\widetilde{\hat{j}_x}$ (Eq. E.54) and $\widetilde{\hat{j}_y}$ (Eq. E.55) and evaluating the commutator $[\widetilde{\hat{j}_x}, \widetilde{\hat{j}_y}]$, one obtains

$$[\widetilde{\hat{j}_x}, \widetilde{\hat{j}_y}] = i \begin{pmatrix} -\frac{1}{2} & 0 \\ 0 & \frac{1}{2} \end{pmatrix} = i\widetilde{\hat{j}_z} \tag{E.57}$$

By performing the commutator of all possible permutations of the projected components of the orbital angular momentum operator, it can be shown that the canonical commutation relations of angular momentum normalised are satisfied for the new $|\phi_{\text{SO}}\rangle$ basis, validating the claim that the ground state manifold behaves as $j_{\text{eff}} = \frac{1}{2}$.

E.4 Projection of the Landé g-factor for Co^{2+} onto the $j_{\text{eff}} = \frac{1}{2}$ and $j_{\text{eff}} = \frac{3}{2}$ spin-orbit manifolds

Having calculated the projection factors α' for both the spin and orbital angular momentum operators $\hat{\mathbf{S}}$ and $\hat{\mathbf{l}}$, respectively, the projection of the Landé g-factor onto both $j_{\text{eff}} = \frac{1}{2}$ and $j_{\text{eff}} = \frac{3}{2}$ spin-orbit manifolds is presented.

Recall from first-order perturbation theory [20, 624], the field splitting of the Co^{2+} spin-orbit multiplets is described by the perturbative Hamiltonian $\hat{\mathcal{H}}_m$ given by

$$\hat{\mathcal{H}}_m = \mu_B(g_L\hat{\mathbf{L}} + g_S\hat{\mathbf{S}}) \cdot \mathbf{H}, \tag{E.58}$$

where g_L and g_S denote orbital and spin g-factors, respectively. For the particular case of the d-block metal Co^{2+}, both orbital and spin g-factors are taken to be the electron's g-factors, equal to approximately 1 and 2 [18], respectively, simplifying Eq. E.58 to

$$\hat{\mathcal{H}}_m = \mu_B(\hat{\mathbf{L}} + 2\hat{\mathbf{S}}) \cdot \mathbf{H}. \tag{E.59}$$

Since an effective total angular momentum $\hat{\mathbf{j}}_{\text{eff}}$ was defined with the projected orbital angular momentum operator $\hat{\mathbf{l}}$ with l =1, then the perturbative Hamiltonian in Eq. E.59 becomes

$$\begin{aligned} \hat{\mathcal{H}}_m &= \mu_B(\alpha\hat{\mathbf{l}} + 2\hat{\mathbf{S}}) \cdot \mathbf{H} \\ &= g'_J\mu_B\hat{\mathbf{j}} \cdot \mathbf{H}, \end{aligned} \tag{E.60}$$

for a particular effective spin-orbit j_{eff} manifold. Eq. E.60 incorporates an orbital angular momentum operator $\hat{\mathbf{L}}$ that has been projected onto $\hat{\mathbf{l}}$ *via* a projection factor α, and a projected Landé g-factor g'_J. A comparison between Eqs. E.59 and E.60, where g_L has been replaced by αg_L, suggests that the Landé g-factor — a fundamental proportionality constant that can be derived directly from the Wigner-Eckart theorem — defined as

$$\begin{aligned} g_J = 1 &\left\{ \frac{J(J+1) - S(S+1) + L(L+1)}{2J(J+1)} \right\} \\ + 2 &\left\{ \frac{J(J+1) + S(S+1) - L(L+1)}{2J(J+1)} \right\} \end{aligned} \tag{E.61}$$

for the original non-projected Hamiltonian in Eq. E.59 assumes the form [20]

$$g'_J = \frac{(2+\alpha)j(j+1) - (2-\alpha)l(l+1) + (2-\alpha)S(S+1)}{2j(j+1)}. \tag{E.62}$$

By inserting the values for $\alpha = -\frac{3}{2}$, as was previously deduced in §E.2, $l = 1$ to reflect the ground state crystal field manifold and $S = \frac{3}{2}$ to reflect the high spin d^7 electron configuration in ideal octahedral coordination, a projected Landé g-factor of $\frac{13}{3}$ and $\frac{32}{30}$ is obtained for the $j_{\text{eff}} = \frac{1}{2}$ ground state and $j_{\text{eff}} = \frac{3}{2}$ first excited spin-orbit manifolds, respectively.

Appendix F

Odd Parity of $\chi''(\mathbf{Q},\omega)$ and the Principle of Detailed Balance

This appendix provides a proof that the imaginary part of the susceptibility, denoted by $\chi''(\mathbf{Q},\hbar\omega)$, must possess odd parity with respect to $\hbar\omega$ *if and only if* the principle of detailed balance is obeyed.

Proof ($\Leftarrow$): The fluctuation-dissipation theorem [100, 108, 625] states that the relationship between the dynamic structure factor $S(\mathbf{Q},\hbar\omega)$ and the imaginary part of the susceptibility $\chi''(\mathbf{Q},\hbar\omega)$ is given by

$$S(\mathbf{Q},\hbar\omega) = \frac{1}{\pi}[n(\hbar\omega)+1]\chi''(\mathbf{Q},\hbar\omega), \tag{F.1}$$

where $n(\hbar\omega)$ is the Bose factor defined by

$$n(\hbar\omega) = \frac{1}{e^{\frac{\hbar\omega}{k_BT}}-1}, \tag{F.2}$$

such that

$$n(\hbar\omega)+1 = \frac{1}{1-e^{-\frac{\hbar\omega}{k_BT}}}, \tag{F.3}$$

and the prefactors $g\mu_B$ introduced in Chapter 1 have not been included for the

purposes of generality. By definition [99], the principle of detailed balance states that

$$S(-\mathbf{Q}, -\hbar\omega) = e^{-\frac{\hbar\omega}{k_B T}} S(\mathbf{Q}, \hbar\omega), \tag{F.4}$$

thus, if one assumes that $S(-\mathbf{Q}, -\hbar\omega) = S(\mathbf{Q}, -\hbar\omega)$ as is the case for all centrosymmetric systems under investigation in this Thesis, then $S(\mathbf{Q}, -\hbar\omega)$ can be rewritten in two ways:

$$S(\mathbf{Q}, -\hbar\omega) = \frac{1}{\pi} \frac{1}{1 - e^{\frac{\hbar\omega}{k_B T}}} \chi''(\mathbf{Q}, -\hbar\omega) \tag{F.5a}$$

$$S(\mathbf{Q}, -\hbar\omega) = \frac{1}{\pi} \frac{e^{-\frac{\hbar\omega}{k_B T}}}{1 - e^{-\frac{\hbar\omega}{k_B T}}} \chi''(\mathbf{Q}, \hbar\omega) \equiv \frac{1}{\pi} - \frac{1}{1 - e^{\frac{\hbar\omega}{k_B T}}} \chi''(\mathbf{Q}, \hbar\omega), \tag{F.5b}$$

where Eq. F.5a is Eq. F.1 with a substitution of $\hbar\omega$ to $-\hbar\omega$, whilst Eq. F.5b is a combination of Eqs. F.1 and F.4. Equating Eqs. F.5a and F.5b, one obtains

$$\frac{1}{1 - e^{\frac{\hbar\omega}{k_B T}}} \chi''(\mathbf{Q}, -\omega) = -\frac{1}{1 - e^{\frac{\hbar\omega}{k_B T}}} \chi''(\mathbf{Q}, \omega), \tag{F.6}$$

which implies

$$\chi''(\mathbf{Q}, -\hbar\omega) = -\chi''(\mathbf{Q}, \hbar\omega), \tag{F.7}$$

confirming $\chi''(\mathbf{Q}, \hbar\omega)$ must have odd parity with respect to $\hbar\omega$ if Eq. F.4 is satisfied.

Proof ($\Rightarrow$): By combining the fluctuation-dissipation theorem (Eq. F.1) and the definition of the Bose factor (Eq. F.3) with the replacement of $\mathbf{Q}$ and $\hbar\omega$ by $-\mathbf{Q}$ and $-\hbar\omega$, respectively, then Eq. F.1 becomes

$$S(-\mathbf{Q}, -\hbar\omega) = \frac{1}{\pi} \frac{1}{1 - e^{\frac{\hbar\omega}{k_B T}}} \chi''(-\mathbf{Q}, -\hbar\omega). \tag{F.8}$$

If one assumes that $\chi''(\mathbf{Q}, \hbar\omega)$ is an odd function with respect to $\hbar\omega$ and that

$\chi''(-\mathbf{Q}, \hbar\omega) = \chi''(\mathbf{Q}, \hbar\omega)$, as is the case for all centrosymmetric systems under investigation in this Thesis, then Eq. F.8 becomes

$$S(-\mathbf{Q}, -\hbar\omega) = \frac{1}{\pi} \frac{1}{1 - e^{\frac{\hbar\omega}{k_B T}}} (-1) \chi''(\mathbf{Q}, \hbar\omega). \tag{F.9}$$

Multiplying both sides of Eq. F.9 by $\frac{e^{-\frac{\hbar\omega}{k_B T}}}{e^{-\frac{\hbar\omega}{k_B T}}}$, then Eq. F.9 becomes

$$S(-\mathbf{Q}, -\hbar\omega) = \frac{1}{\pi} \frac{e^{-\frac{\hbar\omega}{k_B T}}}{e^{-\frac{\hbar\omega}{k_B T}} - 1} (-1) \chi''(\mathbf{Q}, \hbar\omega) \equiv \frac{1}{\pi} \frac{e^{-\frac{\hbar\omega}{k_B T}}}{1 - e^{-\frac{\hbar\omega}{k_B T}}} \chi''(\mathbf{Q}, \hbar\omega) \tag{F.10}$$

The last term on the RHS of Eq. F.10 may be rewritten as

$$S(-\mathbf{Q}, -\hbar\omega) = e^{-\frac{\hbar\omega}{k_B T}} \left\{ \frac{1}{\pi} \frac{1}{1 - e^{-\frac{\hbar\omega}{k_B T}}} \chi''(\mathbf{Q}, \hbar\omega) \right\}, \tag{F.11}$$

where the $\{\dots\}$ term corresponds to the definition of $S(\mathbf{Q}, \hbar\omega)$ in Eq. F.1. Consequently, an equivalent expression to Eq. F.11 is given by

$$S(-\mathbf{Q}, -\hbar\omega) = e^{-\frac{\hbar\omega}{k_B T}} S(\mathbf{Q}, \hbar\omega), \tag{F.12}$$

corresponding to the principle of detailed balance, as summarised by Eq. F.4 above.

■

Appendix G

Wigner-Eckart and Projection Theorems

The following appendix provides a derivation for both the Wigner-Eckart and Projection Theorems. For the purposes of completion, an additional section utilising the projection theorem in the case of projecting the spin $\hat{\mathbf{S}}$ and orbital angular momentum operators $\hat{\mathbf{l}}$ onto the ground state spin-orbit $j_{\text{eff}} = \frac{1}{2}$ manifold of Co^{2+} is included. For the interested reader, both derivations are based on Sakurai's *Modern Quantum Mechanics* [624] and Wigner's *Group Theory and its Application to the Quantum Mechanics of Atomic Spectra* [626] and references contained therein. Any additional references will be stated explicitly in the text.

G.1 Derivation of the Wigner-Eckart Theorem & "Dipole" Selection Rules

The derivation of the Wigner-Eckart theorem begins by first defining irreducible spherical tensors. An irreducible spherical tensor of rank k is a set of $2k+1$ operators $T_q^{(k)}$, where $-k \leq q \leq k$, which transform among themselves in an identical manner to the $2j+1$ angular momentum eigenstates in the $|j, m\rangle$

basis, given by

$$\hat{U}^{\dagger}(R)\hat{T}_{q}^{(k)}\hat{U}(R) = \sum_{q'=-k}^{k} \left(\hat{\mathcal{D}}_{qq'}^{(k)}(R)\right)^{*} \hat{T}_{q'}^{(k)}, \tag{G.1}$$

where $\hat{U}(R)$ is the orthogonal rotation operator in three dimensions and $\mathcal{D}_{qq'}(R)$ is the unitary Wigner $\mathcal{D}$-matrix. Since the set of rotations in three dimensions form a continuous Lie group $SO(3)$ with a Lie algebra $\mathfrak{so}(3)$ and thus forms a differentiable manifold. Consequently, by Stone's theorem [627], there exists an exponential map

$$\hat{U}(R) = e^{i\hat{g}_R v^R}, \tag{G.2}$$

where $\hat{U}(R)$, $\hat{g}_R$ and v^R are a generic element in the group, the set of generators and the set of parameters, respectively. Since the set of rotations forms a continuous symmetry (rotational invariance), then by Wigner's theorem, the exponential map must be unitary and thus the generators must be Hermitian. Utilising the differentiable properties of the $SO(3)$ group, by defining an infinitesimally small change in the rotation parameter $\delta\theta$ about a particular axis defined by $\hat{\theta}$, it can be shown that the generator of $SO(3)$ is the angular momentum $\hat{\mathbf{J}}$ and thus Eq. G.2 can be rewritten as

$$\hat{U}(R) = e^{\frac{-i\theta\hat{\theta}\cdot\hat{\mathbf{J}}}{\hbar}}. \tag{G.3}$$

By truncating a Taylor expansion of Eq. G.3 to $O(\theta)$, $\hat{U}(R)$ can be expressed as

$$\hat{U}(R) \simeq \mathbb{I} - \frac{i}{\hbar}\theta\hat{\theta}\cdot\hat{\mathbf{J}}, \tag{G.4}$$

where $\mathbb{I}$ is the identity element. Inserting Eq. G.4 into the LHS of Eq. G.1, one obtains

$$\left(\mathbb{I} + \frac{i}{\hbar}\theta\hat{\theta}\cdot\hat{\mathbf{J}}\right)\hat{T}_{q}^{(k)}\left(\mathbb{I} - \frac{i}{\hbar}\theta\hat{\theta}\cdot\hat{\mathbf{J}}\right) = \sum_{q'=-k}^{k}\left(\hat{\mathcal{D}}_{qq'}^{(k)}(R)\right)^{*}\hat{T}_{q'}^{(k)}. \tag{G.5}$$

Truncating the polynomial expansion of the LHS to $O(\theta)$, Eq. G.5 becomes

$$\hat{T}_{q}^{(k)} + \frac{i}{\hbar}[\hat{\theta}\cdot\hat{\mathbf{J}}, T_{q}^{(k)}]\theta = \sum_{q'=-k}^{k}\left(\hat{\mathcal{D}}_{qq'}^{(k)}(R)\right)^{*}\hat{T}_{q'}^{(k)}. \tag{G.6}$$

By inserting the definition of the Wigner $\mathcal{D}$-matrix, corresponding to the representation of $\hat{U}(R)$ in the $|j,m\rangle$ basis, Eq. G.6 becomes

$$\hat{T}_q^{(k)} + \frac{i}{\hbar}[\hat{\theta}\cdot\hat{\mathbf{J}}, T_q^{(k)}]\theta = \sum_{q'=-k}^{k} \Big(\langle kq|\hat{U}(R)|kq'\rangle\Big)^* \hat{T}_{q'}^{(k)}. \tag{G.7}$$

Utilising the definition of the complex conjugate of the Wigner $\mathcal{D}$-matrix qq'-element then Eq. G.7 can be rewritten as

$$\hat{T}_q^{(k)} + \frac{i}{\hbar}[\hat{\theta}\cdot\hat{\mathbf{J}}, T_q^{(k)}]\theta = \sum_{q'=-k}^{k} \langle kq'|\hat{U}^\dagger(R)|kq\rangle \hat{T}_{q'}^{(k)}. \tag{G.8}$$

By inserting the Hermitian adjoint of the rotation operator $\hat{U}(R)$ given by Eq. G.4 into the RHS, Eq. G.8 can be further simplified to

$$\hat{T}_q^{(k)} + \frac{i}{\hbar}[\hat{\theta}\cdot\hat{\mathbf{J}}, T_q^{(k)}]\theta = \sum_{q'=-k}^{k} \langle kq'|\mathbb{I} + \frac{i}{\hbar}\theta\hat{\theta}\cdot\hat{\mathbf{J}}|kq\rangle \hat{T}_{q'}^{(k)}. \tag{G.9}$$

Polynomial expansion of the RHS, combined by the orthonormality relations of the $|j,m\rangle$ basis vectors, yields

$$\hat{T}_q^{(k)} + \frac{i}{\hbar}[\hat{\theta}\cdot\hat{\mathbf{J}}, T_q^{(k)}]\theta = \sum_{q'=-k}^{k} \delta_{q'q} T_q^{(k)} + \frac{i}{\hbar}\sum_{q'=-k}^{k} \langle kq'|\theta\hat{\theta}\cdot\hat{\mathbf{J}}|kq\rangle \hat{T}_{q'}^{(k)}. \tag{G.10}$$

Without the loss of generality, setting the z-axis as the axis of rotation, *i.e.* $\hat{\theta} = \hat{e}_z$, then Eq. G.10 becomes

$$\hat{T}_q^{(k)} + \frac{i}{\hbar}[\hat{J}_z, \hat{T}_q^{(k)}]\theta = \hat{T}_q^{(k)} + \frac{i}{\hbar}\sum_{q'=-k}^{k} \langle kq'|\hat{J}_z|kq\rangle \theta \hat{T}_{q'}^{(k)}, \tag{G.11}$$

where the first sum on the RHS was simplified due to the presence of the Kronecker delta $\delta_{q'q}$ and the scalar variable parameter θ was factored out of the bra-ket. By cancelling similar terms, utilising both the definition of $\hat{L}_z|j,m\rangle = m\hbar|j,m\rangle$ and the orthonormality relations of the $|jm\rangle$ basis, Eq. G.11 becomes

$$[\hat{J}_z, \hat{T}_q^{(k)}] = \hbar q \hat{T}_q^{(k)}. \tag{G.12}$$

Similarly, utilising $J_\pm$, in lieu of J_z, by redefining $\hat{\theta}$ in Eq. G.11, it can be shown that

$$[\hat{J}_\pm, \hat{T}_q^{(k)}] = \hbar\sqrt{(k\mp q)(k\pm q+1)}\hat{T}_{q+1}^{(k)}. \tag{G.13}$$

The logic encompassing Eqs. G.2-G.11 demonstrate that Eqs. G.12 and G.13 are equivalent definitions of the irreducible spherical tensor operator $\hat{T}_q^{(k)}$ that was first defined by Eq. G.1.

Projecting the definition of the irreducible spherical tensor operator given by Eq. G.13 onto the $|j,m\rangle$ basis, one obtains

$$\langle j'm'|[\hat{J}_\pm, \hat{T}_q^{(k)}]|jm\rangle = \hbar\sqrt{(k \mp q)(k \pm q + 1)}\langle j'm'|\hat{T}_{q+1}^{(k)}|jm\rangle. \tag{G.14}$$

Expanding the commutator on the LHS, Eq. G.14 becomes

$$\langle j'm'|\hat{J}_\pm\hat{T}_q^{(k)}|jm\rangle - \langle j'm'|\hat{T}_q^{(k)}\hat{J}_\pm|jm\rangle = \hbar\sqrt{(k \mp q)(k \pm q + 1)}\langle j'm'|\hat{T}_{q+1}^{(k)}|jm\rangle. \tag{G.15}$$

By utilising the definition of $\hat{J}_\pm|jm\rangle = \hbar\sqrt{(j \mp m)(j \pm m + 1)}|jm \pm 1\rangle$, in combination with the observation that $(\hat{J}_\pm)^\dagger = \hat{J}_\mp$, then Eq. G.15 becomes

$$\begin{aligned} &\hbar\sqrt{(j' \pm m')(j' \mp m' + 1)}\langle j'm' \mp 1|\hat{T}_q^{(k)}|jm\rangle \\ &-\hbar\sqrt{(j \mp m)(j \pm m + 1)}\langle j'm'|\hat{T}_q^{(k)}|jm \pm 1\rangle \\ &= \hbar\sqrt{(k \mp q)(k \pm q + 1)}\langle j'm'|\hat{T}_{q+1}^{(k)}|jm\rangle, \end{aligned} \tag{G.16}$$

which bears a strong similarity to the recursion relations for the Clebsch-Gordan coefficients given by

$$\begin{aligned} &\sqrt{(j' \pm m')(j' \mp m' + 1)}(j'm' \mp 1|mq\rangle \\ &-\sqrt{(j \mp m)(j \pm m + 1)}(j'm'|m \pm 1q\rangle \\ &= \sqrt{(k \mp q)(k \pm q + 1)}(j'm'|mq \pm 1\rangle \end{aligned} \tag{G.17}$$

for coupling of two angular momenta j and k with z-projections m and q, respectively, and where $|\ )$ denote coupled angular momentum eigenstates, whilst $|\ \rangle$ denote uncoupled product or factored momentum eigenstates. Since both Eqs. G.16 and G.17 have identical coefficients, then it follows that

$$\frac{x_\xi}{y_\xi} = \rho \qquad \forall\ \xi, \tag{G.18}$$

where x_ξ and y_ξ denote the ξ^{th} terms of Eqs. G.16 and G.17, respectively, and ρ is a constant ratio. Without the loss of generality, choosing the ratio of the first terms in Eqs. G.16 and G.17, *i.e.* setting $\xi = 1$, then Eq. G.18 can be stated as

$$\frac{\langle j'm' \mp 1|\hat{T}_q^{(k)}|jm\rangle}{(j'm' \mp 1|mq\rangle} = \rho. \tag{G.19}$$

It is important to note that the value of ρ must hold for all values of ξ and thus it can be concluded that the value of ρ must depend only on j' and k and thus must be independent of m and q. It is conventional* to define ρ as the reduced matrix element

$$\rho = \frac{\langle j' \left\| T^{(k)} \right\| j \rangle}{\sqrt{2j'+1}}, \tag{G.20}$$

where the denominator is a normalisation constant determined by integrating over all angles and is stated explicitly as per the convention established by Sakurai. Combining Eq. G.19 with Eq. G.20 and relabelling $m' \mp 1$ as simply m', one obtains the Wigner-Eckart Theorem

$$\langle j'm'|T_q^{(k)}|jm\rangle = \frac{\langle j' \left\| T^{(k)} \right\| j \rangle}{\sqrt{2j'+1}} (j'm'|mq\rangle, \tag{G.21}$$

where the inner product $(j'm'|mq\rangle \equiv ((jk)j'm'|jmkq\rangle$ is the relevant Clebsch-Gordon coefficient. Since a quantum system is completely described by a set of good quantum numbers (*i.e.* a set of eigenvalues from compatible observations), the Wigner-Eckart theorem is conventionally stated as

$$\langle \mu'j'm'|T_q^{(k)}|\mu jm\rangle = \frac{\langle \mu'j' \left\| T^{(k)} \right\| \mu j \rangle}{\sqrt{2j'+1}} (j'm'|mq\rangle, \tag{G.22}$$

where μ denotes the set of good quantum numbers excluding j and m, whilst the Clebsch-Gordon coefficient is independent of μ and thus not stated explicitly.

An important consequence of the Wigner-Eckart theorem is the set of "dipole" selection rules [628]. By definition, the neutron cross-section $\left(\frac{d^2\sigma}{d\omega d\Omega}\right)_{\lambda\to\lambda'} \propto \Gamma_{\lambda\to\lambda'}$, corresponding to the number of transitions (per unit time) from state λ to λ'. Utilising time-dependent perturbation theory, if one considers the presence of a small, possibly time-dependent perturbation $\hat{H}' = \hat{V}$, then

$$\Gamma_{\lambda\to\lambda'} \propto |\langle\lambda'|\hat{V}|\lambda\rangle|^2. \tag{G.23}$$

Eq. G.23 is called Fermi's Golden Rule and is equivalent to the first order Born approximation where the transition operator $\hat{T}$ is approximated as the first term in the Born perturbation series. In the case of magnetic neutron inelastic scattering, the perturbation $\hat{V}$ can be approximated by $\hat{\mathbf{M}} = \hat{\mathbf{L}} + 2\hat{\mathbf{S}}$. Using Fermi's Golden Rule, the transition probability (per unit time) for an neutron

*The form of the reduced matrix element presented here is that of Sakurai.

inelastic scattering process is given by

$$\Gamma_{\lambda\to\lambda'} \propto |\langle\lambda'|\hat{\mathbf{M}}|\lambda\rangle|^2, \tag{G.24}$$

where the first term in $\hat{\mathbf{M}}$ represents the interaction of the neutron's magnetic dipole moment and the magnetic field produced by the electric current corresponding to the orbital motion of electrons, whilst the second refers to the interaction between the dipole moment of the neutron and the intrinsic spin magnetic moment of the electrons. Since $\hat{\mathbf{M}}$ is a tensor operator of rank $k = 1$ (*i.e.* a vector operator), then the Wigner-Eckart theorem can be rewritten as

$$\langle\mu' j' m'|T_q^{(1)}|\mu j m\rangle = \frac{\langle\mu' j' \left\|T^{(1)}\right\| \mu j\rangle}{\sqrt{2j'+1}}(j'm'|mq\rangle, \tag{G.25}$$

where the LHS is equivalent to the matrix element on the RHS of Eq. G.24. Since the Clebsch-Gordon coefficient $(j'm'|mq\rangle$ is zero unless $m' = m + q$, where $-k = -1 \leq q \leq k = 1$, then the cross section will be zero unless $\Delta m = m' - m$ is ± 1, 0. Furthermore, by the addition theorem of angular momentum, which is essentially a restatement of the triangle inequality, $|j - k| \leq j' \leq j + k$ or equivalently $|j' - j| \leq k \leq j' + j$, then $\Delta j = j' - j = \pm 1$, 0, with the exception of $j' = j = 0$. The restrictions of $\Delta m = \pm 1$, 0 and $\Delta j = \pm 1$, 0 are called the "dipolar" selection rules for $k = 1$.

The term "dipolar" refers to the observation that the perturbative operator $\hat{\mathbf{M}}$ can be approximated as dipolar interactions in the low energy/long wavelength limit [38]. Commonly referred to as the "dipolar approximation", its application is particularly important when addressing the interaction between the neutron's magnetic moment and the orbital motion of the electrons. Since such an interaction is conventionally described by a term $\hat{\mathbf{A}} \cdot \hat{\mathbf{p}}$, where $\hat{\mathbf{A}}$ and $\hat{\mathbf{p}}$ denotes a vector potential field and the momentum operators, respectively, it can be shown that $\hat{H}' \approx \hat{p}_i$, corresponding to the momentum along a particular quantisation axis $i = x, y, z$. Utilising the observation that the commutator $[\hat{\mathbf{r}}_i, \hat{H}_o] \propto \hat{\mathbf{p}}_i$, where $\hat{\mathbf{r}}_i$ and $\hat{H}_o$ denote the i^{th} component of the position operator and the unperturbed Hamiltonian, respectively, then the transition probability (per unit time) or equivalently the cross section must be given by

$$\frac{d^2\sigma}{d\omega d\Omega} \propto \Gamma_{\lambda\to\lambda'} \propto |\langle\lambda'|[\hat{\mathbf{r}}_i, \hat{H}_o]|\lambda\rangle|^2. \tag{G.26}$$

Since the unperturbed Hamiltonian contribution will simply yield the difference

between initial and final energies, then since the constant of proportionality $\mathcal{C}$ contains the charge q, the perturbative Hamiltonian $\hat{H}' = \hat{V} \propto q\hat{r}_i$ which is equivalent to the definition of an electric dipole in classical electromagnetism, and hence the name "dipolar approximation".

In the next subsection, a special case of the Wigner-Eckart theorem called the projection theorem will be derived.

G.2 Derivation of the Projection Theorem

In lieu of Cartesian coordinates, tensor operators of rank $k = 1$ are more conveniently (and conventionally) treated in the spherical basis. The relationship between spherical and Cartesian bases is summarised by

$$\hat{e}_x = -\frac{1}{\sqrt{2}}\hat{e}_1 + \frac{1}{\sqrt{2}}\hat{e}_{-1}, \tag{G.27a}$$

$$\hat{e}_z = \hat{e}_0, \tag{G.27b}$$

$$\hat{e}_y = \frac{i}{\sqrt{2}}\hat{e}_1 + \frac{i}{\sqrt{2}}\hat{e}_{-1}, \tag{G.27c}$$

where indices 1, 0 and -1 are conventionally labelled as $+$, z and $-$, respectively. A combination of eqs. G.27a-G.27c implies that the inner product between the angular momentum $\hat{\mathbf{J}}^{(1)}$ and another rank $k = 1$ tensor operator $\hat{\mathbf{V}}^{(1)}$ is given by

$$\hat{\mathbf{J}} \cdot \hat{\mathbf{V}} = \hat{J}_0\hat{V}_0 - \hat{J}_+\hat{V}_- - \hat{J}_-\hat{V}_+, \tag{G.28}$$

which implies that

$$\langle \mu' jm|\hat{\mathbf{J}} \cdot \hat{\mathbf{V}}|\mu jm\rangle = \langle \mu' jm|\hat{J}_0\hat{V}_0|\mu jm\rangle - \langle \mu' jm|\hat{J}_+\hat{V}_-|\mu jm\rangle - \langle \mu' jm|\hat{J}_-\hat{V}_+|\mu jm\rangle. \tag{G.29}$$

Utilising $(J_\pm)^\dagger = J_\mp$, then it follows that

$$\begin{aligned}\langle \mu' jm|\hat{\mathbf{J}} \cdot \hat{\mathbf{V}}|\mu jm\rangle = m\hbar\langle \mu' jm|\hat{V}_0|\mu jm\rangle - \\ \hbar\sqrt{j(j+1) - m(m-1)}\langle \mu' jm-1|\hat{V}_-|\mu jm\rangle - \\ \hbar\sqrt{j(j+1) - m(m+1)}\langle \mu' jm+1|\hat{V}_+|\mu jm\rangle\end{aligned} \tag{G.30}$$

By applying the Wigner-Ekhart theorem (Eq. G.22) to each of the three individual terms on the RHS of Eq. G.30, then it follows that

$$\langle \mu' j m | \hat{\mathbf{J}} \cdot \hat{\mathbf{V}} | \mu j m \rangle = \mathcal{C} \frac{\langle \mu' j \| \hat{\mathbf{V}}^{(1)} \| \mu j \rangle}{\sqrt{2j+1}}, \tag{G.31}$$

where the constant of proportionality is given by

$$\begin{aligned} \mathcal{C} = m\hbar(j\ m|m\ 0\rangle - \hbar\sqrt{j(j+1)-m(m-1)}(j\ m-1|m\ -1\rangle \\ -\hbar\sqrt{j(j+1)-m(m+1)}(j\ m+1|m\ 1\rangle, \end{aligned} \tag{G.32}$$

where $(\ \ \rangle$ denotes the relevant Clebsch-Gordan coefficient. Since Eq. G.31 must hold for any rank $k = 1$ tensor. As a consequence, if one lets $\hat{\mathbf{V}}^{(1)} = \hat{\mathbf{J}}^{(1)}$, then it must follow that

$$\langle \mu j m | \hat{J}^2 | \mu j m \rangle = \mathcal{C} \frac{\langle \mu j \| \hat{\mathbf{J}}^{(1)} \| \mu j \rangle}{\sqrt{2j+1}}, \tag{G.33}$$

where the constant of proportionality is given by Eq. G.32. Since the three term expansion on the RHS for both Eqs. G.31 and G.33 have identical coefficients, then it follows that

$$\frac{\langle \mu' j m' | \hat{V}_q | \mu j m \rangle}{\langle \mu' j \| \hat{\mathbf{V}} \| \mu j \rangle} = \frac{\langle \mu' j m' | \hat{J}_q | \mu j m \rangle}{\langle \mu j \| \hat{\mathbf{J}} \| \mu j \rangle}, \tag{G.34}$$

or equivalently stated as

$$\frac{\langle \mu' j m' | \hat{V}_q | \mu j m \rangle}{\langle \mu' j m' | \hat{J}_q | \mu j m \rangle} = \frac{\langle \mu' j \| \hat{\mathbf{V}} \| \mu j \rangle}{\langle \mu j \| \hat{\mathbf{J}} \| \mu j \rangle}. \tag{G.35}$$

Utilising the same logic and taking advantage of the equivalence of Eqs. G.31 and G.33, then the following must hold

$$\frac{\langle \mu' j m' | \hat{V}_q | \mu j m \rangle}{\langle \mu j m' | \hat{J}_q | \mu j m \rangle} = \frac{\langle \mu' j m | \hat{\mathbf{J}} \cdot \hat{\mathbf{V}} | \mu j m \rangle}{\langle \mu j m | \hat{J}^2 | \mu j m \rangle}. \tag{G.36}$$

Rearrangement and the identification of $\langle \mu j m | \hat{J}^2 | \mu j m \rangle = j(j+1)\hbar^2$ yields

$$\langle \mu' j m' | \hat{V}_q | \mu j m \rangle = \frac{\langle \mu' j m | \hat{\mathbf{J}} \cdot \hat{\mathbf{V}} | \mu j m \rangle}{j(j+1)\hbar^2} \langle j m' | \hat{J}_q | j m \rangle. \tag{G.37}$$

where the rightmost matrix element $\langle \mu j m' | \hat{J}_q | \mu j m \rangle$ is independent of quantum numbers α and thus α has been omitted as per convention.

Known as the projection theorem, Eq. G.37 states that the matrix elements of the vector operator $\hat{\mathbf{V}}$ are proportional to the corresponding matrix elements of $\hat{\hat{\mathbf{J}}}$, with a proportionality constant $\mathcal{C} = \frac{\langle \mu' \ j \ m | \hat{\mathbf{J}} \cdot \hat{\mathbf{V}} | \alpha \ j \ m \rangle}{j(j+1)}$, if $\hbar$ is set to 1, and thus the projection theorem can be equivalently stated as

$$\hat{\mathbf{V}} = \frac{\langle \hat{\mathbf{J}} \cdot \hat{\mathbf{V}} \rangle}{j(j+1)} \hat{\mathbf{J}}, \tag{G.38}$$

if $\mu' = \mu$ or if the dot product $\hat{\mathbf{J}} \cdot \hat{\mathbf{V}}$ does not concern itself with μ, where the former is applicable for the projections performed for Co^{2+} contained in this Thesis.

G.3 Projection of $\hat{\mathrm{S}}$ and $\hat{\mathrm{l}}$ onto the $j_{\mathrm{eff}} = \frac{1}{2}$ Manifold of Co^{2+} via the Projection Theorem

As described in the studies on α-CoV_3O_8 and $Co_{0.03}Mg_{0.97}O$, by limiting neutron inelastic spectroscopic measurements to be performed at both low temperatures and low incident energies, only transitions within the ground state $j_{eff} = \frac{1}{2}$ spin-orbit manifold are probed [20, 425, 457]. Such a claim can be rationalised by observing that low temperatures limit possible excitations measured to those exclusively *from* the spin-orbit $j_{\mathrm{eff}} = \frac{1}{2}$ manifold, whilst low incident energies further limits possible excitations to those exclusively within the ground state spin-orbit manifold. As described in Appendix E, the projection factor α' associated with the projection of operators onto the $j_{\mathrm{eff}} = \frac{1}{2}$ manifold could be determined by a comparison of matrices. An alternative and equally valid approach consists of taking advantage that the projection theorem (Eq. G.38) contains the total angular momentum operator $\hat{\mathbf{J}}$. By employing the projection theorem, the projection of the spin and orbital angular momentum operators onto an effective total angular momentum operator $\hat{\mathbf{j}}$ is accomplished

by

$$\hat{\mathbf{S}} = \frac{\langle \hat{\mathbf{S}} \cdot \hat{\mathbf{j}} \rangle}{j_{\text{eff}}(j_{\text{eff}}+1)} \hat{\mathbf{j}}, \tag{G.39}$$

$$\hat{\mathbf{l}} = \frac{\langle \hat{\mathbf{l}} \cdot \hat{\mathbf{j}} \rangle}{j_{\text{eff}}(j_{\text{eff}}+1)} \hat{\mathbf{j}}, , \tag{G.40}$$

where $\hat{\mathbf{J}}$ in Eq. G.38 has been substituted for by an effective total angular momentum operator is defined as $\hat{\mathbf{j}} = \hat{\mathbf{l}} + \hat{\mathbf{S}}$, with corresponding eigenvalue j_{eff} and where l corresponds to the orbital angular momentum $\hat{\mathbf{L}}$ projected onto $\hat{\mathbf{l}}$ with corresponding eigenvalue $l = 1$ [18]. Utilising the following identity

$$\hat{\mathbf{l}} \cdot \hat{\mathbf{S}} = \frac{1}{2}(\hat{\mathbf{j}} \cdot \hat{\mathbf{j}} - \hat{\mathbf{l}} \cdot \hat{\mathbf{l}} - \hat{\mathbf{S}} \cdot \hat{\mathbf{S}}), \tag{G.41}$$

Eqs. G.39 and G.40 become:

$$\hat{\mathbf{S}} = \left\{ \frac{1}{2} + \left(\frac{s(s+1) - l(l+1)}{2j_{\text{eff}}(j_{\text{eff}}+1)} \right) \right\} \hat{\mathbf{j}}, \tag{G.42}$$

and

$$\hat{\mathbf{l}} = \left\{ \frac{1}{2} + \left(\frac{l(l+1) - s(s+1)}{2j_{\text{eff}}(j_{\text{eff}}+1)} \right) \right\} \hat{\mathbf{j}}, \tag{G.43}$$

respectively, where s denotes the eigenvalue of the spin angular momentum operator $\hat{\mathbf{S}}$. Inserting the values of s, l and j_{eff} as $\frac{3}{2}$, 1 and $\frac{1}{2}$, respectively, Eqs. G.42 and G.43 reduce to

$$\hat{\mathbf{S}} = \frac{5}{3} \hat{\mathbf{j}}, \tag{G.44}$$

$$\hat{\mathbf{l}} = -\frac{2}{3} \hat{\mathbf{j}}, \tag{G.45}$$

implying that $\alpha' = \frac{5}{3}$ and $-\frac{2}{3}$ for $\hat{\mathbf{S}}$ and $\hat{\mathbf{l}}$, respectively, in agreement with the matrix approach outlined in Appendix E.

As stated in the main text and illustrated in Fig. 4.3, the pair Hamiltonian

$$\hat{\mathcal{H}}_{pair} = \alpha\lambda \hat{\mathbf{l}}_1 \cdot \hat{\mathbf{S}}_1 + \alpha\lambda \hat{\mathbf{l}}_2 \cdot \hat{\mathbf{S}}_2 + 2J \hat{\mathbf{S}}_1 \cdot \hat{\mathbf{S}}_2, \tag{G.46}$$

describes a linear dependence on J for the splitting of the $j_{\text{eff}} = \frac{1}{2}$ manifold in the limit of $\lambda \gg J$. In order to deduce the constant of proportionality $\tilde{\alpha}$, each term of the pair Hamiltonian must be first projected onto the $j_{\text{eff}} = \frac{1}{2}$ manifold yielding

$$\hat{\mathcal{H}}_{pair} = \alpha\lambda\left(-\frac{2}{3}\hat{\mathbf{j}}_1\right)\cdot\frac{5}{3}\hat{\mathbf{j}}_1 + \alpha\lambda\left(-\frac{2}{3}\hat{\mathbf{j}}_2\right)\cdot\frac{5}{3}\hat{\mathbf{j}}_2 + 2J\frac{5}{3}\hat{\mathbf{j}}_1\cdot\frac{5}{3}\hat{\mathbf{j}}_2, \tag{G.47}$$

which can be simplified to

$$\hat{\mathcal{H}}_{pair} = \frac{50}{9}J\hat{\mathbf{j}}_1\cdot\hat{\mathbf{j}}_2 - \frac{10}{9}\alpha\lambda\left\{\hat{\mathbf{j}}_1\cdot\hat{\mathbf{j}}_1 + \hat{\mathbf{j}}_2\cdot\hat{\mathbf{j}}_2\right\}. \tag{G.48}$$

Utilising the identity of $\mathbf{j}\cdot\mathbf{j} \equiv j^2$, with corresponding eigenvalues $j_{\text{eff}}(j_{\text{eff}}+1)$, then Eq. G.48 reduces to

$$\hat{\mathcal{H}}'_{dimer} = \frac{50}{9}J\hat{\mathbf{j}}_1\cdot\hat{\mathbf{j}}_2 - \frac{10}{9}\alpha\lambda(j_{1,\text{eff}}(j_{1,\text{eff}}+1) + j_{2,\text{eff}}(j_{2,\text{eff}}+1)). \tag{G.49}$$

Since $j_{1,\text{eff}} = j_{2,\text{eff}} = \frac{1}{2}$, α and $\widetilde{\lambda}$ are all constants, then Eq. G.49 becomes

$$\hat{\mathcal{H}}_{pair} = \frac{50}{9}J\hat{\tilde{\mathbf{j}}}_1\cdot\hat{\tilde{\mathbf{j}}}_2 + \Phi, \tag{G.50}$$

where the spin-orbit contributions are reduced to a constant Φ, and thus Eq. G.50 can be stated equivalently as

$$\hat{\mathcal{H}}_{pair} = \frac{50}{9}J\hat{\mathbf{j}}_1\cdot\hat{\mathbf{j}}_2, \tag{G.51}$$

where the exchange contribution $\hat{\mathcal{H}}_{ex}$ between pairs of Co^{2+} ions is exclusively considered. Eq. G.51 states that the energy splitting ΔE between the triplet $\Gamma_{\text{eff}} = 1$ and the singlet $\Gamma_{\text{eff}} = 0$ total spin states within the $j_{\text{eff}} = \frac{1}{2}$ ground state spin orbit manifold, varies linearly as a function of J with a proportionality constant $\widetilde{\alpha} = \frac{50}{9}$.

It is important to re-emphasise that the linear behaviour of ΔE with respect to J and the associated proportionality constant $\widetilde{\alpha}$ in Eq. G.51 assumes that only the $j_{\text{eff}} = \frac{1}{2}$ ground state spin orbit manifold is accessible. The validity of such an assumption only holds if, albeit not limited to $|J| \ll |\lambda|$. In other words,

strict linearity of ΔE with respect to J only is valid if the splitting of the spin-orbit manifolds due to the local magnetic field introduced by J is small enough, resulting in minimal entanglement [20, 346]. As will discussed in Chapter 4, the assumption $|J| \ll |\lambda|$ is not completely fulfilled for some of the exchange constants present in $Co_{0.03}Mg_{0.97}O$, particularly J_2. Consequently, an analysis algorithm described in Chapter 4 was created to accommodate the deviation from linearity of ΔE with respect to J, by numerically calculating ΔE as a function of J or more accurately, $|J|$ itself.

Appendix H

Derivation of the Total (Zeroth) Moment Sum Rule, First Moment Sum Rule & Single Mode Approximation for the Heisenberg-Dirac Spin Hamiltonian

The following appendix provides a derivation of both the total (zeroth) and first moment sum rules of neutron scattering for the Heisenberg-Dirac Spin Hamiltonian given by

$$\hat{\mathcal{H}} = \sum_{jj'} J_{jj'} \hat{\mathbf{S}}_j \cdot \hat{\mathbf{S}}_{j'}. \tag{H.1}$$

The exchange interactions are assumed to be isotropic, *i.e.* $J^{\alpha}_{jj'} = J^{\beta}_{jj'} = J^{\gamma}_{jj'} = J_{jj'}$, where the indices α, β, γ conventionally denote the Cartesian axes x, y, z, respectively. Once a general expression for the first moment sum rule is obtained, a powder-averaged expression is derived. This appendix finishes with a derivation of the general expression for the single mode approximation applied to the first moment sum rule. All derivations are based on Zhu's *Modern Techniques for Characterizing Magnetic Materials* [101] and references contained therein. Any additional references will be stated explicitly in the text.

H.1 Derivation of Total (Zeroth) Moment Sum Rule

The derivation of both the total (zeroth) and the first moment sum rules of neutron scattering begin by first defining the dynamic structure factor $S(\mathbf{Q}, \hbar\omega)$ given by

$$S^{\alpha\beta}(\mathbf{Q}, \hbar\omega) = \int_{-\infty}^{\infty} e^{-i\omega t} \frac{1}{N} \sum_{jj'} \left\langle e^{-i\mathbf{Q}\cdot\mathbf{r}_{jj'}} \hat{S}_j^{\alpha} \hat{S}_{j'}^{\beta}(t) \right\rangle \frac{dt}{2\pi\hbar}, \tag{H.2}$$

corresponding to the Fourier transform of the two-point spin correlation function, where N denotes a normalisation constant (*e.g.* number of unit cells) and $\mathbf{r}_{jj'} = \mathbf{r}_j - \mathbf{r}_{j'}$ denotes the displacement vector between sites j and j'. By applying the n^{th} derivative with respect to time

$$\frac{d^n}{dt^n} S^{\alpha\beta}(\mathbf{Q}, \hbar\omega) = \frac{d^n}{dt^n} \left\{ \int_{-\infty}^{\infty} e^{-i\omega t} \frac{1}{N} \sum_{jj'} \left\langle e^{-i\mathbf{Q}\cdot\mathbf{r}_{jj'}} \hat{S}_j^{\alpha} \hat{S}_{j'}^{\beta}(t) \right\rangle \frac{dt}{2\pi\hbar} \right\}, \tag{H.3}$$

and applying the product rule of differentiation, one obtains

$$\begin{aligned} (i\omega)^n \int_{-\infty}^{\infty} e^{-i\omega t} \frac{1}{N} \sum_{jj'} \left\langle e^{-i\mathbf{Q}\cdot\mathbf{r}_{jj'}} \hat{S}_j^{\alpha} \hat{S}_{j'}^{\beta}(t) \right\rangle \frac{dt}{2\pi\hbar} = \\ \int_{-\infty}^{\infty} e^{-i\omega t} \frac{1}{N} \sum_{jj'} \left\langle e^{-i\mathbf{Q}\cdot\mathbf{r}_{jj'}} \hat{S}_j^{\alpha} \frac{d^n}{dt^n} \hat{S}_{j'}^{\beta}(t) \right\rangle \frac{dt}{2\pi\hbar}. \end{aligned} \tag{H.4}$$

Recognising that the LHS is simply a restatement of the definition of the dynamic structure factor given by Eq. H.2, up to a prefactor of $(i\omega)^n$, one can rewrite the expression in Eq. H.4 as

$$(i\omega)^n S(\mathbf{Q}, \hbar\omega) = \int_{-\infty}^{\infty} e^{-i\omega t} \frac{1}{N} \sum_{jj'} \left\langle e^{-i\mathbf{Q}\cdot\mathbf{r}_{jj'}} \hat{S}_j^{\alpha} \frac{d^n}{dt^n} \hat{S}_{j'}^{\beta}(t) \right\rangle \frac{dt}{2\pi\hbar} \tag{H.5}$$

By adding a factor of $\hbar^n$, dividing by i^n on both sides, integrating both sides with

respect to $d(\hbar\omega)$, and utilising the integral identity of $\int_{-\infty}^{\infty} e^{-i\omega t} d(\omega) = 2\pi\delta(t)$, then Eq. H.5 becomes

$$\int_{-\infty}^{\infty} (\hbar\omega)^n S^{\alpha\beta}(\mathbf{Q}, \hbar\omega) d(\hbar\omega) = \left(\frac{\hbar}{i}\right)^n \frac{1}{N} \sum_{jj'} \left\langle e^{-i\mathbf{Q}\cdot\mathbf{r}_{jj'}} \hat{S}_j^{\alpha} \left\{ \frac{d^n}{dt^n} \hat{S}_{j'}^{\beta}(t) \right\}_{t=0} \right\rangle, \tag{H.6}$$

where the δ-function removes the integral and fixes the evaluation to $t = 0$. Equation H.6 is a general expression for the n^{th}-moment of the dynamic structure factor, irrespective of the details of the Hamiltonian $\hat{\mathcal{H}}$.

In the case of the zeroth moment sum rule, commonly referred to as the total moment sum rule, the value of n in Eq. H.6 is set to 0, yielding

$$\int_{-\infty}^{\infty} S^{\alpha\beta}(\mathbf{Q}, \hbar\omega) d(\hbar\omega) = \frac{1}{N} \sum_{jj'} \left\langle e^{-i\mathbf{Q}\cdot\mathbf{r}_{jj'}} \hat{S}_j^{\alpha} \hat{S}_{j'}^{\beta} \right\rangle \equiv \frac{1}{N} \left\langle \hat{S}_{\mathbf{Q}}^{\alpha} \hat{S}_{-\mathbf{Q}}^{\beta} \right\rangle, \tag{H.7}$$

corresponding to the static structure factor $S(\mathbf{Q})$, where $\hat{S}_{\mathbf{Q}}^{\alpha} = \sum_j \hat{S}_j^{\alpha} e^{-i\mathbf{Q}\cdot\mathbf{r}_j}$ denotes the corresponding Fourier transformed spin component. Integrating the static structure factor over the first Brillouin zone and calculating the trace, Eq. H.7 becomes

$$\sum_{\alpha} \int_{-\infty}^{\infty} S^{\alpha\alpha}(\mathbf{Q}) \frac{V_o}{(2\pi)^3} d^3(\mathbf{Q}) = \sum_{\alpha} \int_{-\infty}^{\infty} \frac{1}{N} \sum_{jj'} \left\langle e^{-i\mathbf{Q}\cdot\mathbf{r}_{jj'}} \hat{S}_j^{\alpha} \hat{S}_{j'}^{\alpha} \right\rangle \frac{V_o}{(2\pi)^3} d^3(\mathbf{Q}), \tag{H.8}$$

where the factor $\frac{(2\pi)^3}{V_o}$ denotes the volume of the first Brillouin zone and V_o corresponds to the volume of the crystal's primitive unit cell. **N.B.** Only as otherwise stated, Einstein summation convention is not being used in these derivations, *i.e.* repeated indices do not imply summation. Summations over a particular index or quantity will be labelled explicitly. The value of V_o is conventionally fixed to unity as all length quantities are normalised to relative length units (r.l.u). Utilising the identity $\int_{-\infty}^{\infty} e^{iQr} dQ = 2\pi\delta(r)$, the integral in

Eq. H.8 is simplified to

$$\sum_{\alpha}\int_{-\infty}^{\infty} S^{\alpha\alpha}(\mathbf{Q})\frac{V_o}{(2\pi)^3}d^3(\mathbf{Q}) = \sum_{\alpha}\frac{1}{N}\sum_{jj'}\left\langle \hat{S}_j^{\alpha}\hat{S}_{j'}^{\alpha}\right\rangle (2\pi)^3\delta(\mathbf{r}_{jj'})\frac{1}{(2\pi)^3}, \qquad \text{(H.9)}$$

where the $\delta(\mathbf{r}_{jj'})$ implies that $\mathbf{r}_{jj'} = 0$, which holds only if $j = j'$. Consequently, the δ-function behaves as a Kronecker delta $\delta_{jj'}$ and the double summation index jj' is replaced by j, then Eq. H.9 can be simplified to

$$\sum_{\alpha}\int_{-\infty}^{\infty} S^{\alpha\alpha}(\mathbf{Q})\frac{V_o}{(2\pi)^3}d^3(\mathbf{Q}) = \sum_{\alpha}\frac{1}{N}\sum_{j}\left\langle \hat{S}_j^{\alpha}\hat{S}_{j}^{\alpha}\right\rangle (2\pi)^3\frac{1}{(2\pi)^3}. \qquad \text{(H.10)}$$

By performing the sum over all sites j and indices α, one obtains a quantity of $N(\sum_{\alpha} S^{\alpha}S^{\alpha})$ which is equivalent to $N\mathbf{S}\cdot\mathbf{S}$. By inserting this identity into Eq. H.10, one obtains

$$\sum_{\alpha}\int_{-\infty}^{\infty} S^{\alpha\alpha}(\mathbf{Q})\frac{V_o}{(2\pi)^3}d^3(\mathbf{Q}) = \left\langle \hat{\mathbf{S}}\cdot\hat{\mathbf{S}}\right\rangle = S(S+1), \qquad \text{(H.11)}$$

where the second equality is due to the observation that the expectation value $\left\langle \hat{\mathbf{S}}\cdot\hat{\mathbf{S}}\right\rangle \equiv \left\langle \hat{S}^2\right\rangle = S(S+1)$.

H.2 Derivation of the First Moment Sum Rule

The derivation of the first moment sum rule begins by setting $n = 1$ in the expression for the n^{th}-moment of the dynamic structure factor (Eq. H.6) corresponding to

$$\int_{-\infty}^{\infty}\hbar\omega S^{\alpha\beta}(\mathbf{Q},\hbar\omega)d(\hbar\omega) = \left(\frac{\hbar}{i}\right)\frac{1}{N}\sum_{jj'}\left\langle e^{-i\mathbf{Q}\cdot\mathbf{r}_{jj'}}\hat{S}_j^{\alpha}\left\{\frac{d}{dt}\hat{S}_{j'}^{\beta}(t)\right\}_{t=0}\right\rangle. \qquad \text{(H.12)}$$

Utilising the Heisenberg picture formulation of quantum mechanics [38, 267, 624],

as summarised by

$$\frac{d}{dt}\hat{A}(t) = \frac{i}{\hbar}\left[\hat{\mathcal{H}}, \hat{A}(t)\right] + \frac{\partial \hat{A}(t)}{\partial t}, \tag{H.13}$$

where, in contrast to Schrödinger, the operators $\hat{A}(t)$ assume time dependence and the state vectors $|\psi\rangle$ are assumed to be time-independent, then the time derivative on the RHS in Eq. H.12 can be rewritten as

$$\int_{-\infty}^{\infty} (\hbar\omega) S^{\alpha\beta}(\mathbf{Q}, \hbar\omega) d(\hbar\omega) = \frac{1}{N} \sum_{jj'} \left\langle e^{-i\mathbf{Q}\cdot\mathbf{r}_{jj'}} \hat{S}_j^{\alpha} [\hat{\mathcal{H}}, \hat{S}_{j'}^{\beta}] \right\rangle. \tag{H.14}$$

Since $\mathbf{r}_{jj'} = \mathbf{r}_j - \mathbf{r}_{j'}$, Eq. H.14 can be rewritten as

$$\int_{-\infty}^{\infty} \hbar\omega S^{\alpha\beta}(\mathbf{Q}, \hbar\omega) d(\hbar\omega) = \frac{1}{N} \sum_{jj'} \left\langle e^{-i\mathbf{Q}\cdot\mathbf{r}_{j}} \hat{S}_j^{\alpha} [\hat{\mathcal{H}}, e^{i\mathbf{Q}\cdot\mathbf{r}_{j'}} \hat{S}_{j'}^{\beta}] \right\rangle, \tag{H.15}$$

or equivalently as

$$\int_{-\infty}^{\infty} \hbar\omega S^{\alpha\beta}(\mathbf{Q}, \hbar\omega) d(\hbar\omega) = \frac{1}{N} \left\langle \hat{S}_{\mathbf{Q}}^{\alpha} [\hat{\mathcal{H}}, \hat{S}_{-\mathbf{Q}}^{\beta}] \right\rangle, \tag{H.16}$$

where the spin operator components are expressed in terms of their Fourier transformed analogues. By observing that the Hamiltonian $\hat{\mathcal{H}}$ can be shifted from the right to the left when evaluating the expectation value due to its Hermitian character and assuming a centrosymmetric lattice, *i.e.* $S_{\mathbf{Q}}^{\alpha} = S_{-\mathbf{Q}}^{\alpha}$, then a main diagonal element of the dynamic structure can be expressed as

$$\int_{-\infty}^{\infty} \hbar\omega S^{\alpha\alpha}(\mathbf{Q}, \hbar\omega) d(\hbar\omega) = \frac{1}{2N} \left\langle \left[\left[\hat{S}_{\mathbf{Q}}^{\alpha}, \hat{\mathcal{H}} \right], \hat{S}_{-\mathbf{Q}}^{\alpha} \right] \right\rangle. \tag{H.17}$$

In contrast to the total (zeroth) moment sum rule given by Eq. H.11, the expression for the first moment sum rule is dependent on the particular Hamiltonian $\hat{\mathcal{H}}$ under consideration. As alluded to by Eq. H.17, the derivation for an expression of the first moment sum rule is simpler in the Fourier transformed-basis. It can be shown that the Heisenberg-Dirac Spin Hamiltonian given by Eq. H.1 in the Fourier transformed-basis is given by

$$\hat{\mathcal{H}} = \frac{1}{N} \sum_{\mathbf{Q}} J_{\mathbf{Q}} \hat{\mathbf{S}}_{\mathbf{Q}} \cdot \hat{\mathbf{S}}_{-\mathbf{Q}}, \tag{H.18}$$

or equivalently

$$\hat{\mathcal{H}} = \frac{1}{N}\sum_{\mathbf{Q}} J(\mathbf{Q})\hat{S}^{j}(\mathbf{Q})\hat{S}_{j}(-\mathbf{Q}), \tag{H.19}$$

where the $\mathbf{Q}$-dependence will no longer be written as a subscript since Einstein summation notation will utilised and thus the presence of the repeated index j implies summation. The Fourier transformed exchange and spin operator components are given by

$$J(\mathbf{Q}) = \sum_{\mathbf{r}_{aa'}} J(\mathbf{r}_a - \mathbf{r}_{a'})e^{i\mathbf{Q}\cdot\mathbf{r}_{aa'}} \tag{H.20a}$$

$$\hat{\mathbf{S}}(\mathbf{Q}) = \sum_{a} \hat{\mathbf{S}}(\mathbf{r}_a)e^{i\mathbf{Q}\cdot\mathbf{r}_a}, \tag{H.20b}$$

respectively, where the traditional indices j and j' are avoided since they were used for the implied summation above. By inserting the Hamiltonian in the Fourier transformed-basis into Eq. H.17 and replacing $\mathbf{Q}$ and $-\mathbf{Q}$ by $\mathbf{q}$ and $\mathbf{q}'$ for the purposes of generality, the first (inner) commutator that must be evaluated becomes

$$\left[\hat{S}^{\alpha}(\mathbf{q}), \hat{H}\right] = \left[\hat{S}^{\alpha}(\mathbf{q}), \frac{1}{N}\sum_{\mathbf{Q}} J(\mathbf{Q})\hat{S}^{j}(\mathbf{Q})\hat{S}_{j}(-\mathbf{Q})\right], \tag{H.21}$$

which is equivalent to

$$\left[\hat{S}^{\alpha}(\mathbf{q}), \hat{H}\right] = \frac{1}{N}\sum_{\mathbf{Q}} J(\mathbf{Q})\left[\hat{S}^{\alpha}(\mathbf{q}), \hat{S}^{j}(\mathbf{Q})\hat{S}_{j}(-\mathbf{Q})\right]. \tag{H.22}$$

Utilising the three term commutator identity [A,BC] = [A,B]C + B[A,C], then Eq. H.22 becomes

$$\left[\hat{S}^{\alpha}(\mathbf{q}), \hat{H}\right] = \frac{1}{N}\sum_{\mathbf{Q}} J(\mathbf{Q})\left\{\left[\hat{S}^{\alpha}(\mathbf{q}), \hat{S}^{j}(\mathbf{Q})\right]\hat{S}_{j}(-\mathbf{Q}) + \hat{S}^{j}(\mathbf{Q})\left[\hat{S}^{\alpha}(\mathbf{q}), \hat{S}^{j}(-\mathbf{Q})\right]\right\}. \tag{H.23}$$

Before proceeding, it is important to note that

$$\left[\hat{S}_k(\mathbf{q}), \hat{S}_j(\mathbf{q}')\right] = \int d^3\mathbf{r} \int d^3\mathbf{r}' e^{i\mathbf{q}\cdot\mathbf{r}} e^{i\mathbf{q}'\cdot\mathbf{r}'} \left[\hat{S}_k(\mathbf{r}), \hat{S}_j(\mathbf{r}')\right], \tag{H.24}$$

By noting that the commutator on the RHS of Eq. H.24 is simply the canonical commutation relations of angular momentum given by

$$\left[\hat{S}_k(\mathbf{r}), \hat{S}_j(\mathbf{r}')\right] = i\epsilon_{kjl}\hat{S}^l(\mathbf{r})\delta^{(3)}(\mathbf{r}-\mathbf{r}'). \tag{H.25}$$

Inserting Eq. H.25 into Eq. H.24, the Kronecker delta simplifies the double integral to

$$\left[\hat{S}_k(\mathbf{q}), \hat{S}_j(\mathbf{q}')\right] = i\epsilon_{kjl} \int d^3\mathbf{r} e^{i\mathbf{r}\cdot(\mathbf{q}+\mathbf{q}')} \hat{S}^l(\mathbf{r}). \tag{H.26}$$

Utilising the definition of the Fourier transformed component of the spin operator given by H.20b (one must simply change from discrete to continuous coordinates), Eq. H.26 is equivalent to

$$\left[\hat{S}_k(\mathbf{q}), \hat{S}_j(\mathbf{q}')\right] = i\epsilon_{kjl}\hat{S}^l(\mathbf{q}+\mathbf{q}'). \tag{H.27}$$

Inserting Eq. H.27 into Eq. H.23, one obtains

$$\left[\hat{S}^\alpha(\mathbf{q}), \hat{H}\right] = \frac{1}{N}\sum_{\mathbf{Q}} J(\mathbf{Q}) \left\{ i\epsilon^{\alpha jk}\hat{S}_k(\mathbf{Q}+\mathbf{q})\hat{S}_j(-\mathbf{Q}) + i\hat{S}_j(\mathbf{Q})\epsilon^{\alpha jk}\hat{S}_k(\mathbf{q}-\mathbf{Q}) \right\}, \tag{H.28}$$

which is equivalent to

$$\left[\hat{S}^\alpha(\mathbf{q}), \hat{H}\right] = \frac{i\epsilon^{\alpha jk}}{N}\sum_{\mathbf{Q}} J(\mathbf{Q}) \left\{ \hat{S}_k(\mathbf{Q}+\mathbf{q})\hat{S}_j(-\mathbf{Q}) + \hat{S}_j(\mathbf{Q})\hat{S}_k(\mathbf{q}-\mathbf{Q}) \right\}. \tag{H.29}$$

Proceeding to the second commutator in Eq. H.17 but for the purposes of generality, defining α as a different index α', the commutator becomes

$$\left[\left[\hat{S}^{\alpha}(\mathbf{q}),\hat{H}\right],\hat{S}^{\alpha'}(\mathbf{q}')\right]=-\frac{i\epsilon^{\alpha jk}}{N}\sum_{\mathbf{Q}}J(\mathbf{Q})\left\{\left[\hat{S}^{\alpha'}(\mathbf{q}'),\hat{S}_k(\mathbf{Q}+\mathbf{q})\hat{S}_j(-\mathbf{Q})\right]\right.$$
$$\left.+\left[\hat{S}^{\alpha'}(\mathbf{q}'),\hat{S}_j(\mathbf{Q})\hat{S}_k(\mathbf{q}-\mathbf{Q})\right]\right\}, \quad \text{(H.30)}$$

where the negative sign in Eq. H.30 is a result of the commutator identity $[A,B]=-[B,A]$. Employing the three term commutator identity, Eq. H.30 can be simplified to

$$\left[\left[\hat{S}^{\alpha}(\mathbf{q}),\hat{H}\right],\hat{S}^{\alpha'}(\mathbf{q}')\right]=-\frac{i\epsilon^{\alpha jk}}{N}\sum_{\mathbf{Q}}J(\mathbf{Q})\left\{\hat{S}_k(\mathbf{Q}+\mathbf{q})\left[\hat{S}^{\alpha'}(\mathbf{q}'),\hat{S}_j(-\mathbf{Q})\right]+\right.$$
$$\left[\hat{S}^{\alpha'}(\mathbf{q}'),\hat{S}_k(\mathbf{Q}+\mathbf{q})\right]\hat{S}_j(-\mathbf{Q})+\hat{S}_j(\mathbf{Q})\left[\hat{S}^{\alpha'}(\mathbf{q}'),\hat{S}_k(\mathbf{q}-\mathbf{Q})\right]$$
$$\left.+\left[\hat{S}^{\alpha'}(\mathbf{q}'),\hat{S}_j(\mathbf{Q})\right]\hat{S}_k(\mathbf{q}-\mathbf{Q})\right\}. \quad \text{(H.31)}$$

Utilising the commutation relations defined by Eq. H.27 then Eq. H.31 becomes

$$\left[\left[\hat{S}^{\alpha}(\mathbf{q}),\hat{H}\right],\hat{S}^{\alpha'}(\mathbf{q}')\right]=\frac{\epsilon^{\alpha jk}}{N}\sum_{\mathbf{Q}}J(\mathbf{Q})\left\{\hat{S}_k(\mathbf{Q}+\mathbf{q})\epsilon^{\alpha' jl}\hat{S}_l(\mathbf{q}'-\mathbf{Q})+\right.$$
$$\epsilon^{\alpha' kl}\hat{S}_l(\mathbf{q}'+\mathbf{Q}+\mathbf{q})\hat{S}_j(-\mathbf{Q})+\hat{S}_j(\mathbf{Q})\epsilon^{\alpha' kl}\hat{S}_l(\mathbf{q}'+\mathbf{q}-\mathbf{Q})+$$
$$\left.\epsilon^{\alpha' jl}\hat{S}_l(\mathbf{q}'+\mathbf{Q})\hat{S}_k(\mathbf{q}-\mathbf{Q})\right\}. \quad \text{(H.32)}$$

By utilising the following Levi-Civita identities [629]:

$$\epsilon^{\alpha jk}\epsilon^{\alpha' jl}\equiv\epsilon^{j\alpha k}\epsilon^{j\alpha' l}=\delta^{\alpha\alpha'}\delta^{kl}-\delta^{\alpha l}\delta^{\alpha' k} \quad \text{(H.33a)}$$
$$\epsilon^{\alpha jk}\epsilon^{\alpha' kl}\equiv\epsilon^{kj\alpha}\epsilon^{k\alpha' l}=\delta^{j\alpha'}\delta^{\alpha l}-\delta^{jl}\delta^{\alpha\alpha'}, \quad \text{(H.33b)}$$

into Eq. H.32, one obtains

$$\left[\left[\hat{S}^{\alpha}(\mathbf{q}),\hat{H}\right],\hat{S}^{\alpha'}(\mathbf{q}')\right]=\frac{\epsilon^{\alpha jk}}{N}\sum_{\mathbf{Q}}J(\mathbf{Q})\Big\{\hat{S}_k(\mathbf{Q}+\mathbf{q})\hat{S}_l(\mathbf{q}'-\mathbf{Q})\left(\delta^{\alpha\alpha'}\delta^{kl}-\delta^{\alpha l}\delta^{\alpha' k}\right)$$
$$+\hat{S}_l(\mathbf{q}'+\mathbf{Q}+\mathbf{q})\hat{S}_j(-\mathbf{Q})\left(\delta^{j\alpha'}\delta^{\alpha l}-\delta^{jl}\delta^{\alpha\alpha'}\right)+\hat{S}_j(\mathbf{Q})\hat{S}_l(\mathbf{q}'+\mathbf{q}-\mathbf{Q})\left(\delta^{j\alpha'}\delta^{\alpha l}-\delta^{jl}\delta^{\alpha\alpha'}\right)$$
$$+\hat{S}_l(\mathbf{q}'+\mathbf{Q})\hat{S}_k(\mathbf{q}-\mathbf{Q})\left(\delta^{\alpha\alpha'}\delta^{kl}-\delta^{\alpha l}\delta^{\alpha' k}\right)\Big\}. \tag{H.34}$$

The presence of the Kronecker deltas simplifies Eq. H.34 to

$$\left[\left[\hat{S}^{\alpha}(\mathbf{q}),\hat{H}\right],\hat{S}^{\alpha'}(\mathbf{q}')\right]=\frac{\epsilon^{\alpha jk}}{N}\sum_{\mathbf{Q}}J(\mathbf{Q})\Big\{\hat{S}_k(\mathbf{Q}+\mathbf{q})\hat{S}^{k}(\mathbf{q}'-\mathbf{Q})$$
$$-\hat{S}^{\alpha'}(\mathbf{Q}+\mathbf{q})\hat{S}^{\alpha}(\mathbf{q}'-\mathbf{Q})+\hat{S}^{\alpha'}(\mathbf{q}'+\mathbf{Q}+\mathbf{q})\hat{S}^{\alpha}(-\mathbf{Q})-\hat{S}_k(\mathbf{q}'+\mathbf{Q}+\mathbf{q})\hat{S}^{k}(-\mathbf{Q})$$
$$+\hat{S}^{\alpha'}(\mathbf{Q})\hat{S}^{\alpha}(\mathbf{q}'+\mathbf{q}-\mathbf{Q})-\hat{S}_k(\mathbf{Q})\hat{S}^{k}(\mathbf{q}'+\mathbf{q}-\mathbf{Q})$$
$$+\hat{S}_k(\mathbf{q}'+\mathbf{Q})\hat{S}^{k}(\mathbf{q}-\mathbf{Q})-\hat{S}^{\alpha'}(\mathbf{q}'+\mathbf{Q})\hat{S}^{\alpha}(\mathbf{q}-\mathbf{Q})\Big\}. \tag{H.35}$$

Recalling that $\mathbf{q}'$ must equal to $-\mathbf{q}$ (compare Eqs. H.17 and H.21), then Eq. H.35 simplifies further into

$$\left[\left[\hat{S}^{\alpha}(\mathbf{q}),\hat{H}\right],\hat{S}^{\alpha'}(-\mathbf{q})\right]=\frac{\epsilon^{\alpha jk}}{N}\sum_{\mathbf{Q}}J(\mathbf{Q})\Big\{\hat{S}_k(\mathbf{Q}+\mathbf{q})\hat{S}^{k}(-\mathbf{q}-\mathbf{Q})$$
$$-\hat{S}^{\alpha'}(\mathbf{Q}+\mathbf{q})\hat{S}^{\alpha}(-\mathbf{q}-\mathbf{Q})+\hat{S}^{\alpha'}(\mathbf{Q})\hat{S}^{\alpha}(-\mathbf{Q})-\hat{S}_k(\mathbf{Q})\hat{S}^{k}(-\mathbf{Q})$$
$$+\hat{S}^{\alpha'}(\mathbf{Q})\hat{S}^{\alpha}(-\mathbf{Q})-\hat{S}_k(\mathbf{Q})\hat{S}^{k}(-\mathbf{Q})$$
$$+\hat{S}_k(-\mathbf{q}+\mathbf{Q})\hat{S}^{k}(\mathbf{q}-\mathbf{Q})-\hat{S}^{\alpha'}(-\mathbf{q}+\mathbf{Q})\hat{S}^{\alpha}(\mathbf{q}-\mathbf{Q})\Big\}, \tag{H.36}$$

which is equivalent to

$$\left[\left[\hat{S}^{\alpha}(\mathbf{q}),\hat{H}\right],\hat{S}^{\alpha'}(-\mathbf{q})\right]=\frac{\epsilon^{\alpha jk}}{N}\sum_{\mathbf{Q}}J(\mathbf{Q})\Big\{2\left(\hat{S}^{\alpha'}(\mathbf{Q})\hat{S}^{\alpha}(-\mathbf{Q})-\hat{S}_k(\mathbf{Q})\hat{S}^k(-\mathbf{Q})\right)$$
$$+\hat{S}_k(\mathbf{Q}+\mathbf{q})\hat{S}^k(-\mathbf{q}-\mathbf{Q})+\hat{S}_k(-\mathbf{q}+\mathbf{Q})\hat{S}^k(\mathbf{q}-\mathbf{Q})+$$
$$\hat{S}^{\alpha'}(\mathbf{Q}+\mathbf{q})\hat{S}^{\alpha}(-\mathbf{q}-\mathbf{Q})+\hat{S}^{\alpha'}(-\mathbf{q}+\mathbf{Q})\hat{S}^{\alpha}(\mathbf{q}-\mathbf{Q})\Big\}. \tag{H.37}$$

By observing that the second and the third lines of Eq. H.37 have essentially the same form and furthermore, by utilising the definition of the Fourier transformed spin components (Eq. H.20b) then for example, the second line of Eq. H.37 becomes

$$\hat{S}_k(\mathbf{Q}+\mathbf{q})\hat{S}^k(-\mathbf{q}-\mathbf{Q})+\hat{S}_k(-\mathbf{q}+\mathbf{Q})\hat{S}^k(\mathbf{q}-\mathbf{Q})=$$
$$\sum_a\hat{S}_k(\mathbf{r}_a)e^{i(\mathbf{Q}+\mathbf{q})\cdot\mathbf{r}_a}\sum_{a'}\hat{S}^k(\mathbf{r}_{a'})e^{-i(\mathbf{Q}+\mathbf{q})\cdot\mathbf{r}_{a'}}+$$
$$\sum_a\hat{S}_k(\mathbf{r}_a)e^{i(\mathbf{Q}-\mathbf{q})\cdot\mathbf{r}_a}\sum_{a'}\hat{S}^k(\mathbf{r}_{a'})e^{-i(\mathbf{Q}-\mathbf{q})\cdot\mathbf{r}_{a'}}, \tag{H.38}$$

which is equivalent to

$$\hat{S}_k(\mathbf{Q}+\mathbf{q})\hat{S}^k(-\mathbf{q}-\mathbf{Q})+\hat{S}_k(-\mathbf{q}+\mathbf{Q})\hat{S}^k(\mathbf{q}-\mathbf{Q})=$$
$$\sum_{a,a'}\hat{S}_k(\mathbf{r}_a)e^{i(\mathbf{Q})\cdot\mathbf{r}_a}\hat{S}^k(\mathbf{r}_{a'})e^{-i(\mathbf{Q})\cdot\mathbf{r}_{a'}}\left(e^{i\mathbf{q}\cdot\mathbf{a}}e^{-i\mathbf{q}\cdot\mathbf{r}_{a'}}+e^{-i\mathbf{q}\cdot\mathbf{r}_a}e^{i\mathbf{q}\cdot\mathbf{r}_{a'}}\right), \tag{H.39}$$

or equivalently

$$\hat{S}_k(\mathbf{Q}+\mathbf{q})\hat{S}^k(-\mathbf{q}-\mathbf{Q})+\hat{S}_k(-\mathbf{q}+\mathbf{Q})\hat{S}^k(\mathbf{q}-\mathbf{Q})=$$
$$\sum_{a,a'}\hat{S}_k(\mathbf{r}_a)e^{i(\mathbf{Q})\cdot\mathbf{r}_a}\hat{S}^k(\mathbf{r}_{a'})e^{-i(\mathbf{Q})\cdot\mathbf{r}_{a'}}\left(e^{i\mathbf{q}\cdot(\mathbf{r}_a-\mathbf{r}_{a'})}+e^{-i\mathbf{q}\cdot(\mathbf{r}_a-\mathbf{r}_{a'})}\right). \tag{H.40}$$

Utilising the definition of cosine in terms of exponentials given by $\cos(x)=\frac{e^{ix}+e^{-ix}}{2}$, Eq. H.40 becomes

$$\hat{S}_k(\mathbf{Q}+\mathbf{q})\hat{S}^k(-\mathbf{q}-\mathbf{Q}) + \hat{S}_k(-\mathbf{q}+\mathbf{Q})\hat{S}^k(\mathbf{q}-\mathbf{Q}) =$$
$$\sum_{a,a'} \hat{S}_k(\mathbf{r}_a)e^{i(\mathbf{Q})\cdot\mathbf{r}_a}\hat{S}_k(\mathbf{r}_{a'})e^{-i(\mathbf{Q})\cdot\mathbf{r}_{a'}}\left(2\cos(\mathbf{q}\cdot(\mathbf{r}_a-\mathbf{r}_{a'})\right)$$
$$\equiv \hat{S}_k(\mathbf{Q})\hat{S}^k(-\mathbf{Q})\left(2\cos(\mathbf{q}\cdot(\mathbf{r}_a-\mathbf{r}_{a'})\right). \tag{H.41}$$

Applying the same logic summarised by Eq. H.41 to the fourth line of Eq. H.37, it can be shown that Eq. H.37 can be expressed as

$$\left[\left[\hat{S}^\alpha(\mathbf{Q}),\hat{H}\right],\hat{S}^{\alpha'}(-\mathbf{Q})\right]$$
$$= -\frac{2}{N}\sum_{\mathbf{Q}} J(\mathbf{Q})\left\{\left(\hat{S}_l(\mathbf{Q})\hat{S}^l(-\mathbf{Q}) - \hat{S}^{\alpha'}(\mathbf{Q})\hat{S}^\alpha(-\mathbf{Q})\right)\left(1-\cos(\mathbf{Q}\cdot(\mathbf{r}_a-\mathbf{r}_{a'}))\right)\right\}, \tag{H.42}$$

where $\mathbf{q}$ was replaced by $\mathbf{Q}$ as specified in the first moment sum rule (Eq. H.17). By performing the inverse Fourier transform, the factor of N in the denominator is eliminated and inserting the prefactor of $\frac{1}{2N}$ from Eq. H.17, Eq. H.42 becomes

$$\frac{1}{2N}\left[\left[\hat{S}^\alpha(\mathbf{Q}),\hat{H}\right],\hat{S}^{\alpha'}(-\mathbf{Q})\right]$$
$$= -\frac{1}{N}\sum_{a,a'} J(\mathbf{r}_a-\mathbf{r}_{a'})\left\{\left(\hat{S}_l(\mathbf{r}_a)\hat{S}^l(\mathbf{r}_{a'}) - \hat{S}^{\alpha'}(\mathbf{r}_a)\hat{S}^\alpha(\mathbf{r}_{a'})\right)\left(1-\cos(\mathbf{Q}\cdot(\mathbf{r}_a-\mathbf{r}_{a'}))\right)\right\}. \tag{H.43}$$

Inserting the summation over the index l explicitly and recalling that $\alpha = \alpha'$ by the definition of the first moment sum rule (Eq. H.17) then Eq. H.43 can be expressed as

$$\int_{-\infty}^{\infty} \hbar\omega S^{\alpha\alpha}(\mathbf{Q},\hbar\omega)d(\hbar\omega) =$$
$$= -\frac{1}{N}\sum_{aa',\beta}(1-\delta_{\alpha\beta})J(\mathbf{r}_a-\mathbf{r}_{a'})\left\langle \hat{S}^{\beta}(\mathbf{r}_a)\hat{S}^{\beta}(\mathbf{r}_{a'})\right\rangle \{1-\cos(\mathbf{Q}\cdot(\mathbf{r}_a-\mathbf{r}_{a'}))\}. \tag{H.44}$$

Finally, by performing a sum of Eq. H.44 over all indices α, an expression for the first moment sum rule of neutron scattering for a magnetic system with isotropic exchange is given by

$$\int_{-\infty}^{\infty} \hbar\omega S(\mathbf{Q},\hbar\omega)d(\hbar\omega) = -\frac{2}{3}\sum_{aa'}J(\mathbf{r}_a-\mathbf{r}_{a'})\left\langle \hat{\mathbf{S}}(\mathbf{r}_a)\cdot\hat{\mathbf{S}}(\mathbf{r}_{a'})\right\rangle \{1-\cos(\mathbf{Q}\cdot(\mathbf{r}_a-\mathbf{r}_{a'}))\}. \tag{H.45}$$

The factor of $\frac{2}{3}$ comes from a combination of two key observations. Firstly, the factor of 2 originates from the observation that the summation over α yields six terms (two for each index) and all six terms corresponds to $2\hat{\mathbf{S}}\cdot\hat{\mathbf{S}}$. Secondly, the factor of $\frac{1}{3}$ stems from the paramagnetic approximation corresponding to $\chi^{\alpha\alpha}(\mathbf{Q},\hbar\omega) = \chi^{\beta\beta}(\mathbf{Q},\hbar\omega) = \chi^{\gamma\gamma}(\mathbf{Q},\hbar\omega)$ (or equivalently the main diagonal components of S *via* the fluctuation-dissipation theorem) [107]. As a consequence of the magnetic projection factor [99], only two out of three components can be probed simultaneously, thus an extra factor of $\frac{2}{3}$ must be placed in front of $S(\mathbf{Q},E) = \sum_{\alpha} S^{\alpha\alpha}(\mathbf{Q},\hbar\omega)$. It should be noted that the additional factor of 2 is conventionally [106, 108, 391] not included in the first moment sum rule since it is accounted for by the paramagnetic cross section in the normalisation procedure that converts $I(\mathbf{Q},\hbar\omega)$ to $S(\mathbf{Q},\hbar\omega)$. By relabelling a as i and a' and j, $\mathbf{r}_a-\mathbf{r}_{a'}$ as $\mathbf{d}_{ij}$, defining positions $\mathbf{r}_i$, $\mathbf{r}_j$ by subscript indices (*i.e.* $\hat{\mathbf{S}}(\mathbf{r}_i)\equiv\hat{\mathbf{S}}_i$ and $J(\mathbf{r}_i-\mathbf{r}_j)\equiv J_{ij}$) and accounting for the presence for multiple $(i.j)$ pairs, then Eq. H.45 can be written in its more conventional form as

$$\langle E\rangle(\mathbf{Q}) = -\frac{2}{3}\sum_{i,j} n_{ij}J_{ij}\langle\hat{\mathbf{S}}_i\cdot\hat{\mathbf{S}}_j\rangle(1-\cos(\mathbf{Q}\cdot\mathbf{d}_{ij})), \tag{H.46}$$

where J_{ij}, $n_{ij}\langle\mathbf{S}_i\cdot\mathbf{S}_j\rangle$, $\mathbf{d}_{ij}$ denote the exchange constant, spin-spin correlator and

displacement vector between spins i and j, respectively.

H.3 Derivation of the Powder-Averaged First Moment Sum Rule

By applying the definition of the powder average [390] given by

$$S(|\mathbf{Q}|, E) = \int d\Omega_{\hat{\mathbf{Q}}} \frac{S(\mathbf{Q}, E)}{4\pi}, \tag{H.47}$$

to the first moment sum rule (Eq. H.46), and utilising the property of linearity of the integral, one obtains

$$-\frac{\mathcal{B}_{ij}}{12\pi} \int_0^{\pi} \int_0^{2\pi} (1 - \cos(|\mathbf{Q}||\mathbf{d}_{ij}| \cos\theta)) d\phi \sin\theta d\theta, \tag{H.48}$$

where the prefactor $\mathcal{B}_{ij}$ denotes $2n_{ij}J_{ij}\langle \hat{\mathbf{S}}_i \cdot \hat{\mathbf{S}}_j \rangle$ for a particular (i, j) pair type. Using the substitution of $x = |\mathbf{Q}||\mathbf{d}_{ij}| \cos\theta$ in Eq. H.48, one obtains

$$\frac{\mathcal{B}_{ij}}{3} \left(\frac{1}{4\pi}\right) \int_{|\mathbf{Q}||\mathbf{d}_{ij}|}^{-|\mathbf{Q}||\mathbf{d}_{ij}|} \int_0^{2\pi} (1 - \cos(x)) d\phi \frac{dx}{|\mathbf{Q}||\mathbf{d}_{ij}|}. \tag{H.49}$$

Employing the linearity property of the integral, the first term in Eq. H.49 is reduced to

$$\frac{\mathcal{B}_{ij}}{3} \left(\frac{1}{4\pi}\right) \int_{|\mathbf{Q}||\mathbf{d}_{ij}|}^{-|\mathbf{Q}||\mathbf{d}_{ij}|} \int_0^{2\pi} \frac{d\phi dx}{|\mathbf{Q}||\mathbf{d}_{ij}|} = -\frac{\mathcal{B}_{ij}}{3}. \tag{H.50}$$

The second term in Eq. H.49 becomes

$$-\frac{\mathcal{B}_{ij}}{3} \left(\frac{1}{4\pi}\right) \int_{|\mathbf{Q}||\mathbf{d}_{ij}|}^{-|\mathbf{Q}||\mathbf{d}_{ij}|} \int_0^{2\pi} \cos(x) \frac{d\phi dx}{|\mathbf{Q}||\mathbf{d}_{ij}|}, \tag{H.51}$$

which can be simplified by first integrating out $d\phi$,

$$-\frac{\mathcal{B}_{ij}}{3} \left(\frac{2\pi}{4\pi}\right) \int_{-|\mathbf{Q}||\mathbf{d}_{ij}|}^{|\mathbf{Q}||\mathbf{d}_{ij}|} \cos(x) \frac{dx}{|\mathbf{Q}||\mathbf{d}_{ij}|}, \tag{H.52}$$

which is equal to

$$-\frac{\mathcal{B}_{ij}}{3}\left(\frac{2\pi}{4\pi}\right)(\sin(-|\mathbf{Q}||\mathbf{d}_{ij}|)-\sin(|\mathbf{Q}||\mathbf{d}_{ij}|)). \tag{H.53}$$

Since sine is an odd function, Eq. H.53 reduces to

$$\frac{\mathcal{B}_{ij}}{3}\left(\frac{\sin(|\mathbf{Q}||\mathbf{d}_{ij}|}{|\mathbf{Q}||\mathbf{d}_{ij}|}\right). \tag{H.54}$$

Combining both terms, one obtains the final expression for the powder-averaged first moment sum rule as

$$\langle E\rangle(|\mathbf{Q}|)=-\frac{\mathcal{B}_{ij}}{3}\left(1-\frac{\sin(|\mathbf{Q}||\mathbf{d}_{ij}|}{|\mathbf{Q}||\mathbf{d}_{ij}|}\right). \tag{H.55}$$

The expression in Eq. H.55 is for one particular (i,j) pair. By utilising the linearity property of the integral and replacing $\mathcal{B}_{ij}$ by its definition in Eq. H.48, one obtains the general expression for the powder-averaged first moment sum rule as

$$\langle E\rangle(|\mathbf{Q}|)=-\frac{2}{3}\sum_{i,j}n_{ij}J_{ij}\langle\hat{\mathbf{S}}_i\cdot\hat{\mathbf{S}}_j\rangle\left(1-\frac{\sin(|\mathbf{Q}||\mathbf{d}_{ij}|}{|\mathbf{Q}||\mathbf{d}_{ij}|}\right). \tag{H.56}$$

H.4 The Single Mode Approximation

A particular common approximation employed in this Thesis is that if the inelastic dynamic structure factor $S(\mathbf{Q},\hbar\omega)$ is dominated by a single excitation, then one can can rewrite the dynamic structure factor $S(\mathbf{Q},\hbar\omega)$ as

$$S(\mathbf{Q},\hbar\omega)\approx S(\mathbf{Q})\delta(\hbar\omega-\epsilon(\mathbf{Q})), \tag{H.57}$$

where $\epsilon(\mathbf{Q})$ is the particular dispersion relation of interest and the δ-function assures energy conservation [76, 349, 351]. Known as the single mode approximation (SMA), its application to the first moment sum rule is accomplished by

introducing a $\delta(\omega - \epsilon(\mathbf{Q}))$ on both sides of Eq. H.46, yielding

$$\int \hbar\omega S(\mathbf{Q},\hbar\omega)d(\hbar\omega)\delta(\hbar\omega-\epsilon(\mathbf{Q})) = -\frac{2}{3}\sum_{i,j} J_{ij}\langle\hat{\mathbf{S}}_i\cdot\hat{\mathbf{S}}_j\rangle(1-\cos(\mathbf{Q}\cdot\mathbf{d}_{ij})\delta(\hbar\omega-\epsilon(\mathbf{Q})). \tag{H.58}$$

The presence of the δ-function in Eq. H.58 allows the integral to be quickly simplified to

$$S(\mathbf{Q},\hbar\omega) = -\frac{2}{3}\left(\frac{1}{\epsilon(\mathbf{Q})}\right)\sum_{i,j} J_{ij}\langle\hat{\mathbf{S}}_i\cdot\hat{\mathbf{S}}_j\rangle(1-\cos(\mathbf{Q}\cdot\mathbf{d}_{ij})\delta(\hbar\omega-\epsilon(\mathbf{Q})), \tag{H.59}$$

where $S(\mathbf{Q},\hbar\omega)$ corresponds to a product of an exclusively $\mathbf{Q}$-dependent term and a $\delta(\omega - \epsilon(\mathbf{Q}))$, as desired in Eq. H.57.

Appendix I

Normalisation of Neutron Inelastic Scattering Intensities to Absolute Units

This appendix provides an outline for the normalisation procedure used to convert the raw (vanadium-corrected) neutron scattering intensity of α-CoV_3O_8 measured on the direct time-of-flight spectrometer MARI with an E_i=15 meV at 5 K into absolute units, *i.e.* the neutron cross section. This particular normalisation procedure has been used previously in literature (*e.g.* α-$NaMnO_2$ [106]), consisting of treating constituent cations (and anions) as internal incoherent standards. For the interested reader, this appendix is based on the normalisation procedure outlined by Xu *et al.* and references contained therein [107]. Any additional references will be stated explicitly in the text. The procedure is as follows:

- as is the case for traditional methods for normalisation, an incoherent contribution to the total scattering ultimately determines the normalisation constant. Consequently, a range in $|\mathbf{Q}|$ containing no Bragg peaks was selected. As illustrated in Fig. I.1(a), a $|\mathbf{Q}|$ range of [0.93,1.05] $Å^{-1}$ was chosen between the (020) and (200) Bragg peaks. The absence of Bragg peaks is a necessary condition since these peaks may contain both nuclear coherent, as well as magnetic contributions due to $T<T_N$. It should also be

noted that the process outlined below is valid under the assumption that diffuse scattering, both nuclear and magnetic, are absent or minimal, as is the case for α-CoV_3O_8 (Fig. 3.2(c)).

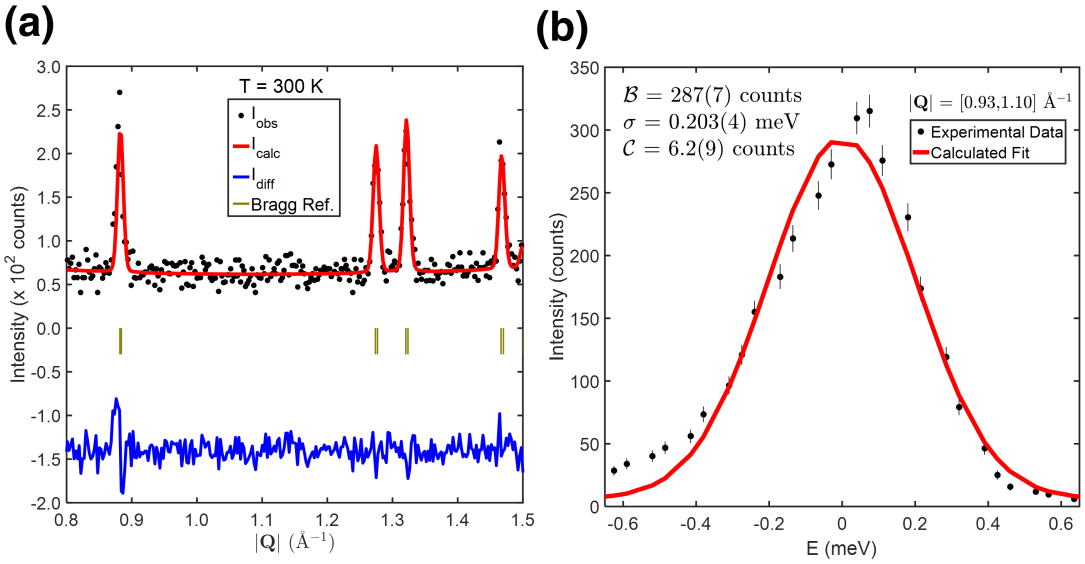

Figure I.1 (a) Room temperature diffraction profile of polycrystalline α-CoV_3O_8 collected on a Bruker D2 Phaser x-ray diffractometer utilising a monochromated Cu $K_{\alpha,1,2}$ source, confirming the absence of any discernible impurities. A Rietveld refinement ($\chi^2 = 1.487$, $R_p = 10.26\%$, $R_{wp} = 14.05\%$) indicates α-CoV_3O_8 crystallises in the orthorhombic *Ibam* (S.G. #72) structure ($a = 14.292(1)$ Å, $b = 9.8844(9)$ Å, $c = 8.3969(8)$ Å). (b) $|\mathbf{Q}|$-integrated ($|\mathbf{Q}|$=[0.93,1.10] Å^{-1}) cut of the inelastic scattering intensity $I(|\mathbf{Q}|, E)$ of α-CoV_3O_8 measured on MARI with an E_i=15 meV at 5 K. A fit to a Gaussian (Eq. I.1) yields an area of 146(5) meV·counts.

- Once an appropriate $|\mathbf{Q}|$-range was chosen, a constant $|\mathbf{Q}|$-cut along E was performed on the raw experimental data. Subsequently, a fit to a simple Gaussian given by

$$I(E) = \mathcal{B}e^{-\frac{(E-E_o)^2}{2\sigma^2}} + \mathcal{C}, \tag{I.1}$$

was calculated using a least-squares optimisation, where $\mathcal{B}$, E_o, σ and $\mathcal{C}$ denote the scale, centre-of-mass, width and vertical offset parameters, respectively. For simplicity, the centre-of-mass parameter E_o for the calculated fit illustrated in Fig. I.1(b) was fixed to 0.0 meV and detailed balance was not included. Utilising the mathematical identity

$$\int_{-\infty}^{\infty} I(E) = \sqrt{2\pi}\mathcal{B}\sigma \tag{I.2}$$

for the area under a Gaussian given by Eq. I.1, an area of 146(5) counts · meV was calculated.

- As alluded to in Chapter 3, since the constant-$|\mathbf{Q}|$ cut was performed in a $|\mathbf{Q}|$ range with only incoherent scattering contributions, the area of the Gaussian in Fig. I.1 must correspond to only a sum of the incoherent cross section of the constituent cations/anions present in the system of interest. In the case of α-CoV_3O_8, only Co^{2+} and V^{4+} possess significant incoherent cross sections, corresponding to 4.8 and 5.08 barns, respectively, whilst O^{2-} possesses a negligible incoherent cross section $8{\times}10^{-4}$ barns [630]. Adding the contributions of both cobalt and vanadium to the total incoherent cross section per formula unit of α-CoV_3O_8, one obtains the following key conversion: 20.04 barns = 146(5) counts · meV.

- Before proceeding, it is important to note that all neutron inelastic scattering measurements on α-CoV_3O_8 were performed on polycrystalline samples. Consequently, the expression describing the relation between the neutron scattering cross section and the dynamic structure factor given by

$$\frac{d^2\sigma}{dEd\Omega}(\mathbf{Q},E) = \left(\frac{\gamma r_o}{2}\right)^2 g_J^2 2|f(\mathbf{Q})|^2 S(\mathbf{Q},E), \tag{I.3}$$

where $\left(\frac{\gamma r_o}{2}\right)^2$ and g_J equals to 73 mb sr^{-1} and the Landé g-factor, respectively, whilst the factor of 2 corresponds to the paramagnetic cross section [106], must be modified to reflect the fact that the powder-averaged neutron scattering intensity $I(|\mathbf{Q}|,E)$ and not $I(\mathbf{Q},E)$ was measured. Such a modification would consist of powder-integrating Eq. I.3 over all solid angles

$$\int \frac{d^2\sigma}{dEd\Omega}(\mathbf{Q},E)\frac{d\Omega}{4\pi} = \left(\frac{\gamma r_o}{2}\right)^2 g_J^2 2|f(|\mathbf{Q}|)|^2 \int S(\mathbf{Q},E)\frac{d\Omega}{4\pi}, \tag{I.4}$$

where the magnetic form factor was approximated into an expression that is only dependent on $|\mathbf{Q}|$ (Appendix A) in order to assure both sides have the same functional dependence. By inserting the definition [390] of the powder-averaged dynamic structure factor given by

$$S(|\mathbf{Q}|,E) = \int S(\mathbf{Q},E)\frac{d\Omega}{4\pi}, \tag{I.5}$$

into Eq. I.4, then it must hold that

$$\left(\frac{1}{4\pi}\right)\frac{d\sigma}{dE}(|\mathbf{Q}|,E) = \left(\frac{\gamma r_o}{2}\right)^2 g_J^2 2|f(|\mathbf{Q}|)|^2 S(|\mathbf{Q}|,E). \tag{I.6}$$

Through dimensional analysis, it can be shown that both sides of Eq. I.6 are consistent since

$$\frac{[\text{barns}]}{[\text{meV}][\text{sr}]} = \frac{[\text{barns}]}{[\text{sr}]}\frac{1}{[\text{meV}]}, \tag{I.7}$$

where the Landé g-factor, the paramagnetic cross section and the magnetic form factor are all unitless, whilst the steradian in the denominator of the LHS is from the factor of 4π.

- The raw powder-averaged neutron scattering intensities $I(|\mathbf{Q}|,E)$ can be converted into the LHS of Eq. I.6 by recalling the conversion factor of 20.04 barns = 146(5) counts · meV. By defining a conversion factor $\mathcal{A} = \frac{20.04 \text{ barns}}{146 \text{ counts} \cdot \text{meV}}$, then the desired conversion of the neutron scattering intensity into absolute units, *i.e.* $I(|\mathbf{Q}|,E)$ to $\frac{d\sigma}{dE}$, is summarised by

$$\frac{d\sigma}{dE} = \mathcal{A}I(|\mathbf{Q}|,E), \tag{I.8}$$

which can be quickly shown to be dimensionally consistent

$$\frac{[\text{barns}]}{[\text{meV}]} = \frac{[\text{barns}]}{[\cancel{\textit{counts}}][\text{meV}]}[\cancel{\textit{counts}}]. \tag{I.9}$$

- Finally, by inserting the conversion given by Eq. I.8 into Eq. I.6 and moving all the pre-factors of the RHS of Eq. I.6 to the LHS of Eq. I.6, one obtains the relationship

$$\left(\frac{1}{4\pi}\right)\frac{\mathcal{A}I(|\mathbf{Q}|,E)}{2g_J^2|F(|\mathbf{Q}|)|^2\left(\frac{\gamma r_o}{2}\right)^2} = S(|\mathbf{Q}|,E), \tag{I.10}$$

summarising the conversion between the powder-averaged raw neutron scattering intensities and the powder-averaged dynamic structure factor in absolute units.

Appendix J

Derivation of the Equations-of-Motion for Equilibrium Green's Functions in the Random Phase Approximation

As described in Chapter 5, the behaviour of the spin wave excitations in the Mott insulator CoO was approached utilising a multi-level spin wave theory based on the equations-of-motion-Green's function method. In this appendix, it will be shown that by applying a Fock-like decoupling random phase approximation (RPA), the equations-of-motion of the Green's functions are reduced to a set of coupled linear equations. The following derivation is based on a partial derivation reported by Buyers, Holden & Perreault [515] and references contained therein. Any additional references will be stated explicitly in the text. A complete derivation is presented here for the interested reader as a pedagogical introduction to the use of the equation-of-motion-Green's function method in describing spin-wave excitations.

J.1 Single-Ion and Inter-Ion Hamiltonians

The derivation begins by first defining the relevant Hamiltonian $\hat{\mathcal{H}}$ that describes a cation with total spin S, exposed to an electric crystalline field and coupled to one another by isotropic exchange. Such a Hamiltonian is given by

$$\hat{\mathcal{H}} = \sum_i \hat{\mathcal{H}}_{CF}(i) + \sum_{ij} J(ij)\hat{\mathbf{S}}(i) \cdot \hat{\mathbf{S}}(j), \tag{J.1}$$

where the indices i, j denote individual sites. It should be noted that the form of Eq. J.1 corresponds to rare earth cations where spin-orbit coupling is the dominant energy scale and the crystal field is treated as a perturbation. In contrast, for the case of Co^{2+}, the first term in Eq. J.1 would be spin-orbit coupling. As will be shown in the next two steps, the difference between both cases are irrelevant in the context of this particular derivation.

The Hamiltonian $\hat{\mathcal{H}}$ in Eq. J.1 can be separated into a single-ion and inter-ion terms. The single-ion term is defined as

$$\hat{\mathcal{H}}_1 = \sum_i \hat{\mathcal{H}}_{CF}(i) + \sum_i \hat{S}_z(i) \left(2 \sum_j J(ij) \langle \hat{S}_z(j) \rangle \right), \tag{J.2}$$

where the second term represents a molecular field, $\hat{\mathcal{H}}_{MF}$ and defined as

$$\hat{\mathcal{H}}_{MF} = \sum_i H_{MF}(i)\hat{S}_z(i), \tag{J.3}$$

where

$$H_{MF}(i) = \left(2 \sum_j J(ij) \langle \hat{S}_z(j) \rangle \right). \tag{J.4}$$

The expectation term $\langle \hat{S}_z(j) \rangle$ denotes a thermal average

$$\langle \hat{S}_\alpha \rangle = \sum_n f_n \langle n | \hat{S}_\alpha | n \rangle \equiv \sum_n \hat{S}_{\alpha nn} f_n, \tag{J.5}$$

where f_n defines the thermal weighting factor of

$$f_n = \frac{e^{\frac{-\omega_n}{k_B T}}}{\sum_m e^{\frac{-\omega_m}{k_B T}}} \tag{J.6}$$

and where $\hat{S}_{\alpha nn}$ denotes

$$\hat{S}_{\alpha nn} = \langle n|\hat{S}_\alpha|n\rangle. \tag{J.7}$$

In addition to the single-ion term, a second term, called the inter-ion term, is defined as

$$\hat{\mathcal{H}}_2 = \sum_{ij} J(ij)\hat{S}_z(i)[\hat{S}_z(j) - 2\langle\hat{S}_z(j)\rangle] + \frac{1}{2}\sum_{ij}[\hat{S}_+(i)\hat{S}_-(j) + \hat{S}_-(i)\hat{S}_+(j)]. \tag{J.8}$$

The first term represents longitudinal fluctuations/deviations away from an average value $\langle\hat{S}_z\rangle$, whilst the second term represents transverse fluctuations.

The separation of the Hamiltonian $\hat{\mathcal{H}}$ into $\hat{\mathcal{H}}_1$ (Eq. J.2) and $\hat{\mathcal{H}}_2$ (Eq. J.8) can be shown by first utilising the following definitions of $\hat{S}_x$ and $\hat{S}_y$ in terms of the raising and lowering operators $\hat{S}_+$ and $\hat{S}_-$, respectively:

$$\hat{S}_x = \frac{1}{2}(\hat{S}_+ + \hat{S}_-) \tag{J.9a}$$

$$\hat{S}_y = \frac{1}{2i}(\hat{S}_+ - \hat{S}_-) \tag{J.9b}$$

Utilising the definition of the inner product

$$\sum_{ij} J_{ij}\hat{\mathbf{S}}(i)\cdot\hat{\mathbf{S}}(j) = \sum_{ij} J_{ij}\left(\hat{S}_x(i)\hat{S}_x(j) + \hat{S}_y(i)\hat{S}_y(j) + \hat{S}_z(i)\hat{S}_z(j)\right), \tag{J.10}$$

and inserting the definitions of Eqs. J.9a and J.9b into Eq. J.10, one obtains

$$\sum_{ij} J(ij) \left[\frac{1}{2} \left(\hat{S}_+(i)\hat{S}_-(j) + \hat{S}_-(i)\hat{S}_+(j) \right) + \hat{S}_z(i)\hat{S}_z(j) \right]. \tag{J.11}$$

Observe that if one adds the term

$$\sum_{ij} \hat{S}_z(i) \left(2 \sum_j J(ij) \langle \hat{S}_z(j) \rangle \right) - \sum_{ij} \hat{S}_z(i) \left(2 \sum_j J(ij) \langle \hat{S}_z(j) \rangle \right) \equiv 0, \tag{J.12}$$

to Eq. J.11, the positive term in Eq. J.12 becomes the second term in Eq. J.2, whilst the negative term in Eq. J.12 when added to the $\hat{S}_z(i)\hat{S}_z(j)$ in Eq. J.10 becomes the first term in Eq. J.8.

It is important to note that the single-ion portion of Eq. J.2 is a known function in terms of the spin operator since $\hat{\mathcal{H}}_{CF}$ can be written in terms of Stevens operators [261, 264]. $\hat{\mathcal{H}}_1$ can be diagonalised, yielding a set of eigenfunctions $|n\rangle$ and corresponding eigenvalues ω_n such that

$$\hat{\mathcal{H}}_1 |n\rangle = \omega_n |n\rangle, \tag{J.13}$$

where the eigenvalue-eigenvector problem in Eq. J.13 describes the energy eigenvalues of a spin S that is placed at a site i in the presence of both a crystalline electric field and a molecular field.

J.2 Creation and Annihilation Operators

Having separated the Hamiltonian $\hat{\mathcal{H}}$ into single-ion and inter-ion terms, the derivation now proceeds by defining both $\hat{\mathcal{H}}_1$ and $\hat{\mathcal{H}}_2$ in terms of creation and annihilation operators $\hat{C}_n^\dagger$ and $\hat{C}_n$, respectively.

Utilising Eq. J.13, the single-ion term can be rewritten as

$$\hat{\mathcal{H}}_1 = \sum_i \sum_n \omega_n \hat{C}_n^\dagger(i) \hat{C}_n(i), \tag{J.14}$$

where $\hat{C}_n(i)$ annihilates the state $|n\rangle$ at site i. It is worthwhile to note that since $\hat{C}^\dagger\hat{C}$ is the number operator $\hat{N}$, Eq. J.14 contains an implicit factor of N^{-1}. This extra factor will be important when a Fourier transform from real space to **Q**-space is performed later in this derivation.

Since all portions of $\hat{\mathcal{H}}$, in particular $\hat{\mathcal{H}}_2$, are defined in terms of the components of the spin operator $\hat{\mathbf{S}}$, these operators can be projected onto the Hilbert space spanned by the creation/annihilation operators by the following identities:

$$\hat{S}_+ = \sum_{mn} \hat{S}_{+mn} C_m^\dagger C_n \tag{J.15a}$$

$$\hat{S}_- = \sum_{mn} \hat{S}_{-mn} C_m^\dagger C_n \tag{J.15b}$$

$$\hat{S}_z = \sum_{mn} \hat{S}_{zmn} C_m^\dagger C_n, \tag{J.15c}$$

The first term in Eqs. J.15a-J.15c are matrix elements of the components of $\hat{\mathbf{S}}$ and are present to provide the proper matrix elements. It is important to note that the aforementioned projection is valid assuming only the $2S+1$ or $(2S+1) \times (2l+1)$ ground state multiplet is under consideration.

Before proceeding to the projection of $\hat{\mathcal{H}}_2$, the term of $\hat{\mathcal{H}}$ that describes the spin waves, there are a few identities and properties that must be introduced.

- The creation and annihilation operators have the following commutation relations:

$$[\hat{C}_m, \hat{C}_n^\dagger]_\pm = \delta_{mn}, \tag{J.16}$$

  where $\pm$ denotes the anticommutator(+) and commutator(-), respectively.

- As discussed thoroughly in Appendix E, the projected components of the spin operator $\hat{\mathbf{S}}$ onto the Hilbert space spanned by the creation and annihilation operators **must** preserve the canonical commutation relations of angular momentum, succinctly summarised as

$$\hat{\mathbf{S}} \times \hat{\mathbf{S}} = i\hat{\mathbf{S}}. \tag{J.17}$$

The expression in Eq. J.17 is equivalent to the conventional form of the commutation relations of angular momentum given by

$$[\hat{S}_\alpha, \hat{S}_\beta] = i\epsilon_{\alpha\beta\gamma}\hat{S}_\gamma \tag{J.18}$$

for each individual component $\alpha, \beta, \gamma = x, y, z$. Such an equivalence can be shown by expressing both sides of Eq. J.17 as its individual components

$$(\hat{S}_y\hat{S}_z - \hat{S}_z\hat{S}_y, \hat{S}_z\hat{S}_x - \hat{S}_x\hat{S}_z, \hat{S}_x\hat{S}_y - \hat{S}_y\hat{S}_x) = i(\hat{S}_x, \hat{S}_z, \hat{S}_z). \tag{J.19}$$

By comparing both sides of the equation for each individual component of $\hat{\mathbf{S}}$, one retrieves Eq. J.18.

- Utilising the commutation relation defined by Eq. J.16, two other commutation relations can be shown to be true

$$[\hat{C}_m^\dagger\hat{C}_n, \hat{C}_r^\dagger\hat{C}_s] = \delta_{nr}\hat{C}_m^\dagger\hat{C}_s - \delta_{sm}\hat{C}_r^\dagger\hat{C}_n \tag{J.20a}$$

$$\sum_{rs}[\hat{C}_m^\dagger\hat{C}_n, \hat{C}_r^\dagger\hat{C}_s]\hat{S}_{\alpha rs} = \sum_s \left(\hat{C}_m^\dagger\hat{C}_s\hat{S}_{\alpha ns} - \hat{C}_s^\dagger\hat{C}_n\hat{S}_{\alpha sm}\right) \tag{J.20b}$$

Eq. J.20a can be derived by utilising the four term commutation identity given by

$$[\hat{\mathcal{A}}\hat{\mathcal{B}}, \hat{\mathcal{C}}\hat{\mathcal{D}}] = \hat{\mathcal{A}}[\hat{\mathcal{B}}, \hat{\mathcal{C}}]\hat{\mathcal{D}} + [\hat{\mathcal{A}}, \hat{\mathcal{C}}]\hat{\mathcal{B}}\hat{\mathcal{D}} + \hat{\mathcal{C}}\hat{\mathcal{A}}[\hat{\mathcal{B}}, \hat{\mathcal{D}}] + \hat{\mathcal{C}}[\hat{\mathcal{A}}, \hat{\mathcal{D}}]\hat{\mathcal{B}}, \tag{J.21}$$

and Eq. J.16, Eq. J.20a becomes

$$\begin{aligned}
[\hat{C}_m^\dagger\hat{C}_n, \hat{C}_r^\dagger\hat{C}_s] &= \hat{C}_m^\dagger[\hat{C}_n, \hat{C}_r^\dagger]\hat{C}_s + [\hat{C}_m^\dagger, \hat{C}_r^\dagger]\hat{C}_n\hat{C}_s \\
&\quad + \hat{C}_r^\dagger\hat{C}_m^\dagger[\hat{C}_n, \hat{C}_s] + \hat{C}_r^\dagger[\hat{C}_m^\dagger, \hat{C}_s]\hat{C}_n && \text{(J.22a)} \\
&= \hat{C}_m^\dagger[\hat{C}_n, \hat{C}_r^\dagger]\hat{C}_s + \hat{C}_r^\dagger[\hat{C}_m^\dagger, \hat{C}_s]\hat{C}_n && \text{(J.22b)} \\
&= \hat{C}_m^\dagger\delta_{nr}\hat{C}_s - \hat{C}_r^\dagger\delta_{sm}\hat{C}_n && \text{(J.22c)}
\end{aligned}$$

Note that in Eq. J.22b, we have utilised the fact that the commutators $[\hat{C}_n, \hat{C}_m]$ and $[\hat{C}_n^\dagger, \hat{C}_m^\dagger]$ are zero $\forall\ m, n$. Eq. J.20b can be derived by first utilising the identity in Eq. J.20a.

$$\sum_{rs}[\hat{C}_m^\dagger\hat{C}_n, \hat{C}_r^\dagger\hat{C}_s]\hat{S}_{\alpha rs} = \sum_{rs}\{\delta_{nr}\hat{C}_m^\dagger\hat{C}_s - \delta_{sm}\hat{C}_r^\dagger\hat{C}_n\}\hat{S}_{\alpha rs} \tag{J.23}$$

The Kronecker delta eliminates the indices r and s in the first and second series, respectively, yielding

$$\sum_{s} \hat{C}_m^\dagger \hat{C}_s \hat{S}_{\alpha ns} - \sum_{r} \hat{C}_r^\dagger \hat{C}_n \hat{S}_{\alpha rm}. \tag{J.24}$$

By replacing the index r by a dummy index s in the second series, and combining both series into one series, one obtains

$$\sum_{s} \{\hat{C}_m^\dagger \hat{C}_s \hat{S}_{\alpha ns} - \hat{C}_s^\dagger \hat{C}_n \hat{S}_{\alpha sm}\}. \tag{J.25}$$

- A final identity is to recognise that for the transverse spin operators $\hat{S}_\pm$, the matrix elements must be entirely non-diagonal, and thus

$$\hat{S}_{\pm nn} = 0, \tag{J.26}$$

must hold true $\forall\ n$. This particular identity will play an important role when addressing the transverse fluctuations portion of $\hat{\mathcal{H}}_2$. It is important to note that this does **not** mean that the longitudinal spin component will be itself entirely diagonal (*e.g.* Davydov excitations [631]).

J.3 Inter-Ion Coupling and the Equation-of-Motion

In this section, the final form of the equations-of-motion of the Green's function in the random phase approximation will be derived. First, recall that the full Hamiltonian $\hat{\mathcal{H}} = \hat{\mathcal{H}}_1 + \hat{\mathcal{H}}_2$ is given by

$$\begin{aligned}\hat{\mathcal{H}} = \sum_i \sum_n \omega_n \hat{C}_n^\dagger(i)\hat{C}_n(i) + \sum_{ij} J(ij)\hat{S}_z(i)[\hat{S}_z(j) - 2\langle \hat{S}_z(j)\rangle] \\ + \frac{1}{2}\sum_{ij}[\hat{S}_+(i)\hat{S}_-(j) + \hat{S}_-(i)\hat{S}_+(j)],\end{aligned} \tag{J.27}$$

where second term, the inter-ion term $\hat{\mathcal{H}}_2$ describes the spin waves of interest. Having established the relevant Hamiltonian, the derivation now proceeds

by defining the transverse term and longitudinal term of the Green's function:

$$G^{\alpha\beta}(ij,t) \equiv G(\hat{S}_\alpha(i), \hat{S}_\beta(j), t) = -i\Theta(t)\langle[\hat{S}_\alpha(i,t), \hat{S}_\beta(j,0)]\rangle \tag{J.28}$$

where $\alpha, \beta = +$ or -, and

$$G^{zz}(ij,t) - i\Theta(t)\langle[\hat{S}_z(i,t), \hat{S}_z(j,0)]\rangle, \tag{J.29}$$

respectively; and the Fourier transform and its inverse are given by:

$$G(\mathbf{Q},t) = \frac{1}{\mathcal{N}}\sum_i G(ij,t)e^{i\mathbf{Q}\cdot(\mathbf{i}-\mathbf{j})} \tag{J.30}$$

and

$$G(ij,\omega) = \sum_i G(ij,t)e^{i\omega t}. \tag{J.31}$$

The prefactor $\Theta(t)$ is the Heavyside function ensuring causality. It is important to note that in Eq. J.28, $\alpha \neq \beta$ since the cases of $-,-$ or $+,+$ would correspond to the physically unrealisable situations of simultaneous creation of two holes or two excitations, respectively. Instead, a hole must be created at the same time as creating an excitation (*i.e.* you excite an electron which creates a hole that must move as the electron moves between energy levels).

Having defined the Green's function and its Fourier transform, the derivation now proceeds in deriving the Heisenberg equation-of-motion of the Green's function by utilising: (1) the definition of the Green's function (e.g. Eq. J.28), (2) the Heisenberg picture of quantum mechanics and (3) the Fourier transform given by Eq. J.31. The derivation will focus on $(+-)$ but it can be readily shown that the form follows for other (allowed) combinations of $+$, $-$ and z. The derivation is as follows:

Taking the time derivative of the definition of the Green's function yields

$$\partial_t G(\hat{S}_+(i), \hat{S}_-(j), t) = -i\delta(t)\langle[\hat{S}_+(i,t), \hat{S}_-(j,0)]\rangle - i\Theta(t)\langle[\partial_t\hat{S}_+(i,t), \hat{S}_-(j,0)]\rangle. \tag{J.32}$$

Utilising the Heisenberg picture of quantum mechanics which states

$$\partial_t \hat{A}(t) = -i[\hat{A}(t), \hat{\mathcal{H}}] + \left(\frac{\partial \hat{A}}{\partial t}\right)_{\hat{\mathcal{H}}} \tag{J.33}$$

but since none of the spin operators have an explicit time dependence themselves, the second term is zero and moving i to the LHS, one obtains

$$i\partial_t \hat{A}(t) = [\hat{A}(t), \hat{\mathcal{H}}] \tag{J.34}$$

Inserting Eq. J.34 into Eq. J.32, we obtain

$$\partial_t G(\hat{S}_+(i), \hat{S}_-(j), t) = -i\delta(t)\langle[\hat{S}_+(i,t), \hat{S}_-(j,0)]\rangle - \Theta(t)\langle[[\hat{S}_+(i,t), \hat{\mathcal{H}}], \hat{S}_-(j,0)]\rangle \tag{J.35}$$

Taking the Fourier transform of Eq. J.35 defined by Eq. J.31, one obtains

$$\int_{-\infty}^{\infty} dt e^{i\omega t} \partial_t G(\hat{S}_+(i), \hat{S}_-(j), t) =$$
$$-i\int_{-\infty}^{\infty} dt e^{i\omega t}\delta(t)\langle[\hat{S}_+(i,t), \hat{S}_-(j,0)]\rangle - i\int_{-\infty}^{\infty} dt e^{i\omega t}\{-i\Theta(t)\langle[[\hat{S}_+(i,t), \hat{\mathcal{H}}], \hat{S}_-(j,0)]\rangle\} \tag{J.36}$$

The first term on the RHS is quickly simplified due to the presence of the delta function $\delta(t)$

$$\int_{-\infty}^{\infty} dt e^{i\omega t} \partial_t G(\hat{S}_+(i), \hat{S}_-(j), t) =$$
$$-i\langle[\hat{S}_+(i,0), \hat{S}_-(j,0)]\rangle - i\int_{-\infty}^{\infty} dt e^{i\omega t}\{-i\Theta(t)\langle[[\hat{S}_+(i,t), \hat{\mathcal{H}}], \hat{S}_-(j,0)]\rangle\} \tag{J.37}$$

Notice that the second term on the RHS contains the definition of the Green's function (Eq. J.28) but with $[\hat{S}_+(i,t), \hat{\mathcal{H}}]$ instead of $\hat{S}_+$, and thus can be relabelled

$$\int_{-\infty}^{\infty} dt e^{i\omega t} \partial_t G(\hat{S}_+(i), \hat{S}_-(j), t) =$$
$$-i\langle[\hat{S}_+(i,0), \hat{S}_-(j,0)]\rangle - i\int_{-\infty}^{\infty} dt e^{i\omega t} G([\hat{S}_+(i,t), \hat{\mathcal{H}}], \hat{S}_-(j,0)) \tag{J.38}$$

Focussing on the LHS, by applying the product rule, one obtains

$$\delta_t\{e^{i\omega t} G(i,j,t)\} = i\omega e^{i\omega t} G(i,j,t) + e^{i\omega t}\partial_t G(i,j,t). \tag{J.39}$$

Rearranging one obtains

$$e^{i\omega t}\partial_t G(i,j,t) = \delta_t\{e^{i\omega t} G(i,j,t)\} - i\omega e^{i\omega t} G(i,j,t). \tag{J.40}$$

Performing integration-by-parts, aided by substituting the above expression into Eq. J.38, one obtains

$$\int_{-\infty}^{\infty} dt \left\{\delta_t e^{i\omega t} G(\hat{S}_+(i,t), \hat{S}_-(j,0)) - i\omega e^{i\omega t} G(\hat{S}_+(i,t), \hat{S}_-(j,0))\right\} =$$
$$-i\langle[\hat{S}_+(i,0), \hat{S}_-(j,0)]\rangle - i\int_{-\infty}^{\infty} dt e^{i\omega t} G([\hat{S}_+(i,t), \hat{\mathcal{H}}], \hat{S}_-(j,0), t). \tag{J.41}$$

The RHS can be simplified further by noting that the second term on the RHS is the Fourier transform defined in Eq. J.31, thus mapping from t onto ω yields

$$\int_{-\infty}^{\infty} dt \left\{\delta_t e^{i\omega t} G(\hat{S}_+(i,t), \hat{S}_-(j,0)) - i\omega e^{i\omega t} G(\hat{S}_+(i,t), \hat{S}_-(j,0))\right\} =$$
$$-i\langle[\hat{S}_+(i,0), \hat{S}_-(j,0)]\rangle - iG([\hat{S}_+(i,\omega), \hat{\mathcal{H}}], \hat{S}_-(j,0), t) \tag{J.42}$$

The LHS of Eq. J.42 can be simplified by utilising the boundary conditions of the Green's functions. These functions must be well-behaved and thus normalisable, implying that they must approach zero in the limit of $\pm\infty$. Consequently, the first term on the LHS vanishes, whilst the second term is simply the definition of

the Fourier transform from t to ω (Eq. J.31), thus simplifying the equation to

$$-i\omega G(\hat{S}_+(i,\omega),\hat{S}_-(j,0)) = -i\langle[\hat{S}_+(i,0),\hat{S}_-(j,0)]\rangle - iG([\hat{S}_+(i,\omega),\hat{\mathcal{H}}],\hat{S}_-(j,0),t) \tag{J.43}$$

Dividing by $-i$, one obtains

$$\omega G(\hat{S}_+(i,\omega),\hat{S}_-(j,0)) = \langle[\hat{S}_+(i,0),\hat{S}_-(j,0)]\rangle + G([\hat{S}_+(i,\omega),\hat{\mathcal{H}}],\hat{S}_-(j,0),t). \tag{J.44}$$

Without the loss of generality, the Heisenberg equation-of-motion of the Green's functions can thus be summarised as

$$\omega G(\hat{A},\hat{B},\omega) = \langle[\hat{A},\hat{B}]\rangle + G([\hat{A},\hat{\mathcal{H}}],\hat{B},\omega), \tag{J.45}$$

where $\hat{A}$ and $\hat{B}$ denote components of spin operators. The presence of the commutator with respect to the Hamiltonian $\hat{\mathcal{H}}$ demonstrates that the Green's functions contain information concerning the dynamics of the system under investigation. The rest of the derivation will involve addressing this particular commutator with the Hamiltonian $\hat{\mathcal{H}}$.

Before proceeding, it will prove useful [515] to define the inter-level susceptibility $\hat{G}$ given by

$$G^{\alpha\beta}(i,j,\omega) = \sum_{mn} \hat{S}_{\alpha mn}\hat{G}^{\beta}(m,n,i,j,\omega), \tag{J.46}$$

where α,β can assume the values of $+$, $-$ or z. The motivation for such a definition is that one of the operators $\hat{A}$ in Eq. J.45 is reduced to the term $C_m^\dagger C_n$, whilst the operator $\hat{B}$ is given by the explicit spin operator $\hat{S}^\beta$. After all the algebraic steps are completed, the total Green's function can be retrieved by simply multiplying $\hat{G}^\beta$ by $\hat{S}_{\alpha mn}$ and summing over mn as defined in Eq. J.46.

Referring to the Hamiltonian $\hat{\mathcal{H}}$ in Eq. J.27, it becomes apparent that there will be three commutators that will need to be evaluated. In fact, this is expected for $SU(2)$ (or $SO(3)$), since there are four members that must be considered: $\{\mathbb{I},z,x,y\}$, corresponding to the diagonal term, longitudinal and

transverse fluctuation terms, respectively, reflecting the three terms of the $\hat{\mathcal{H}}_2$ contribution to Eq. J.27.

J.3.1 Diagonal Commutator

The first commutator that must be evaluated is a term that involves the $\hat{C}^\dagger(k)\hat{C}(k)$ contribution to Eq. J.27. It can be shown that its commutator in Eq. J.46 is given by

$$\sum_k \sum_r [\hat{C}_m^\dagger(i)\hat{C}_n(i), \hat{C}_r^\dagger(k)\hat{C}_r(k)]\omega_r = \delta_{ij}(\omega_n - \omega_m)\hat{C}_m^\dagger(i)\hat{C}_n(j) \tag{J.47}$$

Eq. J.47 can be derived by utilising the four term commutator identity (Eq. J.21), yielding

$$\begin{aligned}\sum_k \sum_r [\hat{C}_m^\dagger(i)\hat{C}_n(i), \hat{C}_r^\dagger(k)\hat{C}_r(k)]\omega_r = \\ \sum_k \sum_r \Big\{ \hat{C}_m^\dagger(i)[\hat{C}_n(j), \hat{C}_r^\dagger(k)]\hat{C}_r(k)\omega_r + [\hat{C}_m^\dagger(i), \hat{C}_r^\dagger(k)]\hat{C}_n(j)\hat{C}_r(k)\omega_r \\ + \hat{C}_r^\dagger(k)\hat{C}_m^\dagger(i)[\hat{C}_n(j), \hat{C}_r(k)]\omega_r + \hat{C}_r^\dagger(k)[\hat{C}_m^\dagger(i), \hat{C}_r(k)]\hat{C}_n(j)\omega_r \Big\}\end{aligned} \tag{J.48}$$

Utilising the commutator identity Eq. J.16 for both indices pairs for states m, n and sites i, j, one can simplify Eq. J.48 to

$$\begin{aligned}\sum_k \sum_r [\hat{C}_m^\dagger(i)\hat{C}_n(i), \hat{C}_r^\dagger(k)\hat{C}_r(k)]\omega_r = \\ \sum_k \sum_r \Big\{ \hat{C}_m^\dagger(i)\delta_{nr}\delta_{jk}\hat{C}_r(k)\omega_r + \hat{C}_r^\dagger(k)\delta_{rm}\delta_{ik}\hat{C}_n(j)\omega_r \Big\}\end{aligned} \tag{J.49}$$

where the second and third terms are removed due to the observation that $[\hat{C}_m^\dagger(i)\hat{C}_n^\dagger(j)] = 0$ and $[\hat{C}_m(i)\hat{C}_n(j)] = 0 \;\; \forall \; \{m, n, i, j\}$. Expanding the sum and utilising the fact that the Kronecker delta will remove both indices k and r, one obtains

$$\sum_k \sum_r [\hat{C}_m^\dagger(i)\hat{C}_n(i), \hat{C}_r^\dagger(k)\hat{C}_r(k)]\omega_r = (\omega_n - \omega_m)\hat{C}_m^\dagger(i)\hat{C}_n(j). \tag{J.50}$$

Finally, it is important to notice that this quantity will be non-zero only if the raising and lowering operators operate on the same site, thus $i = j$ must be true. This physical interpretation can then be summarised as the final expression

$$\sum_k \sum_r [\hat{C}_m^\dagger(i)\hat{C}_n(i), \hat{C}_r^\dagger(k)\hat{C}_r(k)]\omega_r = \delta_{ij}(\omega_n - \omega_m)\hat{C}_m^\dagger(i)\hat{C}_n(i). \tag{J.51}$$

The removal of the j index in $\hat{C}_n$ in Eq. J.51 is simply to reflect that all indices need to be the same for the value to be non-zero.

J.3.2 Transverse Commutator & Random Phase Approximation

The commutator involving the transverse term, corresponding to the third term in Eq. J.27, may be summarised as

$$\begin{aligned}
&\sum_{kl} J(kl)[\hat{C}_m^\dagger(i)\hat{C}_n(i), \hat{S}_+(k)\hat{S}_-(l)] = \\
&\sum_l J(il) \sum_s [\hat{S}_{+ns}(i)\hat{C}_m^\dagger(i)\hat{C}_s(i) - \hat{S}_{+sm}(i)\hat{C}_s^\dagger(i)\hat{C}_n(i)] \sum_{pq} \hat{S}_{-qp}(l)\hat{C}^\dagger(l)\hat{C}_p(l) \\
+ &\sum_l J(il) \sum_s [\hat{S}_{-ns}(i)\hat{C}_m^\dagger(i)\hat{C}_s(i) - \hat{S}_{-sm}(i)\hat{C}_s^\dagger(i)\hat{C}_n(i)] \sum_{pq} \hat{S}_{+qp}(l)\hat{C}^\dagger(l)\hat{C}_p(l)
\end{aligned} \tag{J.52}$$

Since the transverse term have two terms with effectively the same form $\hat{S}_\alpha(i)\hat{S}_\beta(j)$ (*i.e.* two different spin operators on two different sites), then only one term needs to be evaluated and later doubled, and thus the factor of $\frac{1}{2}$ is removed. The derivation of Eq. J.52 can be summarised as the following steps:

Beginning from the LHS of Eq. J.52, by switching the positions of the spin and raising/lowering operarators in the commutator, a negative sign is introduced to the anticommutivity property

$$\sum_{kl} J(kl)[\hat{C}_m^\dagger(i)\hat{C}_n(i), \hat{S}_+(k)\hat{S}_-(l)] =$$
$$\sum_{kl} J(kl)\{-[\hat{S}_+(k)\hat{S}_-(l), \hat{C}_m^\dagger(i)\hat{C}_n(i)]\}. \tag{J.53}$$

Utilising the four term commutation identity given by

$$[\hat{A}\hat{B}, \hat{C}\hat{D}] = \hat{A}[\hat{B}, \hat{C}\hat{D}] + [\hat{A}, \hat{C}\hat{D}]\hat{B}, \tag{J.54}$$

then Eq. J.53 becomes

$$\sum_{kl} J(kl)[\hat{C}_m^\dagger(i)\hat{C}_n(i), \hat{S}_+(k)\hat{S}_-(l)] =$$
$$\sum_{kl} \left\{-\hat{S}_+(k)[\hat{S}_-(l), \hat{C}_m^\dagger(i)\hat{C}_n(i)] - [\hat{S}_+(k), \hat{C}_m^\dagger(i)\hat{C}_n(i)]\hat{S}_-(l)\right\}. \tag{J.55}$$

Recalling from Eqs. J.15a-J.15c that $\hat{S}_\alpha = \sum_{pq} \hat{S}_{\alpha pq}\hat{C}_p^\dagger\hat{C}_q$, then by substituting the definition of the spin operators $\hat{S}$ into the equation above, one obtains

$$\sum_{kl} J(kl)[\hat{C}_m^\dagger(i)\hat{C}_n(i), \hat{S}_+(k)\hat{S}_-(l)] =$$
$$\sum_{kl} J(kl) \left\{-\hat{S}_+(k) \sum_{pq} \hat{S}_{-pq}(l)[\hat{C}_p^\dagger(l)\hat{C}_q(l), \hat{C}_m^\dagger(i)\hat{C}_n(i)]\right.$$
$$\left. - \sum_{pq} \hat{S}_{+pq}(k)[\hat{C}_p^\dagger(k)\hat{C}_q(k), \hat{C}_m^\dagger(i)\hat{C}_n(i)]\hat{S}_-(l)\right\} \tag{J.56}$$

Reversing both commutators to remove the negative sign yields

$$\sum_{kl} J(kl)[\hat{C}_m^\dagger(i)\hat{C}_n(i), \hat{S}_+(k)\hat{S}_-(l)] =$$
$$\sum_{kl}\Bigg\{\hat{S}_+(k)\sum_{pq}\hat{S}_{-pq}(l)[\hat{C}_m^\dagger(i)\hat{C}_n(i), \hat{C}_p^\dagger(l)\hat{C}_q(l)]$$
$$+\sum_{pq}\hat{S}_{+pq}(k)[\hat{C}_m^\dagger(i)\hat{C}_n(i), \hat{C}_p^\dagger(k)\hat{C}_q(k)]\hat{S}_-(l)\Bigg\}. \tag{J.57}$$

A comparison between Eq. J.20b and Eq. J.57 demonstrates that both equations have the same form if $r = p$ and $s = q$. Also note that the terms $\hat{S}_{\alpha mn}$ are scalars and thus commute with the commutator itself. Applying the identity and renaming q as a dummy variable s, Eq. J.57 becomes

$$\sum_{kl} J(kl)[\hat{C}_m^\dagger(i)\hat{C}_n(i), \hat{S}_+(k)\hat{S}_-(l)] =$$
$$\sum_{kl} J(kl)\Bigg\{\hat{S}_+(k)\sum_{s}\left(\hat{C}_m^\dagger(i)\hat{C}_s(k)\hat{S}_{-ns}(l) - \hat{C}_s^\dagger(k)\hat{C}_n(i)\hat{S}_{-sm}(l)\right) +$$
$$+\sum_{s}\left(\hat{C}_m^\dagger(i)\hat{C}_s(k)\hat{S}_{+ns}(k) - \hat{C}_s^\dagger(k)\hat{C}_n(i)\hat{S}_{+sm}(k)\right)\hat{S}_-(l)\Bigg\}. \tag{J.58}$$

It is worthwhile to note that in order for the sum over s to be physically relevant, all indices in the triple terms must be equal. Thus for the second sum for example, $k = i$ while for the first term $k = l = i$, and thus Eq. J.58 can be rewritten as

$$\sum_{kl} J(kl)[\hat{C}_m^\dagger(i)\hat{C}_n(i), \hat{S}_+(k)\hat{S}_-(l)] =$$
$$\sum_{kl} J(kl)\Bigg\{\hat{S}_+(k)\sum_{s}\left(\hat{C}_m^\dagger(i)\hat{C}_s(k)\hat{S}_{-ns}(l) - \hat{C}_s^\dagger(k)\hat{C}_n(i)\hat{S}_{-sm}(l)\right)\delta_{kl}\delta_{ik} +$$
$$+\sum_{s}\left(\hat{C}_m^\dagger(i)\hat{C}_s(k)\hat{S}_{+ns}(k) - \hat{C}_s^\dagger(k)\hat{C}_n(i)\hat{S}_{+sm}(k)\right)\mathcal{S}_-(l)\delta_{ik}\Bigg\}. \tag{J.59}$$

By applying the sum over k, one obtains

$$\sum_{kl} J(kl)[\hat{C}_m^\dagger(i)\hat{C}_n(i), \hat{S}_+(k)\hat{S}_-(l)] =$$
$$\sum_l J(il) \Bigg\{ \hat{S}_+(l) \sum_s \left(\hat{C}_m^\dagger(i)\hat{C}_s(i)\hat{S}_{-ns}(i) - \hat{C}_s^\dagger(i)\hat{C}_n(i)\hat{S}_{-sm}(i) \right) +$$
$$+ \sum_s \left(\hat{C}_m^\dagger(i)\hat{C}_s(i)\hat{S}_{+ns}(i) - \hat{C}_s^\dagger(i)\hat{C}_n(i)\hat{S}_{+sm}(i) \right) \hat{S}_-(l) \Bigg\}. \tag{J.60}$$

By inserting the definition of $\hat{S}_\alpha$ (Eqs. J.15a-J.15c) using dummy indices q and p, whilst utilising the fact that the $\hat{S}_\alpha$ operators in Eq. J.60 are at site l and thus commute with site i, one obtains

$$\sum_{kl} J(kl)[\hat{C}_m^\dagger(i)\hat{C}_n(i), \hat{S}_+(k)\hat{S}_-(l)] =$$
$$\sum_l J(il) \sum_s [\hat{S}_{+ns}(i)\hat{C}_m^\dagger(i)\hat{C}_s(i) - \hat{S}_{+sm}(i)\hat{C}_s^\dagger(i)\hat{C}_n(i)] \sum_{pq} \hat{S}_{-qp}(l)\hat{C}^\dagger(l)\hat{C}_p(l)$$
$$+ \sum_l J(il) \sum_s [\hat{S}_{-ns}(i)\hat{C}_m^\dagger(i)\hat{C}_s(i) - \hat{S}_{-sm}(i)\hat{C}_s^\dagger(i)\hat{C}_n(i)] \sum_{pq} \hat{S}_{+qp}(l)\hat{C}^\dagger(l)\hat{C}_p(l) \tag{J.61}$$

which is identical to Eq. J.52 as stated above. By multiplying through, one obtains

$$\sum_{kl} J(kl)[\hat{C}_m^\dagger(i)\hat{C}_n(i), \hat{S}_+(k)\hat{S}_-(l)] =$$
$$\sum_l \sum_s \sum_{pq} J(il) \Big\{ \hat{S}_{+ns}(i)\hat{S}_{-qp}(l)\hat{C}_m^\dagger(i)\hat{C}_s(i)\hat{C}_q^\dagger(l)\hat{C}_p(l)$$
$$- \hat{S}_{+sm}(i)\hat{S}_{-qp}(l)\hat{C}_s^\dagger(i)\hat{C}_n(i)\hat{C}_q^\dagger(l)\hat{C}_p(l)$$
$$+ \hat{S}_{-ns}(i)\hat{S}_{+qp}(l)\hat{C}_m^\dagger(i)\hat{C}_s(i)\hat{C}_q^\dagger(l)\hat{C}_p(l)$$
$$- \hat{S}_{-sm}(i)\hat{S}_{+qp}(l)\hat{C}_s^\dagger(i)\hat{C}_n(i)\hat{C}_q^\dagger(l)\hat{C}_p(l) \Big\}. \tag{J.62}$$

It is important to note that Eq. J.62 produces terms with the following form $\hat{C}_m^\dagger(i)\hat{C}_n\hat{C}_q^\dagger(l)\hat{C}_p(l)$. Terms with this form represents mn and qp transitions at

sites i and l at the same time. If one assumes that only one site is being excited at a time, a Fock-type random phase approximation (RPA) can be applied [519–522]. Such an approximation is given by

$$\hat{C}_m^\dagger(i)\hat{C}_n\hat{C}_q^\dagger(l)\hat{C}_p(l) \simeq f_m(i)\delta_{ms}\hat{C}_q^\dagger(l)\hat{C}_p(l) + f_q(l)\delta_{pq}\hat{C}_m^\dagger(i)\hat{C}_s(i). \tag{J.63}$$

Inserting Eq. J.63 into Eq. J.62, one obtains

$$\begin{aligned}\sum_{kl} J(kl)[\hat{C}_m^\dagger(i)\hat{C}_n(i), \hat{S}_+(k)\hat{S}_-(l)] = \\ \sum_l\sum_s\sum_{pq} J(il)\Big\{\hat{S}_{+ns}(i)\hat{S}_{-qp}(l)(f_m(i)\delta_{ms}\hat{C}_q^\dagger(l)\hat{C}_p(l) + f_q(l)\delta_{pq}\hat{C}_m^\dagger(i)\hat{C}_s(i)) \\ -\hat{S}_{+sm}(i)\hat{S}_{-qp}(l)(f_s(i)\delta_{sn}\hat{C}_q^\dagger(l)\hat{C}_p(l) + f_q(l)\delta_{pq}\hat{C}_s^\dagger(i)\hat{C}_n(i)) \\ +\hat{S}_{-ns}(i)\hat{S}_{+qp}(l)(f_m(i)\delta_{ms}\hat{C}_q^\dagger(l)\hat{C}_p(l) + f_q(l)\delta_{pq}\hat{C}_m^\dagger(i)\hat{C}_s(i)) \\ -\hat{S}_{-sm}(i)\hat{S}_{+qp}(l)(f_s(i)\delta_{sn}\hat{C}_q^\dagger(l)\hat{C}_p(l) + f_q(l)\delta_{pq}\hat{C}_s^\dagger(i)\hat{C}_n(i))\Big\}.\end{aligned} \tag{J.64}$$

The equation above can be simplified by observing there is a δ_{pq} in four out of the eight terms in Eq. J.64. This observation reduces the sum over p, q to $p = q$. Recall that $\hat{S}_{\pm nn}$ must be zero since these represent transverse terms and thus any term with δ_{pq} can be neglected. Therefore the four remaining terms are

$$\begin{aligned}\sum_{kl} J(kl)[\hat{C}_m^\dagger(i)\hat{C}_n(i), \hat{S}_+(k)\hat{S}_-(l)] = \\ \sum_l\sum_s\sum_{pq} J(il)\Big\{\hat{S}_{+ns}(i)\hat{S}_{-qp}(l)(f_m(i)\delta_{ms}\hat{C}_q^\dagger(l)\hat{C}_p(l)) \\ -\hat{S}_{+sm}(i)\hat{S}_{-qp}(l)(f_s(i)\delta_{sn}\hat{C}_q^\dagger(l)\hat{C}_p(l)) \\ \hat{S}_{-ns}(i)\hat{S}_{+qp}(l)(f_m(i)\delta_{ms}\hat{C}_q^\dagger(l)\hat{C}_p(l)) \\ -\hat{S}_{-sm}(i)\hat{S}_{+qp}(l)(f_s(i)\delta_{sn}\hat{C}_q^\dagger(l)\hat{C}_p(l))\Big\}.\end{aligned} \tag{J.65}$$

Due to the presence of the Kronecker deltas, the index s is replaced by m or n for terms 2 and 4 or 1 and 3, respectively. Therefore, the final expression for the transverse commutator is

$$\sum_{kl} J(kl)[\hat{C}_m^\dagger(i)\hat{C}_n(i), \hat{S}_+(k)\hat{S}_-(l)] = \sum_l J(il) \left\{ \hat{S}_{+nm}(f_m - f_n) \sum_{pq} \hat{S}_{-qp}\hat{C}_q^\dagger(l)\hat{C}_p(l) + \hat{S}_{-nm}(f_m - f_n) \sum_{pq} \hat{S}_{+qp}\hat{C}_q^\dagger(l)\hat{C}_p(l) \right\}. \tag{J.66}$$

It should be noted that the site indices have been dropped for f since it assumed that in a perfect crystal the values of the single ion energy levels are identical.

J.3.3 Longitudinal Commutator

The longitudinal commutator, corresponding to the second term in Eq. J.27, is given by

$$\sum_{lk} J(kl)[\hat{C}_m^\dagger(i)\hat{C}_n(i), \hat{S}_z(k)\{\hat{S}_z(l) - 2\langle\hat{S}_z(l)\rangle\}] = + 2\sum_l J_{il}\hat{S}_{znm}(f_m - f_n) \sum_{pq} \hat{S}_{zpq}\hat{C}_q^\dagger(l)\hat{C}_p(l). \tag{J.67}$$

The derivation of Eq. J.67 consists of the observation that the first commutator of the LHS is identical to the commutator that was solved for the transverse terms. One major difference is that terms with δ_{pq} do not immediately cancel since $\hat{S}_{zpp}$ is not zero. These terms cancel due to the $-2\langle\hat{S}_z(l)\rangle$ contribution, leaving the identical contribution as the transverse terms but with an extra factor of 2 since $\hat{S}_{+nm}$ and $\hat{S}_{-nm}$ are now both $\hat{S}_{znm}$.

To demonstrate this cancellation, recognise that if one takes the commutator of the second term (ignoring the first for now), one obtains

$$\sum_{lk} J(kl) \left\{ -2\langle\hat{S}_z(l)\rangle[\hat{C}_m^\dagger(i)\hat{C}_n(i), \sum_{qp} \hat{S}_{zqp}(k)\hat{C}^\dagger(k)\hat{C}_p(k)] \right\}. \tag{J.68}$$

Pulling out the sum over qp, one obtains

$$\sum_{lk}\sum_{qp} J(kl)\left\{-2\langle\hat{S}_z(l)\rangle\hat{S}_{zqp}(k)[\hat{C}^\dagger_m(i)\hat{C}_n(i),\hat{C}^\dagger(k)\hat{C}_p(k)]\right\}. \tag{J.69}$$

Employing the commutator identity from Eq. J.20b, one obtains

$$\sum_{lk}\sum_{p} J(kl)\left\{-2\langle\hat{S}_z(l)\rangle(\hat{C}^\dagger_m(i)\hat{C}_p(k)\hat{S}_{znp}(k)-\hat{C}^\dagger_p(k)\hat{C}_n(i)\hat{S}_{zpm}(k))\right\}. \tag{J.70}$$

Replacing $\langle\hat{S}_z\rangle$ by its definition given by Eq. J.5, then one obtains

$$\sum_{lk}\sum_{p}\sum_{a} J(kl)\left\{-2(f_a(l)\hat{S}_{zaa}(l))(\hat{C}^\dagger_m(i)\hat{C}_p(k)\hat{S}_{znp}(k)-\hat{C}^\dagger_p(k)\hat{C}_n(i)\hat{S}_{zpm}(k))\right\} \tag{J.71}$$

and by relabelling of the indices a as p and p as s, these terms are identical to the terms containing δ_{pq} in Eq. J.64.

J.3.4 Determination of $\langle[\hat{A},\hat{B}]\rangle$

Recall that in the equation-of-motion given by Eq. J.45, the first term is $\langle[\hat{A},\hat{B}]\rangle$ where $\hat{A}=\hat{C}_m(i)\hat{C}_n(i)$ and $\hat{B}=\hat{S}_\beta$, thus the expectation value can be expressed as

$$\langle[\hat{C}_m(i)\hat{C}_n(i),\sum_{pq}\hat{S}_{\beta pq}(j)\hat{C}^\dagger_p(j)\hat{C}_q(j)]\rangle. \tag{J.72}$$

Pulling out the sum over pq and $\hat{S}_{\beta pq}$, one obtains

$$\langle\sum_{pq}[\hat{C}_m(i)\hat{C}_n(i),\hat{C}^\dagger_p(j)\hat{C}_q(j)]\hat{S}_{\beta pq}(j)\rangle. \tag{J.73}$$

Utilising the commutation identity (Eq. J.20b), one obtains

$$\langle \sum_{q} \Big\{ \hat{C}_m^\dagger(i)\hat{C}_q(i)\hat{S}_{\beta nq}(j) - \hat{C}_q^\dagger(i)\hat{C}_n(i)\hat{S}_{\beta qm}(j) \Big\} \rangle. \tag{J.74}$$

It is clear that all the indices must be equal to one another for the expression above to be non-zero, thus a δ_{ij} must be introduced, yielding

$$\langle \sum_{q} \Big\{ \hat{C}_m^\dagger(i)\hat{C}_q(i)\hat{S}_{\beta nq}(i)\delta_{ij} - \hat{C}_q^\dagger(i)\hat{C}_n(i)\hat{S}_{\beta qm}(i)\delta_{ij} \Big\} \rangle. \tag{J.75}$$

Separating the two terms, the first term will be first addressed. Pulling the sum and $\hat{S}_{\beta nq}$ out of the expectation value since this corresponds to a scalar, one obtains

$$\sum_{q} \hat{S}_{\beta nq}(i)\delta_{ij}\langle \hat{C}_m^\dagger(i)\hat{C}_q(i) \rangle. \tag{J.76}$$

Notice that based on the definition of the total Hamiltonian given by Eq. J.27, the term $\hat{C}_m^\dagger(i)\hat{C}_q(i)$ is simply an operator. By the definition of the expectation value, the equation above is equivalent to

$$\sum_{q} \hat{S}_{\beta nq}\delta_{ij} \sum_{m} f_m(i)\langle m|\hat{C}_m^\dagger(i)\hat{C}_q(i)|m\rangle. \tag{J.77}$$

But this inner product will only be non-zero if $q = m$, therefore the above can be rewritten as

$$\sum_{q}\sum_{m} \hat{S}_{\beta nq}(i)\delta_{ij} f_m(i)\langle m|\hat{C}_m^\dagger(i)\hat{C}_q(i)\delta_{qm}|m\rangle \tag{J.78}$$

which reduces the sum over q to

$$\sum_{m} \hat{S}_{\beta nm}(i)\delta_{ij} f_m(i)\langle m|\hat{C}_m^\dagger(i)\hat{C}_m(i)|m\rangle. \tag{J.79}$$

But based on the definition of the single ion Hamiltonian, $\langle m|\hat{C}_m^\dagger(i)\hat{C}_m(i)|m\rangle$

must be unity and thus the first term is equal to

$$\hat{S}_{\beta nm}(i)\delta_{ij}f_m(i), \tag{J.80}$$

where the sum over m is implied based on the definition of G^β. The process repeated for the second term simply yields

$$\hat{S}_{\beta nm}(i)\delta_{ij}f_n(i), \tag{J.81}$$

and thus a sum of both terms yields

$$\langle[\hat{A},\hat{B}]\rangle = (f_m(i) - f_n(i))\hat{S}_{\beta nm}(i)\delta_{ij}. \tag{J.82}$$

J.3.5 Final Expression for $G^{\alpha\beta}$

By first combining the expressions for all three commutators: diagonal, transverse and longitudinal given by Eqs. J.47, J.66 and J.67, respectively, with the first inner product given by Eq. J.82 and secondly, removing all site indices since it is assumed that all sites are equal for a perfect lattice — a fact reflected by the fact that each expression for the diagonal, transverse, longitudinal and first commutator $\langle[\hat{A},\hat{B}]\rangle$ given at the beginning of their respective subsections have no site indices — the final expression for the inter-level susceptibility is given by

$$\begin{aligned}\omega\hat{G}^\beta(n,m,i,j,\omega) = (f_m - f_n)\hat{S}_{\beta nm}\delta_{ij} + (\omega_n - \omega_m)\hat{G}^\beta(n,m,i,j,\omega)\\ + \sum_l J(il)[\hat{S}_{+nm}(f_m - f_n)\sum_{pq}\hat{S}_{-qp}\hat{G}^\beta(q,p,l,j,\omega)\\ + \hat{S}_{-nm}(f_m - f_n)\sum_{pq}\hat{S}_{+qp}\hat{G}^\beta(q,p,l,j,\omega)]\\ +2\sum_l J(il)\hat{S}_{znm}(f_m - f_n)\sum_{qp}\hat{S}_{zqp}\hat{G}^\beta(q,p,l,j,\omega).\end{aligned} \tag{J.83}$$

The functional dependence of G^β on j requires further explanation. Recall from Eq. J.37 that the second term on the RHS is in fact proportional to $\langle[[\hat{S}_\alpha(i,t),\hat{\mathcal{H}}],\hat{S}_\beta(j,0)]\rangle$. So far, only the inner commutator has been addressed.

The second term which provides the β index, also provides the j site dependence as well. To be more precise, the definition of the Green's function (*e.g.* Eq. J.28 after being Fourier transformed into ω space) as

$$G^{\alpha\beta} = \langle [\hat{S}_\alpha(i,\omega), \hat{S}_\beta(j,0)] \rangle \tag{J.84}$$

can be utilised. In the current case, there is no α index because it has been factored out as $\sum_{mn} \hat{S}_{\alpha mn}$ *via* the definition of G^β. But there still remains an operator of the form $\hat{C}_q^\dagger \hat{C}_p$, both of which have an implicit l dependence (refer to the equations before the indices were dropped) and with the additional $\hat{S}_\beta$ operator that provides j-dependence. The ω-dependence comes from the definition of the Green's function. This is seen explicitly in the example presented above.

One can define the single site susceptibility, $g^{\alpha\beta}$ by the following algorithm:

- set $J(il) = 0$ in Eq. J.83,
- Fourier transform from real to **Q**-space,
- multiply by $\hat{S}_{\alpha mn}$,
- divide by $\omega - \omega_n + \omega_m$, and
- sum over m, n, then one obtains

$$g^{\alpha\beta}(\mathbf{Q},\omega) \equiv g^{\alpha\beta}(\omega) = \sum_{mn} \frac{\hat{S}_{\alpha mn}\hat{S}_{\beta nm}(f_m - f_n)}{\omega - \omega_n + \omega_m}. \tag{J.85}$$

Applying the same algorithm to Eq. J.83 but with a non-zero $J(ij)$, one obtains

$$\begin{aligned} G^{\alpha\beta}(\mathbf{Q},\omega) = g^{\alpha\beta}(\omega) + g^{\alpha+}(\omega)J(\mathbf{Q})G^{-\beta}(\mathbf{Q},\omega) + \\ g^{\alpha-}(\omega)J(\mathbf{Q})G^{+\beta}(\mathbf{Q},\omega) + 2g^{\alpha z}(\omega)J(\mathbf{Q})G^{z\beta}(\mathbf{Q},\omega). \end{aligned} \tag{J.86}$$

Note that the only non-zero single site susceptibilities for Co^{2+} in such a highly symmetric environment are: g^{+-}, g^{-+} and g^{zz} [20, 346]. Going through all

possible combinations of α, β, one obtains only three non-zero Green's functions:

$$G^{+-}(\mathbf{Q},\omega) = g^{+-}(\omega) + g^{+-}(\omega)J(\mathbf{Q})G^{+-}(\mathbf{Q},\omega) \tag{J.87a}$$

$$G^{-+}(\mathbf{Q},\omega) = g^{-+}(\omega) + g^{-+}(\omega)J(\mathbf{Q})G^{-+}(\mathbf{Q},\omega) \tag{J.87b}$$

$$G^{zz}(\mathbf{Q},\omega) = g^{zz}(\omega) + 2g^{zz}(\omega)J(\mathbf{Q})G^{zz}(\mathbf{Q},\omega) \tag{J.87c}$$

It is important to note that G^{++} and G^{--} have not been included in the above expressions because both must be zero. One can rationalise this statement by recalling that a Green's function can be interpreted as a simultaneous tracking of both excitations and their corresponding holes [531]. Performing either $+,+$ or $-,-$ operations do not correspond to a physically relevant process. Another way to prove such a statement is to use the definition of $G^{\alpha\beta}$ in Eq. J.86. For example, set $\alpha = \beta = +$, one will obtain

$$G_{ij}^{++}(\mathbf{Q},\omega) = g_{ij}^{+-}(\omega)J(\mathbf{Q})G_{ij}^{++}(\mathbf{Q},\omega).. \tag{J.88}$$

Eq. J.88 must be true $\forall\ \{\mathbf{Q},\omega,i,j\}$ and thus $g_{ij}^{+-}(\omega)J(\mathbf{Q}) = 1,\ \forall\ \{\mathbf{Q},\omega,i,j\}$, corresponding to a non-physically relevant situation. Instead, the trivial solution to Eq. J.88 is that $G_{ij}^{++}(\mathbf{Q},\omega) = 0,\ \forall\{\mathbf{Q},\omega,i,j\}$. The same logic can be applied to $G_{ij}^{--}(\mathbf{Q},\omega)$.

Finally, Eqs. J.87a-J.87c may be succinctly summarised as

$$G_{ij}^{\alpha\beta}(\mathbf{Q},\omega) = \delta_{ij}g_i^{\alpha\beta}(\omega) + \sum_k g_i^{\alpha\beta}(\omega)\Phi J_{i,i+k}(\mathbf{Q})G_{i+k,j}^{\alpha\beta}(\mathbf{Q},\omega), \tag{J.89}$$

using the single hopping model describing transitions between sites i and j that are coupled by J, where the prefactor

$$\Phi = \begin{cases} 1 & \text{when } \alpha = + \text{ or } - \\ 2 & \text{when } \alpha = z, \end{cases}$$

if α, β is restricted to the following combinations: $+-$, $-+$ or zz.

Appendix K

Reprint of Publications

Evidence for the confinement of magnetic monopoles in quantum spin ice

P.M. Sarte, A.A. Aczel, G. Ehlers, C. Stock, B.D. Gaulin, C. Mauws, M.B. Stone, S. Calder, S.E. Nagler, J.W. Hollett, H.D. Zhou, J.S. Gardner, J.P. Attfield and C.R. Wiebe, *J. Phys.: Condens. Matter*, **29** 45LT01 (2017). Reproduced from [1] with permission, copyrighted by the Institute of Physics.

Ordered magnetism in the intrinsically decorated $j_{\text{eff}} = \frac{1}{2}$ α-CoV_3O_8

P.M. Sarte, A.M. Arévalo-López, M. Songvilay, D. Le, T. Guidi, V. Garcìa-Sakai, S. Mukhopadhyay, S.C. Capelli, W.D. Ratcliff, K.H. Hong, G.M. McNally, E. Pachoud, J.P. Attfield and C. Stock, *Phys. Rev. B* **98**, 224410 (2018). Reproduced from [2] with permission, copyrighted by the American Physical Society.

Disentangling orbital and spin exchange interactions for Co^{2+} on a rocksalt lattice

P.M. Sarte, R.A. Cowley, E.E. Rodriguez, E. Pachoud, D. Le, V. Garcìa-Sakai, J. W. Taylor, C.D. Frost, D. Prabhakaran, C. MacEwen, A. Kitada, A.J. Browne, M. Songvilay, Z. Yamani, W.J.L. Buyers, J.P. Attfield and C. Stock, *Phys. Rev. B* **98**, 024415 (2018). Reproduced from [3] with permission, copyrighted by the American Physical Society.

Letters

IOP Publishing

Journal of Physics: Condensed Matter

J. Phys.: Condens. Matter **29** (2017) 45LT01 (6pp)

https://doi.org/10.1088/1361-648X/aa8ec2

Letter

Evidence for the confinement of magnetic monopoles in quantum spin ice

P M Sarte[1,2], A A Aczel[3], G Ehlers[3], C Stock[2,4], B D Gaulin[5,6,7], C Mauws[12], M B Stone[3], S Calder[3], S E Nagler[3], J W Hollett[8], H D Zhou[9], J S Gardner[10,11], J P Attfield[1,2] and C R Wiebe[5,6,8,12,13]

[1] School of Chemistry, University of Edinburgh, Edinburgh EH9 3FJ, United Kingdom
[2] Centre for Science at Extreme Conditions, University of Edinburgh, Edinburgh EH9 3FD, United Kingdom
[3] Quantum Condensed Matter Division, Oak Ridge National Laboratory, Oak Ridge, TN 37831, United States of America
[4] School of Physics and Astronomy, University of Edinburgh, Edinburgh EH9 3FD, United Kingdom
[5] Department of Physics and Astronomy, McMaster University, Hamilton, ON L8S 4M1, Canada
[6] Canadian Institute for Advanced Research, Toronto, ON M5G 1Z8, Canada
[7] Brockhouse Institute for Materials Research, McMaster University, Hamilton, ON, L8S 4M1, Canada
[8] Department of Chemistry, University of Winnipeg, Winnipeg, MB R3B 2E9 Canada
[9] Department of Physics and Astronomy, University of Tennessee, Knoxville, TN 37996, United States of America
[10] Center for Condensed Matter Sciences, National Taiwan University, Taipei 10617, Taiwan
[11] Neutron Group, National Synchrotron Radiation Research Center, Hsinchu 30076, Taiwan
[12] Department of Chemistry, University of Manitoba, Winnipeg, MB R3T 2N2, Canada

E-mail: ch.wiebe@uwinnipeg.ca

Received 14 August 2017, revised 21 September 2017
Accepted for publication 25 September 2017
Published 20 October 2017

Abstract

Magnetic monopoles are hypothesised elementary particles connected by Dirac strings that behave like infinitely thin solenoids (Dirac 1931 *Proc. R. Soc.* A **133** 60). Despite decades of searching, free magnetic monopoles and their Dirac strings have eluded experimental detection, although there is substantial evidence for deconfined magnetic monopole quasiparticles in spin ice materials (Castelnovo *et al* 2008 *Nature* **326** 411). Here we report the detection of a hierarchy of unequally-spaced magnetic excitations *via* high resolution inelastic neutron spectroscopic measurements on the quantum spin ice candidate $Pr_2Sn_2O_7$. These excitations are well-described by a simple model of monopole pairs bound by a linear potential (Coldea *et al Science* **327** 177) with an effective tension of 0.642(8) K $\cdot$ Å^{-1} at 1.65 K. The success of the linear potential model suggests that these low energy magnetic excitations are direct spectroscopic evidence for the confinement of magnetic monopole quasiparticles in the quantum spin ice candidate $Pr_2Sn_2O_7$.

Keywords: neutron scattering, spin ice, geometrically frustrated magnetism, quantum spin ice, magnetic monopoles

S Supplementary material for this article is available online

(Some figures may appear in colour only in the online journal)

[13] Author to whom any correspondence should be addressed.

1. Introduction

Magnetic monopoles remained at the periphery of physics until Dirac published his quantum theory of magnetic charge [1] in which he envisioned a monopole as the end of an infinitesimally thin solenoid construct known as a Dirac string. Dirac proposed that not only were magnetic monopoles consistent with quantum theory, but their existence would result in the quantisation of electrical charge [1, 2]. While the latter has been verified experimentally [3], the identification of magnetic monopoles has been challenging. Establishing the existence of this elusive elementary particle would lead to a beautiful symmetrisation of Maxwell's equations and validate several modern physical theories [4].

Recently, the discovery of a class of magnets known as spin ices has made the study of magnetic monopole quasiparticles viable [2, 5, 6]. Spin ices are found in a series of magnetic pyrochlore oxides $A_2^{3+}B_2^{4+}O_7$, which have moments residing on the A-site, corner-sharing tetrahedra sublattice. At low temperatures, the moments assume a two-in/two-out short-ranged magnetically ordered state as shown in figure 1(a), possessing Pauling's configurational entropy [7]. Castelnovo *et al* [5] first proposed that dipolar spin ices (DSIs) may host mobile mangetic monopole quasiparticles as illustrated in figure 1(b). These monopoles are expected to interact *via* a magnetic Coulomb law suggesting deconfinement [2, 5], and the strings connecting them in pairs (see figures 1(c) and (d)) have not been easily measurable. Consequently, although there is mounting experimental evidence [2, 8] supporting the existence of monopoles in the DSIs, the exact nature of the interaction between these monopoles is still under active investigation [9].

In an attempt to measure interactions between magnetic monopoles, our attention has shifted to quantum spin ices (QSIs) [10–14]. This family of materials differs from DSIs in the nature of the interactions between the magnetic moments [10], as their magnetic Hamiltonians consist of transverse coupling terms leading to significant fluctuations of the moments away from the local [1 1 1] quantisation axes. As a result, the correlation time of the two-in/two-out state at low temperatures tends to be much shorter for a QSI as compared to its DSI counterparts [15]. There are predictions [16] for the properties of monopoles in QSIs, but their detection has remained elusive. We report here evidence for the direct observation of interacting magnetic monopoles in $Pr_2Sn_2O_7$ using inelastic neutron spectroscopy. Our measurements allow for both an estimate of the monopole pair creation energy and a lower bound of the effective tension between monopoles.

2. Experimental

Polycrystalline samples of $Pr_2Sn_2O_7$ were prepared by a standard solid-state reaction of stoichiometric amounts of Pr_6O_{11} (99.99%, Alfa Aesar) and SnO_2 (99.99%, Alfa Aesar). The powder reagents were mixed together, finely ground and pressed into a pellet using a uniaxial press. The pellets were placed in an alumina crucible and were pre-reacted by heating in air at 1000 °C for 24 h. The pellets were then reground, repelletised and heated in air at 1400 °C for approximately 48 h with intermittent grindings until room temperature powder x-ray diffraction measurements with a Bruker D2 phaser laboratory diffractometer at the University of Edinburgh using a Cu $K_{\alpha_{1,2}}$ source confirmed no discernable impurities.

Low energy transfer inelastic neutron scattering experiments were performed on the direct-geometry time-of-flight cold neutron chopper spectrometer CNCS at the spallation neutron source (SNS) at Oak Ridge National Laboratory (ORNL). Approximately five grams of polycrystalline $Pr_2Sn_2O_7$ and select members of $Pr_2Sn_{2-x}Ti_xO_7$ ($x = 0.40$ and 0.60) were sealed in aluminium cans under a helium atmosphere for the experiment. The sample cans were mounted on the CNCS automatic three sample rotator stick (SS-003) with a boron nitride (BN) spacer adapted for a top loading 100 mm orange cryostat (CRYO-006). Measurements utilised incident energies $\hbar\omega_i$ of 3.32 meV and 25 meV in high flux mode, providing an energy resolution at the elastic line of approximately 0.01 and 2 meV, respectively. Additional measurements were collected with an incident energy of 4.1 meV in medium resolution mode, providing an energy resolution at the elastic line of approximately 0.08 meV. An empty aluminium can was also measured for approximately half the counting time at identical experimental conditions, and the resulting spectra were subtracted from the corresponding sample spectra. The high flux and medium resolution modes were accomplished by spinning the high speed double disk chopper located just before the sample at a frequency of 300 Hz and 240 Hz, respectively.

3. Results and discussion

The pyrochlore $Pr_2Sn_2O_7$ has been well characterised as a potential QSI candidate [10, 17]. Despite susceptibility measurements suggesting net ferromagnetic interactions ($\theta_{CW} = 0.3$ K), there is an absence of long-range magnetic order [17, 18]. The ground state crystal field scheme is well understood [17, 19], consisting of a thermally-isolated non-Kramers doublet. The lower Pr^{3+} effective moment of 2.61(1) μ_B, as compared to $\sim$10 μ_B for DSIs, implies $Pr_2Sn_2O_7$ is more susceptible to quantum fluctuations [19]. In fact, low energy spin fluctuations persist to well below 1 K and possess an anomalously low activation energy, which is attributed to the quantum nature of the system [17].

We have remeasured these low-energy spin fluctuations in a well-characterised powder sample of $Pr_2Sn_2O_7$ using the cold neutron chopper spectrometer (CNCS). Broad, quasi-elastic scattering previously measured [17] was confirmed in our sample at 1.65 K. However, the high resolution and time-integrated flux of the CNCS also enabled the observation of a discernible fine structure to the scattering, as shown in figure 2. A hierarchy of nearly-dispersionless excitations was identified and measured up to $\hbar\omega \sim 2$ meV. These excitations are also visible with different incident energies while obeying detailed balance, confirming they are not spurious in origin. Furthermore, as shown in figure 3, they exhibit a remarkably

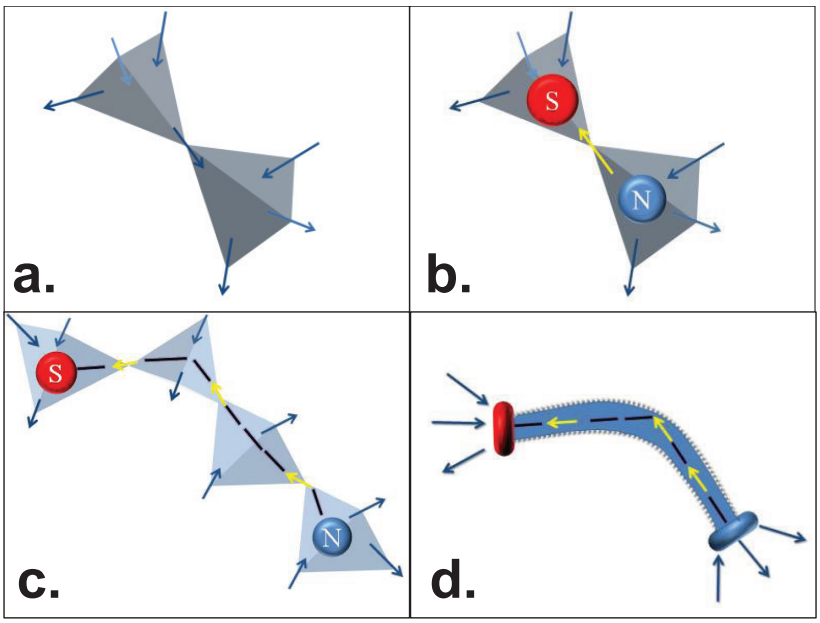

Figure 1. Local spin configurations in quantum spin ices leading to magnetic monopoles and Dirac strings. (a) Schematic of one possible two-in/two-out spin ice configuration in adjacent tetrahedra of the pyrochlore lattice. (b) A defect spin ice state is created by the flipping of a spin labeled in yellow and results in the creation of a magnetic monopole pair labeled N and S. (c) The monopole pair can separate further *via* adjacent spin flips. (d) A schematic of an effective 'Dirac string', which consists of an infinitesimally thin solenoid (one unit of flux width) connecting the monopole pair.

similar temperature dependence to the magnetic diffuse scattering observed in the elastic channel. This similar temperature dependence suggests that the excitations are associated with the quantum spin ice state. Finally, these modes are not due to chemical disorder, as this is well understood through doping studies of $Pr_2Sn_{2-x}Ti_xO_7$ and related materials [20]. Please refer to *supplementary discussion* section 3 for further details.

As summarised by figure 2, the excitation spectrum was analysed by fitting the data to a series of free-width Lorentzians convolved with fixed-width Gaussians. The lowest-energy Lorentzian function models a prominent quasi-elastic background centered at 0.2 meV, previously attributed to quantum tunnelling between degenerate spin ice configurations [17]. The higher-energy Lorentzians represent the five quantised excitations observed here. The analysis reveals that these modes are not evenly-spaced and decrease in relative intensity with increasing temperature, which taken together rule out a possible quantum harmonic oscillator interpretation [21] and imply a magnetic origin instead. We therefore consider possible mechanisms that lead to quantised, unevenly-spaced magnetic excitations. The dynamic response for the spin defects of a quasi-one-dimensional Ising $S = \frac{1}{2}$ spin chain such as $CoNb_2O_6$ [22] below the magnetic ordering temperature has the desired characteristics. While the spin defects are created in pairs, they are ultimately bound together in the ordered state due to an attractive linear potential arising from the finite molecular field [23–25]. A similar spin defect confinement model may apply to $Pr_2Sn_2O_7$, under the assumption that the relevant defects in this case are magnetic monopole quasiparticles and not solitons, while the linear confining potential may be a consequence of the QSI state. Note that the analogy between spin defects and monopoles in a spin ice has been discussed previously [2, 6]. If the monopole confinement model is valid for $Pr_2Sn_2O_7$, then the energies of the excitations should be described by the following:

$$\hbar\omega_n = 2\hbar\omega_o + z_n\lambda^{\frac{2}{3}}\left(\frac{\hbar^2}{\mu}\right)^{\frac{1}{3}}, \qquad (1)$$

where n is a positive integer, μ is the reduced mass, $\hbar\omega_n$ is the n^{th} excitation energy, $2\hbar\omega_o$ is the energy cost to produce a pair of monopoles, λ is an effective tension and z_n are the negative zeros of the Airy function [22, 26]. Furthermore, if one fixes μ to the appropriate value based on previous work by Pan *et al* [27] on another quantum spin ice candidate $Yb_2Ti_2O_7$, then the linear relationship between $\hbar\omega_n$ and z_n also provides an estimate for the lower bound of the effective tension λ between monopoles via the slope of equation (1). Please refer to *supplementary discussion sections 3.3–3.5* for further details.

Figure 4(a) plots the observed energy levels versus the excitation number to facilitate a direct comparison between three different candidate scenarios. Two possibilities, the monopole confinement and QHO [21] models, have already been discussed in detail above. We consider a third model here, based on localised high S clusters. The magnetic excitation spectrum for an isolated spin cluster also consists of a series of quantised energy levels, and the spacing between the modes

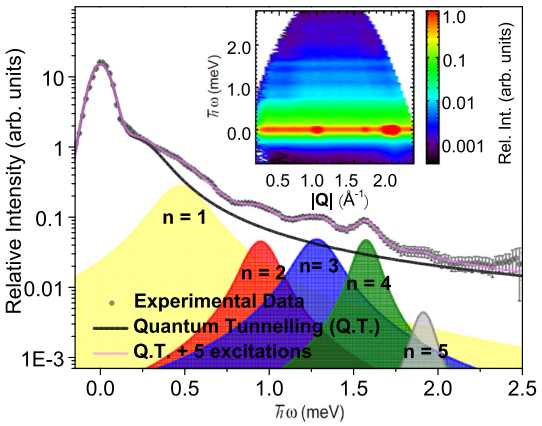

Figure 2. Fine structure in the low energy excitation spectrum of $Pr_2Sn_2O_7$. A $|\mathbf{Q}|$-integrated ($|\mathbf{Q}| = [1.0, 1.5]$ Å^{-1}) cut along $\hbar\omega$ of (inset) the empty aluminium can-subtracted $S(|\mathbf{Q}|, \omega)$ spectrum of polycrystalline $Pr_2Sn_2O_7$ at 1.65 K with an incident energy $\hbar\omega_i = 3.32$ meV on the CNCS operating in high flux mode, displaying unequally-spaced nearly-dispersionless excitations. High flux mode was accomplished by spinning the high speed double disk chopper located just before the sample at a frequency of 300 Hz. A fitting routine, as described in *supplementary discussion section 3.3.* (stacks.iop.org/JPhysCM/29/45LT01/mmedia), was applied exclusively to positive energy transfers with the fit to each excitation shown and labelled by its quantum number n. The strong, broad Lorentzian feature centered at approximately 0.2 meV was observed in previous work [17] and is attributed to quantum tunnelling between degenerate spin ice configurations. The relative intensity axis is presented on a logarithmic scale for both the constant $|\mathbf{Q}|$-cut and $S(|\mathbf{Q}|, \omega)$ spectrum inset to assist with data visualisation due to the relatively low intensity of the excitations as compared to the elastic line.

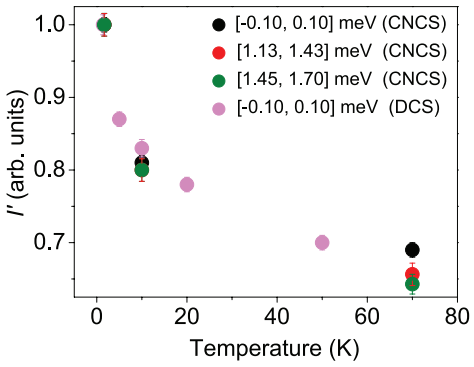

Figure 3. Temperature dependence of the magnetic scattering in $Pr_2Sn_2O_7$. Comparison of the temperature dependence of the normalised integrated intensity I' of the magnetic diffuse scattering and the two lowest energy magnetic excitations observed on the CNCS. For the purposes of comparison, the temperature dependence of the integrated intensity of the magnetic diffuse scattering from previous DCS data [17] is also shown. Both data sets are integrated over identical ranges in $|\mathbf{Q}| = [0.35, 1.75]$ Å^{-1}. The similar temperature dependence of all four data sets suggests that the low energy magnetic excitations are associated with the quantum spin ice state. Please refer to *supplementary discussion section 3.4.* for further details.

can be non-trivial or follow the simple relationship $\hbar\omega_n \propto n^2$ depending on the specific details of the magnetic Hamiltonian [28, 29]. We fit our data to each of these models with the phenomenological expression $\hbar\omega_n = A + Bx_n$, where A and B are constants and x_n is n, n^2, or z_n for the QHO, localised spin cluster or monopole confinement models, respectively. The solid curves in figure 4(a) represent the best fit to each of the models and they clearly illustrate that the monopole confinement model provides the best agreement. Additional details are presented in table 1. Furthermore, a plot of $\hbar\omega_n$ versus z_n, as shown in figure 4(b), produces a linear relationship in agreement with the predictions of this model [22]. Therefore, we interpret these excitations as direct spectroscopic evidence of interacting magnetic monopoles within the pyrochlore lattice.

The linear fit shown in figure 4(b) yields zero as an estimate for $2\hbar\omega_o$ and a lower bound of 0.642(8) K · Å^{-1} for the effective tension between monopoles at 1.65 K. Some physical insights can be made from the measurement of these two parameters. Firstly, the value of the tension is positive and non-negligible, implying that the monopoles are confined $Pr_2Sn_2O_7$ unlike in DSIs [2, 6]. Secondly, the application of an identical analysis algorithm to data collected at 10 K

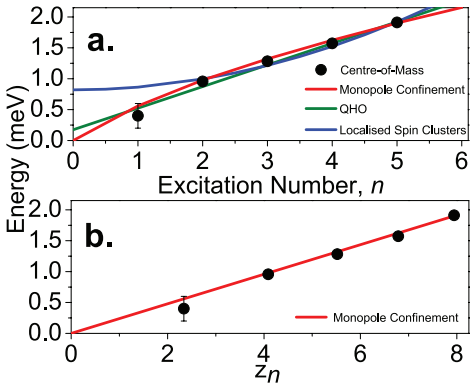

Figure 4. Validation of the monopole confinement model for $Pr_2Sn_2O_7$. (a) The direct comparison between the observed low energy magnetic excitations at 1.65 K and the predicted behaviour from three competing models: quantum harmonic oscillator [21], localised spin clusters [29], and monopole confinement [22]. The predicted values of $\hbar\omega$ for each model were obtained by fitting the corresponding observed values to each model's fitting function as described in the main text, and are connected by interpolated lines as a guide to the eye. The calculated goodness-of-fit metric χ^2_ν is the lowest for the monopole confinement model. (b) The plot of excitation energies against the negative zeros of the Airy function z_n exhibits linear behaviour as predicted by the monopole confinement model [22]. A least squares fit with the linear equation (1) in the main text (shown by the solid red line in both panels (a) and (b)) yielded a lower bound for the effective tension λ of 0.642(8) K · Å^{-1} and a monopole pair creation energy $2\hbar\omega_o$ of 0 meV at 1.65 K (see *supplementary discussion sections 3.5.2. and 3.5.3.*).

Table 1. Comparison between the observed and predicted values of the energy transfer $\hbar\omega$ for the quantum harmonic oscillator, localised spin cluster and monopole confinement models at 1.65 K. The calculated values were obtained by fitting the five observed low energy excitations to the functional form of the individual models, with further details of the fitting described in the main text. Numbers in parentheses indicate statistical errors. The goodness-of-fit metric χ^2_ν (see *supplementary discussion section 3.3.*) for each model is provided to enable quantitative comparison.

Model / Mode	$n = 1$	$n = 2$	$n = 3$	$n = 4$	$n = 5$
Observed (1.65 K)	0.4(2)	0.96(2)	1.28(4)	1.57(2)	1.912(9)
Monopole confinement ($\chi^2_\nu = 5.7$)	0.559(5)	0.978(8)	1.32(1)	1.62(1)	1.90(2)
Quantum harmonic oscillator ($\chi^2_\nu = 22$)	0.524(5)	0.873(9)	1.22(1)	1.57(2)	1.92(2)
Localised spin clusters ($\chi^2_\nu = 8.6$)	0.86(6)	1.00(7)	1.22(9)	1.5(1)	1.9(1)

yields a larger lower bound of 0.667(8) K $\cdot$ Å^{-1} for the effective tension, an increase that would be expected if the confining potential was attributed—to some extent—to the spin ice state. Thirdly, the value of $\lambda \sim$ 0.6 K$\cdot$ Å^{-1} is surprisingly large for the expected energy scale with $J \sim 1$ K [17]. In fact, the energy cost to separate two monopoles by the distance between the centres of adjacent Pr^{3+} tetrahedra corresponds to approximately a temperature scale of 3 K. This strong tension prevents the propagation of monopoles over long distances. The confinement of these monopoles can be roughly quantified, since exact analytical solutions for the Schrödinger equation with an $|x|$-potential are known [30]. The expectation value $\langle|x|\rangle$ for the highest energy excitation clearly observed, $n = 5$, corresponds to a relatively short distance of approximately 20 Å, or two unit cells. Finally, it should be noted that although the linear fit of both 1.65 K and 10 K data yields a value of zero (within error) as an estimate of $2\hbar\omega_o$, its absolute value is extremely sensitive to the energy of the first excitation and thus should be interpreted with caution. Please refer to *supplementary discussion section 3.5.* for further details.

4. Conclusion

High resolution cold inelastic neutron scattering measurements on polycrystalline $Pr_2Sn_2O_7$ have revealed a previously unreported fine structure to the low energy excitation spectrum consisting of a series of unevenly spaced nearly-dispersionless magnetic excitations. A quantum confinement model with a linear potential $\lambda|x|$ accounts for the fine structure suggesting these magnetic excitations are a direct spectroscopic observation of interacting magnetic monopole quasiparticles resulting from a finite tension between them. One natural extension of this work would be to remeasure the low energy dynamics of other QSI candidates (e.g. $Pr_2Zr_2O_7$ [31]) to determine if these systems exhibit similar non-negligible monopole tensions, while another prospect is to explore the effects of external perturbations on the tension such as the application of external magnetic fields and pressure. The success of the monopole confinement model for $Pr_2Sn_2O_7$ encourages future studies on QSIs with the ultimate goal of understanding exactly how monopole confinement affects other physical properties of QSIs.

Acknowledgments

We would like to acknowledge K H Hong, A J Browne, G M McNally, D Le and S E Maytham for helpful comments and discussions. This work was supported by NSERC, ACS, PRF, CFI, NSF, STFC and EPSRC. PMS acknowledges the University of Edinburgh for funding through the Global Research and Principal's Career Development Scholarships and the Canadian Centennial Scholarship Fund. CRW acknowledges financial support from the CRC (Tier II) program, PRF, CIFAR and NSERC. JWH and CM acknowledges financial support from NSERC. JPA and CS acknowledges financial support from the STFC, EPSRC and the ERC. Concerning previously obtained data from the DCS, CRW and HDZ acknowledge financial support from the NSF, the EIEG program (FSU) and the state of Florida. We acknowledge the support of the National Institute of Standards and Technology, US Department of Commerce, in providing the neutron research facilities used in this work. A portion of this research at Oak Ridge National Laboratory's Spallation Neutron Source was sponsored by the Scientific User Facilities Division, Office of Basic Energy Sciences, US Department of Energy. Finally, the authors thank the Carnegie Trust for the Universities of Scotland for providing facilities and equipment for chemical synthesis.

ORCID iDs

A A Aczel https://orcid.org/0000-0003-1964-1943
C Mauws https://orcid.org/0000-0003-1826-6432
M B Stone https://orcid.org/0000-0001-7884-9715
C R Wiebe https://orcid.org/0000-0002-3681-0182

References

[1] Dirac P A M 1931 *Proc. R. Soc.* A **133** 60
[2] Morris D J P *et al* 2009 *Science* **326** 411
[3] Millikan R A 1913 *Phys. Rev.* **2** 109
[4] Acharya B *et al* 2014 *Int. J. Mod. Phys.* B **29** 1430050
[5] Castelnovo C, Moessner R and Sondhi S 2008 *Nature* **451** 42
[6] Bramwell S T, Giblin S R, Calder S, Aldus R, Prabhakaran D and Fennell T 2009 *Nature* **461** 956
[7] Ramirez A P, Hayashi A, Cava R J, Siddharthan R and Shastry B S 1999 *Nature* **399** 333

[8] Fennell T, Deen P P, Wildes A R, Schmalzl K, Prabhakaran D, Boothroyd A T, Aldus R J, McMorrow D F and Bramwell S T 2009 *Science* **326** 415
[9] Paulsen C, Giblin S R, Lhotel E, Prabhakaran D, Matsuhira K and Bramwell S T 2016 *Nat. Phys.* **12** 661
[10] Gingras M J P and McClarty P A 2014 *Rep. Prog. Phys.* **77** 056501
[11] Sibille R, Lhotel E, Hatnean M C, Balakrishnan G, Fåk B, Gauthier N, Fennell T and Kenzelmann M 2016 *Phys. Rev.* B **94** 024436
[12] Wen J-J *et al* 2017 *Phys. Rev. Lett.* **118** 107206
[13] Lee S, Onoda S and Balents L 2012 *Phys. Rev.* B **86** 104412
[14] Benton O, Sikora O and Shannon N 2012 *Phys. Rev.* B **86** 075154
[15] Ehlers G, Cornelius A L, Orendac M, Kajnakova M, Fennell T, Bramwell S T and Gardner J S 2006 *Phys. Rev.* B **73** 174429
[16] Wan Y and Tchernyshyov O 2012 *Phys. Rev. Lett.* **108** 247210
[17] Zhou H D, Wiebe C R, Janik J A, Balicas L, Yo Y J, Qiu Y, Copley J R D and Gardner J S 2008 *Phys. Rev. Lett.* **101** 227204
[18] Matsuhira K, Sekine C, Paulsen C and Hinatsu Y 2004 *J. Magn. Magn. Mater.* **272** 981
[19] Princep A J, Prabhakaran D, Boothroyd A T and Adroja D T 2013 *Phys. Rev.* B **88** 104421
[20] Gaulin B D *et al* 2015 *Phys. Rev.* B **91** 245141
[21] Aczel A A, Granroth G E, MacDougall G J, Buyers W J L, Abernathy D L, Samolyuk G D, Stocks G M and Nagler S E 2012 *Nat. Commun.* **3** 1124
[22] Coldea R, Tennant D A, Wheeler E M, Wawrzynska E, Prabhakaran D, Telling M, Habicht K, Smeibidl P and Kiefer K 2010 *Science* **327** 177
[23] Torrance J and Tinkham M 1969 *Phys. Rev.* **187** 587
[24] Torrance J and Tinkham M 1969 *Phys. Rev.* **187** 595
[25] Shiba H 1980 *Prog. Theor. Phys.* **64** 466
[26] McCoy B and Wu T 1978 *Phys. Rev.* D **18** 1259
[27] Pan L D, Laurita N J, Ross K A, Gaulin B D and Armitage N P 2016 *Nat. Phys.* **12** 361
[28] Rau J G *et al* 2016 *Phys. Rev. Lett.* **116** 257204
[29] Stock C *et al* 2016 *Phys. Rev. Lett.* **117** 017201
[30] Hohlfeld R G and Sandri G 2011 *Wavelet Technol. White Pap.* **11** 1
[31] Kimura K *et al* 2013 *Nat. Commun.* **4** 1934

Ordered magnetism in the intrinsically decorated $j_{\text{eff}} = \frac{1}{2}$ α-CoV_3O_8

P. M. Sarte,[1,2] A. M. Arévalo-López,[1,2,3] M. Songvilay,[2,4] D. Le,[5] T. Guidi,[5] V. García-Sakai,[5] S. Mukhopadhyay,[5] S. C. Capelli,[5] W. D. Ratcliff,[6] K. H. Hong,[1,2] G. M. McNally,[1,2,7] E. Pachoud,[1,2] J. P. Attfield,[1,2] and C. Stock[2,4]

[1]*School of Chemistry, University of Edinburgh, Edinburgh EH9 3FJ, United Kingdom*
[2]*Centre for Science at Extreme Conditions, University of Edinburgh, Edinburgh EH9 3FD, United Kingdom*
[3]*Université Lille 1 Sciences et Technologies, UMR 8181 CNRS, Unité de Catalyse et Chimie du Solide "UCCS", 59655 Villeneuve d'ASCQ, France*
[4]*School of Physics and Astronomy, University of Edinburgh, Edinburgh EH9 3FD, United Kingdom*
[5]*ISIS Facility, Rutherford Appleton Laboratory, Chilton, Didcot OX11 0QX, United Kingdom*
[6]*NIST Center for Neutron Research, National Institute of Standards and Technology, Gaithersburg, Maryland 20899, USA*
[7]*Max-Planck-Institut für Festkörperforschung, D-70569 Stuttgart, Germany*

(Received 8 May 2018; revised manuscript received 29 October 2018; published 6 December 2018)

The antiferromagnetic mixed valence ternary oxide α-CoV_3O_8 displays disorder on the Co^{2+} site that is inherent to the *Ibam* space group resulting in a local selection rule requiring that one Co^{2+} and one V^{4+} reside next to each other, thus giving rise to an intrinsically disordered magnet without the need for external influences such as chemical dopants or porous media. The zero-field structural and dynamic properties of α-CoV_3O_8 have been investigated using a combination of neutron and x-ray diffraction, dc susceptibility, and neutron spectroscopy. The low-temperature magnetic and structural properties are consistent with a random macroscopic distribution of Co^{2+} over the 16*k* metal sites. However, by applying the sum rules of neutron scattering we observe that the collective magnetic excitations are parametrized with an ordered Co^{2+} arrangement and critical scattering consistent with a three-dimensional Ising universality class. The low-energy spectrum is well described by Co^{2+} cations coupled via a three-dimensional network composed of competing ferromagnetic and stronger antiferromagnetic superexchange within the *ab* plane and along *c*, respectively. While the extrapolated Weiss temperature is near zero, the 3D dimensionality results in long-range antiferromagnetic order at $T_N \sim 19$ K. A crystal field analysis finds two bands of excitations separated in energy at $\hbar\omega \sim 5$ meV and 25 meV, consistent with a $j_{\text{eff}} = \frac{1}{2}$ ground state with little mixing between spin-orbit split levels. A comparison of our results to the random 3D Ising magnets and other compounds where spin-orbit coupling is present indicate that the presence of an orbital degree of freedom, in combination with strong crystal field effects and well-separated j_{eff} manifolds, may play a key role in making the dynamics largely insensitive to disorder.

DOI: 10.1103/PhysRevB.98.224410

I. INTRODUCTION

Introducing disorder into condensed matter systems often suppresses common mean-field phases and transitions in favor of states that exhibit unusual critical properties [1–12]. Examples of such exotic behavior in insulating systems include the study of quenched disorder through doping in both model magnets [13,14] and liquid crystal systems [15–17]. While the presence of strong disorder disrupts translational symmetry, often resulting in a glassy phase [18] with long-range order destroyed for all length scales, the presence of weak disorder can give rise to phases displaying distinct responses for differing length scales. For example, in model random field systems near a phase transition, critical thermal fluctuations dominate until the length scale of the order parameter becomes large enough where static terms originating from the induced disorder dominate [19,20]. Examples of new disorder-induced phases include the concept of "Bragg glasses" [21–25] that were first postulated in the context of flux lattices in superconductors [26–28] where Bragg peaks exist; however other properties reflect a glass type response. A further example of unusual phases in the presence of disorder is the Griffiths phase [29–31] that was first suggested in the context of Ising ferromagnets, where an ordered local region coexists within a globally disordered phase. So far, the search for new disorder-induced phases has been limited to introducing disorder by doping in the case of solid state materials, or porous media for liquid crystals [16,32–34] and quantum fluids [35–39].

One example of theoretical efforts to understand the effects of quenched disorder on the order parameter near a phase transition is random field theory which relates disorder to the lowering of the dimensionality of the underlying universality class [40,41]. Model random magnets [13,14,42,43] have played a significant role in the development and validation of such theories with an important example being the dilute Ising antiferromagnets such as $Fe_xZn_{1-x}F_2$ [6,44–46] (Fe^{2+}, $L = 2$, and $S = 2$) and $Mn_xZn_{1-x}F_2$ [47,48] (Mn^{2+}, $L = 0$, and $S = \frac{5}{2}$). In these magnets, the random occupancy introduced through doping combined with a magnetic field results in a tunable random field. While these systems show a competition between static and thermal fluctuations driving magnetic order, the dynamics are largely unaltered by the

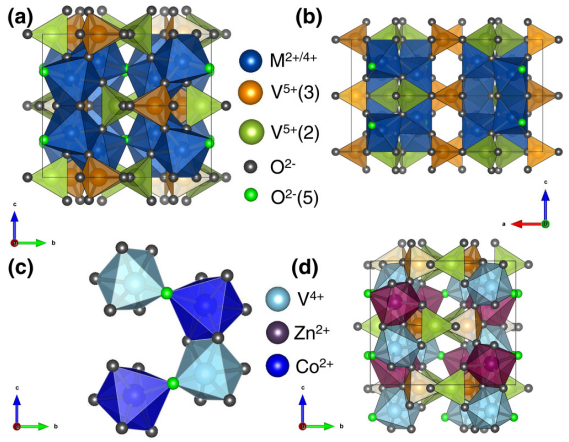

FIG. 1. Proposed [52] crystal structure of α-CoV_3O_8 (*Ibam*, No. 72) along the (a) *bc* and (b) *ac* planes, consisting of zigzag chains of edge-sharing MO_6 ($M = Co^{2+}$, V^{4+}) octahedra running parallel to *c* that are interspaced with nonmagnetic V^{5+} in tetrahedral [V^{5+}(2)] and trigonal bipyramidal [V^{5+}(3)] coordination. (c) Local constraint of the *Ibam* structure. Metal sites opposite of the bridging O(5) must be occupied by one Co^{2+} and one V^{4+}, with the O(5) situated closer to the V^{4+} site. (d) Crystal structure of α-ZnV_3O_8 (*Iba*2, No. 45). In contrast to *Ibam*, the *Iba*2 structure consists of an ordered alternating distribution of Zn^{2+} and V^{4+} along the zigzag chains [53].

introduction of weak disorder [49,50] and therefore the magnets with weak quenched disorder have collective dynamics very similar to the parent compounds. Despite significant interest in the community [51], the amount of systems that have been shown to host such exotic phases as described above have been limited; in particular, there are few examples of definitive Bragg glass and Griffiths phases. In this paper, we discuss a system where disorder is not introduced through doping, but rather is inherent to the crystallographic symmetry and therefore is a situation where magnetic disorder is present despite the presence of structural order.

In contrast to the disordered systems described above, where the disorder is a consequence of an addition external to the original system (e.g., doping [6,44–48], porous media [32,37,38], etc.), and thus can be finely tuned [54], the disorder in α-CoV_3O_8 is simply inherent to its *Ibam* crystal structure. As illustrated in Figs. 1(a) and 1(b), the proposed [52] crystal structure of α-CoV_3O_8 consists of zigzag chains of edge-sharing MO_6 octahedra ($M = Co^{2+}$ and V^{4+}) running along *c*. With the exception of a single crystallographic constraint corresponding to a local selection rule requiring that one Co^{2+} and one V^{4+} reside on opposite sides of the O(5) bridging oxygen [Fig. 1(c)], the *Ibam* structure of α-CoV_3O_8 consists of a random distribution of metal cations along the zigzag chains. A combination of the proposed random metal cation distribution with evidence [52] for both dominant antiferromagnetic exchange coupling from dc susceptibility and Ising anisotropy due to local axial octahedral distortions and spin-orbit coupling suggests that α-CoV_3O_8 may represent a potential alternative route for the investigation of disorder-induced physics. Indeed the study of disorder on electronic structures has found that by introducing correlations, localization [55] can be suppressed [56,57].

In this paper, we characterize both the crystal-magnetic structure and fluctuations of α-CoV_3O_8. This paper consists of five sections discussing our results including this introduction and a subsequent section on experimental details. We first present the characterization of the static nuclear-magnetic structure. High-resolution single-crystal x-ray and neutron diffraction data confirm both the disordered *Ibam* crystal structure and the presence of local octahedral distortions. A combination of single-crystal magnetic neutron diffraction and single-crystal dc susceptibility identify the presence of ferromagnetic correlations between Co^{2+} cations within the *ab* plane, in addition to a dominant antiferromagnetic coupling along *c*. Low-energy critical scattering is consistent with 3D Ising behavior attributable to the $j_{\text{eff}} = \frac{1}{2}$ Co^{2+} ions. However, in contrast to the intrinsically disordered *Ibam* crystal structure, by applying the first moment sum rule of neutron scattering, we find the excitations are well described by an ordered Co^{2+} arrangement. We conclude the paper with a section discussing our results in the context of models for disordered magnets and discuss the role of spin-orbit coupling through a comparison of model magnets in a random field.

II. EXPERIMENTAL DETAILS

Sample preparation. Single crystals of α-CoV_3O_8 were grown using a modified "self-flux" heating routine for α-CoV_2O_6 [58]. Precursor polycrystalline samples of α-CoV_2O_6 were first synthesized by a standard solid state reaction consisting of heating a stoichiometric mixture of $Co(CH_3CO_2)_2 \cdot 4\,H_2O$ (Sigma-Aldrich, 98%) and V_2O_5 (Alfa Aesar, 99.6%) in air for 12 h at 650 °C, then for 48 h at 725 °C, followed by quenching in liquid nitrogen [59,60]. A mixture of the α-CoV_2O_6 polycrystalline precursor and V_2O_5 in a 3:2 ratio in the presence of approximately 0.01% (w/w) of B_2O_3 (Alfa Aesar, 98.5%) was heated in a vacuum-sealed quartz tube at 780 °C for 24 h and subsequently cooled to 700 °C at a rate of 1 °C hr^{-1}. After 24 h of heating at 700 °C, the sample was cooled to 600 °C at a rate of 1 °C hr^{-1} and subsequently quenched to room temperature.

Polycrystalline samples of α-CoV_3O_8 and α-ZnV_3O_8 were synthesized by a standard solid state reaction consisting of heating a stoichiometric mixture of CoO (Alfa Aesar, 95%) or ZnO (Alfa Aesar, 99.99%), VO_2 (Alfa Aesar, 99%), and V_2O_5 for 96 h at 650 °C under static vacuum in a sealed quartz tube with intermittent grindings until laboratory powder x-ray diffraction confirmed no discernible impurities [53,61]. All stoichiometric mixtures of polycrystalline precursors were first mixed thoroughly together and finely ground to homogeneity with acetone using an agate mortar and pestle. The mixtures were pressed into ∼2 g pellets using a uniaxial press and subsequently placed in alumina crucibles or directly in quartz ampoules for reactions performed in air and in vacuum, respectively. Unless otherwise stated, all heating routines involved a ramping rate of 5 °C min^{-1} and samples were furnace-cooled back to room temperature.

Laboratory x-ray diffraction. Single-crystal x-ray diffraction was performed at 120 K on a 0.011 mg single crystal of α-CoV_3O_8 with dimensions of $0.40\times0.11\times0.09\,mm^3$ using monochromated Mo K_α radiation on an Oxford Diffraction SuperNova dual wavelength diffractometer equipped with an Atlas CCD detector and an Oxford Cryostream-Plus low-temperature device. Data collection, integration, scaling, multiscan absorption corrections, and indexing were performed using the CrysAlisPro v1.171.37.35e software package [62]. The structure solution was performed using a direct-approach method with the SHELXS-97 program in Olex2 [63].

Room temperature powder diffraction patterns of α-CoV_2O_6, α-CoV_3O_8, and α-ZnV_3O_8 were collected over $2\theta = [5, 70]^\circ$ in 0.0365° steps on a Bruker D2 Phaser laboratory x-ray diffractometer using monochromated Cu K_α radiation.

All structural refinements for single-crystal and polycrystalline measurements were performed using the JANA2006 [64] and GSAS [65] Rietveld refinement program packages, respectively, and are summarized in Appendix A. For the single-crystal refinement, the solved structure was refined by a full-matrix least squares against F^2 using only data $I > 3\sigma(I)$.

dc magnetic susceptibility. A 7.7 mg single crystal of α-CoV_3O_8 with dimensions of $2\times1\times1\,mm^3$ was aligned along the three principal axes. All crystal alignments were performed with polychromatic Laue backscattering diffraction employing adapted photostimulable plates using the Fujifilm FCR Capsula XL II system [66]. The temperature dependence of ZFC magnetization for all three principal axes was measured on a Quantum Design MPMS in an external dc field $\mu_0 H_{ext} = 0.5$ T applied parallel to the particular axis of interest. Measurements were performed in 2 K steps spaced linearly from 2 K to 300 K.

Neutron single-crystal diffraction. Neutron single-crystal diffraction experiments were performed on the SXD [67,68] time-of-flight instrument at the ISIS spallation source. The SXD diffractometer employs the time-of-flight Laue technique. The combination of a polychromatic incident beam falling on a stationary sample surrounded by 11 ZnS scintillator PSDs covering $\Omega \sim 2\pi$ sr enables quick access to a large amount of reciprocal space with minimal sample movement during data collection. A 0.4312 g single crystal of α-CoV_3O_8 with dimensions of $13.2\times4.1\times2.1\,mm^3$ as illustrated in Fig. 2(d) was mounted on the end of a 6 mm aluminum pin with aluminum tape, vertically suspended from a liquid helium 50 mm bore orange cryostat providing ω motion in an accessible temperature range of 1.5 to 300 K. Diffraction data were collected at both 5 K and 50 K for three different single-crystal frames with an accumulated charge of 1300 μA h (~8 h). After each temperature change, the sample was allowed to thermalize for 15 minutes. Reflection intensities were extracted, reduced, and integrated to structure factors using standard SXD procedures, as implemented in SXD2001 [67–69].

Inelastic neutron time-of-flight scattering spectroscopy. All inelastic neutron scattering experiments were performed on the direct-geometry MARI [70,71] and indirect-geometry IRIS [72] time-of-flight spectrometers located at ISIS. Neutron spectroscopic measurements were performed on powders as preliminary measurements found the signal from single crystals to be weak. High-energy measurements (>2 meV) on 32.6 g of α-CoV_3O_8 and 31.9 g of α-ZnV_3O_8 were performed on the direct-geometry MARI spectrometer. The t_0 chopper was operated at 50 Hz in parallel with a Gd chopper spun at 350, 300, and 250 Hz with incident energies $E_i = 150$, 60, and 15 meV, respectively, providing an elastic resolution of 5.87, 1.82, and 0.321 meV, respectively. A thick disk chopper spun at $f = 50$ Hz reduced the background from high-energy neutrons. A top-loading Displex CCR provided an accessible temperature range of 5 to 600 K.

For lower energies, measurements on 15.1 g of α-CoV_3O_8 were performed on the indirect-geometry IRIS spectrometer. As an indirect-geometry spectrometer, the final energy E_f was fixed at 1.84 meV by cooled PG002 analyzer crystals in near-backscattering geometry. The graphite analyzers were cooled to reduce thermal diffuse scattering [73], providing an elastic resolution of 17.5 μeV. A top-loading Displex CCR provided an accessible temperature range of 5 to 580 K.

Neutron powder diffraction. Neutron diffraction measurements on 1.8 g of polycrystalline α-CoV_3O_8 were performed on the BT-4 thermal triple-axis spectrometer [74] at the NIST Center for Neutron Research (NCNR). Incident and scattering neutron energies were set to 14.7 meV ($\lambda = 2.3592$ Å), selected by vertically focusing PG002 monochromator and analyzer crystals with PG filters located before and after the sample to reduce higher-order neutron contamination. The Söller horizontal collimator configuration downstream order was 60′-monochromator-80′-sample-80′-analyzer-60′-detector. A top-loading liquid helium 50 mm bore orange cryostat provided an accessible temperature range of 1.5 to 300 K. θ-2θ measurements were collected at both 3 K and 300 K over $2\theta = [15, 90]^\circ$ in 0.2° steps ($|\mathbf{Q}| = [0.695, 3.766]$ Å^{-1} in 0.009 Å^{-1} steps). Magnetic order parameter measurements were performed at $2\theta = 41.6^\circ$ ($|\mathbf{Q}| = 1.89$ Å^{-1}) over $T = [3, 32]$ K in 0.1 K steps.

III. RESULTS AND ANALYSIS

A. Crystal structure

As illustrated in Fig. 2(a) and summarized in Tables V and VI in Appendix A, single-crystal x-ray diffraction at 120 K confirmed an orthorhombic unit cell [$a = 14.29344(4)$ Å, $b = 9.8740(3)$ Å, $c = 8.34000(3)$ Å] with a volume of 1185.60(6) Å^3, corresponding to $Z = 8$. Systematic extinctions provided $Ibam$ [No. 72, Figs. 1(a) and 1(b)] and $Iba2$ [No. 45, Fig. 1(d)] as possible space groups, with statistical analysis of the intensity data favoring the centrosymmetric $Ibam$. In a procedure analogous to previous studies on hydrothermally grown single crystals, the structure was solved using a direct method [52]. The corresponding unit cell was found to consist of three metal sites with octahedral (16k), tetrahedral (8j), and trigonal bipyramidal (8j) coordination, with Co^{2+} and V^{4+} with half occupancies independently distributed over the 16k site and V^{5+} with full occupancies in the latter two 8j sites. Structural refinements utilizing 910 out of a total of 985 measured reflections confirmed two important conclusions

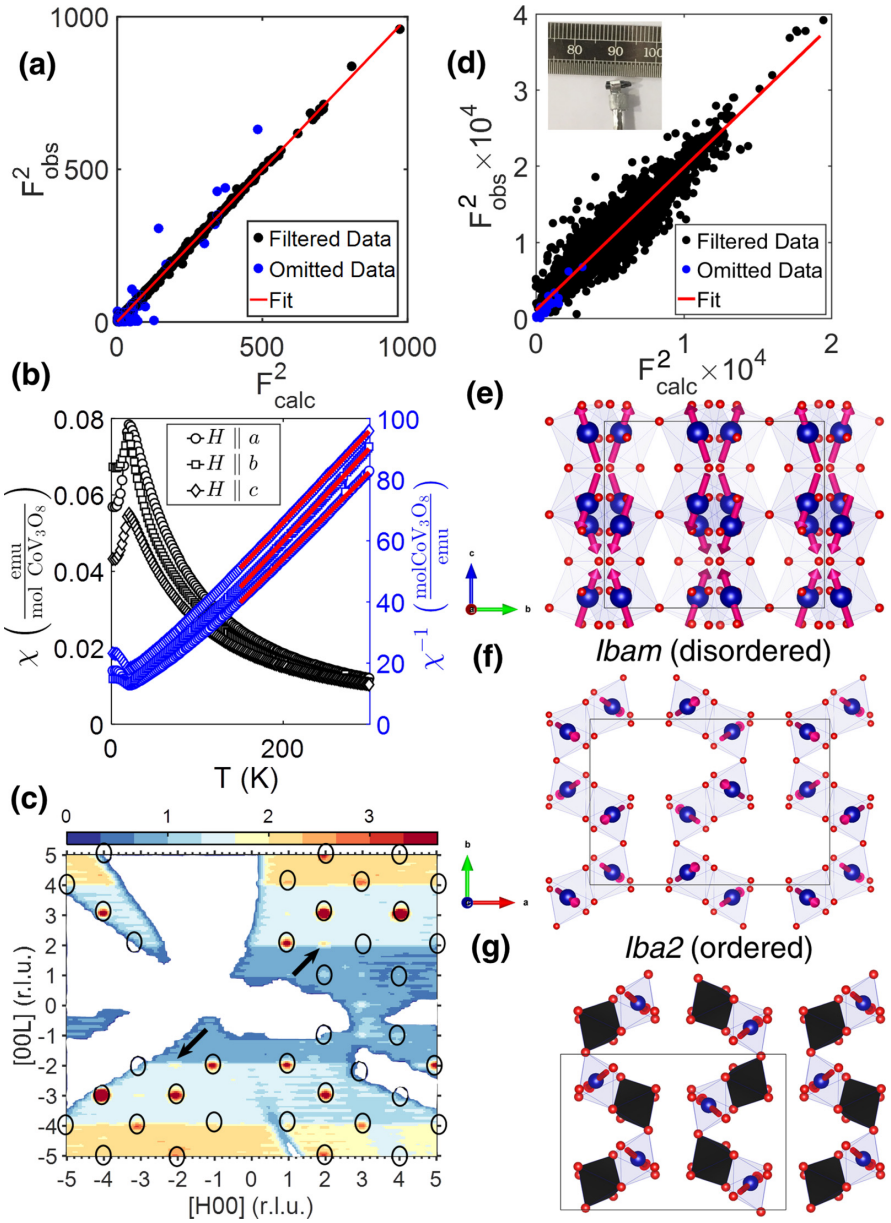

FIG. 2. (a) Refinement of single-crystal x-ray diffraction data collected at 120 K yielding a refined *Ibam* unit cell [$a = 14.29344(4)$ Å, $b = 9.8740(3)$ Å, $c = 8.34000(3)$ Å], in agreement with previous studies [52]. (b) Temperature dependence of the dc magnetic susceptibility of α-CoV_3O_8 in an external dc field $\mu_0 H_{ext} = 0.5$ T applied parallel to the three principal axes. Red lines indicate Curie-Weiss fits to high-temperature data and are summarized by Table I. (c) Single-crystal neutron diffraction intensity pattern collected at 5 K in the $(H0L)$ scattering plane. Black ellipses indicate nuclear Bragg reflections. Arrows indicate strong magnetic Bragg reflections at (-21-2) and (212). (d) Refinement of single-crystal neutron diffraction data on a (inset) 0.4312 g single crystal of α-CoV_3O_8 collected at 5 K. Schematic illustration of the refined magnetic structure of α-CoV_3O_8 along the (e) bc and (f) ab planes with the Co^{2+} having 50% occupancy. The orientation of the refined magnetic moments on Co^{2+} are indicated by red arrows. (g) illustrates the ordered $Iba2$ space group with each Co^{2+} site fully occupied and the black octahedra representing V^{4+} sites. Both panels (f) and (g) show a single layer of Co^{2+} ions.

TABLE I. Curie-Weiss parameters (calculated over a range of $150 \leqslant T \leqslant 300$ K) for α-CoV_3O_8 in an external dc field $\mu_0 H_{ext} = 0.5$ T applied parallel to the three principal axes. Numbers in parentheses indicate statistical errors.

Crystallographic Axis	C (emu K/mol)	p_{eff} (μ_B)	θ_{CW} (K)
a	3.525(9)	5.310(7)	9.5(7)
b	3.31(2)	5.15(2)	2(1)
c	3.354(2)	5.180(2)	−21.3(2)
Average	3.396(7)	5.213(7)	−3.2(4)

from previous studies [52,61]. First, Co^{2+} and V^{4+} are both randomly and equally distributed over the 16k site with refined occupancies of 0.506(6) and 0.494(4), respectively. Second, the large refined anisotropic displacements resulting from placing the O(5) oxygen in the 8f position with full occupancy support the local selection rule consisting of Co^{2+} and V^{4+} occupying respective positions on opposite sides of the O(5) bridging oxygen ligand, as illustrated in Fig. 1(c).

B. dc magnetic susceptibility

As summarized by Table I and Fig. 2, dc susceptibility measurements along all three principal axes indicate that α-CoV_3O_8 behaves as a Curie-Weiss paramagnet at high temperatures and undergoes an antiferromagnetic transition at 19.5(5) K, corresponding to a T_N much greater than the previously reported T_N of 8.2 K for crystals grown hydrothermally [52]. A fit of the high-temperature data [Fig. 2(b)] to the Curie-Weiss law yielded Curie-Weiss temperatures θ_{CW} of 9.5(7), 2(1), −21.3(2) K for $\mu_0 H_{ext}$ applied along a, b, and c, respectively. The small θ_{CW} with an average $\theta_{CW} = -3.2(4)$ K is suggestive of either weak exchange interactions or the presence of multiple and nearly canceling ferro-/antiferromagnetic interactions resulting in the experimentally observed small average. The differences in the constants measured along different directions is also indicative of an anisotropy in the system likely originating from the distortion of the local octahedra [60,75].

As illustrated in Fig. 2(b), the magnetization does not approach zero in the low-temperature limit after the antiferromagnetic transition. Instead, its value for all three principal axes plateaus at 2 K which indicates the possibility of the presence of paramagnetism at lower temperatures, although no measurements were conducted below 2 K. In contrast to the d^7 Co^{2+} moments that can couple via e_g orbitals, coupling between the d^1 V^{4+} moments are exclusively via t_{2g} orbitals which is predicted to be much weaker [76–78] and thus more likely to exhibit paramagnetic behavior. In fact, V^{4+} paramagnetism is supported by the observation that the saturated moment in the low-temperature limit corresponds to 0.150(2) μ_B, a value consistent with a strongly reduced V^{4+} effective paramagnetic moment predicted to occur in the presence of strong spin-orbit coupling and octahedral distortions as has been previously observed experimentally in $Na_2V_3O_7$ [79,80]. Finally, the average effective paramagnetic moment of 5.213(7) μ_B is smaller than the predicted moment of 5.6 μ_B, for Co^{2+} in an octahedral environment as studied in CoO [81] and assuming a 1:1 ratio of high-spin Co^{2+} and V^{4+}, confirming that both spin-orbit and distortion effects play a significant role [59,82] in the magnetism of α-CoV_3O_8, a topic that will be later addressed with inelastic neutron scattering.

TABLE II. Comparison of the refined magnetic moment's components assuming random ($Ibam$) and ordered ($Iba2$) distribution of Co^{2+} and V^{4+} on the metal sites of α-CoV_3O_8. The goodness-of-fit metric χ^2 and residuals from the magnetic refinement of neutron single crystal diffraction data collected at 5 K suggest that Co^{2+} and V^{4+} are randomly distributed. Numbers in parentheses indicate statistical errors.

Parameter	Value ($Ibam$)	Value ($Iba2$)
μ_a	1.35(5) μ_B	1.30(6) μ_B
μ_b	1.16(5) μ_B	1.09(8) μ_B
μ_c	3.05(4) μ_B	2.32(5) μ_B
χ^2	3.18	5.15
R_{F^2}	8.38%	10.59%
R_{wF^2}	8.99%	14.57%
$R_{F^2_{mag}}$	24.13%	32.28%

C. Magnetic structure

As shown in Fig. 2(c) and summarized in Tables VII and VIII in Appendix A, single-crystal neutron diffraction confirmed both an absence of any structural distortion away from the $Ibam$ space group down to 5 K and the appearance of additional Bragg reflections confirming long-range magnetic ordering as measured by previous dc susceptibility measurements [52]. Since dc susceptibility measurements suggested that V^{4+} remained paramagnetic down to at least 2 K, the refinement of single-crystal neutron diffraction data collected at 5 K assumed that the magnetic Bragg reflections were exclusively due to Co^{2+} that were randomly distributed throughout the 16k metal sites. The random distribution of Co^{2+} was accomplished by constraining the occupancy of each metal site to a value of $\frac{1}{2}$. The additional magnetic Bragg reflections were successfully indexed using a propagation vector $\mathbf{k} = (1, 1, 1)$ with the P_Iccn (No. 56.376) Shubnikov space group [83]. The propagation vector $\mathbf{k} = (1, 1, 1)$ was initially chosen as it corresponds to the first point of symmetry reduction by removing body-centering symmetry with the same structural unit cell [84]. Subsequently, utilizing the aforementioned value of $\mathbf{k}$, a symmetry analysis was performed in JANA2006 [64]. With a $\mathbf{k} = (1, 1, 1)$, the symmetry analysis considers which models were compatible—following the symmetry operations of the group, but excluding body centering—with the restriction that moments at (x, y, z) are antiferromagnetically aligned with those moments at $(x + \frac{1}{2}, y + \frac{1}{2}, z + \frac{1}{2})$. Four models were found to be compatible, with the P_Iccn (No. 56.376) Shubnikov space group yielding the best match.

Table II summarizes the results of a joint nuclear and magnetic refinement utilizing 5086 out of a total of 5120 measured reflections at 5 K [Fig. 2(d)], confirming a strong preference for the P_Iccn Shubnikov space group of $Ibam$ over P_Icc2 of $Iba2$. The refined magnetic moment for Co^{2+} was found to be $\mu = 3.53(2)$ μ_B with μ_a, μ_b, and μ_c as 1.35(5) μ_B, 1.16(5) μ_B, and 3.05(5) μ_B, respectively. α-CoV_3O_8 adopts a magnetic structure consisting of effective pairs of 2D layers

in the ab plane, separated from one another by a nonmagnetic layer consisting of tetrahedrally coordinated V^{5+}, as illustrated in Fig. 2(f). Within these 2D layers, Co^{2+} spins are ferromagnetically coupled along both a and b, corresponding to interchain superexchange interactions. These 2D layers come in pairs with each offset from one another by [0.1858a, 0.1508b, and 0.1194c] with the pair being antiferromagnetically coupled to the adjacent pair along c, corresponding to intrachain superexchange interactions.

D. Inelastic neutron scattering

Motivated by the random distribution of Co^{2+} and V^{4+}, multiple ferro-/antiferromagnetic interactions, and the presence of strong spin-orbit coupling, the spin dynamics of α-CoV_3O_8 was investigated with inelastic neutron scattering. All inelastic scattering intensities were normalized to absolute units using the paramagnetic approximation [85]. Normalization was performed by using both Co and V as internal incoherent standards [86,87] to calculate an absolute calibration constant $\mathcal{A}$ converting vanadium-corrected scattering intensities $\widetilde{I}(\mathbf{Q}, E)$ to the differential scattering cross section $\frac{d^2\sigma}{dEd\Omega}$ which was then converted to the dynamic structure factor $S(\mathbf{Q}, E)$ by

$$\mathcal{A}\widetilde{I}(\mathbf{Q}, E) \equiv \frac{d^2\sigma}{dEd\Omega} = \left(\frac{\gamma r_o}{2}\right)^2 g_J^2 2|f(\mathbf{Q})|^2 S(\mathbf{Q}, E), \quad (1)$$

where it is understood [88] that $S(\mathbf{Q}, E)$ is $S^{zz}(\mathbf{Q}, E) = \frac{\mathrm{Tr}\{S^{\alpha\beta}(\mathbf{Q},E)\}}{3}$, $(\frac{\gamma r_o}{2})^2$ and g_J are 73 mb sr^{-1} and the Landé g factor, respectively, while the factor of 2 corresponds to the paramagnetic cross section [85,87,89,90]. The value for the Landé g factor is discussed in Appendix B 2. Hereafter, all neutron scattering quantities with a tilde [for example $\widetilde{S}(|\mathbf{Q}|, E)$] denote the inclusion of the magnetic form factor squared $|f(\mathbf{Q})|^2$.

1. Spin-orbit transitions

As discussed in Appendix B 1, Co^{2+} ($L = 3$ and $S = \frac{3}{2}$) in an octahedral crystal field environment can be projected onto a ground state with an effective orbital angular momentum of $l = 1$ with a projection factor α of $-\frac{3}{2}$ [60,75,81]. Diagonalizing the projected spin-orbit Hamiltonian $\hat{\mathcal{H}}_{SO} = \alpha\lambda\hat{\mathbf{l}}\cdot\hat{\mathbf{S}}$ results in three spin-orbit manifolds characterized by an effective angular momentum $\hat{\mathbf{j}} = \hat{\mathbf{l}} + \hat{\mathbf{S}}$ with eigenvalues $j \equiv j_{\mathrm{eff}}$ of $\frac{1}{2}$, $\frac{3}{2}$, and $\frac{5}{2}$ [91–93]. The $j_{\mathrm{eff}} = \frac{3}{2}$ and $\frac{5}{2}$ manifolds are separated in energy from the $j_{\mathrm{eff}} = \frac{1}{2}$ ground state doublet manifold by $\frac{3}{2}\alpha\lambda$ and $\frac{5}{2}\alpha\lambda$, respectively [75]. For pure CoO [91], $|\alpha\lambda| \sim 24$ meV, and therefore for an undistorted octahedra, one would expect a crystal field excitation at ∼36 meV. In this section, we study the magnetic excitations in α-CoV_3O_8 in order to determine whether its ground state can be considered as a $j_{\mathrm{eff}} = \frac{1}{2}$.

Given that only small single crystals were available of α-CoV_3O_8, preliminary neutron inelastic scattering data failed to produce a measurable signal. To extract information on the low-temperature magnetic dynamics, we therefore used powders and time-of-flight neutron spectroscopy techniques. Neutron inelastic scattering measurements [Figs. 3(a)–3(c)] on polycrystalline α-CoV_3O_8 with an $E_i = 150$, 60, and 15 meV, respectively at 5 K revealed two clear low-$|\mathbf{Q}|$ excitations at ∼5 meV and ∼25 meV. To prevent any weak magnetic signal of interest from being masked by strong phonon bands, a scaled inelastic scattering spectrum $\widetilde{\gamma}\widetilde{S}(|\mathbf{Q}|, E)$ of an approximate isostructural compound α-ZnV_3O_8 [53] collected with identical experimental conditions was subtracted as a background [94]. Neutron inelastic scattering investigations of α-ZnV_3O_8 on MARI found no evidence of correlated V^{4+} moments over the energy range reported here. The scaling factor $\widetilde{\gamma}$ for the background was calculated from the ratio between energy-integrated cuts of $\widetilde{S}(|\mathbf{Q}|, E)$ of α-CoV_3O_8 and α-ZnV_3O_8 along $|\mathbf{Q}|$ at high $|\mathbf{Q}|$, thereby normalizing by the phonon scattering. The use of α-ZnV_3O_8 as a background not only removes the constant and $|\mathbf{Q}|^2$-dependent background contributions but the presence of V^{4+} in both compounds allows for the isolation of magnetic fluctuations solely attributable to Co^{2+}. As illustrated in Figs. 3(d)–3(g), the use of α-ZnV_3O_8 as an effective background revealed that the origin of the low-$|\mathbf{Q}|$ excitations must be due to Co^{2+} exclusively, excluding the possibility of any contribution from V^{4+}.

Following the analysis of inelastic scattering measurements on monoclinic and triclinic polymorphs of CoV_2O_6 [60], the low-$|\mathbf{Q}|$ excitations in α-CoV_3O_8 can be understood as transitions between different spin-orbit manifolds. A comparison between the inelastic spectra of CoV_2O_6 and α-CoV_3O_8 suggests that the excitations at ∼5 meV and ∼25 meV are due to transitions within the $j_{\mathrm{eff}} = \frac{1}{2}$ manifold and between the $j_{\mathrm{eff}} = \frac{1}{2}$ and $j_{\mathrm{eff}} = \frac{3}{2}$ manifolds, respectively. In α-CoV_3O_8, these modes appear much broader than in CoV_2O_6; this will be discussed later. Such an assignment is supported by the observation that the transition at ∼5 meV is gapped at 5 K in the magnetically ordered regime, as illustrated in Figs. 5(a) and 5(b). Such a gap would be a consequence of the Zeeman splitting of the $j_{\mathrm{eff}} = \frac{1}{2}$ manifold due to the internal molecular field caused by long-range ordering in the Néel phase [60]. Once the temperature is raised above T_N, the molecular field would be significantly reduced due to the loss of magnetic order, resulting in the disappearance of a gap, as is experimentally observed in Fig. 3(g).

In the context of this assignment in terms of j_{eff} spin-orbit split manifolds, a difference between α-CoV_3O_8 and monoclinic α-CoV_2O_6 is the absence of an observable ∼110 meV magnetic excitation [Fig. 3(a)]. As was previously calculated for CoV_2O_6 [60], in addition to the strong excitations for the intra-$j_{\mathrm{eff}} = \frac{1}{2}$ and the $j_{\mathrm{eff}} = \frac{1}{2}$ to $j_{\mathrm{eff}} = \frac{3}{2}$ transitions, the intensity of the $j_{\mathrm{eff}} = \frac{1}{2}$ to $j_{\mathrm{eff}} = \frac{5}{2}$ transition scales with the distortion of the local coordination octahedra [95,96] with the transition being absent for a perfect octahedra like in rocksalt and cubic CoO [91]. The distortion of the local octahedra can quantified by the parameter δ defined by

$$\delta = \frac{1}{\mathcal{N}}\sum_i \left\{\left(\frac{d_i - \langle d\rangle}{\langle d\rangle}\right)^2 \times 10^4\right\}, \quad (2)$$

where $\mathcal{N} = 6$ and $\langle d\rangle$ denotes the average distance [60,97]. α-CoV_3O_8 exhibits a much weaker octahedral distortion [$\delta = 11.106(8)$] than α-CoV_2O_6 ($\delta = 55$) and is thus expected to have a significantly weaker intensity. This is also in agreement with previous results on triclinic γ-CoV_2O_6 (with $\delta = 2.1$ and 4.8 for the two different Co^{2+} sites) which failed to observe a

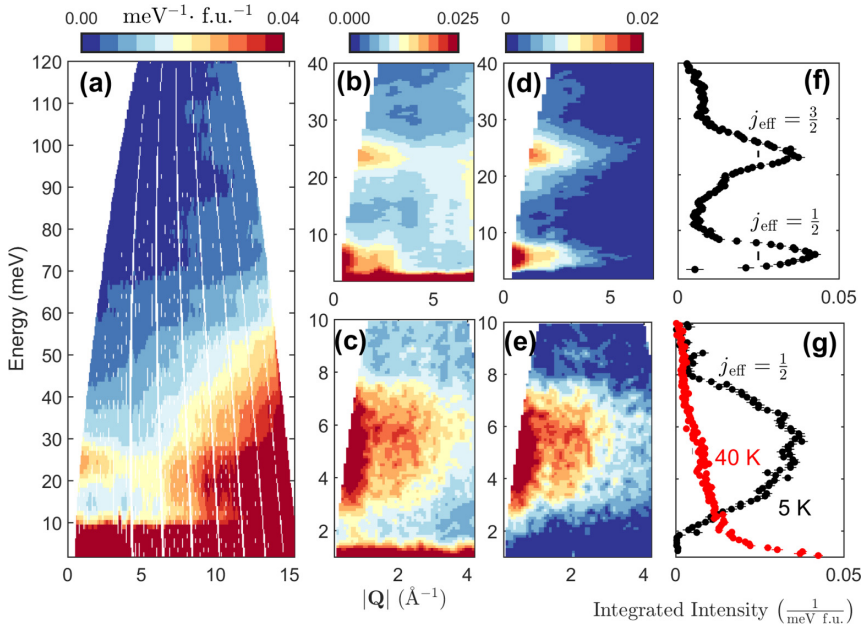

FIG. 3. $\widetilde{S}(|\mathbf{Q}|, E)$ measured on MARI at $T = 5$ K with an E_i of (a) 150 meV, (b) 60 meV, and (c) 15 meV. (d), (e) Magnetic scattering $\widetilde{S}_M(|\mathbf{Q}|, E)$ and (f), (g) corresponding $|\mathbf{Q}|$-integrated cuts ($|\mathbf{Q}| = [0, 3]$ Å^{-1}). Vertical lines in (f), (g) indicate instrumental resolution. $\widetilde{S}_M(|\mathbf{Q}|, E)$ was calculated by the subtraction of corresponding $\widetilde{S}(|\mathbf{Q}|, E)$ for α-ZnV_3O_8 measured at identical experimental conditions. All inelastic scattering intensities have been normalized to absolute units.

$j_{\text{eff}} = \frac{5}{2}$ transition [60]. A distortion of the local octahedra around the Co^{2+} site should result in an anisotropic term in the magnetic Hamiltonian [96,98,99]. Given the powder-average nature of the dynamics (discussed below), we are not sensitive to this term. However, the consistency of the inelastic response with the j_{eff} description discussed above in terms of the energy response is also consistent with other Co^{2+}-based magnets where a local distortion of the octahedra exists [60,95]. We now discuss further evidence for our interpretation in terms of j_{eff} levels by applying the sum rules of neutron scattering to the integrated inelastic scattering intensity.

2. *Total moment sum rule*

To confirm the assignment of the 5 meV signal as excitations within the ground state $j_{\text{eff}} = \frac{1}{2}$ manifold, the total integrated spectral weight at 5 K of the lowest-lying excitation was calculated. As summarized by the total moment sum rule of neutron scattering [87,100–103], the sum of all spectral weights is defined by

$$\frac{3\int d^3\mathbf{Q}\int dE S(\mathbf{Q}, E)}{\int d^3\mathbf{Q}} = j(j+1), \tag{3}$$

where $S(\mathbf{Q}, E) \equiv S^{zz}(\mathbf{Q}, E)$ denotes the magnetic component of the dynamic structure factor $\widetilde{S}^{zz}_M(\mathbf{Q}, E)$ that has been further renormalized by $|f(\mathbf{Q})|^2$. The extra factor of 3 has been included to assure consistency with the definition of $S(\mathbf{Q}, E) \equiv S^{zz}(\mathbf{Q}, E)$ given by Eq. (1) in the paramagnetic approximation. A measurement of the integrated intensity is therefore sensitive to the effective j of the manifold of levels being integrated over. Equation (3) can be simplified by integrating out the angular dependence and canceling common terms resulting in an integral $\mathcal{L}$ defined by

$$\mathcal{L}(|\mathbf{Q}|) = \frac{3\int d|\mathbf{Q}|\mathbf{Q}|^2\int dE S(|\mathbf{Q}|, E)}{\int d|\mathbf{Q}||\mathbf{Q}|^2}. \tag{4}$$

The total integral $\mathcal{L}$ is uniquely a function of $|\mathbf{Q}|$ and represents an integration of the magnetic density of states over all energies including both elastic and inelastic channels in the cross section [87]. With $j_{\text{eff}} = \frac{1}{2}$, the total moment sum rule [Eq. (3)] would predict a value of 0.75 for the total integrated intensity.

Since the assignment discussed above based on spin-orbit transitions assumes that the ∼5 meV excitation and the elastic cross section is exclusively due to excitations within the $j_{\text{eff}} = \frac{1}{2}$ manifold, all quantities in Eq. (3) were projected onto the ground state doublet manifold by the projection theorem of angular momentum [93,94,104]. As discussed in Appendix B 2, the projection onto the ground state doublet required defining the projected value of the Landé g factor g_J as $g'_J = \frac{13}{3}$ and the effective angular momentum j_{eff} as $\frac{1}{2}$ [75,105]. As illustrated in Fig. 4, the total integrated inelastic intensity given by $\mathcal{L}(|\mathbf{Q}|)$ [Eq. (4)] saturates at 0.15(1). Combining the total integral of the inelastic contribution and an elastic contribution [106] of $(\frac{\mu}{g'_J\mu_B})^2 = 0.66$ yields a total integral of 0.81 ± 0.14, in excellent agreement with the total moment prediction for $j_{\text{eff}} = \frac{1}{2}$ of 0.75. The agreement further confirms our assignment of the low-energy excitations to

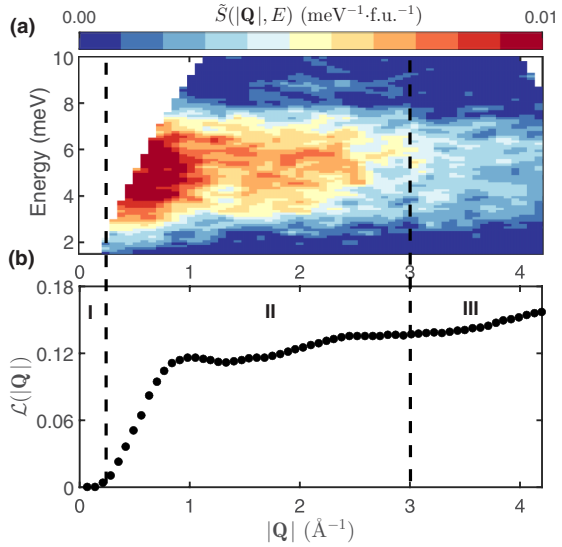

FIG. 4. (a) Magnetic scattering $\widetilde{S}_M(|\mathbf{Q}|, E)$ of α-CoV_3O_8 measured on MARI at $T = 5$ K with an E_i of 15 meV and the corresponding (b) $|\mathbf{Q}|$ dependence of the total integrated inelastic ($E = [2, 8]$ meV) magnetic scattering intensity $\mathcal{L}$. Regions I, II, and III denote "get-lost" tube-, magnetic-, and phonon/form factor–dominated regions, respectively.

transitions within the ground state $j_{\text{eff}} = \frac{1}{2}$ spin-orbit doublet manifold.

With the low-energy excitations being successfully approximated by pure j_{eff} manifolds, we may now rationalize the effective paramagnetic moment p_{eff} of 5.213(7) μ_B that was calculated from dc susceptibility. Given that the $j_{\text{eff}} = \frac{1}{2}$ and $j_{\text{eff}} = \frac{3}{2}$ manifolds are separated by ∼24 meV (∼278 K), both are significantly thermally populated at the high temperatures used for the Curie-Weiss fit. In such a high-temperature regime, we would expect a p_{eff} of $g_s\sqrt{S(S+1)} = 3.9\ \mu_B$, which is significantly less than the measured value as has been commonly observed for other magnets based on Co^{2+} in octahedral coordination [59,60,92,107]. The extra component measured with susceptibility may be accounted for by noting that V^{4+} contributes $g_s\sqrt{S(S+1)} = 1.7\ \mu_B$. Therefore the addition of the contributions to p_{eff} from both Co^{2+} and V^{4+} corresponds to a total predicted $p_{\text{eff}} = 5.6\ \mu_B$, in close agreement with the experimental data, with the small discrepancy potentially attributable to the fact that the $j_{\text{eff}} = \frac{5}{2}$ manifold is still not significantly populated at $T \sim 300$ K. However it is worth noting that an additional and distinct possibility for a much larger measured effective paramagnetic moment may be a strong orbital contribution as has been observed for the case of CoO [108,109], where the orbital contribution is significant, corresponding to approximately $\frac{1}{3}$ of the total ordered moment.

E. Critical exponents

Despite the similarities between the inelastic spectra of α-CoV_3O_8 and CoV_2O_6, one difference is the bandwidth of the low-energy excitation that we have assigned to the $j_{\text{eff}} = \frac{1}{2}$ manifold. As illustrated in Fig. 3(g), in contrast to both polymorphs of CoV_2O_6, α-CoV_3O_8 exhibits a broad peak in energy whose bandwidth is approximately 20 times that of instrumental resolution. Such a large bandwidth could be accounted for by magnetic exchange coupling between spins [60,110,111]. However, an alternative explanation may lie in the intrinsic cationic disorder inherent to the disordered *Ibam* structure of α-CoV_3O_8 [52]. Such large cationic disorder would result in a distribution of cationic sites and correspondingly a spread of spin-orbit transitions as has been shown for multiple doped systems [46,49,112–116], and thus perhaps such disorder may also explain the large bandwidth in α-CoV_3O_8 due to a distribution of molecular fields splitting the $j_{\text{eff}} = \frac{1}{2}$ manifold. We investigate this possibility in this section using scaling.

1. Scaling analysis

The presence of such disorder would result in temperature being the dominant energy scale. To investigate this possibility, the temperature dependence of the Co^{2+} spin fluctuations was analyzed using a scaling analysis previously employed for the charge-doped cuprates [117–121]. For paramagnetic fluctuations, critical scattering theory assumes that a single energy scale, the relaxation rate Γ, is dominant [122]. If Γ is driven by temperature, then it can be shown that the energy-temperature dependence of the uniform dynamic susceptibility $\chi''(E, T)$, follows $\frac{E}{T}$ scaling [117,118] given by

$$\frac{\chi''(T, E)}{\chi''(T = 0\ K, E)} = \arctan\left\{\sum_{i=0} a_i \left(\frac{E}{T}\right)^{2i+1}\right\}, \quad (5)$$

where $\chi''(T = 0\ K, E)$ denotes the value of χ'' in the limit of $T = 0$ K and all even powers are excluded in the sum to satisfy detailed balance, requiring χ'' to be an odd function of energy [120]. For this particular analysis, the value of $\chi''(T, E)$ was calculated by first subtracting a temperature-independent background from the measured $S(T, |\mathbf{Q}|, E)$. The contribution of the background was determined by an algorithm previously employed for $Fe_{1+x}Te_{0.7}Se_{0.3}$ [123] and polymer quantum magnets [124]. The algorithm is based on the requirement that all inelastic scattering must obey detailed balance accounting for both sample environment and other temperature-independent scattering contributions, and thus isolating the fluctuations exclusively due to Co^{2+}. The background-subtracted dynamic structure factor was then converted to $\chi''(T, |\mathbf{Q}|, E)$ via the fluctuation-dissipation theorem [125]

$$\chi''(T, |\mathbf{Q}|, E) = g^2\mu_B^2\pi\left\{\frac{1}{n(E, T) + 1}\right\}S(T, |\mathbf{Q}|, E), \quad (6)$$

where $n(E, T)$ is the Bose factor. Finally, $\chi''(T, |\mathbf{Q}|, E)$ was integrated over $|\mathbf{Q}| = [0, 3]$ and $[0, 2]$ Å^{-1} for measurements on MARI and IRIS, respectively. As illustrated in Fig. 5(c), $\frac{E}{T}$ scaling adequately accounts for the experimental data with the need for only two refined constants of 3.2(1) and 0.8(2) for a_0 and a_2, respectively, since the inclusion of higher-order terms in Eq. (5) did not improve the fit. The success of $\frac{E}{T}$ scaling

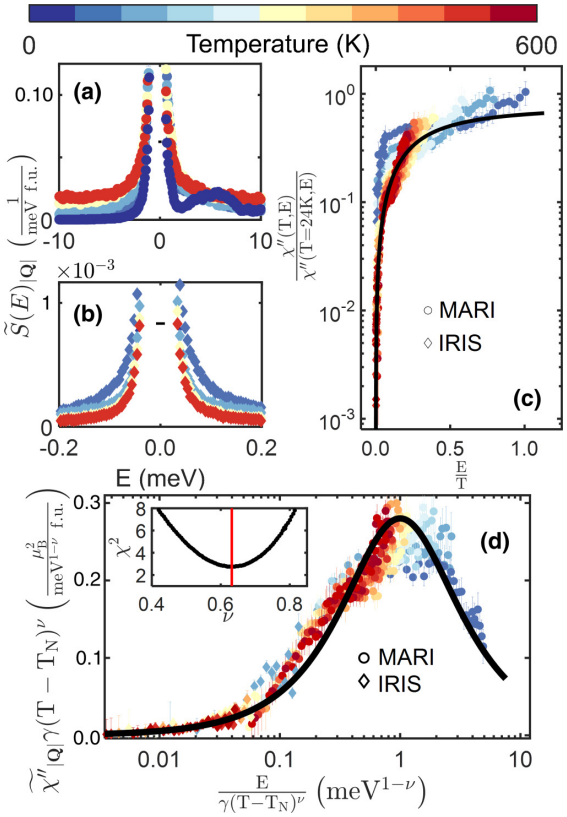

FIG. 5. $|\mathbf{Q}|$-integrated cuts of $\widetilde{S}(|\mathbf{Q}|, E)$ measured on (a) MARI and (b) IRIS at various temperatures. Horizontal lines indicate instrumental resolution. (c) Energy and temperature dependence of the normalized χ'' calculated from $|\mathbf{Q}|$-integrated cuts of $\widetilde{S}_M(|\mathbf{Q}|, E)$ measured on both IRIS at MARI. (d) Compilation of the energy-temperature dependence of $|\mathbf{Q}|$-integrated χ'' as calculated in (c). As discussed in the main text, the data are described by a Lorentzian relaxational form [Eq. (8)], revealing scaling behavior consistent with $\Gamma \propto (T - T_N)^{\nu}$. The line of best fit yields $\nu = 0.636(10)$, corresponding to a global minimum of χ^2 as illustrated in the inset. All panels share the same temperature scale (top horizontal intensity bar). All $|\mathbf{Q}|$-integrated cuts on MARI and IRIS are from $|\mathbf{Q}| = [0, 3]$ Å^{-1} for $E_i = 15$ meV and from $|\mathbf{Q}| = [0, 2]$ Å^{-1} for $E_f = 1.84$ meV, respectively.

suggests that $\Gamma \propto T^{\nu}$ and the larger value of a_0 over all other terms suggests $\nu \leqslant 1$.

The value of ν was refined using a modified scaling algorithm previously employed to detect anomalous scaling in the vicinity of a quantum critical point for $CeCu_2Si_2$ and $CeCu_{6-x}Au_x$ [126–128]. Utilizing the single relational energy mode approximation and the Kramers-Kronig relations [129], the uniform dynamic susceptibility can be approximated as a Lorentzian-like response [95,117,130–135] given by

$$\chi'' = \chi' \left\{ \frac{E\Gamma}{E^2 + \Gamma^2} \right\}, \tag{7}$$

where χ' denotes the static susceptibility and $\Gamma \propto \xi^{-1}$, where ξ is the correlation length [136]. If one assumes both the single energy scale $\Gamma = \gamma(T - T_N)^{\nu}$ and the static susceptibility $\chi' = \frac{C}{\Gamma}$, where γ and C are constants, then Eq. (7) assumes the form

$$\chi'' = \frac{C}{\gamma(T - T_N)^{\nu}} \left\{ \frac{\frac{E}{\gamma(T-T_N)^{\nu}}}{1 + \left(\frac{E}{\gamma(T-T_N)^{\nu}}\right)^2} \right\}. \tag{8}$$

The first assumption leading to Eq. (8) stems from the fact that the scaling properties of the dynamics are being investigated near the vicinity of an ordering transition at $T_N \sim 19$ K and not a quantum critical point as in the cuprates and heavy-fermion systems [106,128,137], a fact that was reflected in Fig. 5(c) by defining $\chi''(T = 0, E)$ as the value at 24 K. The second assumption is based on the paramagnetic behavior observed with dc susceptibility at high temperatures, suggesting χ' should adopt a Curie-Weiss form [106,117]. As illustrated in Fig. 5(d), the scaling relation [Eq. (8)] provides a good description of the experimental data over four orders of magnitude in $\frac{E}{T}$, yielding a refined ν of 0.636(10). It is important to note that the refined value of ν is not consistent with random dilute 3D Ising behavior where $\nu = 0.683(2)$, but instead is consistent with the ordered 3D Ising universality class with a $\nu = 0.6312(3)$ [122,138–142]. While scaling and critical scattering typically only apply near the phase transition, work on other transition-metal-based compounds has found critical scattering that scales up to high temperatures in the paramagnetic regime [110,143].

2. *Magnetic order parameter*

The scaling analysis in the previous section found that the critical fluctuations are both consistent with an ordered three-dimensional Ising universality class and with the dc susceptibility data presented above. Consequently, while the excitations are separated into distinct j_{eff} manifolds, the scaling analysis indicates that the distortion does introduce an anisotropy term in the magnetic Hamiltonian influencing the critical dynamics outlined in the previous section. In an attempt to further deduce the universality class of α-CoV_3O_8, neutron diffraction measurements were performed on polycrystalline α-CoV_3O_8 to extract further critical exponents. As illustrated in Fig. 6(a), polycrystalline α-CoV_3O_8 exhibits long-range magnetic ordering at 3 K, in agreement with both single-crystal dc susceptibility [Fig. 2(b)] and single-crystal neutron diffraction [Fig. 2(c)] measurements. The temperature dependence of the scattering intensity of the (212) magnetic Bragg reflection is displayed in Fig. 6(b), corresponding to the square of the magnetic order parameter ϕ, given by the power-law dependence [144]

$$I(T) \equiv \phi^2(T) \propto (T_N - T)^{2\beta}, \tag{9}$$

yields a refined T_N of 18.8(6) K in agreement with dc susceptibility measurements and a refined β of 0.28(7). Although the value of β is in agreement with the predicted value of 0.326 for the ordered 3D Ising universality class [122], the large statistical error also implies agreement with the predicted value for the random dilute 3D Ising model of 0.35 [138–141]. Therefore, the critical magnetic fluctuations are in agreement

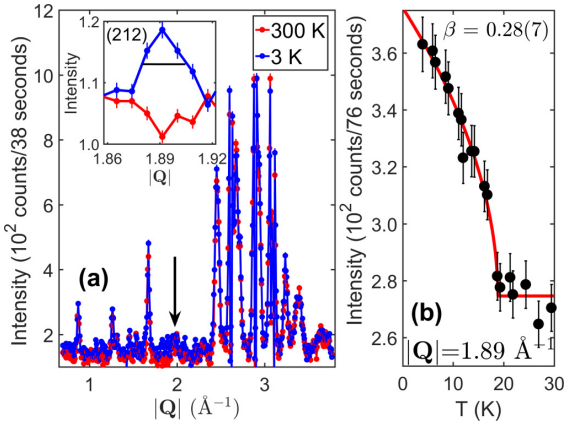

FIG. 6. (a) Neutron diffraction profiles of polycrystalline α-CoV_3O_8 collected at 3 and 300 K on BT-4. Inset: Additional scattering intensity on the (212) magnetic Bragg reflection at 3 K confirms long-range magnetic order. The horizontal line indicates instrumental resolution. (b) Temperature dependence of the elastic intensity at $|\mathbf{Q}| = 1.89$ Å^{-1} ($2\theta = 41.6°$), corresponding to the maximum of the (212) magnetic Bragg reflection as indicated by the arrow in (a). A fit to $(T_N - T)^{2\beta}$ yields $T_N = 18.8(6)$ K and $\beta = 0.28(7)$.

with expectations from both ordered and disordered 3D Ising behavior.

F. First moment sum rule, local cation ordering, and single-mode approximation

In order to deduce further information concerning both the dimensionality d and the microscopic exchange constants J, a combination of the first moment sum rule of neutron scattering and the single-mode approximation was employed. The determination of the values for J and d begins with the Hohenberg-Brinkman first moment sum rule [145] given by

$$\langle E\rangle(\mathbf{Q}) = \int dE E S(\mathbf{Q}, E) = -\frac{2}{3}\sum_{i,j} n_{ij} J_{ij} \langle \hat{\mathbf{S}}_i \cdot \hat{\mathbf{S}}_j\rangle [1 - \cos(\mathbf{Q}\cdot\mathbf{d}_{ij})] \quad (10)$$

and its powder average

$$\langle E\rangle(|\mathbf{Q}|) = -\frac{2}{3}\sum_{i,j} n_{ij} J_{ij} \langle \hat{\mathbf{S}}_i \cdot \hat{\mathbf{S}}_j\rangle \left\{1 - \frac{\sin(|\mathbf{Q}||\mathbf{d}_{ij}|)}{|\mathbf{Q}||\mathbf{d}_{ij}|}\right\}, \quad (11)$$

as derived in Appendix C, where n_{ij}, J_{ij}, $\langle \hat{\mathbf{S}}_i \cdot \hat{\mathbf{S}}_j\rangle$, and $\mathbf{d}_{ij}$ denote the number of individual exchange interactions, the exchange constant, the spin-spin correlator, and the displacement vector between spins at sites i and j, respectively [60,102,146].

Since all of the inelastic intensity measured at 5 K on MARI with an $E_i = 15$ meV shown in Fig. 3(g) corresponds to excitations within the ground state $j_{\text{eff}} = \frac{1}{2}$, proven by the total moment sum rule, then the single-mode approximation (SMA) can be applied [102,147]. The single-mode approximation, applicable to a situation where the excitation spectrum is dominated by a single coherent mode, allows for the dynamic structure factor to be written as $S(\mathbf{Q}, E) = S(\mathbf{Q})\delta[\epsilon(\mathbf{Q}) - E]$, where $\delta[\epsilon(\mathbf{Q}) - E]$ assures energy conservation [60,87,100,124,148]. Applying the single-mode approximation to the first moment sum rule yields

$$S(\mathbf{Q}, E) = -\frac{2}{3}\frac{1}{\epsilon(\mathbf{Q})}\sum_{i,j} n_{ij} J_{ij} \langle \hat{\mathbf{S}}_i \cdot \hat{\mathbf{S}}_j\rangle \cdot \{1 - \cos(\mathbf{Q}\cdot\mathbf{d}_{ij})\}\delta[\epsilon(\mathbf{Q}) - E], \quad (12)$$

providing a quantitative relationship between $S(\mathbf{Q}, E)$ and the dispersion $\epsilon(\mathbf{Q})$ and by extension, a measure of the dimensionality [60,87,149,150]. For numerical purposes, the delta function was approximated as a Lorentzian with a FWHM equal to that of the calculated experimental resolution width of 0.24 meV at 5 meV transfer on MARI. Equations (10)–(12) assume the presence of Heisenberg exchange and thus exclude exchange anisotropy [60,100,102,147]. It is important to note that the exclusion of any anisotropy terms is simply a first approximation based on the success of the isotropic exchange model to account for experimental data in a variety of other Co^{2+}-based systems such as CoV_2O_6, $KMn_{1-x}Co_xF_3$, and $Mn_{1-x}Co_xF_2$ [13,60,92,105,151]. In fact, there is evidence that anisotropic exchange is not negligible in α-CoV_3O_8. Such experimental evidence includes equal intensities for transitions within the ground state manifold and between the ground state and first excited state manifolds [75,92], as illustrated in Fig. 3(f). Another piece of evidence is the presence of a weak signal at ~1 meV at low-energy transfer measurements, as illustrated in Fig. 3(g), that may be indicative of anisotropic breakdown of magnetic excitations [60,75,87,100,152]. The non-negligible value of anisotropic exchange in α-CoV_3O_8 is indeed expected due to the distorted octahedra around Co^{2+} ($\delta \sim 11$) and has been observed in α, γ-CoV_2O_6 with similar distortion parameters [60,82] but will be excluded in the context of the current discussion.

1. First moment sum rule and cation order

This section utilizes the first moment sum rule of neutron scattering to provide an estimate of the exchange constants in α-CoV_3O_8. Figure 7(a) shows that the background-subtracted first moment $\widetilde{\langle E\rangle}(|\mathbf{Q}|)$ at 5 K was successfully described by the powder-averaged first moment sum rule [Eq. (11)] incorporating all possible 15 Co^{2+}-Co^{2+} distances in the α-CoV_3O_8 unit cell from $|\mathbf{d}_{ij}| = [3.209, 7.669]$ Å. As summarized by Table III, a least-squares optimization revealed that only six unique distances possess non-negligible $-n_{ij}J_{ij}\langle \hat{\mathbf{j}}_i \cdot \hat{\mathbf{j}}_j\rangle$ values, where the use of $\hat{\mathbf{j}}$ in the correlator instead of $\hat{\mathbf{S}}$ is due to the use of g'_J in the normalization process. Two particular distances with negligible $-n_{ij}J_{ij}\langle \hat{\mathbf{j}}_i \cdot \hat{\mathbf{j}}_j\rangle$ contributions are 3.209 Å and 3.540 Å, corresponding to the nearest neighbor and metal site distances across the O(5) bridging ligand, respectively. The absence of the latter is expected due to the local selection rule [52] as illustrated in Fig. 1(c), but the absence of the nearest neighbor distance is inconsistent with a random distribution of Co^{2+} inherent to the disordered *Ibam* structure previously deduced by diffraction measurements that are summarized in Fig. 2. Upon closer inspection of the α-CoV_3O_8 unit cell, these six distances were shown to correspond to the unique distances found exclusively

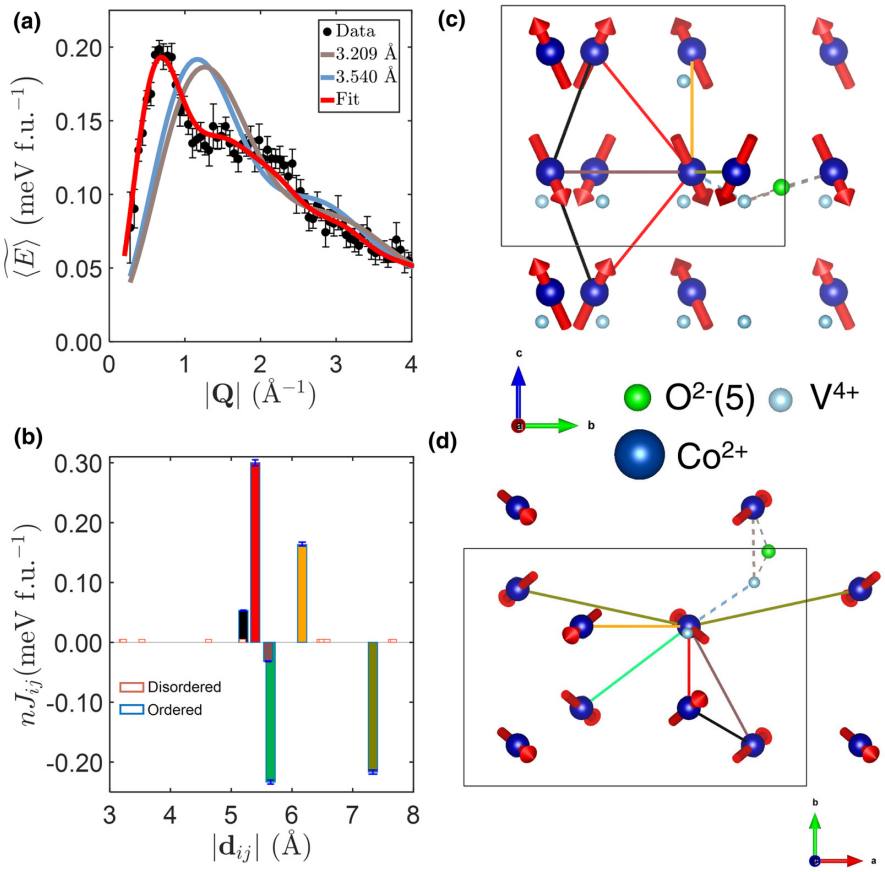

FIG. 7. (a) $|\mathbf{Q}|$ dependence of the background-subtracted first moment $\widetilde{\langle E \rangle}$ as measured on MARI at $T = 5$ K with an $E_i = 15$ meV integrated over $E = [2, 8]$ meV. A fit to the first moment sum rule [Eq. (11)] reveals that only six distances $|\mathbf{d}_{ij}|$ out to 7.5 Å possess non-negligible nJ_{ij} values as illustrated in (b), and summarized in Table III. For the purposes of comparison, distances present only in the ordered and disordered atomic arrangements are distinguished by purple and dark pink outline colors, respectively. Distances with non-negligible nJ_{ij} contributions have a face color corresponding to the illustration of the corresponding six interactions along the (c) *bc* and (d) *ac* planes of the α-CoV_3O_8 unit cell. Both nonbridging oxygen atoms have been excluded and V^{4+} ions have been reduced in size for the purposes of clarity. Two particular distances, 3.209 Å and 3.540 Å, are absent as noted in (a), corresponding to nearest neighbor and bridging metal site distances, respectively.

in the ordered $Iba2$ structure [53] as illustrated in Figs. 7(c) and 7(d), confirming an ordered arrangement of Co^{2+}.

While this analysis indicates the distances are consistent with the ordered $Iba2$ structure, there are two potential caveats. Because we measure the product $-n_{ij}J_{ij}\langle\hat{\mathbf{j}}_i \cdot \hat{\mathbf{j}}_j\rangle$, (i) the value of n_{ij} may not be negligible but instead it may be the correlator $\langle\hat{\mathbf{j}}_i \cdot \hat{\mathbf{j}}_j\rangle$ whose value is negligible; (ii) and/or the exchange constants J_{ij} may themselves be negligible. To address issue (i), we have calculated the correlator $\langle\hat{\mathbf{j}}_i \cdot \hat{\mathbf{j}}_j\rangle$ based on energy-integrated magnetic diffraction data (Table III) and found it to be substantial for all distances. We address argument (ii) by pointing out that some distances with negligible $-n_{ij}J_{ij}\langle\hat{\mathbf{j}}_i \cdot \hat{\mathbf{j}}_j\rangle$ have a Co^{2+}-O^{2-}-Co^{2+} angle close to 180°, predicted by the Goodenough-Kanamori-Anderson rules to yield strong antiferromagnetic exchange [76–78].

We now extract the exchange constants J_{ij} by dividing out the correlator from the $-n_{ij}J_{ij}\langle\hat{\mathbf{j}}_i \cdot \hat{\mathbf{j}}_j\rangle$. By inserting the 6 values of $n_{ij}J_{ij}$ in the mean-field expression for the Curie-Weiss temperature [153,154]

$$\widetilde{\theta}_{\mathrm{CW}} = -\frac{S(S+1)\sum_{i,j} n_{ij}J_{ij}}{3\zeta}, \tag{13}$$

where ζ is a scale factor of 1.9 calculated by Kanamori [81], one obtains $-0.24(15)$ K, a value that is both small and negative, in agreement with the experimentally determined value of $-3.2(4)$ K. The close similarity between the calculated and experimentally determined values of θ_{CW} suggests that all relevant exchange interactions have been accounted for by the $Iba2$ structure. It is important to emphasize that this analysis assumes isotropic exchange and thus assumes the isotropic part of the magnetic Hamiltonian is dominant. While susceptibility data indicate some anisotropy, the similarity between the extracted exchange constants and the θ_{CW} lends

TABLE III. Distances $|\mathbf{d}_{ij}|$ with corresponding non-negligible refined values of $-n_{ij}J_{ij}\langle\hat{\mathbf{j}}_i\cdot\hat{\mathbf{j}}_j\rangle$ and $n_{ij}J_{ij}$ from the fit of the first moment $\langle E\rangle(|\mathbf{Q}|)$ ($E=[2,8]$ meV) at 5 K to the first moment sum rule [145]. The corresponding calculated spin-orbit corrected Curie-Weiss constant $\widetilde{\theta}_{\mathrm{CW}}$ [Eq. (13)] is in close agreement with the experimentally determined Curie-Weiss constant averaged over all three principal directions $\bar{\theta}_{\mathrm{CW,exp}}$. Numbers in parentheses indicate statistical errors.

$\lvert\mathbf{d}_{ij}\rvert$ (Å)	$-n_{ij}J_{ij}\langle\hat{\mathbf{j}}_i\cdot\hat{\mathbf{j}}_j\rangle$ (meV f.u.$^{-1}$)	$\langle\hat{\mathbf{j}}_i\cdot\hat{\mathbf{j}}_j\rangle$	$n_{ij}J_{ij}$ (meV f.u.$^{-1}$)
5.200(2)	0.023(1)	−0.420(2)	0.055(1)
5.395(3)	0.173(1)	−0.594(3)	0.30(1)
5.6083(14)	0.016(2)	0.484(2)	−0.033(1)
5.649(4)	0.099(2)	0.417(3)	−0.24(1)
6.168(3)	0.08(1)	−0.483(3)	0.17(1)
7.3321(9)	0.13(1)	0.595(4)	−0.22(1)
$\bar{\theta}_{\mathrm{CW,exp}}$			−3.2(4) K
$\widetilde{\theta}_{\mathrm{CW}}$			−0.24(15) K

support for the isotropic approximation, while the slightly larger negative measured value may possibly be indicative of some anisotropic contributions. Future advances in both single-crystal growth of this material and also higher flux neutron instrumentation will allow single-crystal data to be obtained and the parameters refined.

2. *Single-mode approximation and dimensionality*

Since the first moment sum rule indicates the presence of multiple unique interactions spanning all three crystallographic directions in the $Iba2$ structure [53], it was suspected that a more intricate dispersion relation should be chosen for Eq. (12), such as the expression given by

$$\begin{aligned}\epsilon(\mathbf{Q}) = \{&B_0 + B_h\cos(2\pi h) + B_k\cos(2\pi k) + B_l\cos(2\pi l)\\ &+ B_{hk}\{\cos[2\pi(h+k)] + \cos[2\pi(h-k)]\}\\ &+ B_{hl}\{\cos[2\pi(h+l)] + \cos[2\pi(h-l)]\}\\ &+ B_{kl}\{\cos[2\pi(k+l)] + \cos[2\pi(k-l)]\}\\ &+ B_{2h}\cos(4\pi h) + \beta_{2k}\cos(4\pi k) + B_{2l}\cos(4\pi l)\}^{\frac{1}{2}},\end{aligned} \tag{14}$$

where B_i are the dispersion parameters. The dispersion relation $\epsilon(\mathbf{Q})$ in Eq. (14) satisfies Bloch's theorem [89] and has been previously used to parametrize the dispersion for more complex systems involving multiple exchange interaction pathways such as PHCC [100], whose large dispersions could not be adequately described with the heuristic model $\epsilon(\mathbf{Q}) = \beta_0 + \sum_i \beta_i\cos(\mathbf{Q}\cdot\mathbf{d}_{ij})$ [60,124,155].

As a first approximation, the parameters in Eq. (14) involving interactions between the principal axes were set to zero and each parameter along a particular principal axis was set to be equal (e.g., $B_h = B_{2h}$). This simple model effectively reduces Eq. (14) to the aforementioned simple heuristic model [60,124,155] and treats every exchange interaction as a combination of interactions along the three principal axes. As illustrated in Fig. 8, all major features of $\widetilde{S}_M(|\mathbf{Q}|, E)$ collected at 5 K, including the large bandwidth, were successfully accounted for by a least-squares optimization of the dispersion parameters. As summarized in Table IV, the refined dispersion parameters indicate the presence of three-

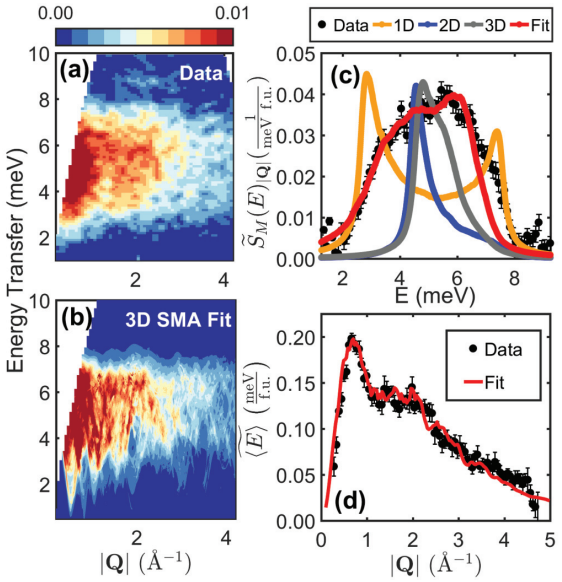

FIG. 8. (a) $\widetilde{S}_M(|\mathbf{Q}|, E)$ measured on MARI at $T = 5$ K with an $E_i = 15$ meV. (b) $\widetilde{S}_M(|\mathbf{Q}|, E)$ calculated by the optimization of all parameters B_i in the heuristic model of $\epsilon(\mathbf{Q})$ in the single-mode approximation of $\widetilde{S}(\mathbf{Q}, E)$ utilizing the refined values of $-n_{ij}J_{ij}\langle\hat{\mathbf{j}}_i\cdot\hat{\mathbf{j}}_j\rangle$ from the first moment sum rule. (c) Comparison of $|\mathbf{Q}|$-integrated cuts ($|\mathbf{Q}| = [0, 3]$ Å^{-1}) of measured and calculated $\widetilde{S}_M(|\mathbf{Q}|, E)$. For the purposes of comparison, nonoptimized $|\mathbf{Q}|$-integrated cuts for all three types of dimensionality d are also presented. These cuts assume both that $\epsilon(\mathbf{Q})$ possesses the same gap parameter B_0 obtained from the 3D SMA fit in (b) and that each permissible set of parameters is equally weighted. (d) Comparison of the measured and calculated $|\mathbf{Q}|$ dependence of the first moment $\langle E\rangle$ integrated over $E = [2, 8]$ meV.

TABLE IV. Refined parameters of the heuristic dispersion relation in the single-mode approximation of $\widetilde{S}(|\mathbf{Q}|, E)$ utilizing the refined values of $-n_{ij}J_{ij}\langle\hat{\mathbf{j}}_i\cdot\hat{\mathbf{j}}_j\rangle$ at 5 K summarized in Table III. As a first approximation, the intraplane dispersion parameters were fixed to zero. Numbers in parentheses indicate statistical errors.

Dispersion Parameter	Refined Value (meV^2)
B_0	28.2(3)
B_h	−1.13(2)
B_k	−4.63(4)
B_l	6.8(7)
B_{hk}	0
B_{hl}	0
B_{kl}	0
B_{2h}	−1.13(2)
B_{2k}	−4.63(4)
B_{2l}	6.8(7)

dimensional magnetism, consistent with the lack of significant asymmetry in the $|\mathbf{Q}|$-integrated cut $\widetilde{S}_M(E)_{|\mathbf{Q}|}$ displayed in Fig. 8(c), as would be expected for both 1D and 2D magnetic fluctuations [87,156,157]. As summarized by Table IV, the dispersion parameters along h and l are both negative while the dispersion parameters along k are positive with a larger magnitude. Both the signs and relative magnitudes of the dispersion parameters can be reconciled using the spin-flip hopping model [60,158], where B_i for a particular direction i is interpreted as a hopping term whose value is proportional to the energy cost of a spin-flip $t \sim SJ$ along that particular direction. The negative h and k dispersion parameters correspond to ferromagnetic coupling along a and b, respectively, while the larger positive l dispersion parameters correspond to stronger antiferromagnetic coupling along c, all consistent with both dc susceptibility and the refined magnetic structure presented in Fig. 2. The ability to describe the powder-averaged magnetic dynamic response in terms of a coherent sharp mode is consistent with the cation order deduced from the critical scaling analysis and thus further evidence that the broadening of the magnetic excitations is due to powder averaging and not due to the underlying disorder.

IV. DISCUSSION

A. Experimental limitations

There are several limitations to the analysis presented in this paper. The first is the use of α-ZnV_3O_8 as a background for the analysis of the low-temperature inelastic spectrum of α-CoV_3O_8. As shown in Fig. 1(d), α-ZnV_3O_8 crystallizes in the cation-ordered $Iba2$ space group [53] and is thus not completely isostructural to α-CoV_3O_8. It can be argued that the local cation ordering deduced is an artifact of the $Iba2$ structure of the α-ZnV_3O_8 background. To counter such a claim, we point out that the scaling analysis utilizing the same inelastic neutron scattering data, but after the subtraction of an independently calculated temperature-independent background derived from detailed balance [123,124], provided a critical exponent ν consistent with pure 3D Ising behavior. Such pure 3D Ising behavior would be unexpected if Co^{2+} was locally disordered.

Another limitation is the observation that the low-temperature cooperative magnetism of α-CoV_3O_8 can be treated as exclusively due to coupling between Co^{2+} moments. The presence of a second magnetic disordered "counter"-cation is in contrast to the model dilute 3D Ising antiferromagnets where the "counter"-cations are nonmagnetic and thus interactions between magnetic ions of one type (e.g., Fe^{2+}) are exclusively considered [6,13,47,48,159]. Such a situation was assumed to apply to α-CoV_3O_8 in the analysis presented so far as a first approximation since there is evidence that V^{4+} behaves paramagnetically, but it is highly unlikely that coupling between V^{4+} and other V^{4+} or Co^{2+} plays no role in the low-temperature magnetism and thus the analogy to the dilute antiferromagnets such as $Fe_xZn_{1-x}F_2$ should be approached with caution. It is important to note that the apparent lack of influence of V^{4+} coupling, relative to coupling between Co^{2+} cations, may be due to the exclusive use of t_{2g} orbitals by V^{4+}, in contrast to the e_g orbitals utilized by Co^{2+} which is predicted to give much stronger coupling [76–78,93,160].

A further limitation concerns the nature of the competing ferromagnetic and antiferromagnetic interactions in α-CoV_3O_8. In contrast to the $Fe_xZn_{1-x}F_2$ series [13,49,161], α-CoV_3O_8 exhibits both distinct ferromagnetic interchain and antiferromagnetic intrachain coupling along the ab plane and along c, respectively. Both ferromagnetic and antiferromagnetic coupling possess similar magnitudes as proven by their near cancellation corresponding to a Weiss temperature near zero. With a Weiss temperature near zero, combined with a $T_N \sim 19$ K, the frustration index $f = |\frac{\theta_{CW}}{T_N}| \lesssim 1$ implies the absence of frustration, a key contributor to the rich phase diagram of the dilute 3D Ising antiferromagnets [6]. To address the concurrent presence of both ferromagnetic and antiferromagnetic couplings, it is worth noting that such a situation is reminiscent of another random dilute 3D Ising magnet system $Fe_xMg_{1-x}Cl_2$ where $x > 0.55$, a series of compounds whose magnetic properties have been shown consistently to be qualitatively similar to that of $Fe_xZn_{1-x}F_2$ [162,163]. To address the absence of frustration, it is worth noting that in contrast to the current study, previous work [52] on smaller hydrothermally grown crystals of α-CoV_3O_8 reported a $T_N = 8.2$ K and a Weiss temperature of -32.1 K, corresponding to a frustration index $f \sim 4$, indicating evidence for significant frustration. Such contrasting behavior provides strong evidence that sample dependence may play a significant role in determining the magnetic properties of α-CoV_3O_8, as has been consistently observed for the dilute antiferromagnets, whose response functions are significantly influenced by both sample quality and nonequilibrium physics [1,13,161]. The particular dependence on sample quality can be partially rationalized using recent work by Volkova [164] on α-ZnV_3O_8. Numerical simulations indicated that although the ordered-$Iba2$ arrangement was predicted to exhibit minimal frustration, if one instead assumed a disordered-$Ibam$ arrangement, significant magnetic frustration was predicted to manifest itself as competing interchain couplings of similar magnitudes in the presence of a dominant antiferromagnetic intrachain coupling. The contrasting behavior between $Iba2$ and $Ibam$ cationic arrangement may provide an explanation for the aforementioned difference in the experimentally determined frustration indices with samples possessing more disorder exhibiting a larger value of f.

B. Disordered $Ibam$ versus ordered $Iba2$?

A contradiction arises from a combined analysis of x-ray and neutron diffraction, dc susceptibility, and inelastic neutron spectroscopy measurements in that the disordered-$Ibam$ structure is derived from diffraction measurements; however the dynamics are more consistent with an ordered-$Iba2$ arrangement of Co^{2+} ions. Diffraction indicates that statically the arrangement of Co^{2+} ions is disordered; however the collective long-wavelength fluctuations seem to average out this disorder. α-CoV_3O_8 therefore appears to be magnetically ordered for longer length scales. The disorder in α-CoV_3O_8 differs from a Griffiths phase where local order is present and may be more analogous to the situation in water ice where local selection rules are present [165]. However, the

lack of strong diffuse scattering in our single-crystal experiments makes a comparison to these correlated disordered systems difficult. However, the presence of the local structural selection for Co^{2+} and V^{4+} distinguishes α-CoV_3O_8 from a doped random magnet where no such local order is required. The apparent robustness of α-CoV_3O_8 to disorder is discussed below in the context of spin-orbit coupling and comparison to other model magnets in a random field.

C. Universality class of α-CoV_3O_8

Ising anisotropy is experimentally supported by several observations discussed above: the presence of a significant octahedral distortion ($\delta \sim 11$) as deduced from a combination of single-crystal x-ray and neutron diffraction data, the presence of 3D Ising fluctuations as deduced from both critical exponents ν and β, and the presence of strong spin-orbit coupling supported by neutron spectroscopy. 3D dimensionality ($d = 3$) is suggested based on the following: the values of the critical exponents ν and β, the nonzero refined values of all h, k, and l dispersion parameters in $\epsilon(\mathbf{Q})$ reflecting strong coupling in both the ab plane and along c, in combination with the relatively weak anisotropy of the dc susceptibility.

The random magnetic cation distribution is supported by the refined $Ibam$ structure from both single-crystal x-ray and neutron diffraction and the value of β. An additional observation is the intrinsic width of the AFM transition as measured with dc susceptibility, reflected by the large experimental error of β caused by the rounding of the order parameter measurement, as has been experimentally observed in other dilute 3D Ising antiferromagnets such as $Co_xZn_{1-x}F_2$ [166]. The dilution of 3D Ising magnetism can be rationalized by the key observation that V^{4+} appears to remain purely paramagnetic down to 2 K and thus has no significant influence on the low-temperature cooperative magnetic properties of α-CoV_3O_8, as proven by a combination of inelastic neutron scattering and dc susceptibility measurements.

D. Comparison between α-CoV_3O_8 and random field Ising magnets

If one disregards the magnetic influence of V^{4+}, effectively treating the cation as a "counter"-ion such as Zn^{2+} in $Fe_xZn_{1-x}F_2$ or $Mn_xZn_{1-x}F_2$, then the magnetism due to Co^{2+} in α-CoV_3O_8 may be regarded as being magnetically diluted by 50%. Additionally, it is important to note that the failure to observe strong structural diffuse scattering with x-ray and neutron diffraction measurements is suggestive of a lack of local cation ordering or gradients. These concentration gradients were noted in dilute model antiferromagnets [1,159,161,167–169]. Such a combination of significant dilution and disorder would be expected to have a significant effect on the dynamics [1,11,12,20,49,51,116,170–172]. In this sense, it is surprising that there seems to be little effect on the magnetic dynamics in α-CoV_3O_8, where the magnetic excitations are consistent with a fully ordered cation arrangement. Such behavior is suggestive that hydrodynamic and long-wavelength fluctuations are not strongly sensitive to the disorder in α-CoV_3O_8, in contrast with expectations based on theory [173,174]. The robust nature of the dynamics to dilution, and in particular disorder, is analogous to several observations in dilute random field magnets and in particular the $Fe_xZn_{1-x}F_2$ series [46,175,176], where sharp excitations are still observable for large amounts of doping [49]. Unlike members of the $Fe_xZn_{1-x}F_2$ series closer to the percolation threshold ($x_p \sim 0.24$) that exhibit spin glass behavior [6,45,49,170], $Fe_{0.5}Zn_{0.5}F_2$ assumes long-range antiferromagnetic order in zero field with a T_N corresponding to half of that of FeF_2 [177,178]. The appearance of long-range antiferromagnetic order as measured by dc susceptibility with a $\mu_0 H_{ext} = 0.5$ T supports the claim that α-CoV_3O_8 is not close to the percolation threshold, where even the smallest external field destroys long-range order, as is the case for $M_xZn_{1-x}F_2$, where $M = Co^{2+}$ and Fe^{2+} [131]. However, the random field Ising magnet $Mn_xZn_{1-x}F_2$ [179,180] does show strong effects of the disorder on the dynamics. Such behavior is consistent with cases of random fields introduced through confinement, where when the critical fluctuations have a similar length scale to the underlying disorder, the phase transition is strongly altered [1,11,20,39,172].

A key difference between MnF_2 and both α-CoV_3O_8 and FeF_2 is the presence of strong crystal field effects and spin-orbit coupling in the latter two compounds [133,175]. It is also worth noting that unlike the case of pure CoO [81,91,94,181–184] where the large and far-reaching exchange constants result in a significant and ultimately problematic entanglement of spin-orbit levels [94], in the case of α-CoV_3O_8, the exchange constants are weak and the Weiss temperature is near 0 K. Both observations suggest that the presence of both strong crystal field effects and spin-orbit coupling with well-separated j_{eff} manifolds, as is the case for α-CoV_3O_8, may be central to making the dynamics robust against strong disorder.

V. CONCLUDING REMARKS

In summary, a combination of zero-field diffraction, dc susceptibility, and neutron spectroscopy measurements have indicated that the low-temperature cooperative magnetism of α-CoV_3O_8 is dominated by $j_{\text{eff}} = \frac{1}{2}$ Co^{2+} cations randomly distributed over the 16k metal site of the $Ibam$ structure, thus corresponding to an intrinsically disordered magnet without the need for any external influences such as chemical dopants or porous media. Despite the intrinsic disorder, by employing the sum rules of neutron scattering, the collective excitations have been shown to not be significantly affected by the disorder, displaying behavior consistent with an ordered-$Iba2$ arrangement of $j_{\text{eff}} = \frac{1}{2}$ Co^{2+} moments over a macroscopic scale. These Co^{2+} moments are coupled via a 3D network of competing ferromagnetic and stronger antiferromagnetic superexchange interactions within the ab plane and along c, respectively, resulting in long-range antiferromagnetic order of the Co^{2+} moments at $T_N \sim 19$ K, despite a Weiss temperature near 0 K. A comparison of our results to the random 3D Ising magnets and other compounds where spin-orbit coupling is present indicates that both the presence of an orbital degree of freedom, in combination with strong crystal field effects and well-separated j_{eff} manifolds, may be key in making the dynamics robust against disorder.

TABLE V. Crystal data and experimental and structural refinement parameters for single-crystal x-ray diffraction measurements on α-CoV_3O_8. Numbers in parentheses indicate statistical errors.

Parameter	Value
Empirical formula	CoV_3O_8
Formula weight	339.7529 g mol^{-1}
Temperature	120.0(1) K
Crystal dimensions	0.40×0.11×0.09 mm^3
Wavelength	0.71073 Å (Mo K_α)
Crystal system	Orthorhombic
Space group	*Ibam* (No. 72)
a	14.29344(4) Å
b	9.8740(3) Å
c	8.34000(3) Å
V	1185.60(6) Å^3
Z	8
ρ	3.8069(3) g cm^{-3}
θ range for data collection	$4.13^\circ \leqslant \theta \leqslant 30.18^\circ$
Limiting indices	$-19 \leqslant h \leqslant 20$, $-13 \leqslant k \leqslant 14$, and $-11 \leqslant l \leqslant 11$
Number of reflections $I > 0$	985
Number of reflections $I > 3\sigma(I)$	910
Absorption correction method	Gaussian
Extinction method	B-C type 1 Gaussian isotropic
Extinction coefficient	2300(100)
Refinement method	Full matrix least squares on F^2
Number of parameters (constraints)	67 (9)
R_{F^2} [$I > 3\sigma(I)$, all]	1.65%, 1.90%
R_{wF^2} [$I > 3\sigma(I)$, all]	2.38%, 2.46%
Goodness of fit χ^2 [$I > 3\sigma(I)$, all]	1.47%, 1.48%

ACKNOWLEDGMENTS

We acknowledge discussions with J. A. M. Paddison, C. R. Wiebe, A. J. Browne, G. Perversi, S. E. Maytham (HBS), and D. R. Jarvis. We are grateful to the Royal Society, the STFC, the ERC, and the EPSRC for financial support. P.M.S. acknowledges financial support from the CCSF, the RSC, and the University of Edinburgh through the GRS and PCDS. We acknowledge the support of the National Institute of Standards and Technology, US Department of Commerce, in providing a portion of the neutron research facilities used in this work. Finally, the authors would like to thank the Carnegie Trust for the Universities of Scotland for providing facilities and equipment for chemical synthesis.

APPENDIX A: CRYSTALLOGRAPHIC DATA

Crystallographic data are summarized in Tables V–X and Fig. 9.

TABLE VI. Structural parameters of α-CoV_3O_8 obtained from the refinement of single-crystal x-ray diffraction data collected at 120 K. Numbers in parentheses indicate statistical errors.

Atom (Label)	Wyckoff Position	x	y	z	B_{iso} (Å^2)	Fractional Occupancy
Co	16k	0.654760(16)	0.33285(2)	0.81060(3)	0.39(2)	0.506(6)
V(1)	16k	0.654760(16)	0.33285(2)	0.81060(3)	0.39(2)	0.494(6)
V(2)	8j	0.52271(2)	0.16672(4)	0.5	0.321(5)	1
V(3)	8j	0.70168(2)	0.94348(4)	0.5	0.252(6)	1
O(1)	8j	0.73349(11)	0.41325(16)	0	0.52(2)	1
O(2)	8j	0.58248(10)	0.27500(16)	0	0.50(2)	1
O(3)	16k	0.76787(8)	0.35258(11)	0.66386(15)	0.53(2)	1
O(4)	8f	0.61080(11)	0.5	0.75	1.2(1)	1[a]
O(5)	16k	0.57900(8)	0.22361(12)	0.65802(16)	0.79(3)	1
O(6)	8j	0.57973(10)	0.98272(16)	0.5	0.48(2)	1

[a]The assignment of full occupancy in the 8f position corresponding to the bridging oxygen is in agreement with the initial refinement by Oka *et al.* [52].

TABLE VII. Crystal data and experimental and structural refinement parameters for single-crystal neutron diffraction measurements on α-CoV_3O_8. Numbers in parentheses indicate statistical errors.

Parameter	Value
Empirical formula	CoV_3O_8
Formula weight	339.7529 g mol^{-1}
Temperature	5.00(3) K
Crystal dimensions	13.2×4.1×2.1 mm^3
Wavelength	Polychromatic (time of flight)
Crystal system	Orthorhombic
Nuclear space group	$Ibam$ (No. 72)
Magnetic space group (BNS setting)	P_Iccn (No. 56.376) or (I_Pbam' OG 72.10.639)
k	(111)
a	14.3280(4) Å
b	9.9213(3) Å
c	8.4160(3) Å
V	1196.35(7) Å^3
Z	8
ρ	3.773(3) g cm^{-3}
θ range for data collection	$2.94^\circ \leqslant \theta \leqslant 76.22^\circ$
Limiting indices	$-35 \leqslant h \leqslant 33$, $-25 \leqslant k \leqslant 19$, and $-16 \leqslant l \leqslant 22$
Number of reflections $I > 0$	5120
Number of reflections $I > 3\sigma(I)$	5086
Refinement method	Full matrix least squares on F^2
Absorption correction	None
Extinction method	B-C type 1 Gaussian isotropic
Extinction coefficient	348(8)
Number of parameters (constraints)	34(10)
μ_a	1.35(4) μ_B
μ_b	1.16(5) μ_B
μ_c	3.05(4) μ_B
R_{F^2} [$I > 3\sigma(I)$, all]	8.34%, 8.38%
R_{wF^2} [$I > 3\sigma(I)$, all]	8.98%, 8.99%
$R_{F^2_{\mathrm{mag}}}$ [$I > 3\sigma(I)$, all]	23.44%, 24.13%
Goodness of fit χ^2 [$I > 3\sigma(I)$, all]	3.18, 3.19

TABLE VIII. Structural parameters for the nuclear structure of α-CoV_3O_8 obtained from the refinement of single-crystal neutron diffraction data collected at 5 K. Numbers in parentheses indicate statistical errors.

Atom (Label)	Wyckoff Position	x	y	z	U_{iso} (Å^2)	Fractional Occupancy[a]
Co	16k	0.9068(3)	0.5765(3)	1.0616(5)	0.0005(5)	0.504(4)
V(1)	16k	0.9068(3)	0.5765(3)	1.0616(5)	0.0005(5)	0.496(4)
V(2)	8j	0.771	0.416	0.75	0.0042	1
V(3)	8j	0.957	1.198	0.75	0.0042	1
O(1)	8j	0.98357(9)	0.66282(11)	0.25	0.00356(16)	1
O(2)	8j	0.83242(8)	0.52523(11)	0.25	0.00388(16)	1
O(3)	16k	1.01787(6)	0.60246(8)	0.91384(10)	0.00392(11)	1
O(4)	8f	0.86076(9)	0.75	1	0.0126(4)	1
O(5)	16k	0.82899(6)	0.47373(8)	0.90801(10)	0.00556(12)	1
O(6)	8j	0.82973(8)	1.23252(10)	0.75	0.00269(15)	1

[a]The value of the fractional occupancies were fixed to the refined values obtained from a refinement of single crystal neutron diffraction data collected at 50 K.

TABLE IX. Cell parameters, fit residuals, and agreement factors for α-CoV_3O_8 obtained from the Rietveld refinement of laboratory powder x-ray diffraction data collected at 300 K. Numbers in parentheses indicate statistical errors.

Parameter	Value
a	14.292(1) Å
b	9.8844(9) Å
c	8.3969(8) Å
V	1186.2(3) Å^3
χ^2	1.487
R_p	10.26%
R_{wp}	14.05%

APPENDIX B: PROJECTION FACTORS

As outlined in the main text, a comparison between the current study and previous studies on other Co^{2+}-based magnets [60,75,81,91,94,166,185] suggests that the low-temperature magnetism of α-CoV_3O_8 may be solely attributed to the ground state doublet spin-orbit manifold, and thus can be simplified to a $j = \frac{1}{2}$ model. To utilize such a model in the current study, the Landé g factor g_J was required to be projected onto individual $j \equiv j_{\text{eff}}$ manifolds.

1. Calculation of the orbital angular momentum operator projection factor α

Before proceeding with the projection of the Landé g factor onto the $j_{\text{eff}} = \frac{1}{2}$ ground state spin-orbit manifold, it is important to note that such a doublet manifold is a consequence of an approach commonly used [60,75,81,91,94] to address the orbital triplet ground state in Co^{2+}. Such an approach first defines an effective total angular momentum $\hat{\mathbf{j}}_{\text{eff}} = \hat{\mathbf{l}} + \hat{\mathbf{S}}$, where $\hat{\mathbf{l}}$ is a fictitious orbital angular momentum operator, with eigenvalue $l = 1$ to reflect an triplet orbital degeneracy [104]. Thus, a projection of g_J and any angular momentum operators onto the $j = \frac{1}{2}$ manifold requires a concurrent projection of $\hat{\mathbf{L}}$ onto $\hat{\mathbf{l}}$, via a projection factor α.

TABLE X. Cobalt-oxygen distances and corresponding octahedral distortion parameter δ for α-CoV_3O_8 at 5 K deduced from the Rietveld refinement of single-crystal neutron diffraction data. Numbers in parentheses indicate statistical errors.

Oxygen Label	d (Å)	$(\frac{d-\langle d\rangle}{\langle d\rangle})^2 \times 10^4$
O(1)	2.12527(5)	27.79(3)
O(2)	1.98916(5)	2.162(8)
O(3)	2.07872(5)	8.79(2)
O(3)′	2.02358(5)	0.0549(13)
O(4)	1.92213(5)	22.95(3)
O(5)	1.97422(4)	4.89(1)
	$\frac{1}{N}\sum\{(\frac{d-\langle d\rangle}{\langle d\rangle})^2 \times 10^4\}$	11.106(8)

The determination of the projection factor α begins by first defining the crystal field Hamiltonian $\hat{\mathcal{H}}_{\text{CEF}}$ describing the effects of the crystalline electric field on the free ion states of the d^7 Co^{2+} resulting from the symmetry imposed by the crystal lattice [75,81,91,186]. Assuming both negligible distortions away from purely octahedral coordination and negligible admixture between the ^4F ground and first excited ^4P free ion states, a weak-intermediate crystal field approach can be employed [187] whereby $\hat{\mathcal{H}}_{\text{CEF}}$ can be written in terms of the Stevens operators $\hat{\mathcal{O}}_4^0$, $\hat{\mathcal{O}}_4^4$ and the numerical coefficient B_4 as

$$\hat{\mathcal{H}}_{\text{CEF}} = B_4\left(\hat{\mathcal{O}}_4^0 + 5\hat{\mathcal{O}}_4^4\right). \tag{B1}$$

The numerical coefficient B_4 is defined as $\beta\langle r^4\rangle$, where β is the Stevens multiplicative factor, while the Stevens operators are defined in terms of the $\hat{L}^2$, $\hat{L}_z$, and $\hat{L}_\pm$ orbital angular momentum operators [104,187] as

$$\hat{\mathcal{O}}_4^0 = 35\hat{L}_z^4 - 30\hat{L}^2\hat{L}_z^2 + 25\hat{L}_z^2 - 6\hat{L}^2 + 3\hat{L}^4 \tag{B2}$$

and

$$\hat{\mathcal{O}}_4^4 = \tfrac{1}{2}\left[\hat{L}_+^4 + \hat{L}_-^4\right]. \tag{B3}$$

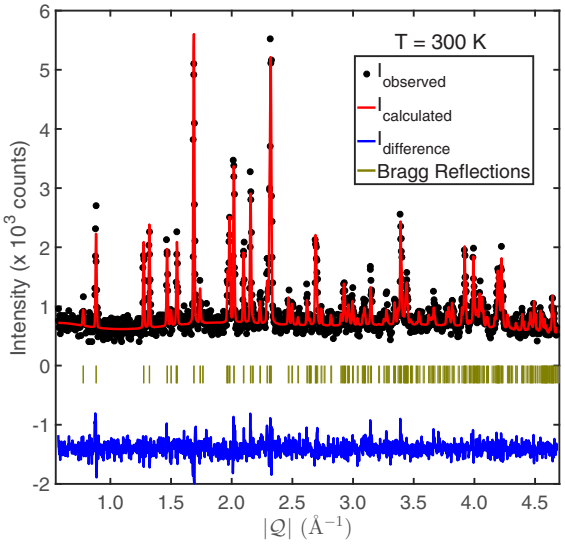

FIG. 9. Room temperature diffraction profile of polycrystalline α-CoV_3O_8 collected on a Bruker D2 Phaser x-ray diffractometer utilizing a monochromated Cu $K_{\alpha,1,2}$ source, confirming the absence of any discernible impurities. A Rietveld refinement ($\chi^2 = 1.487$, $R_p = 10.26\%$, $R_{wp} = 14.05\%$) indicates α-CoV_3O_8 crystallizes in the orthorhombic $Ibam$ (space group No. 72) structure [$a = 14.292(1)$ Å, $b = 9.8844(9)$ Å, $c = 8.3969(8)$ Å].

By combining Eqs. (B1)–(B3) and setting B_4 as -1, the crystal field Hamiltonian is given by

$$\begin{bmatrix} -180 & 0 & 0 & 0 & -232.4 & 0 & 0 \\ 0 & 420 & 0 & 0 & 0 & -300 & 0 \\ 0 & 0 & -60 & 0 & 0 & 0 & -232.4 \\ 0 & 0 & 0 & -360 & 0 & 0 & 0 \\ -232.4 & 0 & 0 & 0 & -60 & 0 & 0 \\ 0 & -300 & 0 & 0 & 0 & 40 & 0 \\ 0 & 0 & -232.4 & 0 & 0 & 0 & -180 \end{bmatrix} \tag{B4}$$

in the $|L = 3, m_L\rangle$ basis where each operator has been normalized by $\hbar$. Before proceeding, it is worth noting that by setting $|B_4|$ as 1, all energy eigenstates will be in terms of B_4 while the negative sign is due to the d^7 electron configuration of Co^{2+}, producing a triplet and not a singlet ground state like Ni^{2+} [186,188].

Diagonalizing the crystal field Hamiltonian yields

$$\begin{bmatrix} -360 & 0 & 0 & 0 & 0 & 0 & 0 \\ 0 & -360 & 0 & 0 & 0 & 0 & 0 \\ 0 & 0 & -360 & 0 & 0 & 0 & 0 \\ 0 & 0 & 0 & 120 & 0 & 0 & 0 \\ 0 & 0 & 0 & 0 & 120 & 0 & 0 \\ 0 & 0 & 0 & 0 & 0 & 120 & 0 \\ 0 & 0 & 0 & 0 & 0 & 0 & 720 \end{bmatrix} \tag{B5}$$

corresponding to a triply degenerate ground state (Γ_4), a triply degenerate first excited state (Γ_5), and a singlet second excited state (Γ_2), where $\Delta(\Gamma_4 \rightarrow \Gamma_5) = 480B_4$ and $\Delta(\Gamma_5 \rightarrow \Gamma_2) = 600B_4$.

Utilizing the diagonalized crystal field Hamiltonian above, a transformation matrix $\mathcal{C}$ can be defined as

$$\mathcal{C} = \begin{bmatrix} 0 & 0 & -0.79 & 0.61 & 0 & 0 & 0 \\ 0 & 0 & 0 & 0 & -0.71 & 0 & -0.71 \\ 0.61 & 0 & 0 & 0 & 0 & -0.79 & 0 \\ 0 & 1.00 & 0 & 0 & 0 & 0 & 0 \\ 0 & 0 & -0.61 & -0.79 & 0 & 0 & 0 \\ 0 & 0 & 0 & 0 & -0.71 & 0 & 0.71 \\ 0.79 & 0 & 0 & 0 & 0 & 0.61 & 0 \end{bmatrix}, \tag{B6}$$

where the columns of $\mathcal{C}$ are the eigenvectors corresponding to the eigenvalues in Eq. (B5). The eigenvectors are arranged in the order of increasing eigenvalues from left to right. In the case of degenerate eigenvalues, the eigenvectors are arranged in the order of increasing eigenvalues from left to right after the application of a small perturbative magnetic field $\hat{\mathcal{H}}_{MF} = H_{MF}\hat{S}_z$. The transformation matrix $\mathcal{C}$ rotates operators from the $|L = 3, m_L\rangle$ basis to a $|\phi_{\text{CEF}}\rangle$ basis defined by the crystal field eigenvectors by

$$\hat{\mathcal{O}}_{|\phi_{\text{CEF}}\rangle} = \mathcal{C}^{-1}\hat{\mathcal{O}}_{|L,m_L\rangle}\mathcal{C}. \tag{B7}$$

Since the ground state multiplet of the crystal field Hamiltonian corresponds to the triply orbitally degenerate manifold, then the top-left 3×3 block matrix of the z component of the orbital angular momentum operator projected onto the crystal field basis must (1) have its matrix entries arranged in a format equivalent to its corresponding angular momentum operator with $l = 1$, while (2) the entries in both matrices must be equal up to the projection constant α [160]. Projecting the $\hat{L}_z$ operator from the $|L = 3, m_L\rangle$ basis to the $|\phi_{\text{CEF}}\rangle$ basis via Eq. (B7), one obtains

$$\mathcal{C}^{-1}\hat{L}_z\mathcal{C} = \left[\begin{array}{ccc|ccc|c} 1.50 & 0 & 0 & 0 & 0 & -1.94 & 0 \\ 0 & 0 & 0 & 0 & 0 & 0 & 0 \\ 0 & 0 & -1.50 & -1.94 & 0 & 0 & 0 \\ \hline 0 & 0 & -1.94 & -0.50 & 0 & 0 & 0 \\ 0 & 0 & 0 & 0 & 0 & 0 & 2.00 \\ -1.94 & 0 & 0 & 0 & 0 & 0.50 & 0 \\ \hline 0 & 0 & 0 & 0 & 2.00 & 0 & 0 \end{array}\right]. \tag{B8}$$

A comparison of the top-left and middle-center 3×3 block matrices in Eq. (B8) to the $\hat{L}_z$ operator (normalized by $\hbar$) in the $|l = 1, m_l\rangle$ basis given by

$$\hat{L}_z = \begin{bmatrix} -1 & 0 & 0 \\ 0 & 0 & 0 \\ 0 & 0 & 1 \end{bmatrix} \tag{B9}$$

confirms that both block matrices have equivalent arrangements of matrix elements to the $\hat{L}_z$ operator in the $|l = 1, m_l\rangle$ basis, with projection factors $\alpha = -\frac{3}{2}$ and $\frac{1}{2}$ for the ground and first excited manifolds, respectively, in agreement with previous derivations utilizing group theory [81,91,104,186].

As a final confirmation of the validity of the projection described by Eq. (B7), both $\hat{L}_+$ and $\hat{L}_-$ were projected onto the $|\phi_{\text{CEF}}\rangle$ basis. Both $\hat{L}_x$ and $\hat{L}_y$ were then calculated using the following identities:

$$\hat{L}_x = \frac{\hat{L}_+ + \hat{L}_-}{2} \tag{B10}$$

and

$$\hat{L}_y = \frac{\hat{L}_+ - \hat{L}_-}{2i}, \tag{B11}$$

yielding

$$\hat{L}_x = \left[\begin{array}{ccc|ccc|c} 0 & 1.1 & 0 & 0 & -1.4 & 0 & 0 \\ 1.1 & 0 & -1.1 & -1.4 & 0 & -1.4 & 0 \\ 0 & -1.1 & 0 & 0 & 1.4 & 0 & 0 \\ \hline 0 & -1.4 & 0 & 0 & 0.4 & 0 & -1.4 \\ -1.4 & 0 & 1.4 & 0.4 & 0 & 0.4 & 0 \\ 0 & -1.4 & 0 & 0 & 0.4 & 0 & 1.4 \\ \hline 0 & 0 & 0 & -1.4 & 0 & 1.4 & 0 \end{array}\right], \tag{B12}$$

$$\hat{L}_y = i\left[\begin{array}{ccc|ccc|c} 0 & 1.1 & 0 & 0 & 0 & 0 & 0 \\ -1.1 & 0 & -1.1 & -1.4 & 0 & 1.4 & 0 \\ 0 & 1.1 & 0 & 0 & 1.4 & 0 & 0 \\ \hline 0 & 1.4 & 0 & 0 & 0.4 & 0 & -1.4 \\ -1.4 & 0 & -1.4 & -0.4 & 0 & 0.4 & 0 \\ 0 & -1.4 & 0 & 0 & -0.4 & 0 & -1.4 \\ \hline \xi & 0 & 0 & 1.4 & 0 & 1.4 & 0 \end{array}\right]. \tag{B13}$$

Finally, by extracting the top-left 3×3 block matrices, denoted by a prime, from the definitions of $\hat{L}_z$ [Eq. (B8)], $\hat{L}_x$ [Eq. (B12)], and $\hat{L}_y$ [Eq. (B13)] and evaluating the commutator $[\hat{L}'_x, \hat{L}'_y]$, one obtains

$$[\hat{L}'_x, \hat{L}'_y] = i\begin{bmatrix} 1.5 & 0 & 0 \\ 0 & 0 & 0 \\ 0 & 0 & -1.5 \end{bmatrix} = i\hat{L}'_z. \tag{B14}$$

By performing the commutator of all possible permutations of the projected components of the orbital angular momentum operator, it can be shown that the canonical commutation relations of angular momentum [104], normalized by $\hbar$,

$$[\hat{L}'_x, \hat{L}'_y] = i\epsilon_{xyz}\hat{L}'_z, \tag{B15}$$

are satisfied for the new $|\phi_{\text{CEF}}\rangle$ basis.

2. Calculation of projected Landé g factor g'_J

Recall from first-order perturbation theory [75] that the field splitting of the Co^{2+} spin-orbit multiplets is described by the perturbative Hamiltonian $\hat{\mathcal{H}}_m$ given by

$$\hat{\mathcal{H}}_m = \mu_B(g_L\hat{\mathbf{L}} + g_S\hat{\mathbf{S}}) \cdot \mathbf{H}, \tag{B16}$$

where g_L and g_S denote orbital and spin g factors, respectively. For the particular case of the d-block metal Co^{2+}, both orbital and spin g factors are taken to be the electron's g factors, equal to approximately 1 and 2, respectively, simplifying Eq. (B16) to

$$\hat{\mathcal{H}}_m = \mu_B(\hat{\mathbf{L}} + 2\hat{\mathbf{S}}) \cdot \mathbf{H}. \tag{B17}$$

Since an effective total angular momentum $\hat{\mathbf{j}}_{\text{eff}}$ was defined with the projected orbital angular momentum operator $\hat{\mathbf{l}}$ with $l = 1$, then the perturbative Hamiltonian in Eq. (B17) becomes

$$\begin{aligned} \hat{\mathcal{H}}_m &= \mu_B(\alpha\hat{\mathbf{l}} + 2\hat{\mathbf{S}}) \cdot \mathbf{H} \\ &= g'_J\mu_B\hat{\mathbf{j}} \cdot \mathbf{H}, \end{aligned} \tag{B18}$$

for a particular effective spin-orbit j_{eff} manifold. Equation (B18) incorporates an orbital angular momentum operator $\hat{\mathbf{L}}$ that has been projected onto $\hat{\mathbf{l}}$ via a projection factor α, and a projected Landé g factor g'_J. A comparison between Eqs. (B17) and (B18) suggests that the Landé g factor—a fundamental proportionality constant that can be derived

directly from the Wigner-Eckart theorem [94]—defined as

$$g_J = 1\left\{\frac{J(J+1)-S(S+1)+L(L+1)}{2J(J+1)}\right\} + 2\left\{\frac{J(J+1)+S(S+1)-L(L+1)}{2J(J+1)}\right\} \quad \text{(B19)}$$

for the original nonprojected perturbative Hamiltonian in Eq. (B17), assumes the form

$$g'_J = \frac{(2+\alpha)j(j+1)-(2-\alpha)l(l+1)+(2-\alpha)S(S+1)}{2j(j+1)}. \quad \text{(B20)}$$

As required, Eq. (B20) reduces to Eq. (B19) if $\alpha = 1$. By inserting the values of $S = \frac{3}{2}$ to reflect the high-spin d^7 electron configuration in ideal octahedral coordination, $l = 1$ to reflect the ground state crystal field manifold and the associated projection factor $\alpha = -\frac{3}{2}$, the projected Landé g factor of $\frac{13}{3}$ is obtained for the $j_{\text{eff}} = \frac{1}{2}$ ground state spin-orbit manifold [75].

3. Calculation of spin angular momentum operator projection factor α'

As discussed in previous work [75,81,91,94,166,185] on other systems whose magnetism is based on Co^{2+} in octahedral coordination, multiple projections of different angular momentum operators are necessary to consolidate the measured low-temperature magnetic excitations and the theoretical framework for a $j_{\text{eff}} = \frac{1}{2}$ ground state. One method [160] for such projections was presented in Appendix B 1 and involved the use of linear transformations in the matrix representation of operators. Although powerful, this method relies on access to computation software and quickly becomes tedious as the dimension of the Hilbert space of interest increases. For the purposes of completion, we present an alternative method to project angular momentum operators onto a particular j_{eff} manifold. This method consists of a special case of the Wigner-Eckart theorem [93,104], called the projection theorem, given by

$$\hat{\mathcal{O}} = \alpha'\hat{\mathbf{j}}_{\text{eff}} = \frac{\langle\hat{\mathcal{O}}\cdot\hat{\mathbf{j}}_{\text{eff}}\rangle}{j(j+1)}\hat{\mathbf{j}}_{\text{eff}}, \quad \text{(B21)}$$

describing the projection of an angular momentum operator $\hat{\mathcal{O}}$ onto an effective total angular momentum operator $\hat{\mathbf{j}}_{\text{eff}}$ via a projection factor α'. As introduced in Appendix B 1, the operator $\hat{\mathbf{j}}_{\text{eff}} = \hat{\mathbf{l}} + \hat{\mathbf{S}}$ denotes an effective total angular momentum operator that utilizes a projection of an orbital angular momentum operator $\hat{\mathbf{L}}$ with $L = 3$ onto a fictitious orbital angular momentum operator $\hat{\mathbf{l}}$ with $l = 1$ via α.

For illustrative purposes, let $\hat{\mathcal{O}}$ be the spin angular momentum operator $\hat{\mathbf{S}}$. The numerator of the projection factor α' in Eq. (B21) can be simplified by first using the distributive property of the inner product

$$\hat{\mathbf{S}}\cdot\hat{\mathbf{j}}_{\text{eff}} = \hat{\mathbf{S}}\cdot(\hat{\mathbf{l}}+\hat{\mathbf{S}}) = \hat{S}^2 + \hat{\mathbf{l}}\cdot\hat{\mathbf{S}}. \quad \text{(B22)}$$

The inner product $\hat{\mathbf{l}}\cdot\hat{\mathbf{S}}$ on the right-hand side of Eq. (B22) can be simplified to

$$\hat{\mathbf{l}}\cdot\hat{\mathbf{S}} = \tfrac{1}{2}[(\hat{j}_{\text{eff}})^2 - \hat{l}^2 - \hat{S}^2], \quad \text{(B23)}$$

since the inner product of $\hat{\mathbf{j}}_{\text{eff}}$ with itself is equal to

$$(\hat{j}_{\text{eff}})^2 = (\hat{\mathbf{l}}+\hat{\mathbf{S}})\cdot(\hat{\mathbf{l}}+\hat{\mathbf{S}}) = \hat{l}^2 + \hat{S}^2 + 2\hat{\mathbf{l}}\cdot\hat{\mathbf{S}}. \quad \text{(B24)}$$

Combining Eqs. (B22) and (B23), the numerator of α' in Eq. (B21) becomes

$$\langle\hat{\mathbf{S}}\cdot\hat{\mathbf{j}}_{\text{eff}}\rangle = S(S+1) + \tfrac{1}{2}[j(j+1) - l(l+1) - S(S+1)], \quad \text{(B25)}$$

where j_{eff} was relabeled as j. Inserting Eq. (B25) into Eq. (B21), one obtains

$$\hat{\mathbf{S}} = \frac{S(S+1)+\frac{1}{2}[j(j+1)-l(l+1)-S(S+1)]}{j(j+1)}\hat{\mathbf{j}}_{\text{eff}}, \quad \text{(B26)}$$

which can be simplified algebraically to

$$\hat{\mathbf{S}} = \left\{\frac{1}{2} + \frac{S(S+1)-l(l+1)}{2j(j+1)}\right\}\hat{\mathbf{j}}_{\text{eff}}. \quad \text{(B27)}$$

Finally, by inserting the aforementioned values of $S = \frac{3}{2}$, $l = 1$, and $j \equiv j_{\text{eff}} = \frac{1}{2}$ for high-spin Co^{2+}, Eq. (B27) simplifies to

$$\hat{\mathbf{S}} = \tfrac{5}{3}\hat{\mathbf{j}}_{\text{eff}}. \quad \text{(B28)}$$

A comparison between Eqs. (B21) and (B28) indicates that the projection factor α' of the spin-orbital angular momentum operator is $\frac{5}{3}$ for the $j = \frac{1}{2}$ ground state spin-orbit manifold [94]. It can be shown [81] that one obtains the same value of α' employing the method outlined in Appendix B 1 with the transformation matrix $\mathcal{C}$ defined as the eigenvectors of the spin-orbit Hamiltonian $\hat{\mathcal{H}}_{SO} = \alpha\lambda\hat{\mathbf{l}}\cdot\hat{\mathbf{S}}$, where $\alpha = -\frac{3}{2}$ as derived in Appendix B 1, $\lambda = -16$ meV as measured by Cowley *et al.* [91], and $\hat{\mathbf{l}}$ is a fictitious orbital angular momentum operator with an eigenvalue $l = 1$ as discussed above and in the main text.

APPENDIX C: DERIVATION OF THE POWDER-AVERAGED FIRST MOMENT SUM RULE OF NEUTRON SCATTERING

The first moment sum rule of neutron scattering [145] states that

$$\langle E\rangle(\mathbf{Q}) = -\frac{2}{3}\sum_{i,j} n_{ij}J_{ij}\langle\hat{\mathbf{S}}_i\cdot\hat{\mathbf{S}}_j\rangle[1-\cos(\mathbf{Q}\cdot\mathbf{d_{ij}})], \quad \text{(C1)}$$

where J_{ij}, $n_{ij}\langle\hat{\mathbf{S}}_i\cdot\hat{\mathbf{S}}_j\rangle$, $\mathbf{d}_{ij}$ denote the exchange constant, spin-spin correlator, and displacement vector between spins i and j, respectively. Applying the definition of the powder average [146], Eq. (C1) becomes

$$S(|\mathbf{Q}|, E) = \int d\Omega_{\hat{\mathbf{Q}}}\frac{S(\mathbf{Q}, E)}{4\pi}, \quad \text{(C2)}$$

and utilizing the property of linearity of the integral, one obtains

$$-\frac{\mathcal{B}_{ij}}{12\pi}\int_0^{\pi}\int_0^{2\pi}[1-\cos(|\mathbf{Q}||\mathbf{d}_{ij}|\cos\theta)]d\phi\sin\theta d\theta, \quad \text{(C3)}$$

where $\mathcal{B}_{ij}$ denotes $2n_{ij}J_{ij}\langle\hat{\mathbf{S}}_i\cdot\hat{\mathbf{S}}_j\rangle$ for a particular ij pair type. Using the substitution of $x = |\mathbf{Q}||\mathbf{d}_{ij}|\cos\theta$ in Eq. (C3), one

obtains

$$\frac{\mathcal{B}_{ij}}{3}\left(\frac{1}{4\pi}\right)\int_{|\mathbf{Q}||\mathbf{d}_{ij}|}^{-|\mathbf{Q}||\mathbf{d}_{ij}|}\int_0^{2\pi}[1-\cos(x)]d\phi\frac{dx}{|\mathbf{Q}||\mathbf{d}_{ij}|}. \quad \text{(C4)}$$

Employing the linearity property of the integral, the first term in Eq. (C4) is reduced to

$$\frac{\mathcal{B}_{ij}}{3}\left(\frac{1}{4\pi}\right)\int_{|\mathbf{Q}||\mathbf{d}_{ij}|}^{-|\mathbf{Q}||\mathbf{d}_{ij}|}\int_0^{2\pi}\frac{d\phi dx}{|\mathbf{Q}||\mathbf{d}_{ij}|}=-\frac{\mathcal{B}_{ij}}{3}. \quad \text{(C5)}$$

The second term in Eq. (C4) becomes

$$-\frac{\mathcal{B}_{ij}}{3}\left(\frac{1}{4\pi}\right)\int_{|\mathbf{Q}||\mathbf{d}_{ij}|}^{-|\mathbf{Q}||\mathbf{d}_{ij}|}\int_0^{2\pi}\cos(x)\frac{d\phi dx}{|\mathbf{Q}||\mathbf{d}_{ij}|}, \quad \text{(C6)}$$

which can be simplified by first integrating out $d\phi$,

$$-\frac{\mathcal{B}_{ij}}{3}\left(\frac{2\pi}{4\pi}\right)\int_{|\mathbf{Q}||\mathbf{d}_{ij}|}^{-|\mathbf{Q}||\mathbf{d}_{ij}|}\cos(x)\frac{dx}{|\mathbf{Q}||\mathbf{d}_{ij}|}, \quad \text{(C7)}$$

which is equal to

$$-\frac{\mathcal{B}_{ij}}{3}\left(\frac{2\pi}{4\pi}\right)[\sin(-|\mathbf{Q}||\mathbf{d}_{ij}|)-\sin(|\mathbf{Q}||\mathbf{d}_{ij}|)]. \quad \text{(C8)}$$

Since sine is an odd function, Eq. (C8) reduces to

$$\frac{\mathcal{B}_{ij}}{3}\left(\frac{\sin(|\mathbf{Q}||\mathbf{d}_{ij}|)}{|\mathbf{Q}||\mathbf{d}_{ij}|}\right). \quad \text{(C9)}$$

Combining both terms, one obtains the final expression for the $|\mathbf{Q}|$ dependence of the powder-averaged first moment as

$$\langle E\rangle(|\mathbf{Q}|)=-\frac{\mathcal{B}_{ij}}{3}\left(1-\frac{\sin(|\mathbf{Q}||\mathbf{d}_{ij}|)}{|\mathbf{Q}||\mathbf{d}_{ij}|}\right). \quad \text{(C10)}$$

The expression in Eq. (C10) pertains to one particular ij pair type. Utilizing the linearity property of the integral and replacing $\mathcal{B}_{ij}$ by its definition, one can recover the sum from Eq. (C1),

$$\langle E\rangle(\mathbf{Q})=-\frac{2}{3}\sum_{i,j}n_{ij}J_{ij}\langle\hat{\mathbf{S}}_i\cdot\hat{\mathbf{S}}_j\rangle\left(1-\frac{\sin(|\mathbf{Q}||\mathbf{d}_{ij}|)}{|\mathbf{Q}||\mathbf{d}_{ij}|}\right), \quad \text{(C11)}$$

corresponding to Eq. (11) in the main text.

[1] D. S. Fisher and A. Khurana, Phys. Today **41**(12), 56 (1988).
[2] N. Martin, P. Bonville, E. Lhotel, S. Guitteny, A. Wildes, C. Decorse, M. Ciomaga Hatnean, G. Balakrishnan, I. Mirebeau, and S. Petit, Phys. Rev. X **7**, 041028 (2017).
[3] R. Sibille, E. Lhotel, M. C. Hatnean, G. J. Nilsen, G. Ehlers, A. Cervellino, E. Ressouche, M. Frontzek, O. Zaharko, V. Pomjakushin *et al.*, Nat. Commun. **8**, 892 (2017).
[4] S. F. Edwards and P. W. Anderson, J. Phys. F: Met. Phys. **5**, 965 (1975).
[5] S. F. Edwards and P. W. Anderson, J. Phys. F: Met. Phys. **6**, 1927 (1976).
[6] E. P. Raposo and M. D. Coutinho-Filho, Phys. Rev. B **57**, 3495 (1998).
[7] O. Narayan and D. S. Fisher, Phys. Rev. B **42**, 7869 (1990).
[8] L. Savary and L. Balents, Phys. Rev. Lett. **118**, 087203 (2017).
[9] E. Altman, Y. Kafri, A. Polkovnikov, and G. Refael, Phys. Rev. Lett. **93**, 150402 (2004).
[10] P. B. Weichman, Mod. Phys. Lett. B **22**, 2623 (2008).
[11] J. A. Hoyos and T. Vojta, Phys. Rev. Lett. **100**, 240601 (2008).
[12] T. Vojta, J. Phys. A: Math. Gen. **39**, R143 (2006).
[13] R. A. Cowley and W. J. L. Buyers, Rev. Mod. Phys. **44**, 406 (1972).
[14] T. M. Nieuwenhuizen and C. N. A. van Duin, Eur. Phys. J. B **7**, 191 (1999).
[15] L. Radzihovsky and J. Toner, Phys. Rev. B **60**, 206 (1999).
[16] T. Bellini, L. Radzihovsky, J. Toner, and N. A. Clark, Science **294**, 1074 (2001).
[17] J. Toner and D. P. DiVincenzo, Phys. Rev. B **41**, 632 (1990).
[18] K. Binder and A. P. Young, Rev. Mod. Phys. **58**, 801 (1986).
[19] H. Barghathi and T. Vojta, Phys. Rev. Lett. **109**, 170603 (2012).
[20] T. Vojta, Computing quantum phase transitions, in *Reviews in Computational Chemistry* (Wiley-Blackwell, Hoboken, NJ, 2009), Chap. 4, pp. 167–221.
[21] T. Giamarchi and P. Le Doussal, Phys. Rev. B **52**, 1242 (1995).
[22] T. Klein, I. Joumard, S. Blanchard, J. Marcus, R. Cubitt, T. Giamarchi, and P. Le Doussal, Nature (London) **413**, 404 (2001).
[23] A. D. Hernández and D. Domínguez, Phys. Rev. Lett. **92**, 117002 (2004).
[24] P. Olsson, Phys. Rev. Lett. **98**, 097001 (2007).
[25] D. Li and B. Rosenstein, Phys. Rev. Lett. **90**, 167004 (2003).
[26] M. J. P. Gingras and D. A. Huse, Phys. Rev. B **53**, 15193 (1996).
[27] D. S. Fisher, Phys. Rev. Lett. **78**, 1964 (1997).
[28] T. Giamarchi and P. Le Doussal, Phys. Rev. Lett. **72**, 1530 (1994).
[29] R. B. Griffiths, Phys. Rev. Lett. **23**, 17 (1969).
[30] A. J. Bray, Phys. Rev. Lett. **59**, 586 (1987).
[31] B. M. McCoy, Phys. Rev. Lett. **23**, 383 (1969).
[32] S. Park, R. L. Leheny, R. J. Birgeneau, J.-L. Gallani, C. W. Garland, and G. S. Iannacchione, Phys. Rev. E **65**, 050703 (2002).
[33] R. L. Leheny, S. Park, R. J. Birgeneau, J.-L. Gallani, C. W. Garland, and G. S. Iannacchione, Phys. Rev. E **67**, 011708 (2003).
[34] P. S. Clegg, C. Stock, R. J. Birgeneau, C. W. Garland, A. Roshi, and G. S. Iannacchione, Phys. Rev. E **67**, 021703 (2003).
[35] H. R. Glyde, Rep. Prog. Phys. **81**, 014501 (2018).
[36] H. R. Glyde, O. Plantevin, B. Fåk, G. Coddens, P. S. Danielson, and H. Schober, Phys. Rev. Lett. **84**, 2646 (2000).
[37] J. V. Porto and J. M. Parpia, Phys. Rev. Lett. **74**, 4667 (1995).
[38] D. T. Sprague, T. M. Haard, J. B. Kycia, M. R. Rand, Y. Lee, P. J. Hamot, and W. P. Halperin, Phys. Rev. Lett. **75**, 661 (1995).
[39] M. Chan, N. Mulders, and J. Reppy, Phys. Today **49**(8), 30 (2018).
[40] Y. Imry and S.-k. Ma, Phys. Rev. Lett. **35**, 1399 (1975).

[41] A. Aharony, Y. Imry, and S.-k. Ma, Phys. Rev. Lett. **37**, 1364 (1976).
[42] S. M. A. Tabei, M. J. P. Gingras, Y.-J. Kao, P. Stasiak, and J.-Y. Fortin, Phys. Rev. Lett. **97**, 237203 (2006).
[43] D. Silevitch, D. Bitko, J. Brooke, S. Ghosh, G. Aeppli, and T. Rosenbaum, Nature (London) **448**, 567 (2007).
[44] Z. Slanič, D. P. Belanger, and J. A. Fernandez-Baca, Phys. Rev. Lett. **82**, 426 (1999).
[45] G. Álvarez, N. Aso, D. P. Belanger, A. M. Durand, V. Martín-Mayor, K. Motoya, and Y. Muro, Phys. Rev. B **86**, 024416 (2012).
[46] Y. W. Rodriguez, I. E. Anderson, D. P. Belanger, H. Nojiri, F. Ye, and J. A. Fernandez-Baca, J. Magn. Magn. Mater. **310**, 1546 (2007).
[47] R. A. Cowley, H. Yoshizawa, G. Shirane, and R. J. Birgeneau, Z. Phys. B: Condens. Matter **58**, 15 (1984).
[48] R. J. Birgeneau and Y. J. Uemura, J. Appl. Phys. **61**, 3692 (1987).
[49] C. Paduani, D. P. Belanger, J. Wang, S.-J. Han, and R. M. Nicklow, Phys. Rev. B **50**, 193 (1994).
[50] R. Leheny, Y. Lee, G. Shirane, and R. Birgeneau, Eur. Phys. J. B **32**, 287 (2003).
[51] T. Vojta, AIP Conf. Proc. **1550**, 188 (2013).
[52] Y. Oka, T. Yao, N. Yamamoto, and Y. Ueda, J. Solid State Chem. **141**, 133 (1998).
[53] D. J. Lloyd and J. Galy, Cryst. Struct. Commun. **2**, 209 (1973).
[54] S. Fishman and A. Aharony, J. Phys. C: Solid State Phys. **12**, L729 (1979).
[55] P. W. Anderson, Phys. Rev. **109**, 1492 (1958).
[56] A. Croy, P. Cain, and M. Schreiber, Eur. Phys. J. B **82**, 107 (2011).
[57] F. A. B. F. de Moura and M. L. Lyra, Phys. Rev. Lett. **81**, 3735 (1998).
[58] Z. He, J.-I. Yamaura, Y. Ueda, and W. Cheng, J. Am. Chem. Soc. **131**, 7554 (2009).
[59] M. Markkula, A. M. Arévalo-López, and J. P. Attfield, J. Solid State Chem. **192**, 390 (2012).
[60] F. Wallington, A. M. Arévalo-López, J. W. Taylor, J. R. Stewart, V. García-Sakai, J. P. Attfield, and C. Stock, Phys. Rev. B **92**, 125116 (2015).
[61] S. Ichikawa, M. Hibino, and T. Yao, Asian J. Energy Environ. **8**, 490 (2007).
[62] Agilent-CrysAlisPRO, Yarnton, Oxfordshire, England, 2013.
[63] O. V. Dolomanov, L. J. Bourhis, R. J. Gildea, J. A. Howard, and H. Puschmann, J. Appl. Crystallogr. **42**, 339 (2009).
[64] V. Petříček, M. Dušek, and L. Palatinus, Z. Kristallogr. Cryst. Mater. **229**, 345 (2014).
[65] B. H. Toby, J. Appl. Crystallogr. **34**, 210 (2001).
[66] W. Whitley, C. Stock, and A. D. Huxley, J. Appl. Crystallogr. **48**, 1342 (2015).
[67] C. L. Bull, M. W. Johnson, H. Hamidov, K. Komatsu, M. Guthrie, M. J. Gutmann, J. S. Loveday, and R. J. Nelmes, J. Appl. Crystallogr. **47**, 974 (2014).
[68] M. J. Gutmann, V. Petříček, M. A. Daoud-Aladine, and C. Y. Martin, Meas. Sci. Technol. **19**, 034005 (2008).
[69] M. Gutmann, Acta Cryst. A **61**, c164 (2005).
[70] C. Stock, R. A. Cowley, J. W. Taylor, and S. M. Bennington, Phys. Rev. B **81**, 024303 (2010).
[71] K. H. Andersen, Nucl. Instrum. Methods Phys. Res., Sect. A **371**, 472 (1996).
[72] F. Hippert, E. Geissler, J. L. Hodeau, E. Lelièvre-Berna, and J.-R. Regnard, *Neutron and X-ray Spectroscopy* (Springer Science & Business Media, Berlin, 2006).
[73] C. J. Carlile, M. A. Adams, P. S. R. Krishna, M. Prager, K. Shibata, and P. Westerhuijs, Nucl. Instrum. Methods Phys. Res., Sect. A **338**, 78 (1994).
[74] National Institute of Standards and Technology, *NIST Center for Neutron Research Accomplishments and Opportunities*, ASTM Special Technical Publication, Vol. 962 (Department of Commerce, United States of America, 2001).
[75] W. Buyers, T. Holden, E. Svensson, R. Cowley, and M. Hutchings, J. Phys. C **4**, 2139 (1971).
[76] J. B. Goodenough, Phys. Rev. **100**, 564 (1955).
[77] J. B. Goodenough, J. Phys. Chem. Solids **6**, 287 (1958).
[78] J. Kanamori, J. Phys. Chem. Solids **10**, 87 (1959).
[79] Z. Ropka and R. J. Radwanski, Czech J. Phys. **54**, 427 (2004).
[80] J. L. Gavilano, D. Rau, S. Mushkolaj, H. R. Ott, P. Millet, and F. Mila, Phys. Rev. Lett. **90**, 167202 (2003).
[81] J. Kanamori, Prog. Theor. Exp. Phys. **17**, 177 (1957).
[82] B. Kim, B. H. Kim, K. Kim, H. C. Choi, S.-Y. Park, Y. H. Jeong, and B. I. Min, Phys. Rev. B **85**, 220407 (2012).
[83] D. B. Litvin, *Magnetic Group Tables: 1-, 2- and 3-Dimensional Magnetic Subperiodic Groups and Magnetic Space Groups* (IUCR, Hoboken, NJ, 2013).
[84] M. De Graef, Metall. Mater. Trans. A **41**, 1321 (2010).
[85] G. Xu, Z. Xu, and J. Tranquada, Rev. Sci. Instrum. **84**, 083906 (2013).
[86] Z. Xu, J. Wen, T. Berlijn, P. M. Gehring, C. Stock, M. B. Stone, W. Ku, G. Gu, S. M. Shapiro, R. J. Birgeneau, and G. Xu, Phys. Rev. B **86**, 174419 (2012).
[87] C. Stock, L. C. Chapon, O. Adamopoulos, A. Lappas, M. Giot, J. W. Taylor, M. A. Green, C. M. Brown, and P. G. Radaelli, Phys. Rev. Lett. **103**, 077202 (2009).
[88] H. F. Fong, P. Bourges, Y. Sidis, L. P. Regnault, J. Bossy, A. Ivanov, D. L. Milius, I. A. Aksay, and B. Keimer, Phys. Rev. B **61**, 14773 (2000).
[89] G. L. Squires, *Introduction to the Theory of Thermal Neutron Scattering*, 3rd ed. (Cambridge University Press, Cambridge, UK, 2012).
[90] C. Stock, W. J. L. Buyers, R. Liang, D. Peets, Z. Tun, D. Bonn, W. N. Hardy, and R. J. Birgeneau, Phys. Rev. B **69**, 014502 (2004).
[91] R. A. Cowley, W. J. L. Buyers, C. Stock, Z. Yamani, C. Frost, J. W. Taylor, and D. Prabhakaran, Phys. Rev. B **88**, 205117 (2013).
[92] W. J. L. Buyers, R. A. Cowley, T. M. Holden, and R. W. H. Stevenson, J. Appl. Phys. **39**, 1118 (1968).
[93] D. I. Khomskii, *Transition Metal Compounds* (Cambridge University Press, Cambridge, UK, 2014).
[94] P. M. Sarte, R. A. Cowley, E. E. Rodriguez, E. Pachoud, D. Le, V. García-Sakai, J. W. Taylor, C. D. Frost, D. Prabhakaran, C. MacEwen, A. Kitada, A. J. Browne, M. Songvilay, Z. Yamani, W. J. L. Buyers, J. P. Attfield, and C. Stock, Phys. Rev. B **98**, 024415 (2018).
[95] R. A. Cowley, W. J. L. Buyers, P. Martel, and R. W. H. Stevenson, J. Phys. C: Solid State Phys. **6**, 2997 (1973).

[96] P. Martel, R. A. Cowley, and R. W. H. Stevenson, Can. J. Phys. **46**, 1355 (1968).

[97] A. M. Abakumov, R. Erni, A. A. Tsirlin, M. D. Rossell, D. Batuk, G. Néer, and G. V. Tendeloo, Chem. Mater. **25**, 2670 (2013).

[98] H. M. Gladney, Phys. Rev. **146**, 253 (1966).

[99] U. Walter, J. Phys. Chem. Solids **45**, 401 (1984).

[100] M. B. Stone, I. Zaliznyak, D. H. Reich, and C. Broholm, Phys. Rev. B **64**, 144405 (2001).

[101] J. Lorenzana, G. Seibold, and R. Coldea, Phys. Rev. B **72**, 224511 (2005).

[102] K. W. Plumb, J. R. Morey, J. A. Rodriguez-Rivera, H. Wu, A. A. Podlesnyak, T. M. McQueen, and C. L. Broholm, Phys. Rev. X **6**, 041055 (2016).

[103] P. R. Hammar, D. H. Reich, C. Broholm, and F. Trouw, Phys. Rev. B **57**, 7846 (1998).

[104] A. Abragam and B. Bleaney, *Electron Paramagnetic Resonance of Transition Ions* (Dover Publications, New York, 1986).

[105] T. Holden, W. Buyers, E. Svensson, R. Cowley, M. Hutchings, D. Hukin, and R. Stevenson, J. Phys. C **4**, 2127 (1971).

[106] C. Stock, C. Broholm, F. Demmel, J. Van Duijn, J. W. Taylor, H. J. Kang, R. Hu, and C. Petrovic, Phys. Rev. Lett. **109**, 127201 (2012).

[107] S. A. J. Kimber, H. Mutka, T. Chatterji, T. Hofmann, P. F. Henry, H. N. Bordallo, D. N. Argyriou, and J. P. Attfield, Phys. Rev. B **84**, 104425 (2011).

[108] R. Radwanski and Z. Ropka, Phys. B (Amsterdam, Neth.) **345**, 107 (2004).

[109] W. Neubeck, C. Vettier, F. de Bergevin, F. Yakhou, D. Mannix, L. Ranno, and T. Chatterji, J. Phys. Chem. Solids **62**, 2173 (2001).

[110] R. Birgeneau, A. Aharony, N. Belk, F. Chou, Y. Endoh, M. Greven, S. Hosoya, M. Kastner, C. Lee, Y. Lee, G. Shirane, S. Wakimoto, B. Wells, and K. Yamada, J. Phys. Chem. Solids **56**, 1913 (1995).

[111] M. Greven, R. J. Birgeneau, Y. Endoh, M. A. Kastner, M. Matsuda, and G. Shirane, Z. Phys. B: Condens. Matter **96**, 465 (1995).

[112] M. Songvilay, S. Petit, V. Hardy, J. P. Castellan, G. André, C. Martin, and F. Damay, Phys. Rev. B **91**, 054408 (2015).

[113] J. van Duijn, K. H. Kim, N. Hur, D. Adroja, M. A. Adams, Q. Z. Huang, M. Jaime, S.-W. Cheong, C. Broholm, and T. G. Perring, Phys. Rev. Lett. **94**, 177201 (2005).

[114] B. D. Gaulin, E. Kermarrec, M. L. Dahlberg, M. J. Matthews, F. Bert, J. Zhang, P. Mendels, K. Fritsch, G. E. Granroth, P. Jiramongkolchai, A. Amato, C. Baines, R. J. Cava, and P. Schiffer, Phys. Rev. B **91**, 245141 (2015).

[115] J. Gaudet, D. D. Maharaj, G. Sala, E. Kermarrec, K. A. Ross, H. A. Dabkowska, A. I. Kolesnikov, G. E. Granroth, and B. D. Gaulin, Phys. Rev. B **92**, 134420 (2015).

[116] Y. J. Uemura and R. J. Birgeneau, Phys. Rev. B **36**, 7024 (1987).

[117] C. Stock, W. J. L. Buyers, Z. Yamani, Z. Tun, R. J. Birgeneau, R. Liang, D. Bonn, and W. N. Hardy, Phys. Rev. B **77**, 104513 (2008).

[118] R. J. Birgeneau, R. W. Erwin, P. M. Gehring, M. A. Kastner, B. Keimer, M. Sato, S. Shamoto, G. Shirane, and J. Tranquada, Z. Phys. B.: Condens. Matter **87**, 15 (1992).

[119] W. Bao, Y. Chen, Y. Qiu, and J. L. Sarrao, Phys. Rev. Lett. **91**, 127005 (2003).

[120] B. Keimer, R. J. Birgeneau, A. Cassanho, Y. Endoh, R. W. Erwin, M. A. Kastner, and G. Shirane, Phys. Rev. Lett. **67**, 1930 (1991).

[121] S. D. Wilson, S. Li, P. Dai, W. Bao, J.-H. Chung, H. J. Kang, S.-H. Lee, S. Komiya, Y. Ando, and Q. Si, Phys. Rev. B **74**, 144514 (2006).

[122] M. Collins, *Magnetic Critical Scattering*, Oxford Series on Neutron Scattering in Condensed Matter (Oxford University Press, New York, NY, 1989).

[123] C. Stock, E. E. Rodriguez, and M. A. Green, Phys. Rev. B **85**, 094507 (2012).

[124] T. Hong, M. Kenzelmann, M. M. Turnbull, C. P. Landee, B. D. Lewis, K. P. Schmidt, G. S. Uhrig, Y. Qiu, C. Broholm, and D. Reich, Phys. Rev. B **74**, 094434 (2006).

[125] T. Mason, in *High-Temperature Superconductors. II*, Handbook on the Physics and Chemistry of Rare Earths (Elsevier, Amsterdam, Netherlands, 2001), Vol. 31, pp. 281–314.

[126] A. Schröder, G. Aeppli, R. Coldea, M. Adams, O. Stockert, H. Löhneysen, E. Bucher, R. Ramazashvili, and P. Coleman, Nature (London) **407**, 351 (2000).

[127] O. Stockert, M. Enderle, and H. v. Löhneysen, Phys. Rev. Lett. **99**, 237203 (2007).

[128] A. J. Millis, Phys. Rev. B **48**, 7183 (1993).

[129] J. D. Jackson, *Classical Electrodynamics*, 3rd ed. (Wiley, New York, NY, 1999).

[130] B. L. Bean and J. R. Izatt, J. Opt. Soc. Am. **63**, 832 (1973).

[131] M. Hagen, R. A. Cowley, S. K. Satija, H. Yoshizawa, G. Shirane, R. J. Birgeneau, and H. J. Guggenheim, Phys. Rev. B **28**, 2602 (1983).

[132] W. Bao, C. Broholm, G. Aeppli, S. A. Carter, P. Dai, T. F. Rosenbaum, J. M. Honig, P. Metcalf, and S. F. Trevino, Phys. Rev. B **58**, 12727 (1998).

[133] M. T. Hutchings, M. P. Schulhof, and H. J. Guggenheim, Phys. Rev. B **5**, 154 (1972).

[134] M. F. Collins, V. J. Minkiewicz, R. Nathans, L. Passell, and G. Shirane, Phys. Rev. **179**, 417 (1969).

[135] M. P. Schulhof, R. Nathans, P. Heller, and A. Linz, Phys. Rev. B **4**, 2254 (1971).

[136] H. Chou, J. M. Tranquada, G. Shirane, T. E. Mason, W. J. L. Buyers, S. Shamoto, and M. Sato, Phys. Rev. B **43**, 5554 (1991).

[137] Q. Si, S. Rabello, K. Ingersent, and J. L. Smith, Nature (London) **413**, 804 (2001).

[138] M. Hasenbusch, F. P. Toldin, A. Pelissetto, and E. Vicari, J. Stat. Mech. (2007) P02016.

[139] H. G. Ballesteros, L. A. Fernández, V. Martín-Mayor, A. Muñoz Sudupe, G. Parisi, and J. J. Ruiz-Lorenzo, Phys. Rev. B **58**, 2740 (1998).

[140] P. Calabrese, V. Martín-Mayor, A. Pelissetto, and E. Vicari, Phys. Rev. E **68**, 036136 (2003).

[141] P. Calabrese, A. Pelissetto, and E. Vicari, Phys. Rev. B **68**, 092409 (2003).

[142] M. J. George and J. J. Rehr, Phys. Rev. Lett. **53**, 2063 (1984).

[143] C. Stock, L. C. Chapon, A. Schneidewind, Y. Su, P. G. Radaelli, D. F. McMorrow, A. Bombardi, N. Lee, and S.-W. Cheong, Phys. Rev. B **83**, 104426 (2011).

[144] S. D. Wilson, Z. Yamani, C. R. Rotundu, B. Freelon, E. Bourret-Courchesne, and R. J. Birgeneau, Phys. Rev. B **79**, 184519 (2009).
[145] P. C. Hohenberg and W. F. Brinkman, Phys. Rev. B **10**, 128 (1974).
[146] J. T. Haraldsen, T. Barnes, and J. L. Musfeldt, Phys. Rev. B **71**, 064403 (2005).
[147] G. Xu, C. Broholm, D. H. Reich, and M. A. Adams, Phys. Rev. Lett. **84**, 4465 (2000).
[148] E. E. McCabe, C. Stock, E. E. Rodriguez, A. S. Wills, J. W. Taylor, and J. S. O. Evans, Phys. Rev. B **89**, 100402 (2014).
[149] S. Ma, C. Broholm, D. H. Reich, B. J. Sternlieb, and R. W. Erwin, Phys. Rev. Lett. **69**, 3571 (1992).
[150] S. M. Girvin, A. H. MacDonald, and P. M. Platzman, Phys. Rev. B **33**, 2481 (1986).
[151] E. C. Svensson, W. J. L. Buyers, T. M. Holden, R. A. Cowley, and R. H. W. Stevenson, Can. J. Phys. **47**, 1983 (1969).
[152] M. Ramazanoglu, C. P. Adams, J. P. Clancy, A. J. Berlinsky, Z. Yamani, R. Szymczak, H. Szymczak, J. Fink-Finowicki, and B. D. Gaulin, Phys. Rev. B **79**, 024417 (2009).
[153] K. Lee, J. Lee, C. Lee, and M. Whangbo, Bull. Korean Chem. Soc. **35**, 1277 (2014).
[154] C. Kittel, *Introduction to Solid State Physics* (Wiley, New York, 2005).
[155] M. B. Stone, Y. Chen, J. Rittner, H. Yardimci, D. H. Reich, C. Broholm, D. V. Ferraris, and T. Lectka, Phys. Rev. B **65**, 064423 (2002).
[156] R. J. Birgeneau, Q. Feng, Q. J. Harris, J. P. Hill, A. P. Ramirez, and T. R. Thurston, Phys. Rev. Lett. **75**, 1198 (1995).
[157] Y. J. Kim, R. J. Birgeneau, F. C. Chou, M. Greven, M. A. Kastner, Y. S. Lee, B. O. Wells, A. Aharony, O. Entin-Wohlman, I. Y. Korenblit, A. B. Harris, R. W. Erwin, and G. Shirane, Phys. Rev. B **64**, 024435 (2001).
[158] I. Cabrera, J. D. Thompson, R. Coldea, D. Prabhakaran, R. I. Bewley, T. Guidi, J. A. Rodriguez-Rivera, and C. Stock, Phys. Rev. B **90**, 014418 (2014).
[159] A. P. Young, *Spin Glasses and Random Fields*, Directions in Condensed Matter Physics (World Scientific, London, UK, 1998).
[160] G. L. Stamokostas and G. A. Fiete, Phys. Rev. B **97**, 085150 (2018).
[161] A. R. King and V. Jaccarino, J. Appl. Phys. **52**, 1785 (1981).
[162] J. Mattsson, J. Kushauer, D. Bertrand, J. Ferré, and W. Kleemann, J. Magn. Magn. Mater. **130**, 216 (1994).
[163] N. G. Fytas, V. Martín-Mayor, M. Picco, and N. Sourlas, J. Stat. Phys. **172**, 665 (2018).
[164] L. M. Volkova, J. Phys.: Condens. Matter **19**, 176208 (2007).
[165] D. A. Keen and A. L. Goodwin, Nature (London) **521**, 303 (2015).
[166] R. S. Cowley and K. Carneiro, J. Phys. C: Solid State Phys. **13**, 3281 (1980).
[167] G. D'Ariano and F. Borsa, Phys. Rev. B **26**, 6215 (1982).
[168] C. A. Ramos, A. R. King, and V. Jaccarino, Phys. Rev. B **37**, 5483 (1988).
[169] D. P. Belanger, A. R. King, I. B. Ferreira, and V. Jaccarino, Phys. Rev. B **37**, 226 (1988).
[170] D. P. Belanger and H. Yoshizawa, Phys. Rev. B **47**, 5051 (1993).
[171] T. Terao, K. Yakubo, and T. Nakayama, Phys. Rev. E **50**, 566 (1994).
[172] M. Vojta, Phys. Rev. Lett. **111**, 097202 (2013).
[173] I. Y. Korenblit and E. F. Shender, Phys. Rev. B **48**, 9478 (1993).
[174] C. C. Wan, A. B. Harris, and D. Kumar, Phys. Rev. B **48**, 1036 (1993).
[175] M. Hutchings, B. Rainford, and H. Guggenheim, J. Phys. C: Solid State Phys. **3**, 307 (1970).
[176] C. B. de Araujo, Phys. Rev. B **22**, 266 (1980).
[177] R. J. Birgeneau, R. A. Cowley, G. Shirane, H. Yoshizawa, D. P. Belanger, A. R. King, and V. Jaccarino, Phys. Rev. B **27**, 6747 (1983).
[178] J. P. Hill, Q. Feng, Q. J. Harris, R. J. Birgeneau, A. P. Ramirez, and A. Cassanho, Phys. Rev. B **55**, 356 (1997).
[179] P. W. Mitchell, R. A. Cowley, H. Yoshizawa, P. Böni, Y. J. Uemura, and R. J. Birgeneau, Phys. Rev. B **34**, 4719 (1986).
[180] G. J. Coombs, R. A. Cowley, W. J. L. Buyers, E. C. Svensson, T. M. Holden, and D. A. Jones, J. Phys. C: Solid State Phys. **9**, 2167 (1976).
[181] Z. Yamani, W. J. L. Buyers, R. A. Cowley, and D. Prabhakaran, Phys. B (Amsterdam, Neth.) **403**, 1406 (2008).
[182] T. Satoh, R. Iida, T. Higuchi, Y. Fujii, A. Koreeda, H. Ueda, T. Shimura, K. Kuroda, V. I. Butrim, and B. A. Ivanov, Nat. Commun. **8**, 638 (2017).
[183] K. Tomiyasu and S. Itoh, J. Phys. Soc. Jpn. **75**, 084708 (2006).
[184] M. Feygenson, X. Teng, S. E. Inderhees, Y. Yiu, W. Du, W. Han, J. Wen, Z. Xu, A. A. Podlesnyak, J. L. Niedziela, M. Hagen, Y. Qiu, C. M. Brown, L. Zhang, and M. C. Aronson, Phys. Rev. B **83**, 174414 (2011).
[185] K. A. Ross, J. W. Krizan, J. A. Rodriguez-Rivera, R. J. Cava, and C. L. Broholm, Phys. Rev. B **93**, 014433 (2016).
[186] F. Seitzand D. Turnbull, *Solid State Physics* (Elsevier Science, Amsterdam, Netherlands, 1959), Vol. 9.
[187] H. T. Hutchings, Solid State Phys. **16**, 227 (1964).
[188] Y.-J. Kim, A. P. Sorini, C. Stock, T. G. Perring, J. van den Brink, and T. P. Devereaux, Phys. Rev. B **84**, 085132 (2011).

Disentangling orbital and spin exchange interactions for Co^{2+} on a rocksalt lattice

P. M. Sarte,[1,2] R. A. Cowley,[3,*] E. E. Rodriguez,[4] E. Pachoud,[1,2] D. Le,[5] V. García-Sakai,[5] J. W. Taylor,[5] C. D. Frost,[5] D. Prabhakaran,[3] C. MacEwen,[6] A. Kitada,[7] A. J. Browne,[1,2] M. Songvilay,[2,6] Z. Yamani,[8] W. J. L. Buyers,[8,9] J. P. Attfield,[1,2] and C. Stock[2,6]

[1]*School of Chemistry, University of Edinburgh, Edinburgh EH9 3FJ, United Kingdom*
[2]*Centre for Science at Extreme Conditions, University of Edinburgh, Edinburgh EH9 3FD, United Kingdom*
[3]*Department of Physics, Clarendon Laboratory, University of Oxford, Park Road, Oxford OX1 3PU, United Kingdom*
[4]*Department of Chemistry and Biochemistry, University of Maryland, College Park, Maryland 20742, USA*
[5]*ISIS Facility, Rutherford Appleton Laboratory, Chilton, Didcot OX11 0QX, United Kingdom*
[6]*School of Physics and Astronomy, University of Edinburgh, Edinburgh EH9 3FD, United Kingdom*
[7]*Department of Materials Science and Engineering, Kyoto University, Yoshida-honmachi, Sakyo, Kyoto 606-8501, Japan*
[8]*National Research Council, Chalk River, Ontario K0J 1JO, Canada*
[9]*Canadian Institute of Advanced Research, Toronto, Ontario M5G 1Z8, Canada*

(Received 23 October 2017; revised manuscript received 16 June 2018; published 17 July 2018)

Neutron spectroscopy was applied to study the magnetic interactions of orbitally degenerate Co^{2+} on a host MgO rocksalt lattice where no long-range spin or orbital order exists. The paramagnetic nature of the substituted monoxide $Co_{0.03}Mg_{0.97}O$ allows for the disentanglement of spin exchange and spin-orbit interactions. By considering the prevalent excitations from Co^{2+} spin pairs, we extract seven exchange constants out to the fourth coordination shell. An antiferromagnetic next-nearest-neighbor 180° exchange interaction is dominant; however, dual ferromagnetic and antiferromagnetic interactions are observed for pairings with other pathways. These interactions can be understood in terms of a combination of orbital degeneracy in the t_{2g} channel and the Goodenough-Kanamori-Anderson rules. Our work suggest that such a hierarchy of exchange interactions exists in transition-metal-based oxides with a t_{2g} orbital degeneracy.

DOI: 10.1103/PhysRevB.98.024415

I. INTRODUCTION

The combination of magnetic exchange and orbital degeneracy has provided the basis for a number of topics in condensed-matter physics including metal-insulator transitions, high-temperature superconductors, colossal magnetoresistance [1–3], and, more recently, Kitaev interactions [4–6]. Rocksalt CoO was the first orbitally degenerate compound to have its magnetic structure investigated using neutron diffraction [7–10], but the underlying exchange interactions are still not known. Indeed, calculations and experiment have been hindered by the complex electronic and orbital ground state of Co^{2+}. While e_g mediated magnetic exchange has been well understood (for example, in $KCuF_3$ [11]), the case of exchange involving degenerate t_{2g} orbitals has proven more difficult [12]. We investigate the magnetic exchange interactions in the case of a t_{2g} orbital degeneracy by performing neutron spectroscopy on MgO substituted with Co^{2+}. We extract seven exchange interactions and observe dual ferro- and antiferromagnetic exchange interactions with comparable magnitudes. The dual exchange interactions are a direct result of the underlying t_{2g} orbital degeneracy of Co^{2+}.

The starting point for understanding the spin-orbital Hamiltonian for paramagnetic Co^{2+} ions is crystal-field theory based on octahedral coordination [13,14] [Fig. 1(a) for rocksalt CoO] [15–17]. As schematically shown in Fig. 1(b), the octahedral crystal field ($\hat{\mathcal{H}}_{CF}$) splits the five degenerate d orbitals (^4F) such that the d^7 electronic structure consists of five electrons occupying the lower-energy t_{2g} states and two electrons in the higher-energy e_g orbitals. This constitutes two orbital triplets ($^4T_{1,2}$) levels separated by $10Dq \sim 900$ meV [17]. The triplet degenerate $^4T_1$ ground state can be approximated to have an effective orbital angular momentum of $\tilde{l} = 1$ [16–24]. Applying spin-orbit coupling (defined by $\hat{\mathcal{H}}_{SO} = \tilde{\lambda}\vec{l} \cdot \vec{S}$, with $S = \frac{3}{2}$) to this orbital ground state results in three effective spin-orbit manifolds classified by an effective angular momentum of $j_{\text{eff}} = \frac{1}{2}, \frac{3}{2}$, and $\frac{5}{2}$ (with $\vec{j}_{\text{eff}} = \vec{l} + \vec{S}$). The $j_{\text{eff}} = \frac{1}{2}$ ground state is separated from the higher-energy $j_{\text{eff}} = \frac{3}{2}$ states by $\frac{3}{2}\tilde{\lambda} \sim 36$ meV [17].

In the presence of long-range magnetic order (as exists in CoO at low temperatures), the total single-ion Hamiltonian for Co^{2+} can then be summarized by

$$\hat{\mathcal{H}}_{SI} = \hat{\mathcal{H}}_{CF} + \hat{\mathcal{H}}_{SO} + \hat{\mathcal{H}}_{MF}, \tag{1}$$

where $\hat{\mathcal{H}}_{CF}$, $\hat{\mathcal{H}}_{SO}$, and $\hat{\mathcal{H}}_{MF}$ are the octahedral crystal-field, spin-orbit, and magnetic-order-induced molecular field. The effect of magnetic ordering on the three spin-orbit manifolds discussed above can be illustrated by considering a single dominant next-nearest-neighbor 180° $Co^{2+} - O^{2-} - Co^{2+}$ superexchange J_2 with

$$\hat{\mathcal{H}}_{MF} = 2J_2 z_2 \langle \hat{\mathbf{S}} \rangle_{av} \hat{\mathcal{S}}^z, \tag{2}$$

*Deceased.

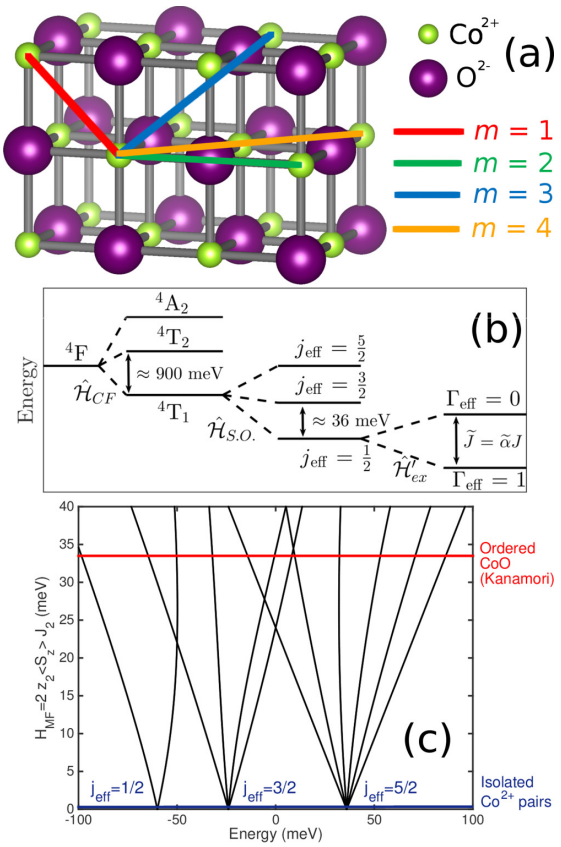

FIG. 1. (a) Cubic (room-temperature) rocksalt $Fm\bar{3}m$ crystal structure of CoO [25]. The pair distances between first shell (nearest) neighbors, second shell (next-nearest) neighbors, etc. are denoted by $m = 1,2$, etc., respectively. (b) The effective pair Hamiltonian $\hat{\mathcal{H}}_{\text{pair}}$ for $Co_{0.03}Mg_{0.97}O$. (c) The energy eigenvalues of the single-ion Hamiltonian including a molecular field from magnetic order with Kanamori's estimate [16] of J_2 shown by the solid red line.

where z_2 and $\hat{\mathcal{S}}^z$ denote the number of Co^{2+} neighbors and the z axis of the spin operator [15]. As illustrated in Fig. 1(c), by considering only the predicted value of J_2 by Kanamori [16] in the mean-field expression for $\hat{\mathcal{H}}_{\text{MF}}$, a complex admixture of different molecular-field split Co^{2+} spin-orbit manifolds occurs in the presence of magnetic order [15–17].

The strong magnetic-order-induced mixing of multiple j_{eff} manifolds in CoO is in contrast to many other Co^{2+}-based magnets that have both weak exchange and molecular fields and thus exhibit weak mixing [18,26–28]. CoO is further complicated by the possibility of multiple long-range spin-spin interactions [29–32]. The extraction of the multiple-spin exchanges in CoO is thus experimentally very difficult despite the simplicity of its crystal structure [15,17,22,23,30,31,33–35].

We have extracted the magnetic exchange interactions on a rocksalt lattice by investigating weakly substituted $Co_{0.03}Mg_{0.97}O$ using neutron scattering and through considering excitations from the dominant Co^{2+} pair response. This paper is divided into four sections, including this introduction. In Sec. II, we first describe the experimental methods including materials preparation and characterization techniques, where we conclude that our dilute sample can be described by a Co^{2+} pair response. An expanded description of the characterization is given in the Supplemental Material [36], illustrating the x-ray, susceptibility, and energy dispersive x-rays (EDX) data [36]. In Sec. III, the theory required to extract both the exchange constant and the distance associated with the interaction is outlined. We then show the experimental data used to derive the exchange interactions. We finally conclude with a discussion of the results, including a comparison with thermodynamic data from pure CoO, and also how we can understand the results in terms of the Goodenough-Kanamori-Anderson (GKA) rules.

II. EXPERIMENTAL DETAILS AND MATERIALS CHARACTERIZATION

To extract individual J constants for Co^{2+}, we have followed the pioneering work on dilute Mn^{2+} [37,38] and Co^{2+} [22] compounds and measured the dilute monoxide $Co_{0.03}Mg_{0.97}O$ using inelastic neutron spectroscopy. The high magnetic dilution removes the problematic molecular field discussed above [Fig. 1(c)] and suppresses the mixing between j_{eff} manifolds, allowing us to consider a dominant response for Co^{2+} pairs. Probabilistic arguments can be used to illustrate this and are based on the observation that for a given random distribution of xCo^{2+} and $(1-x)Mg^{2+}$ ions, the number of Co^{2+} pairs and the number of pairwise interactions for a given geometry present in the lattice far outweighs the number of Co^{2+} triplets and corresponding interactions between three Co^{2+} cations. For example, if there are N ways that a cluster with a particular geometry of three sites XYZ can occur in a given crystal, the relative probabilities of an arrangement of 3 Mg^{2+}, 1 Co^{2+}, and 2 Mg^{2+} (and its permutations), 2 Co^{2+} and 1 Mg^{2+} (and its permutations), and 3 Co^{2+} occupying the three sites XYZ are $(1-x)^3$, $x(1-x)^2$, $x^2(1-x)$, and x^3, respectively. Hence the ratio of numbers of spin pairs with XY, XZ, and YZ geometry to spin triplets with XYZ geometry in the lattice is $\frac{1-x}{x}$, and thus for small x, the number and hence inelastic neutron-scattering intensities of Co^{2+} pair excitations far outweigh those from larger Co^{2+} clusters. We summarize the sample preparation and characterization techniques confirming the dominant pair response in this section, and an expanded description, including data from the techniques, of the characterization is provided in the Supplemental Material [36]. We also discuss the neutron experiments applied to these materials.

Materials preparation. Two polycrystalline samples of $Co_{0.03}Mg_{0.97}O$ were synthesized for this particular investigation. The first was synthesized by traditional solid-state methods as outlined by Cowley *et al.* [17]. A second sample of $Co_{0.03}Mg_{0.97}O$ was made using solution techniques by mixing stoichiometric amounts of $Mg(NO_3)_2 \times 6H_2O$ and $Co(NO_3)_2 \times 6H_2O$. The solid mixture was dissolved in CH_3CH_2OH and stirred for 1 h and heated to 70 °C for 12 h, yielding a pink gel. The gel was heated in air to 600 °C with

a heating rate of 20 °C/h, reacted for 24 h, subsequently heated to 1000 °C with a heating rate of 150 °C/h, held for an additional 48 h, and finally cooled to room temperature by switching off the furnace. Details concerning the synthesis and treatment of MgO and CoO samples are outlined by Cowley *et al.* [17]. We note that both magnetically substituted MgO samples gave consistent results and the comparison is shown in the Supplemental Material [36].

Laboratory x-ray diffraction. Room-temperature powder-diffraction patterns of the end members (CoO and MgO) and $Co_xMg_{1-x}O$ synthesized by sol-gel were collected over $2\theta = [25, 100]^\circ$ in 0.02° steps on a Bruker D2 Phaser laboratory x-ray diffractometer utilizing a monochromated Cu $K_{\alpha,1,2}$ source. As illustrated in the Supplemental Material [36], Rietveld refinement of $Mg_{1-x}Co_xO$ indicates that the solid solution assumes a rocksalt structure ($Fm\bar{3}m$) with a unit-cell parameter $a = 4.2131(2)$ Å. Utilizing the measured values of the end members CoO (4.2594(4) Å) and MgO (4.2118(1) Å), the unit-cell parameter of 4.2131(2) Å corresponds to an $x = 0.025(5)$ according to Vegard's law [39], supporting that approximately 3% of the Mg^{2+} sites contain Co^{2+}.

Energy-dispersive x-ray analysis. As a final direct confirmation of the concentration of Co^{2+} in our sample, we performed energy-dispersive x-ray measurements. Elemental analysis was performed using scanning electron microscopy (SEM) on a Hitachi SU-70 Schottky field-emission gun SEM with an equipped Bruker Quantax energy-dispersive x-ray detector. Energy-dispersive x-ray spectroscopy (EDS) was carried out at 15 keV. The results are illustrated in the Supplemental Material [36] show the effective substitution and the homogeneous distribution of cobalt throughout the sample. The spatially resolved analysis also confirms a homogenous distribution of cobalt throughout the sample.

DC magnetic susceptibility. Temperature dependence of magnetization was measured on a Quantum Design MPMS for a 32.5 mg of polycrystalline $Co_{0.03}Mg_{0.97}O$ synthesized by sol-gel in an external dc field $\mu_o H_{ext} = 0.1$ T. Zero-field-cooling (ZFC) measurements were performed in 2 K steps spaced linearly from 2 to 300 K, while FC measurements were performed in 5 K steps spaced linearly from 2 to 170 K. As described in the Supplemental Material [36], the Curie-Weiss constant was found to be consistent with pairs of Co^{2+} with an exchange interaction reported by Kanamori [16]. The Curie constant was found to agree with a concentration of Co^{2+} ions, consistent with starting concentrations, x-ray powder diffraction, and also EDX measurements. Susceptibility measurements therefore confirm the following key experimental properties of our substituted samples: the lack of magnetic ordering; the absence of measurable clustering of Co^{2+} evidenced from no measurable difference between zero-field and field-cooled sweeps; a Curie-Weiss constant consistent with a dominant 180° superexchange interaction; and finally a Curie constant consistent with starting concentrations.

Inelastic neutron-scattering details. 45.8, 45.2, 32.5, and 15.7 g of $Co_{0.03}Mg_{0.97}O$ synthesized by the standard solid-state and sol-gel methods, annealed MgO and CoO, respectively, were placed in separate airtight aluminum cans under helium. The high-energy measurements were made on the direct geometry MARI spectrometer. For measurements concerning the $Co_{0.03}Mg_{0.97}O$ sample synthesized by traditional solid-state methods, MgO and CoO powders, the t_o chopper was operated at 50 Hz in parallel with a Gd chopper spun at frequencies $f = 350$, 250 and 150 Hz with incident energies $E_i = 30$, 10, and 5 meV, respectively, providing an elastic resolution of 0.7, 0.2, and 0.1 meV, respectively. For measurements concerning the $Co_{0.03}Mg_{0.97}O$ sample synthesized by sol-gel, the Gd chopper was spun at $f = 350$ and 250 Hz with an E_i of 29.50 and 14.50 meV, providing an elastic resolution of 0.7 and 0.2 meV, respectively. For both $Co_{0.03}Mg_{0.97}O$ samples, a thick disk chopper with $f = 50$ Hz reduced the background from high-energy neutrons. A top-loading Displex CCR cooled the samples to a base temperature of approximately 5 K. We note that further neutron inelastic scattering results comparing pure MgO, CoO, and our substituted MgO sample are presented in the Supplemental Material [36].

For lower energies, measurements were made on the indirect geometry IRIS spectrometer. The final energy was fixed at 1.84 meV by PG002 analyzer crystals in near backscattering geometry. The graphite analyzers are cooled to reduce thermal diffuse scattering, providing an elastic resolution of 17.5 μeV. A combination of IRIS' long path length and its array of disk choppers allowed us to select multiple time windows, resulting in the measured bandwidth being selectively increased to include energy transfers up to ~2 meV. A top-loading Displex CCR was used to cool the sample to a base temperature of approximately 11 K. For all samples, identical instrumental and environmental parameters were employed on IRIS.

III. Co^{2+} PAIR INTERACTIONS

Having discussed the materials preparation and characterization, we conclude that our rocksalt MgO sample substituted with Co^{2+} can be considered to be dominated by pairs of Co^{2+} ions. We now discuss the neutron-scattering response of an isolated pair of magnetic ions and how it can be used to extract both the interaction distance and also the energy-exchange interaction. By considering Co^{2+} pair interactions and only low-energy excitations within the lowest $j_{\text{eff}} = \frac{1}{2}$ doublet (with $\hat{\tilde{\mathbf{j}}} = \beta\hat{\mathbf{S}}$), the interaction energy $\hat{\mathcal{H}}_{\text{ex}}$ between a pair of Co^{2+} ions in substituted $Mg_{0.97}Co_{0.03}O$ is approximated by

$$\hat{\mathcal{H}}'_{\text{ex}} = 2J\hat{\mathbf{S}}_1 \cdot \hat{\mathbf{S}}_2 \sim \tilde{\alpha} J\, \hat{\tilde{\mathbf{j}}}_1 \cdot \hat{\tilde{\mathbf{j}}}_2, \tag{3}$$

where $\hat{\tilde{\mathbf{j}}}$ and $\tilde{\alpha} = 2\beta^2$ denote an effective total angular momentum operator with $j = \frac{1}{2}$ and a projection factor, respectively. As summarized by Fig. 1(b), the $\hat{\mathcal{H}}'_{\text{ex}}$ describes individual $j_{\text{eff}} = \frac{1}{2}$ pair excitations as transitions between triplet ($\Gamma_{\text{eff}} = 1$) and singlet ($\Gamma_{\text{eff}} = 0$) levels separated by an energy of $\Delta E = \tilde{\alpha} J$ [43–45]. The projection factor $\tilde{\alpha}$, in this low-energy approximation, can be calculated by diagonalizing $\hat{\mathcal{H}}_{\text{SI}} + \hat{\mathcal{H}}'_{\text{ex}}$, with $\hat{\mathcal{H}}_{\text{MF}} = 0$ owing to the lack of long-range magnetic order in $Co_{0.03}Mg_{0.97}O$ [17]. This is equivalent to the following Hamiltonian for two (labeled 1 and 2) interacting Co^{2+} ions:

$$\hat{\mathcal{H}}' = \tilde{\lambda}\hat{\tilde{\mathbf{l}}}_1 \cdot \hat{\mathbf{S}}_1 + \tilde{\lambda}\hat{\tilde{\mathbf{l}}}_2 \cdot \hat{\mathbf{S}}_2 + 2J\hat{\mathbf{S}}_1 \cdot \hat{\mathbf{S}}_2. \tag{4}$$

By considering $\tilde{l} = 1$ and $S = \frac{3}{2}$, this amounts to 144 basis states and a 144 × 144 matrix for this particular Hamiltonian in terms of the two-particle basis of $|\tilde{l}_1, m_{\tilde{l},1}, s_1, m_{s,1}\rangle \otimes$

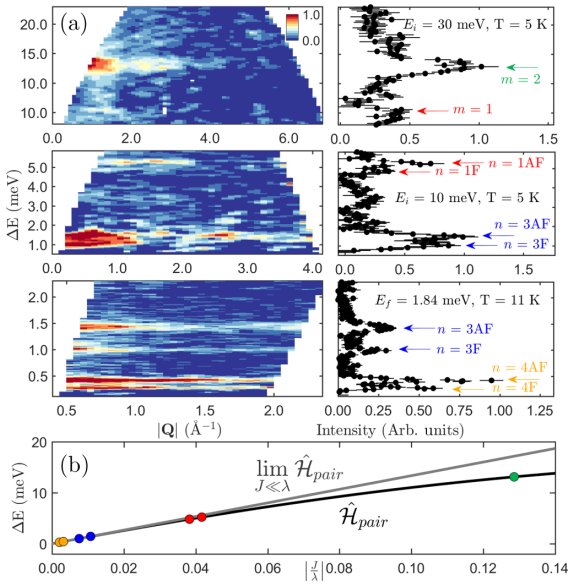

FIG. 2. (a) Background (using pure and nonmagnetic MgO) subtracted powder-averaged neutron-scattering intensity maps of $Co_{0.03}Mg_{0.97}O$ measured on (a, top left) MARI at 5 K with an $E_i = 30$ meV, (a, middle left) MARI at 5 K with an $E_i = 10$ meV and (a, bottom left) IRIS at 11 K with an E_f of 1.84 meV revealing seven low-energy bands of dispersionless magnetic excitations. The right column shows $|\mathbf{Q}|$-integrated cuts. Labels denote the coordination shell m and the type of coupling present with label n, both of which are determined in Fig. 3. (b) The black curve denotes the pair energy splitting as a function of the normalized exchange $\Delta E(|\frac{J}{\lambda}|)$. The points are measured energy positions from (a). The gray line is the same relationship derived using the projection theorem in the large-λ limit [19,20].

$|\widetilde{l}_2, m_{\widetilde{l},2}, s_2, m_{s,2}\rangle$, where $\widetilde{l}_i$, $m_{\widetilde{l},i}$, s_i, and $m_{s,i}$ denote the eigenvalues corresponding to the $\hat{\widetilde{\mathbf{l}}}_i$, $\hat{\widetilde{\mathbf{l}}}_{z,i}$, $\hat{\mathbf{S}}_i$, and $\hat{\mathbf{S}}_{z,i}$ operators, respectively, for the ith particle. As illustrated in Fig. 2(b), in the limit of $J \ll \lambda$, $\Delta E(J)$ is linear with $\widetilde{\alpha} = \frac{50}{9}$, in agreement with the projection theorem of angular momentum [20,44]. Therefore, measuring pair excitations with neutron spectroscopy provides a direct way to estimate the magnitude of exchange constant $|J|$ between neighboring Co^{2+} ions when this projection factor is taken into account. We note that this is independent of the sign of J and we discuss how that can be determined from the temperature dependence below.

While the excitation energy provides the magnitude $|J|$, the neutron spectroscopic momentum dependence can be used to extract the corresponding intrapair distance $\mathbf{R}_m$, where m denotes the coordination shell. By applying the Hohenberg-Brinckman first-moment sum rule and the single-mode approximation for an isolated pair, excitations from a Co^{2+} pair have the following $|\mathbf{Q}|$ dependence [43,50,51]:

$$S(|\mathbf{Q}|) \propto \frac{|F(|\mathbf{Q}|)|^2}{\Delta E_o}\left(1 - \frac{\sin(|\mathbf{Q}||\mathbf{R}_m|)}{|\mathbf{Q}||\mathbf{R}_m|}\right), \tag{5}$$

with $|F(|\mathbf{Q}|)|^2$ the magnetic form factor. Since the modulation is solely dependent on the intrapair distance $\mathbf{R}_m$, the excitation can be assigned to a particular pair and corresponding coordination shell in the $Fm\bar{3}m$ structure, as illustrated in Fig. 1(a).

IV. RESULTS AND DISCUSSION

Having discussed the theory for isolated pairs in dilute $Co_{0.03}Mg_{0.97}O$, we now present the experimental data. As illustrated by Fig. 2(a), low-temperature/incident-energy inelastic neutron spectroscopic measurements on powder $Co_{0.03}Mg_{0.97}O$ display a hierarchy of dispersionless excitations up to $\Delta E \sim 15$ meV. Based on the energy value of the excitations, we can assign an exchange constant as shown in Fig. 2(b) using the previously measured value for the spin-orbit-coupling constant $\widetilde{\lambda}$ [17] for isolated Co^{2+} on a rocksalt lattice. The intensities for each of the seven excitations in Fig. 2(a) exhibit a modulated $|\mathbf{Q}|$ dependence, characteristic of pairwise interactions and thus distinguishing them from single-ion dispersionless crystal-field excitations [43]. As shown in Figs. 3(a) and 3(b), by fitting the intensity of each mode at different energies to Eq. (5), the different pair excitations could be assigned to relative coordination shells ranging from $m = 1$ to $m = 4$.

We now discuss the temperature dependence with the goal of extracting the sign of J. Antiferromagnetically coupled ($J > 0$) pairs of $j_{\text{eff}} = \frac{1}{2}$ spins consist of a singlet ground state and a triplet excited state, while ferromagnetic coupling ($J < 0$) gives a triplet ground state and a single excited state. These two different coupling scenarios give distinct temperature dependences of the integrated intensity that scales as the thermal population difference between the ground and excited states [51,52], with antiferromagnetic pairs following

$$I_{\text{AF}}(T) \propto (1 - e^{-\Delta E/k_B T})/(1 + 3e^{-\Delta E/k_B T}) \tag{6}$$

and ferromagnetic pairs following

$$I_{\text{F}}(T) \propto (1 - e^{-\Delta E/k_B T})/(3 + e^{-\Delta E/k_B T}), \tag{7}$$

such that as $T \to 0$ K, the ratio

$$\frac{I_{\text{AF}}}{I_{\text{F}}} = \frac{3 + e^{-\Delta E/k_B T}}{1 + 3e^{-\Delta E/k_B T}} \to 3. \tag{8}$$

As illustrated in Fig. 3(d), by normalizing the temperature dependence by $I_{\text{F}}(T)$, all integrated intensities fall onto either one of two universal curves describing antiferromagnetism or ferromagnetism.

All extracted values of J based on the energy, momentum, and temperature dependence discussed above are summarized in Table I. All coordination shells, with the exception of $m = 2$, display two closely spaced excitations with differing signs for the exchange constant, as illustrated in Fig. 3(c) for the ∼5 meV excitation. This presence of dual ferro- and antiferromagnetic interactions for $m = 1$, 3, and 4 is consistent with the GKA rules [40–42,53] since each of these exchange pathways consists of at least one 90° $Co^{2+} - Co^{2+}$ interaction involving the overlap of half and filled orbitals. Indeed, the GKA rules predict that the combination of the orbital degree of freedom for *each* Co^{2+} and a lack of orbital ordering (or anisotropy) would manifest itself as either a direct antiferromagnetic ${t_{2g}}^1 - {t_{2g}}^1$ or a weaker ferromagnetic

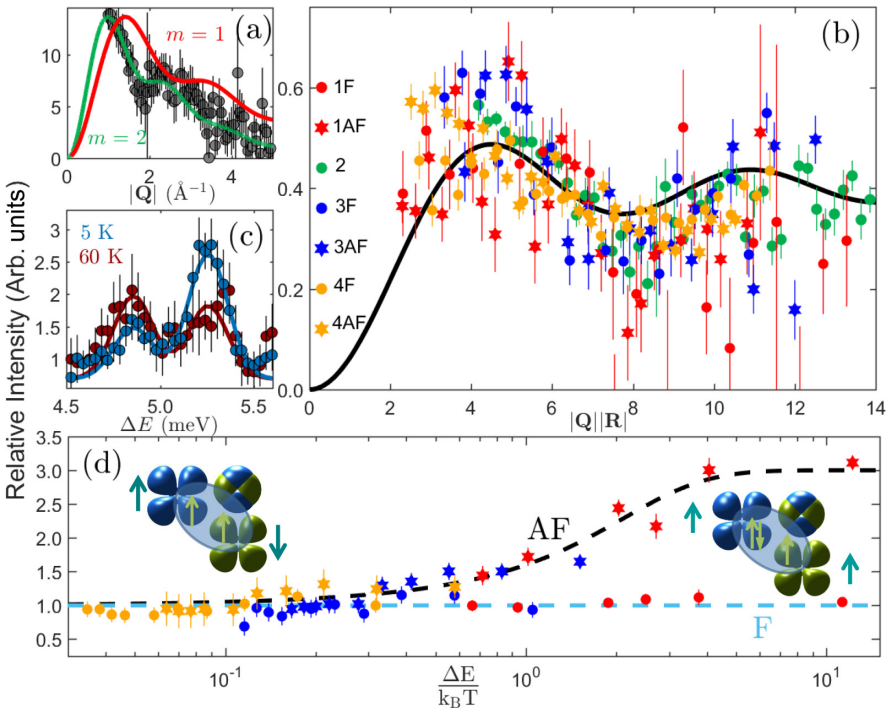

FIG. 3. (a) Constant-E cut ($\Delta E = [12,14]$ meV) from MARI at 5 K with an $E_i = 30$ meV. The green curve is a fit to Eq. (5) with $|\mathbf{R}| = 4.2(3)$ Å ($m = 2$ pairs). The red curve is with $|\mathbf{R}|$ fixed as 2.98 Å ($m = 1$ pairs). (b) Scaled and form-factor-corrected $|\mathbf{Q}|$ dependence of the intensities for all magnetic excitations with $|\mathbf{R}|$ calculated from the fitting routine described in (a). The solid black curve is $1 - \frac{\sin(|\mathbf{Q}||\mathbf{R}_n|)}{|\mathbf{Q}||\mathbf{R}_n|}$. (c) Constant-$|\mathbf{Q}|$ cut (MARI, $E_i = 10$ meV) showing a different temperature dependence for the two peaks despite both being from $m = 1$ pairs. (d) Normalized temperature dependence of the Bose-factor-corrected integrated intensity for all seven excitations (Fig. 2) showing two universal curves calculated (dashed lines) for antiferromagnetic and ferromagnetic coupling. Both the integrated intensities and the calculated behavior of antiferromagnetic or ferromagnetically coupled pairs were normalized by $I_F(T)$, as described in the main text. The inset is a pictorial representation of the sign of J as predicted by the GKA rules [40–42]—antiferromagnetism (left) is a result of exchange between two half-filled and completely filled t_{2g} orbitals, while weaker ferromagnetism (right) is a result of exchange between a half-filled and completely filled t_{2g} orbitals. Yellow arrows denote local t_{2g} spin configurations and teal arrows denote total spin configurations on each Co^{2+}.

${t_{2g}}^1 - {t_{2g}}^2$ exchange interaction. As summarized in Fig. 3(d) and Table I, the experimental results verify the GKA rules [40–42,53] as the antiferromagnetic interaction is stronger than the ferromagnetic alternative for all the $m \neq 2$ excitations, while the 180° $Co^{2+} - O^{2-} - Co^{2+}$ m = 2 coupling leads to only a strong antiferromagnetic interaction.

Having assigned the signs of the seven exchange constants for dilute $Co_{0.03}Mg_{0.97}O$, we now provide a comparison with thermodynamic data and previously measured and calculated exchange constants for bulk CoO. The additional complication of dual ferro- and antiferromagnetic interactions for most m exchange pathways in combination with the entanglement of individual spin-orbit manifolds in the presence of magnetic order provides a possible explanation for the large range of J values reported for CoO [16,30,31,35,54–58]. As summarized in Table I, the values of J show good agreement with three general trends reported by experiment [30]: (i) dominant $J_2 > 0$, (ii) a $J_1 < 0$, and (iii) a significantly smaller but non-negligible J_3, all in broad agreement with the trends concluded from a recent generalized gradient approximation (GGA)+U density functional theory (DFT) calculation on CoO (though no such dual exchange was predicted) [32]. In terms of thermodynamic data, the Curie-Weiss constant is related to the exchange interactions via $\Theta_{CW} = -\frac{2}{3}S(S+1)\sum_i z_i J_i$, where the spin value $S = \frac{3}{2}$ and z_i is the number of neighbors for each ith exchange interaction [48,49]. Following Kanamori [16] and applying a correction for spin-orbit coupling, the effective Curie-Weiss temperature $\widetilde{\theta}_{CW}$ is listed in Table I and compared against a mean-field T_N calculated based just on J_2. The estimated $\widetilde{\theta}_{CW}$ of $-295(5)$ K [$-25.4(5)$ meV] and a mean-field estimate of T_N of 283(5) K [24.4(3) meV] demonstrate close similarities with experimentally determined values of $\theta_{CW} = -330(4)$ K [46,47] and $T_N = 291(4)$ K [25], respectively, for CoO. The excellent agreement results from the near-perfect cancellation of antiferromagnetic and ferromagnetic interactions for all coordinations with the exception of $m = 2$ (the 180° interaction). Although the $Co_{0.03}Mg_{0.97}O$ lattice ($a = 4.21$ Å) is contracted relative to that of pure CoO ($a = 4.26$ Å), the above agreements of energy scale are highly suggestive that the $Co^{2+} - Co^{2+}$ exchange interactions are not greatly

TABLE I. Magnetic exchange constants for $Co_{0.03}Mg_{0.97}O$ determined by the current study, magnetic exchange constants for CoO as cited in literature [30,31], and calculated for CoO by Deng *et al.* [32] using GGA+U DFT. The values from GGA+U DFT have been renormalized such that J_2 is equal to the value from this current study. The values of T_N, θ_{CW}, and λ reported in the literature [17,25,46,47] for CoO have been included for the purposes of a comparison to the mean-field value [48,49] of θ_{CW} corresponding to the J values determined by the current study.

Quantity/Source	Current study (meV)	Literature studies (meV)	Calculated (meV) [32]
$\widetilde{\lambda}$		24(5) [17]	
J_{1AF}	1.000(8)	0.60 to −0.31 [16,30]	−0.97(2)
J_{1F}	−0.918(6)		
J_2 or J_{2AF}	3.09(5)	2.8 to 0.0013 [30]	3.09(5)
J_{3AF}	0.258(1)	−0.67 [31]	−0.461(8)
J_{3F}	−0.182(1)		
J_{4AF}	0.0759(4)		−0.0085(1)
J_{4F}	−0.0504(4)		
T_N	24.4(3)[a]	25.1(4) [25]	
θ_{CW}	−25.4(5)	−28.4(4) [46,47]	

[a]Calculated using the mean-field estimate $T_N \sim |\frac{2}{3}S(S+1)z_2J_2|$.

changed, or at least any changes are smaller than systematic errors introduced by attempting to simplify the scheme in pure CoO. Hence the present results represent a comprehensive set of interaction-energy estimates for CoO.

In summary, we have disentangled the exchange and spin-orbit interactions for Co^{2+} on a rocksalt lattice. Through a combined analysis of the energy, momentum, and temperature dependence, we have extracted seven exchange constants out to four coordination shells. Both ferro- and antiferromagnetic interactions are observed, with the exception of second-neighbor interactions through linear $Co^{2+} - O^{2-} - Co^{2+}$ bridges, in agreement with both the GKA rules and thermodynamic data. The results demonstrate that in the case of an orbital degeneracy in the t_{2g} channel, dual ferro- and antiferromagnetic interactions occur with comparable magnitudes.

ACKNOWLEDGMENTS

We acknowledge useful conversations with T. Guidi, J. R. Stewart, M. A. Green, T. J. Williams, K. H. Hong, G. M. McNally, and S. E. Maytham. We are grateful to the Carnegie Trust for the Universities of Scotland, the Royal Society, the STFC, the ERC, and the EPSRC for financial support. P.M.S. acknowledges financial support from the CCSF and the University of Edinburgh through the GRS and PCDS.

[1] Y. Tokura and N. Nagaosa, Science **288**, 462 (2000).
[2] E. Dagotto, Science **309**, 257 (2005).
[3] K. I. Kugel and D. I. Khomskii, Sov. Phys. JETP **136**, 621 (1982).
[4] Y. Okamoto, M. Nohara, H. A. Katori, and H. Takagi, Phys. Rev. Lett. **99**, 137207 (2007).
[5] R. Wang, A. Go, and A. J. Millis, Phys. Rev. B **95**, 045133 (2017).
[6] G. Jackeli and G. Khaliullin, Phys. Rev. Lett. **102**, 017205 (2009).
[7] C. G. Shull, W. A. Strauser, and E. O. Wollan, Phys. Rev. **83**, 333 (1951).
[8] Y. Y. Li, Phys. Rev. **100**, 627 (1955).
[9] W. L. Roth, Phys. Rev. **110**, 1333 (1958).
[10] B. van Laar, Phys. Rev. **138**, A584 (1965).
[11] S. K. Satija, J. D. Axe, G. Shirane, H. Yoshizawa, and K. Hirakawa, Phys. Rev. B **21**, 2001 (1980).
[12] A. M. Oles, P. Horsch, L. F. Feiner, and G. Khaliullin, Phys. Rev. Lett. **96**, 147205 (2006).
[13] M. W. Haverkort, A. Tanaka, L. H. Tjeng, and G. A. Sawatzky, Phys. Rev. Lett. **99**, 257401 (2007).
[14] B. C. Larson, W. Ku, J. Z. Tischler, C.-C. Lee, O. D. Restrepo, A. G. Eguiluz, P. Zschack, and K. D. Finkelstein, Phys. Rev. Lett. **99**, 026401 (2007).
[15] J. Sakurai, W. J. L. Buyers, R. A. Cowley, and G. Dolling, Phys. Rev. **167**, 510 (1968).
[16] J. Kanamori, Prog. Theor. Phys. **17**, 177 (1957).
[17] R. A. Cowley, W. J. L. Buyers, C. Stock, Z. Yamani, C. Frost, J. W. Taylor, and D. Prabhakaran, Phys. Rev. B **88**, 205117 (2013).
[18] F. Wallington, A. M. Arévalo-Lopez, J. W. Taylor, J. R. Stewart, V. García-Sakai, J. P. Attfield, and C. Stock, Phys. Rev. B **92**, 125116 (2015).
[19] D. I. Khomskii, *Transition Metal Compounds* (Cambridge University Press, Cambridge, 2014).
[20] A. Abragam and B. Bleaney, *Electron Paramagnetic Resonance of Transition Ions* (Oxford University Press, Oxford, 2012).
[21] J. Kanamori, Prog. Theor. Phys. **17**, 197 (1957).
[22] W. J. L. Buyers, T. M. Holden, E. C. Svensson, R. A. Cowley, and M. T. Hutchings, J. Phys. C: Solid State Phys. **4**, 2139 (1971).
[23] W. J. L. Buyers, T. M. Holden, E. C. Svensson, and D. J. Lockwood, Phys. Rev. B **30**, 6521 (1984).
[24] R. A. Cowley, W. J. L. Buyers, P. Martel, and R. W. H. Stevenson, J. Phys. C: Solid State Phys. **6**, 2997 (1973).
[25] W. Jauch, M. Reehuis, H. J. Bleif, F. Kubanek, and P. Pattison, Phys. Rev. B **64**, 052102 (2001).
[26] R. Coldea, D. A. Tennant, E. M. Wheeler, E. Wawrzynska, D. Prabhakaran, M. Telling, K. Habicht, P. Smeibidl, and K. Kiefer, Science **327**, 177 (2010).

[27] B. Grenier, S. Petit, V. Simonet, E. Canévet, L.-P. Regnault, S. Raymond, B. Canals, C. Berthier, and P. Lejay, Phys. Rev. Lett. **114**, 017201 (2015).
[28] H. D. Zhou, C. Xu, A. M. Hallas, H. J. Silverstein, C. R. Wiebe, I. Umegaki, J. Q. Yan, T. P. Murphy, J.-H. Park, Y. Qiu, J. R. D. Copley, J. S. Gardner, and Y. Takano, Phys. Rev. Lett. **109**, 267206 (2012).
[29] A. L. Dalverny, J. S. Filhol, F. Lemoigno, and M. L. Doublet, J. Phys. Chem. C **114**, 21750 (2010).
[30] M. Feygenson, X. Teng, S. E. Inderhees, Y. Yiu, W. Du, W. Han, J. Wen, Z. Xu, A. A. Podlesnyak, J. L. Niedziela, M. Hagen, Y. Qiu, C. M. Brown, L. Zhang, and M. C. Aronson, Phys. Rev. B **83**, 174414 (2011).
[31] K. Tomiyasu and S. Itoh, J. Phys. Soc. Jpn. **75**, 084708 (2006).
[32] H.-X. Deng, J. Li, S.-S. Li, J.-B. Xia, A. Walsh, and S.-H. Wei, Appl. Phys. Lett. **96**, 162508 (2010).
[33] Z. Yamani, W. J. L. Buyers, R. A. Cowley, and D. Prabhakaran, Can. J. Phys. **88**, 729 (2010).
[34] G. Fischer, M. Däne, A. Ernst, P. Bruno, M. Lüeders, Z. Szotek, W. Temmerman, and W. Hergert, Phys. Rev. B **80**, 014408 (2009).
[35] C. Kant, T. Rudolf, F. Schrettle, F. Mayr, J. Deisenhofer, P. Lunkenheimer, M. V. Eremin, and A. Loidl, Phys. Rev. B **78**, 245103 (2008).
[36] See Supplemental Material at http://link.aps.org/supplemental/10.1103/PhysRevB.98.024415 for a description of sample characterization.
[37] A. Furrer, A. Podlesnyak, and K. W. Krämer, Phys. Rev. B **92**, 104415 (2015).
[38] E. C. Svensson, M. Harvey, W. J. L. Buyers, and T. M. Holden, J. Appl. Phys. **49**, 2150 (1978).
[39] L. Vegard, Z. Phys. **5**, 17 (1921).
[40] J. B. Goodenough, J. Phys. Chem. Solids **6**, 287 (1958).
[41] J. Kanamori, J. Phys. Chem. Solids **10**, 87 (1959).
[42] P. W. Anderson, Phys. Rev. **79**, 350 (1950).
[43] J. T. Haraldsen, T. Barnes, and J. L. Musfeldt, Phys. Rev. B **71**, 064403 (2005).
[44] M. Rose, *Elementary Theory of Angular Momentum, Dover Books on Physics and Chemistry* (Dover, New York, 1995).
[45] A. Furrer and O. Waldmann, Rev. Mod. Phys. **85**, 367 (2013).
[46] T. Nagamiya, K. Yosida, and R. F. Kubo, Adv. Phys. **4**, 1 (1955).
[47] J. R. Singer, Phys. Rev. **104**, 929 (1956).
[48] K. Lee, J. Lee, C. Lee, and M. Whangbo, Bull. Korean Chem. Soc. **35**, 1277 (2014).
[49] C. Kittel, *Introduction to Solid State Physics* (Wiley, New York, 2005).
[50] P. C. Hohenberg and W. F. Brinkman, Phys. Rev. B **10**, 128 (1974).
[51] M. B. Stone, M. D. Lumsden, S. Chang, E. C. Samulon, C. D. Batista, and I. R. Fisher, Phys. Rev. Lett. **100**, 237201 (2008).
[52] Y. Zhu, *Modern Techniques for Characterizing Magnetic Materials* (Springer Science & Business Media, New York, 2005).
[53] J. B. Goodenough, Phys. Rev. **100**, 564 (1955).
[54] M. Tachiki, J. Phys. Soc. Jpn. **19**, 454 (1964).
[55] M. El-Batanouny, J. Phys.: Condens. Matter **14**, 6281 (2002).
[56] H.-h. Chou and H. Y. Fan, Phys. Rev. B **13**, 3924 (1976).
[57] R. R. Hayes and C. H. Perry, Solid State Commun. **13**, 1915 (1973).
[58] T. Satoh, R. Iida, T. Higuchi, Y. Fujii, A. Koreeda, H. Ueda, T. Shimura, K. Kuroda, V. I. Butrim, and B. A. Ivanov, Nat. Commun. **8**, 638 (2017).

Glossary

Airy Function of the First Kind Conventionally denoted by Ai, it is one of the two linearly independent solutions to the Airy equation $\frac{d^2y}{dx^2} - xy = 0$. The Airy function of the first kind is the solution to the Schrödinger equation with a linear potential, and the resulting quantised energy eigenvalues are parametrised by the negative zeros of Ai. This function plays a key role in the proposed quantum confinement of monopole quasi-particles that is the subject of Chapter 2.

Antiferromagnetic Order Magnetic moments are all aligned anti-parallel to one another and cancel completely. Such an arrangement results in zero net magnetisation below a critical temperature that is known as the Néel Temperature T_N.

Atomic Form Factor The Fourier transform of the spatial density distribution from real space to reciprocal space. The atomic form factor is a measure of the scattering amplitude of a wave by an isolated atom. The spatial density distribution that is utilised is dependent on the specific type of interaction involved in the scattering process and thus the type of radiation used to scatter off the system. X-ray form factor utilise the electron charge density. Neutron nuclear form factor utilises the spatial density of the nucleus, whilst its magnetic counterpart utilises the spatial density of the unpaired electrons. Since the form factor is the Fourier transform of the spatial density distribution, it possesses an intrinsic $\mathbf{Q}$-dependence that is reflective of said distribution and is a powerful tool when one attempts to identify particular types of scattering. Approximated analytical expressions for the magnetic form factors of Pr^{3+} and Co^{2+} are presented in Appendix A.

Aufbauprinzip For the ground state configuration of a system, the electrons fill orbitals with the lowest energy available before proceeding to those

with higher energies. Further elaboration on the ground state electron configuration, particularly in the case of degenerate orbitals, is given by a combination of the Pauli Exclusion Principle and Hund's Rules. This principle is also known as the "building-up principle", a literal translation of the original German term.

Bose Factor Provides the effective population of phonons with a given energy at a specific temperature. Defined as $\frac{1}{e^{\frac{E}{k_B T}}-1}$ and usually denoted as $n(E)$, the Bose factor plays a particularly crucial role in neutron inelastic scattering with its presence in the fluctuation-dissipation theorem (Eq. 1.109).

Ceramic Method The most common method for preparing metal oxides. The method consists of grinding reagents together, pelletising the resulting mixture, and heating the mixture at a desired temperature. The process is usually repeated multiple times for the purposes of reaction completeness and chemical homogeneity. This method was employed in all experimental chapters.

Clebsch-Gordan Coefficients Expansion coefficients of the coupled angular momentum eigenstates into the uncoupled product momentum eigenstates basis. In this thesis, the former is denoted by $|\ )$, whilst the latter is denoted by $|\ \rangle$.

Commutation Relations of Angular Momentum The commutation relations between the individual components of angular momentum operators. These commutation relations are a consequence of the canonical commutation relations $[\hat{\mathbf{r}}_i, \hat{\mathbf{p}}_j] = i\hbar\delta_{ij}$. The commutation relations is the Lie algebra $\mathfrak{so}(3)$ of the Lie group SO(3). It should be noted that there exists a 2-to-1 group homomorphism from SU(2) to SO(3) and their respective Lie algebras $\mathfrak{su}(2)$ and $\mathfrak{so}(3)$ are isomorphic.

Convolution A mathematical operation between two functions that produces a third function that quantifies how the shape of one of the functions is influenced by the other. The mathematical definition of the convolution of two functions f and g is given by: $(f * g)(t) = \int_{-\infty}^{\infty} f(\tau)g(t-\tau)d\tau$.

Cold Neutrons Neutrons possessing energies between 0 and 25 meV. So-called ultra-cold neutrons are a subcategory of cold neutrons with energies of $\sim 10^{-4}$ meV.

Collimator A device used to mechanically reduce the neutron beam divergence.

Critical Exponents Exponents that describe the behaviour of physical quantities in close proximity to a continuous phase transition. A more rigorous mathematical definition consists of the following: if a quantity $f(x)$ has a critical exponent λ in close proximity to the critical point defined by $x = 0$ as the critical point is approached from positive x, then $f(x) \sim x^{\lambda}$ for $x \to 0^{+}$, where the critical exponent λ can be defined as $\lambda = \lim_{x \to 0^{+}} \frac{\ln f(x)}{\ln x}$, such that λ defines the asymptotic behaviour of $f(x)$ as $x \to 0^{+}$. Examples of critical exponents β and ν are presented in Eqs. 1.60 and 1.61, respectively.

Crystalline Electric Field The total electrostatic field produced at a particular point in the lattice by the charged ligands. The description of the electrostatic interaction of the metal centres with the crystalline electric field is the basis of crystal field theory. First developed by Bethe and van Vleck, crystal field theory describes how the presence of the crystalline electric field breaks the metal centres' orbital degeneracy.

Cubic Crystal System A crystal system where the unit cell has $a = b = c$ and $\alpha = \beta = \gamma = 90°$.

Curie Law The mathematical relationship between a paramagnetic material's magnetisation, applied magnetic field and absolute temperature. The Curie law, given by Eq. 1.49, only holds for high temperatures and low applied magnetic fields.

Curie-Weiss Law A mean-field modification of the Curie law due to the presence of an internal molecular Weiss field. As is convention, the Curie-Weiss law is introduced as Eq. 1.66 corresponding to the mathematical relationship between a material's magnetic susceptibility and its absolute temperature in the paramagnetic regime.

de Broglie Hypothesis All matter can exhibit wave-like property. One of the two converse pillars of wave-particle duality.

Debye-Walker Factor A mathematical tool to describe the attenuation of coherent neutron scattering and x-ray scattering due to thermal motion of sample's constituents. Usually denoted by $e^{-2W(\mathbf{Q})} = \langle e^{i\mathbf{Q}\cdot\mathbf{u}_l} \rangle$, where $\mathbf{Q}$ and $\mathbf{u}_l$ are the momentum transfer and displacement of the l^{th} atom, respectively. The low $\mathbf{Q}$ and temperatures considered in this Thesis reduces the Debye-Waller factor to effectively one, and thus it may be neglected during the normalisation process.

Diagaonlisable Matrix A square matrix M is diagonalisable if the matrix M is similar to a diagonal matrix D. In other words, there exists an invertible matrix C such that $C^{-1}MC = D$.

Diffuse Scattering Scattering that arises due to any departure of a material's structure from a perfect periodic crystalline lattice. Diffuse scattering is measured between the Bragg peaks and are indicative of short-ranged correlations/fluctuations.

Dimension The minimum number of coordinates required to specify any arbitrary point in a mathematical space.

Dipole Selection Rules for Magnetic Neutron Inelastic Scattering Only transitions where $\Delta m = \pm 1, 0$ and $\Delta j = \pm 1, 0$ have non-zero transition matrix elements. These rules are a direct consequence of the Wigner-Eckart theorem.

Dirac String A hypothetical infinitesimally thin one-dimensional construct that stretches between two magnetic monopoles of opposite charges or from one magnetic monopole out to infinity.

Direct Methods A group of structure solution reciprocal-space methods that attempts to determine the phase of the structure factor directly from the measured amplitudes by exploiting well-defined relationships between the phases and corresponding amplitudes. The condition that the atoms are peaks in the measured density maps and these peaks are well-separated are usually satisfied for single crystal diffraction, unlike their powder counterparts due to the extensive overlap that results from powder-averaging.

Dispersion Relation The relationship between the frequency ω (Energy) and the wavevector $\mathbf{k}$ ($\mathbf{Q}$ or $\mathbf{q}$). For neutron inelastic scattering, dispersion relations are commonly denoted as $\epsilon(\mathbf{Q})$ or $\epsilon(\mathbf{q})$ and an example of one such relation is given as Eq. 3.13 in Chapter 3.

Double Differential Scattering Neutron Cross Section number of neutrons that are scattered into a particular solid angle element $d\Omega$ with a particular final energy lying in the range dE_f from E_f, whilst being normalised to the incoming flux Φ. This definition is the most generic and is defined more strictly in actual experiments as a function of incoming energy E_i and direction (θ, ϕ) as illustrated in Fig. 1.20.

Dynamic Structure Factor Double inverse Fourier transform of the time-dependent pair-correlation function. As a rule-of-thumb, the dynamic structure factor is the desired quantity in neutron inelastic scattering experiments. It is conventionally denoted by $S(\mathbf{Q}, E)$ and is introduced as Eq. 1.110.

Principle of Detailed Balance The mathematical relationship between the dynamic structure factor for up-scattering and down-scattering processes, corresponding to E $<$ 0 and E $>$ 0 energy transfers, respectively. The mathematical relationship is introduced in Eq. 1.108.

Elastic Scattering The particle's kinetic energy in the centre-of-mass frame is conserved throughout the scattering process.

Emergence A broad and widely applicable concept of the appearance of collective behaviour or properties that are absent in its constituent parts.

Energy-Dispersive X-ray Spectroscopy The use of a focussed beam of high-energy charged particles or X-rays to stimulate the emission of X-ray radiation. Since the wavelength of the emitted X-ray radiation is characteristic of the atomic structure for a particular element being irradiated and its intensity is directly proportional to the amount of the element present, energy-dispersive x-ray spectroscopy is a powerful tool for elemental analysis.

Epithermal Neutrons Neutrons possessing energies between 25 meV and approximately 1 eV. Depending on the classification scheme, some restrict Epithermal neutrons to energies between 25 meV and 400 meV, whilst neutrons between 400-600 meV and 600-1000 meV are classified as Cadmium and EpiCadmium neutrons.

Equations-of-Motion Equations that describe the behaviour of a system in terms of functions of dynamic variables.

Exchange Interaction A quantum mechanical effect between indistinguishable particles with no true classical analogue. Such an effect exists due to wavefunctions of indistinguishable particles being subject to exchange symmetry. The exchange interaction increases (reduces) the expectation value of two or more indistinguisable fermions (bosons) when their wavefunctions overlap. The exchange interaction is the underlying mechanism for a significant portion of conventional collective magnetic behaviour.

Experimental Resolution The minimum difference in energy (or $\mathbf{Q}$) such that two or more signals can be distinguished from one another. It is a parameter, often quoted by the full-width-at-half-maximum (FWHM), that is characteristic of the spectrometer at a particular energy and momentum transfer.

Fermi's Golden Rule An equation for the calculation of the transition rate from an initial state $|i\rangle$ to a final state $|f\rangle$ that is part of continuum, in the presence of a perturbation that may possess time-dependence. A common form of the Golden Rule is that the transition rate is directly proportional to the strength of the coupling between states $|i\rangle$ and $|f\rangle$ and the number of potential paths for the transition to occur, given by $|\langle i|\hat{V}|f\rangle|^2$ and the density of final states ρ_f, respectively. It is also known as the Golden Rule of Time-Dependent Perturbation Theory.

Ferrimagnetic Order Magnetic moments, usually from different types of atoms or ions, are all aligned anti-parallel to one another but do not cancel completely. Such an arrangement results in a net magnetisation below a critical temperature that is also known as the Curie Temperature $\mathrm{T_C}$.

Ferromagnetic Order Magnetic moments are all aligned parallel to one another. Such an arrangement results in a net magnetisation below a critical temperature that is known as the Curie Temperature $\mathrm{T_C}$.

First Brillouin Zone The Wigner-Seitz primitive unit cell about a lattice point in reciprocal space.

First Moment Sum Rule In the case of isotropic exchange, the first moment is periodic in $\mathbf{Q}$. Its periodicity is uniquely defined by the sum of displacement vectors between moments, whilst the intensity is defined by a combination of a sum of the spin-spin correlators and the spin-spin exchange constants. A derivation of the first moment sum rule is presented in Appendix H.2 and is summarised by Eq. H.45.

Fluctuation-Dissipation Theorem The mathematical relationship between the dynamic structure factor and the imaginary component of the susceptibility. The power of the fluctuation-dissipation theorem is that it allows the description of the auto-correlation function (a microscopic quantity) in terms of the dynamic susceptibility (a macroscopic quantity). Following directly from the Langevin equation and is a hallmark of linear

response theory. Its namesake is based on the observation that equilibrium fluctuations and energy dissipations have the same origins and are thus inseparable from one another, whilst their magnitudes must obey certain relationships. The mathematical relationship is introduced in Eq. 1.109.

Flux Method A solution growth method for growing single crystals which involves dissolving reagents in a solvent called the flux. This method was employed extensively in Chapter 3.

Frustration A phenomenon where all pairwise interactions cannot be simultaneously minimised.

Frustration Index A metric for measuring the level of frustration in magnetic systems. The frustration index f is defined as $\left|\frac{\theta_{\mathrm{CW}}}{T_c}\right|$, where θ_{CW} and T_c denote the Curie-Weiss and critical (Curie or Néel) temperatures, respectively. A value of $f > 5$ indicates the presence of significant frustration.

General Wyckoff Position A Wyckoff position that is invariant only with respect to the identity operation (E).

Geometric Frustration Frustration that is a result of the incompatibility of the interaction between magnetic degrees of freedom with the geometric constraints imposed by the underlying symmetry of the crystal structure.

g-factor A dimensionless constant-of-proportionality between the magnetic moment and the angular momentum of a particle, an atom or a nucleus.

Goodenough-Kanamori-Anderson Rules A set of semi-empirical rules for determining the sign and relative strength of the superexchange interactions for a particular set of electronic arrangements on various metal centres placed in a given geometric arrangement.

Green's Function A solution of a linear differential equation with a Dirac delta inhomogeneous source with homogeneous boundary conditions. The importance of the Green's function in this Thesis is that it acts as a propagator.

Hamiltonian The observable operator for the total energy (kinetic and potential) of the system. It is conventionally denoted by $\hat{\mathcal{H}}$.

Heisenberg-Dirac-van Vleck Hamiltonian The Hamiltonian of the Heisenberg model. Often referred to simply as the Heisenberg Hamiltonian, $\hat{\mathcal{H}} = \sum_{i,j} J_{ij}\hat{\mathbf{S}}_i \cdot \hat{\mathbf{S}}_j$ describes the total energy of the system with pairwise interactions *via* isotropic exchange with an exchange constant J_{ij} between spins $\mathbf{S}_i$ and $\mathbf{S}_j$ at sites i and j of an infinite lattice, respectively, where it is understood that $i \neq j$.

Hilbert Space A real or complex inner product space that is also a complete metric space with respect to the distance function inherent to the inner product. In this Thesis, the Hilbert space is denoted by H.

Holstein-Primakoff Transformation A transformation of the spin operators for a system of S-moments on a lattice onto bosonic creation and annihilation operators. The transformed operators satisfy the commutation relations exactly and this transformation plays a central role in conventional (linear) spin wave theory.

Hund's Rules A set of three semi-empirical rules used to determine the term symbol ${}^{2S+1}L_J$ corresponding to the ground state electron configuration of a multi-electron atom.

Inelastic Scattering The particle's kinetic energy in the centre-of-mass frame is not conserved throughout the scattering process.

in vacuo Performed in a vacuum.

Jahn-Teller Theorem Any non-linear coordination complex with a spatially degenerate electronic ground state will undergo a geometric distortion to remove the degeneracy. This particular type of geometric distortion is called a Jahn-Teller distortion and occurs for coordination complexes with certain electronic configurations.

Kagomé Lattice A lattice structure that consists of the vertices and edges of the trihexagonal tiling pattern. The use of the name Kagomé stems from the presence of the trihexagonal tiling pattern in the traditional Japanese woven bamboo basket.

Kitaev Model Spin-$\frac{1}{2}$ degrees of freedom placed on the vertices of a tri-coordinated lattice, where nearest neighbours interact *via* a highly anisotropic Ising exchange, whose easy-axis is dependent on the bonding direction. The Kitaev Hamiltonian is $\hat{\mathcal{H}} = \sum \langle i,j \rangle J^\gamma K^\gamma_{j,k}$, where $K^\gamma_{j,k} = \sigma^\gamma_j \sigma^\gamma_k$ is the

bond operator for $\langle j,k\rangle$ bond of γ-type. The Kitaev model is a quantum mechanical model which is exactly solvable, possesses topological order and is a model that hosts a variety of gapped and non-gapped quantum spin liquids.

Kramers Theorem For any half-integer spin system possessing time-reversal symmetry, every energy eigenstate is degenerate.

Lattice Fourier Transform of the Exchange Interactions Sometimes referred to as the Fourier transformed exchange function, $J(\mathbf{Q}) = \sum_{i\neq j} J_{ij} e^{\mathbf{Q}\cdot\mathbf{d}_{ij}}$, specifies both the strength and $\mathbf{Q}$-dependence of the coupling of the single-site susceptibilities that is described by the equation-of-motion for the Green's functions in the random phase approximation (Eq. 5.1).

Lie Algebra A vector space $\mathfrak{g}$ over some field $\mathbb{F}$ equipped with a bilinear map called a Lie bracket. The Lie bracket is a non-associative, alternating bilinear map $[\cdot,\cdot] : \mathfrak{g}\times\mathfrak{g}\to\mathfrak{g}$ that satisfies the Jacobi identity.

Ligand An ion or molecule that binds to the central metal atom in a coordination complex.

Lineshape A description of the form of an excitation in spectroscopy. Rarely, if ever, are excitations perfect delta functions, instead they are broadened and possess characteristic shapes. Physical origins of broadening are numerous are include: proximity broadening and lifetime broadening. The final subsection in Chapter 1 introduces various possible analytic approximations to describe observed lineshapes.

Magnetic Anisotropy The directional (spatial orientation) dependence of a system's magnetic properties.

Mean Field Theory The study of the behaviour of large and complex stochastic systems in terms of much simpler models. Mean field theory reduces models that involve large numbers of particles interacting with one another to a model consisting of individual particles that are each influenced by the same single averaged effect from all its neighbours, *i.e.* the so-called *mean field*. The power of mean field theory is its attempt to reduce a complex many-body problem to a much simpler one-body problem. Mean field theory is introduced as the physical motivation for the Weiss field that led to the Curie-Weiss equation (Eq. 1.66) in Chapter 1. Its highly

related counterpart in **Q**-space is the Random Phase Approximation that is employed in Chapter 5.

Metal Oxides Chemical compounds formed from metal(s) and oxygen.

Magnetic Monopole A hypothetical elementary particle that is a magnet consisting of one magnetic pole and would correspond to the magnetic analogue of electrical charges. Interest in monopoles stems from a combination of symmetrisation of Maxwell's equations of electromagnetism and the Dirac quantisation condition.

Master Equation The mathematical relationship between the scattering cross section and the perturbative potential from which the neutrons are scattering from. The equation is given by Eq. 1.93.

Monoclinic Crystal System A crystal system where the unit cell has $a \neq b \neq c$ and $\alpha = \beta = 90^\circ \neq \gamma$.

Mott Insulator A class of insulating materials that are predicted to be conductors using conventional band theory. Deviations from conventional band theory stem from electron-electron interactions.

Neutron Flux The number of neutrons incident on a unit area per unit time.

Neutron Inelastic Scattering A special type of spectroscopy that utilises how the neutron is scattered from a sample, consisting of changes in energy and direction, to infer information about the sample's atomic and/or magnetic dynamics.

Neutron Moderator A medium at which neutrons are brought to thermal equilibrium at a particular temperature. Conventionally, moderators denote media located adjacent to the reactor that reduces the energy of fast neutrons. The reduction in energy optimises the nuclear chain reaction, whilst achieving neutron energies that are optimal for studying matter. Moderators located much further away from the fission (or spallation process) are called sources. Sources that are held at cryogenic temperatures are called cold sources and provide neutrons that are optimised to study magnetism, whilst sources that are heated such as hot graphite, provide neutrons that are optimised to study electronic transitions. Moderators are typically composed of light nuclei with low neutron absorption cross sections with modest stopping power.

Neutron Spectrometer A tool used to perform neutron inelastic scattering experiments.

Normalisation The conversion of vanadium-corrected neutron scattering intensities into the absolute units, *i.e.* the double differential scattering neutron cross section in units of barns $\cdot$ sr^{-1} $\cdot$ meV^{-1}. The normalisation procedure utilising internal incoherent standards is summarised in Appendix I.

Nuclear Fission A nuclear reaction or a nuclear decay process that results in the splitting of a nucleus into smaller pieces.

Observable Operator A Hermitian operator $\hat{\mathcal{O}}$ that is associated with a measurement of a particular observable, *i.e.* a physical quantity that can be measured. Such an association is a fundamental posulate of quantum mechanics.

Octahedral Distortion Parameter A parameter used to quantify the degree of distortion of a coordination complex with six ligands away from ideal octahedral coordination. Conventionally denoted by δ, the parameter is introduced as Eq. 1.75.

Optical Floating Zone Method A crucible-free melt growth method for single crystal growth. The method consists of melting a translatable section, termed the molten zone, of a precursor, usually the desired crystal in polycrystalline form, in the form of compressed cylindrical rods. Zone melting is achieved by a focussed beam of light from optically-based heating sources, most commonly halogen lamps. The counter-rotating feed and seed rods are held together by surface tension and are both vertically translated in a controlled atmosphere throughout the growth process. As the feed and seed rods are vertically translated, more precursor material is melting at the melt edge, whilst the molten mixture crystallises at the newly cooled end, known as the growth edge. This method was employed extensively in Chapter 5.

Orthorhombic Crystal System A crystal system where the unit cell has $a \neq b \neq c$ and $\alpha = \beta = \gamma = 90°$.

Paramagnetic Approximation An approximation where it is assumed that only isotropic spin excitations are being measured. With the assumption that all magnetic anisotropy is absent, as is the case in the paramagnetic

regime, and thus its namesake, the system must be rotationally invariant and thus $S^{zz}_{\text{mag}}(\mathbf{Q}, E) = S^{yy}_{\text{mag}}(\mathbf{Q}, E) = S^{xx}_{\text{mag}}(\mathbf{Q}, E)$.

Parasitic Scattering Scattering that occurs whilst the sample is absent. This type of scattering is often caused, but not limited to, scattering off the edges of the beam collimators.

Partial Differential Equation An equation summarising the mathematical relationship between two (or more) independent variables, a previously undetermined multivariable function of the variables, and the partial derivatives of the multivariable function with respect to the variables.

Pauli Exclusion Principle No two or more identical fermions can occupy the same quantum mechanical state in a quantum mechanical system simultaneously.

Penetration Depth The depth inside the material at which the intensity of radiation is $\frac{1}{e}$ of its incident intensity.

Perturbation Theory A set of approximation schemes used to describe a complicated (non-ideal) quantum system in terms of much a simpler (ideal) quantum system, where a solution is already known. The approach is to re-frame the complicated Hamiltonian $\hat{\mathcal{H}}$ as the simpler Hamiltonian $\hat{\mathcal{H}}_o$, whose solutions are known, that is being perturbed by a potential $\epsilon\hat{V}$, where ϵ is a small parameter and $\hat{V}$ is the potential describing the perturbation. If the perturbation is small, then the solution of $\hat{\mathcal{H}}$ is simply the known solutions of $\hat{\mathcal{H}}_o$ subject to corrections. If the perturbing potential has explicit time-dependence, one will utilise time-dependent perturbation theory, otherwise, time-independent perturbation is employed.

Point Group A group of isometries that keep at least one point fixed in space.

Power Density The amount of power per unit volume.

Projection The mapping of a mathematical structure onto an idempotent sub-structure.

Projection Factor In this Thesis, it is a multiplicative factor that accompanies the projection of angular momentum operators. The determination of the projection factor is the central theme for both Appendices E and G.

Projection Theorem The matrix elements of a vector operator $\hat{\mathbf{V}}$ are directly proportional to those of angular momentum operator $\hat{\mathbf{J}}$ with a proportionality constant $\mathcal{C} = \frac{\langle \hat{\mathbf{V}} \cdot \hat{\mathbf{J}} \rangle}{j(j+1)}$. The projection theorem is the Wigner-Eckart theorem for the case of vector operators $\hat{\mathbf{V}}$, *i.e.* tensor operators of rank $k = 1$. A derivation of the projection theorem is presented in Appendix G.2 and is summarised by Eq. G.38.

Propogation Vector The relation between the spatial orientation of magnetic moments of equivalent magnetic atoms in different nuclear unit cells. By convention, the propagation vector is denoted by $\mathbf{k}$.

Pyrochlore Structure Denoted by $Fd\bar{3}m$, the structure consists of an interpenetrating network of corner-sharing tetrahedra, with each network consisting of cations occupying the two respective special crystallographic positions 16*d* and 16*c*. Alternative views of the structure include alternating Kagomé and triangular layers along the [111] crystallographic direction for both the 16*d* and 16*c* sites.

Quantum Numbers Numbers that parametrise conserved quantities in the dynamics of a quantum system. These numbers specify the particular quantum state that the quantum system occupies.

Quantum Spin Liquid A novel state of matter that is composed of highly correlated spins that do not achieve long range magnetic order down to absolute zero due to quantum effects/fluctuations. This state of matter is characterised by their strong long-range quantum entanglement that preserves symmetries and possesses many exotic and often novel properties including topological ground state degeneracy and fractionalised spin excitations.

Quenching of Orbital Angular Momentum The reduction of the effective orbital angular momentum L to values near (partial) or equal (complete) to zero.

Random Phase Approximation The replacement of products of operators by averages, as is performed in mean field theory, where the fluctuation of averages is neglected. This approximation plays a crucial role in the simplification of the equation-of-motion (Eq. 5.1) in Chapter 5, as shown in its derivation in Appendix J.

Rietveld Refinement A multi-parameter curve fitting procedure. The procedure consists of performing a least-squares optimisation of a model function to the entire data set comprising the diffraction scan. The parameters of the model function used to match the data's peaks' positions, heights and widths contain pieces of information regarding the unit cell's parameters, details of the crystal's unit cell (*e.g.* thermal factors, atomic coordinates, *etc.*), whilst incorporating other effects such as instrumental background, resolution convolution and sample absorption.

Rock Salt Structure Denoted by $Fm\bar{3}m$, the structure is composed of two inter-penetrating face-centred cubic lattices with each lattice composed of atoms A and B occupying the two respective special crystallographic positions $4a$ and $4b$.

Scanning Electron Microscopy The use of a focussed beam of high-energy electrons to deduce a variety of information concerning the surface of a sample. Such information is deduced from electron-sample interactions and include texture, structure, and chemical composition.

Scattering Physical process by which radiation or particles deviate from a straight trajectory due to some form of interaction with a particular system.

Scattering Triangle A pictorial representation of the scattering geometry for an neutron inelastic process. The triangle consists of the geometric interpretation of $\mathbf{Q} = \mathbf{k}_i - \mathbf{k}_f$, with an angle of 2θ between vectors $\mathbf{k}_i$ and $\mathbf{k}_f$. Two examples of scattering triangles are given in Fig. 1.17.

Schrödinger Equation A partial differential equation that describes how a quantum system changes over time. The equation can be considered the quantum analogue of the conservation of energy. In the case that the potential does not have explicit time dependence, the equation is reduced to a much simpler eigenvalue equation, known as the time-independent Schrödinger Equation.

Single Mode Approximation The approximation of $S(\mathbf{Q}, E)$ as $S(\mathbf{Q})\delta(E - \epsilon(\mathbf{Q}))$, where $\epsilon(\mathbf{Q})$ is the dispersion relation of interest. Such an approximation is employed when $S(\mathbf{Q}, E)$ is dominated by a single well-defined excitation.

Single-Site Susceptibility The dynamic susceptibility at the level of the single-site, denoted by $g^{\alpha\beta}$. Such an interpretation, and hence its name,

stems from the observation that $g^{\alpha\beta}$ appears in Appendix J as the solution to the equation-of-motion given by Eq. J.83 when $J(il)$ is set to zero. $g^{\alpha\beta}$ is the quantity that is coupled by $J(\mathbf{Q})$ *via* the equations-of-motion of the Green's functions in the random phase approximation. The analysis that forms the basis of Chapter 5 employs the form of the single-site susceptibility in the limit of $T \to 0$ K and is summarised by Eq. 5.10.

Sol-Gel Method Solution-based alternative to the ceramic method, requiring much lower synthesis temperatures. The method first involves the creation of the *sol*, a colloidal solution of monomer precursors. The *sol* is aged or heated under moderate temperatures, thus creating a continuous and porous network of the desired product, called the *gel*. Sintering the *gel* results in its decomposition and densification into a ceramic (or glass). This method was employed extensively in Chapter 4.

Space Group A group of symmetry elements on the points of a space lattice. In other words, a space group is a group of symmetry elements that keeps the periodicity of the Bravais lattice of interest invariant.

Spallation The emission of nucleons from a nucleus as a result of the collision of a high energy with said nucleus.

Special Wyckoff Position A Wyckoff position that is invariant with respect to both the identity operation (E) and at least one other operation of the space group.

Spin Glass Commonly referred to as the magnetic analogue of glass. An intuitive definition treats spin glasses as disordered magnets whose spins' spatial orientation are arranged in an non-periodic, amorphous manner. Rigorous mathematical definitions vary from source to source but the common theme is that spin glasses possess an exponential number of locally stable minima, resulting in such systems exhibiting dynamics on all time scales.

Spin Ice A crystalline material whose local moment arrangement maps directly onto the statistical mechanical problem of local proton coordination in water ice investigated by Linus Pauling in the early 20^{th} Century.

Spin-Orbit Coupling A relativistic interaction between a particle's intrinsic spin angular momentum and its motion inside a potential.

Spurious Scattering A broad term referring to any scattering that is not due the intrinsic features of the sample's scattering function. The physical origins of such scattering are various and include: resolution function artefacts, scattering from materials (other than the sample) present in the beam such as the sample environment, accidental Bragg scattering, and higher order harmonics.

SQUID An extremely sensitive magnetometer used to measure magnetic fields with both great accuracy and precision. Corresponding to the acronym **S**uperconducting **Qu**antum **I**nterference **D**evice, these magnetometers consist of loops of superconducting materials containing Josephson junctions, thus allowing SQUIDs to utilise the Josephson effect, resulting in extreme sensitivity for detecting weak magnetic fields.

Stevens Operators In the Stevens approach (Stevens formalism), the crystal field Hamiltonian $\hat{\mathcal{H}}_{CEF}$ is written as a linear combination of the product of Stevens operators $\hat{O}_l^m$ and their corresponding Stevens parameters B_l^m. Stevens operators are a function of angular momentum operators and transform like the real tesseral harmonics $Z(\theta, \phi)$ under rotations. The mathematical motivation of Stevens formalism is the projection theorem (the Wigner-Eckart theorem for vector operators). The Stevens operators that are employed in this Thesis are summarised in Appendix D.

Stone's Theorem $(\hat{U}_t)_{t\in\Re}$ is a strongly continuous one-parameter unitary group, if and only if there exists an exponential map $\hat{U}_t = e^{it\hat{A}}$, where $\hat{A}$: $\mathcal{D}_{\hat{A}} \rightarrow H$ is an infinitesimal group generator with domain $\mathcal{D}_{\hat{A}} = \{\psi \in H | \lim_{\epsilon\rightarrow 0} \frac{-i}{\epsilon}(\hat{U}_\epsilon(\psi) - \psi)\}$. The theorem is also known as Stone's Theorem on One-Parameter Unitary Groups.

Sum Rules of Neutron Scattering Mathematical relationships that allow for the extraction of system-specific parameters from the n^{th}-moments of the dynamic structure factor.

Systematic Errors Non-random, predictable, and repeatable errors with a non-zero mean and whose influence will not be reduced by repeating measurements.

Taylor's Theorem Suppose that a function f is defined on an interval I containing a point a and suppose that the function is $N + 1$ times differentiable on this interval. Then for each $x \neq a$ in I, there exists a value

c between x and a so that $f(x) = \sum_{n=0}^{N} \frac{f^{(n)}(a)}{n!}(x-a)^n + \frac{f^{(N+1)}(c)}{(N+1)!}(x-a)^{N+1}$. The power series $\sum_{n=0}^{N} \frac{f^{(n)}(a)}{n!}(x-a)^n$ is known as the Taylor series of $f(x)$ about a point $x = a$ and can be thought of a polynomial that approximates $f(x)$ in an interval containing a. When $a = 0$, the Taylor series is called the Maclaurin series. The Taylor (or Maclaurin) series will converge only for specific values of x as determined by the series' radius of convergence.

Thermal Neutrons Neutrons possessing an energy of approximately 25 meV. The name *thermal* is derived from the observation that the energy of 25 meV corresponds to the maximum of the Maxwell-Boltzmann distribution of neutron energy (speeds) for room temperature.

Time-of-Flight Neutron Spectrometer A neutron spectrometer that utilises neutron velocities in either monochromatisation or energy discrimination or both. All key elements of a time-of-flight spectrometer are presented in Figs. 1.18 and 1.19.

Triple Axis Neutron Spectrometer A neutron spectrometer where monochromatisation and energy discrimination are accomplished *via* Bragg optics with a crystal monochromator and analyser, respectively. All key elements of a triple axis spectrometer are presented in Fig. 1.16.

Type-II Antiferromagnet An antiferromagnet where magnetic moments within a (111) plane are aligned parallel, whilst moments between adjacent (111) planes are aligned antiparallel to one another. In other words, an antiferromagnet constructed from the antiferromagnetic stacking of ferromagnetic (111) sheets.

Universality A hypothesis which states for a continuous phase transition, the static critical exponents depend on: (i) the dimensionality of the system d, (ii) the dimensionality of the order parameter D, and (iii) whether the forces are of short- or long-range.

Vegard's Law A heuristic empirical rule that states the lattice parameter of a solid solution of two constituents at a temperature T is equal to a rule of mixtures of the constituents' individual lattice parameters at the same temperature T.

Wigner-Eckart Theorem In the angular momentum basis states, the matrix elements of the spherical tensor operators $T_q^{(k)}$ can be expressed as a product

of the Clebsch-Gordan coefficient and the reduced matrix element, where the latter's value is independent of angular momentum orientation. A derivation of the theorem is presented in Appendix G.1 and is summarised by Eq. G.22.

Wigner's Theorem of Symmetry Representation Any symmetry transformation can be represented on a Hilbert space H of physical states by an operator $\hat{\mathcal{O}}$ that is either linear and unitary or anti-linear and anti-unitary. A corollary of Wigner's Theorem is that continuous symmetries have unitary representations.

Zeeman Effect The splitting of a spectral line into individual components in the presence of a magnetic field. The magnetic field analogue of the Stark Effect.

Zeroth Moment Sum Rule The integral of $S(\mathbf{Q}, E)$ over all $(\mathbf{Q}, E)$ is sensitive to the effective total(spin) angular momentum of the manifolds being integrated over. A derivation of the zeroth moment sum rule is presented in Appendix H.1 and is summarised by Eq. H.11.